Ing. Dipl.-Ing. Martin Nuss, BSc

Low-dimensional correlated fermions out-of-equilibrium: steady-state Green's function cluster methods and space-time evolution

DOCTORAL THESIS

For obtaining the academic degree of

Doktor der technischen Wissenschaften

Doctoral Programme of Technical Sciences
Technical Physics

Graz University of Technology

Supervisor:

Univ.-Prof. Dipl.-Phys. Dr.rer.nat. Wolfgang von der Linden

Institute of Theoretical and Computational Physics

Graz, June 25, 2015

Contents

Abstract

This thesis is about the theoretical description of strongly correlated fermions out-of-equilibrium in a condensed matter context. In particular, we explore the impact of electronic correlations on charge transport in low-dimensional or geometrically confined electronic systems. The out-of-equilibrium aspects of strong electronic correlations are discussed under three major viewpoints i) linear-response transport characteristics, ii) transient real-time dynamics and iii) the steady-state, where each one of these sheds light on a different aspect of recent experimental developments.

The *transport characteristics of effectively low-dimensional materials* are obtained using the well established linear-response formalism in a combined *ab initio* plus correlation methods approach. We build an effective model for the material $Li_{0.9}Mo_6O_{17}$ which exhibits an effectively one-dimensional electronic structure. This electronic structure is explained in terms of maximally-localized orbitals and the dominant processes for charge transport are characterized. A good agreement of experimentally measured angle resolved photo emission data with calculated spectral functions in dynamical mean field theory as well as the extended variational cluster approach is attained. The linear-response conductivity is found to be highly anisotropic along linear chains of molecular-like orbitals and compares well to recent experimental data.

The *transient dynamics of quantum impurities* is obtained using a matrix product state based real time evolution in a density matrix renormalization group and time evolving block decimation framework. This method is especially suited to study the time evolution of one-dimensional quantum systems, for which it is the highly accurate method of choice. We apply this scheme to study transport across a quantum dot tunnel coupled to source and drain leads under bias voltage at zero temperature, where electronic correlations are most pronounced. The transient dynamics after a quantum quench as well as a quasi-exact time evolution into the steady-state current-voltage characteristics is studied. The steady-state characteristics will serve as a benchmark for further investigation of the steady-state using perturbative approaches. We investigate the physics inside and outside the light cone of causal information spreading following the quench and characterize the emergent Kondo spin-screening cloud by means of time and space dependent spin-spin and charge-charge correlation functions. An emergent dynamic scale proportional to the Kondo temperature is found in these correlations.

The *steady-state of nano-devices and molecular junctions* is obtained using a combined quantum master equation and nonequilibrium Green's function based many-body quantum cluster methods approach. A large part of this thesis is devoted to the development and improvement of numeric nonequilibrium Green's function based quantum many-body cluster methods to study the steady-state of correlated systems out-of-equilibrium. We focus on the development of i) the steady-state cluster perturbation theory, ii) its variational improvement, the steady-state variational cluster approach which includes a self-consistent feedback and iii) a consistent unperturbed state representation in the master equation based steady-state cluster perturbation theory. Besides these perturbative approaches we also make use of the auxiliary master equation approach which maps the original system to an exactly solvable auxiliary Lindblad equation. We apply these approximation schemes to study charge transport in the Kondo regime in single quantum dots under bias voltage and find a remarkable success of the self-consistent feedback implemented in the steady-state variational cluster approach which allows for an accurate description of the

steady-state current-voltage characteristics at low to medium bias voltages including the correct linear-response conductivity. Calculated stability diagrams compare well to experimental data. The splitting of the Kondo resonance under bias voltage is analyzed in detail and results of the auxiliary master equation approach are compared to data from the steady-state variational cluster approach. Following the success of the newly developed methods for a single correlated orbital, we extend the calculations to multi-orbital molecular junctions. The Aharonov-Bohm effect and the role of electronic correlations on charge transport are studied in a Benzene molecular junction in a magnetic field using steady-state cluster perturbation theory, which is able to describe the system well up to interference mediated current blocking effects. Further, we study such interaction induced, magnetism mediated current blocking effects in a quantum dot diode with polarized leads in master equation based steady-state cluster perturbation theory and interaction induced, quantum interference mediated current blocking in a ring triple quantum dot junction. This new approach is capable of reproducing the current blocking as predicted by the plain quantum master equation solution. In using the master equation based steady-state cluster perturbation theory we however go beyond the approximate quantum master equation solutions and are able to include lead induced broadening effects. Finally, a combined insight of quasi-exact real-time evolution, perturbative steady-state calculations and the auxiliary master equation approach provides evidence for a strong impact of electronic correlations on the charge transport even at high bias voltages if the electronic density of states of the leads is finite.

Kurzfassung

Diese Arbeit behandelt die theoretische Beschreibung von Systemen stark korrelierter Fermionen außerhalb des Gleichgewichts, wie sie im Rahmen von aktuellen Problemstellungen im Bereich der kondensierten Materie auftreten. Insbesondere behandeln wir die Fragestellung wie elektronische Korrelationen den Ladungstransport in niedrigdimensionalen oder geometrisch eingeschlossenen elektronischen Systemen beeinflussen. Dabei werden die besonderen Aspekte starker elektronischer Korrelationen unter drei Hauptgesichtspunkten beleuchtet: i) durch Transporteigenschaften in der Theorie der linearen Antwort ii) durch Einschaltvorgänge in Echtzeitdynamik und iii) durch den stationären Zustand.

Die *Transporteigenschaften von Materialien mit einer effektiv niedrigdimensionalen elektronischen Struktur* werden im etablierten Formalismus der Theorie der linearen Antwort basierend auf der elektronischen Struktur von *ab initio* plus Korrelationsmethoden berechnet. Insbesondere wird ein effektives Modell für das Material $Li_{0.9}Mo_6O_{17}$ hergeleitet, welches eine effektiv eindimensionale elektronische Struktur aufweist. Diese wird im Rahmen von lokalen Orbitalen charakterisiert und die dominanten Transportprozesse werden identifiziert. Eine gute Übereinstimmung ergibt sich zwischen winkelaufgelösten Photoemissionsspektren aus dem Experiment und den mittels Dynamischer Molekularfeld Theorie und dem erweiterten Variationellen Cluster Zugang berechneten Spektralfunktionen. Die lineare Leitfähigkeit ist stark anisotrop entlang von Ketten molekularer Orbitale und passt gut zu den Ergebnissen zahlreicher aktueller Experimente.

Die *zeitliche Dynamik von Quanten-Störstellenproblemen* wird mittels einer auf Matrixproduktzuständen basierenden Echtzeitentwicklung in einem kombinierten Verfahren, bestehend aus Dichtematrix Renormierungsgruppe und Time Evolving Block Decimation ermittelt. Diese Methode eignet sich besonders um die Zeitentwicklung von eindimensionalen Quantensystemen zu bestimmen. In diesem Kontext kann sie oftmals sogar quasi-exakte Ergebnisse liefern. In dieser Arbeit wird dieses Verfahren angewendet um den Ladungstransport über einen Quantenpunkt, welcher über Tunnelamplituden an einen Quell- und einen Senk- Kontakt gekoppelt ist, am absoluten Temperaturnullpunkt, wo elektronische Korrelationen am stärksten ausgeprägt sind, zu ermitteln. Hierbei charakterisieren wir sowohl die Einschaltdynamik nach einem Quanten-Quench als auch die Langzeitentwicklung in einen stationären Zustand. Die dabei ermittelte, quasi-exakte, Strom-Spannungs-Kennlinie nutzen wir später als Vergleichsbasis um die Zuverlässigkeit approximativer Verfahren beurteilen zu können. Getrennt, untersuchen wir die physikalischen Eigenschaften innerhalb, und außerhalb des Lichtkegels kausaler Informationsausbreitung, welcher sich nach dem Quanten-Quench bildet. Insbesondere charakterisieren wir die sich bildende Kondo-Spin-Abschirmungswolke durch zeit- und ortsabhängige Spin-Spin- und Ladungs-Ladungs- Korrelationsfunktionen. Hierbei finden wir eine dynamische Skala in den Korrelationen welche proportional zur Kondotemperatur ist.

Im größten Bereich dieser Arbeit untersuchen wir den *stationären Zustand von Nanostrukturen und molekularen Bauteilen* mittels einem kombinierten Zugang aus einer Quanten-Mastergleichung und den auf Nichtgleichgewichts-Greensfunktionen basierenden Vielteilchen-Quanten-Clustermethoden. Dabei liegt ein großes Augenmerk auf der Entwicklung und Verbesserung dieser numerischen Verfahren um zuverlässige Näherungsverfahren für den stationären Zustand korrelierter Schaltungen zur Verfügung zu stellen. Insbesondere entwickeln wir i) die Stationäre-Zustands Cluster Störungsrechnung, ii) deren variationelle Verbesserung, den Stationären-Zustands Variationellen

Clusterzugang, welcher eine selbstkonsistente Rückkopplung beinhaltet und iii) einen konsistenten ungestörten Zustand für die mastergleichungsbasierte Cluster Störungsrechnung. Neben diesen störungstheoretischen Verfahren wird auch der Hilfssystem-Mastergleichungszugang benutzt, welcher das ursprüngliche System auf ein exakt lösbares offenes Quanten-Hilfssystem abbildet. Mit Hilfe dieser Methoden untersuchen wir den Ladungstransport im Kondoregime eines Quantenpunktes unter Spannung und finden einen beachtlichen Erfolg der selbstkonsistenten Rückkopplung im Stationären-Zustands Variationellen Clusterzugang, welche eine genaue Beschreibung der Strom-Spannungs-Kennlinie bei niedrigen und mittleren Spannungen erlaubt und auch die lineare Leitfähigkeit genau wiedergeben kann. Die berechneten Stabilitätsdiagramme zeigen gute Übereinstimmung mit aktuellen experimentellen Messungen. Die Aufspaltung der Gleichgewichts-Kondoresonanz mit der angelegten Spannung wird im Detail diskutiert und die Ergebnisse des Hilfssystems-Mastergleichungszugang und des Stationären-Zustands Variationellen Clusterzugang verglichen. Motiviert durch den großen Erfolg der entwickelten Methoden bei der Beschreibung eines korrelierten Orbitals, verallgemeinern wir die Rechnungen auf molekulare Bauteile mit mehreren korrelierten Orbitalen. Wir untersuchen den Einfluss elektronischer Korrelationen auf den Ladungstransport und den Aharonov-Bohm Effekt in einem kontaktierten Benzol Molekül in einem magnetischen Feld. Hierbei liefert bereits die Stationäre-Zustands Cluster Störungsrechnung gute Ergebnisse, nur kann das Interferenz-induzierte Strom-Blocking nicht abgebildet werden. Die mastergleichungsbasierte Cluster Störungsrechnung kann auch diese Effekte behandeln und wird benutzt um wechselwirkungsinduzierte und durch den Magnetismus vermittelte Strom-Blocking Effekte in einer Quantenpunkt-Diode mit polarisierten Kontakten zu erforschen. Ebenso studieren wir wechselwirkungsinduzierte und durch den Quanteninterferenz vermittelte Strom-Blocking Effekte in einem Ringmolekül mit drei Orbitalen. Die mastergleichungsbasierte Cluster Störungsrechnung schafft es hierbei, die reinen Mastergleichungsergebnisse zu verbessern indem kontaktinduzierte Linienverbreiterungseffekte besser beschrieben werden können. Abschließend finden wir durch kombinierte Ergebnisse aus der Zeitentwicklung und den störungstheoretischen Methoden im stationären Zustand, dass elektronische Korrelationen selbst bei sehr großen Spannungen einen starken Einfluss auf den Ladungstransport haben können, vorausgesetzt die elektronische Zustandsdichte der Kontakte ist endlich.

Acknowledgements

Three years have passed since Univ.-Prof. Dipl.-Phys. Dr.rer.nat. Wolfgang von der Linden and Univ.-Prof. Dr.rer.nat. Enrico Arrigoni appointed me to work on the highly interesting topic of strongly correlated systems out-of-equilibrium. Since then, our shared enthusiasm and curiosity for this topic has always been a common denominator in this work. I remember the great joy and pleasure of working on this assignment although and because our research provided a constant challenge.

Sustaining my studies and keeping motivated all the time was only possible due to my parents Maria and Albert Nuss whom I would like to express my thanks for their unending love, encouragement and support. For her support and comradeship, especially in our common time in the students dorm I would like to express my gratitude to my sister Mag. Franziska Nuss who concluded her studies two years ago. After all this thesis provided the basis for meeting my girlfriend Dipl.-Ing. Dr.tech. Kerstin Traudel Oppelt who I would like to thank for her affection and support which provides me with energy and reason.

Especially I want to thank my supervisors Univ.-Prof. Dipl.-Phys. Dr.rer.nat. Wolfgang von der Linden and Univ.-Prof. Dr.rer.nat. Enrico Arrigoni who guided me through this work with great intuition, valuable suggestions and brilliant ideas. I thank both of them for spending a lot of time on our discussions and being always available for questions.

I would like to thank my co-supervisors and scientific collaborators Ao.Univ.-Prof. Dipl.-Phys. Dr.rer.nat. Hans Gerd Evertz, Dipl.-Ing. Dr.techn. Markus Aichhorn, Dipl.-Ing. Antonius Dorda, Dipl.-Ing. Dr.techn. Christoph Heil, Dipl.-Ing. Dr. Michael Knap, Gerhard Dorn, Dipl.-Ing. Dr.techn. Martin Ganahl, Dipl.-Ing. Maximilian Sorantin and Dipl.-Ing. Jakob Neumayr for the pleasant cooperations and for making all our scientific output possible. Further, I would like to thank everybody who supported me during my studies, especially Ass.Prof. Dipl.-Ing. Dr.techn. Winfried Kernbichler who gave me the opportunity to work at the institute very early, and encouraged me all the time. I enjoyed working in the quantum many-body theory group at the Institute of Theoretical and Computational Physics with Dipl-Ing. Dr. Peter Pippan, Dipl.-Ing. Dr. Ralf Gamilscheg, Mag. Faruk Geles, Dipl.-Ing. Klaus Lang, Dipl.-Ing. Benjamin Kollmitzer, Dipl.-Ing. Dr.-techn. Anna Fulterer, Dipl.-Ing. Hubert Antlinger, Delia Fugger and Dipl.-Ing. Dr.-techn. Valentin Zauner, Dipl.-Ing. Dr. Elias Assmann, Dr. Irakli Tidvinidze, Dr. Balazs Hetenyi, Dr. Mohammad Zhian Asadzadeh, Dr. Liviu Chioncel, Dipl.-Ing. Christopher Albert, Mag. Peter Leitner, Dr. Lilia Boeri, Dipl.-Ing Manuel Zingl, Dipl,-Ing. Robert Triebl, Dipl.-Ing Gernot Kapper and Dipl.-Ing. Andreas Martitsch. For helping me with lots of bureaucratic work I thank Brigitte Schwarz and for keeping our computers up and running, Andreas Hirczy.

This work was supported by the Austrian Science Fund (FWF) Grants No. P18551, P24081, P26508 and the START Project Grant No. Y746 as well as SFB-ViCoM projects F04103 and F04104. The author acknowledges further support by NaWi Graz and the Leistungsstipendium and Förderungsstipendium of Graz University of Technology as well as NSF under Grant No. NSF PHY05-51164. The author thanks the Forschungszentrum Jülich, in particular the autumn school on correlated electrons and the MPI-PKS Dresden, in particular Masud Haque and the QSOE13, for hospitality and support.

Numerical calculations have been conducted at the cluster infrastructure of the Institute of

Theoretical and Computational Physics of Graz University of Technology, the Vienna Scientific Cluster VSC-I and VSC-II, as well as the d-cluster of Graz University of Technology. We made use of the CT-QMC code of the TRIQS toolkit [1], the *NRG LJUBLJANA* code of Rok Zitko [2] as well as the MPS core library of Martin Ganahl. The computer codes for the nonequilibrium Green's functions and quantum master equation methods have been developed by Martin Nuss in C/C++ and Matlab. We made use of the standard software Gaussian09 [3], Wien2k [4], Wannier90 [5] and XCrysden [6].

We are grateful to Robert Peters for providing his DMRG and NRG data, Christoph Karrasch for providing his FRG and NRG data, Philipp Werner for providing his continuous time QMC data as well as Andreas Dirks for providing his QMC data. The author thanks Kurt Schönhammer, Thomas Pruschke, Piet Dargel, Olivier Parcollet, Michel Ferrero, Sabine Andergassen, Steve R. White, Fabian Heidrich-Meisner, Philipp Werner, Andreas Dirks, Jim W. Allen, Peter Prelovsek, Janez Bonca, Lev Vidmar, Jerne Mravlje, Karsten Held, Angelo Valli, Fakher Assaad, Piotr Chudzinski, Karin Zojer, Dmitry A. Ryndyk, Ferdinand Schürrer, Heinrich Sormann, Achim Rosch, Walter Hofstetter, Sebastian Diehl, Andreas Honecker, Daniel Rost, Frauke Schwarz, Masud Haque and Shreyoshi Ghosh for fruitful and valuable discussions as well as feedback on our work.

Affidavit

EIDESSTATTLICHE ERKLÄRUNG

AFFIDAVIT

Ich erkläre an Eides statt, dass ich die vorliegende Arbeit selbstständig verfasst, andere als die angegebenen Quellen/Hilfsmittel nicht benutzt, und die den benutzten Quellen wörtlich und inhaltlich entnommenen Stellen als solche kenntlich gemacht habe. Das in TUGRAZonline hochgeladene Textdokument ist mit der vorliegenden Masterarbeit/Diplomarbeit/Dissertation identisch.

I declare that I have authored this thesis independently, that I have not used other than the declared sources/resources, and that I have explicitly indicated all material which has been quoted either literally or by content from the sources used. The text document uploaded to TUGRAZonline is identical to the present master's thesis/diploma thesis/doctoral dissertation.

_____ _____

Datum / Date Unterschrift / Signature

Abbreviations

1PI ..... **o**ne-**p**article **i**rreducible functional approach
AMEA ..... **a**uxiliary **m**aster **e**quation **a**pproach
ARPES ..... **a**ngle **r**esolved **p**hoto **e**mission **s**pectroscopy
BA ..... **B**ethe-**A**nsatz
BMsme ..... **B**orn-**M**arkov-**s**ecular **m**aster **e**quation
CMOS ..... **c**omplimentary **m**etal **o**xide **s**emiconductor
CPT ..... **c**luster **p**erturbation **t**heory
CT-QMC ..... **c**ontinous **t**ime **q**uantum **M**onte **C**arlo
dc ..... **d**irect **c**urrent
DF ..... **d**ual **f**ermions
DFT ..... **d**ensity **f**unctional **t**heory
DMET ..... **d**ensity **m**atrix **e**mbedding **t**heory
DMF^{2}RG ..... **d**ynamical **m**ean **f**ield **t**o functional **r**enormalization **g**roup
DMFT ..... **d**ynamical **m**ean **f**ield **t**heory
DMRG ..... **d**ensity **m**atrix **r**enormalization **g**roup
DOS ..... electronic **d**ensity **o**f **s**tates
DΓA ..... **d**ynamical **v**ertex **a**pproximation
ED ..... **e**xact **d**iagonalization
eVCA ..... **e**xtended **V**ariational **C**luster **A**pproach
FRG ..... **f**unctional **r**enormalization **g**roup
LDA ..... **l**ocal **d**ensity **a**pproximation
MC ..... **M**onte **C**arlo
MCBJ ..... **m**echanically **c**ontrolled **b**reak **j**unction
ME ..... **m**aster **e**quation
meCPT ..... **m**aster **e**quation enhanced steady-state **c**luster **p**erturbation **t**heory
MFT ..... **m**ean **f**ield **t**heory
MPS ..... **m**atrix **p**roduct **s**tates
NEGF ..... **n**onequilibrium **G**reen's **f**unctions
NRG ..... **n**umerical **r**enormalization **g**roup
PT ..... **p**erturbation **t**heory
QMC ..... **q**uantum **M**onte **C**arlo
QME ..... **q**uantum **m**aster **e**quation

RG ..... **r**enormalization **g**roup
RPA ..... **r**andom **p**hase **a**pproximation
SET ..... **s**ingle **e**lectron **t**ransistor
SFA ..... **s**elf **e**nergy **f**unctional **a**pproach
SIAM ..... **s**ingle-**i**mpurity **A**nderson **m**odel
STM ..... **s**canning **t**unneling **m**icroscopy
stsCPT ..... **st**eady-**s**tate **c**luster **p**erturbation **t**heory
stsVCA ..... **st**eady-**s**tate **v**ariational **c**luster **a**pproach
SVD ..... **s**ingular **v**alue **d**ecomposition
TEBD ..... **t**ime **e**volving **b**lock **d**ecimation
TRIQS ..... a **T**oolbox for **R**esearch on **I**nteracting **Q**uantum **S**ystems [1]
VCA ..... **v**ariational **c**luster **a**pproach

1. Introduction and outline

This thesis is about the physics of strongly correlated electron systems out-of-equilibrium. A large number of properties of typical condensed matter systems can be described remarkably well by a non-interacting quasi-particle approach. The main reason being the effective screening of the mutual interaction of their quantum particles which demotes this interaction to a mere renormalization of the parameters of quasi-particles as described by Landau's Fermi-liquid theory [7, 8, 9, 10]. Systems are referred to as strongly correlated if the theoretical description of their physical properties facilitating effectively non-interacting theories fails qualitatively. That is the contribution to the electronic energy arising from Coulomb repulsion between electrons is not small compared to the kinetic energy or lattice potential. A prime example is the material NiO, which is predicted to be a metal in conventional solid-state methods like the DFT in the LDA, but turns out to be a Mott insulator [11] due to its partly localized electrons. Strongly correlated electron systems can be found all over condensed matter physics [12, 13]. Prominent examples in the solid state are the cuprate superconductors [14], the Mott physics of transition metal oxides [15, 16], spatially confined physics of artificial nano-structures [17, 18, 19], hetero-structures [20, 21, 22], effectively low-dimensional bulk materials [23, 24], vacancies [25], ad-atoms at surfaces [26], quantum liquids [27], molecular electronics [28, 29] or artificially engineered quantum simulators [30]. Such systems pose an additional challenge to theoretical approaches, however, they offer a great range of interesting phenomena which might very well lead to revolutionary technological applications in the foreseeable future. Most of these applications will see a realization in an inherent nonequilibrium environment, such as solar cells [21] or nano-scale electronics [31, 32]. Recent years have indeed seen fascinating advances in experimental preparation and measurement techniques to probe correlated systems out-of-equilibrium [28, 33, 34, 35]. Their theoretical modelling, however, is complicated already in equilibrium [36] and poses a great challenge out-of-equilibrium [37, 38]. Due to the importance of describing recent experiments and guiding future research, the development of new theoretical methods, schemes and algorithms for an accurate description of interacting quantum particles out-of-equilibrium is in order.

In this thesis we report on our recent contributions to the field of strongly correlated low-dimensional electronic systems out-of-equilibrium. Starting from equilibrium simulations we apply linear-response transport theory to effectively low-dimensional materials, study the quasi-exact numerical time evolution of quantum dots and finally arrive at the steady-state transport characteristics of molecular junctions. In employing these three approaches to nonequilibrium physics we focus on the one hand on the development of new numeric methods and approximation schemes and on the other hand on basic physical insight using also state-of-the-art many-body methods. A brief analysis of current experimental efforts in nonequilibrium correlated physics will be given in Ch. 2. Subsequently, an overview of theoretical developments and an introduction to the methods and models developed and used in this work is provided in Ch. 3. A conclusion is presented in Ch. 4. The main results are available in the form of a collection of papers at the end of this thesis in Ch. 5. Their content shall be outlined in the following.

In order to enter the realm of nonequilibrium physics we apply linear-response theory [39, 40] to calculate the dc properties of a highly anisotropic real material. Linear-response theory is based entirely on the equilibrium ground state properties of the system and its application is limited to small external fields. In Sec. 5.1 we discuss the physical properties of the correlated effectively

one-dimensional conductor $Li_{0.9}Mo_6O_{17}$ starting from *ab initio* band structure calculations [41]. We obtain an effective electronic model in terms of Wannier orbitals and analyse its equilibrium properties, the Fermi surface and DOS. Electron-electron interactions are then considered in state-of-the-art DMFT [42] and the quantum cluster methods CPT [43, 44] and VCA [45] to obtain correlated spectral functions. These quantum cluster methods will be generalized to steady-state nonequilibrium methods in the third part of this thesis. On the methods side we generalize the eVCA method [46] to *ab initio* Hamiltonians. Material properties are discussed on the basis of the electronic structure. In particular we analyse why this material shows such an extreme degree of anisotropy in its electronic properties. We elaborate on the degree of correlation and find good agreement of our theoretical results with recent ARPES experiments [47]. The calculated highly anisotropic conductivity qualitatively agrees with recent experimental observations [48].

In order to probe genuine nonequilibrium phenomena beyond linear-response it is necessary to prepare a given system in a non-eigenstate and study its real time evolution. If such a calculation is feasible, in principle all information starting from transient behaviour up to the steady-state becomes available. In Sec. 5.2 we apply the quasi-exact MPS [49] based DMRG [50] + TEBD [51] scheme to obtain the time dependent transport characteristics across a single quantum dot [52] and in Sec. 5.3 the spatio-temporal evolution of the Kondo [53] screening cloud in the SIAM [54]. The DMRG+TEBD is a well established scheme especially suited for one-dimensional systems. On the methods oriented side we add to it a data analysis scheme to obtain steady-state observables from the real time domain and investigate the beneficial aspects of an auxiliary damping term in the time evolution. We investigate the physical properties of the prime model of correlated physics: the SIAM [55]. In equilibrium, accurate methods exist to probe its thermodynamic properties [56, 57] and even its spectral function [58, 59]. Out-of-equilibrium many open questions remain of which some are discussed in this thesis. The discussion of the physics of the SIAM out-of-equilibrium is a major point of this work. In the following chapters a range of methods will be developed and applied to analyse this model. Here we present accurate results for the time dependent current. We analyse transient properties and finally arrive at a faithful current-voltage characteristics in the steady-state. The effects of electron-electron interactions in different parameter regimes are discussed. We identify parameter regimes where the method works particularly well and those where the time evolution is limited to shorter times by considering the entanglement entropy. Considering the time evolution of distance dependent spin-spin and charge-charge correlation functions we gain insight into the emerging time and length scales of the Kondo screening cloud and discuss the physics inside and outside of the light-cone [60] following a quantum quench.

Often experiments probe the steady-state of a system which settles as a consequence of a large external influence like a bias voltage. Most of the time a treatment in a conventional linear-response way is not appropriate because the external influence is not small and excited states have a significant influence on the nonequilibrium behaviour. Following the real time evolution into the steady-state is often prohibited due to finite available simulation times of the method at hand in combination with long time-scales in the physical problem. It is therefore desirable to directly obtain the steady-state in a nonequilibrium framework. A large part of our work is focused on the development of numeric approximate steady-state quantum cluster methods stsCPT, stsVCA and meCPT as generalizations of their equilibrium counterparts CPT and VCA. These steady-state methods are based on strong-coupling first order real space perturbation theory for which an unperturbed (reference) state is necessary. In the course of this thesis we explore three reference states. In stsCPT the naive zero temperature ground state of a real space partition of the system is used. For stsVCA a self-consistent feedback to the steady-state is created using variational single-particle fields on these partitions. In meCPT a second order

QME [61] is facilitated to obtain a mixed reference state for the cluster partitions. In Sec. 5.4 we find the steady-state quantum cluster methods and the self-consistent feedback to yield good results in equilibrium for the case of strongly inhomogeneous systems as needed for transport problems [62]. To some extent the methods are even capable of capturing the essential features of the Kondo physics of a single quantum dot like the correct linear-response current, the Friedel sum rule and the exponential scaling of the Kondo scale with interaction strength. Based on this work we extended and apply the stsCPT and stsVCA in Sec. 5.5 and Sec. 5.6 to study steady-state transport across single quantum dots [63, 62]. In this part we develop and benchmark the self-consistent feedback of the stsVCA method. We find that stsVCA shows a rapid convergence in the control parameter, the size of the interacting part of the system. In the SIAM, we find it to yield superior results to the plain stsCPT in the low bias regime where electronic correlations are pronounced. Recent experiments obtained stability diagrams [64], which are well described by the stsVCA method. We analyse the splitting of the Kondo resonance in detail and find a linear splitting with bias voltage in stsVCA, as also predicted by other methods.

Recently experiments on molecular junctions and molecular electronic devices have become state-of-the-art. The poor agreement of the experimentally obtained transport characteristics and the theoretical *ab initio* values from LDA+NEGF calculations is attributed to strong electron-electron interaction effects in the highly confined geometries [37, 38]. Thus the development of methods which are capable of treating the electronic correlations on a more appropriate footing are in order. In Sec. 5.7 we apply the stsCPT method to predict the transport characteristics of such a junction consisting of two metallic leads and one Benzene molecule [65]. We extend the stsCPT to include the effects of magnetic fields. Obtained transmission and circular current-voltage characteristics as well as the nonequilibrium charge distribution and magnetization show pronounced effects of electron-electron interactions beyond mean field. A crucial influence on the quality and convergence of the stsCPT and stsVCA approximations has the reference state on which the perturbative solution is based. In Sec. 5.8 we develop an advanced reference state based on the solution of a QME for meCPT [66]. This mixed reference state incorporates information about the environment characteristics like temperature or chemical potential. We apply meCPT to electron-electron interaction based quantum diodes and triple-ring quantum junctions to study interaction induced quantum interference mediated blocking [67]. Within meCPT not only dynamic single-particle expectation values in the steady-state but also full information about the distribution of the reference state becomes available. We discuss stability diagrams, state-occupations, transmission functions and finally the steady-state blocking mechanism.

In Sec. 5.9, an alternative to the perturbative treatment of the steady-state is provided by the AMEA approach [68, 69]. Within this Green's function method the nonequilibrium self-energy is computed from an auxiliary system which is described by a Lindblad master equation. The parameters of the Lindbladian of the auxiliary system are found by requiring the Keldysh space hybridization functions to match the ones of the physical problem. The development of the AMEA is advanced and applied to the SIAM. A rapid convergence of steady-state observables was found and the splitting of the Kondo resonance under bias voltage was studied in detail. A promising outlook is the application of the AMEA as a steady-state DMFT solver.

Finally, in Sec. 5.10, using the combined efforts of DMRG+TEBD, stsCPT, stsVCA, the AMEA and the BMsme we give insight into the behaviour of electronic correlations at high bias voltages [70]. It is commonly believed that electronic correlations play an important role at low bias voltages. On the contrary high bias voltages seem to act effectively like a high temperature, rendering the system effectively free [71, 72, 73]. Based on the current-voltage characteristics, steady-state charge and spin fluctuations, the nonequilibrium spectral function and the nonequilibrium distribution function we argue that electronic correlations become enhanced at high bias voltages at the band edge, for finite lead DOS.

2. Experimental facts

The history of condensed matter physics has, to a large extent, been devoted to the study of complex phenomena and phases in equilibrium, such as high temperature superconductivity, charge density waves or magnetism. Nowadays a good understanding of the underlying many-body problem has been developed based on both experimental insight as well as theoretical considerations. However, still major open questions remain unsolved, such as a complete understanding of superconductivity. In the past decade the attention has shifted to research in time-dependent and out-of-equilibrium steady-state phenomena. These do not only provide the basis for tomorrow's applications which will dominantly operate in a nonequilibrium setup but also add time as an additional dimension, to help understand the inner workings of condensed matter systems. Driven by ultra fast electronics (femtosecond time-scales), cryogenic devices and clean vacuum technology it has become possible to generalize successful experimental techniques from equilibrium to nonequilibrium setups. One of these methods is time dependent ARPES [74] which allows to study electronic states in a pump-probe like fashion and monitor the excitation and relaxation of electronic occupations. In the solid-state the dynamics of complex phases like the melting of a charge density wave [75, 76, 77], the population of surface-states in topological insulators [78, 79], the dynamics of cooper pairs in cuprate superconductors [80, 81] or electron motion in low-dimensional materials [82] have been characterized. Strong laser pulses can be used to control e.g. the superconducting state [83] or the Mott insulating state [84, 85] in pump-probe experiments. In time resolved x-ray diffraction the study of anti-ferromagnetic order and the interplay of lattice and electron behaviour is studied [86]. These new methods will prove especially handy to characterize designed multilayer structures with engineered correlations [87] for the application in microelectronics or solar technology [21]. Even more experimental control and tune-ability has become available when creating the condensed matter system artificially in quantum simulators. Such devices allow to trap quantum particles by optical means and study their mutual interactions, the impact of the confinement lattice, as well as the influence of external fields. In this way one of the most prominent phases of condensed matter physics, the Mott insulating phase has been realized artificially [88, 89]. Out-of-equilibrium, the spreading of correlations can nowadays be monitored reliably [90]. This work focuses on out-of-equilibrium phenomena of impurities in metals or on surfaces and effectively low-dimensional electronic structure as both realized in nano-structures and molecular electronics. In the following a brief introduction into the state-of-the-art findings of these research areas is provided.

2.1. Nano-technology

The broad field of research of matter at the nano-metre scale is termed nano-technology [91, 92]. Since initial dreams of manipulating objects of atomic or molecular extent at the beginning of the sixties [93], it has evolved to its active goal of fabricating new materials and devices that have novel properties and functionality due to their tiny structure. Often nano-systems consist of small clusters of atoms or macromolecules in solution or adsorbed onto or structured into surfaces or layered materials. These units constitute effectively zero-, one-, two- or three dimensional systems with unique properties depending on their composition, structure, arrangement, dimensionality and environment which promote their quantum mechanical features. Nano-technology already

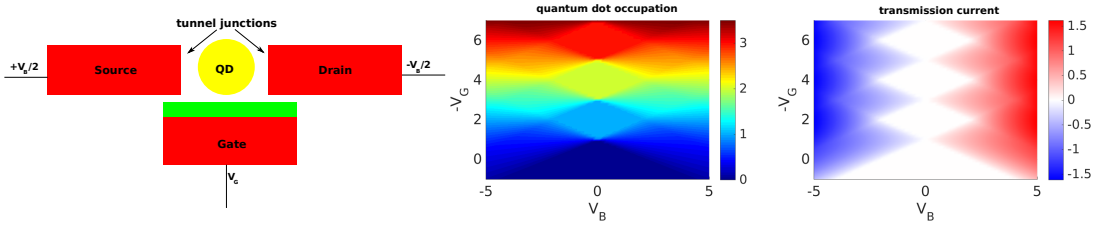

Figure 2.1.: *Single electron transistor.* **(Left)** Schematic setup. **(Middle)** Quantum dot occupation as function of bias voltage V_B and gate voltage V_G. **(Right)** Transmission current.

found a lot of industrial applications today: The high surface area of nano-structured materials provides perfect conditions for catalysis or storage functionality. Plastics and lacks are enhanced by nano-additives. Nano-coatings are well known for their mechanical strength and self-cleaning features. In our everyday life nano-particles appear in sunscreen, pans or cosmetic products. The public awareness for nano-technology sky-rocketed in 1985 with the discovery of the C_{60} buckminsterfullerene [94] and carbon nano-tubes, both a by-product of auto mobile exhaust. In technological application they however offer brilliant mechanical and electrical properties and the possibility of designing low-dimensional thermoelectric materials [95].

In this thesis we study electrical transport properties of nano-structures under voltage bias. So-called quantum dots are created as confined regions in space for example on a surface or in a hetero-structure where the available electronic states are quantized due to the strong geometric confinement [96, 97, 98, 99, 100]. They are often referred to as artificial atoms [101] due to properties similar to their natural pedants. However quantum dots offer tune ability and control over their energy structure, which enables device engineering. They can be realized via local anodic oxidation (LAO) on a GaAs/AlGaAs heterostructure [20] which enables tunable few electron control [102] or in a graphene nano-structure [103, 104]. Recently complex setups including superconducting leads and topological materials have been developed. In one of them the realization of the long elusive Majorana particle has been proposed [105].

Quantum dots contacted to nano-wires offer control over single electrons as realized e.g. in a SET. Such a device consists of a geometrically confined electronic dot tunnel coupled to a source and a drain lead as well as a gate electrode which allows to control the dot occupation, see Fig. 2.1. At low enough temperatures and small tunnel couplings the dot can be tuned into a sequential tunnelling regime when the time scale for electrons to "reside" on the dot is much larger than the tunnelling time scale. In this regime the source-drain current shows a stepwise behaviour which can be attributed to the Coulomb repulsion of the electrons on the dot, the so-called Coulomb blockade. The simplest model for such a device is a metallic "constant interaction" spinless fermion quantum dot [106]. The quantum dot is modeled by $\hat{\mathcal{H}}^S = \sum_k \epsilon_k f_k^\dagger f_k + U(N)$ with $U(N) = uN^2 - V_G N$ where N denotes the number of particles on the dot and the gate is described by the parameter V_G. The dot is tunnel coupled to a metallic source and drain lead via $\hat{\mathcal{H}}^{SE}_{S/D} = \sum_{kk'} t^{S/D}_{kk'} f_k^\dagger c_{k'} + h.c.$, where f denote the dot degrees of freedom and c the lead degrees of freedom. Using Fermi's golden rule [107] the transition between an initial state on the dot $|i_a\rangle$ and a final state $|f_b\rangle$ due to $\hat{\mathcal{H}}^{SE}_{S/D}$ is given by

$$\Gamma^{S/D}_{ba} = 2\pi \sum_{i_a f_b} \left|\langle f_b|\hat{\mathcal{H}}^{SE}_{S/D}|i_a\rangle\right|^2 p_{i_a} \delta\left(\omega_{f_b} - \omega i_a\right) ,$$

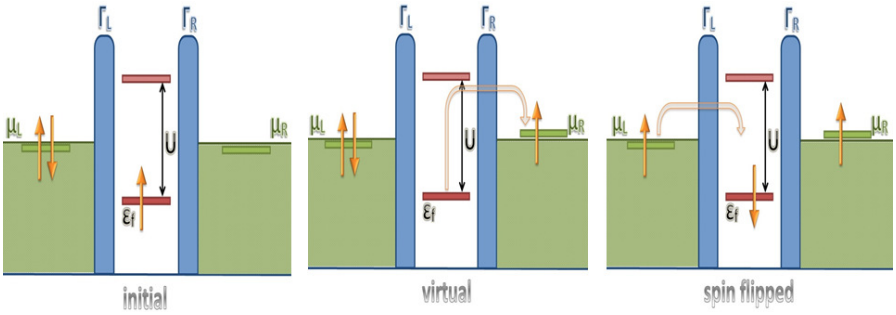

Figure 2.2.: *Higher order processes.* Visualization of a higher order process in a quantum dot tunnel-coupled via $\Gamma_{L/R}$ to two electronic leads at chemical potentials $\mu_{L/R}$. The on-site energy of the dot is denoted ϵ_f and the on-site Coulomb repulsion U. The initially singly-↑ occupied dot transitions via a virtual empty (doubly occupied) state to a singly-↓ occupied state.

where p_{i_a} is the initial state distribution of the isolated dot. Based on these transition rates, the distribution function P_a can be obtained from a Pauli master equation [61] (see Sec. 3.3.3) which equates inflow into state a and outflow

$$0 = \sum_{b,\lambda\epsilon\{S,D\}} \left(\Gamma^{\lambda}_{ab} P_b - \Gamma^{\lambda}_{ba} P_a\right) .$$

Assuming thermal initial distributions and a flat lead DOS one finds, labelling the dot states by particle number N, $\Gamma^{S/D}_{N+1,N} = \gamma^{S/D} f(U(N+1) - U(N) - \mu_{S/D})$ and $\Gamma^{S/D}_{N-1,N} = \gamma^{S/D} f(U(N-1) - U(N) + \mu_{S/D})$ with $f(\omega) = \frac{\omega}{e^{\beta\omega}-1}$, $\Gamma = \sum_{\lambda\epsilon\{S,D\}} \Gamma^{\lambda}$ and $\gamma^{S/D}$ the effective coupling to the source and the drain. The resulting steady-state distribution P_α is provided by the eigenvector corresponding to eigenvalue zero of

$$0 = \Gamma_{N,N-1} P_{N-1} - (\Gamma_{N+1,N} + \Gamma_{N-1,N}) P_N + \Gamma_{N,N+1} P_{N+1} ,$$

together with the normalization condition $\sum_N P_N = 1$. The resulting steady-state occupation and transmission current are plotted in Fig. 2.1. The occupation increases stepwise with V_G in a quantized fashion. This is because the interaction energy u between the particles on the dot needs to be overcome before another particle can be added. As a result one finds diamonds of constant particle number in the $V_G - V_B$ plane at which also no current can flow because the device is blocked due to Coulomb interaction. Experimentally the stability diagram is well understood [108] through characterization and transport measurements [20, 109, 110]. In this work we investigate two devices in the single-electron transistor regime: a single quantum dot diode and a ring triple-quantum dot transistor, see Sec. 5.8.

Even lower temperatures and stronger coupling promote coherent transport phenomena, like elastic co-tunnelling arising from the Kondo effect [111, 112]. Virtual transitions via energetically unfavourable states, as shown in Fig. 2.2, can lead to a strongly enhanced electronic transport if they occur coherently. In the equilibrium spin-Kondo effect a virtual spin-flip transition between the degenerate spin-↑ and spin-↓ states is the driving feature for non-trivial many-body phenomena [53]. For a detailed introduction to this topic see the section on the SIAM in Sec. 3.1. This work explores the steady-state transport of nano-devices in the Kondo regime (see Sec. 5.7,

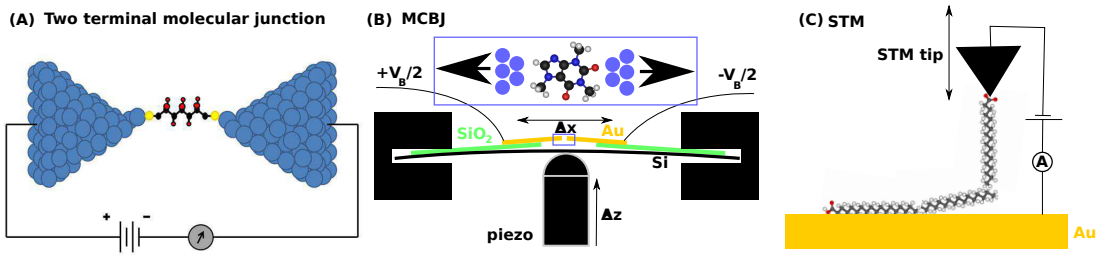

Figure 2.3.: *Experimental characterization of molecular junctions.* **(A)** A molecule contacted to two electronic leads under bias voltage. **(B)** Model of a MCBJ. **(C)** Model of a STM.

Sec. 5.7, Sec. 5.5, Sec. 5.6, Sec. 5.10) as well as the time dependent formation of the Kondo effect (see Sec. 5.2, Sec. 5.3).

2.2. Molecular junctions

What has become known as the field of molecular electronics [28, 31, 113, 19, 32, 18] is still a relatively young playground for a joint effort of physicists, chemists, material scientists and device engineers [29, 114]. Already in the 1970ies molecular scale electronic devices were proposed, notably the molecular current rectifier by Aviram and Ratner [115] or the molecular tunnel junction by Polymeropoulos and Sagiv [116]. Molecular electronic devices are highly anticipated miniaturized alternatives to the well established CMOS technology of today's microelectronic industry. While the latter approaches the limit of the photo-lithographic manufacturing method, molecular electronic devices offer the perspective of still higher packing density and therefore faster processing power and higher memory density [117]. Conventional microelectronics already is on the verge of leaving the realm of classical transport due to quantum mechanical tunnelling phenomena in junctions smaller than a few nano-metres although its concept is entirely based on conventional classical electronics. Engineers are working hard to develop concepts minimizing these spurious quantum influences. In contrast molecular junctions specifically avail quantum effects for a more flexible design and more powerful applications. The long term goal of research in molecular electronics is to integrate millions of molecules into one functional chip. Its short term goals are to understand the fundamental processes of charge transfer in small devices and to build functional molecular junctions acting as sensors or switches.

Molecules can either actively serve as tailored conducting elements in a junction or alter the device properties passively by changing the transport properties of the electrodes. The transport characteristics of molecular electronic devices directly reflect the electronic properties of the junction molecule [118]. As such, on the one hand these devices can be seen as molecular spectrographs, revealing the quantum states and inner workings of the molecule. On the other hand, the functional properties of the device are highly flexible and can be tuned directly via the electronic properties of the molecule either statically by side group design or dynamically for example using tailored vibrations. In today's research, many promising device layouts are explored including single molecular junctions, mono layers or thin films [119]. In this introduction we focus on transport through single molecules in two terminal setups, which have been a topic of active research in this thesis.

The ultimate limit of miniaturization consists in contacting a single atom or molecule, ideally hosting some sort of functionality, see Fig. 2.3 (A). As is, such a junction looks innocent and straight forward as it consists of a left and right lead under bias voltage and a molecule contacted in-between those two electrodes. However, many challenges have had to be overcome until finally the transport characteristics of such a device could be recorded. Organic molecules offer a wide range of functionalization possibilities and their manufacturing process is well established. In order to make such molecules "stick" to the metallic reservoirs commonly contacting thiol anchor groups are facilitated [120, 121, 122, 123]. Contacting to gold electrodes [121, 124, 29] or platinum leads [123] has become feasible. To actually catch the molecule in-between the leads has become possible due to advances in experimental fabrication [34] and device assembly [33, 125] for example via electro migration [33, 126, 127, 128, 129, 130, 131, 132, 133]. Newly designed, improved and adopted measurement techniques [134] enabled electrical transport measurements across molecular junctions [31]. In the following we shortly comment on two of the most common methods: MCBJ and STM.

In the MCBJ [121, 113] the current-voltage characteristics can be obtained in a statistical way [124]. The MCBJ usually operates in ultra high vacuum and at cryogenic temperatures. This technique provides an accurate way to control the spacing between two metallic electrodes on the picometer level stable on time-scales required for transport experiments [34, 135, 124, 123], see Fig. 2.3 (B). A piezo is used to bend a flexible rod in a three-point bending mechanism, which in turn stretches the metal on top of it until it breaks. Often thin gold electrodes are deposited onto an insulating buffer like SiO_2 which is grown on a flexible base material like a phosphor-bronze substrate. The gold electrode is pre-structured using electron beam lithography to form a narrow constriction of about 100 nm. When bending the substrate (Δz), a controlled gap (Δx) forms between the two new electrodes. The molecules are then dissolved in an appropriate solvent and the thiol end groups of the molecules will become trapped between electrodes in the MCBJ. This setup allows to measure transport depending on bias voltage as well as to perform stretching experiments and study the behaviour of transport as a function of electrode separation. The difficulty in a single measurement often consists in determining which molecule is trapped, how many of them, in which orientation and in which contacting layout. Therefore a statistical way of obtaining the transport characteristics has been suggested [124]. The trapping experiment is repeated over and over and each time the current-voltage curve is recorded. A post processing step then allows to narrow down the many individual curves onto a few characteristics of one or two molecules.

The widespread STM [136] has become an established tool in many areas of surface characterization, nano-technology and single-atom manipulation. Due to its flexibility and precision it has also become one of the most favourite techniques to study transport through individual molecules [137, 138, 125, 139, 140, 35, 141, 134, 139], see Fig. 2.3 (C). In ultra high vacuum conditions and at cryogenic temperatures the STM is used to locate pre-deposited molecules on a surface. The molecule is approached and then gently pulled off the surface using the STM tip. In this way the molecule becomes contacted between the two electrodes, the surface and the STM tip. Like in the MCBJ the electrode separation can be controlled with high accuracy.

Typically the resulting quantum point contacts in the ballistic regime display a quantized conductance in steps of $2\frac{e^2}{h} \approx 13\,k\Omega^{-1}$, where e is the electron charge and h is Planck's constant [142, 143]. This quantized conduction has been experimentally observed by pulling apart two gold electrodes and assigning the conductance to the observed number of atomic gold chains linking the electrodes in the final position. Already simple junctions like a benzene-1,4-dithiol molecule connected to two gold electrodes offer a rich current-voltage characteristics [124]. The high sensitivity of the transport characteristics on the electronic structure of the device promotes the theoretical modelling and understanding of the electronic characteristics out-of-equilibrium

to an important task. A well established formalism to predict these transport characteristics is provided by the DFT+NEGF scheme [144, 145, 146, 147, 148, 149, 150, 151, 152, 153]. Within this method the electronic structure of the molecule and the tips of the leads is obtained using equilibrium *ab initio* band structure methods in some approximation of the DFT. NEGF transport calculations are then run based on these electronic states. Although this method offers the appealing advantage to obtain the transport behaviour from first principles and therefore design devices directly on the computer, the experimental and theoretical transport characteristics are in poor agreement [37, 38]. This failure to predict device characteristics has been attributed to the improper treatment of electronic correlations which can become large in molecular junctions.

Quite generally, molecular junctions are low-dimensional and arranged in a highly confined geometries which both promote electronic correlation effects. Therefore the theoretical investigation of transport through molecular junctions is a highly non-trivial challenge which however promises new and improved device designs from first principles. This work contributes to the study of correlated single molecular two-terminal junctions where the molecule is the active conductor. In this work we develop NEGF based methods to specifically study the impact of electronic correlations on steady-state transport in molecular junctions and apply an accurate numeric real-time evolution to study time dependent phenomena. We discuss a single correlated orbital with two electronic leads as the simplest model of a molecular junction, see Sec. 5.2, Sec. 5.3, Sec. 5.5, Sec. 5.6 Sec. 5.9 and Sec. 5.10. This simple model junction already features strong correlation phenomena like the Kondo effect [53] at low temperatures and describes the well known Coulomb blockade at elevated temperatures. We then discuss a single orbital diode with polarized leads Sec. 5.8 which features NDC. In Ring molecules, in addition to electronic correlations also quantum interference effects influence the transport characteristics. These are explored in a benzene like ring molecule in a magnetic field in Sec. 5.7 and a three ring molecule transistor which features interaction induced quantum interference mediated current blocking, see Sec. 5.8.

3. Theoretical approach

Equilibrium statistical physics is characterized by the state of lowest energy and can be described by a thermodynamic state function like the one for the ideal gas $pV = Nk_BT$, relating its pressure and volume to the particle number and temperature [154]. A nonequilibrium steady-state is, although time independent, not an equilibrium state and does not respect the fluctuation-dissipation relations. When and if a system can be described by an equilibrium theory, ultimately, reduces to the magnitude of involved time-scales, like the relaxation rate and the observation time scale. In this thesis we consider the nonequilibrium behaviour of interacting many-body systems. The many-body problem is in general unsolvable exactly, even in classical physics, like in the study of planetary motion, and in semi-classical physics, like in the study of fusion plasma dynamics and therefore insightful approximate solutions need to be designed.

The setups discussed in the previous chapter consist of many interacting microscopic particles, which are described by a quantum theory. Quantum mechanics assigns probabilities to quantum states which can be realized for microscopic particles [155, 156, 157, 158, 107]. The evolution of quantum particles follows Schrödinger's equation [159, 160]

$$i\hbar\frac{\partial}{\partial t}|\Psi(\mathbf{r},t)\rangle = \hat{\mathcal{H}}|\Psi(\mathbf{r},t)\rangle\,,$$

where the pure quantum state $|\Psi\rangle$ evolves according to the Hamiltonian operator $\hat{\mathcal{H}}$ and $\hbar = \frac{h}{2\pi} \approx 1.054\cdot10^{-34}\,\frac{\mathrm{m^2kg}}{\mathrm{s}}$ is the reduced Planck constant. The stationary state is found by the eigenvalue equation

$$E|\Psi(\mathbf{r})\rangle = \hat{\mathcal{H}}|\Psi(\mathbf{r})\rangle\,.$$

A condensed matter system typically consists of a large number of electrons and atomic-nuclei. The general many-body Hamiltonian takes the form [161]

$$\hat{\mathcal{H}} = \sum_{\mu=1}^{N_I}\left(-\frac{\hbar^2}{2M_\mu}\hat{\nabla}_\mu^2\right) + \frac{1}{4\pi\varepsilon_0}\sum_{\mu<\nu}^{N_I}\frac{Q_\mu Q_\nu}{|\mathbf{R}_\mu-\mathbf{R}_\nu|} + \sum_{i=1}^{N_e}\left(-\frac{\hbar^2}{2m_e}\hat{\nabla}_i^2\right) + \frac{1}{4\pi\varepsilon_0}\sum_{i<j}^{N_e}\frac{e^2}{|\mathbf{r}_i-\mathbf{r}_j|} + \frac{1}{4\pi\varepsilon_0}\sum_{i\mu}\frac{eQ_\mu}{|\mathbf{r}_i-\mathbf{R}_\mu|}\,,$$

and consists of a kinetic term for N_I nuclei with mass M_μ and charge Q_μ at positions $\mathbf{R}_\mu$ and N_e electrons with mass m_e and charge e at positions $\mathbf{r}_i$ as well as the Coulomb interaction between electrons, nuclei and electrons and nuclei. $\varepsilon_0 \approx 8.854\cdot10^{-12}\,\frac{\mathrm{F}}{\mathrm{m}}$ is the vacuum permittivity. An exact solution of such a large system of coupled differential equations is hopelessly out of reach in the general case. A lot of interesting physical properties depend however only on the electronic degrees of freedom which can be separated from the nuclear motion because the dynamics of the nuclei is much slower than the electronic time scale. In the Born-Oppenheimer [162] approximation one treats the nuclei classically and the dynamics of the electrons is augmented by a static lattice potential $\hat{V}_{\mathrm{ext}}(r_i)$

$$\hat{\mathcal{H}}_{\mathrm{BO}} = \sum_{i=1}^{N_e}\left(-\frac{\hbar^2}{2m_i}\hat{\nabla}_i^2\right) + \frac{1}{4\pi\varepsilon_0}\sum_{i<j}^{N_e}\frac{e^2}{|\mathbf{r}_i-\mathbf{r}_j|} + \sum_i \hat{V}_{\mathrm{ext}}(\mathbf{r}_i)\,. \tag{3.1}$$

The still problematic term which renders the equation untractable is the one involving the interaction between two electrons i and j. In the history of theoretical condensed matter physics mainly two routes have been followed to gain insight into the physics of such an interacting electronic system.

In the first approach one attempts to solve Eq. (3.1) directly using an approximate expression for the interaction term. The resulting equations are either perturbative or result in an effective single-particle description, as exercised in the most successful working horse of condensed matter physics: the density functional theory (DFT) [163, 164] in the local density approximation (LDA) [165]. This theory allows to computationally obtain reliable electronic properties for most standard materials and systems even in a black box fashion nowadays. However, standard exchange-correlation functionals like the LDA are not suited to describe strongly correlated systems.

The second major approach is to construct so-called model Hamiltonians, which describe the essential and important parts of the physical properties at low energies. The most famous of these model Hamiltonians is the single-band Hubbard model [166]

$$\hat{\mathcal{H}}_{\mathrm{Hub}} = -t \sum_{\langle ij\rangle,\sigma} (c^{\dagger}_{i\sigma} c_{j\sigma} + c^{\dagger}_{j\sigma} c_{i\sigma}) + U \sum_{i=1}^{N} \hat{n}_{i\uparrow} \hat{n}_{i\downarrow} \,,$$

which describes the physics of electrons in a single correlated band, as for example formed by strongly localized d- or f-electrons. It is described in terms of second quantized fermionic creation/annihilation operators $c^{\dagger}_{i\sigma}/c_{i\sigma}$ at site i with spin σ [167, 106]. The particle number operator is defined as $\hat{n}_{i\sigma} = c^{\dagger}_{i\sigma}/c_{i\sigma}$. Particles are allowed to hop from site i to nearest-neighbour site j with a hopping amplitude t which sets the kinetic energy scale. The long-range Coulomb interaction is rendered to a caricature interaction which only penalizes electrons residing on the same orbital with an energy cost U. Models like the Hubbard model significantly reduce the number of degrees of freedom and the complication of the interaction terms while retaining the most important physical mechanisms. Unfortunately most of these models are still intractable in the general case and approximate methods have been and are developed to gain understanding. The advantage with respect to the full approximate solution is that those approximate methods are usually much more controlled and interactions can be treated more accurately.

In recent times these two different techniques of investigating condensed matter systems converge again onto common grounds, most prominently in the LDA+DMFT method for strongly correlated systems. Such approaches start from the full Born-Oppenheimer Hamiltonian in an effective treatment like LDA but treat the strong electron-electron interactions within a model Hamiltonian formalism like DMFT in a self-consistent framework, harnessing advantages of both approaches.

This work is mainly concerned with the approximate or quasi-exact solution of model Hamiltonians and the development of numerical methods for this purpose. The combined *ab initio* + correlation methods approach is followed in the first part of this thesis, see Sec. 5.1.

3.1. Model Hamiltonians

The first part of this thesis (Sec. 5.1) discusses an extended Hubbard model which is explained therein. The Hamiltonian for molecular and nano-junctions will be outlined in Sec. 3.3.1 when it comes in handy in conjunction with outlining steady-state quantum cluster methods. A large part of this thesis is devoted to the study of the single-impurity Anderson model (SIAM) [55] which shall be reviewed briefly at this point since it helps to introduce the notation and provides

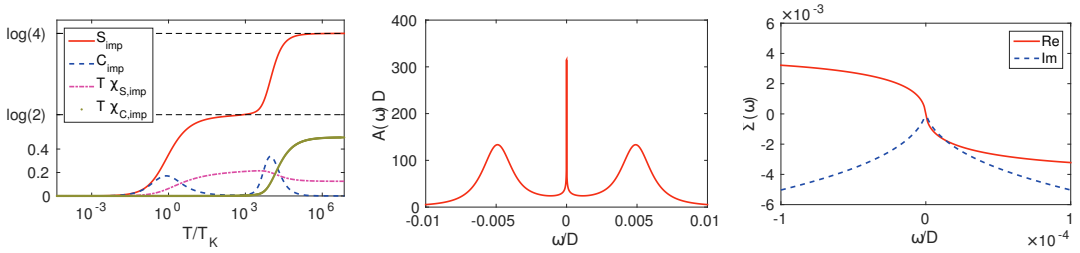

Figure 3.1.: *Equilibrium properties of the SIAM.* **(Left)** Thermodynamics of the impurity. **(Middle)** Zero temperature spectral function. **(Right)** Self-energy. All data have been obtained using the NRG Ljubljana code [2] for $U = 20\,\Delta$.

the basis for a lot of effects which are also important in the other models. the SIAM consists of a single correlated fermionic site coupled to an infinite electronic environment

$$\hat{\mathcal{H}}^{\mathrm{SIAM}} = \epsilon_f \sum_{\sigma} f_\sigma^\dagger f_\sigma + U\,\hat{n}_\uparrow^f\,\hat{n}_\downarrow^f + \sum_{\lambda k\sigma} \epsilon_{\lambda k\sigma}\, c_{\lambda k\sigma}^\dagger\, c_{\lambda k\sigma} + \sum_{\lambda k} \left(t'_{\lambda k\sigma} f_\sigma^\dagger c_{\lambda k\sigma}\right) + h.c.\,.$$

Here $f_\sigma / f_\sigma^\dagger$ denote fermionic annihilation/creation operators for the impurity orbital with spin $\sigma \in \{\uparrow, \downarrow\}$ respectively. The impurity site is subject to a local Coulomb repulsion U repelling spin-$\uparrow$ and spin-$\downarrow$ type particles where the particle number operator is defined in the usual way as $\hat{n}_\sigma^f = f_\sigma^\dagger f_\sigma$ and the impurity on-site potential is ϵ_f and takes the value $\epsilon_f = -\frac{U}{2}$ at particle-hole symmetry. This correlated impurity is hybridized with an environment of free electrons described by $c_{\lambda k\sigma} / c_{\lambda k\sigma}^\dagger$, with dispersion $\epsilon_{\lambda k\sigma}$ where λ denotes a reservoir index. In equilibrium typically one reservoir e.g. an s-electron conduction band is of interest while for the nonequilibrium description the impurity is coupled to $N_\lambda = 2$ reservoirs to apply a bias voltage or a temperature gradient.

The SIAM has originally been devised to study magnetic impurities in metallic hosts [168] and explore their anomalous resistance minimum at a finite, low temperature [169, 170] which is accompanied by an anomalous magnetic susceptibility and specific heat. The cause for this phenomenon was found in a non-perturbative many-body effect which lies at the heart of the physics of the SIAM, the Kondo effect [171, 53], which manifests itself at a low temperature scale T_K, known as the Kondo temperature. In equilibrium, the electronic environment is described by a Fermi energy ϵ_F. Considering the atomic limit ($t'_{\lambda k\sigma} = 0$) for the interacting impurity, it is empty $\epsilon_f > 0$ and doubly occupied if $\epsilon_f < -U$ if the conduction band energy ϵ_F behaves accordingly. The interesting local moment regime occurs for values of ϵ_f in-between where the ground-state is degenerate in spin. This includes the particle-hole symmetric point $\epsilon_f = -\frac{U}{2}$ on which we focus the following discussion. These systems however only behave as local moments at sufficiently high temperatures $T \gg T_K$. To gain deeper understanding one has to give up the simple atomic limit which predicts a spurious immediate splitting of the impurity DOS into charge excitations at $\omega \pm \frac{U}{2}$. On the one hand, a self-consistent static mean field treatment of the spin resolved impurity densities obtains an erroneous phase transition at $U_C = \pi\Delta\left(1 + \cot\left(\frac{\pi\langle n^f\rangle}{2}\right)\right)$. This solution predicts a magnetic state which is non-physical for an effective zero dimensional system [55]. On the other hand, a low order perturbative treatment encounters a logarithmic divergence [53]. This "Kondo problem" could be resolved by Kondo [171] and Anderson [172]. The low energy behaviour of the SIAM can be described in terms of the Kondo Hamiltonian which is derived via a projection technique onto the singly-occupied subspace in the Schrieffer-Wolff transformation [173, 174]. In this model the impurity is effectively described by a local spin degree of freedom coupled to the electronic conduction band via an effective exchange interaction

$J\hat{\vec{S}}_f \cdot \vec{\tau}_{\sigma\sigma'} c^\dagger_{k\sigma} c_{k'\sigma'}$ with $J = -\frac{8t'^2}{U} < 0$ driven by virtual spin flips between the Kramers doublet. For a ferromagnetic exchange interaction $J \to +\infty$ the low energy physics can be described in terms of elastic potential scattering. In the SIAM, one encounters an anti-ferromagnetic exchange interaction $J < 0$ which promotes a ground state which is a bound state of the impurity and conduction electron spins, the Kondo singlet. The success of the poor man's scaling RG was to show that even for arbitrary small (positive) U this strong coupling fixed point is reached in the RG flow, and the Kondo singlet state is approached. The energy scale below this RG flow remains meaningful is one way to define the Kondo temperature $T_K \propto e^{-U}$. The physics of the impurity can be very well understood by considering thermodynamic observables which are available analytically from seminal Bethe Ansatz results [175, 176] and numerically from highly accurate NRG calculations [58, 59, 177]. As shown in Fig. 3.1 (left), the impurity entropy S_{imp} signals the contribution of 4 states at high temperatures i.e. empty, double-occupied and spin-$\uparrow$/spin-$\downarrow$ respectively. At lower temperatures, still above T_K the 2 energetically favoured singly occupied states contribute and below the T_K only a single state, the singlet, remains. The specific heat C_{imp} indicates two "transitions", one where the charge degrees of freedom freeze out at high temperatures and one where the spin degrees of freedom condense to the singlet state at T_K, which are visible in the charge-susceptibility $\chi_{C,imp}$ and spin-susceptibility $\chi_{S,imp}$, respectively. The NRG spectral function of the SIAM is shown in Fig. 3.1 (middle). It is especially accurate at low energies where the Kondo resonance is found. This peak at $\omega = 0$ signifies the Kondo state and is pinned at the chemical potential as expected for a local Fermi liquid and described by the Friedel sum rule. In addition the spectral function shows to Hubbard bands at energies $\omega \propto U$ which are caused by charge excitations. The low energy self-energy (Fig. 3.1 (right)) exhibits a quadratic imaginary and linear real part, typical for Fermi liquids.

As of today, the equilibrium physics of the SIAM has been well characterized owing to an additional combined insight gained from sophisticated computational approaches like e.g. perturbation theory [178, 179, 180, 181], FRG [182, 183, 184], DMRG [185, 186, 187], slave particle methods [188, 189], methods based on Hubbard's X-operator technique [166, 190] or variational wave functions [26].

The SIAM has emerged as one of the prime models and important tool of correlated condensed matter systems [26, 42]. Quantum impurity models describe the adsorption of atoms onto surfaces [26, 191, 192, 193]. Additionally, they are of theoretical interest as solvable models of quantum field theories [58, 194]. The behaviour of a plethora of magnetic phenomena and the field of heavy fermion physics is described by strongly correlated quantum impurity models [195, 196], like the periodic Anderson impurity model.

A renewed interest in understanding and calculating dynamic quantities of the SIAM was created with the advent of DMFT [42, 197, 198, 199, 200, 201]. DMFT provides a flexible framework to study general fermionic lattice models. The electronic self-energy provided by DMFT is the one of the auxiliary impurity system which is local and becomes exact for the Hubbard model in infinite dimensions [197]. In DMFT, the frequency dependent self-energy of the impurity model has to be determined, which has led to advanced methods for the calculation of dynamic quantities like self-consistent QMC [202], Hirsch-Fye QMC [203, 204], projective QMC [205] or continuous-time QMC [206] which however suffer from analytic continuation ambiguities [207, 208]. Real axis solvers include ED, which has achieved exact results for truncated baths [209], NRG [210], IPT [201], NCA [211, 212] or the local moment approach [213, 214]. With the MPS framework several approaches exist to obtain the dynamic self-energy, correction-vector DMRG [215, 216], dynamical DMRG [217], an MPS based Lanczos algorithm [218], Chebyshev expansion [219] or real time evolution using TEBD [220].

Recently the SIAM in a nonequilibrium setup has become of major importance in the understanding of transport through quantum dots [221, 112, 222], correlated nano-structures and

molecules [223, 224, 126, 128, 225]. In this context the quantum impurity models have been studied using semi-classical methods [226] and Green's function techniques [227, 228, 229, 230]. The SIAM is predicted to stay in the strong coupling regime even under the influence of a bias voltage [231] which permits a full characterization under special circumstances only [232, 233, 234]. Beyond the linear-response result in the Kondo regime, which is characterized by the conductance quantum, some fundamental aspects of the impurity out-of-equilibrium are known [235, 236, 237]. Nonequilibrium correlated impurity models still pose an exciting challenge to theory as of today. A major part of this work is devoted to address this issue. Among the existing approaches to the SIAM out-of-equilibrium are [52, 69] scattering-state BA [238], scattering-state NRG (SNRG) [239, 240, 241], non-crossing approximation studies [229, 242], fourth order Keldysh PT [243], other perturbative methods [244, 245] in combination with the renormalization group (RG) [246, 247, 248, 249, 250], iterative summation of real-time path integrals [251], time dependent NRG [252], flow equation techniques [253, 254], the time dependent DMRG [51, 50, 255, 256, 49, 257], applied to the SIAM [258, 52], the FRG [259, 260], diagrammatic QMC [261, 262], CT-QMC calculations on an auxiliary system with an imaginary bias [263, 264, 265, 266, 267], non-equilibrium CPT [62], the non-equilibrium VCA [268, 269], super-operator techniques [270, 271], dual fermions [272], many-body PT and time-dependent DFT [273], real-time RG (rtRG) [274], generalized slave-boson methods [275], time dependent Gutzwiller mean field calculations [276] and generalized master equation approaches [277]. Comparisons of the results of some of these methods are available in literature [278, 52, 279] and time-scales have been discussed in [280]. The advent of nonequilibrium DMFT [281, 282, 283] further stimulated the efforts on solvers out-of-equilibrium [284].

3.2. From equilibrium to the steady-state

Quantum systems in equilibrium can be very well characterized thanks to methods developed in the past decade. Statistical mechanics is successful in describing ensemble averaged properties of thermodynamic systems connected to equilibrium reservoirs. The grand-canonical state $\hat{\rho}_0$ of a system described by $\hat{\mathcal{H}}_0$ is given by [285]

$$\hat{\rho}_0 = \frac{e^{-\beta(\hat{\mathcal{H}}_0 - \mu\hat{N})}}{\mathrm{tr}\left\{e^{-\beta(\hat{\mathcal{H}}_0 - \mu\hat{N})}\right\}},$$

where μ denotes the chemical potential controlling the particle number $\hat{N}$ and β is the inverse temperature $\frac{1}{k_B T}$. Properties of the system $\hat{A}$ are obtained as averages

$$\langle \hat{A} \rangle_0 = \mathrm{tr}\left\{\hat{\rho}_0 \hat{A}\right\}.$$

In this thesis we will be concerned with the reaction of a system onto an external influence $\hat{\mathcal{H}}_E(t) = f(t)\hat{B}$, where $\hat{B}$ is again some observable of the system. The full system is now described by its initial state $\hat{\mathcal{H}}_0$ and the time dependent influence $\hat{\mathcal{H}}_E(t)$, $\hat{\mathcal{H}} = \hat{\mathcal{H}}_0 + \hat{\mathcal{H}}_E(t)$. The expectation value of $\hat{A}$ changes to $\langle \hat{A}(t) \rangle = \mathrm{tr}\left\{\hat{\rho}(t)\hat{A}\right\}$, where the time dependent density matrix can be found from the von-Neumann equation

$$i\hbar\dot{\hat{\rho}}(t) = \left[\hat{\mathcal{H}}, \hat{\rho}(t)\right]_- . \tag{3.2}$$

The most simple way to obtain the reaction of the system onto $\hat{\mathcal{H}}_E(t)$ is via causal response functions as obtained in the well known linear-response formalism. Upon transforming to the

interaction representation with respect to $\hat{\mathcal{H}}_0$

$$\hat{\rho}_I(t) = e^{\frac{i}{\hbar}\hat{\mathcal{H}}_0 t}\hat{\rho}(t)e^{-\frac{i}{\hbar}\hat{\mathcal{H}}_0 t}\,,$$

and expanding Eq. (3.2) into powers of $\hat{\mathcal{H}}_E(t)$ up to linear order one finds [285]

$$\hat{\rho}(t) = \hat{\rho}_0 - \frac{i}{\hbar}\int_{-\infty}^{t} dt' e^{-\frac{i}{\hbar}\hat{\mathcal{H}}_0 t'}\left[\hat{\mathcal{H}}_E(t'), \hat{\rho}_0\right]_- e^{\frac{i}{\hbar}\hat{\mathcal{H}}_0 t'}\,.$$

The response of the system onto $\hat{\mathcal{H}}_E(t)$ is finally given by

$$\langle\hat{A}(t)\rangle - \langle\hat{A}\rangle_0 = -\frac{i}{\hbar}\int_{-\infty}^{t} dt' f(t')\langle\left[\hat{A}_I(t), \hat{O}_I(t')\right]_-\rangle_0\,. \tag{3.3}$$

Most importantly, within this approximation the action of the external influence can be computed from an expectation value of the unperturbed system at the initial time $\langle\rangle_0$. At the heart of Eq. (3.3) lies the causal response function $G^R_{\hat{A}\hat{O}}(t,t') = -i\theta(t-t')\langle\left[\hat{A}(t), \hat{O}(t')\right]_-\rangle_0$ which we will discuss in detail in Sec. 3.3.1.

For now we consider transport properties like the resistivity $\rho = \frac{k_B t}{e^2 A_0}$, the thermopower $S = -\frac{k_B A_1}{|e| A_0}$ or the thermal conductivity $\kappa = k_B\left(A_2 - \frac{A_1^2}{A_0}\right)$ which can be expressed in terms of kinetic coefficients A_n [286, 287]. In the first part of this thesis we obtained the transport characteristics of the effectively one-dimensional material $Li_{0.9}Mo_6O_{17}$ based on realistic *ab initio* calculations including electronic correlations within DMFT and eVCA, see Sec. 5.1. In linear-response, the transport coefficients are given by

$$\mathcal{A}^n_{\nu\mu} = N_{\text{spin}}\pi\hbar\int_{-\infty}^{\infty} d\omega\,(\beta\omega)^n \times p_{\text{FD}}(\omega,\mu,\beta)p_{\text{FD}}(-\omega,-\mu,\beta)\Gamma_{\nu\mu}(\omega,\omega)\,, \tag{3.4}$$

where $N_{\text{spin}} = 2$ is due to spin degeneracy, the indices $\nu,\mu = \{a,b,c\}$ denote the real space coordinate system, and we neglect vertex corrections. The Fermi-Dirac distribution $p_{\text{FD}}(\omega,\mu,\beta) = \frac{1}{e^{\beta(\omega-\mu)}+1}$ restricts the interval of integration to $\beta^{-1} \sim k_B T$ around the Fermi energy ϵ_F (k_B is Boltzmann's constant, and T and β denote temperature and inverse temperature, resp.). The transport distribution

$$\Gamma_{\nu\mu}(\omega_1,\omega_2) = \frac{1}{V}\frac{1}{N_{1.\text{BZ}}}\sum_{\mathbf{k}\epsilon 1.\text{BZ}} \text{tr} \times \left[v_\nu(\mathbf{k})A(\omega_1,\mathbf{k})v_\mu(\mathbf{k})A(\omega_2,\mathbf{k})\right], \tag{3.5}$$

(V is the unit cell volume) is given in terms of the velocities

$$v^{\alpha\beta}_\nu(\mathbf{k}) = -\frac{\hbar}{m}\langle\Psi_\alpha(\mathbf{k})|\nabla_\nu|\Psi_\beta(\mathbf{k})\rangle\,, \tag{3.6}$$

and the spectral function

$$A_{\alpha\beta}(\omega,\mathbf{k}) = -\frac{1}{\pi}\Im\text{m}(G^R_{\alpha\beta}(\omega,\mathbf{k}))\,, \tag{3.7}$$

which both are matrices in orbital indices α,β, which the trace tr runs over.

We use velocities $v^{\alpha\beta}_\nu(\mathbf{k})$ (Eq. (3.6)) in the Peierls approximation (neglecting the gradient of

the Wannier orbital itself leading to a diagonal representation)

$$v_\nu^{\alpha\beta}(\mathbf{k}) = \frac{1}{\hbar}\left(\langle\omega_\alpha(\mathbf{k})|\frac{\partial\hat{\mathcal{H}}(\mathbf{k})}{\partial k_\nu}|\omega_\beta(\mathbf{k})\rangle - \alpha\,(r_\alpha - r_\beta)\,\langle\omega_\alpha(\mathbf{k})|\hat{\mathcal{H}}(\mathbf{k})|\omega_\beta(\mathbf{k})\rangle\right) \approx \frac{1}{\hbar}\frac{\partial E_\alpha(\mathbf{k})}{\partial k_\nu}\delta_{\alpha\beta} \quad (3.8)$$

where the second term in the first expression takes intra-unit cell processes into account [287], and r_α is the position of Wannier orbital α inside the unit cell.

Often the linear-response treatment provides insufficient information, for example, when the perturbation is strong or details of the transient behaviour become important. For such systems a real time evolution becomes of interest. For strongly correlated systems, as discussed in this thesis, this task becomes highly non-trivial due to the complexity of the problem. When not resorting to effectively free approximations like a time dependent mean field theory, very successful approaches for tackling the interacting problem include the time dependent Lanczos method [288, 289] or Arnoldi time evolution [290]. In addition conventional Runge-Kutta schemes [291] and Laplace transformation of the differential equation and subsequently solving numerically a sparse system of equations [292, 293] have been applied [290]. In this work we investigate the time dependence of a quantum impurity (see Sec. 5.2 and Sec. 5.3) using another very successful method: the time evolving block decimation [51, 49]. This method provides a quasi-exact way to time evolve the quantum state due to an efficient state representation in terms of matrix product states. It is especially well suited for one-dimensional systems. Reaching long times is limited by the growth of the entanglement in the quantum state which lets the state representation become more and more inefficient at constant computation time. We do not attempt to give a detailed overview of the method here but refer the interested reader to the excellent existing literature [49]. In this thesis we consider quenches (sudden changes in the Hamiltonian) from an equilibrium state at time $\tau = 0$: $\hat{\mathcal{H}}_0$ to a state under voltage bias $\hat{\mathcal{H}}^> = \hat{\mathcal{H}}_0 + \theta(\tau - \tau_0)\hat{\mathcal{H}}_1$ for times $\tau > \tau_0$. The equilibrium state of $\hat{\mathcal{H}}_0$ is obtained using the DMRG [294, 50, 295]. Then the state is time evolved with $\hat{\mathcal{H}}^>$. For this purpose the quantum state of a one-dimensional system of L sites consisting of quantum objects $\{s_i\} = s_1, s_2, \ldots, s_L$ of local dimension d

$$|\psi\rangle = \sum_{\{s_i\}} c_{\{s_i\}}|\{s_i\}\rangle\,,$$

is expressed in terms of local matrices A^{i,s_i} as a matrix product state

$$|\psi\rangle = \sum_{\{s_i\}}\sum_{\{\mu_i\}} A^{1,s_1}_{\mu_1} A^{2,s_2}_{\mu_1\mu_2} A^{3,s_3}_{\mu_2\mu_3} \ldots A^{L-1,s_{L-1}}_{\mu_{L-2}\mu_{L-1}} A^{L,s_L}_{\mu_L}|\{s_i\}\rangle\,.$$

In TEBD, the time evolution is implemented via a Suzuki-Trotter decomposition [49] on a bipartite lattice writing e.g. in second order

$$e^{-\frac{i}{\hbar}\hat{\mathcal{H}}^> T} = \left(e^{-\frac{i}{\hbar}\hat{\mathcal{H}}_o\frac{\tau}{2}} e^{-\frac{i}{\hbar}\hat{\mathcal{H}}_e\tau} e^{-\frac{i}{\hbar}\hat{\mathcal{H}}_o\frac{\tau}{2}} + O(\tau^3)\right)^{N_\tau}\,,$$

with N_τ time slices of step size $T = N_\tau\tau$. One step of the time evolution proceeds by applying the evolution alternatingly on the odd/even sub lattice $\hat{\mathcal{H}}_{o/e} = \prod_{i\in\{\text{odd/even}\}} \hat{\mathcal{H}}^>_{ii+1}$. MPS time evolution requires the application of local two-site matrix product operators which increases the size of the A matrices $\chi \to d\chi$ in each step. The beauty in the method lies in its efficient state representation which allows to truncate the state based on the least significant entries in the reduced density matrix. This becomes possible by expressing the MPS in its canonical form $A^{i,s_i}_{\mu_{i-1}\mu_i} = \lambda^{i-1}_{\mu_{i-1}}\Gamma^{i,s_i}_{\mu_{i-1}\mu_i}$ where $\lambda^{i-1}_{\mu_{i-1}}$ are the weights of the reduced density matrix ρ which can be

obtained via a Schmidt decomposition of the quantum state into two subsystems between bond i and $i+1$: $|\psi\rangle = \sum_{ij} c_{ij}|i\rangle_A|j\rangle_B = \sum_{\mu} \lambda_\mu |A\rangle_\alpha |B\rangle_\alpha$ using an SVD [296] $c_{ij} = U_{ik}\lambda_{kk}V^\dagger_{kj}$ with $\sum_\alpha \lambda^2_\alpha = 1$. The entanglement entropy $S = -\mathrm{tr}_B\left\{\hat{\rho}_A \ln\left(\hat{\rho}_A\right)\right\} = \sum_\mu \lambda^2_\mu \ln\left(\lambda^2_\mu\right)$ takes its maximum value $\ln(\chi)$ when all states participate equally. In ground state DMRG for one-dimensional systems one finds however that the weights λ^2_μ decay rapidly yielding a small entanglement entropy. In this case a truncation of the state by discarding the smallest weights is efficient. Indeed one finds that the needed dimension of Γ to represent such a state faithfully scales with the surface of the boundary between subsystems A and B. When the one-dimensional Hamiltonian consists of short range couplings only, all correlations need to go through one point which leads to $\chi \propto \ln(L_c)$ where L_c is the spatial correlation length. For time dependent systems this criterion does not hold but is strongly dependent on the system and type of quench. Nevertheless the representation stays efficient up to interesting time-scales. Note that all calculations performed in TEBD simulate a canonical ensemble which can only reach a steady-state locally. For the DMRG and TEBD simulations we adapt a highly parallelized and well tested code developed at the institute in the group of Prof. Hans Gerd Evertz [297, 298, 299, 300, 301, 302].

Starting from linear-response we have arrived via the real time evolution at the problem of addressing the long time limit, the steady-state. The steady-state is especially viable for device engineering. However it is often inaccessible in real time evolution for numerical reasons, see Sec. 5.2. Therefore we generalized approximate quantum many-body cluster methods to nonequilibrium situations which allow to directly access the steady-state properties. The following chapter will provide a detailed overview of the development of the steady-state cluster perturbation theory and its improvements as applied in Sec. 5.7, Sec. 5.5, Sec. 5.6, Sec. 5.8 and Sec. 5.10.

3.3. Steady-state quantum cluster methods

In the past decade, quantum cluster methods have seen quite some success in describing the properties of strongly correlated systems in equilibrium. The central idea of these Green's function based techniques [303] is to construct an approximate solution of an unsolvable large system of interest (typically in the thermodynamic limit) based on an extrapolation of the solution of a small interacting finite size system which solution is accessible [212]. This finite size system can either be used to supply a direct guess for the electronic self-energy $\Sigma(\omega)$ in a perturbative scheme or serve as an artificial reference system constrained by the properties of the physical system.

The general idea is most easily outlined by considering the well known static mean field approach for an interacting translationally invariant model [304]. Within this effective medium approach, appropriate order parameters are chosen for a single site $\hat{\mathcal{H}}\left(\hat{n}_\uparrow.\hat{n}_\downarrow\right) \rightarrow \hat{\widetilde{\mathcal{H}}}\left(\phi_\uparrow.\hat{n}_\downarrow\right)$ and are determined self-consistently via the expectation values of their corresponding operators $\phi_\sigma = \langle \hat{n}_\sigma \rangle$. Likewise in a cluster mean field approach a larger subsystem of size L_C is chosen and the order parameters may acquire a spatial modulation if it lowers the free energy [305] permitting a more accurate description of the relevant degrees of freedom at long wavelengths.

Another very successful effective medium approach is the DMFT [42, 197, 198, 199, 200, 201] which in contrast to the static mean field theory includes information of excited states. In DMFT the system of interest is mapped onto an effective auxiliary impurity system via the noninteracting Green's function. The approximation consists in replacing the lattice self-energy by the self-energy of the impurity, which is local and becomes exact in the limit of infinite dimensions for the single-band Hubbard model [197]. As in the static mean field approach, also the DMFT

has been generalized to its cluster variants to include short scale variations in the self-energy. Including such non-local contributions to the self-energy becomes possible in cluster extensions such as the DCA [306, 307, 308] or the CDMFT [309] or by diagrammatic or RG extensions like DF [310], DΓA [311], 1PI [312] and DMF^{2}RG [313].

A quantum cluster method which proofs highly accurate for static ground state properties is the DMET [314, 315] which performs a cluster embedding based on a Schmidt decomposition into an interacting cluster and an effectively noninteracting environment. The DMET shows good performance with various embedding strategies [316]. The phase diagrams of Hubbard models [317] can be captured well and it has been extended to obtain spectral functions [318].

In the following we focus on the so far unmentioned perturbative quantum cluster methods CPT and VCA which are improved and extended to nonequilibrium problems in this thesis.

Consider a lattice of interacting fermions in the translationally invariant Hubbard model in equilibrium. The atomic limit, or Hubbard-1 approximation [319] is to compute the electronic self-energy Σ considering just one site. This implies a poor representation of electronic correlations. A straight forward generalization is to compute the self-energy from larger subsystems, say $L = 2$, $L = 3$ or $L = 4$ sites. Since the complexity for solving these clusters grows exponentially with their size one can in practice never reach the exact solution at $L \to \infty$. However one can hope for a systematic improvement and a faithful extrapolation of observables into the thermodynamic limit. A methodical formulation for this process is provided by CPT [43, 44] which is the lowest order [320] result of a strong coupling expansion of the self-energy [321]. CPT and its variants are very well outlined in the excellent review articles by D. Sénéchal [322, 323]. Within CPT the given lattice Hamiltonian $\hat{\mathcal{H}}$ is dissolved into finite size clusters in block diagonal form $\hat{H}^C$ by cutting all single-particle bonds connecting them $\hat{H}^I$. The clusters are chosen such that their interacting single-particle Green's functions $g(z)$ can be obtained exactly. Note that $g(z)$ is a block diagonal matrix in site i and spin σ space and a function of a complex energy z. The argument z defines the type of Green's function, $z = i\omega + i0^+$ (where ω is a real energy) yields the retarded Green's component, $z = i\omega - i0^+$ yields the advanced component and $z = i\omega$ yields the Matsubara component [324]. The Green's function $g(z)$ is usually computed by applying full diagonalization [296, 325] or sparse diagonalization like the Lanczos [326] or band-Lanczos method [325]. Also a kernel polynomial method [327], QMC [328] and an MPS base Lanczos scheme [329] were used to reach larger cluster sizes. The single-particle Green's function of the lattice model $G(z)$ is computed from $g(z)$ by reintroducing the cut single-particle bonds perturbatively $T_{ij} = \langle i|\hat{H}_I|j\rangle$

$$G^{-1}(z) = g^{-1}(z) - T\,. \tag{3.9}$$

A derivation of this central CPT equation is possible within the functional integral formalism [36] and can be found in [330]. This Dyson like equation implies that for the self-energy of the lattice system $\Sigma(\omega)$ the self-energy of the clusters is used [331, 329]. CPT becomes exact in non-interacting systems i.e. when the self-energy vanishes. It trivially also yields the exact solution in the atomic limit. CPT is systematically improvable by increasing the cluster size.

CPT has initially seen much success in describing the properties of the fermionic Hubbard model [320, 332, 333]. It has been applied to study the Mott transition in the two dimensional Hubbard model [334, 335, 336] as well as cuprates [337, 338, 339] and to study superconductivity [340], stripe phases in doped anti-ferromagnets [341] as well as in gap states in doped Mott insulators [342]. The dynamics of even lower dimensional structures like ladder systems [343] or purely one-dimensional Hubbard chains [344] featuring spin-charge separation [345] have been obtained using CPT. It has been applied to two- [346] and three- band [347, 348] generalizations of the Hubbard model and to multi-orbital systems [349]. Besides the accurate descriptions of

fullarenes [350], also the recently emerged iron pnictide superconductors [351] have been subject to CPT studies. CPT has seen much success in evaluating the dynamics of Hubbard-Holstein polarons [352, 353, 354, 355, 356]. It has been applied to the SIAM [357, 358] and more recently to study topologically non-trivial phases in the Kitaev-Hubbard model for quantum Hall states [359] and topological invariants in interacting quantum spin Hall systems [360]. CPT has been combined with *ab initio* calculations to study effectively low-dimensional materials [41]. There exist extensions to the t-J model [361, 341] and to pure spin Hamiltonians [362] as well as an improvement based on periodized cluster variables [363].

A variational extension of CPT is provided by the VCA [45] which is based on the SFA [364, 365]. In VCA the self-energy Σ is computed from a reference system which is constructed based on a CPT cluster tiling with optimized single-particle parameters. VCA is discussed in the very good review articles [366, 367, 368, 369] on which this short summary is based. Typically the interacting lattice system $\hat{\mathcal{H}}(x,U)$ is composed of single-particle $\hat{\mathcal{H}}_I(x)$ and two or more particle terms $\hat{\mathcal{H}}_{II}(U)$. The VCA reference system (primed quantities) is defined on the same lattice with the same interaction terms as the original Hamiltonian: $\hat{\mathcal{H}}'(x',U) = \hat{\mathcal{H}}'_I(x') + \hat{\mathcal{H}}_{II}(U)$ but may differ in the one-particle terms x. In the SFA a generalized grand potential functional $\Omega[G,G_0] = \Phi[G] - \mathrm{Tr}\left\{\left(G_0^{-1} - G^{-1}\right)G\right\} + \mathrm{Tr}\left\{\ln\left(-G\right)\right\}$ is constructed from the Luttinger-Ward functional $\frac{\delta\Phi[G]}{\delta G} = \Sigma$ [370]. Systems featuring the same interaction terms have the same "universal" Luttinger-Ward functional which in general cannot be computed exactly. Within VCA the Legendre transformed Luttinger-Ward functional $F[\Sigma] = \Phi[\Sigma] - \mathrm{Tr}\left\{\Sigma G\right\}$ is eliminated by comparing the generalized grand potential for the original $\Omega[\Sigma,G_0] = F[\Sigma] - \mathrm{Tr}\left\{\ln\left(-G_0^{-1} + \Sigma\right)\right\}$ and the reference system $\Omega'[\Sigma,G_0'] = F[\Sigma] - \mathrm{Tr}\left\{\ln\left(-G_0'^{-1} + \Sigma\right)\right\}$:

$$\Omega[\Sigma,G_0] = \Omega'[\Sigma,G_0'] - \mathrm{Tr}\left\{\ln\left(-G'[\Sigma]\right)\right\} + \mathrm{Tr}\left\{\ln\left(-G[\Sigma]\right)\right\}.$$

The functional derivative of the self-energy functional $\Omega[\Sigma,G_0]$ with respect to Σ yields Dyson's equation at the stationary point

$$\frac{\delta\Omega[\Sigma,G_0]}{\delta\Sigma} = -G + \left(G_0^{-1} - \Sigma\right)^{-1} \stackrel{!}{=} 0.$$

The last two equations comprise a set of two equations for the two unknown functions G and Σ. These equations would yield the exact self-energy given the functional derivative could be done in the space of all self-energies. In practice the self-energies are parametrised by those obtainable from the reference system leaving the Luttinger-Ward functional and therefore the interaction therms invariant. This implies that the functional $\Omega[\Sigma,G_0]$ becomes a function of the single-particle parameters x' [371]

$$\Omega(x') = \Omega'(x') + \mathrm{Tr}\left\{\ln\left(-G(x,x')\right)\right\} - \mathrm{Tr}\left\{\ln\left(-G'(x')\right)\right\}, \tag{3.10}$$

where the trace Tr includes a sum over site and spin indices as well as an integral over energy or sum over Matsubara frequencies. The VCA approximation ultimately means restricting the space of available self-energies to those generated by the reference system and its single-particle parametrization. The stationary condition determining the optimal parameters in the restricted space is given by

$$\nabla_{x'}\Omega(x') \stackrel{!}{=} 0.$$

VCA implements a dynamic variational principle since it involves $G(\omega)$ and therefore excited states. The Green's function G is obtained in the CPT approximation. The CPT perturbation

$T = T_0'^{-1} - T_0^{-1}$ contains all inter cluster terms and in addition introduced by VCA the difference in variational parameters $\mathbf{\Delta} \equiv x' - x$, which leaves the original system invariant in the non-interacting case. If additional bath sites are added to the system in the spirit of VCA, the method is often referred to as DIA [322]. We note that the DMFT can also be derived within the SFA.

VCA has seen much success in application to fermionic- [372, 373, 374, 375, 376] and bosonic -lattice systems [377]. In contrast to CPT, VCA capable of describing symmetry broken phases like ferromagnetism [378] or the competition between anti-ferromagnetism and superconductivity [379]. VCA has been extended to the super-fluid phase [380, 381], to extended Hubbard models [46] as well as to disordered systems [382, 383]. The dynamic properties of the fermionic Hubbard model have been studied in detail [384, 385] with a focus on nematicity in two dimensions [386], the Mott transition [374, 387, 388] and superconductivity [389] in cuprates [374]. It has been extended to the three band Hubbard model [390] and to include Hund's coupling [391]. VCA was used to treat organic materials [392] and one-dimensional Hubbard chains [393]. VCA has been applied with great success to the Bose Hubbard model [394, 395, 396], the Falicoff-Kimball model [397], the Periodic Anderson model [398, 399], the Jaynes-Cummings-Lattice model [400], the Tavis-Cummings lattice model [401] and the SIAM [357]. VCA has proven useful to obtain the dynamics of the attractive Hubbard model [402] and heavy fermion superconductors [403]. Recent studies include time reversal symmetry breaking [404], frustrated Hubbard systems [375, 405] and topological aspects [406] of the Kane-Mele-Hubbard model [407, 408], the Hubbard model on a triangular- [409, 410], Kagome- [411, 412] and honeycomb-lattice [360] as well as the Bernevig-Hughes-Zhang model [413]. VCA is capable of describing fermions in optical lattices [414], solid-light systems [415], Dirac fermions [416], polaritons [417] and the compass model [418]. Also realistic materials can be modeled within VCA [419, 420, 421] in an LDA+VCA framework [422, 423, 424, 425, 426, 427, 41]. So far applications to spin systems suffered from severe limitations [428, 429] which have been resolved recently by applying the pseudo particle approach on auxiliary bosons [430, 380, 381].

3.3.1. Steady-state cluster perturbation theory

In the following we are going to present the extension of the CPT and the VCA to nonequilibrium situations, in particular to the steady-state [381]. A common framework is provided by the nonequilibrium self-energy functional theory in [269]. CPT has been generalized to time dependent problems in [431] and has been applied to spin systems [430]. The steady-state CPT was used to study charge transport through molecules [432, 433], also as part of this thesis [65]. The stsVCA has been used to study transport through nano-structures in this thesis ([62, 63] and Sec. 5.10). A generalization to a consistent reference states is provided in Sec. 5.8 as part of this thesis [66].

At first, we will start out by generalizing the CPT to the framework of Keldysh-Schwinger nonequilibrium Green's functions. Second, we discuss a steady-state self-consistency criterion for stsVCA. Third, we outline how a consistent reference state can be found using a QME. Finally we present ideas how the representation of non-interacting reservoirs can be optimized within the interacting clusters.

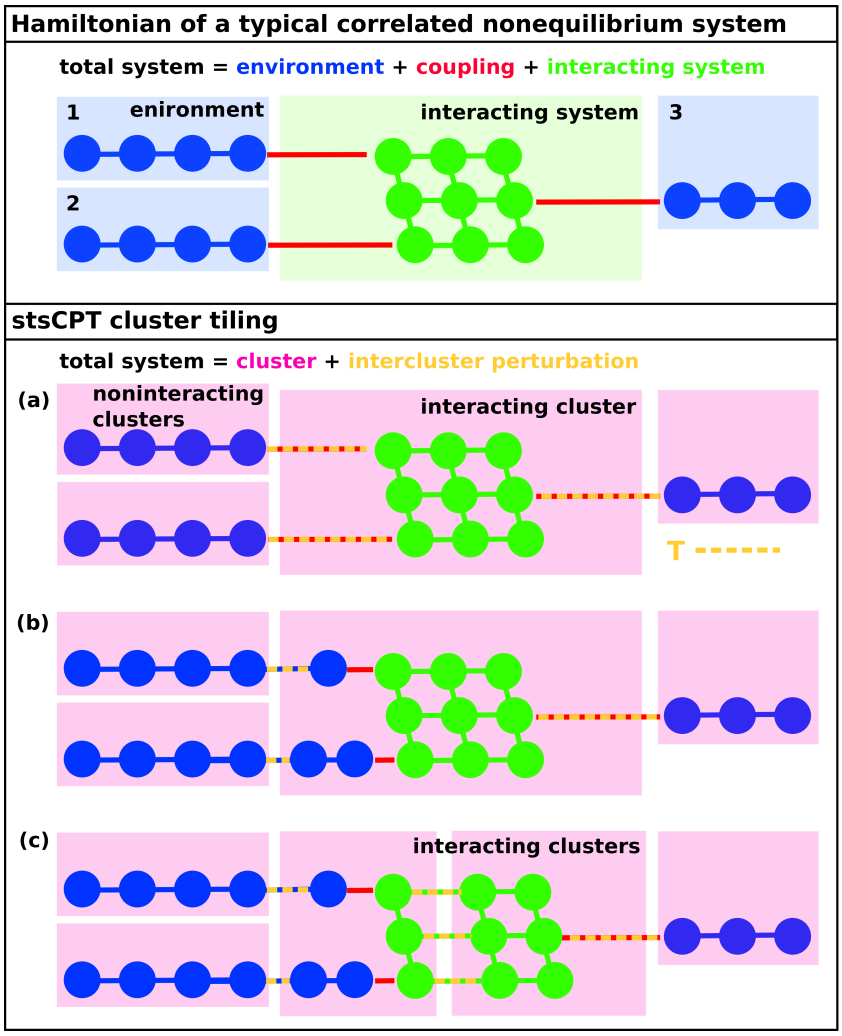

Figure 3.2.: *Setup of a correlated nonequilibrium system.* **(Top)** We discuss finite size fermionic systems coupled to infinite electronic environments. **(Bottom)** For stsCPT, the system is tiled into exactly solvable clusters. Some possible cluster tilings: (a) Tiling at the system-environment coupling. (b) Several sites of the environment are incorporated into the central interacting cluster. (c) For large interacting systems, in addition the interacting cluster can be split into several parts.

Lattice partition

Typical nano- and molecular- junctions can be modelled by a small interacting system $\hat{\mathcal{H}}^S$ tunnel-coupled via $\hat{\mathcal{H}}^{SE}$ to N_λ non-interacting leads of infinite extent $\hat{\mathcal{H}}^E$, see Fig. 3.2 (top)

$$\hat{\mathcal{H}} = \hat{\mathcal{H}}^S + \hat{\mathcal{H}}^E + \hat{\mathcal{H}}^{SE} . \tag{3.11}$$

The interacting system Hamiltonian $\hat{\mathcal{H}}^S$ typically describes the electronic degrees of freedom of e.g. a molecule, a nano-structure or a correlated layer in terms of the fermionic creation/annihilation operators $f^\dagger_{i\sigma}/f_{i\sigma}$ on site i with spin σ. The non-interacting environment Hamiltonian $\hat{\mathcal{H}}^E$ models free electron reservoirs i.e. electronic leads

$$\hat{\mathcal{H}}^E = \sum_{\lambda k\sigma} \epsilon_{\lambda k\sigma} c^\dagger_{\lambda k\sigma} c_{\lambda k\sigma} .$$

Lead λ is described by the dispersion relation $\epsilon_{\lambda k\sigma}$ of the quasi-particles $c^\dagger_{\lambda k\sigma}/c_{\lambda k\sigma}$. The system and environment are coupled by single-particle tunnelling amplitudes $t'_{i\lambda k\sigma}$

$$\hat{\mathcal{H}}^{SE} = \sum_{i\lambda k\sigma} \left(t'_{i\lambda k\sigma} f^\dagger_{i\sigma} c_{\lambda k\sigma} \right) + h.c. .$$

For stsCPT one partitions $\hat{\mathcal{H}}$, Eq. (3.11), into individually solvable clusters $\hat{\mathcal{H}}^C$ and single-particle terms $\hat{\mathcal{H}}^I$ mediating between them, see Fig. 3.2 (a)

$$\hat{\mathcal{H}}(t) \stackrel{a.}{=} \hat{\mathcal{H}}^C + \theta(t - t_0)\hat{\mathcal{H}}^I . \tag{3.12}$$

Formally we consider the inter-cluster perturbation $\hat{\mathcal{H}}^I$ to be switched on at a time t_0. The most natural and simple cluster decomposition would be into a block diagonal cluster Hamiltonian $\hat{\mathcal{H}}^C$ consisting of the interacting system $\hat{\mathcal{H}}^S$ and the non-interacting leads $\hat{\mathcal{H}}^E$ which leaves the system-environment coupling $\hat{\mathcal{H}}^{SE}$ as inter-cluster perturbation $\hat{\mathcal{H}}^I$. In general it is possible and sometimes necessary or desirable to choose a different cluster tiling. A different tiling becomes necessary when $\hat{\mathcal{H}}^S$ is too large and its full solution is prohibited. In this case $\hat{\mathcal{H}}^S$ has to be split into several parts by removing single-particle hoppings which then enter $\hat{\mathcal{H}}^I$, see Fig. 3.2 (c). As mentioned above, the stsCPT approximation is the lowest order cluster expansion in the electronic self-energy. Electronic correlations in the cluster can be taken into account to higher accuracy when some parts of the non-interacting leads are assigned to $\hat{\mathcal{H}}^C$ (and also the according $\hat{\mathcal{H}}^{SE}$). The new inter-cluster perturbation $\hat{\mathcal{H}}^I$ then consists of a set of cut intra-environment hoppings, see Fig. 3.2 (b).

Nonequilibrium Green's functions

In the following we briefly review the underlying framework of the stsCPT, the Keldysh-Schwinger nonequilibrium Green's function formalism. Within this technique relations for steady-state perturbation theory are retained which are formally equivalent to their well known equilibrium counterparts. The equilibrium time-ordering becomes replaced by a formal contour integration which boils down to a 2×2 matrix structure for Green's functions in Keldysh space. The Keldysh-Schwinger Green's function technique was proposed by Keldysh [434], although earlier related approaches exist by Schwinger [435] and by Feynman and Vernon [436]. This chapter is based based on the book by Haug and Jauho [437] and the review article by Rammer and Smith [438]. The presented description is tailored towards fermionic systems. A similar presentation is also available in the books [439, 440, 441, 442, 443], review articles [444, 445, 446] and lecture notes

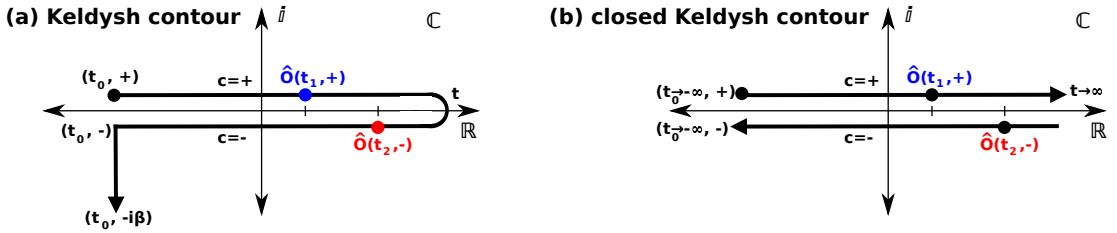

Figure 3.3.: *Keldysh contour.* **(a)** Keldysh (interaction) contour $\mathcal{K}$. **(B)** Keldysh closed path contour $\mathcal{C}$ for the steady-state.

[447, 448, 449, 450].

The dynamics of of the entire system defined by $\hat{\mathcal{H}}$, Eq. (3.12), is given by the von-Neumann equation

$$i\dot{\hat{\rho}} = \left[\hat{\mathcal{H}}, \hat{\rho}\right]_- , \tag{3.13}$$

where the commutator is defined as $\left[\hat{A}, \hat{B}\right]_- = \hat{A}\hat{B} - \hat{B}\hat{A}$. The formal solution of the von-Neumann equation defines the unitary time evolution operator ($\hbar \equiv 1$)

$$\hat{U}(t, t_0) = \hat{\hat{T}} e^{-i\int_{t_0}^{t} dt' \hat{\mathcal{H}}(t')} , \tag{3.14}$$

where the time-ordering operator

$$\begin{aligned}\hat{\hat{T}}\left(\hat{A}(t)\hat{B}(t')\right) &= \begin{cases} \hat{A}(t)\hat{B}(t') & \text{if } t > t' \\ \hat{B}(t')\hat{A}(t) & \text{if } t' > t \end{cases} \\ &= \theta(t-t')\,\hat{A}(t)\hat{B}(t') - \theta(t'-t)\,\hat{B}(t')\hat{A}(t) ,\end{aligned}$$

orders the operators with increasing time from right to left.

We start from a system in thermal equilibrium for times $t \leq t_0$ defined by the disconnected cluster Hamiltonian $\hat{\mathcal{H}}(t \leq t_0) = \hat{\mathcal{H}}^C$ which is described by the density operator

$$\hat{\rho}^C = \frac{e^{-\beta\hat{\mathcal{H}}^C}}{\mathrm{tr}\left\{e^{-\beta\hat{\mathcal{H}}^C}\right\}} ,$$

with inverse temperature $\beta = \frac{1}{T}$ ($k_B \equiv 1$). In the following it is assumed that the interacting part of the Hamiltonian is switched on adiabatically long before all other processes begin. For times $t > t_0$ we switch on the inter-cluster perturbation in addition $\hat{\mathcal{H}}(t > t_0) = \hat{\mathcal{H}}$ and seek to evaluate nonequilibrium observables

$$\langle \hat{O}(t) \rangle = \mathrm{tr}\left\{\hat{\rho}^C \hat{O}_H(t)\right\} , \tag{3.15}$$

where the Heisenberg time evolution with respect to the full Hamiltonian is given by

$$\hat{O}_H(t) = \hat{U}(t_0, t)\hat{O}\hat{U}(t, t_0) .$$

We denote operators in the Schrödinger picture without a subscript H. The well-known repre-

sentation of the expectation value on the Keldysh contour is obtained by rewriting the density operator at time t_0 in terms of time evolution operators, Eq. (3.14)

$$\hat{U}(t_0 - i\beta, t_0) = \hat{\hat{T}} e^{-i\int_{t_0}^{t_0-i\beta} dt' \hat{\mathcal{H}}(t')} = e^{-\beta\hat{\mathcal{H}}(t_0)} = e^{-\beta\hat{\mathcal{H}}^C} = \hat{\rho}^C \,.$$

Inserting these expressions into Eq. (3.15) one finds

$$\langle \hat{O}(t) \rangle = \frac{\mathrm{tr}\left\{\hat{U}(t_0 - i\beta, t_0)\hat{U}(t_0, t)\hat{O}\hat{U}(t, t_0)\right\}}{\mathrm{tr}\left\{\hat{U}(t_0 - i\beta, t_0)\right\}} = \frac{\mathrm{tr}\left\{\hat{\hat{T}}_{\mathcal{K}}\left(e^{-i\int_{\mathcal{K}} dt' \hat{\mathcal{H}}(t')}\hat{O}\right)\right\}}{\mathrm{tr}\left\{\hat{U}(t_0 - i\beta, t_0)\right\}} \,, \tag{3.16}$$

where we have formally introduced the integral on the Keldysh-contour $\mathcal{K}$ which renders the treatment of nonequilibrium Green's functions structurally equivalent to the equilibrium case. Instead of the equilibrium time ordering $\hat{\hat{T}}$, the contour-ordering operator

$$\hat{\hat{T}}_{\mathcal{K}}\left(\hat{A}(t,c)\hat{B}(t',c')\right) = \begin{cases} \hat{A}(t,c)\hat{B}(t',c') & \text{if } \{t,c\} > \{t',c'\} \\ \hat{B}(t',c')\hat{A}(t,c) & \text{if } \{t',c'\} > \{t,c\} \end{cases} ,$$

orders operators according to the path on the Keldysh contour $\mathcal{K}$. As shown in Fig. 3.3 (a) the contour starts at the upper branch $c = +$ at time t_0 to t and runs back on the lower branch $c = -$ from at time t to t_0. The initial correlations are included in the last part which runs parallel to the imaginary axis from t_0 to $t_0 - i\beta$.

This last part plays an important role in the description of time dependent transient phenomena. It vanishes if interactions are turned on adiabatically. We are interested in the description of steady-state transport. The steady-state itself, in general, does not depend on the way how it is reached. Therefore it seems plausible that the initial correlations have been washed out and the information has been transported away into the infinite reservoirs [447]. This furthermore allows us to extend the initial time to $t_0 \to -\infty$ which simplifies further treatment. In this case the Keldysh contour $\mathcal{K}$ simplifies to the closed Keldysh-contour $\mathcal{C}$, see Fig. 3.3 (b), which runs at the upper branch $c = +$ from time $-\infty$ to $t \to +\infty$ and on the lower branch $c = -$ back to time time $-\infty$. Steady-state observables then read

$$\langle \hat{O} \rangle_{\mathrm{sts}} := \langle \hat{O}(t \to +\infty) \rangle = \langle \hat{U}(-\infty, +\infty)\hat{O}\hat{U}(+\infty, -\infty) \rangle = \langle \hat{\hat{T}}_{\mathcal{C}}\left(e^{-i\int_{\mathcal{C}} dt' \hat{\mathcal{H}}(t')}\hat{O}\right) \rangle \,.$$

This expression can be generalized to the single-particle Green's function, which is given by

$$\begin{aligned} g^{c_1 c_2}(i, t_1; j, t_2) &= -i\langle f_i(t_1) f_j^\dagger(t_2) \rangle_{\mathrm{sts}} \\ &= -i\mathrm{tr}\left\{\hat{U}(-\infty, -; t_1, c_1) f_i(t_1, c_1) \hat{U}(t_1, c_1; t_2, c_2) f_j^\dagger(t_2, c_2) \hat{U}(t_2, c_2; -\infty, +)\right\} \,. \end{aligned}$$

Here i, j denote compound indices for all the fermionic degrees of freedom e.g. site or spin. When replacing the contour integral by real time integrals (analytic continuation) this Green's function takes on one of the four possible combinations:

i) The time-ordered (causal) Green's function ($c_1 = +, c_2 = +$)

$$g_{ij}^T(t_1, t_2) = -i\langle \hat{\hat{T}}\left(f_i(t_1) f_j^\dagger(t_2)\right) \rangle = g^{++}(i, t_1; j, t_2) \,,$$

which is known from equilibrium perturbation theory.

ii) Fully inverting the "direction" one finds the anti-time-ordered Green's function ($c_1 = -, c_2 = -$)

$$g_{ij}^{\bar{T}}(t_1,t_2) = -i\langle \hat{\bar{T}}\left(f_i(t_1) f_j^\dagger(t_2)\right)\rangle = g^{--}(i,t_1;j,t_2)\,.$$

iii) The lesser Green's function ($c_1 = +, c_2 = -$)

$$g_{ij}^{<}(t_1,t_2) = i\langle f_j^\dagger(t_2) f_i(t_1)\rangle = g^{+-}(i,t_1;j,t_2)\,,$$

describes the propagation of a hole in the system.

iv) While the greater Green's function ($c_1 = -, c_2 = +$)

$$g_{ij}^{>}(t_1,t_2) = -i\langle f_i(t_1) f_j^\dagger(t_2)\rangle = g^{-+}(i,t_1;j,t_2)\,,$$

describes the propagation of a particle.

Out of these four components only three are independent and a convenient rotation is given in terms of:

i) The retarded Green's function

$$g_{ij}^{R}(t_1,t_2) = -i\theta(t_1-t_2)\langle\left[f_i(t_1), f_j^\dagger(t_2)\right]_+\rangle = \theta(t_1-t_2)\left(g_{ij}^{>}(t_1,t_2) - g_{ij}^{<}(t_1,t_2)\right)\,, \tag{3.17}$$

with the anti-commutator $\left[\hat{A}.\hat{B}\right]_+ = \hat{A}\hat{B} + \hat{B}\hat{A}$ and the usual Heaviside function, see App. C.

$$\theta(t) = \begin{cases} 0: & t<0 \\ 1: & t \geq 0 \end{cases}\,.$$

Notice that equivalently $g^R = g^T - g^< = g^> - g^{\bar{T}}$.

ii) The advanced Green's function

$$g_{ij}^{A}(t_1,t_2) = i\theta(t_2-t_1)\langle\left[f_i(t_1), f_j^\dagger(t_2)\right]_+\rangle = \theta(t_2-t_1)\left(g_{ij}^{<}(t_1,t_2) - g_{ij}^{>}(t_1,t_2)\right)\,.$$

Note that equivalently $g^A = g^T - g^> = g^< - g^{\bar{T}}$.

iii) The Keldysh Green's function

$$g_{ij}^{K}(t_1,t_2) = -i\langle\left[f_i(t_1), f_j^\dagger(t_2)\right]_-\rangle = g_{ij}^{<}(t_1,t_2) + g_{ij}^{>}(t_1,t_2)\,. \tag{3.18}$$

Notice that $g^R - g^A = g^> - g^<$, $g^T - g^{\bar{T}} = g^R + g^A$ and $g^T + g^{\bar{T}} = g^> + g^< = g^K$.

Within this representation the Green's function in the closed Keldysh space is conveniently defined in matrix notation

$$\widetilde{g}_{ij}(t_1,t_2) = \begin{pmatrix} g_{ij}^R(t_1,t_2) & g_{ij}^K(t_1,t_2) \\ 0 & g_{ij}^A(t_1,t_2) \end{pmatrix}\,.$$

Its components obey the symmetries $\left(g^R(t_1,t_2)\right)^\dagger = g^A(t_2,t_1)$ and $\left(G^K(t_1,t_2)\right)^\dagger = -G^K(t_2,t_1)$. In the steady-state the system regains its time-translational invariance and therefore the Green's functions do only depend on the time difference $\tau = t_1 - t_2$. Like in non-relativistic equilibrium

systems one finds a more convenient representation in terms of the Fourier transformed

$$\widetilde{g}_{ij}(\omega) = \mathcal{F}[\widetilde{g}_{ij}(\tau)] = \int_{-\infty}^{\infty} d\tau\, e^{+i\omega\tau}\widetilde{g}_{ij}(\tau)\,,$$

$$\widetilde{g}_{ij}(\tau) = \mathcal{F}^{-1}[\widetilde{g}_{ij}(\omega)] = \frac{1}{2\pi}\int_{-\infty}^{\infty} d\omega\, e^{-i\omega\tau}\widetilde{g}_{ij}(\omega)\,,$$

Green's functions

$$\widetilde{g}_{ij}(\omega) = \begin{pmatrix} g_{ij}^R(\omega) & g_{ij}^K(\omega) \\ 0 & g_{ij}^A(\omega) \end{pmatrix}. \tag{3.19}$$

Single-particle Green's function

Equilibrium CPT is based on a perturbative expansion of the electronic self-energy Σ. This expansion remains formally equivalent in the steady-state when replacing the equilibrium quantities by their corresponding nonequilibrium counterparts, the 2×2 Keldysh space steady-state Green's function $\widetilde{g}(\omega)$ (Eq. (3.19)) and self-energy $\widetilde{\Sigma}(\omega)$. The single-particle Green's function $\widetilde{G}(\omega)$ of the entire nonequilibrium system in the steady-state as described by $\hat{\mathcal{H}}$ (Eq. (3.11)) is given by an expression analogously to the equilibrium case (Eq. (3.9))

$$\widetilde{G}(\omega)^{-1} = \widetilde{g}(\omega)^{-1} - \widetilde{T}\,, \tag{3.20}$$

with the inter-cluster perturbation in Keldysh space $T^R = T^A = T$, $T^K = 0$. In our notation all Green's functions $g^\alpha(\omega)$ are block diagonal in the individual clusters and for non-interacting infinite systems only one entry at the coupling site is needed [329]. Besides the usual retarded Green's function $g^R(\omega)$ (Eq. (3.17)) also the Keldysh component $g^K(\omega)$ (Eq. (3.18)) needs to be evaluated. The advanced component follows $g^A(\omega) = \left(g^R(\omega)\right)^\dagger$. Note that for the equilibrium starting point of decoupled clusters, their respective Keldysh component is provided by the fluctuation-dissipation result $g^K(\omega) = \left(g^R(\omega) - g^A(\omega)\right)(1 - 2p_{\mathrm{FD}}(\omega, T, \mu))$, with the Fermi-Dirac distribution $p_{\mathrm{FD}}(\omega, T, \mu) = \frac{1}{1+e^{\frac{(\omega-\mu)}{T}}}$ at an initial temperature T and a chemical potential μ [36].

Evaluation of observables

Within stsCPT single-particle observables can be computed from the Keldysh Green's function $G^K(\omega)$ (Eq. (3.20)). In the stsCPT approximation the single-particle density matrix

$$\kappa_{ij} = \frac{\delta_{ij}}{2} - \frac{i}{2}\int_{-\infty}^{\infty}\frac{d\omega}{2\pi}G_{ij}^K(\omega)\,, \tag{3.21}$$

can be expressed in terms of the retarded CPT Green's function

$$\kappa_{ij} = \frac{\delta_{ij}}{2} - \frac{i}{2}\int_{-\infty}^{\infty}\frac{d\omega}{2\pi}\Big(G_{in}^R(\omega)P_{nj}(\omega) - P_{in}(\omega)(G_{jn}^R(\omega))^* + G_{in}^R(\omega)\left([P(\omega), T]_-\right)_{nm}(G_{jm}^R(\omega))^*\Big),$$

The last line holds within stsCPT, we use the Einstein summation convention and $P_{ij}(\omega) = \delta_{ij}(1 - 2p_{\mathrm{FD}}(\omega, T_i, \mu_i))$.

Important steady-state observables of transport experiments can be readily read off from κ_{ij}. Introducing the spin label explicitly, the site resolved charge density is provided by the diagonal elements $\langle n_i \rangle = \sum_\sigma \kappa_{ii\sigma}$ and the magnetization by $\langle m_i \rangle = \frac{1}{2}(\kappa_{ii\uparrow} - \kappa_{ii\downarrow})$.

The current $\langle j_{\langle ij \rangle} \rangle$ between nearest-neighbour sites $\langle ij \rangle$ is related to the imaginary part of κ_{ij} and reads in symmetrized Meir-Wingreen form [228]

$$\langle j_{\langle ij \rangle} \rangle = \frac{e}{2\hbar} \left(h_{ij}\kappa_{ij} - h_{ji}\kappa_{ji} \right) ,$$

where h_{ij} is the single-particle Hamiltonian.

Equivalently, the transmission current between two environments $\lambda = 1, 2$ can be evaluated in the Landauer-Büttiker form [437, 17, 432]

$$\langle j_{1/2} \rangle = \frac{e}{\hbar} \int_{-\infty}^{\infty} \frac{d\omega}{2\pi} W(\omega) \mathrm{tr} \left\{ \mathcal{T}(\omega) \right\} ,$$

with the transport window

$$W(\omega) = p_{\mathrm{FD}}(\omega, T_1, \mu_1) - p_{\mathrm{FD}}(\omega, T_2, \mu_2) ,$$

and the transmission function

$$\mathcal{T}(\omega) = G^R(\omega) \Gamma_1(\omega) \left(G^R(\omega) \right)^\dagger \Gamma_2(\omega) ,$$

which is given in terms of $G^R(\omega) = \left((g^R(\omega))^{-1} - (\widetilde{\Sigma}_1 + \widetilde{\Sigma}_2) \right)^{-1}$ where the lead broadening functions of lead λ projected onto the system sites i, j are $\widetilde{\Sigma}_{\lambda ij} = T_{i\lambda} g^R_{\lambda\lambda} T_{\lambda j}$ and $\Gamma_\lambda = -2\Im\mathrm{m}\left(\widetilde{\Sigma}_\lambda\right)$.

3.3.2. Steady-state variational cluster approach

In the following we present an extension of the plain stsCPT which allows for a better representation of the electronic self-energy and therefore higher accuracy. In equilibrium, the VCA provides a dynamic variational principle to find an optimized unperturbed reference state using CPT. The strategy for the steady-state is formally equivalent to the equilibrium VCA, see the beginning of Ch. 3.3. One parametrizes the self-energy by a set of single-particle parameters $\boldsymbol{\Delta}$ which span the search-space for the optimal self-energy. The cluster partitioned Hamiltonian $\hat{\mathcal{H}}$ (Eq. (3.12)) does not change if we add a single-particle operator $\hat{\Delta}$ to the cluster Hamiltonian $\hat{\mathcal{H}}^C$ and subtract them again from the inter-cluster perturbation $\hat{\mathcal{H}}^I$

$$\begin{aligned} \hat{\mathcal{H}}^C(\boldsymbol{\Delta}) &= \hat{\mathcal{H}}^C + \hat{\Delta} , \\ \hat{\mathcal{H}}^I(\boldsymbol{\Delta}) &= \hat{\mathcal{H}}^I - \hat{\Delta} . \end{aligned}$$

In particular

$$\hat{\Delta} = \sum_{\delta_1 \delta_2} \Delta_{\delta_1 \delta 2} f^\dagger_{\delta_1} f_{\delta_2} , \tag{3.22}$$

see Fig. 3.4 (top). As in equilibrium VCA, the indices $\delta \in \{\delta_1, \ldots, \delta_{L_C}\}$ usually refer to actual system degrees of freedom. Then $\Delta_{\delta_i \delta j}$ renormalizes the according single-particle parameter of the system in $\hat{\mathcal{H}}^C$. Another possibility is to add L_B auxiliary bath sites $\delta \in \{\delta_{L_C+1}, \ldots, \delta_{L_C+L_B}\}$ described by $f^\dagger_\delta / f_\delta$ which may acquire a finite coupling to the system and an on-site energy

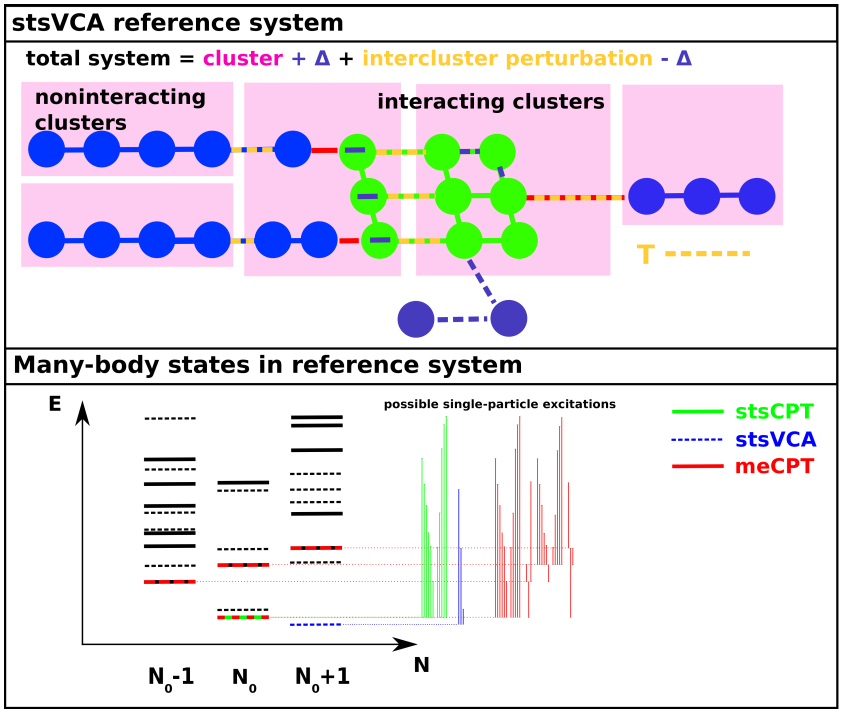

Figure 3.4.: *Reference state.* **(Top)** The stsVCA reference state. **(Bottom)** Contributing many-body states in stsCPT, stsVCA and meCPT.

during the stsVCA self-consistency cycle.

Generalizing the expression for the equilibrium generalized grand potential Eq. (3.10) to time dependent problems, a formally analogous expression is obtained on the Keldysh contour [269]. In the steady-state one obtains

$$\begin{aligned}\Omega[\widetilde{\Sigma}(\boldsymbol{\Delta})] &= \Omega' + \mathrm{Tr}\left\{\ln\left(\widetilde{G}\right)\right\} - \mathrm{Tr}\left\{\ln\left(\widetilde{g}\right)\right\} \\ &= \Omega'(\boldsymbol{\Delta}) + \mathrm{Tr}\left\{\ln\left(\left(\widetilde{G}_0^{-1} - \widetilde{\Sigma}(\boldsymbol{\Delta})\right)^{-1}\right)\right\} - \mathrm{Tr}\left\{\ln\left(\left(\widetilde{g}_0^{-1} - \widetilde{\Sigma}(\boldsymbol{\Delta})\right)^{-1}\right)\right\},\end{aligned}$$

with the VCA variational principle

$$\frac{\partial\Omega[\widetilde{\Sigma}(\boldsymbol{\Delta})]}{\partial\widetilde{\Sigma}(\boldsymbol{\Delta})} \stackrel{!}{=} 0 = \mathrm{Tr}\left\{\frac{\delta\widetilde{\Sigma}(\boldsymbol{\Delta})}{\delta\boldsymbol{\Delta}}\left(\widetilde{G} - \widetilde{g}\right)\right\} = \int \frac{d\omega}{2\pi}\widetilde{\mathrm{tr}}\left\{\widetilde{\sigma}_x \frac{\partial\widetilde{\Sigma}(\omega,\boldsymbol{\Delta})}{\partial\boldsymbol{\Delta}}\left(\widetilde{G}(\omega) - \widetilde{g}(\omega)\right)\right\}, \tag{3.23}$$

where $\widetilde{\sigma}_x = \begin{pmatrix} 0 & 1 \\ 1 & 0 \end{pmatrix}$ is the first Pauli matrix in Keldysh space, see App. B. Noting that $\widetilde{\Sigma}$ is only different from zero on the sites of the interacting clusters, denoted by c. One obtains for the trace in Eq. (3.23)

$$\begin{aligned}&\widetilde{\mathrm{tr}}\left\{\begin{pmatrix} 0 & 1 \\ 1 & 0 \end{pmatrix}\begin{pmatrix} \frac{\partial}{\partial\boldsymbol{\Delta}}\Sigma^R & \frac{\partial}{\partial\boldsymbol{\Delta}}\Sigma^K \\ 0 & \frac{\partial}{\partial\boldsymbol{\Delta}}\Sigma^A \end{pmatrix}\begin{pmatrix} \left(G^R - g^R\right) & \left(G^K - g^K\right) \\ 0 & \left(G^A - g^A\right) \end{pmatrix}\right\} \\ &= \mathrm{tr}\left\{\left(\frac{\partial}{\partial\boldsymbol{\Delta}}\Sigma^R_{cc}\right)\left(G^K_{cc} - g^K_{cc}\right) + \left(\frac{\partial}{\partial\boldsymbol{\Delta}}\Sigma^K_{cc}\right)\left(G^A_{cc} - g^A_{cc}\right)\right\}.\end{aligned} \tag{3.24}$$

Using Dyson's equation [36] in Keldysh space

$$\widetilde{\Sigma} = \widetilde{G}_0^{-1} - \widetilde{G}^{-1},$$

and the CPT equation (Eq. (3.20)) for the non-interacting and interacting Green's functions $\widetilde{G}_0^{-1}$ and $\widetilde{G}^{-1}$

$$\begin{aligned}\widetilde{G}_0^{-1} &= \widetilde{g}_0^{-1} - \widetilde{T}, \\ \widetilde{G}^{-1} &= \widetilde{g}^{-1} - \widetilde{T},\end{aligned}$$

the stsCPT self-energy takes the form

$$\widetilde{\Sigma} = \widetilde{g}_0^{-1} - \widetilde{g}^{-1}.$$

Its retarded (upper left) and Keldysh (upper right) components can be read off from the general structure of an inversion of a matrix $\widetilde{\gamma}$ in Keldysh space

$$\widetilde{\gamma}^{-1} = \begin{pmatrix} \left(\gamma^R\right)^{-1} & -\left(\gamma^R\right)^{-1}\gamma^K\left(\gamma^A\right)^{-1} \\ 0 & \left(\gamma^A\right)^{-1} \end{pmatrix}.$$

Using the expression for the trace (Eq. (3.24)) and plugging in the explicit relation for the self-

energy, the VCA variational principle (Eq. (3.23)) takes the form

$$\frac{\partial\Omega[\widetilde{\Sigma}(\boldsymbol{\Delta})]}{\partial\widetilde{\Sigma}(\boldsymbol{\Delta})} = 0 = \mathrm{tr}\Bigg\{ \int \frac{d\omega}{2\pi}\Bigg(\frac{\partial}{\partial\boldsymbol{\Delta}}\Big(\big(g_0^R\big)^{-1} - \big(g^R\big)^{-1} \Big)_{cc} \big(G_{cc}^K - g_{cc}^K\big) + \Big(\frac{\partial}{\partial\boldsymbol{\Delta}}\Big(-\big(g_0^R\big)^{-1} g_0^K \big(g_0^A\big)^{-1} + \big(g^R\big)^{-1} g^K \big(g^A\big)^{-1} \Big)\Big)_{cc} \big(G_{cc}^A - g_{cc}^A\big) \Bigg)\Bigg\},$$

where $\big(\widetilde{g}^{-1}\big)_{cc}^K = \Big(-\big(g_0^R\big)^{-1} g_0^K \big(g_0^A\big)^{-1}\Big)_{cc} = 0$ for sites c of the interacting finite size clusters. So we are left with

$$\frac{\partial\Omega[\widetilde{\Sigma}(\boldsymbol{\Delta})]}{\partial\widetilde{\Sigma}(\boldsymbol{\Delta})} = 0 = \mathrm{tr}\left\{ \int \frac{d\omega}{2\pi}\left(\frac{\partial\big(g_{0,cc}^R\big)^{-1}}{\partial\boldsymbol{\Delta}} - \frac{\partial\big(g_{cc}^R\big)^{-1}}{\partial\boldsymbol{\Delta}} \right)\big(G_{cc}^K - g_{cc}^K\big) \right\}.$$

Further considering the expression for $\hat{\Delta}$ (Eq. (3.22)) one finds $\frac{\partial}{\partial\boldsymbol{\Delta}}(g_0^R(\boldsymbol{\Delta}))^{-1} = -\delta_{i\delta_1}\delta_{j\delta_2}$, where δ_i are sites out of c at which a variational parameter acts, and finally obtains

$$\begin{aligned}
\frac{\partial\Omega[\widetilde{\Sigma}(\boldsymbol{\Delta})]}{\partial\widetilde{\Sigma}(\boldsymbol{\Delta})} = 0 &= -\mathrm{tr}\left\{ \int \frac{d\omega}{2\pi}\left(\delta_{i\delta_1}\delta_{j\delta_2} + \frac{\partial\big(g_{cc}^R\big)^{-1}}{\partial\boldsymbol{\Delta}} \right)\big(G_{cc}^K - g_{cc}^K\big) \right\} \\
&= -\int \frac{d\omega}{2\pi} G_{\delta_1\delta_2}^K(\omega) + \int \frac{d\omega}{2\pi} g_{\delta_1\delta_2}^K(\omega) - \mathrm{tr}\left\{ \int \frac{d\omega}{2\pi} \frac{\partial\big(g_{cc}^R\big)^{-1}}{\partial\boldsymbol{\Delta}} \big(G_{cc}^K - g_{cc}^K\big) \right\} \\
&= -\left(\frac{\delta_{\delta_1\delta_2}}{2} - \frac{i}{2}\int \frac{d\omega}{2\pi} G_{\delta_1\delta_2}^K(\omega) \right) + \left(\frac{\delta_{\delta_1\delta_2}}{2} - \frac{i}{2}\int \frac{d\omega}{2\pi} g_{\delta_1\delta_2}^K(\omega) \right) \\
&\quad + \frac{i}{2}\mathrm{tr}\left\{ \int \frac{d\omega}{2\pi} \frac{\partial\big(g_{cc}^R\big)^{-1}}{\partial\boldsymbol{\Delta}} \big(G_{cc}^K - g_{cc}^K\big) \right\} \\
&= -\kappa_{\delta_1\delta_2}^{sts} + \kappa_{\delta_1\delta_2}^{cluster} + \frac{i}{2}\mathrm{tr}\left\{ \int \frac{d\omega}{2\pi} \frac{\partial\big(g_{cc}^R\big)^{-1}}{\partial\boldsymbol{\Delta}} \big(G_{cc}^K - g_{cc}^K\big) \right\}
\end{aligned}$$

where $\kappa_{\delta_1\delta_2}^{sts}/\kappa_{\delta_1\delta_2}^{cluster}$ are the elements of the steady-state/reference-state single-particle density matrix as found from Eq. (3.21). Eq. (3.23) provides a system of equations which roots determine the optimal stsVCA parameters $\boldsymbol{\Delta}_{\mathrm{opt.}}$. The last term is often small. Neglecting it leads to an intuitive, alternative self-consistency criterion, as suggested in [268], in terms of the single-particle density matrices of the steady-state and the reference system. The remaining term can be recast in the form $\kappa_{\delta_1\delta_2}^{sts} = \kappa_{\delta_1\delta_2}^{cluster}$ which determines those variational parameters which make the reference system as similar as possible to the steady-state in terms of single-particle expectation values. The alternative self-consistency criterion can be written in compact form [268]

$$0 \stackrel{!}{=} \mathrm{Tr}\left\{ \frac{\partial\widetilde{g}_0^{-1}(\boldsymbol{\Delta})}{\partial\boldsymbol{\Delta}} \big(\widetilde{G} - \widetilde{g}\big) \right\} = \int \frac{d\omega}{2\pi} \widetilde{\mathrm{tr}}\left\{ \widetilde{\sigma}_x \frac{\partial\widetilde{g}_0^{-1}(\omega,\boldsymbol{\Delta})}{\partial\boldsymbol{\Delta}} \big(\widetilde{G}(\omega) - \widetilde{g}(\omega)\big) \right\}, \tag{3.25}$$

compare to the starting point Eq. (3.23).

For terms in $\hat{\Delta}$ which correspond to system degrees of freedom this procedure requires the

reference system to behave as similar as possible to the steady-state in terms of the single-particle expectation value of the variational parameters. Note that when $\hat{\Delta}$ includes the coupling and on-site energies of an infinite number of bath sites, the self-consistency Eq. (3.25) becomes equivalent to nonequilibrium cluster DMFT.

3.3.3. Consistent reference state

In stsCPT $\widetilde{g}(\omega)$ is computed based on an equilibrium reference state obtained for $t < t_0$ i.e. for $\hat{\mathcal{H}}^S$. For the interacting finite size regions S, one typically chooses a temperature $T_S = 0$ and a chemical potential μ_S in-between the ones of the non-interacting leads. For this setup the reference state $|\psi\rangle^S$ is then obtained as the pure zero temperature ground state of $\hat{\mathcal{H}}^S$. This arbitrary choice of the chemical potential μ_S and temperature T_S for finite size interacting clusters would not influence the final solution in an ideal exact treatment. However, since stsCPT is perturbative in $\hat{\mathcal{H}}^I$, the stsCPT solution $\widetilde{G}(\omega)$ will depend on details of the reference state.

As explained above, the stsVCA reference state is improved by variational parameters determined by a dynamic variational principle. The stsVCA reference state, however, again is an equilibrium state $\hat{\rho}^S(\mathbf{\Delta}_{\text{opt.}})$ obtained from $\hat{\mathcal{H}}^S(\mathbf{\Delta}_{\text{opt.}})$. The chemical potential μ_S can be optimized in the stsVCA self-consistency by including it in $\hat{\Delta}$. In principle also an optimization of T_S would be possible but is numerically too demanding [451, 452, 453]. In this way the stsVCA reference state $|\psi\rangle^C$ is typically obtained as the pure zero temperature ground state of $\hat{\mathcal{H}}^S(\mathbf{\Delta}_{\text{opt.}})$.

In the following we pursue a very simple idea to generalize the unperturbed zero order reference state to a consistent nonequilibrium state [66]. In equilibrium the grand-canonical reference state $\hat{\rho}^S_{gc}$ is uniquely determined by the thermodynamic equilibrium situation. This Boltzmann distribution of the weights in $\hat{\rho}^S_{gc}$ is entirely characterized by a chemical potential μ_S and a temperature T_S. This distribution is found by the steady-state solution of a QME in the Born-Markov approximation, when coupling the system to one thermal reservoir. From this viewpoint a natural extension to the nonequilibrium situation is to make use of this QME as well in order to obtain a consistent reference state when coupling the system to non thermal reservoirs or to multiple reservoirs with temperature or voltage differences. In the steady-state, the reference state is then given by the steady-state reduced density operator of the system $\hat{\rho}^S$. In the following we outline how the correct zeroth order reduced density operator $\hat{\rho}^S$ is obtained from a second order Born-Markov QME.

The real time τ evolution of the many-body density matrix $\hat{\rho}$ is given by the von-Neumann equation Eq. (3.13), where $\hat{\mathcal{H}}$ includes the interacting system, the environment and the coupling in-between (Eq. (3.11)) [454]. Typically the large size of the Hilbert space of $\hat{\mathcal{H}}$ prohibits the formal full solution which for time independent Hamiltonians reads, $\hat{\rho}(\tau) = e^{+i\hat{\mathcal{H}}\tau}\hat{\rho}(0)e^{-i\hat{\mathcal{H}}\tau}$. Following the standard approach [61, 455, 456], we consider quantum junctions in the weak coupling limit $|\hat{\mathcal{H}}^{SE}| \ll \{|\hat{\mathcal{H}}^{E}|\}$ and consider a cluster decomposition in $|\hat{\mathcal{H}}^{SE}|$ for simplicity. In the interaction picture with respect to the coupling $\hat{\rho}_I(\tau) = e^{+i(\hat{\mathcal{H}}^S+\hat{\mathcal{H}}^E)\tau}\hat{\rho}(0)e^{-i(\hat{\mathcal{H}}^S+\hat{\mathcal{H}}^E)\tau}$ the von-Neumann equation reads $\dot{\hat{\rho}}_I(\tau) = -i\left[\hat{\mathcal{H}}^{SE}_I, \hat{\rho}_I\right]_-$. We are interested in the reduced system many-body density matrix $\hat{\rho}^S(\tau) = \text{tr}_E\{\hat{\rho}\}$ which takes the form

$$\dot{\hat{\rho}}^S_I(\tau) = -i\text{tr}_E\left\{\left[\hat{\mathcal{H}}^{SE}_I(\tau), \hat{\rho}(0)\right]_-\right\} - \int_0^\tau d\tau' \text{tr}_E\left\{\left[\hat{\mathcal{H}}^{SE}_I(\tau), \left[\hat{\mathcal{H}}^{SE}_I(\tau'), \hat{\rho}_I(\tau')\right]_-\right]_-\right\}.$$

To obtain a tractable equation we perform three standard approximations [61]:

i) The Born approximation is a perturbative expansion of the density matrix $\hat{\rho}_I(\tau) = \hat{\rho}^S_I(\tau) \otimes$

$\bar{\hat{\rho}}_I^E + \mathcal{O}(|\hat{\mathcal{H}}^{SE}|)$

$$\dot{\hat{\rho}}_I^S(\tau) = -i\mathrm{tr}_E\left\{\left[\hat{\mathcal{H}}_I^{SE}(\tau), \hat{\rho}(0)\right]_-\right\} - \int_0^\tau d\tau' \mathrm{tr}_E\left\{\left[\hat{\mathcal{H}}_I^{SE}(\tau), \left[\hat{\mathcal{H}}_I^{SE}(\tau'), \hat{\rho}_I^S(\tau') \otimes \bar{\hat{\rho}}_I^E\right]_-\right]_-\right\} + \mathcal{O}(|\hat{\mathcal{H}}^C|^3)\,.$$

ii) The Markov approximation assumes a memory-less bath, that is the density matrix varies slower in time than the decay time of the bath correlation functions $C_{\alpha\beta}(\tau)$ which decay rapidly, which allows to replace $\hat{\rho}_I^S(\tau')$ with $\hat{\rho}_I^S(\tau)$ and extend the integration limit from τ to $+\infty$. Furthermore one can show that single-particle expectation values vanish and we can therefore neglect the first term yielding

$$\dot{\hat{\rho}}_I^S(\tau) = -\int_0^\infty dt' \mathrm{tr}_E\left\{\left[\hat{\mathcal{H}}_I^{SE}(\tau), \left[\hat{\mathcal{H}}_I^{SE}(\tau'), \hat{\rho}_I^S(\tau) \otimes \bar{\hat{\rho}}_I^E\right]_-\right]_-\right\},$$

which upon transforming back to the Schrödinger picture yields an equation which is is time-local, preserves trace and hermiticity, and has constant coefficients.

iii) To obtain an equation of Lindblad form which in addition preserves positivity, we employ the secular approximation which averages over fast oscillating terms.

Born-Markov-secular master equation

The resulting BMsme for the system density matrix $\rho^S(\tau)$ is valid in the weak coupling limit and takes a convenient form for hermitian system-bath coupling operators [61, 457], for details see App. E

$$\hat{\mathcal{H}}^{SE} = \sum_\alpha \hat{S}_\alpha \otimes \hat{B}_\alpha \text{ with}$$
$$\hat{S}_\alpha = \hat{S}_\alpha^\dagger \text{ and } \hat{B}_\alpha = \hat{B}_\alpha^\dagger\,.$$

The BMsme reads in the energy eigenbasis of the system Hamiltonian $\hat{\mathcal{H}}^S|a\rangle = \omega_a|a\rangle$

$$\dot{\rho}^S(\tau) = -i\left[\hat{\mathcal{H}}^S + \hat{\mathcal{H}}^{LS}, \rho^S(\tau)\right]_- + \sum_{abcd} \Xi_{ab,cd}\left(|a\rangle\langle b|\rho^S(\tau)|d\rangle\langle c| - \frac{1}{2}\left[|d\rangle\langle c||a\rangle\langle b|, \rho^S(\tau)\right]_+\right), \quad (3.26)$$

with

$$\Xi_{ab,cd} = \sum_{\alpha\beta} \xi_{\alpha\beta}(\omega_b - \omega_a)\delta_{\omega_b-\omega_a,\omega_d-\omega_c}\langle a|\hat{S}_\beta|b\rangle\langle c|\hat{S}_\alpha|d\rangle^*\,. \quad (3.27)$$

The Lamb-shift Hamiltonian is defined as

$$\hat{\mathcal{H}}^{LS} = \sum_{ab} \Lambda_{ab}|a\rangle\langle b|\,, \quad (3.28)$$

with

$$\Lambda_{ab} = \frac{1}{2i}\sum_{\alpha\beta}\sum_c \lambda_{\alpha\beta}(\omega_b - \omega_c)\delta_{\omega_b,\omega_a}\langle c|\hat{S}_\beta|b\rangle\langle c|\hat{S}_\alpha|a\rangle^*\,. \quad (3.29)$$

Note that $[\hat{\mathcal{H}}^{LS}, \hat{\mathcal{H}}^{S}]_{-} = 0$. The BMsme in this form is valid if

$$\left[\hat{\mathcal{H}}^{E}, \bar{\rho}^{E}\right]_{-} = 0 \text{ and}$$
$$\mathrm{Tr}\left(\hat{B}_{\alpha}\bar{\rho}^{E}\right) = 0\,.$$

The constants ξ and λ are given by the full even and odd Fourier transforms

$$\xi_{\alpha\beta}(\omega) = \int_{-\infty}^{\infty} d\tau\, C_{\alpha\beta}(\tau) e^{+i\omega\tau} \tag{3.30}$$

$$\lambda_{\alpha\beta}(\omega) = \int_{-\infty}^{\infty} d\tau\, \mathrm{sign}(\tau) C_{\alpha\beta}(\tau) e^{+i\omega\tau} = \frac{i}{\pi} \int\!\!\!\!\!\!\diagup_{-\infty}^{\infty} d\omega' \frac{\xi_{\alpha\beta}(\omega')}{\omega - \omega'}\,, \tag{3.31}$$

of the bath correlation functions

$$C_{\alpha\beta}(\tau) = \mathrm{Tr}\left(e^{+i\hat{\mathcal{H}}^{E}\tau}\hat{B}_{\alpha}e^{-i\hat{\mathcal{H}}^{E}\tau}\hat{B}_{\beta}\bar{\rho}^{E}\right) = \mathrm{Tr}\left(\hat{B}_{\alpha}(\tau)\hat{B}_{\beta}\bar{\rho}^{E}\right)\,, \tag{3.32}$$

where the Heisenberg time evolution is

$$\hat{B}_{\alpha}(\tau) = e^{+i\hat{\mathcal{H}}^{E}\tau}\hat{B}_{\alpha}e^{-i\hat{\mathcal{H}}^{E}\tau}\,.$$

Pauli master equation

We first consider the BMsme for non-degenerate system Hamiltonians, where it reduces to an equation for classical probabilities. For non-degenerate $\hat{\mathcal{H}}^{S}$ the eigenvalues ω_a are unique. Then the structure of Eq. (3.29) and Eq. (3.27) allows to replace $\delta_{\omega_b,\omega_a} \to \delta_{b,a}$ in Eq. (3.29) and $\delta_{\omega_b-\omega_a,\omega_d-\omega_c} \to \delta_{b,d}\,\delta_{a,c}$ in Eq. (3.27). Using these relations we find for the only non-zero elements

$$\Xi_{ab} := \Xi_{ab,ab} = \sum_{\alpha\beta} \xi_{\alpha\beta}(\omega_b - \omega_a)\langle a|\hat{S}_{\beta}|b\rangle\langle a|\hat{S}_{\alpha}|b\rangle^{*}\,, \tag{3.33}$$

and

$$\Lambda_a := \Lambda_{aa} = \frac{1}{2i}\sum_{\alpha\beta}\sum_{c} \lambda_{\alpha\beta}(\omega_a - \omega_c)\langle c|\hat{S}_{\beta}|a\rangle\langle c|\hat{S}_{\alpha}|a\rangle^{*}\,. \tag{3.34}$$

As a result Eq. (3.26) reduces to

$$\dot{\rho}^{S}(\tau) = -i\left[\hat{\mathcal{H}}^{S} + \hat{\mathcal{H}}^{LS}, \rho^{S}(\tau)\right]_{-} + \sum_{a,b}\Xi_{ab}\left(|a\rangle\langle b|\rho^{S}(\tau)|b\rangle\langle a| - \frac{1}{2}\left[|b\rangle\langle b|, \rho^{S}(\tau)\right]_{+}\right)\,, \tag{3.35}$$

with

$$\hat{\mathcal{H}}^{LS} = \sum_{a}\lambda_a|a\rangle\langle a|\,. \tag{3.36}$$

Next we derive equations to obtain the many-body density matrix form the BMsme for non-degenerate systems. One can split the evolution into two independent contributions from the

two terms in Eq. (3.35) seperately, starting out with the first one involving the commutator

$$\begin{aligned}
\dot{\rho}_1^S(\tau) &= -i\left[\hat{\mathcal{H}}^S + \hat{\mathcal{H}}^{LS}, \rho_1^S(\tau)\right]_- \\
&= -i\left[\sum_a \omega_a |a\rangle\langle a| + \sum_b \Lambda_b |b\rangle\langle b|, \sum_{xy} \rho_{1,xy}^S(\tau)|x\rangle\langle y|\right]_- \\
&= -i\sum_{abxy} \rho_{1,xy}^S(\tau)\Big(\omega_a|a\rangle\langle a||x\rangle\langle y| + \Lambda_b|b\rangle\langle b||x\rangle\langle y| - \omega_a|x\rangle\langle y||a\rangle\langle a| - \Lambda_b|x\rangle\langle y||b\rangle\langle b|\Big) \\
&= i\sum_{xy} \rho_{1,xy}^S(\tau)\Big((\omega_y - \omega_x) + (\Lambda_y - \Lambda_x)\Big)|x\rangle\langle y|\,.
\end{aligned}$$

In the non-degenerate case it can be shown that the diagonal elements decouple from the off-diagonal terms. The diagonal terms read ($a = b$)

$$\begin{aligned}
\dot{\rho}_{1,aa}^S(\tau) = \langle a|\dot{\rho}_1^S(\tau)|a\rangle &= i\sum_{xy} \rho_{1,xy}^S(\tau)\Big((\omega_y - \omega_x) + (\Lambda_y - \Lambda_x)\Big)\langle a||x\rangle\langle y||a\rangle \\
&= i\rho_{1,aa}^S(\tau)\Big((\omega_a - \omega_a) + (\Lambda_a - \Lambda_a)\Big) \\
&= 0\,.
\end{aligned}$$

The off-diagonal terms read ($a \neq b$)

$$\begin{aligned}
\dot{\rho}_{1,ab}^S(\tau) = \langle a|\dot{\rho}_1^S(\tau)|b\rangle &= i\sum_{xy} \rho_{1,xy}^S(\tau)\Big((\omega_y - \omega_x) + (\Lambda_y - \Lambda_x)\Big)\langle a||x\rangle\langle y||b\rangle \\
&= i\rho_{1,ab}^S(\tau)\Big((\omega_b - \omega_a) + (\Lambda_b - \Lambda_a)\Big)\,.
\end{aligned}$$

Next we consider the second, non-unitary term in Eq. (3.35)

$$\begin{aligned}
\dot{\rho}_2^S(\tau) &= \sum_{ab} \Xi_{ab}\left(|a\rangle\langle b|\rho_2^S(\tau)|b\rangle\langle a| - \frac{1}{2}\left[|b\rangle\langle b|, \rho_2^S(\tau)\right]_+\right) \\
&= \sum_{ab} \Xi_{ab}\left(|a\rangle\langle b|\sum_{xy} \rho_2^S(\tau)|x\rangle\langle y||b\rangle\langle a| - \frac{1}{2}\left(|b\rangle\langle b|\sum_{xy} \rho_{1,xy}^S(\tau)|x\rangle\langle y| + \sum_{xy} \rho_{1,xy}^S(\tau)|x\rangle\langle y||b\rangle\langle b|\right)\right) \\
&= \sum_{abxy} \Xi_{ab}\rho_{2,xy}^S(\tau)\left(|a\rangle\langle b||x\rangle\langle y||b\rangle\langle a| - \frac{1}{2}|b\rangle\langle b||x\rangle\langle y| - \frac{1}{2}|x\rangle\langle y||b\rangle\langle b|\right) \\
&= \sum_{cx} \Xi_{cx}\rho_{2,xx}^S(\tau)|c\rangle\langle c| - \frac{1}{2}\sum_{cxy}\Big(\Xi_{cx}\rho_{2,xy}^S(\tau) + \Xi_{cy}\rho_{2,xy}^S(\tau)\Big)|x\rangle\langle y|\,.
\end{aligned}$$

The diagonal terms then read ($a = b$)

$$\begin{aligned}\dot{\rho}^S_{2,aa}(\tau) &= \langle a|\dot{\rho}^S_2(\tau)|a\rangle = \sum_{cx}\Xi_{cx}\rho^S_{2,xx}(\tau)\langle a\|c\rangle\langle c\|a\rangle - \frac{1}{2}\sum_{cxy}\Big(\Xi_{cx}\rho^S_{2,xy}(\tau) + \Xi_{cy}\rho^S_{2,xy}(\tau)\Big)\langle a\|x\rangle\langle y\|a\rangle \\ &= \sum_x \Xi_{ax}\rho_2^{S,xx}(\tau) - \frac{1}{2}\sum_c\Big(\Xi_{ca}\rho^S_{1,aa}(\tau) + \Xi_{ca}\rho^S_{2,aa}(\tau)\Big) \\ &= \sum_c\Big(\Xi_{ac}\rho^S_{2,cc}(\tau) - \Xi_{ca}\rho^S_{2,aa}(\tau)\Big).\end{aligned}$$

The off-diagonal terms read ($a \neq b$)

$$\begin{aligned}\dot{\rho}^S_{2,aa}(\tau) &= \langle a|\dot{\rho}^S_2(\tau)|b\rangle = \sum_{cx}\Xi_{cx}\rho^S_{2,xx}(\tau)\langle a\|c\rangle\langle c\|b\rangle - \frac{1}{2}\sum_{cxy}\Big(\Xi_{cx}\rho^S_{2,xy}(\tau) + \Xi_{cy}\rho^S_{2,xy}(\tau)\Big)\langle a\|x\rangle\langle y\|b\rangle \\ &= \sum_x \Xi_{ax}\rho^S_{2,xx}(\tau)\delta_{a,b} - \frac{1}{2}\sum_c\Big(\Xi_{ca} + \Xi_{cb}\Big)\rho^S_{2,ab}(\tau) \\ &= -\frac{1}{2}\sum_c\Big(\Xi_{ca} + \Xi_{cb}\Big)\rho^S_{2,ab}(\tau).\end{aligned}$$

Collecting the individual results of the two terms in Eq. (3.35) we obtain the evolution of the many-body density matrix in the non-degenerate case. The diagonal elements decouple from the off-diagonal evolution. The diagonal components evolve by

$$\begin{aligned}\dot{\psi}_a(\tau) = \dot{\rho}^S_{aa}(\tau) &= \dot{\rho}^S_{1,aa}(\tau) + \dot{\rho}^S_{2,aa}(\tau) \\ &= 0 + \sum_c\Big(\Xi_{ac}\rho^S_{cc}(\tau) - \Xi_{ca}\rho^S_{aa}(\tau)\Big) \\ &= \sum_c\Big(\Xi_{ac}\psi_c(\tau) - \Xi_{ca}\psi_a(\tau)\Big),\end{aligned}$$

where a vector in the reduced space of the diagonals of the reduced many-body density matrix is denoted $\psi_a = \rho^S_{aa}$. The off-diagonal components evolve by

$$\begin{aligned}\dot{\rho}^S_{ab}(\tau) &= \dot{\rho}^S_{1,ab}(\tau) + \dot{\rho}^S_{2,ab}(\tau) \\ &= \left(i(\omega_b + \Lambda_b - \omega_a - \Lambda_a) - \frac{1}{2}\sum_c\Big(\Xi_{ca} + \Xi_{cb}\Big)\right)\rho^S_{ab}(\tau).\end{aligned}$$

The final result in the non-degenerate case reads

$$\dot{\psi}_a(\tau) = \sum_c\Big(\Xi_{ac}\psi_c(\tau) - \Xi_{ca}\psi_a(\tau)\Big), \tag{3.37a}$$

$$\dot{\rho}^S_{ab}(\tau) = \left(i(\omega_b + \Lambda_b - \omega_a - \Lambda_a) - \frac{1}{2}\sum_c\Big(\Xi_{ca} + \Xi_{cb}\Big)\right)\rho^S_{ab}(\tau), \tag{3.37b}$$

where the first line holds for $a = b$ and the second line for $a \neq b$, Ξ_{ab} is defined in Eq. (3.33), ω_a are the non-degenerate eigenenergies of the system Hamiltonian and the non-degenerate Lamb-shift coefficients Λ_a are defined in Eq. (3.34).

Reduced system density matrix

Next we derive the governing equations for the evolution of the reduced many-body density matrix in the general case, i.e. for systems which might be degenerate. Similar to the non-degenerate case, the evolution can be split into two independent contributions from the two terms in Eq. (3.26), starting out with the first one involving the commutator

$$\begin{aligned}
\dot{\rho}_1^S(\tau) &= -i\left[\hat{\mathcal{H}}^S + \hat{\mathcal{H}}^{LS}, \rho_1^S(\tau)\right]_- \\
&= -i\left[\sum_c \omega_c|c\rangle\langle c| + \sum_{ab}\Lambda_{ab}|a\rangle\langle b|, \sum_{xy}\rho_{1,xy}^S(\tau)|x\rangle\langle y|\right]_- \\
&= -i\sum_{xyabc}\rho_{1,xy}^S(\tau)\Big(\omega_c|c\rangle\langle c||x\rangle\langle y| + \Lambda_{ab}|a\rangle\langle b||x\rangle\langle y| - \omega_c|x\rangle\langle y||c\rangle\langle c| - \Lambda_{ab}|x\rangle\langle y||a\rangle\langle b|\Big) \\
&= i\sum_{xyc}\rho_{1,xy}^S(\tau)\Big((\omega_y-\omega_x)|x\rangle\langle y| + \Lambda_{yc}|x\rangle\langle c| - \Lambda_{cx}|c\rangle\langle y|\Big).
\end{aligned}$$

In the general case the diagonal elements do not decouple from the off-diagonal terms. The first part of the evolution for the reduced many-body density matrix reads

$$\begin{aligned}
\dot{\rho}_{1,ab}^S(\tau) = \langle a|\dot{\rho}_1^S(\tau)|b\rangle &= i\sum_{xyc}\rho_{1,xy}^S(\tau)\Big((\omega_y-\omega_x)\langle a||x\rangle\langle y||b\rangle + \Lambda_{yc}\langle a||x\rangle\langle c||b\rangle - \Lambda_{cx}\langle a||c\rangle\langle y||b\rangle\Big) \\
&= i\Big((\omega_b-\omega_a)\rho_{1,ab}^S(\tau) + \sum_c\Big(\rho_{1,ac}^S(\tau)\Lambda_{cb} - \Lambda_{ac}\rho_{1,cb}^S(\tau)\Big)\Big)
\end{aligned}$$

Next we consider the second, non-unitary term in Eq. (3.26)

$$\begin{aligned}
\dot{\rho}_2^S(\tau) &= \sum_{abcd}\Xi_{ab,cd}\left(|a\rangle\langle b|\rho^S(\tau)|d\rangle\langle c| - \frac{1}{2}\left[|d\rangle\langle c||a\rangle\langle b|, \rho^S(\tau)\right]_+\right) \\
&= \sum_{abcdxy}\Xi_{ab,cd}\rho_{2,xy}^S(\tau)\left(|a\rangle\langle b||x\rangle\langle y||d\rangle\langle c| - \frac{1}{2}\Big(|d\rangle\langle c||a\rangle\langle b||x\rangle\langle y| + |x\rangle\langle y||d\rangle\langle c||a\rangle\langle b|\Big)\right) \\
&= \sum_{cdxy}\rho_{2,xy}^S(\tau)\left(\Xi_{cx,dy}|c\rangle\langle d| - \frac{1}{2}\Xi_{cx,cd}|d\rangle\langle y| - \frac{1}{2}\Xi_{cb,cy}|x\rangle\langle d|\right).
\end{aligned}$$

The second part of the evolution for the reduced many-body density matrix reads

$$\begin{aligned}
\dot{\rho}_{2,ab}^S(\tau) = \langle a|\dot{\rho}_2^S(\tau)|b\rangle &= \sum_{cdxy}\rho_{2,xy}^S(\tau)\left(\Xi_{cx,dy}\langle a||c\rangle\langle d||b\rangle - \frac{1}{2}\Xi_{cx,cd}\langle a||d\rangle\langle y||b\rangle - \frac{1}{2}\Xi_{cb,cy}\langle a||x\rangle\langle d||b\rangle\right) \\
&= \sum_{cd}\left(\Xi_{ac,bd}\rho_{2,cd}^S(\tau) - \frac{1}{2}\Xi_{cd,ca}\rho_{2,db}^S(\tau) - \frac{1}{2}\Xi_{cb,cd}\rho_{2,ad}^S(\tau)\right)
\end{aligned}$$

Collecting the individual results of the two terms in Eq. (3.26) we obtain the final result for the evolution of the reduced many-body density matrix in the general (degenerate) case

$$\begin{aligned}\dot{\rho}^S_{ab}(\tau) &= \dot{\rho}^S_{1,ab}(\tau) + \dot{\rho}^S_{2,ab}(\tau) \\ &= i(\omega_b - \omega_a)\rho^S_{ab}(\tau) \\ &+ i\sum_c \left(\rho_{S,ac}(\tau)\Lambda_{cb} - \Lambda_{ac}\rho^S_{cb}(\tau)\right) \\ &+ \sum_{cd}\left(\Xi_{ac,bd}\rho^S_{cd}(\tau) - \frac{1}{2}\Xi_{cd,ca}\rho^S_{db}(\tau) - \frac{1}{2}\Xi_{cb,cd}\rho^S_{ad}(\tau)\right),\end{aligned} \tag{3.38}$$

where $\Xi_{ab,cd}$ is defined in Eq. (3.27), ω_a are the possibly degenerate eigenenergies of the system Hamiltonian and the general Lamb-shift coefficients Λ_{ab} are defined in Eq. (3.29).

Bath correlation functions

The coefficients of the BMsme (Eq. (3.26)) are given in terms of bath correlation functions as outlined in App. E. In summary we obtain for the time dependent correlation functions $C_{\alpha\beta}(\tau)$

$$\begin{aligned}C_{11}(\tau) = C_{22}(\tau) &= \frac{1}{2}\sum_\lambda t'^2_\lambda \sum_k |h_{\lambda k}|^2 \left(2ip_{\mathrm{FD}}(\omega_{\lambda k},\beta_\lambda,\mu_\lambda)\sin(\omega_{\lambda k}\tau) + e^{-i\omega_{\lambda k}\tau}\right) \\ &= \frac{1}{4\pi}\sum_\lambda \int_{-\infty}^{\infty} d\nu\, \Gamma_\lambda(\nu)\left(e^{-i\nu\tau} + 2ip_{\mathrm{FD}}(\nu,\beta_\lambda,\mu_\lambda)\sin(\nu\tau)\right), \\ C_{12}(\tau) = -C_{21}(\tau) &= \frac{i}{2}\sum_\lambda t'^2_\lambda \sum_k |h_{\lambda k}|^2 \left(2p_{\mathrm{FD}}(\omega_{\lambda k},\beta_\lambda,\mu_\lambda)\cos(\omega_{\lambda k}\tau) - e^{-i\omega_{\lambda k}\tau}\right) \\ &= \frac{i}{4\pi}\sum_\lambda \int_{-\infty}^{\infty} d\nu\, \Gamma_\lambda(\nu)\left(-e^{-i\nu\tau} + 2p_{\mathrm{FD}}(\nu,\beta_\lambda,\mu_\lambda)\cos(\nu\tau)\right).\end{aligned}$$

For their respective even Fourier transforms $\gamma_{\alpha\beta}(\omega)$ we find

$$\begin{aligned}\gamma_{11}(\omega) = \gamma_{22}(\omega) &= \frac{1}{2}\sum_\lambda \Gamma_\lambda(-\omega)p_{\mathrm{FD}}(-\omega,\beta_\lambda,\mu_\lambda) + \Gamma_\lambda(\omega)\bar{p}_{\mathrm{FD}}(\omega,\beta_\lambda,\mu_\lambda), \\ \gamma_{12}(\omega) = -\gamma_{21}(\omega) &= \frac{i}{2}\sum_\lambda \Gamma_\lambda(-\omega)p_{\mathrm{FD}}(-\omega,\beta_\lambda,\mu_\lambda) - \Gamma_\lambda(\omega)\bar{p}_{\mathrm{FD}}(\omega,\beta_\lambda,\mu_\lambda).\end{aligned}$$

The odd Fourier transforms $\sigma_{\alpha\beta}(\omega)$ are given by

$$\begin{aligned}\sigma_{11}(\omega) = \sigma_{22}(\omega) &= \frac{i}{2\pi}\sum_\lambda \mathcal{P}\int_{-\infty}^{\infty} d\nu \Gamma_\lambda(\nu)\left(\frac{p_{\mathrm{FD}}(\nu,\beta_\lambda,\mu_\lambda)}{\nu+\omega} - \frac{\bar{p}_{\mathrm{FD}}(\nu,\beta_\lambda,\mu_\lambda)}{\nu-\omega}\right), \\ \sigma_{12}(\omega) = -\sigma_{21}(\omega) &= -\frac{1}{2\pi}\sum_\lambda \mathcal{P}\int_{-\infty}^{\infty} d\nu \Gamma_\lambda(\nu)\left(\frac{p_{\mathrm{FD}}(\nu,\beta_\lambda,\mu_\lambda)}{\nu+\omega} + \frac{\bar{p}_{\mathrm{FD}}(\nu,\beta_\lambda,\mu_\lambda)}{\nu-\omega}\right).\end{aligned}$$

Single-particle density matrix

Next we provide expressions for the basic single-particle observables, typically of interest, in

terms of the reduced many-body density matrix ρ^S. The single-particle density matrix κ reads

$$\kappa_{ij\sigma}(\tau) = \mathrm{tr}\left(c^\dagger_{i\sigma} c_{j\sigma} \rho^S(\tau) \right) = \sum_{ab} \langle b|c^\dagger_{i\sigma} c_{j\sigma}|a\rangle\langle a|\rho^S(\tau)|b\rangle = \sum_{ab} \langle b|c^\dagger_{i\sigma} c_{j\sigma}|a\rangle \rho^S_{ab}(\tau)\,,$$

where a and b denote eigenstates of the system Hamiltonian and i and j are single-particle quantum numbers like site or orbital, for σ we have in mind spin. From the single-particle density-matrix we read off the site occupation $\langle n_i\rangle(\tau) = \sum_\sigma \kappa_{ii\sigma}(\tau)$, the spin resolved occupations $\langle n_{i\sigma}\rangle(\tau) = \kappa_{ii\sigma}(\tau)$, and the magnetization $\langle m_i\rangle(\tau) = \frac{1}{2}(\kappa_{ii\sigma}(\tau) - \kappa_{ii\bar{\sigma}}(\tau))$.

Current to the reservoir

Next we obtain an expression for the current to reservoir λ making use of the operator of total system charge $\hat{Q}$ and total system particle number $\hat{N}$, where q denotes the charge of one charge carrier

$$\begin{aligned} j^\lambda(\tau) &= \frac{d}{d\tau}\langle \hat{Q}(\tau)\rangle = q\frac{d}{d\tau}\langle \hat{N}(\tau)\rangle = q\frac{d}{d\tau}\mathrm{tr}\left(\hat{N}\rho^S(\tau)\right) = q\mathrm{tr}\left(\hat{N}\dot{\rho}_S(\tau)\right) \\ &= q\mathrm{tr}\left(\hat{N}\left(\dot{\rho}^S_{(1)}(\tau) + \dot{\rho}^S_{(2)}(\tau) + \dot{\rho}^S_{(3)}(\tau)\right)\right) \\ &= j^{\lambda,(1)}(\tau) + j^{\lambda,(2)}(\tau) + j^{\lambda,(3)}(\tau)\,, \end{aligned}$$

where we split the calculation into three parts according to the three terms in Eq. (3.26). Note that in the following we use the expressions $\Xi_{ab,cd}$ and λ_{ab} although, only the quantities of bath λ should be considered, so what we really mean is $\Xi^\lambda_{ab,cd}$ and λ^λ_{ab}. This index will be re-instated in the final results at the end of this section. We start out by calculating the term involving the commutator with the system Hamiltonian

$$\begin{aligned} j^{\lambda,(1)}(\tau) &= q\mathrm{tr}\left(\sum_f n_f|f\rangle\langle f|\dot{\rho}^S_{(1)}(\tau)\right) \\ &= q\mathrm{tr}\left(\sum_f n_f|f\rangle\langle f|(-i)\left[\hat{\mathcal{H}}^S, \rho^S(\tau)\right]_-\right) \\ &= q\sum_f n_f \mathrm{tr}\left(|f\rangle\langle f|\left(-i\sum_a \omega_a|a\rangle\langle a|\sum_{xy}\rho^S_{xy}(\tau)|x\rangle\langle y| + i\sum_{xy}\rho^S_{xy}(\tau)|x\rangle\langle y|\sum_a \omega_a|a\rangle\langle a|\right)\right) \\ &= iq\sum_f n_f \mathrm{tr}\left(\sum_a (\omega_a - \omega_f)\,\rho^S_{fa}(\tau)|f\rangle\langle a|\right) \\ &= iq\sum_f n_f \sum_{ac} (\omega_a - \omega_f)\,\rho^S_{fa}(\tau)\langle c\|f\rangle\langle a\|c\rangle \\ &= iq\sum_f n_f\,(\omega_f - \omega_f)\,\rho^S_{ff}(\tau) \\ &= 0\,. \end{aligned}$$

The second term in Eq. (3.26) involves the commutator with the Lamb-shift Hamiltonian

$$
\begin{aligned}
j^{\lambda,(2)}(\tau) &= q\mathrm{tr}\left(\sum_f n_f|f\rangle\langle f|\dot{\rho}^S_{(2)}(\tau)\right)\\
&= q\mathrm{tr}\left(\sum_f n_f|f\rangle\langle f|(-1)\left[\hat{\mathcal{H}}^{LS},\rho^S(\tau)\right]_-\right)\\
&= q\sum_f n_f\mathrm{tr}\left(|f\rangle\langle f|\left(-i\sum_{ab}\Lambda_{ab}|a\rangle\langle b|\sum_{xy}\rho^S_{xy}(\tau)|x\rangle\langle y| + i\sum_{xy}\rho^S_{xy}(\tau)|x\rangle\langle y|\sum_{ab}\Lambda_{ab}|a\rangle\langle b|\right)\right)\\
&= iq\sum_f n_f\mathrm{tr}\left(\sum_{ab}\left(\Lambda_{ab}\rho^S_{fa}(\tau)-\Lambda_{fa}\rho^S_{ab}(\tau)\right)|f\rangle\langle b|\right)\\
&= iq\sum_f n_f\sum_{abc}\left(\Lambda_{ab}\rho^S_{fa}(\tau)-\Lambda_{fa}\rho^S_{ab}(\tau)\right)\langle c||f\rangle\langle b||c\rangle\\
&= iq\sum_{ab}\left(n_b\Lambda_{ab}\rho^S_{ba}(\tau)-n_b\Lambda_{ba}\rho^S_{ab}(\tau)\right)\\
&= iq\sum_{ab}\left(n_a\Lambda_{ba}\rho^S_{ab}(\tau)-n_b\Lambda_{ba}\rho^S_{ab}(\tau)\right)\\
&= iq\sum_{ab}\left(n_a-n_b\right)\Lambda_{ba}\rho^S_{ab}(\tau)\,.
\end{aligned}
$$

For non-degenerate systems ($\lambda_{ab}=\lambda_a\delta_{a,b}$) this takes on the form

$$
\begin{aligned}
j^{\lambda,(2)}_{\text{non-deg}}(\tau) &= iq\sum_{ab}\left(n_a-n_b\right)\Lambda_a\delta_{a,b}\rho^S_{ab}(\tau)\\
&= iq\sum_a\left(n_a-n_a\right)\Lambda_a\rho^S_{aa}(\tau)\\
&= 0\,.
\end{aligned}
$$

At last we treat the third term in Eq. (3.26) which involves the non-unitary part of the evolution

$$
\begin{aligned}
j^{\lambda,(3)}(\tau) &= q\mathrm{tr}\left(\sum_f n_f|f\rangle\langle f|\dot{\rho}^S_{(3)}(\tau)\right)\\
&= q\mathrm{tr}\left(\sum_f n_f|f\rangle\langle f|\left(\sum_{abcd}\Xi_{ab,cd}\left(|a\rangle\langle b|\rho^S(\tau)|d\rangle\langle c| - \frac{1}{2}\left[|d\rangle\langle c||a\rangle\langle b|,\rho^S(\tau)\right]_+\right)\right)\right)\\
&= q\sum_f n_f\mathrm{tr}\Bigg(\sum_{abcdxy}\Xi_{ab,cd}\rho^S_{xy}(\tau)\Bigg(|f\rangle\langle f||a\rangle\langle b||x\rangle\langle y||d\rangle\langle c|\\
&- \frac{1}{2}|f\rangle\langle f||d\rangle\langle c||a\rangle\langle b||x\rangle\langle y| - \frac{1}{2}|f\rangle\langle f||x\rangle\langle y||d\rangle\langle c||a\rangle\langle b|\Bigg)\Bigg)\\
&= q\sum_f n_f\mathrm{tr}\Bigg(\sum_{cxy}\Xi_{fx,cy}\rho^S_{xy}(\tau)|f\rangle\langle c|\\
&- \frac{1}{2}\sum_{axy}\Xi_{ax,af}\rho^S_{xy}|f\rangle\langle y| - \frac{1}{2}\sum_{aby}\Xi_{ab,ay}\rho^S_{fy}|f\rangle\langle b|\Bigg)\\
&= q\sum_f n_f\mathrm{tr}\Bigg(\sum_{axy}\Xi_{fx,ay}\rho^S_{xy}(\tau)|f\rangle\langle a|\\
&- \frac{1}{2}\sum_{axy}\Xi_{ax,af}\rho^S_{xy}(\tau)|f\rangle\langle y| - \frac{1}{2}\sum_{axy}\Xi_{ax,ay}\rho^S_{fy}(\tau)|f\rangle\langle x|\Bigg)\\
&= q\sum_f n_f\Bigg(\sum_{xy}\Xi_{fx,fy}\rho^S_{xy}(\tau)\\
&- \frac{1}{2}\sum_{xy}\Xi_{yx,yf}\rho^S_{xf}(\tau) - \frac{1}{2}\sum_{xy}\Xi_{xf,xy}\rho^S_{fy}(\tau)\Bigg)\\
&= q\sum_{xyc}\left(n_c\Xi_{cx,cy}\rho^S_{xy}(\tau) - \frac{1}{2}n_c\Xi_{yx,yc}\rho^S_{xc}(\tau) - \frac{1}{2}n_c\Xi_{xc,xy}\rho^S_{cy}(\tau)\right)\\
&= q\sum_{xyc}\left(n_c\Xi_{cx,cy}\rho^S_{xy}(\tau) - \frac{1}{2}n_y\Xi_{cx,cy}\rho^S_{xy}(\tau) - \frac{1}{2}n_x\Xi_{cx,cy}\rho^S_{xy}(\tau)\right)\\
&= q\sum_{xyc}\left(n_c - \frac{1}{2}n_y - \frac{1}{2}n_x\right)\Xi_{cx,cy}\rho^S_{xy}(\tau)\\
&= q\sum_{abc}\left(n_c - \frac{1}{2}n_b - \frac{1}{2}n_a\right)\Xi_{ca,cb}\rho^S_{ab}(\tau)\,.
\end{aligned}
$$

For non-degenerate systems ($\Xi_{ab,cd} = \Xi_{ab}\delta_{a,c}\delta_{b,d}$) this takes on the form

$$
\begin{aligned}
j^{\lambda,(3)}_{\text{non-deg}}(\tau) &= q\sum_{abc}\left(n_c - \frac{1}{2}n_b - \frac{1}{2}n_a\right)\Xi_{ca}\delta_{a,b}\rho^S_{ab}(\tau)\\
&= q\sum_{ac}\left(n_c - \frac{1}{2}n_a - \frac{1}{2}n_a\right)\Xi_{ca}\rho^S_{aa}(\tau)\\
&= q\sum_{ab}\left(n_a - n_b\right)\Xi_{ab}\rho^S_{bb}(\tau)\,.
\end{aligned}
$$

Collecting all the results we end up with an expression for the current

$$\begin{aligned} j^{\lambda}(\tau) &= j^{\lambda,(1)}(\tau) + j^{\lambda,(2)}(\tau) + j^{\lambda,(3)}(\tau) \\ &= 0 \\ &+ iq \sum_{ab} (n_a - n_b)\, \Lambda^{\lambda}_{ba} \rho^{S}_{ab}(\tau) \\ &+ q \sum_{abc} \left(n_c - \frac{1}{2} n_b - \frac{1}{2} n_a \right) \Xi^{\lambda}_{ca,cb} \rho^{S}_{ab}(\tau) \\ &= q \sum_{ab} \left(i\,(n_a - n_b)\, \Lambda^{\lambda}_{ba} + \sum_{c} \left(n_c - \frac{1}{2} n_b - \frac{1}{2} n_a \right) \Xi^{\lambda}_{ca,cb} \right) \rho^{S}_{ab}(\tau)\,. \end{aligned}$$

In the non-degenerate case the expression reduces to

$$\begin{aligned} j^{\lambda}_{\text{non-deg}}(\tau) &= j^{\lambda,(1)}_{\text{non-deg}}(\tau) + j^{\lambda,(2)}_{\text{non-deg}}(\tau) + j^{\lambda,(3)}_{\text{non-deg}}(\tau) \\ &= 0 + 0 + q \sum_{ab} (n_a - n_b)\, \Xi_{ab} \rho^{S}_{bb}(\tau) \\ &= q \sum_{ab} (n_a - n_b)\, \Xi_{ab} \psi_b(\tau)\,. \end{aligned}$$

The final results for the current to lead λ in the general (degenerate) and the non-degenerate case are

$$j^{\lambda}(\tau) = q \sum_{ab} \left(i\,(n_a - n_b)\, \Lambda^{\lambda}_{ba} + \sum_{c} \left(n_c - \frac{1}{2} n_b - \frac{1}{2} n_a \right) \Xi^{\lambda}_{ca,cb} \right) \rho^{S}_{ab}(\tau)\,, \tag{3.39}$$

$$j^{\lambda}_{\text{non-deg}}(\tau) = q \sum_{ab} (n_a - n_b)\, \Xi^{\lambda}_{ab} \psi_b(\tau)\,. \tag{3.40}$$

Single-particle Green's function

For CPT we need to evaluate the single-particle Green's function based on the reduced density operator $\hat{\rho}^S$. Starting from a given many-body density matrix $\hat{\rho}^S$ for the system, we obtain a general expression for the equilibrium steady-state single-particle Green's function $g^R_{ij}(\omega) = << c_i ; c_j^\dagger >>_\omega$. $g^R_{ij}(\omega)$ is available from the spectral function $S_{ij}(\omega)$ [285], see also Sec. 3.3.1

$$g^R_{ij}(\omega) = \int_{-\infty}^{\infty} d\omega' \frac{S_{ij}(\omega')}{\omega - \omega' + i0^+}\,.$$

The spectral density $S_{ij}(\omega)$, for Fermions is given by

$$S_{ij}(\omega) = \langle \left[c_i, c_j^\dagger \right]_+ \rangle\,,$$

and can be expressed in terms of elementary correlation functions $C_{\hat{A}\hat{B}}(t,t') = C(\hat{A}(t)\hat{B}(t'))$. Here we use, quite generally, any two Heisenberg operators of the system $\hat{A}(t)$ and $\hat{B}(t')$ instead of the specific choice of annihilation and creation operators. Using eigenstates of the system

Hamiltonian $\hat{\mathcal{H}}_S$: $|\alpha\rangle, |\beta\rangle, |\gamma\rangle$ we find

$$\begin{aligned}
C_{\hat{A}\hat{B}}(t,t') &= \mathrm{Tr}\left(\hat{\rho}^S(t')\hat{A}(t)\hat{B}(t')\right) \\
&= \sum_{\alpha\beta\gamma} \langle\alpha|\hat{\rho}^S(t')|\beta\rangle\langle\beta|\hat{A}(t)|\gamma\rangle\langle\gamma|\hat{B}(t')|\alpha\rangle \\
&= \sum_{\alpha\beta\gamma} \langle\alpha|e^{i\hat{\mathcal{H}}_S t'}\rho^S e^{-i\hat{\mathcal{H}}_S t'}|\beta\rangle\langle\beta|e^{i\hat{\mathcal{H}}_S t}\hat{A}e^{-i\hat{\mathcal{H}}_S t}|\gamma\rangle\langle\gamma|e^{i\hat{\mathcal{H}}_S t'}\hat{B}e^{-i\hat{\mathcal{H}}_S t'}|\alpha\rangle \\
&= \sum_{\alpha\beta\alpha} \rho^S_{\alpha\beta} e^{i(\omega_\alpha-\omega_\beta)t'} e^{i(\omega_\beta-\omega_\gamma)t} e^{i(\omega_\gamma-\omega_\alpha)t'} \langle\beta|\hat{A}|\gamma\rangle\langle\gamma|\hat{B}|\alpha\rangle \\
&= \sum_{\alpha\beta\alpha} \rho^S_{\alpha\beta} e^{i(\omega_\beta-\omega_\gamma)t} e^{-i(\omega_\beta-\omega_\gamma)t'} \langle\beta|\hat{A}|\gamma\rangle\langle\gamma|\hat{B}|\alpha\rangle\,.
\end{aligned}$$

With $\tau = t - t'$ we find

$$C_{\hat{A}\hat{B}}(\tau) = \sum_{\alpha\beta\alpha} \rho^S_{\alpha\beta} e^{i(\omega_\beta-\omega_\gamma)\tau} \langle\beta|\hat{A}|\gamma\rangle\langle\gamma|\hat{B}|\alpha\rangle\,,$$

and its Fourier transform

$$\begin{aligned}
C_{\hat{A}\hat{B}}(\omega) &= \int_{-\infty}^{\infty} d\tau e^{+i\omega\tau} C_{\hat{A}\hat{B}}(\tau) \\
&= \sum_{\alpha\beta\alpha} \rho^S_{\alpha\beta}\langle\beta|\hat{A}|\gamma\rangle\langle\gamma|\hat{B}|\alpha\rangle \int_{-\infty}^{\infty} d\tau e^{+i\omega\tau} e^{i(\omega_\beta-\omega_\gamma)\tau} \\
&= \sum_{\alpha\beta\alpha} \rho^S_{\alpha\beta}\langle\beta|\hat{A}|\gamma\rangle\langle\gamma|\hat{B}|\alpha\rangle \delta\left(\omega + (\omega_\beta - \omega_\gamma)\right)\,.
\end{aligned}$$

The spectral function is then given by

$$\begin{aligned}
S_{\hat{A}\hat{B}}(\omega) &= C_{\hat{A}\hat{B}}(\omega) + C_{\hat{B}\hat{A}}(-\omega) \\
&= \sum_{\alpha\beta\alpha} \rho^S_{\alpha\beta}\langle\beta|\hat{A}|\gamma\rangle\langle\gamma|\hat{B}|\alpha\rangle \delta\left(\omega + (\omega_\beta - \omega_\gamma)\right) + \sum_{\alpha\beta\alpha} \rho^S_{\alpha\beta}\langle\beta|\hat{B}|\gamma\rangle\langle\gamma|\hat{A}|\alpha\rangle \delta\left(-\omega + (\omega_\beta - \omega_\gamma)\right) \\
&= \sum_{\alpha\beta\alpha} \rho^S_{\alpha\beta}\Big(\langle\beta|\hat{A}|\gamma\rangle\langle\gamma|\hat{B}|\alpha\rangle \delta\left(\omega + (\omega_\beta - \omega_\gamma)\right) + \langle\beta|\hat{B}|\gamma\rangle\langle\gamma|\hat{A}|\alpha\rangle \delta\left(\omega - (\omega_\alpha - \omega_\gamma)\right)\Big)\,.
\end{aligned}$$

The retarded single-particle Green's function takes the explicit form

$$g^R_{ij(\sigma)}(\omega) = \sum_{abc} \rho^S_{ab}\delta_{\omega_a,\omega_b}\left(\frac{\langle b|f_{i\sigma}|c\rangle\langle c|f^\dagger_{j\sigma}|a\rangle}{\omega^+ - (\omega_c - \omega_b)} + \frac{\langle b|f^\dagger_{j\sigma}|c\rangle\langle c|f_{i\sigma}|a\rangle}{\omega^+ - (\omega_a - \omega_c)}\right),$$

which can be expressed in terms of Q-matrices [458]

$$
\begin{aligned}
Q^{>(a)\dagger}_{cj\sigma} &= \langle c|f^\dagger_{j\sigma}|a\rangle\,, \quad Q^{<(a)\dagger}_{ci\sigma} = \langle c|f_{i\sigma}|a\rangle \\
Q^{>(b)}_{ic\sigma} &= \langle b|f_{i\sigma}|c\rangle\,, \quad Q^{<(b)}_{jc\sigma} = \langle b|f^\dagger_{j\sigma}|c\rangle \\
\lambda^{>(b)}_c &= (\omega_c - \omega_b)\,, \quad \lambda^{<(a)}_c = (\omega_a - \omega_c) \\
\Lambda^{>(ab)}_c(z) &= \frac{\rho^S_{ab}\delta_{\omega_a,\omega_b}}{z-\lambda^{>(b)}_c}\,, \quad \Lambda^{<(ab)}_c(z) = \frac{\rho^S_{ab}\delta_{\omega_a,\omega_b}}{z-\lambda^{<(a)}_c}\,,
\end{aligned}
$$

so that

$$
g^R_{ij(\sigma)}(\omega) = Q^{>(b)}_{ic\sigma}\Lambda^{>(ab)}_c(\omega^+)Q^{>(a)\dagger}_{cj\sigma} + Q^{<(b)}_{jc\sigma}\Lambda^{<(ab)}_c(\omega^+)Q^{<(a)\dagger}_{ci\sigma}\,, \tag{3.41}
$$

where $\omega^+ = \omega + i0^+$ and Einstein's sum convention applies. The advanced component follows $g^A = g^{R\dagger}$ and the Keldysh component g^K is zero for finite size systems and given by the equilibrium relation for extensive regions in the reference state $g^K(\omega) = (g^R(\omega) - g^A(\omega))(1 - 2p_{\mathrm{FD}}(\omega, T, \mu))$. Once the excitations of the reference state $\hat{\rho}^S$ are determined one can use $\widetilde{g}(\omega)$ in the usual stsCPT equation Eq. (3.20) to obtain the full steady-state Green's function $\widetilde{G}(\omega)$.

3.4. Auxiliary master equation approach

Up to now we have discussed stsCPT and its variants which rely on a perturbation theory in single-particle hoppings. In the stsVCA, in addition a flexible reference state is obtained by introducing self-consistently determined single-particle terms while in the meCPT the reference state is found from the solution of a quantum master equation. Common to all these methods is that the electronic self-energy is determined from a finite size system. The AMEA [68, 69] is again based on a self-energy from a finite size system. However, this system is not obtained through perturbative decomposition of the original one, but rather from an auxiliary open quantum system. Here we focus on the major aspects of the AMEA following [69] closely. The concept behind the AMEA is similar to the ED approach to the DMFT impurity problem in equilibrium [209, 42]. There, the equilibrium electronic reservoir is truncated to a small number of reservoir orbitals, whose parameters are determined by fitting the Keldysh space hybridization function $\widetilde{\Delta}(\omega)$ of the lattice problem. The self-energy is then determined exactly from this system of auxiliary reservoir orbitals plus impurity by Lanczos ED [326]. This approach cannot be straightforwardly extended to the non-equilibrium steady-state for several reasons: (i) since the small bath is finite, its time dependence is (quasi) periodic, i.e. no steady-state is reached, (ii) there is no Matsubara representation out-of-equilibrium, thus, one is forced to use real energies but (iii) in this case $\Im\mathrm{m}(\Delta^R_{\mathrm{aux}}(\omega))$ of the small bath consists of δ-peaks and can hardly be fitted to a smooth $\Delta^R(\omega)$.

In the AMEA these issues are circumvented by coupling the auxiliary reservoir orbitals to an infinite Markovian environment [68] in the framework of open quantum systems. These additional Markovian baths so to say compensate for the missing information in the auxiliary reservoir orbitals, rendering the auxiliary system thermodynamically large. In turn the auxiliary system is capable of yielding a true nonequilibrium self-energy in the steady-state. The dynamics of the auxiliary open system are governed by a Lindblad type quantum master equation which controls the time dependence of the reduced density operator $\hat{\rho}$ [454, 456] and can still be solved

exactly for a small number of auxiliary reservoir orbitals:

$$\dot{\hat{\rho}} = \hat{\tilde{\mathcal{L}}}\hat{\rho}\,. \tag{3.42}$$

The Lindblad super-operator

$$\hat{\tilde{\mathcal{L}}} = \hat{\tilde{\mathcal{L}}}_H + \hat{\tilde{\mathcal{L}}}_D\,, \tag{3.43a}$$

consists of a unitary contribution

$$\hat{\tilde{\mathcal{L}}}_H\hat{\rho} = -i[\hat{\mathcal{H}}_{\mathrm{aux}}, \hat{\rho}]\,,$$

with the Hamiltonian of the auxiliary system (here for one correlated orbital f)

$$\hat{\mathcal{H}}_{\mathrm{aux}} = \sum_{\mu\nu=0}^{N_B}\sum_{\sigma} E_{\mu\nu} d^\dagger_{\mu\sigma} d_{\nu\sigma} + U d^\dagger_{f\uparrow} d_{f\uparrow} d^\dagger_{f\downarrow} d_{f\downarrow}\,, \tag{3.43b}$$

as well as a non-unitary, dissipative term originating from the coupling to the Markovian environment

$$\hat{\tilde{\mathcal{L}}}_D\hat{\rho} \equiv 2\sum_{\mu\nu=0}^{N_B}\sum_{\sigma}\left(\Gamma^{(+)}_{\nu\mu}\left(d_{\mu\sigma}\hat{\rho}\; d^\dagger_{\nu\sigma} - \frac{1}{2}\{\hat{\rho}, d^\dagger_{\nu\sigma} d_{\mu\sigma}\}\right) + + \Gamma^{(-)}_{\nu\mu}\left(d^\dagger_{\nu\sigma}\hat{\rho}\; d_{\mu\sigma} - \frac{1}{2}\{\hat{\rho}, d_{\mu\sigma} d^\dagger_{\nu\sigma}\}\right)\right). \tag{3.43c}$$

The quadratic form of the dissipator (Eq. (3.43c)) corresponds to a non-interacting Markovian environment. In the meCPT a BMsme was used to obtain the reference state for CPT (see Eq. (3.26)) which has the same structure as Eq. (3.43c). In the meCPT however, the coefficients of the equation have been obtained from the bath correlation functions, that is, from the physical system in perturbation theory. In contrast here the coefficients $\Gamma^{\alpha}_{\mu\nu}, E_{\mu\nu}$ are fit parameters which map the auxiliary system to the original one. Similar to the equilibrium case, in the AMEA the mapping is provided by the bath hybridization function in Keldysh space $\widetilde{\Delta}(\omega)$. The fit is obtained by minimizing the cost function

$$\chi(E_{\mu\nu}, \Gamma^{(\kappa)}_{\mu\nu}) = \sum_{\alpha\in\{R,K\}}\int_{-\infty}^{\infty} d\omega\, W^{\alpha}(\omega)\left|\Delta^{\alpha}(\omega) - \Delta^{\alpha}_{\mathrm{aux}}(\omega; E_{\mu\nu}, \Gamma^{(\kappa)}_{\mu\nu})\right|^n . \tag{3.44}$$

with respect to the parameters of the auxiliary system. The advanced component does not need to be considered as $\Delta^A = \Delta^{R*}$. The accuracy of the results will be directly related to the accuracy of the fit to $\widetilde{\Delta}(\omega)$, and this increases rapidly with the number of fit parameters, which obviously increases with N_B as does the computational complexity necessary to exactly diagonalize the interacting auxiliary system. The fit does not present a major numerical difficulty, as the determination of the hybridization functions of both the original model, as well as the one of the auxiliary system $\widetilde{\Delta}_{\mathrm{aux}}(\omega)$ described by the Lindblad equation (3.43) require the evaluation of $\widetilde{G}_0$, i.e. the solution of a non-interacting problem.

Once the auxiliary system is defined in terms of $E_{\mu\nu}$ and $\Gamma^{(\kappa)}_{\mu\nu}$, the corresponding interacting nonequilibrium problem Eq. (3.43) can be solved by exact diagonalization of the non-hermitian super-operator $\hat{\tilde{\mathcal{L}}}$ within the space of many-body density operators. The dimension of this space is equal to the square of the dimension of the many-body Hilbert space, and thus it grows exponentially as a function of N_B. A discussion of the solution of the non-interacting problem is available in App. F as well as [68, 69] while the solution of the interacting system is described

in [69].

3.5. Discussion

We have presented several Green's function based methods for the steady-state. All of them are based on the exact solution of a finite size interacting system, as a reference state from which the single-particle excitations are obtained. While the stsCPT, stsVCA and meCPT are perturbative in the single-particle hopping terms of the inter-cluster Hamiltonian, the AMEA is based upon an auxiliary open quantum system which is mapped onto the original one via the Keldysh space hybridization function. The solution of stsCPT and stsVCA are based on a Hamiltonian system, while for the meCPT and the AMEA a quantum master equation has to be solved with the notable difference that in meCPT the coefficients of this master equation are found directly from the bath correlation functions of the original lattice problem while in the AMEA these are fit parameters to minimize the "distance" to the lattice hybridization function. The perturbative approaches become exact for vanishing interaction-strength and in the atomic limit. All these approaches provide a high degree of flexibility and are able to treat any given fermionic lattice Hamiltonian of a nano-structure, hetero-structure, molecular junction or multi-layer system also starting from *ab initio* calculations. In the AMEA solution an additional anisotropic steady-state DMFT step may be required and for stsCPT, stsVCA and meCPT a mean field extension in the spirit of eVCA might be required if non-local interactions are treated perturbatively. All these approaches are systematically improvable by considering larger cluster sizes L_C. The numerical effort for stsCPT and stsVCA scales exponentially in the size of the interacting clusters L_C while the meCPT and the AMEA scale exponentially in $2L_C$ because their configuration space are the many-body density matrices. On modern computer systems the solution of cluster sizes up to $L_C \approx 16$ is feasible ($L_C \approx 8$ in meCPT and AMEA).

Although the reference state of stsCPT is an ad-hoc equilibrium state at zero temperature and with some chemical potential in-between the ones of the leads see Fig. 3.4 (bottom), good qualitative results can be obtained with this method for standard molecular junctions. To treat broken symmetry states or systems with very strong many-body effects like Kondo systems, the self-consistent feedback implemented in stsVCA has proven vital. Note that also the stsVCA reference state is an equilibrium system, however with optimized single-particle parameters. The meCPT solution is based on a nonequilibrium many-body state and should be used if interferences between the states therein are to be expected, that is for degenerate cluster Hamiltonians. Another reason to use meCPT is at higher bias voltages where the contribution from additional transport channels in the reference state might become large. Finally we mention that the representation of non-interacting clusters, the infinite leads is not unique as soon as some lead orbitals are incorporated in the interacting cluster. Indeed they are invariant under any unitary transformation of the lead degrees of freedom. Because these transformation however alters also the perturbative matrix elements in the inter-cluster terms, these representations are not equivalent when applying a perturbative expansion like stsCPT. A scheme to optimize the representation with respect to the perturbation is outlined in App. G. In the following we discuss a simple toy model for an actual molecular junction to showcase the steady-state methods.

Toy model of Zn-Porphyrin

Porphyrins are a class of highly conjugated aromatic systems. Elementary synthesis and experimental characterization is well established. Classical applications include dyes and catalysts while current research focuses on their application in molecular electronics [459] and solar cells [460]. We obtain a toy model for a Zn-Porphyrin by fitting the parameters of an extended Hub-

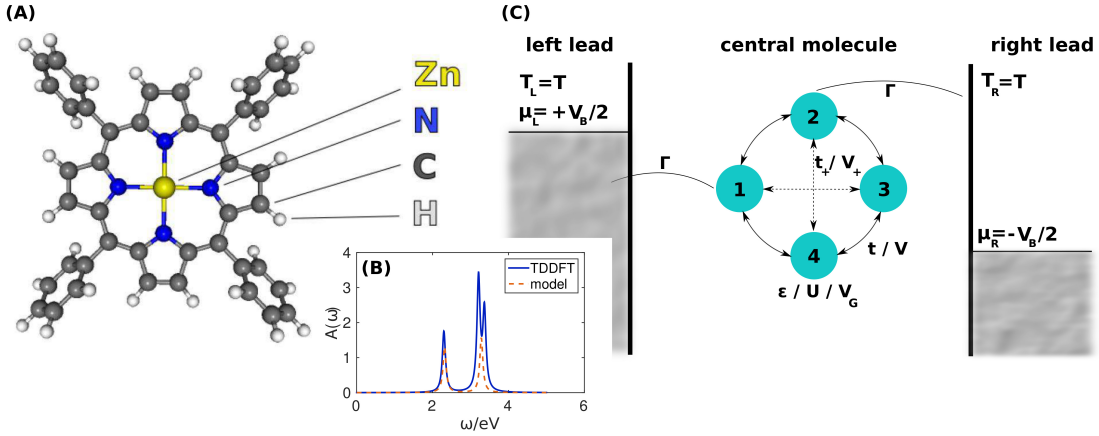

Figure 3.5.: (Color online) *Model of a Zn-Porphyrin* **(A)** Ball and stick representation of the Zn-Porphyrin. **(B)** TDDFT excitation spectrum (solid blue) and model fit (dashed orange). **(C)** The parameters of the four orbital toy model are described in the text.

bard [166] / Pariser-Parr-Pople [461, 462] model to the UV-vis excitation spectrum of the free molecule as obtained by TDDFT in Gaussian09 [3] which qualitatively agrees also to experimental data. Note that the parameters are determined crudely for the free standing molecule and no effects of the leads or respective anchor groups are taken into account in a proper downfolding to local orbitals [463]. Based on the four fold symmetry of the molecule, $L = 4$ local orbitals are chosen, see Fig. 3.5:

$$\begin{aligned}\hat{\mathcal{H}}^S = &(\epsilon + V_G)\sum_{i=1}^{4}\sum_{\sigma}\hat{n}^f_{i\sigma} + \sum_{i=1}^{4} U\left(\hat{n}^f_{i\uparrow} - \frac{1}{2}\right)\left(\hat{n}^f_{i\downarrow} - \frac{1}{2}\right)\\ &+ t\sum_{ij\in\mathcal{N}}\sum_{\sigma}\left(f^\dagger_{i\sigma}f_{j\sigma} + \text{h.c.}\right) + t_+\sum_{ij\in\mathcal{N}\mathcal{N}}\sum_{\sigma}\left(f^\dagger_{i\sigma}f_{j\sigma} + \text{h.c.}\right)\\ &+ V\sum_{ij\in\mathcal{N}}\sum_{\sigma\sigma'}\left(\hat{n}^f_{i\sigma} - \frac{1}{4}\right)\left(\hat{n}^f_{j\sigma'} - \frac{1}{4}\right) + V_+\sum_{ij\in\mathcal{N}\mathcal{N}}\sum_{\sigma\sigma'}\left(\hat{n}^f_{i\sigma} - \frac{1}{4}\right)\left(\hat{n}^f_{j\sigma'} - \frac{1}{4}\right).\end{aligned}$$

The model features a local potential $\epsilon = -0.67\,|t|$ and local Coulomb repulsion $U = 1.48\,|t|$. The geometry suggest that the orbitals are connected via single-particle tunnelling terms $t = 7.5\,\text{eV}$ in a circular manner $\mathcal{N} = \{(1,2),(2,3),(3,4),(4,1)\}$ and a next-nearest neighbour tunnelling $t_+ = -0.83\,|t|$ crosswise $\mathcal{N}\mathcal{N} = \{(1,3),(2,4)\}$. The magnitude of the according off-diagonal Coulomb terms is $V = 0.27\,|t|$, $V_+ = 0.13\,|t|$. The molecule is coupled to two flat band electronic reservoirs with $\Gamma \approx 0.0067\,|t|$ and $T \approx 0.013\,|t|$ in a meta-setup.

Results for the charge current and for the orbital resolved steady-state occupations for $V_G = 0$ are presented in the top panel of Fig. 3.6. The current remains essentially zero until the bias voltage has penetrated the HOMO-LUMO gap. The dominant excitations in the system are visible in the UV-VIS spectrum in Fig. 3.5 at $\omega_1 = 2.318\,\text{eV}$ and $\omega_2 = 3.286\,\text{eV}$. Due to the symmetrically applied bias voltage $\mu_L = -\mu_R = \frac{V_B}{2}$ one would expect contributions to the current at twice the excitation energy, at $V_B \approx 0.618\,|t|$ and at $V_B \approx 0.876\,|t|$. These are indeed observed in the meCPT and the BMsme current. In addition within BMsme these transitions become broadened by temperature only, while in meCPT and stsCPT they are broadened by lead induced effects in addition. For low bias voltages e.g. at $V_B = 0.1\,|t|$, all orbital occupancies

are approximately one and the current vanishes. The reference state within stsCPT is the state of lowest energy in the four particle spin-symmetric sector. Also the meCPT reference state $\hat{\rho}^S$ has only contributions from the four particle sector. The transmission function is depicted in Fig. 3.6. It is proportional to $\left|G^R_{12}(\omega)\right|^2$ which shows only one excitation at $\omega_2 = 3.286\,\mathrm{eV}$ while the diagonal components would also feature an excitation at ω_1. For medium bias voltages like e.g. at $V_B = 0.7\,|t|$ in stsCPT we find a modulation in the orbital occupancies of $\langle n_1\rangle = \langle n_3\rangle = 1.39$, $\langle n_2\rangle = \langle n_4\rangle = 1.00$ and a tiny current of $j = 0.0019\,\Gamma$. In meCPT the modulation is more pronounced: $\langle n_1\rangle = \langle n_3\rangle = 1.34$, $\langle n_2\rangle = \langle n_4\rangle = 0.83$ and a larger current is obtained $j = 0.0795\,\Gamma$ due to the change in reference state $\hat{\rho}^S$ which now consists of the following contributions $7\% : N = 3$, $54\% : N = 4$, $39\% : N = 5$. The plain BMSme yields $\langle n_1\rangle = \langle n_3\rangle = 1.13$, $\langle n_2\rangle = \langle n_4\rangle = 1.03$ and $j = 0.5521\,\Gamma$. In this regime the differences between stsCPT and meCPT are most pronounced. In general the meCPT solution shows more steps in the observables which follow the ones observed in the BMsme curves due to the better reference state. For large bias voltages e.g. at $V_B = 1.2\,|t|$ we obtain in stsCPT $\langle n_1\rangle = \langle n_3\rangle = 1.65$, $\langle n_2\rangle = \langle n_4\rangle = 0.75$ and $j = 0.2443\,\Gamma$. In meCPT the occupancies are $\langle n_1\rangle = \langle n_3\rangle = 1.36$, $\langle n_2\rangle = \langle n_4\rangle = 0.69$ and the current is smaller $j = 0.1427\,\Gamma$ where the reference state $\hat{\rho}^S$ consists of $1\% : N = 2$, $21\% : N = 3$, $53\% : N = 4$, $21\% : N = 5$, $5\% : N = 6$. Again the BMSme yields a smaller variation in orbital occupancy $\langle n_1\rangle = \langle n_3\rangle = 1.12$, $\langle n_2\rangle = \langle n_4\rangle = 0.92$ and a larger current of $j = 0.7626\,\Gamma$. We attribute the reduced current in the meCPT with respect to the BMsme to an increased Coulomb repulsion due to higher orbital occupancies.

For a gate voltage of $V_G = 0.8\,|t|$ an interesting effect is observed. The BMsme predicts a pure two particle state at low bias voltages which crosses over to a pure three particle state at $V_B \approx 0.8\,|t|$. In both parameter regions the current of course vanishes. However in-between at the crossover point a current would be allowed in principle which could result in a blocking state in the $N = 3$ regime, see [66]. We however find that the current vanishes due to matrix-elements.

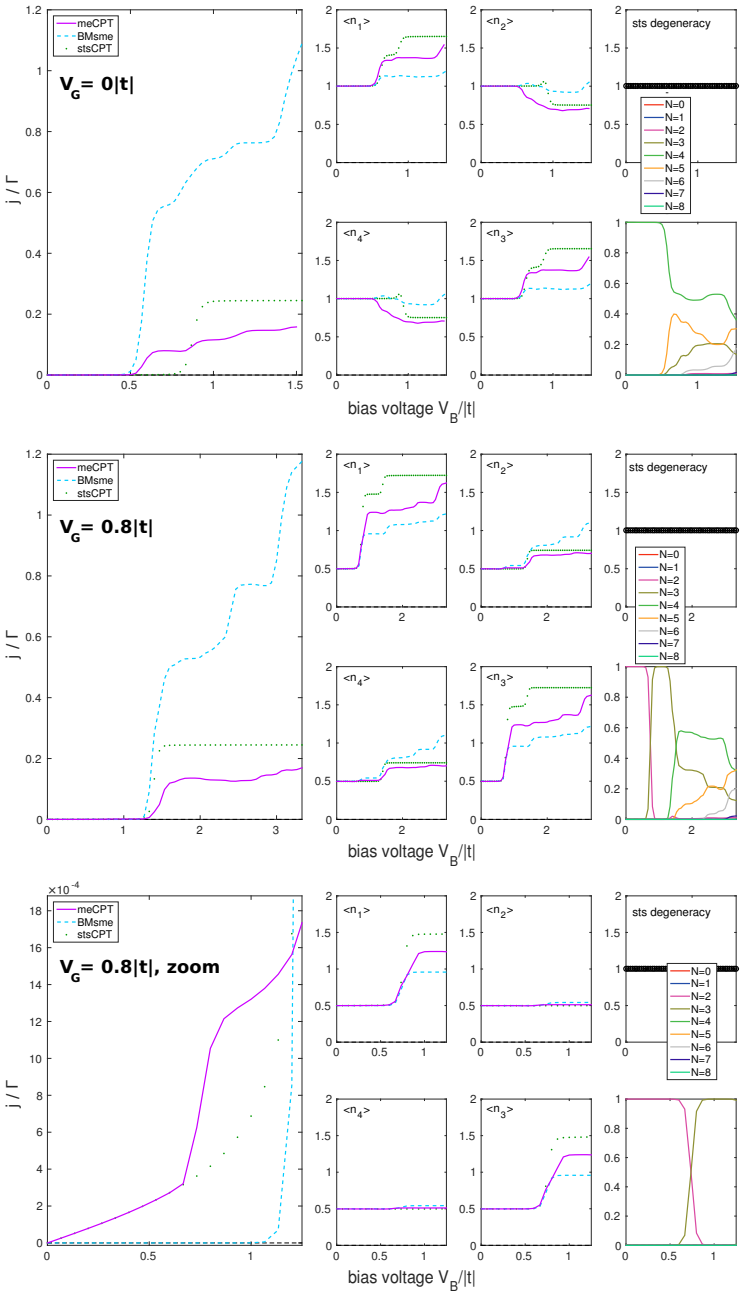

Figure 3.6.: (Color online) *Steady-state transport through Zn-Porphyrin.* **(Top)** No gate voltage $V_G = 0$. **(Middle)** $V_G = 0.8\,|t|$. **(Bottom)** Same as (B), zoom to low bias voltages. The panel on the left of each row shows the charge current j entering the molecule. The four middle panels in each row depict the four local charge densities $\langle n_i \rangle$. The panel on the top right of each row shows the steady-state degeneracy and the one on the bottom right shows the particle number resolved weight of the BMsme steady-state density matrix $\hat{\rho}^S$.

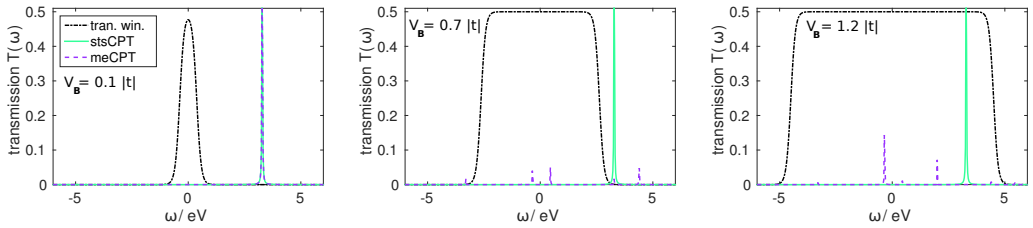

Figure 3.7.: (Color online) *Transmission functions at* $V_G = 0$. **(Left)** Transmission function $\mathcal{T}(\omega)$ for $V_B = 0.1\,|t|$. **(Middle)** Transmission function $\mathcal{T}(\omega)$ for $V_B = 0.7\,|t|$. **(Right)** Transmission function $\mathcal{T}(\omega)$ for $V_B = 1.2\,|t|$.

4. Conclusions

In this thesis we have discussed effectively low-dimensional strongly correlated electron systems out-of-equilibrium. We have applied linear-response transport theory in combination with dynamical mean field theory and the extended variational cluster approach, real-time evolution in a matrix product based framework consisting of the density matrix renormalization group and subsequent time evolving block decimation as well as nonequilibrium Green's function and quantum master equation based steady-state calculations.

In Sec. 5.1, we have obtained a model for the electronic structure of the highly anisotropic effectively low-dimensional purple bronze $Li_{0.9}Mo_6O_{17}$ based on *ab initio* electronic structure calculations. Representation in terms of maximally-localized Wannier orbitals lead to an effective model with two filled bands and two half-filled bands. The anisotropic transport coefficients were obtained in linear-response theory and the results reproduce trends of recent experiments. We were able to analyse the dominant processes for charge transport in terms of linear chains of localized molecular-like orbitals. Including electron-electron interaction in the extended variational cluster approach and dynamical mean field theory we studied the effects of electron-electron interactions. The so obtained spectral functions compare well with recent angle-resolved photo emission experiments.

Linear response theory proved sufficient to obtain qualitatively, the transport characteristics of effectively one-dimensional structures. However, when the external perturbation becomes larger a more accurate treatment is in order. In Sec. 5.2, we went beyond linear-response and studied the real-time evolution of quantum impurities connected to one-dimensional leads after a strong quantum-quench. In particular we studied the single-impurity Anderson model out-of-equilibrium by means of a matrix product state based real-time evolution. This approach allowed us to access relevant time-scales to reach the steady-state. We studied and compared three quenches: quenching the bias voltage, quenching the hybridization to both leads and quenching the hybridization to one lead only. We could show that quenching the lead-dot tunnellings is the most suitable one for obtaining steady-state observables. The characteristic period of oscillations in the transient time evolution of the charge current is already very well described by renormalization group results for a different and simpler model, the interacting resonant level model of spinless fermions. We obtained quasi-exact results for the steady-state current-voltage characteristics for low, medium and high bias voltages. This calculated current-voltage characteristics agrees very well with established results which are available in the low-bias region only. On the methods oriented side we found that a large entanglement entropy correlates positively with a large steady-state current amplitude, rendering the corresponding parameter regions more challenging to simulate. To reduce the entanglement, we also studied a damped version of the time evolution and found that high-energy states have very different significance in the low- and high-bias regimes, respectively.

In Sec. 5.3, we extended our studies of time-dependent impurity problems to resolve space and time dependent correlation functions. We studied the time-dependent formation of the Kondo spin screening cloud in the single-impurity Anderson model. Starting from an unentangled state, we switched on the impurity-reservoir hybridization and followed the subsequent dynamics in real time. From the spin-spin and charge-charge correlation functions we obtained characteristic time and length scales. Our results agree with previous calculations at equilibrium and, for

local observables, out-of-equilibrium. We found that the nonequilibrium correlation functions converge to the equilibrium results for long times. In the time-dependent data, we identified a linear spreading of signals travelling at the lattice Fermi velocity, which has been referred to as a light cone in recent literature. We observed a ferromagnetic response in the wake of the signal at the light cone. We observe directly from the nonequilibrium time evolution of correlation functions that the structure of the correlation functions inside the light cone emerges on two time-scales. The qualitative core of the correlation functions develops rapidly, at the lattice Fermi velocity. This includes the phase and period of oscillations as well as fixed ferromagnetic and anti-ferromagnetic domains. These correlations then reach their equilibrium values exponentially slowly in time, defining a dynamic scale which has the same exponential dependence on interaction-strength as the Kondo temperature. Outside the light cone, we obtain a power-law decay of the correlation functions, with essentially interaction-strength- and time-independent exponents.

Applying the matrix product state based time evolution we could show that reaching even converged steady-state observables is possible, numerically. However, the data analysis is challenging and more complex models might feature longer time-scales which prohibit the full evolution. Therefore we developed approximate numerical methods which directly compute the steady-state. In Sec. 5.4, we conducted an equilibrium cluster perturbation theory study of the single-impurity Anderson model which served the purpose to gauge the abilities of the method in equilibrium and generalize it to strongly anisotropic models, to set it up for a future use out-of-equilibrium. When applying the variational cluster approach we found that the variational extension is a vital ingredient for a good approximation. The cluster perturbation theory and variational cluster approach spectra both yield a Kondo resonance in the impurity density of states with the correct height as predicted by the Friedel sum rule. A close look at the Kondo resonance shows that the variational cluster approach is able to reproduce the resonance and the functional behaviour for the Kondo temperature in a remarkable way. The Kondo temperature is expected to show exponential behaviour in interaction strength in the Kondo regime. The variational cluster approach yielding an exponential behaviour, however, tends to underestimate the exponent. This issue was resolved recently by an optimized bath representation for cluster perturbation theory as presented in App. G. Comparison of dynamic quantities to continuous-time quantum Monte Carlo solidifies the origins of this behaviour. For the asymmetric model, the Friedel sum rule is fulfilled in all parameter regions implying that the Kondo resonance is pinned at the chemical potential in the Kondo region. In addition, a self-consistent formulation of the variational cluster approach, previously introduced in the context of nonequilibrium problems, was explored. Results obtained by the self-consistent approach show agreement with results obtained by the variational cluster approach based on the grand potential for the density of states of the impurity f-orbital. While there are certainly more accurate methods to deal with a single-quantum-impurity model, especially at low energies, our work shows that the variational cluster approach is a flexible and versatile method which provides reasonably accurate results with modest computational resources. Here, the variational cluster approach self-consistency condition proves to be crucial.

Based on the success in equilibrium we generalized cluster perturbation theory and the variational cluster approach to study the steady-state of the single-impurity Anderson model in Sec. 5.5 and Sec. 5.6. Results for the particle-hole symmetric model, which is dominated by Kondo correlations, have been compared to time evolving block decimation and quantum Monte Carlo. At low values of interaction strength they show excellent agreement already for nonequilibrium cluster perturbation theory. For higher values of interaction strength, the self-consistency implemented within the nonequilibrium variational cluster approach proves crucial in order to obtain reasonable results. Both methods coincide with the low bias linear-response data for the

steady-state current. Both methods furthermore become exact in the non-interacting limit. The nonequilibrium local density of states of the quantum dot exhibits a linear and interaction dependent splitting of the bias voltage within the nonequilibrium variational cluster approach which is not visible in the nonequilibrium cluster perturbation theory. At a certain bias voltage we find that this split Kondo resonance merges with the high-energy incoherent part of the spectrum. When applying a gate voltage and thereby leaving the Kondo regime, calculations become a lot easier and nonequilibrium cluster perturbation theory and the nonequilibrium variational cluster approach appear to perform very well, which can be inferred from the convergence of our data. The highest current amplitude is obtained at the crossover from the Kondo to the empty or doubly occupied quantum dot. Experimental stability diagrams are reproduced very well within the variational approach. They show a clear Kondo regime and a Coulomb blockade region. We may conclude that the nonequilibrium variational cluster approach is a promising method for the evaluation of steady-state quantities of strongly correlated model systems.

Based on the good performance of the steady-state method for a single orbital, we generalized the method to study effects of electron-electron interactions in a benzene like molecule in Sec. 5.7, subject to a finite bias voltage induced by two metallic leads, as a function of an applied magnetic field. We make use of a Hubbard-type-model based description of such a device in the charge neutral regime. Using steady-state cluster perturbation theory, observables have been computed for para-, meta-, as well as ortho- setups. Results for the total transmission current and circular current as well as the steady-state charge distribution and magnetization have been presented. By studying physically relevant regimes of electron-electron interactions in addition to an applied magnetic field, we describe the effects of electron-electron interactions on the steady-state beyond the mean field level. We found that these are to shift voltage thresholds and to decrease the magnitude of currents. Additionally, interactions lead to deviating currents in the meta and ortho setup which were comparable in the non-interacting system. The steady-state charge distribution becomes strongly renormalized by interactions respecting the symmetry of the isolated molecule. Due to the Zeeman effect, we obtain a steady-state magnetization which is highly sensitive to bias voltage. Our results may help to validate model calculations at fixed interaction parameters and contribute to the understanding of sophisticated *ab initio* based transport calculations. Our results indicate that the main effect of interactions is to renormalize voltage thresholds and current magnitudes. We showed that the charge density is sensitive to electron-electron interactions and becomes strongly renormalized with every additional electronic level contributing to transport. This fact has to be accounted for in self-consistent approaches.

To resolve current blocking effects in Sec. 5.8 we augmented the steady-state cluster perturbation theory with an appropriate, consistent reference state. This reference state is obtained by the reduced many-body density matrix in the steady-state obtained from a quantum master equation. The resulting hybrid method inherits beneficial aspects of steady-state cluster perturbation theory as well as from the quantum master equation We benchmarked the new method on two experimentally realizable systems: a quantum diode and a triple quantum dot ring, which both feature negative differential conductance and interaction induced current blocking effects. Master equation based cluster perturbation theory is able to improve the bare quantum master equation results by a correct inclusion of lead induced level-broadening effects, and the correct non-interacting limit. In contrast to previous realizations of the steady-state cluster perturbation theory, master equation based cluster perturbation theory is able to correctly predict interaction induced current blocking effects. It is well known that the secular approximation is not applicable to quasi degenerate problems, which is corroborated by our results for the steady-state current. However, master equation based cluster perturbation theory based on the Born-Markov-secular master equation density, is able to repair most of the shortcomings of Born-Markov-secular master equation. The results are very close to those obtained by master equation based cluster

perturbation theory based on the density of Born-Markov-secular master equation, where the quasi-degenerate states are treated consistently. The computational effort of master equation based cluster perturbation theory beyond that of the bare quantum master equation scales with the number of significant entries in the reference state density matrix but is typically small. In the presented formulation the new method is flexible and fast and therefore well suited to study nano-structures, molecular junctions or hetero-structures also starting from an *ab initio* calculation.

In conclusion, the steady-state cluster perturbation theory can be used to obtain reasonably accurate results for the transport through weakly coupled molecular junctions. If electronic correlations are large, like in Kondo systems, the self-consistent feedback implemented in the steady-state variational cluster approach proves essential to obtain accurate results. To study complex transport phenomena like interaction induced blocking, which depend on the interplay of many-body states in the reference system, the master equation based steady-state cluster perturbation theory becomes necessary.

As an alternative, an approximation not based on a direct perturbative expansion of the model but on a mapping to an auxiliary open quantum system is presented in Sec. 5.9. The auxiliary master equation approach to the single-impurity Anderson model is based on a mapping of the original Hamiltonian to an auxiliary open quantum system consisting of the interacting impurity coupled to bath sites as well as to a Markovian environment. The dynamics of the auxiliary open system is controlled by a Lindblad master equation. Its parameters are determined by a fit to the impurity-environment hybridization function. This has many similarities to the procedure used for the exact-diagonalization dynamical mean field theory impurity solver, but has the advantage that one can work directly with real frequencies, which is mandatory for nonequilibrium systems. We have illustrated how the accuracy of the results can be estimated, and systematically improved by increasing the number of auxiliary bath sites. A scheme to introduce linear corrections has been devised. We presented in detail how the nonequilibrium Green's functions of the correlated open quantum system are obtained by making use of non-hermitian Lanczos diagonalization in a super-operator space. These techniques make the whole method fast and efficient as well as particularly suited as an impurity solver for steady-state dynamical mean field theory. In this work, we have applied the approach to the single-impurity Anderson model. We have analyzed in detail the systematic improvement of the current-voltage characteristics as a function of the number of auxiliary bath sites. Already for four auxiliary bath sites, results show a rather good agreement with quasi-exact data from time-evolving block decimation in the low- and medium-bias regimes. In the high-bias regime, the current deviates from the expected result with increasing interaction strength. However, we have shown how to estimate the reliability of the data from the deviation of the hybridization functions and how results can be corrected to linear order in this deviation. The impurity spectral function obtained in our calculation features a linear splitting of the Kondo resonance as a function of bias voltage. Good agreement with data from scattering-state numerical renormalization group was found.

In Sec. 5.10, we discussed the role of electronic correlations at high bias voltage when the reservoir density of states is structured and finite and the bias voltage approaches the bandwidth. As an illustration we discuss the particular example of the steady-state of a single quantum dot connected to two leads of semicircular electronic density of states under bias voltage. We use density matrix renormalization group, time evolving block decimation, the steady-state variational cluster approach, the auxiliary master equation approach and a Born-Markov-secular quantum master equation to evaluate the steady-state double occupancy, charge current, local density of states and the reduced steady-state many-body density matrix. In general one expects electronic correlations to impact transport characteristics at bias voltages smaller than the electronic coherence temperature. For large bias voltages it has been shown that in the wide band limit electronic

correlations are dominated by the perturbing external bias. The system behaves like free and the effect of the high bias voltage is comparable to a high temperature or a high magnetic field. We do not apply the wide band limit but discuss a system which features two electronic leads with a finite and structured electronic density of states. We found that the steady-state can be classified into three regimes in bias voltage, according to the degree of electronic correlation. For low bias voltages the steady-state feels the remnants of the equilibrium spin Kondo effect. It features enhanced magnetic fluctuations and suppressed charge fluctuations. The charge current in this regime is enhanced with respect to an equivalent system without electron-electron interactions. Only states at low energies contribute to transport and their density is high due to electronic correlations. At medium bias voltages many states reside inside the transport window and we find charge and spin fluctuations comparable to those of an equilibrium non-interacting system or for the high bias steady-state in the wide band limit. The current in this regime is also comparable to the one of an equivalent non-interacting system. The finding of this work is that at high bias voltages, close to the band edge of the leads, the transport is again enhanced with respect to the non-interacting equivalent. We observe large charge fluctuations and small magnetic fluctuations in this regime. The small transport window limits the states contributing to transport again to those at low energies. These are strongly enhanced due to electronic correlations. We propose that the high bias state features the characteristics of a charge Kondo effect.

5. Findings collected in publications

In this chapter we present the collected results of this thesis. An overview is given in Tab. 5. Each section of this chapter contains one of the publication listed in Tab. 5 and a preamble. In the preamble the full copyright and citation is given in addition to detailed author credentials. A brief paragraph on the achievements in the respective publications and on how it connects with the rest of this thesis concludes this introduction.

5.1. Effective model for the electronic properties of quasi-one-dimensional purple bronze $Li_{0.9}Mo_6O_{17}$ based on *ab initio* calculations

5.1.1. Preamble

This part of the thesis serves the purpose to enter the realm of nonequilibrium physics by using the well developed linear-response theory [39, 40]. Linear-response theory is based entirely on the equilibrium ground state properties of the system and its application is limited to small external fields, see Sec. 3.2. On the one hand we make contact with *ab initio* band structure calculations and build an electronic model for the correlated effectively one-dimensional conductor $Li_{0.9}Mo_6O_{17}$, which provides the crossroads between model physics and *ab initio* theories. An overview of phenomena in bulk material materials out-of-equilibrium is available in Ch. 2. Basically all methods presented in the remainder of this thesis in Sec. 5.2, Sec. 5.3, Sec. 5.4, Sec. 5.5, Sec. 5.6, Sec. 5.7, Sec. 5.8, Sec. 5.9 and Sec. 5.10 are flexible enough to be applied to real materials if augmented by such a preliminary step. On the other hand we apply equilibrium DMFT [42] and the quantum cluster methods CPT [43, 44] and VCA [45] to obtain correlated spectral functions. A nonequilibrium method analogous to DMFT will be presented in Sec. 5.9 and CPT as well as VCA will be generalized to the steady-state in Sec. 5.4, Sec. 5.5, Sec. 5.6, Sec. 5.7, Sec. 5.8 and Sec. 5.10. We find the transport characteristics of $Li_{0.9}Mo_6O_{17}$ to be strongly anisotropic. It is an effectively one-dimensional conductor as observed in transport experiments [48]. ARPES experiments [47] are well described by correlated spectral functions calculated using our model for the electronic structure. By comparing experimentally obtained Fermi surfaces to our calculations we conclude that this compound constitutes a moderately correlated material. A detailed study of correlated transport along these chains would be possible in the DMRG+TEBD framework, which is applied to the SIAM in this thesis in Sec. 5.2 and Sec. 5.3. Details of the calculations are available in Ch. A.

This research is authored by Martin Nuss (MN) and co-authored by Markus Aichhorn (MA). This research was to a large and significant extent conducted by MN under the supervision of MA. The work was initiated by MN. MA provided guidance throughout the whole working period. MN and MA conducted literature research and worked on developing a model for the electronic

Table 5.1.: List of publications sorted by thematic setting.

#	setting	reference	section	title
1	linear-response	PHYSICAL REVIEW B 89, 045125 (2014) [41]	Sec. 5.1	Effective model for the electronic properties of quasi-one-dimensional purple bronze $Li_{0.9}Mo_6O_{17}$ based on *ab initio* calculations
2	real time evolution	PHYSICAL REVIEW B 88, 045132 (2013) [52]	Sec. 5.2	Steady-state and quench-dependent relaxation of a quantum dot coupled to one-dimensional leads
3	real time evolution	PHYSICAL REVIEW B 91, 085127 (2015) [54]	Sec. 5.3	Nonequilibrium spatiotemporal formation of the Kondo screening cloud on a lattice
4	steady-state	PHYSICAL REVIEW B 85, 235107 (2012)	Sec. 5.4	Variational cluster approach to the single-impurity Anderson model
5	steady-state	AIP Conf. Proc. 1485, 302 (2012) [63]	Sec. 5.5	Non-linear transport through a strongly correlated quantum dot
6	steady-state	PHYSICAL REVIEW B 86, 245119 (2012) [62]	Sec. 5.6	Steady-state spectra, current, and stability diagram of a quantum dot: A nonequilibrium variational cluster approach
7	steady-state	PHYSICAL REVIEW B 89, 155139 (2014) [65]	Sec. 5.7	Effects of electronic correlations and magnetic field on a molecular ring out-of-equilibrium
8	steady-state	submitted to PHYSICAL REVIEW B (2015), arXiv:1505.01683	Sec. 5.8	Master equation based steady-state cluster perturbation theory
9	steady-state	PHYSICAL REVIEW B 89, 165105 (2014) [69]	Sec. 5.9	Auxiliary master equation approach to nonequilibrium correlated impurities
10	steady-state	unpublished (2015) [70]	Sec. 5.10	Strong electronic correlations at high bias voltage and structured electronic leads

structure. MA conducted *ab initio* calculations using Wien2k [4], performed a Wannier down folding [5] and ran DMFT calculations in TRIQS [1]. MN adapted the eVCA method originally proposed by MA *et al.* in [46]. MN wrote computer codes for the CPT and eVCA calculations and tested and ran those simulations. MN calculated and analyzed the linear-response conductivity. MN conducted parameter studies and analyzed the results of interacting methods. MN prepared, collected, interpreted, analyzed and visualized the results and set them in context with recent literature. MN wrote the first version of the manuscript. All authors contributed equally in analysing the data and revising the manuscript. Enrico Arrigoni, Wolfgang von der Linden and Christoph Heil provided help and expertise. We discussed our results with Jim W. Allen, Fakher Assaad, Jerne Mravlje and Piotr Chudzinski.

5.1.2. Manuscript

Effective model for the electronic properties of quasi-one-dimensional purple bronze $Li_{0.9}Mo_6O_{17}$ based on *ab initio* calculations

Martin Nuss* and Markus Aichhorn

Institute of Theoretical and Computational Physics, Graz University of Technology, 8010 Graz, Austria

(Received 10 June 2013; revised manuscript received 18 December 2013; published 16 January 2014)

We investigate the electronic structure of the strongly anisotropic, quasi-low-dimensional purple bronze $Li_{0.9}Mo_6O_{17}$. Building on all-electron *ab initio* band-structure calculations, we obtain an effective model in terms of four maximally localized Wannier orbitals, which turn out to be far from atomiclike. We find *two half-filled* orbitals arranged in chains running along one crystallographic direction and *two full* orbitals in perpendicular directions, respectively. The possibility to reduce this model to only two orbitals forming two chains per unit cell with interchain coupling is discussed. Transport properties of these models show high anisotropy, reproducing trends of the experimentally determined values for the dc conductivity. We also consider basic effects of electron-electron interactions using the (extended) variational cluster approach and dynamical mean field theory. We find good agreement with experimental photoemission data upon adding moderate onsite interaction of the order of the bandwidth to the *ab initio* derived tight-binding Hamiltonian. The obtained models provide a profound basis for further investigations on low-energy Luttinger-liquid properties or to study electronic correlations within computational many-body theory.

DOI: 10.1103/PhysRevB.89.045125 PACS number(s): 71.10.−w, 71.27.+a, 71.20.−b, 72.15.−v

I. INTRODUCTION

The electronic structure of highly anisotropic materials shows a plethora of interesting effects. Quantum many-body dynamics in quasi-low-dimensional systems becomes important and dominant in many regions of their rich phase diagram. This often implies unconventional ground states, such as non-Fermi-liquid or Luttinger-liquid states. One prominent example for this class of materials is the lithium molybdenum purple bronze $Li_{0.9}Mo_6O_{17}$ [1], a molybdenum oxide bronze with quasi-one-dimensional properties. [2]

Experimental structure analysis using x rays [3] as well as neutrons [4] determined a monoclinic crystal structure. The conduction electrons are mostly located on two molybdenum octahedral sites which are arranged in double zigzag chains along the *b* axis. This leads to a very high anisotropy of the material, which has been studied by several techniques using resistivity measurements [5–10], conductivity under pressure [11], magnetoresistance [8,12], thermal expansion [13], optical conductivity [14,15], the Nernst effect [16], thermal conductivity [17], thermopower [18], and muon spectroscopy [19].

The electronic properties have been addressed using angle-resolved photoemission spectroscopy (ARPES) [20–28] and scanning tunneling microscopy (STM) [29,30], which argued for one-dimensional Luttinger-liquid physics [28,31–36]. Other studies disputed this claim [37]. The evolution and the current status of work in that direction is summed up in a recent review article [26]. A temperature-dependent dimensional crossover [38–40], which induces coherence for the perpendicular electron motion, has been studied using neutron diffraction [4].

Apart from intriguing physical effects of effective low dimensionality, the material shows superconductivity below 1.9 K [2,41–44] and a metal-insulator transition is observed at around 24 K [5,14,41,45]. No evidence for a Peierls instability has been reported [46], and a possible charge-density wave (CDW) phase is still under debate [29,47–49]. Recent studies have argued for a compensated metal [50]. All data are summed up in a conjectured electronic phase diagram as presented in [49].

Theoretical *ab initio* studies of the electronic structure using a tight-binding method [51] as well as a linearized muffin-tin orbital (LMTO) [52,53] calculation in the local density approximation (LDA) have been conducted. These approaches were successful in providing a broad picture of the "high-energy" physics of $Li_{0.9}Mo_6O_{17}$, accounting for the high anisotropy. Although experiments testified a wealth of remarkable low-energy properties and different quantum ground states, more detailed theoretical investigations, including interactions and low dimensionality, emerged in recent years only.

Chudzinski *et al.* [48] investigated the quasi-one-dimensionality and have been able to extract an effective *low-energy* theory within the Tomonaga–Luttinger-liquid framework. Their approach is based on an atomic orbital tight-binding model with parameters such that it matches an LDA LMTO band-structure calculation. Motivated by the crystal structure of $Li_{0.9}Mo_6O_{17}$, the model was set up with four molybdenum *d* orbitals in a zigzag ladder arrangement including onsite as well as nonlocal electronic interactions. It was found that within this model, Luttinger-liquid low-energy parameters can be obtained, which are consistent with experimental findings.

Another recent work [49] proposes a two-dimensional model from *Slater-Koster* [54] atomic orbitals also including nonlocal electronic interactions. Again, an ansatz with four Mo orbitals in zigzag ladder arrangement was applied. The authors argue, based on electron counting, that there are two electrons to be shared among the four equivalent Mo atoms, leading to quarter-filled orbitals. The bandwidth obtained with this ansatz for the two bands crossing the Fermi level is in rough agreement with density functional theory (DFT) calculations.

*martin.nuss@student.tugraz.at

Details of the band structure such as curvatures, however, and also the bands just below the Fermi level which are of similar Mo *d* character, can not be reproduced by this *Slater-Koster* model.

The main purpose of this work is to establish an unbiased, *general purpose tight-binding model* for the electronic properties of $Li_{0.9}Mo_6O_{17}$ based on *ab initio* calculations. Such a model is intended to serve as a basis to study the role of electronic correlations by adding interactions, be it in a computational many-body theory or in a one-dimensional renormalization group (RG) framework. In contrast to previous work [49], we propose a model based on maximally localized Wannier orbitals [55,56] instead of linear combination of atomic orbitals. Four molecularlike orbitals are obtained in a fully *ab initio* approach from an all-electron DFT calculation. Our results unambiguously show that, using a set of four Wannier orbitals in the unit cell, the model consists of *two half-filled* as well as *two filled* orbitals. As we will show in the following, the DFT band structure is perfectly reproduced in this basis set of Wannier functions.

This model describes the momentum-resolved electronic structure as observed in ARPES [22] experiments and reproduces highly anisotropic transport characteristics [5–8,12,14,17]. Furthermore, we discuss an even simpler two-orbital effective model which can be derived from the four-orbital model.

In the second part of the paper, we conduct a first (qualitative) study of effects of interactions on the electron dynamics within this effective Wannier model. Even more so due to the low dimensionality, the interacting model is in general difficult to approach. By applying RG as well as density matrix renormalization group (DMRG) [57] in certain limits (chains, ladders), their essential physics can be understood [49]. To solve the full low-dimensional interacting Hubbard-type model, general frameworks as for example (cluster) dynamical mean field theory [(C)DMFT]-like approaches [58] have been applied, where the self-energy of the system is restricted to a finite length scale.

Realistic modeling is a relatively new and rapidly developing field [60–62]. In this work, we study (simple) electron-electron interactions in the effective model using complementary numerical techniques. First, we use cluster perturbation theory (CPT) [63,64] as well as the (extended) [65,66] variational cluster approach [67] [(e)VCA] in the spirit of LDA + VCA [68,69]. The choice of these methods is motivated by the expected reduced effective dimensionality of the material which renders the nonlocal character of the VCA self-energy an interesting perspective. Second, we apply the well-established LDA + DMFT [70–72] approach, which neglects nonlocal correlations, but on the other hand performs superior in describing the quasiparticle features at low energy as compared to VCA. For all applied methods, we find that a moderate value of onsite interactions strength is capable of describing the electron dynamics best and in good agreement with ARPES experiments. We discuss the influence of a hybridization mechanism of the two bands right at the Fermi energy with the two bands slightly below, not accounted for in previous work.

This paper is organized as follows: In Sec. II, we report accurate all-electron DFT data from which we obtain a model in terms of maximally localized Wannier functions. A further simplified model for $Li_{0.9}Mo_6O_{17}$ with reduced number of hopping parameters is discussed in Sec. II C. We present results for the anisotropic conductivity in Sec. III and compare to transport measurements. The electron dynamics of the interacting effective model is presented and compared to ARPES experiments in Sec. IV before concluding in Sec. V.

II. FROM CRYSTAL STRUCTURE TO AN EFFECTIVE ELECTRONIC MODEL

A. *Ab initio* electronic structure

We obtain the electronic structure for ideal $Li_1Mo_6O_{17}$ from a non-spin-polarized, full-potential linearized augmented plane wave (FP-LAPW) [73–76] DFT [77,78] calculation as implemented in the WIEN2K package [79]. The unit-cell parameters and crystal structure are taken from x-ray data [3] which have been recently confirmed by neutron diffraction experiments [4]. The space group is monoclinic (prismatic) $P2_1/m$ with lattice parameters $a = 12.762(2)$ Å, $b = 5.523(1)$ Å, $c = 9.499(1)$ Å, $\beta = 90.61(1)^\circ$, and $Z = 2$, leading to a 48-atom unit cell $[Li_1Mo_6O_{17}]_2$ [80].

All results presented in this work are calculated with the exchange-correlation potential treated in the LDA [81]. We checked that the generalized-gradient approximation (GGA-PBE [82]) gives indistinguishable results for the band structures. Our results are converged in terms of the size of the FP-LAPW basis set, which is determined by the $RK_{\max}$ parameter in WIEN2K. By performing calculations for different $RK_{\max}$ we found that $RK_{\max} = 7.0$ and 6.0 gave the same results, with band energies within 10^{-3} eV, only at $RK_{\max} = 5.0$ deviations become visible. Therefore, also due to the computational complexity of the problem, all results presented here are obtained with a $RK_{\max} = 6.0$ basis set.

The obtained electronic structure $\epsilon_{\mathrm{KS}}(\mathbf{k})$ is visualized along the standard path of the *b*-*c* plane in reciprocal space (Y-G-X-M) (see also Fig. 2) in Fig. 1 (left). In order to compare to ARPES experiment, we modeled lithium-vacant $Li_{0.9}Mo_6O_{17}$ by a rigid band shift of 0.03 eV of the LDA bands [52]. We find a combined bandwidth of the four bands in the vicinity of the Fermi energy ϵ_F of $W \approx 1.82$ eV and two Fermi velocities of $v_{F,1} \approx 0.99 \times 10^5$ m/s and $v_{F,2} \approx 0.93 \times 10^5$ m/s, roughly one order of magnitude lower than in free-electron metals [83]. The corresponding electronic density of states (DOS) is shown in Fig. 1 (right). The LDA DOS is obtained by Gaussian integration ($\sigma \approx 0.02$ eV) using the tetrahedron method on a grid of 216 *k* points in the irreducible Brillouin zone (BZ).

By and large, the electronic structure compares well to previous data reported in early works of Whangbo *et al.* [51] from an empirical tight-binding method, and also to more recent LMTO calculations within the atomic sphere approximation (ASA) from Popovic *et al.* [52]. But note that in particular the band crossings/hybridizations on the X-M line as well as the lowest empty bands at ∼1 eV above ϵ_F are apparently different. Since we checked accurately the convergence of the all-electron FP-LAPW calculations, the difference is most likely to come from the approximations introduced in LMTO-ASA and tight-binding calculations.

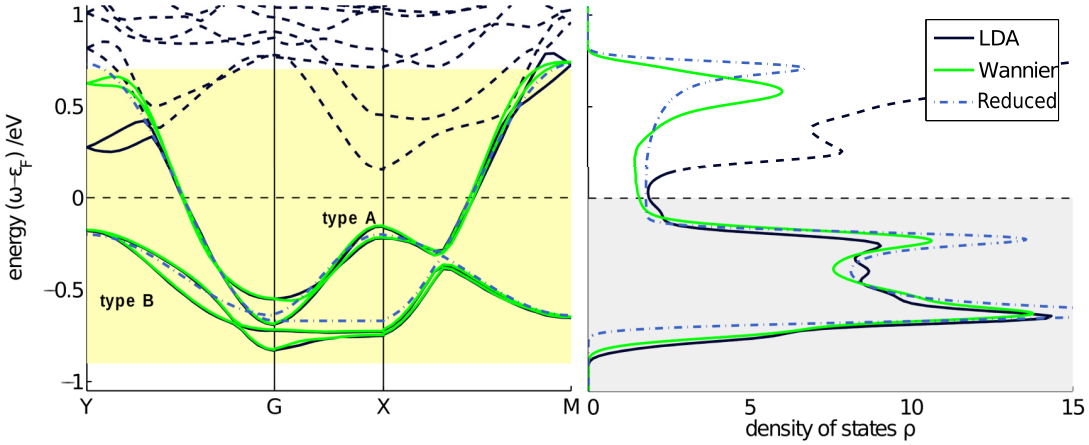

FIG. 1. (Color online) Left: LDA band structure (solid black) in the vicinity of the Fermi energy ϵ_F plotted along a two-dimensional path in the reciprocal b-c plane. The four bands of the full Wannier projected Hamiltonian are shown on top (solid green) next to the data for the reduced model (dashed-dotted blue line). Right: DOS of the LDA calculation (black), the full Wannier model (solid green line), and the reduced model (dashed-dotted blue line).

The one dimensionality of the material becomes manifest in the Fermi surface which is shown in Fig. 2 (left). Arising from two bands crossing the Fermi energy, it consists of two sheets warping in the c direction, cutting the b axis and being roughly constant in the a direction. In experiments [84], the maximum splitting of the Fermi surface ($<10^{-3}$ Å^{-1}) is observed along the $\overline{\text{PK}}$ line. Our LDA calculations yield the maximum splitting along the very same line (see Fig. 2), but the magnitude is much larger ($\approx$0.021 Å^{-1}). In previous LDA calculations [52], an even larger splitting of $\approx$0.045 Å^{-1} was found. This discrepancy of the theoretical results with experiment is likely due to the improper treatment of strong nonlocal electronic correlations in the LDA.

B. Realistic effective model

To construct an effective model, we have to identify the origin (orbital character and atom) of those electronic states which are most important for the physical properties, i.e., those close to the Fermi energy ϵ_F. We plot in the bottom panel of Fig. 3 the partial DOS for the six inequivalent Mo atoms in the unit cell. One can nicely see that Mo_1 and Mo_4 contribute most to the DOS at ϵ_F (for nomenclature see Fig. 2 in Onoda *et al.* [3]). In the top panel of Fig. 3, we show the crystal structure, with emphasis on those Mo_1 and Mo_4 (including the equivalent Mo_1' and Mo_4') atoms. It is evident that these atoms form the two adjacent zigzag chains running along the b axis, giving rise to the two quasi-one-dimensional bands crossing ϵ_F. The atoms Mo_2 and Mo_5 are sitting next to the chains, and thus have some smaller contributions. The other two Mo atoms are far away from the chains, and thus contribute hardly anything to the weight around ϵ_F. This analysis of the orbital character shows clearly that the bands around ϵ_F originate mainly from only four atoms (Mo_1, Mo_4 and Mo_1', Mo_4', respectively) in the unit cell.

To construct an effective model, we take the electronic wave-function data ϕ_{KS} in an energy window of $[-0.9, 0.7]$ eV, that comprises the four relevant bands as shown in Fig. 1. The lower bound of the energy window for projection is straightforward to choose because the gap between the four

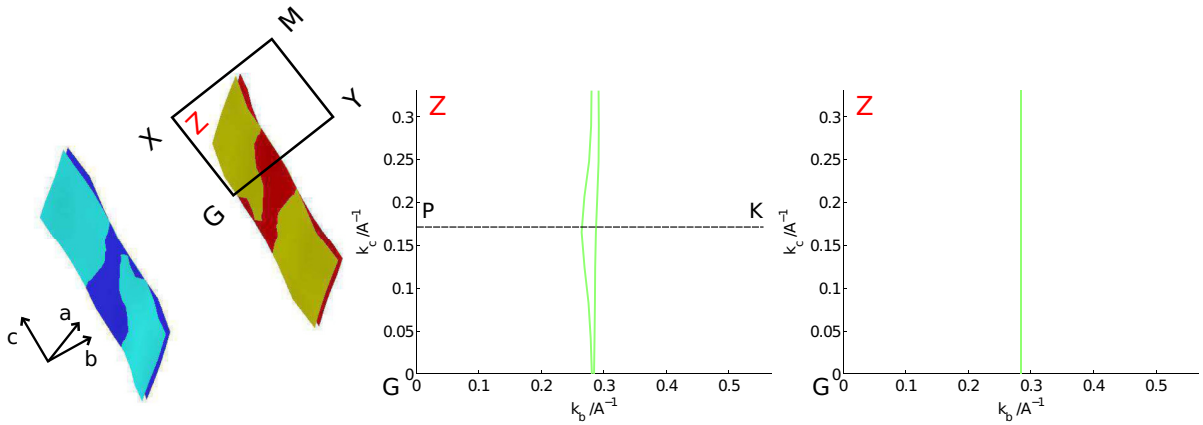

FIG. 2. (Color online) Calculated Fermi surface. Left: The *ab initio* result (image created using XCRYSDEN [59]). Center: In-plane projection of the result for the four-orbital Wannier model. Right: In-plane projection of the result for the reduced model, where type-A orbitals are strictly one dimensional and the two Fermi sheets are degenerate.

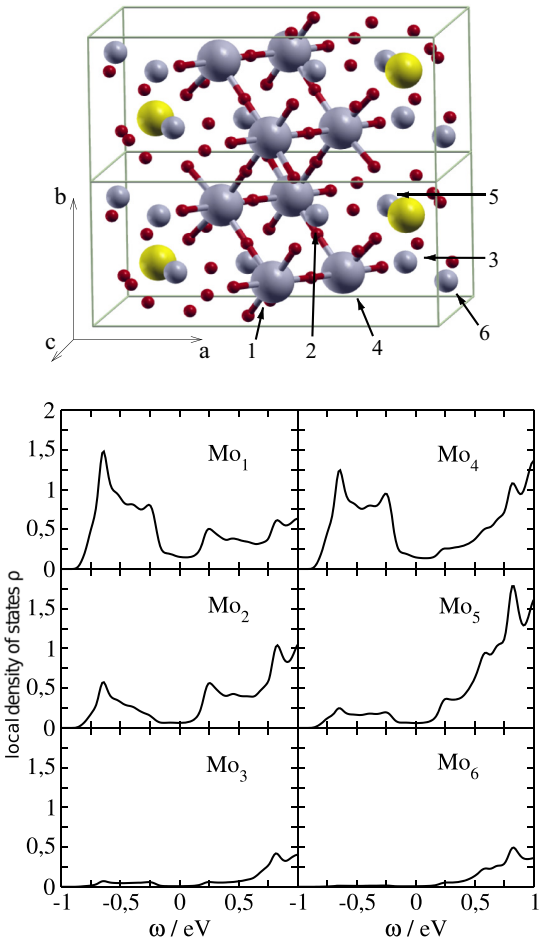

FIG. 3. (Color online) Top plot: Crystal structure. In the a and c directions one unit cell and in the b direction two unit cells are shown. Big gray balls are Mo_1/Mo_1' and Mo_4/Mo_4' atoms, showing the zigzag chain structure along b. Small gray: other Mo sites. The numbers next to the black arrows denote the atom number. Small red balls are oxygen, and the yellow balls Li atoms. This image has been created using XCRYSDEN [59]. Bottom plot: Partial DOS of the six inequivalent Mo atoms in the unit cell. Top row: atoms Mo_1 and Mo_4, forming the zigzag chains. Middle row: Mo_2 and Mo_5. Bottom row: Mo_3 and Mo_6.

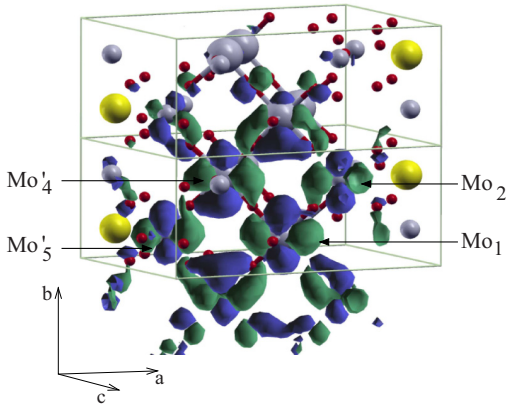

FIG. 4. (Color online) Visualization of one type-A Wannier orbital. Similar as in Fig. 3, two unit cells in the b direction are shown, the Wannier function is centered in the lower unit cell. The center of the Wannier function is located in-between atoms Mo_1 and Mo_4'. Arrows mark the atoms with significant contribution to the Wannier function: in-chain atoms Mo_1 and Mo_4', and adjacent atoms Mo_2 and Mo_5'. Color coding as in the top panel of Fig. 3. For the Wannier functions, blue and green lobes denote positive and negative phases, respectively. The image has been created using XCRYSDEN [59].

considered molybdenum d bands and the next lower bands is larger than 1.5 eV. The upper bound is more involved since bands with different character penetrate the energy window from above, and are entangled with the two bands crossing the Fermi energy. In order to get a good description of the bands, we had to use the disentanglement procedure of WANNIER90 with a frozen energy window of $[-0.9,0.0]$ eV.

We project these data onto four maximally localized Wannier orbitals [55] ω_α using WANNIER90 [85] and the WIEN2WANNIER [86] interfaces. As initial seed, we chose one d_{xy} orbital on each of the Mo_1, Mo_4, Mo_1', and Mo_4' atoms.

Although starting from a seed with atomic orbitals, the calculated Wannier functions, however, have quite different character. They can be divided into two kinds. Type A, which is oriented along chains in the b direction, and type B which is in some sense orthogonal in real space, mediating between the chains in the b direction. The orbitals contributing to the states around ϵ_F are of type A, and one of these orbitals is shown in Fig. 4. One can clearly see the d_{xy} orbital character, forming the zigzag chains, around atoms Mo_1 and Mo_4', where most of the orbital weight is located. In consistency with the partial DOS (Fig. 3), some contribution also comes from atoms Mo_2 and Mo_5' since they are adjacent to the chains, as shown in Fig. 4.

The splitting into two types of orbitals can be understood from the band structure. Only two bands cross ϵ_F, which results in two equivalent Wannier functions (A). The other two bands, lying below ϵ_F, are spanned by another set of two equivalent Wannier functions (B), respecting the crystal symmetry.

We would like to emphasize that these orbitals are far from atomiclike. We estimate their spread from the square root of the spread functional of WANNIER90, which yields 5.2 Å for orbital type A, and 4.4 Å for orbital type B. We also want to note that the Wannier functions are not centered on a Mo site. Instead, Fig. 4 clearly shows that the centers are located in the middle of a bond between two Mo sites. For type A, one orbital has its center between atoms Mo_1 and Mo_4', the other between Mo_1' and Mo_4, respectively. In that sense, these Wannier orbitals can be regarded as bond-centered molecularlike orbitals.

The origin of the large spread in real space is the very limited number of bands that are taken into account in the Wannier construction scheme. Taking all d orbitals of the Mo_1, Mo_1', Mo_4, and Mo_4' atoms as well as the bridging oxygen p orbitals into account would of course result in much better localization. However, the Hamiltonian then describes many bands, and not only the most important four bands in the vicinity of ϵ_F. A similar effect can be observed for instance in the construction of the one-band model in cuprate superconductors. Also there, taking only the $d_{x^2-y^2}$ orbital into the construction results in quite large Wannier orbitals with long tails [87].

Concerning the electron charge in the Wannier orbitals, we find that orbitals of type A are *half-filled*, whereas orbitals of type B are identified as (almost) filled. For lithium-vacant purple bronze, we find a total occupation of ≈5.8 electrons in these four bands since there are two lithium ions in the unit cell, each contributing ≈0.1 hole doping. In the remainder of the paper, we will therefore use for all discussions an average filling of the four bands of $\langle n \rangle = 1.44$ [88].

Specifically, the downfolding procedure yields the matrix elements of a single-particle Hamiltonian [89]

$$H_{\mathrm{Wannier},\alpha\beta}(\mathbf{k}) = \langle \omega_\alpha | \, \hat{\mathcal{H}}_{\mathrm{Wannier}}(\mathbf{k}) \, | \omega_\beta \rangle = \sum_{\delta R} e^{-i\mathbf{k}\cdot\delta R} M_{\mathbf{R}\alpha\mathbf{R}'\beta} \quad (1)$$

in the four-orbital Wannier space $\alpha,\beta = \{\mathrm{A},\mathrm{A}',\mathrm{B},\mathrm{B}'\}$ where the sum runs over all lattice translations $\delta R = (\mathbf{R} - \mathbf{R}')$ and the crystal momentum $\mathbf{k}$ is defined in the first BZ [90].

Our model (1) consists of two filled electronic orbitals, type B, slightly below the Fermi energy ϵ_F ($M_{\mathbf{0B0B}} = M_{\mathbf{0B'0B'}} = -0.423$ eV), as well as two half-filled ones, type A, crossing the Fermi energy ϵ_F ($M_{\mathbf{0A0A}} = M_{\mathbf{0A'0A'}} = 0.005$ eV). The largest energy scale for the hopping matrix elements is the nearest-neighbor hopping along the b direction of orbitals of type A which is $t_{\max} \approx -0.35$ eV.

This 4×4 noninteracting Wannier Hamiltonian can easily be diagonalized by numerical means. Its band structure and DOS are plotted on top of the LDA results in Fig. 1. The Wannier DOS has been calculated from $N_{1.\mathrm{BZ}} = 48^3$ k points in the first BZ, using a numerical broadening of $0^+ = 0.086\, t_{\max}$. We obtain very good agreement except for the upper band edges, where the accuracy is influenced by the entanglement of the bands in this energy region. We find a total bandwidth of the four bands in the vicinity of ϵ_F of $W \approx 1.57$ eV and two Fermi velocities of $v_{F,1} \approx 1.16 \times 10^5$ m/s and $v_{F,2} \approx 1.06 \times 10^5$ m/s. Note that the Fermi velocity is pointing along the b direction, while the other components are three orders of magnitude smaller. The Fermi surface (see Fig. 2, center) is also reproduced very accurately by the Wannier model.

C. Effective interchain coupling

The Wannier model (1) consists of numerous single-particle hopping terms between four Wannier orbitals in a three-dimensional crystal. Many of the terms of the Wannier model are orders of magnitude smaller than the dominant hopping process of type-A orbitals along the b direction with $t_{\mathrm{AA}} \approx -0.35$ eV. For instance, all intra-unit-cell hybridizations are negligibly small (of order 10^{-4} eV). This includes direct hopping $t_{\mathrm{AA}'}$ between adjacent chains. The reason for this is that the two orbitals type A and A′ are aligned parallel to each other in the unit cell, with negligible overlap. The hybridization perpendicular to the chains, which is responsible for the dispersion in perpendicular direction, is predominantly mediated through the type-B orbitals in an (A-B-A) or (A-B-A′) fashion (see Fig. 5). In this section, we derive a two-dimensional model in the b-c plane consisting of two degenerate half-filled chains that comprises the fundamental

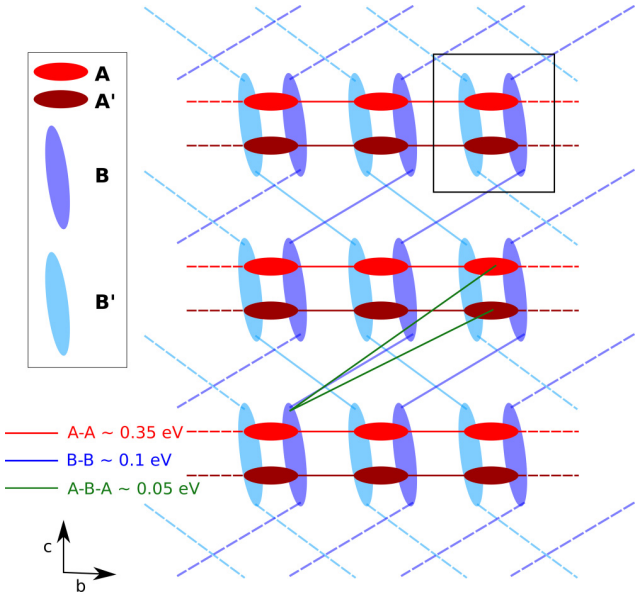

FIG. 5. (Color online) Visualization of the full effective Wannier Hamiltonian (1). A schematic drawing of the most dominant hopping processes is presented: type-A orbitals (red), type-B orbitals (blue). Lines denote the dominant hopping paths, and the black square marks the size of the unit cell.

model. The indirect hopping results only in a small effective hopping between the chains, which we estimate perturbatively.

The starting point for perturbation theory is a Hamiltonian, where orbitals of type A and type B are decoupled. For this purpose we define a complete set of projection operators projected Hamiltonians $\hat{\mathcal{H}}_{\alpha\alpha} = \hat{P}_\alpha \hat{\mathcal{H}} \hat{P}_\alpha$ on the type $\alpha = \{\mathrm{A},\mathrm{B}\}$ orbitals. In zeroth-order approximation, the hybridization terms are set to zero, $\hat{\mathcal{H}}_{\mathrm{AB}} = \hat{\mathcal{H}}_{\mathrm{BA}} = 0$. For our Wannier model, this corresponds to neglecting those matrix elements which are less than 10% of the largest occurring hopping energy $|t_{\max}| = 0.35$ eV and leads to a Hamiltonian

$$H_{\mathrm{reduced}} = \begin{pmatrix} t_{\mathrm{AA}} 2\cos(k_b b) & 0 \\ 0 & \epsilon_B + t_{\mathrm{BB}} 2\cos(k_b b \pm k_c c) \end{pmatrix}, \quad (2)$$

with $t_{\mathrm{AA}} = -0.35$ eV, $t_{\mathrm{BB}} = -0.11$ eV, and $\epsilon_{\mathrm{B}} = -0.45$ eV accompanied by the rigid band shift of $\mu = -0.03$ eV. One has to keep in mind that both bands A and B are doubly degenerate. We will refer to this Hamiltonian as *reduced model* throughout this work.

Note that the two type-B orbitals disperse in orthogonal diagonals. The bands crossing the Fermi energy arise due to the two degenerate type-A orbitals which now represent isolated, one-dimensional chains dispersing in the b direction. Due to the missing hybridization between A and B orbitals, fine features of the perpendicular (c-direction) dispersion are not reproduced. Nevertheless, despite its simplicity, the band structure and density of states (see Fig. 1) are still described very well. Data in the figure have been obtained using $N_{1.\mathrm{BZ}} = 48^3 k$ points in the first BZ and a numerical broadening of $0^+ = 0.086\, t_{\max}$ for the evaluation of the DOS.

We find a bandwidth of the two bands in the vicinity of ϵ_F of $W \approx 1.4$ eV and a Fermi velocity of $v_F \approx 0.93 \times 10^5$ m/s.

In order to estimate the effective interchain coupling, we treat the indirect (A-B-A′) hoppings in second-order perturbation theory. For that purpose, we project the full four-orbital Wannier model (1) onto the type-A bands [91]

$$\hat{\tilde{\mathcal{H}}}_{\mathrm{AA}} = \hat{\mathcal{H}}_{\mathrm{AA}} + \hat{\mathcal{H}}_{\mathrm{AB}}(\omega - \hat{\mathcal{H}}_{\mathrm{BB}})^{-1}\hat{\mathcal{H}}_{\mathrm{BA}}\,.$$

Upon approximating ω by the bare eigenenergies of $\hat{\mathcal{H}}_{\mathrm{AA}}$, we arrive at a two-orbital model which reproduces the band dispersions of the two bands crossing the Fermi energy (not shown). We note in passing that this two-orbital model can also be obtained by a Wannier construction where the basis is restricting to bands of type A alone.

Keeping the number of hopping terms low, we now perform a fit of $\hat{\tilde{\mathcal{H}}}_{\mathrm{AA}}(\mathbf{k})$ with a Hamiltonian that contains perpendicular hopping in addition to the terms of the A orbitals of the reduced model [Eq. (2)] respecting the symmetry of the lattice. In particular, we choose for the perpendicular hopping both intrachain (A-A) terms as well as interchain (A-A′) terms. The χ^2 fit is done using 20^2 k points on an equidistant grid in one fourth of the reciprocal b-c plane ($k_a \approx 0$) plus 3×32 k points on the standard path Y-G-X-M. The only relevant perpendicular hopping processes given by this procedure are nearest-neighbor interchain terms of the order of $t_{\mathrm{AA}'} \approx -0.005$ eV, as well as nearest-neighbor intrachain terms of the order of $t_{\mathrm{AA}} \approx -0.02$ eV. The hopping in the b direction only slightly renormalizes to $t_{\mathrm{AA/A'A'}} \approx -0.37$ eV accompanied by an onsite shift of $\epsilon_{\mathrm{A/A}'} = -0.01$ eV.

Thus, we find an intuitive two-orbital model that consists of two chains dispersing in the b direction with nearest-neighbor perpendicular hoppings of type A-A and A′-A′ which are one order of magnitude smaller than the hopping in the b direction. The direct effective hopping of type A-A′ between the two chains within one unit cell is again one order of magnitude smaller. This small effective coupling explains the robust one dimensionality of the compound. Our calculated values are in good agreement with those discussed in [48].

We want to stress here that only in this section fitting of parameters was performed, in order to estimate the effective perpendicular hopping using only a few parameters. In all other parts of this work, only *ab initio* calculated hopping integrals are used.

III. ANISOTROPIC CONDUCTIVITY

We augment our discussion of the electronic structure by computing the linear response transport and comparing it to experiments. The conductivity tensor of $Li_{0.9}Mo_6O_{17}$ consists of three independent diagonal σ_a,σ_b,σ_c entries as well as one nonzero off-diagonal element $\sigma_{bc} = \sigma_{cb}$ (see Appendix A). Literature provides values for the anisotropic resistivity at room temperature (300 K) and zero magnetic field using several experimental techniques. We summarized the reported data in Table I which all agree on a highly anisotropic resistivity. The ratio between the diagonal elements of the resistivity tensor, however, strongly disagrees in-between the individual measurements. In particular, $\rho_a : \rho_b$ differs by a factor of ≈60 while $\rho_b : \rho_c$ differs even by a factor of ≈640 from the lowest to the highest anisotropy found in experiments. These discrepancies are often attributed to experimental challenges when measuring the resistivity of strongly anisotropic small samples.

TABLE I. Collected data for the anisotropic resistivity at $T = 300$ K and our low-temperature theoretical results for small scattering γ[eV] ∼ 0.05 eV. Data from Refs. [5,12,14] were obtained via four-point measurements, Refs. [6,7] report results using the Montgomery method, Ref. [8] measurements are based on magnetoresistance, and in Ref. [17] a Hall experiment was carried out. Resistivity values which were not given in the respective publications are represented by dashes in the ratio column.

Ref.	ρ_a m Ωcm	ρ_b m Ωcm	ρ_c m Ωcm	Ratio
[5]	2470	9.5		260:1:-
[12]	64.5	16	854	4.5:1:50
[14]		1.7		-:1:-
[6]	110(40)	19(1)	47(5)	6(2):1:2.5(4)
[7]	30	0.4	600	80:1:1600
[8]		0.4		100:1:>100
[17]				100:1:-
Full Wannier model	≈430γ	≈1.8γ	≈600γ	240:1:330
Reduced model		≈2γ		-:1:-

A. Conductivity of the reduced model

The reduced model introduced in Eq. (2) consists of $N_{\mathrm{band}} = 2$ degenerate bands (type A) crossing the Fermi energy dispersing only in the b direction with velocity $v_b^{\mathrm{AA}}(\mathbf{k}) = -\frac{2t_{\mathrm{AA}}}{\hbar} b \sin(k_b b)$ [Eq. (A5)]. In this case of diagonal velocities and spectral functions, the conductivity (see Appendix A1) becomes

$$\sigma_{bb} = \frac{16e^2 t_{\mathrm{AA}}^2}{\hbar}\frac{b^2}{ac}\int_{-\infty}^{\infty} d\omega \frac{\beta}{2\{1+\cosh[\beta(\omega-\mu)]\}} \times \int_0^{\frac{\pi}{b}} dk_b \sin^2(k_b b)\left(\frac{\gamma}{\pi}\right)^2 \times \frac{1}{\{[\omega - 2t_{\mathrm{AA}}\cos(k_b b)]^2 - \gamma^2\}^2},$$

where we introduced a phenomenological scattering $\gamma \sim |\mathrm{Im}[\Sigma(\omega = \mu)]|$ in the Lorentzian-shaped spectral function. In the low-temperature small-scattering limit we find

$$\sigma_{bb} = \frac{16e^2 t_{\mathrm{AA}}^2}{\hbar}\frac{b^2}{ac}\int_{-\infty}^{\infty} d\omega\, \delta(\omega-\mu) \times \int_0^{\frac{\pi}{b}} dk_b \sin^2(k_b b)\frac{\delta[\omega - 2t_{\mathrm{AA}}\cos(k_b b)]}{2\pi\gamma},$$

which evaluates to

$$\sigma_{bb} = \frac{4e^2}{h\gamma}\frac{b}{ac}\sqrt{(2t_{\mathrm{AA}})^2 - \mu^2} \overset{\mu=0}{\approx} N_{\mathrm{spin}} N_{\mathrm{band}} \frac{D}{R_K \gamma}\frac{b}{ac},$$

with $D = 2t_{\mathrm{AA}}$ and $R_K = \frac{h}{e^2}$ the von Klitzing constant. Using this expression we find for the resistivity $\rho_{bb} = \frac{1}{\sigma_{bb}} \approx 2\gamma$[eV] m Ωcm. Considering a reasonable mean-free path d of the order of a unit-cell length and using the calculated Fermi velocity of ≈10^5 m/s we can estimate a scattering

of $\gamma[\mathrm{eV}] = \frac{0.658}{d[\mathrm{\AA}]} \approx 0.05$ eV which implies a resistivity of $\rho_{bb} \approx 0.1$ m Ωcm.

B. Conductivity anisotropy

The reduced model is limited to transport in the b direction. To study the high transport anisotropy suggested by experiments, we calculate the conductivity tensor of the full four-orbital Wannier model. We evaluate Eq. (A1) numerically at $T = 4.2$ K and for small scattering γ (for details see Appendix A2). For the resistivity we obtain $\rho_a \approx 430\gamma$[eV] m Ωcm, $\rho_b \approx 1.8\gamma$[eV] m Ωcm, and $\rho_c \approx 600\gamma$[eV] m Ωcm ($\rho_a : \rho_b : \rho_c \sim 240 : 1 : 330$). Note that the b-axis resistivity in the strictly one-dimensional model (2) is only $\approx$10% larger than the resistivity in the four-orbital model, which means that the reduced model yields already a quite accurate description of the b-axis transport. The a- and c-axis resistivities are roughly two orders of magnitude larger than in the b direction, compatible with experimental data. Using the same phenomenological scattering $\gamma \approx 0.05$ as motivated in the previous section, we obtain $\rho_a \approx 20$ m Ωcm, $\rho_b \approx 0.1$ m Ωcm, and $\rho_c \approx 30$ m Ωcm. The resistivity ratio of $\rho_a/\rho_b \sim 240$ does compare best to the experimental value 260 as obtained in [5] (see Table I).

IV. CORRELATED ELECTRONIC STRUCTURE

The obtained Wannier model is close to being half-filled which indicates that the local part of the Coulomb interactions is most important. The effects of off-diagonal Coulomb interactions are small and further discussed in Appendix B. In the following, we focus on local electron-electron interactions of density-density type, which are added to the *ab initio* tight-binding Wannier model

$$\hat{\mathcal{H}} = \hat{\mathcal{H}}_{\mathrm{Wannier}} + \hat{\mathcal{H}}_{\mathrm{int}}, \tag{3}$$

where the single-particle part $\hat{\mathcal{H}}_{\mathrm{Wannier}}$ is defined in Eq. (1) and

$$\hat{\mathcal{H}}_{\mathrm{int}} = \sum_{\mathbf{R}} \sum_{\alpha} U_\alpha \hat{n}_{\mathbf{R}\alpha\uparrow} \hat{n}_{\mathbf{R}\alpha\downarrow}, \tag{4}$$

where $\hat{n}_{\mathbf{R}\alpha\sigma}$ is the particle-number operator for Wannier orbital $\alpha = \{\mathrm{A},\mathrm{A}',\mathrm{B},\mathrm{B}'\}$ and spin $\sigma = \{\uparrow, \downarrow\}$ in unit cell $\mathbf{R}$. In order to treat the different band fillings in the model properly, we employ a simple double-counting correction [92] in $\hat{\mathcal{H}}_{\mathrm{Wannier}}$,

$$M^{+\mathrm{DC}}_{\mathbf{0}\alpha\mathbf{0}\alpha} = M_{\mathbf{0}\alpha\mathbf{0}\alpha} - U_\alpha \langle n_{\mathbf{0}\alpha} \rangle_{\mathrm{Wannier}}, \tag{5}$$

where the densities $\langle n \rangle_{\mathrm{Wannier}}$ are taken from the noninteracting Wannier model. Adding interactions we furthermore set the chemical potential μ such that the average filling of electrons in the system is at its physical value $\langle n \rangle \approx 1.44$.

This interacting theory is challenging to solve, even more so because the expected results hint to low-dimensional physics which can promote nonlocal self-energy effects. We employ two complementary techniques to study on a first, more qualitative level, the effect of interactions. First, we apply the VCA, which contains nonlocal contributions to the self-energy Σ. Second, we augment these results by a DMFT calculation which neglects contributions of nonlocal self-energy terms, but is superior in the treatment of the low-energy quasiparticle resonance.

A. Variational cluster approach

The VCA [67] is a quantum many-body cluster method which is capable of treating short-range correlations exactly [65,67,93,94]. The given lattice Hamiltonian is partitioned into a cluster and an intercluster Hamiltonian $\hat{\mathcal{H}} = \hat{\mathcal{H}}^{\mathrm{cl}} + \hat{\mathcal{H}}^{\mathrm{inter}}$, where only single-particle terms are allowed in the intercluster part (for details, see Appendix B). Clusters consist of one or more unit cells and are chosen so that their single-particle Green's function $g^\sigma_{ml}(z)$ can be obtained exactly. We use clusters consisting of two unit cells in the b direction ($L_\mathcal{C} = 8$) to capture at least the most basic nonlocal self-energy effects on the quasi-one-dimensional chains which enable signatures of a possible spin-charge separation [66]. In this work, we employ a numerical band Lanczos scheme and the Q-matrix formalism to obtain $g^\sigma_{ml}(z)$ [95]. The CPT approximation to the single-particle Green's function of the full system $G^{-1}(z)$ is given within first-order strong coupling perturbation theory by [63,64]

$$G^{-1}(z) = g^{-1}(z) - H^{\mathrm{inter}}, \tag{6}$$

where H^{inter} are the matrix elements of the intercluster Hamiltonian in the basis of cluster orbitals. If the cluster is larger than the actual unit cell of the crystal, we use a Green's function periodization prescription to project on the original unit cell $G_{\alpha\beta}(z)$ [94].

Within VCA, Eq. (6) is evaluated at the stationary point of the generalized grand potential $\Omega[\mathbf{\Sigma}]$ (for fermions at zero temperature) which is available from G and g [67]. The grand potential is parametrized by the VCA variational parameters $\mathbf{\Delta}$ which are fixed by the VCA condition [67]

$$\nabla_{\mathbf{\Delta}} \Omega(\mathbf{\Delta}) \stackrel{!}{=} \mathbf{0}. \tag{7}$$

The VCA improves the CPT ($\mathbf{\Delta} \equiv \mathbf{0}$) approximation (which is to approximate the self-energy Σ_G of the full system by the self-energy of the cluster Σ_g) by adding flexibility to the cluster self-energy in terms of variational parameters $\mathbf{\Delta}$. We consider the onsite energies of the four Wannier orbitals as independent variational parameters $\mathbf{\Delta} = \{\Delta_{\epsilon_\mathrm{A}}, \Delta_{\epsilon_{\mathrm{A}'}}, \Delta_{\epsilon_\mathrm{B}}, \Delta_{\epsilon_{\mathrm{B}'}}\}$ (which implicitly includes an overall shift of the chemical potential of the cluster) and use $N_{1.\mathrm{BZ}} = 32^3$ k points in the irreducible BZ for the evaluation of Eq. (7).

Advantages of the VCA are that (i) it is exact in the noninteracting system, (ii) the approximation is systematically improvable by enlarging cluster sizes, (iii) or increasing the number of variational parameters $\mathbf{\Delta}$, and (iv) it is possible to work directly in the real energy domain as well as in Matsubara space. VCA on small clusters is inherently biased towards the insulating state, therefore we expect to overestimate a possible Mott gap (see Appendix C for a discussion).

B. Dynamical mean field theory

A complementary approach that neglects nonlocal effects but describes the local dynamical quantum fluctuations better is the DMFT [96]. Within this theory, the interacting lattice problem is mapped on a self-consistent four-orbital impurity model coupled to an infinite electronic bath. The DMFT approximation is to assume a momentum-independent

self-energy of the original model $\Sigma_{\alpha\beta}$:

$$\Sigma_{\alpha\beta}(i\omega,\mathbf{k}) \stackrel{!}{=} \mathcal{S}_{\alpha\beta}(i\omega),$$

where $\mathcal{S}_{\alpha\beta}$ is the local self-energy generated by the auxiliary quantum impurity system.

As impurity solver we use the continuous time quantum Monte Carlo (CT-QMC) code of the TRIQS [97] toolkit and its implementation of the hybridization expansion (CT-HYB) [98,99] algorithm using Legendre polynomials [100]. This sign-problem free method works in Matsubara space and provides statistically exact and reliable results even at very low temperatures [101]. We used a low temperature of $\beta = 150\ \mathrm{eV}^{-1}$ and a k mesh of $N_{1.\mathrm{BZ}} = 800$. The imaginary-time data are continued to the real-frequency axis using a parallel tempering analytic continuation method [102].

Different to VCA, the DMFT as applied here neglects nonlocal correlations. On the other hand, it treats the local dynamical quantum fluctuations accurately.

C. Discussion of the interacting dynamics

For models based on *atomic* orbitals, constrained LDA calculations suggest an onsite interaction for the atomic d Mo orbitals of $U \approx 6.4$ eV and a nearest-neighbor interaction of $V \approx 0.2$ eV [52] in $Li_{0.9}Mo_6O_{17}$, while the bulk Mo value for the onsite interaction is $U \approx 3.8$ eV [48]. As we will discuss in the following, in our model these larger interaction values U, which have been proposed and used for model calculations [48,49], do not give results in accordance with experimental data. Obtaining the interaction parameters in an *ab initio* way by, e.g., the constrained random phase approximation (cRPA) [61,103], would be highly desirable, but is beyond our present computational capabilities due to the very large unit cell of the system.

In the following, based on physical arguments, we will nevertheless argue that a moderate value of U is appropriate for our model. We use uniform *onsite* interactions $U_\alpha = U$ only and estimate the magnitude of the interaction strength to be of the order of a few $t_{\max}$. The reduced value, compared to the atomic one, can be motivated by (i) the large spread of the orbitals [104] and (ii) the effective screening of other Mo $4d$ states near the Fermi level. We want to remind the reader that we are not dealing with atomic orbitals (where for molybdenum the interaction U could be of the order of several electron volts) but with extended, even molecularlike, orbitals (see Fig. 4).

Let us start the discussion using interaction values of the order of the bandwidth, i.e., using $U = 1$ eV. We show results for the single-particle spectrum and orbitally resolved DOS of the interacting model in Figs. 6 (left and center) and 7 [105]. We used a Lorentzian broadening of $0^+ = 0.05$ eV for plotting the spectral functions, as well as $0^+ = 0.025$ eV for plotting the DOS. As discussed in the previous section, the VCA is biased towards an insulating solution (see also Appendix C), that is why there is a small gap in the conduction band visible in the spectral function, which is not seen in the DMFT results.

Comparing the single-particle dynamics to recent experiments (ARPES data from Refs. [21,22]), we find very good agreement for the bands at the Fermi energy (Fig. 6, right). The renormalization of the effective mass of the half-filled orbitals, calculated from the DMFT self-energy, is $m \approx 1.2 m_0$, where m_0 is the LDA band mass.

Regarding the bands crossing the Fermi energy, their slope improves in VCA/DMFT with respect to the LDA data,

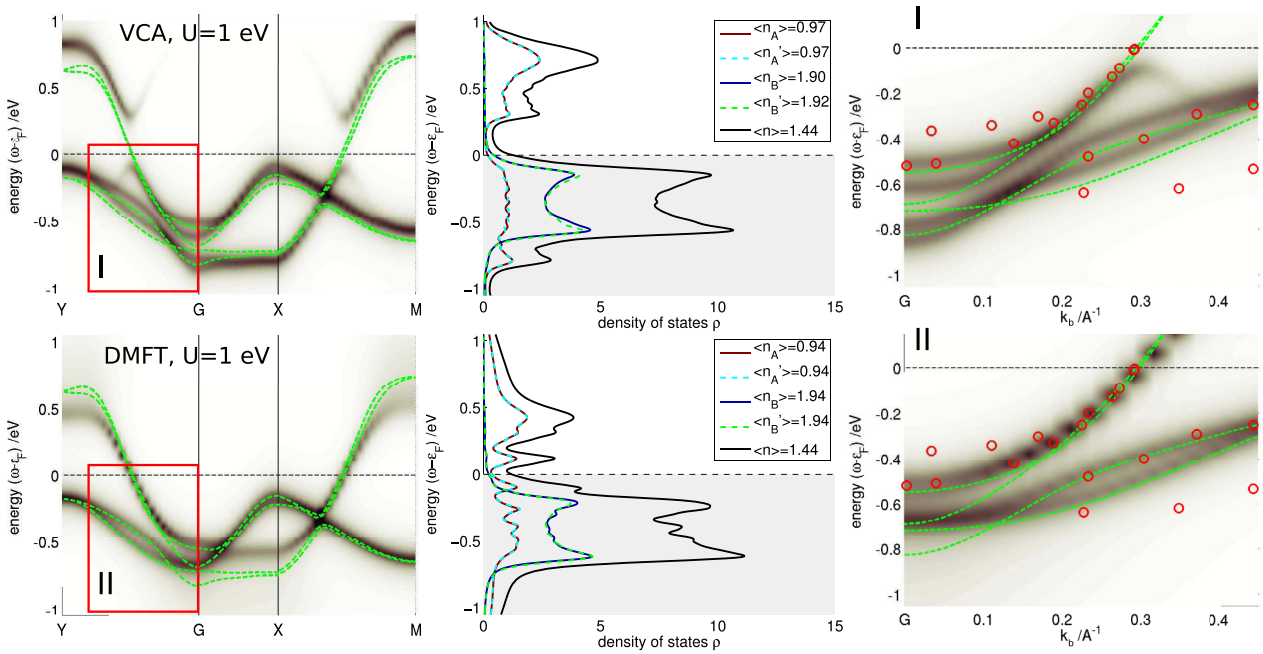

FIG. 6. (Color online) Spectral function and DOS of the interacting model. Top row: VCA data for $U = 1$ eV using eight-orbital clusters. Bottom row: DMFT data for $U = 1$ eV. Left: Spectral function plotted along a two-dimensional path in the reciprocal b-c plane. The noninteracting dispersion is plotted on top (dashed green line). Center: Orbitally resolved density of states. Right: Zoom to the spectral function in the respective red rectangle compared to ARPES data from Ref. [22] which are indicated as red circles.

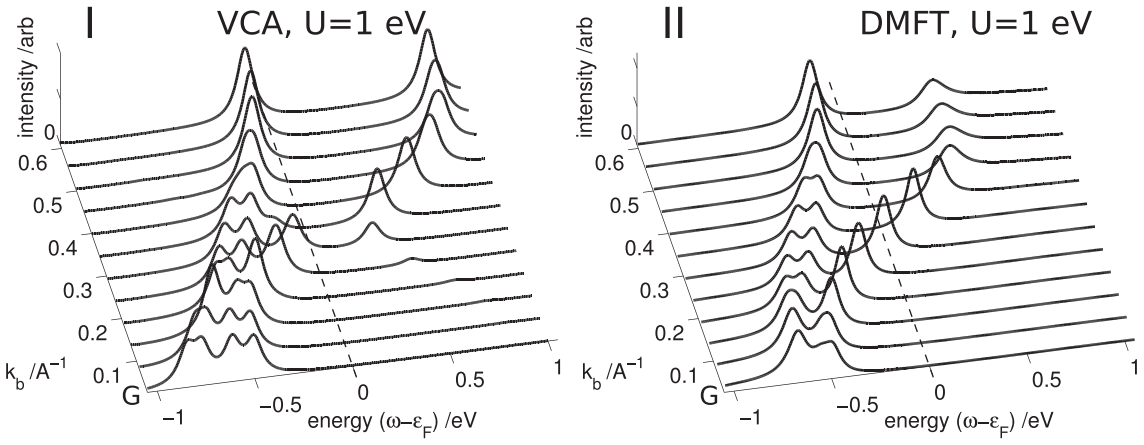

FIG. 7. Cuts through the spectral function along the b axis. The parameters and labels (I, II) correspond to those in Fig. 6.

and compares well with the measured excitations in ARPES experiments [22]. Note that the upmost branch provides only a very weak signal in the ARPES data as compared to the lower branch. In our DMFT calculation, the electronic correlations suppress the hybridizations between chains A and A′, making them equivalent. This leads to only one dispersing feature crossing the Fermi energy (see Fig. 6, lower right panel). The red circles at lower binding energy correspond to the shoulder in the ARPES data, which are very likely due to nonlocal correlation effects that are completely neglected in the single-site DMFT approach. A final statement on the impact of nonlocality of the self-energy and spin-charge separation on the single-particle excitations requires a detailed investigation on large systems, which is beyond the scope of this paper.

Increasing the interaction value further, for instance to $U = 1.5$ eV, does not change results significantly (left aside the artificial gap in the VCA calculation). Above a certain limit, however, which is around $U = 2.5$ eV in our calculations, a Mott gap opens in the two half-filled bands. An extreme example is using the atomic value for the interaction $U = 6$ eV, which is shown in Fig. 8. The half-filled bands are in the Mott insulating state, with the spectral weight transferred to roughly ± 3 eV. The only spectral weight left close to the Fermi level originates from the two almost filled orbitals, type B. This is of course qualitatively different from experimental results.

The values of U given here can only be seen as rough estimates to the actual value, and are by no means *ab initio*. The DMFT overestimates the metallicity of a system, in particular in low dimensions, while the VCA underestimates it. Hence, using different techniques which are tailored more towards low dimensions, the needed value of U to open a Mott gap might be even smaller. As has been shown by Chudzinski *et al.* [48], the system should be metallic, but very close to an insulating state. Our observations can be used as a guideline in further studies to determine the value of U. At very large coupling $U = 6$ eV, however, the system as modeled here is strongly localized, and the insulating state there should be very robust. This is supported by the fact that both methods, VCA and DMFT, give indistinguishable results in this (almost) atomic limit. It clearly shows that taking atomic values

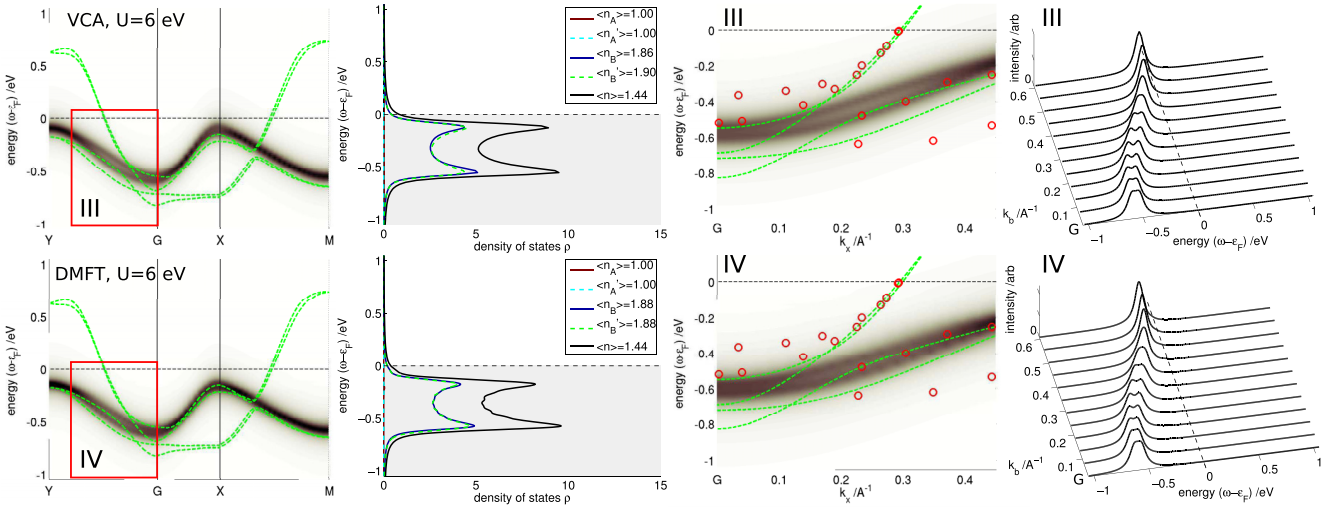

FIG. 8. (Color online) Spectral function and DOS of the interacting model for high values of onsite interaction strength as one would expect for atomiclike molybdenum d orbitals: $U = 6$ eV. For legends, arrangement of the subplots, and color coding, see Fig. 6. On the far right we show cuts through the spectral function as in Fig. 7.

for U is inadequate for the effective model derived in this work.

Let us shortly comment on the effect of correlations in the reduced model (Sec. II C). There, the Hamiltonian of the half-filled and the filled bands decouples exactly, which means that one is left with a standard one-dimensional (almost) half-filled Hubbard model with nearest-neighbor hopping only [106]. As discussed in Secs. II C and III A, this gives a quite good description of the dispersion in chain direction including transport properties. Effects beyond the one-dimensional Hubbard model can be included using the effective perpendicular hopping terms as estimated in Sec. II C. In a recent study on dimensional crossover [40], the critical perpendicular coupling to enter the regime of one-dimensional physics is $t_p \approx 0.18t$ at interaction strength $U = 3t$. Of course, this value depends on model details such as frustrated hopping and interaction strength. However, since our estimated value for t_p in $Li_{0.9}Mo_6O_{17}$ is significantly smaller than this boundary, we suggest that this can explain the robustness of one-dimensional (1D) physics in this compound. We leave a more detailed study of the dimensional crossover in $Li_{0.9}Mo_6O_{17}$ for further investigations.

V. CONCLUSIONS

We have devised a model for the electronic structure of the highly anisotropic low-dimensional purple bronze $Li_{0.9}Mo_6O_{17}$. Starting from *ab initio* calculations, applying density functional theory in the local density approximation, we constructed a four-orbital model based on molybdenum d states in terms of maximally localized Wannier functions. This leads to an effective theory with *two filled bands* slightly below and *two half-filled bands* crossing the Fermi energy. We obtained an even more elementary effective model with reduced dimensionality consisting of two orbitals only, tailored towards studies of interactions at low energies.

We showed that basic electronic properties of our model are in good agreement with experimental data and *ab initio* results. Estimated anisotropic transport coefficients reproduce experimental trends. The model enables us to study effects of many-body correlations. In a first approach, we made use of the (extended) variational cluster approach which takes into account nonlocal contributions to the self-energy and dynamical mean field theory to study the effects of density-density type electron-electron interactions. Our results indicate that moderate onsite interactions (of the order of the bandwidth) are essential, while nearest-neighbor density-density interactions play a minor role. The so-obtained single-particle spectra agree well with recent angle-resolved photoemission experiments. Our study sets some qualitative limits on the value of the interaction parameters. In particular, we could show that the values used for atomiclike molybdenum d orbitals are completely inappropriate for our Wannier model of lithium purple bronze.

We would like to point out that our model is very different from previously proposed descriptions for $Li_{0.9}Mo_6O_{17}$ which were based on atomic orbitals with a comparatively high onsite interaction strength of several electron volts. We suggest that low-energy treatments of this one-dimensional model should start from two half-filled chains with moderate onsite interaction rather than quarter-filled ladder models with high values of onsite interaction strength plus off-diagonal interactions.

Our model is intended to serve as a starting point for future studies of the electronic structure and interactions of $Li_{0.9}Mo_6O_{17}$ be it in a renormalization group Luttinger liquid or computational many-body sense. On the latter side it would certainly be interesting to conduct a more thorough investigation of nonlocal self-energy effects to complement our (extended) variational cluster approach results. In particular, the phenomenon of spin-charge separation deserves further attention. A theoretical understanding of the phase diagram of the system, i.e., the occurrence of superconducting, insulating, or charge ordered states as function of pressure and temperature, remains a challenging open question. These studies could be augmented by an *ab initio* calculation of interaction parameters for the Wannier model by appropriate techniques such as constrained random phase approximation [61,103], making the approach fully *ab initio*. At the moment of writing, this is not feasible due to the computational complexity.

ACKNOWLEDGMENTS

We gratefully acknowledge fruitful discussions with J. W. Allen, W. von der Linden, E. Arrigoni, C. Heil, J. Mravlje, F. Assaad, and in particular P. Chudzinski. M.N. thanks the Forschungszentrum Jülich-Autumn School on Correlated Electrons for hospitality. This work was partly supported by the Austrian Science Fund (FWF) P24081-N16 and SFB-ViCoM subprojects F04103, and some calculations have been performed on the Vienna Scientific Cluster (VSC).

APPENDIX A: LINEAR RESPONSE TRANSPORT

The structure of the conductivity tensor $\sigma_{\alpha\beta}$ of $Li_{0.9}Mo_6O_{17}$ follows from the C_{2h} point symmetry as well as physical symmetry considerations for the conductivity [107] and can easily be established by requiring the conductivity tensor to be (i) symmetric for physical reasons and (ii) invariant under transformations with the four lattice point symmetry operations (identity, inversion, mirror symmetry perpendicular to the a axis and twofold rotation around the a axis) S_α: $\sigma = S_\alpha \sigma S_\alpha^T$.

1. Formalism

Following Refs. [108–110], linear response transport coefficients can be expressed in terms of kinetic coefficients

$$\mathcal{A}^n_{\nu\mu} = N_{\text{spin}} \pi \hbar \int_{-\infty}^{\infty} d\omega\, (\beta\omega)^n \times p_{\text{FD}}(\omega,\mu,\beta) p_{\text{FD}}(-\omega,-\mu,\beta) \Gamma_{\nu\mu}(\omega,\omega), \quad \text{(A1)}$$

where $N_{\text{spin}} = 2$ is due to spin degeneracy, the indices $\nu,\mu = \{a,b,c\}$ denote the real-space coordinate system, and we neglect vertex corrections. The Fermi-Dirac distribution $p_{\text{FD}}(\omega,\mu,\beta) = \frac{1}{e^{\beta(\omega-\mu)}+1}$ restricts the interval of integration to $\beta^{-1} \sim k_B T$ around the Fermi energy ϵ_F (k_B is Boltzmann's constant, and T and β denote temperature and inverse

temperature, respectively). The transport distribution

$$\Gamma_{\nu\mu}(\omega_1,\omega_2) = \frac{1}{V}\frac{1}{N_{1.\mathrm{BZ}}}\sum_{\mathbf{k}\in 1.\mathrm{BZ}} \mathrm{Tr} \times [v_\nu(\mathbf{k})A(\omega_1,\mathbf{k})v_\mu(\mathbf{k})A(\omega_2,\mathbf{k})] \quad \text{(A2)}$$

($V = abc$ is the unit-cell volume) is given in terms of the velocities

$$v_\nu^{\alpha\beta}(\mathbf{k}) = -\frac{\hbar}{m}\langle\Psi_\alpha(\mathbf{k})|\,\nabla_\nu\,|\Psi_\beta(\mathbf{k})\rangle \quad \text{(A3)}$$

and the spectral function

$$A_{\alpha\beta}(\omega,\mathbf{k}) = -\frac{1}{\pi}\mathrm{Im}\left[G^R_{\alpha\beta}(\omega,\mathbf{k})\right], \quad \text{(A4)}$$

which both are matrices in orbital indices $\alpha,\beta = \{\mathrm{A},\mathrm{A}',\mathrm{B},\mathrm{B}'\}$, which the trace Tr runs over.

We use velocities $v_\nu^{\alpha\beta}(\mathbf{k})$ [Eq. (A3)] in the Peierls approximation (neglecting the gradient of the Wannier orbital itself leading to a diagonal representation)

$$v_\nu^{\alpha\beta}(\mathbf{k}) = \frac{1}{\hbar}\Bigg(\langle\omega_\alpha(\mathbf{k})|\,\frac{\partial\hat{\mathcal{H}}(\mathbf{k})}{\partial k_\nu}\,|\omega_\beta(\mathbf{k})\rangle - \alpha(r_\alpha - r_\beta)\,\langle\omega_\alpha(\mathbf{k})|\,\hat{\mathcal{H}}(\mathbf{k})\,|\omega_\beta(\mathbf{k})\rangle\Bigg) \approx \frac{1}{\hbar}\frac{\partial E_\alpha(\mathbf{k})}{\partial k_\nu}\delta_{\alpha\beta}, \quad \text{(A5)}$$

where the second term in the first expression takes intra-unit-cell processes into account [109] and r_α is the position of Wannier orbital α inside the unit cell. This term is neglected in the following because the intra-unit-cell hopping elements are negligibly small. The conductivity tensor is

$$\sigma_{\nu\mu} = \beta e^2 \mathcal{A}^0_{\nu\mu}, \quad \text{(A6)}$$

with e denoting the electron charge.

2. Details on the evaluation of the anisotropic conductivity

In this appendix, we outline the numerical procedure used for the evaluation of the conductivity tensor (A6). These equations contain four additional, auxiliary numerical parameters in which we converge our results: (i) The spectral function $A_{\alpha\beta}(\omega,\mathbf{k})$ [Eq. (A4)] of the Wannier Hamiltonian is available exactly through the noninteracting retarded single-particle Green's function $G^R_{\alpha\beta}(\omega) = \langle\omega_\alpha(\mathbf{k})|\,\frac{1}{\omega+i\gamma-\hat{\mathcal{H}}(\mathbf{k})}\,|\omega_\beta(\mathbf{k})\rangle$. The broadening γ of the spectral function is chosen phenomenologically as described in the main part of the text. For numerical reasons, γ has to be chosen in accordance with (ii) the number of k points $N_{1.\mathrm{BZ}}$ in the first BZ for the sum in Eq. (A2). We obtain converged conductivities for $N_{1.\mathrm{BZ}}^{1/3} \in [1,67]$ to within a relative error of 10^{-3} using an equidistant grid in the irreducible BZ. We use $\gamma = \{0.1,0.075,0.05,0.025\}$ and rescale all conductivities with γ. As a function of γ, the resistivities in the a and b directions are constant at $\rho_a \approx (1.8 \pm 0.05)\gamma$ and $\rho_b \approx (430 \pm 10)\gamma$, while the resistivity in the c direction shows an upward trend. For our values of γ we find $\rho_c \approx \{190,300,480,650\}\gamma$. Since the last data point at $\gamma = 0.025$ is already difficult to converge in $N_{1.\mathrm{BZ}}$, we estimate $\rho_c \approx (600 \pm 150)\gamma$.

(iii) The velocities $v_\nu^{\alpha\beta}(\mathbf{k})$ [Eq. (A3)] are obtained by symmetric first-order numeric gradient approximations $v_\nu^{\alpha\beta}(\mathbf{k}) \approx \frac{\delta_{\alpha\beta}}{\hbar}\frac{E_\alpha(\mathbf{k}+\frac{\delta}{2}\mathbf{e}_\nu)-E_\alpha(\mathbf{k}-\frac{\delta}{2}\mathbf{e}_\nu)}{\delta}$ ($\mathbf{e}_\nu$ denotes the unit vector in real-space dimension ν). The parameter of the finite-difference scheme for the velocities used is $\delta = 10^{-6}$ after finding only negligible changes in a range of $\delta \in [10^{-8},10^{-3}]$. (iv) For reasons of numerical stability, we evaluate Eq. (A6) at a low, but finite temperature of $T = 4.2$ K, keeping in mind that $v_\nu^{ij}(\mathbf{k})$ and $A(\omega,\mathbf{k})$ have been evaluated for zero temperature. We find the results to be independent of this choice in a range of $T \in [1,50]$ K. In this calculation, at fixed γ, the temperature dependence enters through the Fermi-Dirac distribution only and a small scattering is taken into account through the broadening γ in the spectral function. We checked the numeric procedure on the reduced model where analytic results are known (see main text).

APPENDIX B: NONLOCAL INTERACTIONS: EXTENDED VCA

Here, we outline the VCA theory as implemented to obtain the results of the main text including the extensions needed in eVCA to treat nonlocal Coulomb interactions [65]. The single-particle part of the full Hamiltonian is readily decomposed into a cluster and an intercluster part

$$\hat{\mathcal{H}}^{\mathrm{cl}}_{\mathrm{Wannier}} = M_{\boldsymbol{\mathcal{R}}m\boldsymbol{\mathcal{R}}l}\,|\omega_m\rangle\,\langle\omega_l|\,,$$
$$\hat{\mathcal{H}}^{\mathrm{inter}}_{\mathrm{Wannier}} = \sum_{\delta\mathcal{R}} e^{-i\mathbf{k}\cdot\delta\mathcal{R}} M_{\boldsymbol{\mathcal{R}}m\boldsymbol{\mathcal{R}}'l}\,|\omega_m\rangle\,\langle\omega_l|\,,$$

where indices m and l run over the $L_\mathcal{C}$ orbitals in the cluster $\mathcal{C}$ at superlattice [94] position $\boldsymbol{\mathcal{R}}$.

When off-diagonal interaction terms are nonzero, an additional mean field treatment is needed for those two-particle terms which extend over the cluster boundary [65]. This leads to a modified interaction part of the Hamiltonian

$$\hat{\mathcal{H}}_{\mathrm{int}} = \sum_{\mathcal{C}}\left(\hat{\mathcal{H}}^{\mathrm{cl}}_{\mathrm{int}} + \hat{\mathcal{H}}^{\mathrm{cl}}_{\mathrm{mf}}(\boldsymbol{\varphi})\right),$$
$$\hat{\mathcal{H}}^{\mathrm{cl}}_{\mathrm{int}} = \sum_{m=1}^{L_\mathcal{C}} U_m\,\hat{n}_{m\uparrow}\hat{n}_{m\downarrow} + \sum_{\substack{m<l\in\mathcal{C}\\ \sigma\sigma'}} V_{ml}\,\hat{n}_{m\sigma}\hat{n}_{l\sigma'},$$
$$\hat{\mathcal{H}}^{\mathrm{cl}}_{\mathrm{mf}}(\boldsymbol{\varphi}) = \sum_{ml}\widetilde{V}_{ml}\left(\sum_\sigma(\hat{n}_{m\sigma}\varphi_l + \hat{n}_{l\sigma}\varphi_m) - \varphi_l\varphi_m\right),$$

with onsite interaction strength U_m, intracluster off-diagonal interactions V_{ml}, as well as $\widetilde{V}_{ml} = \sum_{\boldsymbol{\mathcal{R}}} V_{0m\boldsymbol{\mathcal{R}}l}$ the interaction elements in the mean field Hamiltonian. The mean fields $\boldsymbol{\varphi}$ (taken as spin independent $\varphi_m = \sum_\sigma\langle\hat{n}_{m\sigma}\rangle$ and restricted by lattice symmetry) need to be determined self-consistently.

This allows us to write the (interacting) cluster Hamiltonian in the VCA as

$$\hat{\mathcal{H}}^{\mathrm{cl}}(\boldsymbol{\Delta},\boldsymbol{\varphi}) = \hat{\mathcal{H}}^{\mathrm{cl}}_{\mathrm{Wannier}}(\boldsymbol{\Delta}) + \hat{\mathcal{H}}^{\mathrm{cl}}_{\mathrm{int}} + \hat{\mathcal{H}}^{\mathrm{cl}}_{\mathrm{mf}}(\boldsymbol{\varphi}),$$

where we introduced the VCA variational parameters [67,93] $\boldsymbol{\Delta}$.

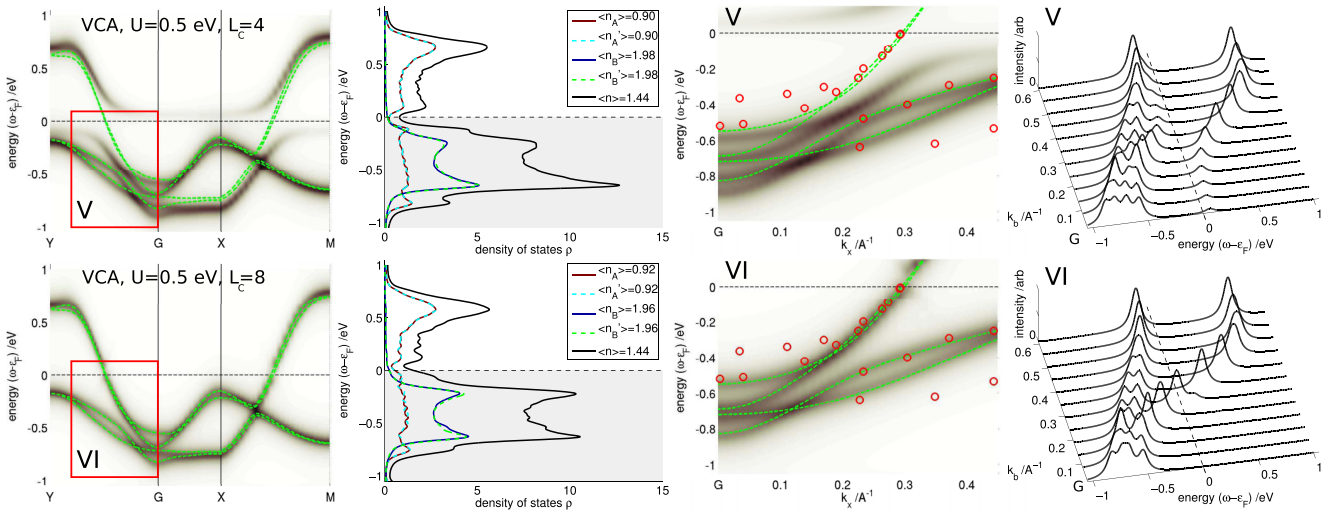

FIG. 9. (Color online) Comparison of VCA cluster sizes for a moderate onsite interaction strength of $U = 0.5$ eV. Top row: VCA data for using four-orbital clusters. Bottom row: VCA data for using eight-orbital clusters. For legends, arrangement of the subplots, and color coding, see Fig. 8.

To study the impact of nonlocal Coulomb interactions, we extend Eq. (4) by

$$\hat{\mathcal{H}}_{\text{int,nl}} = \hat{H}_{\text{int}} + \sum_{\mathbf{R}<\mathbf{R}'} \sum_{\substack{\alpha<\beta \\ \sigma\sigma'}} V_{\mathbf{R}\alpha\mathbf{R}'\beta}\, \hat{n}_{\mathbf{R}\alpha\sigma} \hat{n}_{\mathbf{R}'\beta\sigma'},$$

which also effects the double-counting terms in Eq. (5)

$$M^{+\text{DC,nl}}_{\mathbf{0}\alpha\mathbf{0}\alpha} = M^{+\text{DC}}_{\mathbf{0}\alpha\mathbf{0}\alpha} - \sum_{\mathbf{R}\gamma} V_{\mathbf{0}\alpha\mathbf{R}\gamma} \langle n_{\mathbf{R}\gamma} \rangle_{\text{Wannier}},$$

where the sum over $(\mathbf{R},\gamma)$ runs over all bonds connected to orbital $(\mathbf{0},\alpha)$. The mean fields $\boldsymbol{\varphi}$ [65] which arise due to off-diagonal interaction terms are fixed by the eVCA condition on the generalized grand potential [111]

$$\nabla_{\boldsymbol{\Delta},\boldsymbol{\varphi}} \Omega(\boldsymbol{\Delta},\boldsymbol{\varphi}) \stackrel{!}{=} \mathbf{0}.$$

In order to check the influence of *nearest-neighbor density-density interactions* $V_{\mathbf{R}\alpha\mathbf{R}'\beta}$, we did several eVCA calculations with different values within reasonable limits, i.e., below a value of $\approx \frac{U}{2}$. Our calculations show, however, that these interactions $V_{\mathbf{R}\alpha\mathbf{R}'\beta}$ lead only to minor differences compared to results without them. We did not find the system to be susceptible to any charge ordering. For that reason, and also because the precise value of the parameters $V_{\mathbf{R}\alpha\mathbf{R}'\beta}$ is complicated to estimate, all results presented here are calculated with onsite interaction $U_\alpha = U$ only [112]. Given the band-filling factors and the good agreement with ARPES experiments, we argue that onsite interactions are sufficient to describe the spectral properties of this system within our approximation.

APPENDIX C: VCA CLUSTER SIZE EXTRAPOLATION

Here, we discuss the approximation introduced by choosing eight-orbital clusters for the VCA procedure. Eight-orbital clusters enable nonlocal self-energy effects along the chain direction in the most basic fashion. The VCA on small cluster sizes is inherently biased towards the insulating state [94]. In Fig. 9, we show the behavior of the results when going from one-unit-cell clusters $L_\mathcal{C} = 4$ to two-unit-cell clusters in the b direction $L_\mathcal{C} = 8$. For the same interaction strength, the $L_\mathcal{C} = 4$ calculation clearly shows a pronounced Mott gap in the A-type orbitals while it is still absent in the $L_\mathcal{C} = 8$ calculation. All other basic features are comparable. For numerical reasons, we can not go to larger cluster sizes. Nevertheless, we expect the results of the $L_\mathcal{C} = 8$ calculation to be still heavily biased towards the insulating state. One can regard the critical value $U \approx 0.7$ eV for which the gap opens at $L_\mathcal{C} = 8$ as a lower bound to the true critical interaction.

[1] W. McCarroll and M. Greenblatt, J. Solid State Chem. **54**, 282 (1984).
[2] M. Greenblatt, Chem. Rev. **88**, 31 (1988).
[3] M. Onoda, K. Toriumi, Y. Matsuda, and M. Sato, J. Solid State Chem. **66**, 163 (1987).
[4] M. S. da Luz, J. J. Neumeier, C. A. M. dos Santos, B. D. White, H. J. I. Filho, J. B. Leão, and Q. Huang, Phys. Rev. B **84**, 014108 (2011).
[5] M. Greenblatt, W. McCarroll, R. Neifeld, M. Croft, and J. Waszczak, Solid State Commun. **51**, 671 (1984).
[6] M. S. da Luz, C. A. M. dos Santos, J. Moreno, B. D. White, and J. J. Neumeier, Phys. Rev. B **76**, 233105 (2007).
[7] J.-F. Mercure, A. F. Bangura, X. Xu, N. Wakeham, A. Carrington, P. Walmsley, M. Greenblatt, and N. E. Hussey, Phys. Rev. Lett. **108**, 187003 (2012).
[8] X. Xu, A. F. Bangura, J. G. Analytis, J. D. Fletcher, M. M. J. French, N. Shannon, J. He, S. Zhang, D. Mandrus, R. Jin *et al.*, Phys. Rev. Lett. **102**, 206602 (2009).
[9] C. A. M. dos Santos, M. S. da Luz, Y.-K. Yu, J. J. Neumeier, J. Moreno, and B. D. White, Phys. Rev. B **77**, 193106 (2008).

[10] Y. Matsuda, M. Sato, M. Onoda, and K. Nakao, J. Phys. C: Solid State Phys. **19**, 6039 (1986).

[11] C. E. Filippini, J. Beille, M. Boujida, J. Marcus, and C. Schlenker, Phys. C (Amsterdam) **162–164, Part 1**, 427 (1989).

[12] H. Chen, J. J. Ying, Y. L. Xie, G. Wu, T. Wu, and X. H. Chen, Europhys. Lett. **89**, 67010 (2010).

[13] C. A. M. dos Santos, B. D. White, Y.-K. Yu, J. J. Neumeier, and J. A. Souza, Phys. Rev. Lett. **98**, 266405 (2007).

[14] J. Choi, J. L. Musfeldt, J. He, R. Jin, J. R. Thompson, D. Mandrus, X. N. Lin, V. A. Bondarenko, and J. W. Brill, Phys. Rev. B **69**, 085120 (2004).

[15] L. Degiorgi, P. Wachter, M. Greenblatt, W. H. McCarroll, K. V. Ramanujachary, J. Marcus, and C. Schlenker, Phys. Rev. B **38**, 5821 (1988).

[16] J. L. Cohn, B. D. White, C. A. M. dos Santos, and J. J. Neumeier, Phys. Rev. Lett. **108**, 056604 (2012).

[17] N. Wakeham, A. F. Bangura, X. Xu, J.-F. Mercure, M. Greenblatt, and N. E. Hussey, Nat. Commun. **2**, 1 (2011).

[18] M. Boujida, C. Escribe-Filippini, J. Marcus, and C. Schlenker, Phys. C (Amsterdam) **153–155, Part 1**, 465 (1988).

[19] J. Chakhalian, Z. Salman, J. Brewer, A. Froese, J. He, D. Mandrus, and R. Jin, Phys. B (Amsterdam) **359–361**, 1333 (2005).

[20] J. D. Denlinger, G.-H. Gweon, J. W. Allen, C. G. Olson, J. Marcus, C. Schlenker, and L.-S. Hsu, Phys. Rev. Lett. **82**, 2540 (1999).

[21] F. Wang, J. V. Alvarez, S.-K. Mo, J. W. Allen, G.-H. Gweon, J. He, R. Jin, D. Mandrus, and H. Hochst, Phys. Rev. Lett. **96**, 196403 (2006).

[22] F. Wang, J. V. Alvarez, J. W. Allen, S.-K. Mo, J. He, R. Jin, D. Mandrus, and H. Hochst, Phys. Rev. Lett. **103**, 136401 (2009).

[23] G.-H. Gweon, J. W. Allen, and J. D. Denlinger, Phys. Rev. B **68**, 195117 (2003).

[24] G.-H. Gweon, S.-K. Mo, J. W. Allen, J. He, R. Jin, D. Mandrus, and H. Hochst, Phys. Rev. B **70**, 153103 (2004).

[25] F. Wang, J. Alvarez, S.-K. Mo, J. Allen, G.-H. Gweon, J. He, R. Jin, D. Mandrus, and H. Hochst, Phys. B (Amsterdam) **403**, 1490 (2008).

[26] L. Dudy, J. D. Denlinger, J. W. Allen, F. Wang, J. He, D. Hitchcock, A. Sekiyama, and S. Suga, J. Phys.: Condens. Matter **25**, 014007 (2013).

[27] G.-H. Gweon, J. Denlinger, C. Olson, H. Hochst, J. Marcus, and C. Schlenker, Phys. B (Amsterdam) **312–313**, 584 (2002).

[28] G.-H. Gweon, J. D. Denlinger, J. W. Allen, C. G. Olson, H. Höechst, J. Marcus, and C. Schlenker, Phys. Rev. Lett. **85**, 3985 (2000).

[29] J. Hager, R. Matzdorf, J. He, R. Jin, D. Mandrus, M. A. Cazalilla, and E. W. Plummer, Phys. Rev. Lett. **95**, 186402 (2005).

[30] T. Podlich, M. Klinke, B. Nansseu, M. Waelsch, R. Bienert, J. He, R. Jin, D. Mandrus, and R. Matzdorf, J. Phys.: Condens. Matter **25**, 014008 (2013).

[31] T. Giamarchi, Chem. Rev. **104**, 5037 (2004).

[32] M. Pustilnik, M. Khodas, A. Kamenev, and L. I. Glazman, Phys. Rev. Lett. **96**, 196405 (2006).

[33] M. Khodas, M. Pustilnik, A. Kamenev, and L. I. Glazman, Phys. Rev. B **76**, 155402 (2007).

[34] V. Meden and K. Schönhammer, Phys. Rev. B **46**, 15753 (1992).

[35] J. Voit, Phys. Rev. B **47**, 6740 (1993).

[36] G. León, C. Berthod, and T. Giamarchi, Phys. Rev. B **75**, 195123 (2007).

[37] J. Xue, L.-C. Duda, K. E. Smith, A. V. Fedorov, P. D. Johnson, S. L. Hulbert, W. McCarroll, and M. Greenblatt, Phys. Rev. Lett. **83**, 1235 (1999).

[38] S. Biermann, A. Georges, A. Lichtenstein, and T. Giamarchi, Phys. Rev. Lett. **87**, 276405 (2001).

[39] C. Berthod, T. Giamarchi, S. Biermann, and A. Georges, Phys. Rev. Lett. **97**, 136401 (2006).

[40] M. Raczkowski and F. F. Assaad, Phys. Rev. Lett. **109**, 126404 (2012).

[41] C. Schlenker, H. Schwenk, C. Escribe-Filippini, and J. Marcus, Physica B + C (Amsterdam) **135**, 511 (1985).

[42] Y. Matsuda, M. Onoda, and M. Sato, Physica B + C (Amsterdam) **143**, 243 (1986).

[43] T. Ekino, J. Akimitsu, Y. Matsuda, and M. Sato, Solid State Commun. **63**, 41 (1987).

[44] J.-F. Mercure, A. F. Bangura, X. Xu, N. Wakeham, A. Carrington, P. Walmsley, M. Greenblatt, and N. E. Hussey, arXiv:1203.6672.

[45] M. Sato, Y. Matsuda, and H. Fukuyama, J. Phys. C: Solid State Phys. **20**, L137 (1987).

[46] G.-H. Gweon, J. Denlinger, J. Allen, R. Claessen, C. Olson, H. Hochst, J. Marcus, C. Schlenker, and L. Schneemeyer, J. Electron Spectrosc. Relat. Phenom. **117–118**, 481 (2001).

[47] J. Dumas and C. Schlenker, Int. J. Mod. Phys. B **07**, 4045 (1993).

[48] P. Chudzinski, T. Jarlborg, and T. Giamarchi, Phys. Rev. B **86**, 075147 (2012).

[49] J. Merino and R. H. McKenzie, Phys. Rev. B **85**, 235128 (2012).

[50] J. L. Cohn, P. Boynton, J. S. Triviño, J. Trastoy, B. D. White, C. A. M. dos Santos, and J. J. Neumeier, Phys. Rev. B **86**, 195143 (2012).

[51] M. H. Whangbo and E. Canadell, J. Am. Chem. Soc. **110**, 358 (1988).

[52] Z. S. Popović and S. Satpathy, Phys. Rev. B **74**, 045117 (2006).

[53] T. Jarlborg, P. Chudzinski, and T. Giamarchi, Phys. Rev. B **85**, 235108 (2012).

[54] J. C. Slater and G. F. Koster, Phys. Rev. **94**, 1498 (1954).

[55] N. Marzari, A. A. Mostofi, J. R. Yates, I. Souza, and D. Vanderbilt, Rev. Mod. Phys. **84**, 1419 (2012).

[56] N. Marzari, I. Souza, and D. Vanderbilt, Highlight of the Month, Psi-K Newsletter **57**, 129 (2003).

[57] U. Schollwöck, Ann. Phys. (NY) **326**, 96 (2011).

[58] T. Maier, M. Jarrell, T. Pruschke, and M. H. Hettler, Rev. Mod. Phys. **77**, 1027 (2005).

[59] A. Kokalj, Comput. Mater. Sci. **28**, 155 (2003).

[60] I. V. Solovyev, J. Phys.: Condens. Matter **20**, 293201 (2008).

[61] M. Imada and T. Miyake, J. Phys. Soc. Jpn. **79**, 112001 (2010).

[62] K. Held, I. A. Nekrasov, N. Blümer, V. I. Anisimov, and D. Vollhardt, Int. J. Mod. Phys. B **15**, 2611 (2001).

[63] C. Gros and R. Valenti, Phys. Rev. B **48**, 418 (1993).

[64] D. Sénéchal, D. Perez, and M. Pioro-Ladrière, Phys. Rev. Lett. **84**, 522 (2000).

[65] M. Aichhorn, H. G. Evertz, W. von der Linden, and M. Potthoff, Phys. Rev. B **70**, 235107 (2004).

[66] M. Aichhorn, E. Y. Sherman, and H. G. Evertz, Phys. Rev. B **72**, 155110 (2005).

[67] M. Potthoff, M. Aichhorn, and C. Dahnken, Phys. Rev. Lett. **91**, 206402 (2003).

[68] L. Chioncel, H. Allmaier, E. Arrigoni, A. Yamasaki, M. Daghofer, M. I. Katsnelson, and A. I. Lichtenstein, Phys. Rev. B **75**, 140406 (2007).

[69] M. Aichhorn, T. Saha-Dasgupta, R. Valentí, S. Glawion, M. Sing, and R. Claessen, Phys. Rev. B **80**, 115129 (2009).

[70] V. I. Anisimov, A. I. Poteryaev, M. A. Korotin, A. O. Anokhin, and G. Kotliar, J. Phys.: Condens. Matter **9**, 7359 (1997).

[71] M. I. Katsnelson and A. I. Lichtenstein, J. Phys.: Condens. Matter **11**, 1037 (1999).

[72] L. Chioncel, M. I. Katsnelson, R. A. de Groot, and A. I. Lichtenstein, Phys. Rev. B **68**, 144425 (2003).

[73] J. C. Slater, Phys. Rev. **51**, 846 (1937).

[74] O. K. Andersen, Phys. Rev. B **12**, 3060 (1975).

[75] D. Singh, Phys. Rev. B **43**, 6388 (1991).

[76] E. Sjöstedt, L. Nordström, and D. Singh, Solid State Commun. **114**, 15 (2000).

[77] P. Hohenberg and W. Kohn, Phys. Rev. **136**, B864 (1964).

[78] W. Kohn and L. J. Sham, Phys. Rev. **140**, A1133 (1965).

[79] P. Blaha, K. Schwarz, G. Madsen, D. Kvasnicka, and J. Luitz, WIEN2K, An Augmented Plane Wave + Local Orbitals Program for Calculating Crystal Properties (Karlheinz Schwarz, Techn. Universität Wien, Austria, Wien, Austria, 2001).

[80] For a simplification of the calculation, in particular the structure of the k mesh, we approximated β to 90.0°. We checked that the band structure is indistinguishable along the high-symmetry directions.

[81] D. M. Ceperley and B. J. Alder, Phys. Rev. Lett. **45**, 566 (1980).

[82] J. P. Perdew, K. Burke, and Y. Wang, Phys. Rev. B **54**, 16533 (1996).

[83] N. W. Ashcroft and N. D. Mermin, *Solid State Physics* (Saunders College, Philadelphia, 1976).

[84] J. W. Allen (private communication).

[85] A. A. Mostofi, J. R. Yates, Y.-S. Lee, I. Souza, D. Vanderbilt, and N. Marzari, Comput. Phys. Commun. **178**, 685 (2008).

[86] J. Kunes, R. Arita, P. Wissgott, A. Toschi, H. Ikeda, and K. Held, Comput. Phys. Commun. **181**, 1888 (2010).

[87] E. Pavarini, I. Dasgupta, T. Saha-Dasgupta, O. Jepsen, and O. K. Andersen, Phys. Rev. Lett. **87**, 047003 (2001).

[88] All densities are given in terms of orbital densities $\langle n_i \rangle = \sum_\sigma \langle n_{i\sigma} \rangle$.

[89] Setting the maximum hopping range to fourth-nearest-neighbor unit cells in b, second-nearest-neighbor in c, and nearest neighbor in the a direction, we obtained 2160 single-particle matrix elements $M_{\mathbf{R}\alpha\mathbf{R}'\beta}$. We do not provide a full table of all matrix elements in this text. They are available upon request from aichhorn@tugraz.at.

[90] Since we start from a spin-symmetric calculation, $H_{\text{Wannier},\alpha\beta}$ is independent of spin σ.

[91] When numerically evaluating $\hat{\widetilde{\mathcal{H}}}_{\text{AA}}(\mathbf{k})$, we use $(\omega - \hat{\mathcal{H}}_{\text{BB}})^{-1} \approx (\epsilon_{\text{AA}} - \hat{\mathcal{H}}_{\text{BB}} + i0.05)^{-1}$ followed by a Hermitization of the effective Hamiltonian $\widetilde{\mathcal{H}}_{\text{AA}} = \frac{\widetilde{\mathcal{H}}_{\text{AA}} + \widetilde{\mathcal{H}}_{\text{AA}}^T}{2}$ for stability.

[92] D. A. Ryndyk, A. Donarini, M. Grifoni, and K. Richter, Phys. Rev. B **88**, 085404 (2013).

[93] C. Dahnken, M. Aichhorn, W. Hanke, E. Arrigoni, and M. Potthoff, Phys. Rev. B **70**, 245110 (2004).

[94] D. Senechal, arXiv:0806.2690.

[95] M. Aichhorn, E. Arrigoni, M. Potthoff, and W. Hanke, Phys. Rev. B **74**, 235117 (2006).

[96] A. Georges, G. Kotliar, W. Krauth, and M. J. Rozenberg, Rev. Mod. Phys. **68**, 13 (1996).

[97] M. Ferrero and O. Parcollet, TRIQS: a Toolbox for Research in Interacting Quantum Systems, http://ipht.cea.fr/triqs

[98] P. Werner, A. Comanac, L. de' Medici, M. Troyer, and A. J. Millis, Phys. Rev. Lett. **97**, 076405 (2006).

[99] P. Werner and A. J. Millis, Phys. Rev. B **74**, 155107 (2006).

[100] L. Boehnke, H. Hafermann, M. Ferrero, F. Lechermann, and O. Parcollet, Phys. Rev. B **84**, 075145 (2011).

[101] E. Gull, A. J. Millis, A. I. Lichtenstein, A. N. Rubtsov, M. Troyer, and P. Werner, Rev. Mod. Phys. **83**, 349 (2011).

[102] K. S. D. Beach, arXiv:cond-mat/0403055.

[103] T. Miyake, F. Aryasetiawan, and M. Imada, Phys. Rev. B **80**, 155134 (2009).

[104] J. Ferber, K. Foyevtsova, H. O. Jeschke, and V. Roser, arXiv:1209.4466.

[105] When comparing results of different techniques (LDA, VCA, DMFT, ARPES), we first apply a rigid band shift of 0.03 eV to the LDA data to account for the $\langle n \rangle \approx 1.44$ filling (which matches the as-is ARPES results). In order to be consistent with these LDA data, the VCA and DMFT data have to be shifted further by an offset which is determined by the way k sums are handled in the respective methods. The chemical potential offset of the respective methods, determined for $U = 0$ eV, is ≈0.1 eV for VCA and ≈0.13 eV for DMFT.

[106] F. H. L. Essler, H. Frahm, F. Göhmann, A. Klümper, and V. E. Korepin, *The One-Dimensional Hubbard Model* (Cambridge University Press, Cambridge, 2010).

[107] E. Hartmann, *An Introduction to Crystal Physics* (University College Cardiff Press, Cardiff, UK, 1984).

[108] V. S. Oudovenko, G. Pálsson, K. Haule, G. Kotliar, and S. Y. Savrasov, Phys. Rev. B **73**, 035120 (2006).

[109] J. M. Tomczak and S. Biermann, Phys. Rev. B **80**, 085117 (2009).

[110] X. Deng and J. Mravlje (private communication).

[111] Note that this may be a minimum, a maximum, or in general any stationary point in each of the parameters.

[112] Note that for largely delocalized orbitals, it is expected that the onsite interaction should be slightly larger in a more involved model that includes also off-diagonal Coulomb terms [113].

[113] M. Schüler, M. Rösner, T. O. Wehling, A. I. Lichtenstein, and M. I. Katsnelson, Phys. Rev. Lett. **111**, 036601 (2013).

5.2. Steady-state and quench-dependent relaxation of a quantum dot coupled to one-dimensional leads

5.2.1. Preamble

This part of our work has been published in PHYSICAL REVIEW B 88, 045132 (2013) [52] and is also available as a preprint on arXiv:1301.3068.

This part of the thesis represents the first of two papers concerned with real time evolution of strongly correlated systems under applied bias voltages, see Sec. 3.2. Here we study the real time evolution of the SIAM under bias voltage after a quantum quench using the MPS [49] techniques DMRG [50] + TEBD [51]. The study of out-of-equilibrium properties of the SIAM is a major theme throughout this thesis. An introduction to the model is given in Sec. 3.1. The model describes the physics of correlated solids under many different circumstances which are outlined in Ch. 2. The SIAM is used as an impurity model in Sec. 5.1, dynamic equilibrium properties are obtained in Sec. 5.4 and its time dependent spatial correlations are explored in Sec. 5.3. Here we report data for three quenches, which after strongly quench-dependent transients yield the same steady-state current. We analyse the parameter dependence of bipartite entanglement and compare our quasi-exact results for the current to recently developed other numerical schemes. We will revisit the current-voltage characteristics in later chapters Sec. 5.5 and Sec. 5.6 when we take a look at the SIAM using the approximate steady-state methods: stsCPT and stsVCA, which have been developed in this thesis. Improved steady-state spectral functions are available from the AMEA [68] in Sec. 5.9 and the high bias transport physics will be explored in detail in Sec. 5.10. In these papers the quasi-exact DMRG+TEBD data will serve as a benchmark. The stsCPT and stsVCA will yield additional information and grant access to dynamic quantities like the nonequilibrium spectral function.

This manuscript is authored by Martin Nuss (MN) and co-authored by Martin Ganahl (MG), Hans Gerd Evertz (HE) as well as by MN's supervisors Enrico Arrigoni (EA) and Wolfgang von der Linden (WL). This research was to a large and significant extent conducted by MN under the supervision of WL and EA. EA, HE and WL provided expertise and guidance throughout the work. This research was initiated by HE, EA and WL. MG wrote the basis of the MPS computer code which was adapted to the problem at hand by MN. MG and HE provided expertise for the MPS technique. MN ran the computer simulations and tests and analyzed the resulting data. MN conducted literature research and set the results in context with published results. MN prepared, collected, interpreted, analyzed and visualized the results and set them in context with recent literature. MN wrote the first version of the manuscript. All authors contributed equally in discussing the results and revising the manuscript. Steven R. White initiated the calculations with a damped time evolution to reduce entanglement. We discussed our results with Sabine Andergassen. We thank Fabian Heidrich-Meisner, Philipp Werner, and Andreas Dirks for providing their data in Fig. 5.

5.2.2. Manuscript

PHYSICAL REVIEW B **88**, 045132 (2013)

Steady-state and quench-dependent relaxation of a quantum dot coupled to one-dimensional leads

Martin Nuss,* Martin Ganahl, Hans Gerd Evertz, Enrico Arrigoni, and Wolfgang von der Linden
Institute of Theoretical and Computational Physics, Graz University of Technology, 8010 Graz, Austria
(Received 17 January 2013; revised manuscript received 15 April 2013; published 29 July 2013)

We study the time evolution and steady state of the charge current in a single-impurity Anderson model, using matrix product states techniques. A nonequilibrium situation is imposed by applying a bias voltage across one-dimensional tight-binding leads. Focusing on particle-hole symmetry, we extract current-voltage characteristics from universal low-bias up to high-bias regimes, where band effects start to play a dominant role. We discuss three quenches, which after strongly quench-dependent transients yield the same steady-state current. Among these quenches we identify those favorable for extracting steady-state observables. The period of short-time oscillations is shown to compare well to real-time renormalization group results for a simpler model of spinless fermions. We find indications that many-body effects play an important role at high-bias voltage and finite bandwidth of the metallic leads. The growth of entanglement entropy after a certain time scale $\propto\Delta^{-1}$ is the major limiting factor for calculating the time evolution. We show that the magnitude of the steady-state current positively correlates with entanglement entropy. The role of high-energy states for the steady-state current is explored by considering a damping term in the time evolution.

DOI: 10.1103/PhysRevB.88.045132 PACS number(s): 73.63.Kv, 73.23.−b, 72.10.Fk, 71.15.−m

I. INTRODUCTION

Over the past decade, experimental control over quantum systems has increased considerably. Possible realizations reach from model Hamiltonians[1,2] using ultracold atoms in optical lattices to experimental setups of nanoscopic devices such as molecular junctions, quantum wires, or quantum dots.[3,4] Many of these systems show remarkable properties, often due to reduced effective dimensionality and many-body interactions. A prominent example is the Kondo effect,[5] which plays an essential role in transport across quantum dots. A theoretical understanding of transport in out-of-equilibrium conditions is highly interesting for applications in nanoelectronics and molecular electronics and even in biological systems.

Electron-electron interactions render the theoretical description of nonequilibrium dynamics one of the most challenging problems in today's condensed matter physics.[6] However, with the advent of efficient numerical techniques to simulate one-dimensional (1D) quantum systems,[7–12] many physical problems are well within grasp of theoretical physicists. Even nonequilibrium setups in regimes where the potential bias is large with respect to the energy scales of the unperturbed systems are now feasible to study.[13–15]

In this work, we obtain the steady-state charge current of a single interacting quantum dot under voltage bias, modeled by a single-impurity Anderson model (SIAM).[16] This model is commonly discussed in the wide-band limit[17] approximation, tailored towards a universal, low-bias transport description. Here, we extend the discussion to the case of a finite (semicircular) conduction band in the leads, which has not been explored specifically. A particular realization could consist of two one-dimensional leads such as nanowires[18–21] and a junction between them comprised of a magnetic impurity, i.e., the quantum dot. We use generic one-dimensional tight-binding leads with finite electronic bandwidth which mimic the electronic properties of, for example, carbon nanotubes.[22] In such a device, the electronic density of states (DOS) of the leads would have a bandwidth on the order of 15 eV (Refs. 22 and 23) and effects arising from their specific structure are to be expected when using corresponding bias voltages which are larger than those typically applied in current experiments with nanoscopic devices.

The steady state is obtained by combining density matrix renormalization group[7,11] (DMRG) and time evolving block decimation[9,11] (TEBD) techniques to perform real-time evolution of the system after several different quenches. This technique is known to yield reliable results for a wide parameter range of one-dimensional models[12–14,24–34] and to agree with analytical data.[13]

We focus on the particle-hole-symmetric point which shows the most pronounced many-body effects.[35] The bias voltage for most of our data is much larger than the equilibrium Kondo temperature (see Sec. V A), so that Kondo correlations should not influence the steady-state current. We show that the same steady-state current is reached independent of the type of quench used and identify quenches which are superior to others when it comes to extracting steady-state data. We investigate quench-induced oscillations in the transients and compare to real-time renormalization group results. We have performed a careful convergence study in all auxiliary numerical and system parameters and found the major limitation to be the truncation of the many-body state space in each iteration. The method is well suited for reaching relevant time scales to study the steady-state current. We find that our approach is capable of yielding unbiased results valid in the thermodynamic limit. Data presented in this work reproduce analytical results in the noninteracting system. In the low-bias region, our results for the current-voltage characteristics agree with previous data (Heidrich-Meisner *et al.* [14]). We are able to extend earlier results[14,36–41] to a wider parameter regime and discuss the interplay of finite lead bandwidth and electronic correlations. We find evidence for pronounced many-body effects at

high-bias voltages in interplay with finite electronic bandwidths of the leads.[42] Finally, we discuss the role of high-energy states for the steady-state current in low- and high-bias-voltage regimes.

The text is organized as follows: In Sec. II we introduce our model and describe in detail the different quenches to be performed. We present data for the transient response in Sec. III. Results for the steady-state current are presented in Sec. IV where we also outline how to extract steady-state data from time-evolved quantities. We analyze time scales of individual parameter regimes in Sec. V. The role of high-energy states in different bias regimes is discussed in Sec. VI. A detailed convergence analysis is presented in Appendix A.

II. SETUP

In this section, we define our notation for the SIAM which we use to model a quantum dot. We are interested in electron transport across the quantum dot after each of the several quenches to be described in detail in the following. We explain how we calculate the ground state using DMRG and the real-time evolution using TEBD.

A. Single-impurity Anderson model

We consider a model for a quantum dot including charge as well as spin fluctuations described by the SIAM, consisting of an interacting site connected to a bath of noninteracting electrons. We choose a setup where the quantum dot is located in the middle of a one-dimensional chain of tight-binding electrons. The dynamics is governed by

$$\hat{\mathcal{H}} = \hat{\mathcal{H}}_{\text{dot}} + \hat{\mathcal{H}}_{\text{res}} + \hat{\mathcal{H}}_{\text{coup}}, \tag{1a}$$

$$\hat{\mathcal{H}}_{\text{dot}} = -\frac{U}{2}\sum_{\sigma} f_{\sigma}^{\dagger} f_{\sigma} + U\,\hat{n}_{\uparrow}^{f}\,\hat{n}_{\downarrow}^{f}, \tag{1b}$$

$$\hat{\mathcal{H}}_{\text{res}} = \sum_{\alpha,\sigma}\left(\epsilon_{\alpha}\sum_{i} c_{i\alpha\sigma}^{\dagger} c_{i\alpha\sigma} - t\sum_{\langle i,j\rangle} c_{i\alpha\sigma}^{\dagger} c_{j\alpha\sigma}\right), \tag{1c}$$

$$\hat{\mathcal{H}}_{\text{coup}} = -\sum_{\alpha} t_{\alpha}' \sum_{\sigma}(c_{0\alpha\sigma}^{\dagger} f_{\sigma} + f_{\sigma}^{\dagger} c_{0\alpha\sigma}) \tag{1d}$$

(see Fig. 1) where U parametrizes the onsite interaction strength on the quantum dot, $t_{\alpha}', \alpha \in \{L,R\}$ is the coupling strength between the quantum dot and the left and right leads.

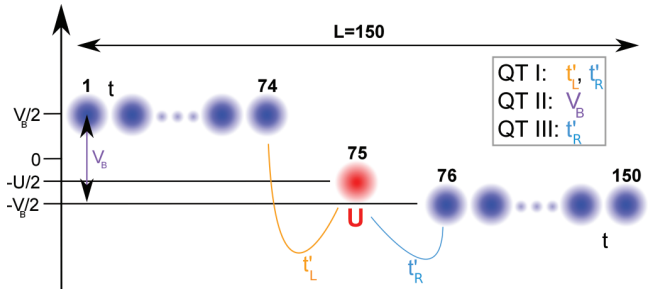

FIG. 1. (Color online) Illustration of the three quenches performed for the SIAM: (i) QT I: quenching of both quantum dot-reservoir tunnelings t_L' and t_R', (ii) QT II: quenching the bias voltage V_B, and (iii) QT III: quenching the dot-lead tunneling t_R' to one lead.

Lead α is characterized by intralead hopping t and onsite potential ϵ_{α}. Particle-hole symmetry is enforced for all chosen parameters. When needed, the onsite energy of the quantum dot will be denoted by ϵ_f.

We choose $t = 1$ and symmetric couplings $t_L' = t_R' = 0.3162\,t$ [Eq. (1d)] for all simulations, yielding a bandwidth of $D = 4\,t$ of the leads and an equilibrium Anderson width[5] of $\Delta \equiv \pi\, t_{\alpha}'^2\, \rho_{\text{reservoir}}(0) = \frac{t_{\alpha}'^2}{t} \approx 0.1\,t$. We choose $t = 1$ and symmetric couplings $t_L' = t_R' = 0.3162\,t$ [Eq. (1d) for all simulations. This yields a bandwidth of $D = 4\,t$ of the leads and an equilibrium Anderson width[5] of $\Delta \equiv \pi\, t_{\alpha}'^2\, \rho_{\text{reservoir}}(\mu) = \frac{t_{\alpha}'^2}{t} \approx 0.1\,t$, where the reservoir DOS at the chemical potential is denoted by $\rho_{\text{reservoir}}(\mu)$. We will display all energies in units of Δ ($\hbar, k_B$ and $e = 1$). We restrict ourselves to the zero-temperature case. Real time will be denoted by τ. In Appendix A we show that within the simulation time τ accessible, the finiteness of the leads does not affect our results.

B. Quench preparation

We are interested in the steady-state current[43] of Eq. (1a) under a finite-bias voltage V_B.[44,45] Our strategy to obtain the steady state is by quenching the Hamiltonian parameters $\mathsf{x}_0 = \{U, t, t_{\alpha}', \epsilon_{\alpha}\}$ at $\tau = 0$ from some initial to their final values $\hat{\mathcal{H}}(\mathsf{x}_0) \to \hat{\mathcal{H}}(\mathsf{x})$ and evolve an initial state $|\Psi_0\rangle$ with $\hat{\mathcal{H}}(\mathsf{x})$. $|\Psi_0\rangle$ is chosen to be the ground state of the initial Hamiltonian $\hat{\mathcal{H}}(\mathsf{x}_0)$ in the canonical ensemble at half-filling with total spin projection $S^z = 0$.

It has been shown that the steady state is independent of the quench rate.[30,31] We apply all quenches at an instant of time, i.e., without a ramp. It could, however, be interesting to study the entanglement growth as a function of the quench ramp.

We consider three different quench types (see Fig. 1) which will be explained in detail below. Unless stated otherwise, we choose a system of $L = 150$ sites with the quantum dot located at site 75. To drive the system out of equilibrium, a bias voltage V_B is applied by setting the respective onsite energies of the leads in an antisymmetric fashion to $\epsilon_L = -\epsilon_R = \frac{V_B}{2}$. For all quenches, the final parameters are $\mathsf{x} = \{U, t = 1, t_{\alpha}' = 0.3162\,t, \epsilon_L = \frac{V_B}{2}, \epsilon_R = -\frac{V_B}{2}\}$, with variable U. The initial setup is quench-type (QT) dependent (see Fig. 1):

1. *QT I: Hybridization quench to both leads $t_{\alpha}' = 0 \to 0.3162\,t$*

For $\tau < 0$ we take $\mathsf{x}_0 = \{U, t, t_{\alpha}' = 0, \epsilon_{\alpha} = \pm V_B/2\}$, i.e., no quantum dot-to-leads coupling, but the bias voltage is already applied. We prepare the ground state of $\hat{\mathcal{H}}(\mathsf{x}_0)$ at half-filling in the left and right leads and a single up electron on the quantum dot. At $\tau = 0$ the tunneling t_{α}' is quenched to its finite value. Note that due to the splitting into three disconnected parts ($t_{\alpha}' = 0$), S^z is not zero on the quantum dot and on the right lead initially.

2. *QT II: Quenching the bias voltage $\epsilon_{\alpha} = 0 \to \pm V_B/2$*

At $\tau < 0$, $\mathsf{x}_0 = \{U, t, t_{\alpha}' = 0.3261\,t, \epsilon_{\alpha} = 0\}$. The system is prepared in the ground state $|\Psi_0\rangle$ at half-filling with overall $S^z = 0$ zero. At $\tau = 0$ the bias voltage is quenched to its desired value. As compared to QT I, this setup has the advantage that no subsystems with finite values of S^z exist in the ground state. Furthermore, correlations between the three

regions are already present in the ground state. Note that the initial state is much more complicated than for QT I. This type of quench has also been used by the authors of Ref. 25.

3. *QT III: Quenching the hybridization $t'_R = 0 \rightarrow 0.3162\,t$ to the right lead*

The initial parameters are chosen $\mathsf{x}_0 = \{U, t, t'_L = 0.3261\,t,\ t'_R = 0,\ \epsilon_\alpha = \pm V_B/2\}$, and the system is again solved for the ground state $|\Psi_0\rangle$ at half-filling. At $\tau = 0$, we quench $t'_R = 0 \rightarrow 0.3162\,t$ and evolve $|\Psi_0\rangle$ with the quenched Hamiltonian.

C. Methods

To prepare the system in the ground state of the initial Hamiltonian, we employ the DMRG (Ref. 7) algorithm in its two- and single-site formulations. Our implementation exploits conservation of spin projection (S^z) and charge (N), which is crucial for obtaining high-precision data. Time evolution is done using the TEBD (Ref. 9) algorithm, within a second-order Suzuki-Trotter decomposition of the propagator

$$e^{-i\hat{\mathcal{H}}T} = (e^{-i\hat{\mathcal{H}}\delta\tau})^{\frac{T}{\delta\tau}} = \left(e^{\frac{\delta\tau}{2}\hat{\mathcal{H}}_o} e^{\delta\tau\hat{\mathcal{H}}_e} e^{\frac{\delta\tau}{2}\hat{\mathcal{H}}_o}\right)^{N_\tau} + \mathcal{O}(\delta\tau^3),$$

where $N_\tau = \frac{T}{\delta\tau}$ is the number of time slices, T is the total simulation time, and $\delta\tau$ the length of a single time step. The operators $\hat{\mathcal{H}}_e$ and $\hat{\mathcal{H}}_o$ act on even and odd bonds of the bipartite lattice, respectively. Unless stated otherwise, we use a TEBD matrix dimension of $\chi_{\mathrm{TEBD}} = 2000$ and a Trotter time step of $\delta\tau = 0.05\,t^{-1}$. For additional details including studies of convergence in system size L and all auxiliary numerical parameters, we refer the reader to Appendix A.

The calculations carried out in this work set very high computational demands (≈one million CPU hours) and were only possible due to a parallel code[46–48] which respects quantum-number (N, S_z) conservation.

III. TRANSIENT RESPONSE

In this section, we present results for the transient current response of the three quenches. We discuss individual bias regimes and identify oscillations in the time evolution of the current which are reminiscent of results for an interacting resonant level model of spinless fermions. We show that QT II leads to much larger initial oscillations than the other two QTs.

A. Low-, medium-, and high-bias regimes

In our simulations, we identify three regimes of bias voltage V_B with qualitatively different behavior. Within each regime, the general features of the time evolution of the current are only moderately dependent on interaction strength. For that reason, we first discuss results for $U/\Delta = 12$ only (see Fig. 2).

For low-bias voltages $[V_B/\Delta \in (0,18)]$, a steady-state current plateau[6,49] is reached within $\tau \approx \Delta^{-1}$. In a region of medium-bias voltages $[V_B/\Delta \in (18,28)]$, we observe a fast increase in current over a time scale of $\tau \approx 0.3\,\Delta^{-1}$ followed by a rather slow decay which, for some model parameters, is too slow to reach a steady-state plateau within accessible simulation times (see below). In the high-bias region $[V_B/\Delta \in (28,40)]$, the time evolution of the current shows a sharp peak followed by fast decrease of the current into a steady-state plateau within $\tau \approx \Delta^{-1}$.

Our data indicate that within a simulation time of $\tau = 3\,\Delta^{-1}$, approximately one particle is transferred from the left reservoir to the right one. As discussed in detail in Sec. IV, all three QTs eventually approach the same steady state, although in quite different manner. QT II, for example, leads to the largest transient current spike, which is one reason for the lower accuracy in determining the steady state for this quench. We also find that quenching the hybridization(s) (QT I or III) yields much cleaner steady-state plateaux as compared to quenching the bias voltage (QT II), which leads to more pronounced oscillations in these plateaux.

B. Characteristic oscillations of the current

The time evolution of the current exhibits oscillations which are more or less pronounced depending on the type of quench. These oscillations become more explicit with increasing interaction strength (not shown). Their period is of the order of $0.5\,\Delta^{-1}$ for low-bias voltages and decreases to about $0.3\,\Delta^{-1}$ for higher-bias voltages, in a range of interaction strengths $U = [0,20]\,\Delta$. These oscillations compare nicely to results from real-time renormalization group (rtRG) for the interacting resonant level model [see Ref. 50, Eq. (107)], which predicts a sinusoidal behavior $[\propto \sin(\frac{\tau}{\tau_C})]$ with a period of

$$\tau_C(U,V) = \frac{2}{V_B + U}.$$

In Fig. 3, we plot $\tau_C(U,V)$ as a function of interaction strength and find remarkable agreement with rtRG results at higher-bias voltages. The period was extracted from the TEBD time evolution data in three ways: (i) by fitting a sine function, (ii) by identifying the dominant Fourier amplitudes, and (iii) by identifying local maxima. These data were combined and their individual uncertainty taken into account. Error bars in Fig. 3 (not shown) would be sharply growing below $V_B = 25\,\Delta$. In the lower-bias regime, our data are not significant for a reliable extraction of the period.

IV. STEADY-STATE CURRENT

In this section, we present the current-voltage characteristics of quantum dot. We outline a scheme to extract the steady-state current and investigate the dependence on the type of quench used. The current-voltage characteristics in the low-bias region is compared to existing data obtained with other methods. Furthermore, we present a detailed comparison between an interacting and a noninteracting quantum dot for finite as well as infinite lead bandwidth.

A. Extracting the steady-state current

We identify the steady-state current as the mean value of the time-dependent current taken over a suitable time domain $[\tau_S, \tau_E]$ over which the current shows an almost constant behavior (apart from small oscillations). τ_S typically depends on the model parameters and was chosen by hand, and τ_E is taken to be the largest time for which simulations yield reliable results (see Fig. 2). Beyond τ_E the current becomes numerically unreliable, resulting in an artificially decaying

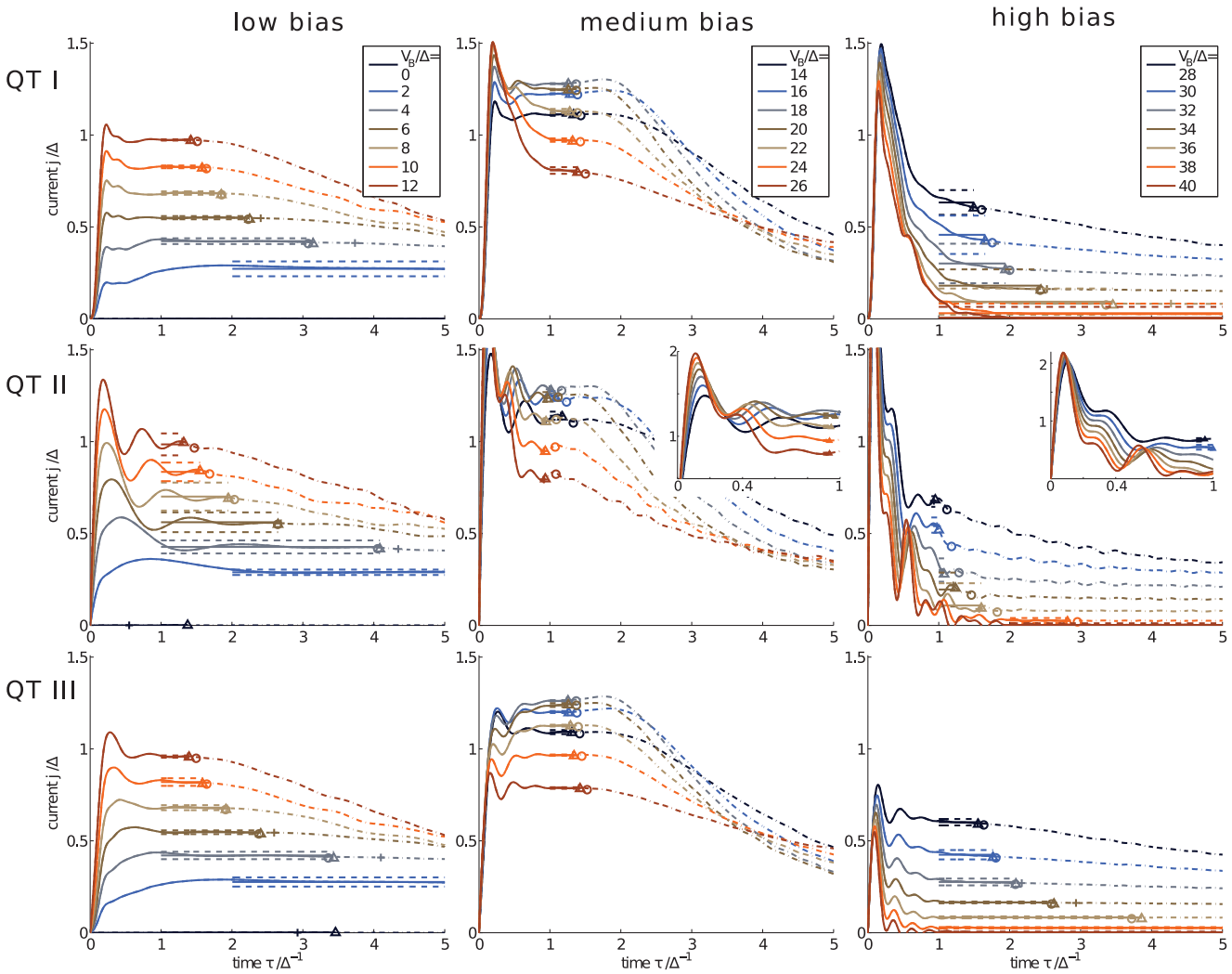

FIG. 2. (Color online) Time dependence of the current [Eq. (A1)] at $U/\Delta = 12$ for the three different QTs and for different bias voltages. The curves are plotted as solid lines up to the last reliable point in the TEBD calculation (see text). Larger times are plotted as dashed-dotted lines. Solid horizontal lines are fits to extract the steady-state currents. The time domain for these fits starts at $\tau \approx \Delta^{-1}$ and ends at a point which is identified as the last reliable data point (symbols, see text). Dashed horizontal lines indicate the uncertainty. The insets in the mid row show respective zooms onto short-time regions, which are not visible in the main part of the figure.

current (see Appendix A for discussion). We find that in most of the parameter regions, the transients have decayed at $\tau_S \approx \Delta^{-1}$. On the other hand, the end point of the plateau strongly depends on the parameter region under consideration. We define it by two distinct measures. One is the time $\tau_E^{(1)}$ for which the truncated weight ϵ [see Eq. (A3)] reaches a threshold of $\epsilon_c = 3 \times 10^{-6}$ at any bond (marked by $+$ in Fig. 2). The second definition ($\tau_E^{(2)}$ marked by $\circ$ in Fig. 2) is given by the time for which two different definitions of the current, namely the expectation value of the current operator [Eq. (A1)] and the time derivative of the particle number [Eq. (A2)], deviate by more than 7×10^{-4}, the latter being more susceptible to accumulation of errors. Both times are in good agreement with each other and can be combined into an effective simulation time $\tau_E = \min(\tau_E^{(1)}, \tau_E^{(2)}) + \alpha|\tau_E^{(1)} - \tau_E^{(2)}|$ (marked by triangles in Fig. 2). We choose a value of $\alpha = 0.1$. Results do not depend on this particular choice. It turns out that this procedure is very robust and does also agree with the point at which the TEBD current starts to deviate from the exact time evolution in the noninteracting system (see Appendix A 5).

The steady-state plateaux obtained in this way usually show oscillations and/or small, parameter- and quench-dependent drifts. We quantify the quality of convergence within the plateau region $[\tau_S, \tau_E]$ by the slope of a linear fit to the current. A large slope indicates that it is not possible to reach the steady state within the given simulation time τ_E, i.e., the physical relaxation time is too long or the reached simulation time is too short. This is further discussed in Sec. V. For these parameter values, we can only provide a likely upper bound for the steady-state current, given by the current at the last reliable simulation time. This is justified because we find the current to always decrease as a function of time (apart from small oscillations). Note that although for some of these parameters the current in some QTs may appear converged but is still

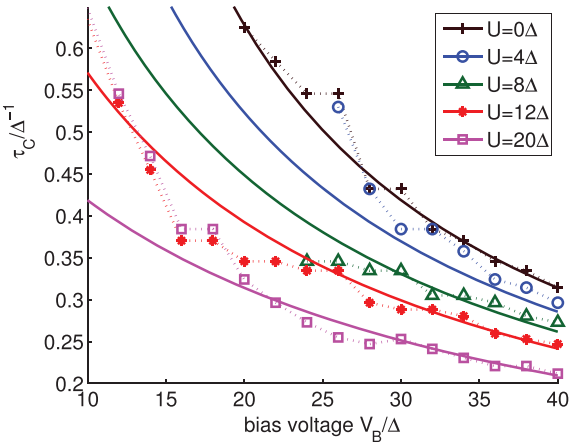

FIG. 3. (Color online) Period of the sinusoidal oscillations of the current in QT II for various values of interaction strength $U/\Delta = 0,4,8,12$, and 20 (symbols). Solid lines indicate the predicted form for the interacting resonant level model (Ref. 50).

considered not converged according to our strict criteria. We consider the current to be converged when the relative slope is below a threshold of $\approx 5 \times 10^{-2}\ \Delta$. Each curve in addition was inspected by hand for convergence. When we consider the steady-state current converged, we estimate its error as three times the standard deviation taken over the data points in the fitting interval $[\tau_S, \tau_E]$ (plotted as dashed lines in Figs. 2 and 4). This coincides most of the time with the maximal deviation of the time-dependent current from its mean value.

As an important test, we obtained the current-voltage characteristics for the noninteracting case and compared it to analytical results[51] (see Fig. 4), finding excellent agreement (see also Appendix A 5). Another indication for the reliability of the scheme outlined above is that all three types of quenches investigated yield the same steady-state current within the uncertainty. We note that this is not *a priori* clear since quench-dependent steady states have been reported in different

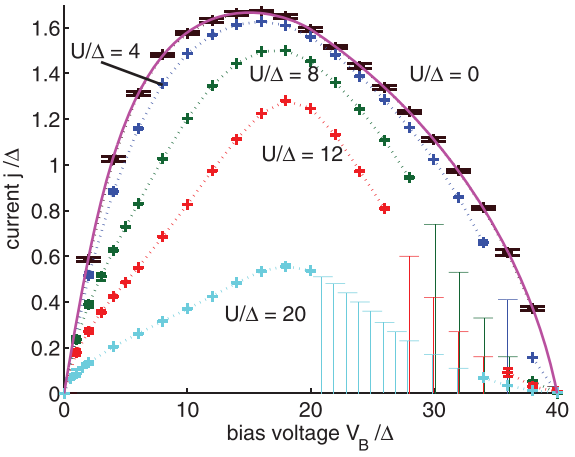

FIG. 4. (Color online) Current-voltage characteristics of the quantum dot. The steady-state currents shown are obtained by a fit of the expectation value of the current operator within the steady-state plateau. Regions where only a likely upper bound for the steady-state current could be obtained are indicated by pedestals (see text).

systems.[52] As noted in Appendix A, the position of the plateau is also stable with respect to variations of technical parameters of the simulation. The quality of the steady-state plateau, however, depends strongly on the values of interaction and bias voltage and may be obscured by initial oscillations or shortened at the end by the truncated weight breakdown.

The behavior of the spin current strongly depends on the quench type and it is even identical to zero for QT II. In this respect, the steady-state charge current does not depend on the properties of the spin current since all three quenches yield the same steady state for the charge current. This turns out to be very advantageous since the time scales in the spin sector are much larger than in the charge sector.[53,54]

From our calculations, we find QT I and QT III to yield more reliable data for the extraction of the steady-state current than QT II. Reasons for this behavior are (i) the much more pronounced oscillations in the data of QT II which enlarge the statistical uncertainty of steady-state values and (ii) the much higher transient spike in QT II accompanied by a slightly higher initial entanglement and shorter τ_E. Entanglement growth is in general parameter dependent and converges towards the same value for all quench types.[54] In the following, we will present steady-state data extracted from QT I and QT III.

B. Current-voltage characteristics

The current-voltage characteristics of the quantum dot for interaction strengths of $U/\Delta = 0,4,8,12$, and 20 are shown in Fig. 4. We plot data as obtained from QTs I and III (other QTs would give the same results but with larger error bars, as discussed in Sec. IV A). Results for the noninteracting case agree with analytic results for an infinite system.[51] In some regions, only a likely upper bound for the steady-state current can be provided. This region does not lie on the extreme end of the parameter space. It shows nontrivial dependence on U and V_B, which is discussed in detail in Sec. V. The current-voltage characteristics has an approximately semicircular shape, with decreasing maximum as a function of interaction strength U. At small bias V_B, the current is linear in V_B and agrees with the linear response result $j_{\text{lin}} = 2G_0 V_B$ (see also Fig. 5). At higher bias, it departs from the linear response result. With increasing U, this departure occurs already at smaller bias V_B, which can be attributed to an exponential thinning of the Kondo resonance with increasing U.

In intermediate-bias regions, we observe a flattening in the current-voltage curve. The maximum steady-state current is obtained in a bias regime from $V_B \approx 15\ \Delta$ to $19\ \Delta$. Increasing the interaction from $U = 0$ to $12\ \Delta$ appears to shift the position of the maximum to higher-bias voltages. For larger values of U our data are not significant to conclude on the behavior of the position of the maximum. We find the maximum current to decrease quadratically with increasing interaction strength: $\frac{j_{\max}}{\Delta} \simeq 1.675 - 0.003(\frac{U}{\Delta})^2$. Note that these features will likely depend on the actual reservoir DOS.

The decrease of the steady-state current for high-bias voltages can be attributed to the diminishing overlap of the DOS of the two reservoirs.[49] Both have a semicircular DOS with a bandwidth of $D = 40\ \Delta$. In the wide-band limit, the curves behave similarly inside the low-bias regime but should

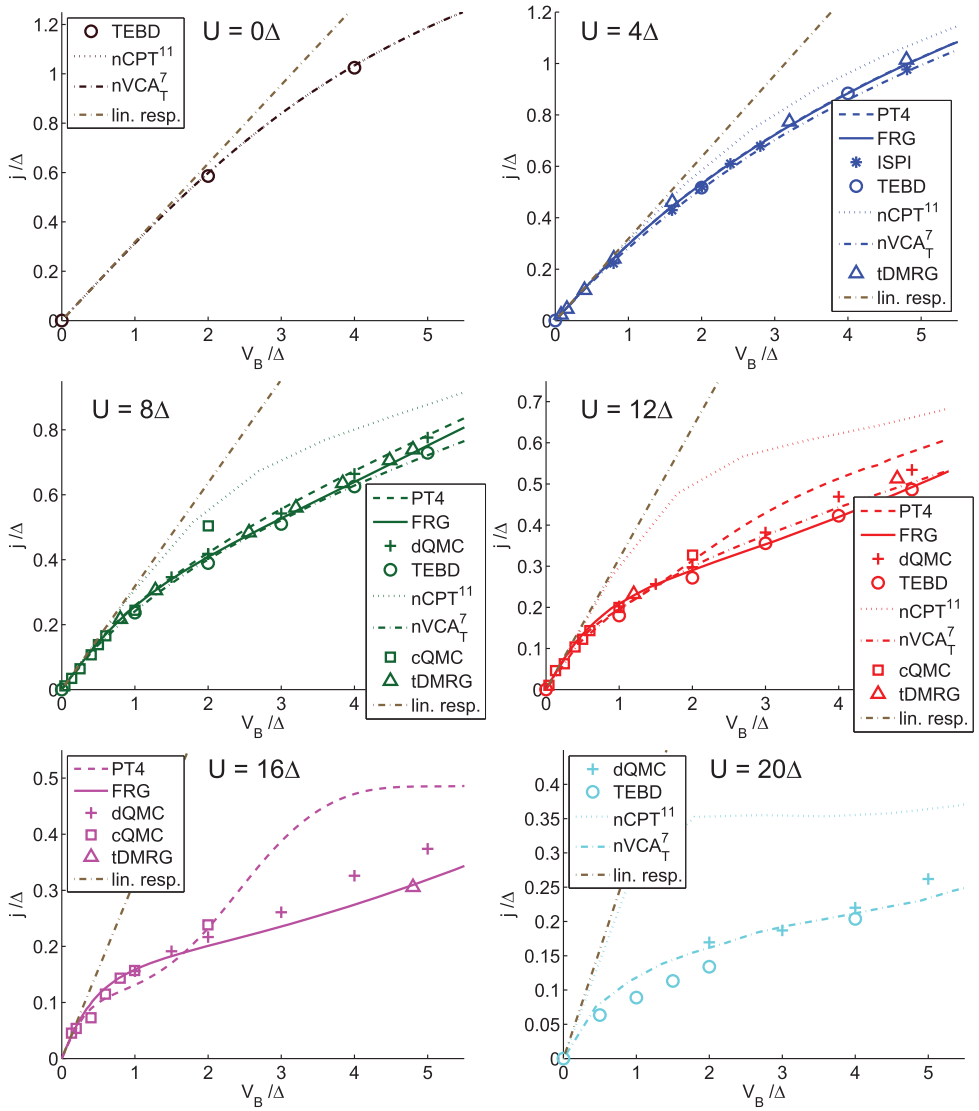

FIG. 5. (Color online) Comparison of the current-voltage characteristics of the SIAM obtained with different methods in the low-bias regime. Some of the methods use a wide-band limit and others a semicircular reservoir DOS which (for equal Δ) become comparable in the low-bias region shown. The methods are (1) diagrammatic QMC for $T = 0$ in the wide-band limit (dQMC) (Ref. 36), (2) fourth-order Keldysh perturbation theory for $T = 0$ in the wide-band limit (PT4) (Ref. 37), (3) time-dependent DMRG for $T = 0$ using a semicircular DOS (tDMRG) (Ref. 14), (4) TEBD for $T = 0$ using a semicircular DOS (TEBD, this work), (5) nonequilibrium fRG for $T = 0$ using a wide-band limit (fRG) (Ref. 38), (6) nonequilibrium cluster perturbation theory for $T = 0$ using a semicircular DOS (nCPT^{11}) (Ref. 39), (7) nonequilibrium variational cluster approach for $T = 0$ using a semicircular DOS (nCPT$^{7}_{T}$) (Ref. 39), (8) imaginary-time QMC for $T = 0.2\,\Delta$ in the wide-band limit (cQMC) (Ref. 40), (9) iterative summation of real-time path integrals for $T = 0.2\,\Delta$ in the wide-band limit (ISPI) (Ref. 41), and (10) the linear response result for the Kondo regime $j_{\text{lin}} = 2G_0V_B$ (lin. resp.).

saturate as a function of V_B for higher-bias voltages (see Fig. 6).

We discuss three simple limits. The TEBD results for the current respect the linear response (j_{lin}) for very low-bias voltages which gives the conductance quantum G_0. Furthermore, they respect the high-bias voltage band cutoff where the current has to go to zero (here at $V_B = 40\,\Delta$) due to diminishing overlap of the DOS of the reservoirs. The third limit is the noninteracting case (nontrivial for the used numerical method), where we obtain perfect agreement with analytical results for the thermodynamic limit.

C. Comparison to previous results

In the low-bias region, results from other techniques are available for the SIAM out of equilibrium. In the following, we discuss our results for various values of interaction strength U together with data previously obtained (see Fig. 5) by diagrammatic quantum Monte Carlo (QMC),[36] fourth-order Keldysh perturbation theory,[37] time-dependent DMRG,[14] TEBD for temperature $T = 0$ (this work), nonequilibrium functional renormalization group (fRG),[38] nonequilibrium cluster perturbation theory,[39] the nonequilibrium variational cluster approach,[39,55] imaginary-time QMC,[40] iterative

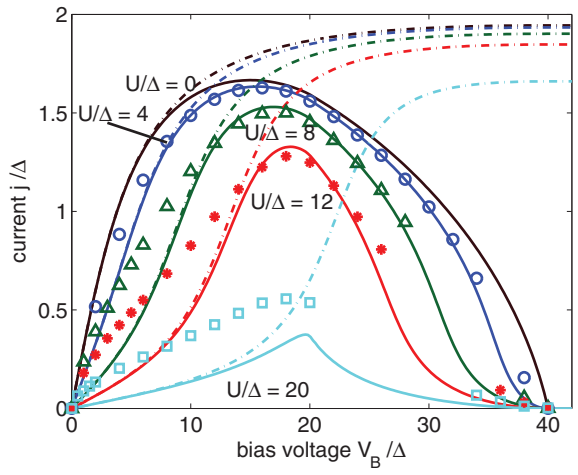

FIG. 6. (Color online) Comparison of the current-voltage characteristics of a *noninteracting*, resonant level device with onsite potential $\epsilon_f = -\frac{U}{2}$ (solid lines) with the TEBD data for the interacting quantum dot (symbols). Both devices have the same specifications with only the interaction U missing in the first case. The comparison is done for four values of interaction strengths resp. onsite potentials: $\frac{U}{\Delta} = \{4,8,12,20\}$ resp. $\frac{\epsilon_f}{\Delta} = \{-2,-4,-6,-10\}$ (blue/circles, green/triangles, red/stars, cyan/squares, respectively). In addition, we show the $U = 0$ result (black/no symbols). The dashed-dotted lines indicate data for a noninteracting device in the wide-band limit.

summation of real-time path integrals,[41] and the linear response result for the Kondo regime $j_{\text{lin}} = 2G_0V_B$. All methods work at or close to zero temperature. Some of the methods use a wide-band limit and others a semicircular reservoir DOS which (for equal Δ) become comparable in the shown low-bias region (see Fig. 6 for a comparison). The newly obtained TEBD results agree very well with the unbiased dQMC (Ref. 36) and quasi-exact tDMRG (Ref. 14) data. An earlier comparison including more details but fewer techniques is available in Ref. 56.

D. Comparison to a noninteracting device: Identifying correlation effects from the steady-state charge current

To gain further understanding of the role of correlations, we compare the steady-state current of the interacting quantum dot (U, onsite potential $\epsilon_f = -U/2$) to the one of a corresponding noninteracting (resonant level) device with $U = 0$ and onsite potential $\epsilon_f = -\frac{U}{2}$ (see Fig. 6). Data for the resonant level device are obtained analytically.[51]

From the plots in Fig. 6, one can see clear differences in the low-bias region between the noninteracting and interacting device for all interaction strengths, which can be attributed to the presence of the low-energy Kondo resonance in the interacting case. For low bias, the Kondo resonance fixes the linear response current to a U-independent constant and causes a higher current than for a noninteracting quantum dot at the same onsite potential. Furthermore, the curvature of the current-voltage characteristics in the low-bias region is negative in the interacting case as compared to positive in the noninteracting system. For larger values of $U = 12\,\Delta$ and $20\,\Delta$, the negative curvature turns into a positive one in the low-bias region.

For low values of interaction strength (see data for $U = 4\,\Delta$) we observe deviations in both the low- and high-bias regions. For the latter, this hints at possible many-body effects which may also be important in the high-bias regime. Data in the medium-bias region are almost indistinguishable from the noninteracting case. For high values of interaction strength, the picture changes and many-body effects are present in the whole bias regime.

Summing up, we find that effects of interaction are most pronounced in the low- and also in the high-bias regime, where a larger current is obtained than in the noninteracting device. Because of the small remaining overlap of the DOS of the leads, this larger current may be due to some low-energy spectral weight in the interacting device, consistent with low-energy excitations observed in Ref. 39 using a nonequilibrium variational cluster approach calculation.

V. DISCUSSION OF TIME SCALES

In the following, we argue that Kondo correlations do not influence the steady-state charge current in the parameter regime under study (large bias V_B compared to Kondo scale). However, our simulations show that depending on bias voltage and interaction strength, the steady-state charge current can not always be reached within the simulation time τ_E (see Sec. IV A), due to (i) weak spots of the method (i.e., small τ_E) and/or (ii) long physical relaxation times. To obtain insight into physical mechanisms as well as the parameter dependence of the performance of TEBD, also relevant for future studies, it is desirable to disentangle these two effects. We identify parameter regimes with such long physical time scales to be at $U + V_B > D$ (low charge-current regime), where we find our method to perform well, as opposed to parameter regimes with high currents, where only smaller times τ_E can be reached, as shown in Appendix B.

A. Finite simulation size/time and Kondo correlations

At the particle-hole-symmetric point of the SIAM, Kondo correlations are especially pronounced. In *equilibrium* they introduce a characteristic energy scale, the Kondo temperature[5] T_K which translates into a length scale of the Kondo singlet ξ_K, given by Bethe ansatz[57]

$$\xi_K \propto \frac{v_F}{k_B T_K} \propto 2t\sqrt{\frac{2}{\Delta U}}\, e^{\frac{\pi}{8\Delta}U}. \tag{2}$$

Due to the exponential dependence on interaction strength, these spin correlations can not fully develop on a finite-size system,[58,59] already for moderate interaction strength. For the parameters used in this work, the equilibrium Kondo correlations have a spatial extent (screening cloud) of approximately $\xi_K \approx 50$ sites for $U = 4\,\Delta$, $\xi_K \approx 200$ sites for $U = 8\,\Delta$, $\xi_K \approx 900$ sites for $U = 12\,\Delta$, and $\xi_K \approx 16\,000$ sites for $U = 20\,\Delta$ [see Eq. (2)]. These amount to equilibrium Kondo temperatures of $T_K \approx 3 \times 10^{-1}\,\Delta$, $9 \times 10^{-2}\,\Delta$, $2 \times 10^{-2}\,\Delta$, and $1 \times 10^{-3}\,\Delta$, respectively.

For very small bias voltages $V_B \ll T_K$ (and large U), the Kondo effect introduces a large time scale. In this work, however, we focus on parameters for which $V_B \gg T_K$. (An exception is $U = 4\,\Delta$ and $V_B < 10\,\Delta$, where the Kondo cloud does fit into our finite-size system.[60]) For the parameter regime under study, recent numeric[61] and analytic[62–64] studies provide strong indications for suppression of the equilibrium Kondo effect.

It is argued in literature that one expects a splitting of the Kondo resonance, possibly a pinning at the lead potentials[65,66] and/or a suppression[61] of the Kondo effect similar to the effect of temperature[4,61,63] or magnetic field.[67] Renormalization group studies concluded that bias voltage is a relevant energy scale in the problem.[62–64] Recent results for the electron dynamics in the steady state indicate a splitting of the Kondo resonance away from zero with bias voltage which further supports our observation that the Kondo induced time scale is not relevant for charge transport at large bias voltages.[39] Note that even in the presence of Kondo correlations, charge relaxation should be orders of magnitudes faster than spin relaxation.[53]

From our current simulation we made the observation that an initial system with Kondo correlations (to be precise, their finite-size remnants) as in QT II yields the *same* steady-state charge current (after a short, and different transient regime) as an initial system without them as in QT I. This indicates that in QT II the Kondo correlations are washed away by bias voltage. We thus conclude that although finite-size systems are not able to capture the full equilibrium Kondo singlet,[58] the steady-state transport in the charge channel is not noticeably affected in the parameter regime under investigation.

B. Time scales in the high-bias regime

We find that relaxation times in the model under discussion are strongly parameter (U, V_B) dependent. These relaxation time scales are estimated by the slope of a linear fit to the plateau region $[\tau_S, \tau_E]$ (see Sec. IV A). In particular, we identify three regions [see Fig. 7 (top)]: region I is characterized by short physical relaxation times and region II exhibits longer relaxation times. Region II overlaps with the regime in which TEBD restricts us to small final simulation times τ_E (high steady-state current regime, see Appendix B for discussion). In region II, we did not obtain a converged steady-state current. In region III, the current is small and the maximum reachable simulation time (see Appendix B) was large enough to determine the steady-state current.

We proceed by providing an intuitive single-particle picture of the transition from region I to II in a Hubbard-I-type description [Fig. 7 (bottom)]. Then, the leads (assuming infinite reservoirs) are described by semicircular bands of bandwidth D, asymmetrically shifted against each other with increasing bias voltage V_B. The quantum dot consists of a single (noninteracting) level, located at the single-particle energy $-\frac{U}{2}$. We find that the transition occurs when this single-particle level of the quantum dot leaves the overlap region of both lead DOS (blue line, $U_{\text{trans}} \approx D - V_B$). We conclude that the existence of an appreciable spectral weight *in the overlap region* of the lead DOS leads to faster relaxation.

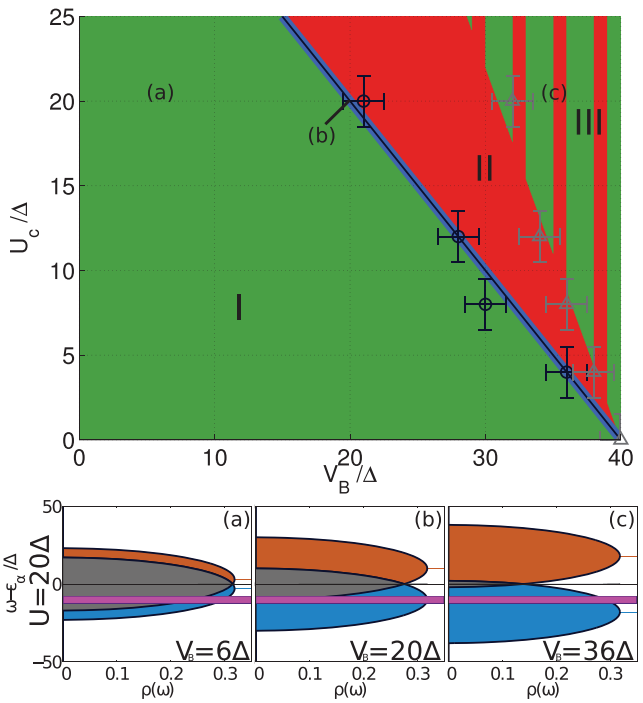

FIG. 7. (Color online) (Top) Parameter regions in the $U - V_B$ of short (I) and long (II) physical relaxation scales as well as a regime of more complex behavior III. Data from the TEBD calculation are indicated with black and gray markers. For region II, pedestals are shown in Fig. 4. (Bottom) Single-particle DOS and single-particle dot level in a Hubbard-I-type picture at $U = 20\,\Delta$, for (a) $V_B = 6\,\Delta$, (b) $V_B = 20\,\Delta$, and (c) $V_B = 36\,\Delta$. The electronic DOS of the left (right) lead is shown in red (blue) and their overlap in brown. The single-particle level of the quantum dot is indicated at $-\frac{U}{2}$ in magenta.

VI. ROLE OF HIGH-ENERGY STATES

To study the role of high-energy states during the time evolution we add a damping term to the propagator

$$\hat{\mathcal{U}}(\tau) = e^{-i\hat{\mathcal{H}}\tau(1-i\Gamma)}, \tag{3}$$

which gradually reduces the contribution of high-energy states.

In Fig. 8, the effects of damping of high-energy modes on the current is visualized. We show results for very low-bias voltage ($V_B = 2\,\Delta$) as well as high-bias voltage ($V_B = 32\,\Delta$). The different influence of overdamping (dashed lines) on low-bias setups in contrast to high-bias setups yields insight into the role of high-energy states in the two respective cases. In low-bias settings, strong overdamping (here $\Gamma = 10\,\Delta$) leads to lower current while in the high-bias case it leads to higher current with respect to the true one. This indicates a qualitatively different role of high-energy states for these two settings.

This result can be made plausible by a simple argument. In the case of small-bias voltage ($V_B \ll t$), the dominant energies should be the kinetic ones and neglecting high-energy states amounts to eliminating those with highest kinetic energy. Such states contribute much to the current and neglecting them leads to a lower total current. On the other hand, for very high-bias voltage ($V_B \gg t$), potential energy is expected to dominate. High-energy states are then those with a lot of particles in the

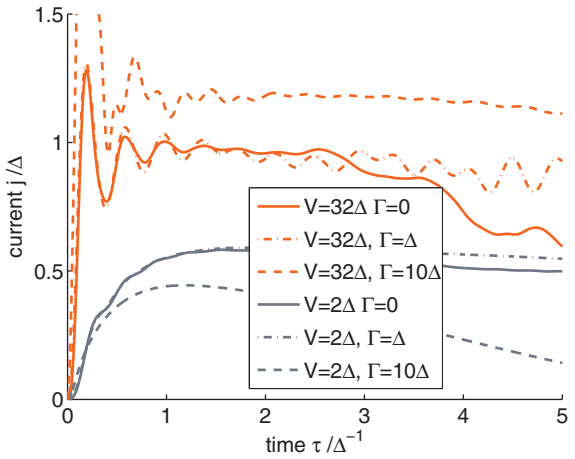

FIG. 8. (Color online) Effects of damping Γ of high-energy modes on the time evolution of the current ($U = 0, \chi_{\mathrm{TEBD}} = 500$, QT I). Data shown are obtained for very low-bias voltage ($V_B = 2\,\Delta$, group of gray curves in lower part of figure) and high-bias voltage ($V_B = 32\,\Delta$, group of orange curves in upper part of figure). For each bias voltage, we compare data obtained by a standard ($\Gamma = 0$) time evolution (full lines), data using an (empirically) optimally damped time evolution ($\Gamma = \Delta$, dashed-dotted lines) as well as for an overdamped evolution ($\Gamma = 10\,\Delta$, dashed lines).

high-bias reservoir. Eliminating them reduces the available state space for hopping of particles back to the side of high potential. Therefore, the current is increased due to less back flow. From a technical point of view, such an approach may reduce entanglement growth (the limiting quantity in real-time evolution using matrix product states), thus reducing the required matrix dimensions of the MPS. Using such an ansatz, however, suffers from two drawbacks. (i) On the one hand, we have just seen that high-energy states can be important for the steady-state current and, on the other hand, estimating *a priori* a suitable magnitude of the damping Γ is not straightforward since it should in principle be dynamically adjusted during the time evolution taking into account energies and truncated weight. Due to these reasons, we refrain from using such an approach in general. However, we show in Fig. 8 that by choosing a phenomenologically good value for the damping ($\Gamma = \Delta$), one can indeed somewhat prolong the stable time evolution.

VII. CONCLUSIONS

We studied the single-impurity Anderson model out of equilibrium beyond the linear response regime by means of density matrix renormalization group. Real-time evolution was performed making use of the time-evolving block decimation algorithm which allows us to access relevant time scales to reach the steady state. Within this framework, we investigated three different quenches: (i) quenching the hybridization with already applied bias voltage, (ii) quenching the bias voltage, and (iii) quenching the hybridization at one side only.

Calculated current-voltage characteristics agree very well with established results which are available in the low-bias region. We find that the period of characteristic oscillations in the time evolution of the charge current is already very well described by renormalization group results for a different model, the interacting resonant level model of spinless fermions. After an initial transient regime, where on the order of one particle is transferred through the quantum dot, the steady-state current agrees among the three quenches investigated. For the identification of steady-state plateaux in time-dependent quantities, the type of quench is however very important. We show that quenching the lead-dot tunnelings is the most suitable one, contrary to expectations whereas quenching the bias voltage results in large initial oscillations of the current. We furthermore show that limitations of the method such as its inherent finite size do not pose a problem for simulations of the setup discussed here within accessible times. Our findings indicate that the steady-state charge current is not influenced by finite-size effects, hinting that incompletely developed Kondo correlations in the spin channel do not influence charge transport noticeably. We find that a large entanglement entropy correlates positively with a large steady-state current amplitude. By studying a damped time evolution, we find that high-energy states have very different significance in the low- and high-bias regimes, respectively.

Aside from reproducing the universal low-bias physics, we open up new perspectives for devices in which a large-bias voltage is combined with a finite electronic DOS of the leads, such as nanotubes. For such devices, we predict that effects of electron-electron interactions are important even at high-bias voltages.

Interesting extensions within the presented approach may be the application of a gate voltage to study stability diagrams, evaluation of spin correlations which could hint on Kondo correlations, to study effects of asymmetric couplings, the interplay of bias and magnetic fields as well as to investigate correlated leads.[34] On the technical side, it would be interesting to evaluate whether more gently ramped quenches over a finite-time interval further decrease oscillations or even entanglement and further improve the extraction of steady-state data.

ACKNOWLEDGMENTS

We gratefully acknowledge fruitful discussions with S. Andergassen and S. R. White. We thank F. Heidrich-Meisner, P. Werner, and A. Dirks for providing their data in Fig. 5. This work was partly supported by the Austrian Science Fund (FWF) P24081-N16, and ViCoM Projects No. F04103 and No. F04104. H.G.E. thanks the KITP for hospitality. This research was supported in part by the NSF under Grant No. NSF PHY05-51164. Most of the numerical calculations have been conducted at the Vienna Scientific Cluster (VSC-I&II).

APPENDIX A: METHOD SETUP, CONVERGENCE ANALYSIS, AND PRELIMINARY CONSIDERATIONS

Here, we present some preliminary considerations concerning the convergence and quality of our data. Uncertainties arise from the approximations made within the method and

from numerical precision. In addition, our setup contains leads of finite size, with two effects in principle. First, this finite size affects the ground state at time zero. We will show in the following that the effect on the current is negligible; it converges already at much smaller lead size than used here.

Second, the finiteness of the reservoirs means that no energy or particle dissipation occurs and eventually the system will show oscillatory behavior. We note in passing that during our simulation time only approximately one particle traverses the quantum dot. The earliest time at which the current can be affected by the finite system size arises from a perturbation which propagates after the quench to the end of a lead and back to the quantum dot. The velocity of this signal is limited by the Lieb-Robinson bound,[68] up to exponentially suppressed parts, and in our case is $v \approx 2t$, which can also be clearly seen in the time evolution of local charge expectation values.[54] The perturbation will hit the left and right ends of the chain and return back to the quantum dot after a time of about $\tau \approx 2(L/2)/(2t) = L/(2t)$, i.e., $\tau/\Delta^{-1} \approx L\Delta/(2t) \approx 7.5$ for $L = 150$. This is far beyond the times τ_E (see Sec. IV A) up to which we calculate the steady-state current, which is therefore not affected. This conclusion is confirmed by the convergence of the current with respect to system size L, discussed below. The measured current may, however, be affected by other possible errors within our approach: (i) the procedure to measure it, (ii) the Trotter error, and (iii) the limited matrix dimension χ_{TEBD} (i.e., truncated weight).

In the following, we will show that the major uncertainty arises from the limited matrix dimension χ_{TEBD}, while other sources are negligible. The definition of the time intervals from which the steady-state current is evaluated (Sec. IV A) is also relevant. A similar conclusion has been drawn before in the framework of adaptive tDMRG (Ref. 25) and for different systems in the framework of TEBD.[49]

1. Obtaining the current

Within the TEBD time evolution, the steady-state current may be obtained via the expectation value of the current operator at each time step[24,69]

$$\hat{j}_{ij}(\tau) = i\, t_{ij} \sum_{\sigma} (a^{\dagger}_{i\sigma}\, a_{j\sigma} - a_{i\sigma}\, a^{\dagger}_{j\sigma}),$$

where i and j denote adjacent sites and $a_{i\sigma}$ and $a^{\dagger}_{i\sigma}$ are annihilation and creation operators for fermions onsite i with spin σ which depend at time τ and t_{ij} is taken to be real. To obtain the current through the quantum dot, a symmetrized version of the inflow and outflow is used:

$$\begin{aligned}\hat{j}(\tau) &= \frac{\hat{j}_{Lf} + \hat{j}_{fR}}{2} \\ &= i\,\pi\, t' \sum_{\sigma} \left(\left(f^{\dagger}_{\sigma} c^{L}_{\mathrm{end}\sigma} - c^{L\dagger}_{\mathrm{end}\sigma} f_{\sigma} \right) - \left(f^{\dagger}_{\sigma}\, c^{R}_{0\sigma} - c^{R\dagger}_{0\sigma}\, f_{\sigma} \right) \right),\end{aligned} \tag{A1}$$

where $c^{L}_{\mathrm{end}\sigma}$, $c^{\dagger L}_{\mathrm{end}\sigma}$ denote operators on the last site of the left reservoir (number 74 in Fig. 1) and $c^{R}_{0\sigma}$, $c^{R\dagger}_{0\sigma}$ denote operators on the first site of the right reservoir (number 76 in Fig. 1).

Another way of computing the current is by calculating the time derivative of the total particle number to the left of the site under consideration:

$$j_{ii+1}(\tau) = \frac{d}{d\tau} \left\langle \sum_{m=1}^{i} \sum_{\sigma} \hat{n}_{m\sigma}(\tau) \right\rangle.$$

Again, a symmetric combination of the dot's ingoing and outgoing current yields the current under consideration

$$\begin{aligned} j(\tau) = \frac{1}{2} \Bigg(&\frac{d}{d\tau} \left\langle \sum_{m\in L} \sum_{\sigma} \hat{n}_{m\sigma}(\tau) \right\rangle \\ &+ \frac{d}{d\tau} \left\langle \sum_{m\in L\cup f} \sum_{\sigma} \hat{n}_{m\sigma}(\tau) \right\rangle \Bigg). \end{aligned} \tag{A2}$$

The current through the dot may be evaluated at each TEBD time step using Eq. (A1) or by computing a finite-difference approximation to the differential Eq. (A2) every two successive time steps.

Aside from the expected additional source of error by evaluating the time derivative numerically, this method is expected to perform less well due to the influence of all sites in the system on the result for the current, the occupation number of each site having its own limited accuracy. A comparison of the current evaluated by means of Eqs. (A1) and (A2) for various values of interaction strength U and applied bias voltage V_B as well as all QTs (I, II, III) shows good agreement in the beginning of the time evolution [see Fig. 9 (left)]. Due to an accumulation of errors in the particle-number expectation values of the individual sites, the results start to deviate at some time $\tau_E^{(2)}$. We do not use results beyond $\tau_E^{(2)}$ (see the discussion in Sec. IV A). Numerical values of all steady-state currents will be obtained using the current operator [Eq. (A1)] which yields a much more stable estimator.

2. Finite-size effects: L

In this section, we discuss the dependence of the results for the current on the length of the system L.[49,70] We quench both dot-lead tunnelings (i.e., QT I). The qualitative behavior for the other QTs (II and III) is virtually identical. Results for the steady-state current for system sizes of $L = 20,40,60,80,100,120$, and 150 sites are shown in Fig. 9 (right) in the noninteracting case. We find that the final results for the steady-state current agree with the analytically available results for an infinite system in all cases within the numerical error. This ensures a reliable determination of steady-state properties even on finite-size systems. As mentioned before, the system size limits the maximum simulation time due to signals back-propagating from the borders. In the main part of this work, all calculations are performed for a system size of $L = 150$ to provide a nice long plateau (maximum simulation time) in the steady-state current. It has been noted in Ref. 71 that in the particle-hole-symmetric half-filled model, the steady-state current is independent of system size. A detailed discussion of finite size and time scales in a model of spinless fermions can be found in Ref. 70.

For completeness, we note that it is possible to extend the available simulation time, when it is limited by the hard boundary conditions of the leads, by applying modified boundary conditions.[34,69,72,73] Exponentially decreasing the matrix elements of the Hamiltonian towards the end of the

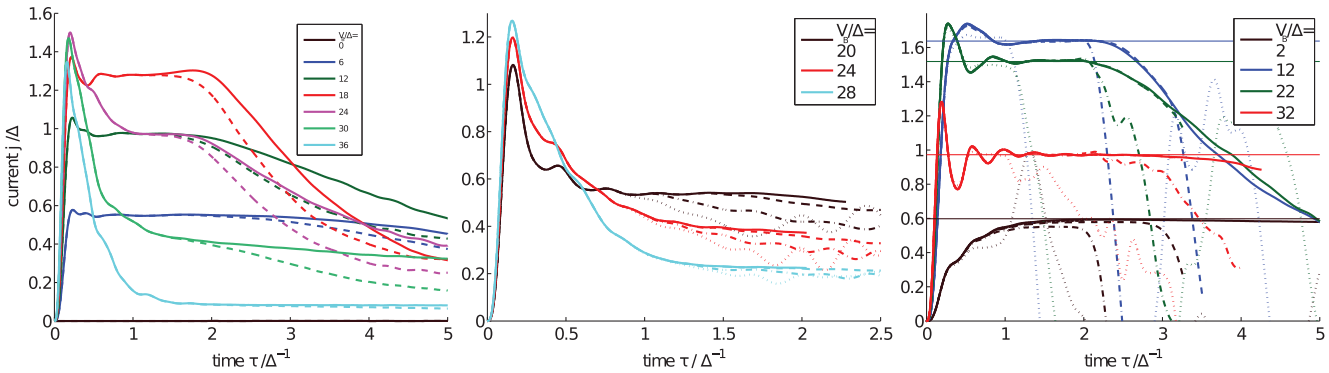

FIG. 9. (Color online) Convergence of the current with respect to several auxiliary numerical parameters. Left: Solid lines denote results obtained evaluating the expectation value of the current operator (A1), while dashed lines indicate data obtained by evaluating the time derivative of the expectation value of the particle number (A2) ($U = 12\,\Delta$, $L = 150$, $\chi_{\mathrm{TEBD}} = 2000$, QT I). Center: Matrix sizes $\chi_{\mathrm{TEBD}} = 250$ (dotted line),500 (dashed-dotted line),2000 (dashed line), and 4000 (solid line) are presented ($U = 20\,\Delta$, $L = 150$, QT I). Right: We show system sizes $L = 20,40,60,80,100,120$, and 150 (dotted, dashed-dotted, dashed, dashed-dashed-dotted-dotted, long-dashed-short-dashed, dashed-gap-dashed, and solid lines) at $U = 0$, $L = 150$, $\chi_{\mathrm{TEBD}} = 2000$ for QT I. The constant solid lines indicate the exact steady-state currents of the respective thermodynamic system.

reservoirs ultimately corresponds to a Wilson chain with logarithmic discretization.[73] In this work, we do not apply any modified boundary conditions because our simulation time is not limited by the size of the chains but the TEBD matrix dimension χ_{TEBD}.

3. Trotter error: $\delta\tau$

The Trotter error grows only linearly with simulation time,[25,74] and can be controlled by choosing sufficiently small $\delta\tau$. Therefore, usually the contribution to the total error arising due to the Trotter approximation is negligible with respect to other approximations. We investigated the influence of the Trotter decomposition on the current. Results for $\delta\tau/t^{-1} = \{0.01,0.05,0.1\}$ were found to agree to within 5×10^{-5}. We do not plot the results because they all lie on top of each other. A good value for the time step was found to be $\delta\tau/t^{-1} = 0.05$ which was used in the main section of the paper.

4. MPS matrix dimension: χ

The quality of the TEBD results is predominantly determined by the maximum matrix size χ_{TEBD} used. A bigger χ_{TEBD} leads to fewer discarded states (i.e., less truncated weight of the reduced density matrices) during the truncation and therefore to a systematically better approximation.[12] The truncated weight is defined by[74]

$$\epsilon = 1 - \sum_{\gamma=1}^{\chi} \lambda_{\gamma}^{2}, \tag{A3}$$

where λ_{γ}^{2} denote the eigenvalues of the reduced density matrices. This quantity is zero if no truncation is done. The computational cost of the TEBD algorithm scales essentially like[74]

$$\mathrm{cost} \propto L(d\ \chi_{\mathrm{TEBD}})^{3},$$

where L is the length of the chain and $d = 4$ the size of the local fermionic Hilbert space. Therefore, it is essential to keep χ_{TEBD} as low as possible. During the simulations we noticed that at a certain time (long before signals propagating back from the ends of the chain would reach the quantum dot), the truncated weight starts to grow quickly and the results become unstable,[75] causing a decaying current. The effects of enlarging χ_{TEBD} are shown in Fig. 9 (center). As the data indicate, the effect of increasing χ_{TEBD} is to make larger simulation times accessible, before the simulation breaks down due to accumulation of truncated weight. Remarkably, no spurious quasi-steady state is entered when χ_{TEBD} is relatively small. The overall shape of the current appears to be unaffected by enlarging χ_{TEBD}, making reliable predictions for $\chi_{\mathrm{TEBD}} = 2000$ possible. We checked our results in all parameter regions for convergence. In the main part of the paper, we always used $\chi_{\mathrm{TEBD}} = 2000$ as a good compromise between run time and accuracy.

5. Comparison to analytical results

In the noninteracting setup $U = 0$, we compare TEBD data to results from an exact time evolution (see Fig. 10). The exact time evolution was obtained for the same system parameters by time evolving the single-particle density matrix. We find that the TEBD time evolution is reliable up to a system-parameter-dependent time. This time (triangles) again is in accordance with the criterion for the maximum reachable simulation time as defined in Sec. IV A and has a nontrivial dependence on bias voltage and interaction strength.

The noninteracting system is nontrivial for the TEBD method. Our data for the entanglement entropy and the truncated weight at low-, medium-, as well as high-bias voltages for increasing interaction strength[54] indicate that indeed the $U = 0$ case does not exhibit a particular low entanglement or truncated weight in comparison with higher interaction strength. Since we reproduce the exact analytic steady-state current in the noninteracting case, we conclude that the agreement with exact results is not a peculiarity of the noninteracting system and our way of data extraction can be applied to finite values of U.

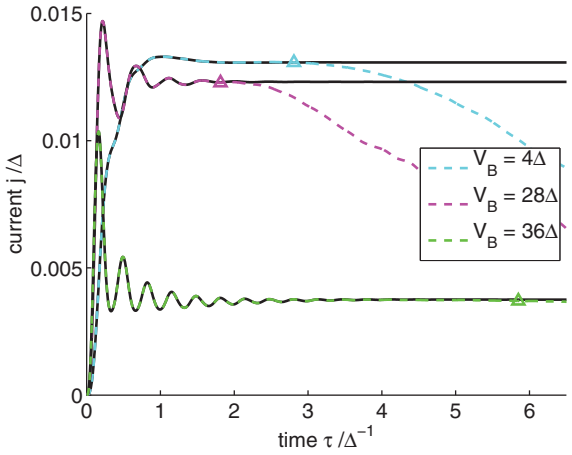

FIG. 10. (Color online) Exact results for the noninteracting system. Comparison of the TEBD current (dashed lines) to an exact time evolution (solid black lines) for $U = 0\,\Delta$, $L = 150$, $\chi_{\mathrm{TEBD}} = 2000$, QT I. We show results for $V_B = 4\,\Delta$ (cyan), $V_B = 28\,\Delta$ (magenta), and $V_B = 36\,\Delta$ (green). The respective maximum reliable simulation times (see Sec. IV A for definition) are indicated as triangles.

6. Setup

Based on the above considerations, all data in the main part of the paper were obtained for the following parameters: (i) The ground state was obtained by DMRG using a matrix size $\chi_{\mathrm{DMRG}} = 400$ and undergoing 10 sweeps of two-site DMRG before switching to 40 runs for single-site DMRG. (ii) The model consists of $L = 150$ sites. Upon performing one of the three above-described quenches (I, II, or III), we used bias voltages in a range of $V_B/\Delta = (0,42)$. We always started from an overall half-filled system in the canonical ensemble with total $S^z = 0$ and alternating up and down spins are chosen from left to right. (iii) The time evolution was performed using a TEBD matrix size of $\chi_{\mathrm{TEBD}} = 2000$, a trotter step of $\delta\tau/\Delta^{-1} = 0.005$ and evolving for 1000 time steps which yielded a final simulation time of $T/\Delta^{-1} = 5$. Requiring a maximum truncated weight of $\epsilon_c = 10^{-15}$, we dynamically adjusted the size of the TEBD matrices with a maximum matrix size of χ_{TEBD}. We measured observables at each time step.

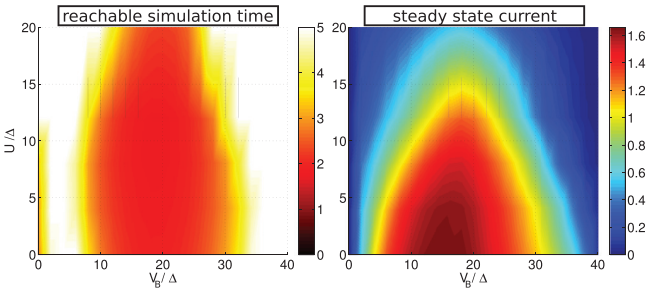

FIG. 11. (Color online) Maximum simulation time reachable (QT I, $\chi_{\mathrm{TEBD}} = 2000$) due to accumulation of entanglement entropy (left) and steady-state current (right). The left plot shows the time until a truncated weight of $\epsilon_c = 5 \times 10^{-5}$ is reached at any bond of the chain for the first time. The right figure corresponds to the data in Fig. 4. Note the inverted color scale in the left image; dark regions correspond to low values of the maximum time reachable.

APPENDIX B: CORRELATION OF ENTROPY AND STEADY-STATE CURRENT

The major limiting factor for time evolution using TEBD is the increase of bipartite entanglement[11]

$$S_i = -\mathrm{tr}[\hat{\rho}_L \ln(\hat{\rho}_L)] = -\mathrm{tr}[\hat{\rho}_R \ln(\hat{\rho}_R)],$$

where $\hat{\rho}_{L/R}$ denotes the reduced density matrix to the left (L) and to the right (R) of a bipartition at bond i. Using a maximum matrix dimension χ_{TEBD}, we stop the simulation (for Fig. 11) whenever the truncated weight at any bond exceeds a threshold value of $\epsilon_c = 5 \times 10^{-5}$, which defines our maximum simulation time $\tau_E^{(1)}$ (see Sec. IV A). In Fig. 11, we plot $\tau_E^{(1)}$ as a function of U and V_B (left) and compare it to the magnitude of the steady-state current for the same parameters (right).

From our data we conclude that reachable simulation times due to accumulation of entanglement (and thus truncated weight) are nonmonotonic in U and V_B but can be characterized roughly by the magnitude of current in the system. We find this behavior to be generic to all investigated QTs.

*martin.nuss@student.tugraz.at

[1]S. Trotzky, P. Cheinet, S. Fölling, M. Feld, U. Schnorrberger, A. M. Rey, A. Polkovnikov, E. A. Demler, M. D. Lukin, and I. Bloch, Science **319**, 295 (2008).
[2]U. Schneider, L. Hackermuller, J. P. Ronzheimer, S. Will, S. Braun, T. Best, I. Bloch, E. Demler, S. Mandt, D. Rasch *et al.*, Nat. Phys. **8**, 213 (2012).
[3]D. Goldhaber-Gordon, J. Gores, M. A. Kastner, H. Shtrikman, D. Mahalu, and U. Meirav, Phys. Rev. Lett. **81**, 5225 (1998).
[4]A. V. Kretinin, H. Shtrikman, and D. Mahalu, Phys. Rev. B **85**, 201301 (2012).
[5]A. C. Hewson, *The Kondo Problem to Heavy Fermions* (Cambridge University Press, Cambridge, UK, 1997).
[6]N. S. Wingreen, A.-P. Jauho, and Y. Meir, Phys. Rev. B **48**, 8487 (1993).
[7]S. R. White, Phys. Rev. B **48**, 10345 (1993).
[8]A. Daley, C. Kollath, U. Schollwoeck, and G. Vidal, J. Stat. Mech.: Theor. Exper. (2004) P04005.
[9]G. Vidal, Phys. Rev. Lett. **93**, 040502 (2004).
[10]S. R. White and A. E. Feiguin, Phys. Rev. Lett. **93**, 076401 (2004).
[11]U. Schollwock, Ann. Phys. (NY) **326**, 96 (2011).
[12]P. Schmitteckert, Phys. Rev. B **70**, 121302 (2004).
[13]E. Boulat, H. Saleur, and P. Schmitteckert, Phys. Rev. Lett. **101**, 140601 (2008).
[14]F. Heidrich-Meisner, A. E. Feiguin, and E. Dagotto, Phys. Rev. B **79**, 235336 (2009).
[15]S. T. Carr, D. A. Bagrets, and P. Schmitteckert, Phys. Rev. Lett. **107**, 206801 (2011).
[16]P. W. Anderson, Phys. Rev. **124**, 41 (1961).
[17]In the wide-band limit, a featureless (constant) electronic density of states of the reservoirs is assumed which has a bandwidth much

larger than the characteristic energy scales of the system coupled to the reservoir. The retarded Green's function is then given by $G^R(\omega) = -\frac{1}{2W}\ln(\frac{\omega-W}{\omega+W})$ where W is the half-bandwidth.

[18] S. J. Tans, M. H. Devoret, H. Dai, A. Thess, R. E. Smalley, L. J. Geerligs, and C. Dekker, Nature (London) **386**, 474 (1997).

[19] A. Hasegawa, K. Yoshizawa, and K. Hirao, Chem. Phys. Lett. **345**, 367 (2001).

[20] K. Grove-Rasmussen, S. Grap, J. Paaske, K. Flensberg, S. Andergassen, V. Meden, H. I. Jørgensen, K. Muraki, and T. Fujisawa, Phys. Rev. Lett. **108**, 176802 (2012).

[21] S. J. Chorley, M. R. Galpin, F. W. Jayatilaka, C. G. Smith, D. E. Logan, and M. R. Buitelaar, Phys. Rev. Lett. **109**, 156804 (2012).

[22] R. Saito, M. Fujita, G. Dresselhaus, and M. S. Dresselhaus, Appl. Phys. Lett. **60**, 2204 (1992).

[23] B. William, *Electronic and Optical Properties of Conjugated Polymers* (Oxford University Press, Oxford, 2005).

[24] K. A. Al-Hassanieh, A. E. Feiguin, J. A. Riera, C. A. Büsser, and E. Dagotto, Phys. Rev. B **73**, 195304 (2006).

[25] F. Heidrich-Meisner, I. González, K. A. Al-Hassanieh, A. E. Feiguin, M. J. Rozenberg, and E. Dagotto, Phys. Rev. B **82**, 205110 (2010).

[26] M. Znidaric, Phys. Rev. Lett. **106**, 220601 (2011).

[27] S. Jesenko and M. Znidaric, Phys. Rev. B **84**, 174438 (2011).

[28] F. Heidrich-Meisner, G. B. Martins, C. A. Büsser, K. A. Al-Hassanieh, A. E. Feiguin, G. Chiappe, E. V. Anda, and E. Dagotto, Eur. Phys. J. B **67**, 527 (2009).

[29] S. Kirino, T. Fujii, J. Zhao, and K. Ueda, J. Phys. Soc. Jpn. **77**, 084704 (2008).

[30] S. Kirino and K. Ueda, J. Phys. Soc. Jpn. **79**, 093710 (2010).

[31] M. A. Cazalilla and J. B. Marston, Phys. Rev. Lett. **88**, 256403 (2002).

[32] H. G. Luo, T. Xiang, and X. Q. Wang, Phys. Rev. Lett. **91**, 049701 (2003).

[33] M. A. Cazalilla and J. B. Marston, Phys. Rev. Lett. **91**, 049702 (2003).

[34] A. Feiguin, P. Fendley, M. P. A. Fisher, and C. Nayak, Phys. Rev. Lett. **101**, 236801 (2008).

[35] M. Nuss, E. Arrigoni, M. Aichhorn, and W. von der Linden, Phys. Rev. B **85**, 235107 (2012).

[36] P. Werner, T. Oka, M. Eckstein, and A. J. Millis, Phys. Rev. B **81**, 035108 (2010).

[37] T. Fujii and K. Ueda, Phys. Rev. B **68**, 155310 (2003).

[38] S. G. Jakobs, M. Pletyukhov, and H. Schoeller, Phys. Rev. B **81**, 195109 (2010).

[39] M. Nuss, C. Heil, M. Ganahl, M. Knap, H. G. Evertz, E. Arrigoni, and W. von der Linden, Phys. Rev. B **86**, 245119 (2012).

[40] A. Dirks, J. E. Han, M. Jarrell, and T. Pruschke, Phys. Rev. B **87**, 235140 (2013).

[41] S. Weiss, J. Eckel, M. Thorwart, and R. Egger, Phys. Rev. B **77**, 195316 (2008).

[42] I. Bâldea and H. Köppel, Phys. Rev. B **81**, 193401 (2010).

[43] Which is in fact a "quasi"-steady state due to the fact that the system is of finite size. We, however, show that it corresponds to the true steady state of the corresponding thermodynamic system.

[44] A. Kawabata, Rep. Prog. Phys. **70**, 219 (2007).

[45] A. Kawabata, J. Phys. Soc. Jpn. **65**, 30 (1996).

[46] M. Ganahl, E. Rabel, F. H. L. Essler, and H. G. Evertz, Phys. Rev. Lett. **108**, 077206 (2012).

[47] V. Zauner, M. Ganahl, H. G. Evertz, and T. Nishino, arXiv:1207.0862.

[48] M. Knap, E. Berg, M. Ganahl, and E. Demler, Phys. Rev. B **86**, 064501 (2012).

[49] M. Einhellinger, A. Cojuhovschi, and E. Jeckelmann, Phys. Rev. B **85**, 235141 (2012).

[50] S. Andergassen, M. Pletyukhov, D. Schuricht, H. Schoeller, and L. Borda, Phys. Rev. B **83**, 205103 (2011).

[51] An expression for the noninteracting steady-state current is given by (Refs. 76 and 77) $j = 4\pi t'^4 \int_{-\frac{V_B}{2}}^{\frac{V_B}{2}} d\omega \frac{\rho_L(\omega)\rho_R(\omega)}{([g_L^A(\omega)+g_R^A(\omega)]t'^2-(\omega-\epsilon_f))(\text{c.c.})}$, where $\rho_{L/R}$ denote the electronic DOS of the (disconnected) left and right leads and $g^A_{L/R}$ their advanced single-particle Green's functions.

[52] E. Perfetto, G. Stefanucci, and M. Cini, Phys. Rev. Lett. **105**, 156802 (2010).

[53] G. Cohen, E. Gull, D. R. Reichman, A. J. Millis, and E. Rabani, Phys. Rev. B **87**, 195108 (2013).

[54] M. Nuss, M. Ganahl, H. G. Evertz, E. Arrigoni, and W. von der Linden (unpublished).

[55] M. Knap, W. von der Linden, and E. Arrigoni, Phys. Rev. B **84**, 115145 (2011).

[56] J. Eckel, F. Heidrich-Meisner, S. G. Jakobs, M. Thorwart, M. Pletyukhov, and R. Egger, New J. Phys. **12**, 043042 (2010).

[57] I. Affleck, arXiv:0911.2209.

[58] T. Hand, J. Kroha, and H. Monien, Phys. Rev. Lett. **97**, 136604 (2006).

[59] A. Holzner, I. P. McCulloch, U. Schollwöck, J. von Delft, and F. Heidrich-Meisner, Phys. Rev. B **80**, 205114 (2009).

[60] I. Titvinidze and M. Potthoff, J. Korean Phys. Soc. **62**, 1434 (2013).

[61] L. Mühlbacher, D. F. Urban, and A. Komnik, Phys. Rev. B **83**, 075107 (2011).

[62] M. Pletyukhov, D. Schuricht, and H. Schoeller, Phys. Rev. Lett. **104**, 106801 (2010).

[63] M. Pletyukhov and H. Schoeller, Phys. Rev. Lett. **108**, 260601 (2012).

[64] A. Rosch, J. Kroha, and P. Wölfle, Phys. Rev. Lett. **87**, 156802 (2001).

[65] S. De Franceschi, R. Hanson, W. G. van der Wiel, J. M. Elzerman, J. J. Wijpkema, T. Fujisawa, S. Tarucha, and L. P. Kouwenhoven, Phys. Rev. Lett. **89**, 156801 (2002).

[66] R. Leturcq, L. Schmid, K. Ensslin, Y. Meir, D. C. Driscoll, and A. C. Gossard, Phys. Rev. Lett. **95**, 126603 (2005).

[67] A. V. Kretinin, H. Shtrikman, D. Goldhaber-Gordon, M. Hanl, A. Weichselbaum, J. von Delft, T. Costi, and D. Mahalu, Phys. Rev. B **84**, 245316 (2011).

[68] E. Lieb and D. Robinson, Commun. Math. Phys. **28**, 251 (1972).

[69] L. G. G. V. Dias da Silva, F. Heidrich-Meisner, A. E. Feiguin, C. A. Büsser, G. B. Martins, E. V. Anda, and E. Dagotto, Phys. Rev. B **78**, 195317 (2008).

[70] A. Branschädel, G. Schneider, and P. Schmitteckert, Ann. Phys. (NY) **522**, 657 (2010).

[71] G. Schneider and P. Schmitteckert, arXiv:cond-mat/0601389.

[72] M. Vekić and S. R. White, Phys. Rev. Lett. **71**, 4283 (1993).

[73] D. Bohr, P. Schmitteckert, and P. Wölfle, Europhys. Lett. **73**, 246 (2006).

[74] U. Schollwöck, Rev. Mod. Phys. **77**, 259 (2005).

[75] D. Gobert, C. Kollath, U. Schollwöck, and G. Schütz, Phys. Rev. E **71**, 036102 (2005).

[76] Y. Meir and N. S. Wingreen, Phys. Rev. Lett. **68**, 2512 (1992).

[77] H. Haug and A. Jauho, *Quantum Kinetics in Transport and Optics of Semiconductors*, 2nd ed. (Springer, Berlin, 1996).

5.3. Nonequilibrium spatiotemporal formation of the Kondo screening cloud on a lattice

5.3.1. Preamble

This part of our work has been published in PHYSICAL REVIEW B 91, 085127 (2015) [54] and is also available as a preprint on arXiv:1312.4586. Reproduced with permission from PHYSICAL REVIEW B 91, 085127 (2015), doi:10.1103/PhysRevB.91.085127 under Creative Commons Attribution 3.0 License.

In this second work on real time evolution we discuss the spatio-temporal formation of the Kondo screening cloud in the SIAM, see Sec. 3.2. Although the SIAM is the role model of correlated physics, its nonequilibrium physics is not fully understood as of today, see Sec. 3.1. Physical developments are discussed in Ch. 2. Especially the spatio-temporal correlations are of importance for nonequilibrium methods. Time evolution methods like the one presented in Sec. 5.2 need to pass the correlation time to reach the steady-state. In the real space cluster methods CPT and VCA and their nonequilibrium representatives, spatial correlations have to be considered due to their real space perturbative nature, see Sec. 5.4, Sec. 5.5, Sec. 5.6, Sec. 5.7, Sec. 5.8 and Sec. 5.10. Further the SIAM is used as an impurity solver in Sec. 5.1 and an auxiliary Lindblad system for it is proposed in Sec. 5.9. In this work we analyse the spatio-temporal correlations following a quantum quench into the Kondo regime using space and time dependent spin-spin and charge-charge correlation functions. We discuss in detail the time-scales and screening lengths and obtain a dynamic scale. The physics inside and outside the light cone which follows the quench is elaborated on in detail.

This paper is authored by Martin Nuss (MN) and co-authored by Martin Ganahl (MG), MN's supervisors Enrico Arrigoni (EA) and Wolfgang von der Linden (WL) as well as by Hans Gerd Evertz (HE). This research was to a large and significant extent conducted by MN under the supervision of WL and EA. HE, MN and MG initiated the work. MG provided his MPS computer code. HE, EA and WL provided guidance and expertise in all stages of the work. MG and HE provided expertise concerning the MPS computer simulations. MN adapted the computer code of MG, ran tests and parameter studies and finally conducted the computer simulations. MN analyzed the large scale data. MN conducted literature research. MN prepared, collected, interpreted, analyzed and visualized the results and set them in context with recent literature. MN wrote the first version of the manuscript. All authors contributed equally in discussing the results and revising the manuscript. We discussed our results with with Sabine Andergassen, Masud Haque, Fabian Heidrich-Meisner, Kerstin T. Oppelt and Shreyoshi Ghosh. We thank Rok Zitko for providing the *NRG LJUBLJANA* computer code [2].

5.3.2. Manuscript

Nonequilibrium spatiotemporal formation of the Kondo screening cloud on a lattice

Martin Nuss,* Martin Ganahl, Enrico Arrigoni, Wolfgang von der Linden, and Hans Gerd Evertz
Institute of Theoretical and Computational Physics, Graz University of Technology, 8010 Graz, Austria
(Received 5 September 2014; revised manuscript received 13 February 2015; published 27 February 2015)

We study the nonequilibrium formation of a spin screening cloud that accompanies the quenching of a local magnetic moment immersed in a Fermi sea at zero temperature. Based on high-precision density matrix renormalization-group results for the interacting single-impurity Anderson model, we discuss the real-time evolution after a quantum quench in the impurity-reservoir hybridization using time-evolving block decimation. We report emergent length and time scales in the spatiotemporal structure of nonlocal correlation functions in the spin and the charge density channel. At equilibrium, our data for the correlation functions and the extracted length scales show good agreement with existing results, as do local time-dependent observables at the impurity. In the time-dependent data, we identify a major signal which defines a "light cone" moving at the Fermi velocity and a ferromagnetic component in its wake. Inside the light cone we find that the structure of the nonequilibrium correlation functions emerges on two time scales. Initially, the qualitative structure of the correlation functions develops rapidly at the lattice Fermi velocity. Subsequently the spin correlations converge to the equilibrium results on a much larger time scale. This process sets a dynamic energy scale, which we identify to be proportional to the Kondo temperature. Outside the light cone we observe two different power-law decays of the correlation functions in space, with time- and interaction-strength-independent exponents.

DOI: 10.1103/PhysRevB.91.085127 PACS number(s): 72.10.Fk, 72.15.Qm, 71.27.+a, 73.21.La

I. INTRODUCTION

Quantum impurities are among the most fundamental paradigms of strongly correlated quantum systems. Equilibrium properties of such systems have been subject to intense investigation and are nowadays well understood. A famous example is the Kondo effect, where a local spin-$\frac{1}{2}$ degree of freedom interacts with the spins of a sea of free electrons [1]. The ground state of this system is a delocalized spin singlet, formed by the local moment and the spin of the free electrons, also called a screening cloud. The present work investigates how such a screening cloud develops over time when a local moment comes into contact with a free electron reservoir.

Quantum impurity systems, quite generally, feature an emergent screening length scale at low temperatures which provides the basis for their complex physics. In the 1950s, magnetic impurities have already been identified as the cause for a large resistivity anomaly at low temperatures when immersed in metallic hosts in dilute quantities [2,3]. It was found theoretically that the impurity's local magnetic moment becomes quenched below a certain temperature, known as the Kondo temperature [1,4], T_K, to form a local Fermi liquid [5]. Increased spin-flip scattering between pairs of degenerate spin-$\frac{1}{2}$ states then leads to an increase in resistivity below T_K.

Meanwhile, the Kondo effect has been observed also in nanoscopic devices like quantum dots [6–12], carbon nanotubes [13], and molecular junctions [14]. Here, the narrow, zero-energy resonance in the local density of states of the impurity, the Kondo-Abrikosov-Suhl resonance, leads to a well-defined unitary conductance in linear response. The Kondo effect has also proven essential to understanding tunneling into single magnetic atoms [15], adsorption of molecules onto surfaces [16], or defects in materials such as graphene [17]. On the theoretical side the Kondo effect lies at the heart of our current understanding of correlated materials, notably within the very successful dynamical mean-field theory [18–20].

Insight into the details of the screening cloud is important not only for the understanding of the physics of a single impurity but also for the understanding of the interplay of many magnetic impurities. Many impurities result in competing effects among conduction electrons and local moments, which form the basis for spin exhaustion scenarios [21,22] as well as for the Doniach phase diagram [23,24], which describes the relationship between Kondo [1] and RKKY interaction [25–27].

Experimental characterization of the structure of the singlet ground state, which is a bound state of the impurity spin and the reservoir electron "screening cloud," has proven difficult so far. Several proposals exist for how to measure the spatial extent of the spin screening cloud or its antiferromagnetic correlation with the impurity spin [28,29]. In principle, the real-space structure could be probed by performing nuclear magnetic resonance/Knight shift [30–32] measurements on bulk metals hosting dilute magnetic impurities, but the approach remains challenging [28]. Indirect observation by measurement of the Kondo resonance, for example, by photo emission, also remains elusive due to the too narrow resonance at the Fermi energy [33]. Other proposals suggest the use of scanning tunneling microscopy [34] and scanning tunneling spectroscopy to analyze adatoms or surface defects with Kondo behavior [35,36]. In the realm of nanodevices, proposals include experiments based on persistent currents [37] or in confined geometries [38,39]. Some progress has been made recently using single magnetic atoms [15], quantum corrals [40], or impurities beneath surfaces [35].

*martin.nuss@tugraz.at

On the theoretical side, however, the structure of the screening cloud has been characterized, at least in the equilibrium spin-spin correlation function [41] and the charge density-density correlation function [42,43]. Theoretical results [44–47] in equilibrium include studies employing quantum Monte Carlo (QMC), [48] numerical renormalization group (NRG) [49–51], and density matrix renormalization group (DMRG) [52], as well as, in the noninteracting system, also exact diagonalization [53].

The fascinating question of how the spatial structure of the Kondo screening cloud develops in the first place, i.e., whether and how it is approached in a nonequilibrium time evolution starting from an initial state without Kondo physics, has recently come under investigation [55–57]. The present work extends previous equilibrium DMRG calculations [52] by investigating the dynamic nonequilibrium formation of Kondo correlations. We study the physical behavior of the single-impurity Anderson model (SIAM) [58] based on results obtained with the DMRG [59–61] and the time-evolving block decimation (TEBD) [62] for matrix product states [63]. The system is sketched in Fig. 1. At time $\tau = 0$ [54] we start from an unentangled state of a singly occupied impurity and a half-filled Fermi sea (FS) of conduction electrons, $|\Psi\rangle = |\uparrow\rangle_{\text{impurity}} \otimes |\text{FS}\rangle_{\text{reservoir}}$. Then, after connecting the impurity to the reservoir, we follow the evolution of correlation functions over time as the system equilibrates and the "impurity spin gets transported to infinity." In this way, we obtain information about the spatiotemporal structure of the screening cloud.

Recently, studies of the time-dependent behavior of length scales in strongly correlated impurity systems were performed for the Toulouse point of the anisotropic Kondo model, where it maps onto a noninteracting system [55,56], and for the symmetric Kondo model [57]. In both these systems a "light cone"–like propagation of excitations with the Fermi velocity was observed and the regions inside as well as outside the light cone were investigated. Both studies identified a common low-energy scale: the inverse Kondo temperature as a time scale, which was seen in a spin correlation function outside the light cone at the Toulouse point [55,56]. For the symmetric Kondo model such a time scale was observed in an equilibrium linear response calculation to a magnetic perturbation [57]. We extend these studies to the SIAM, which shares a common low-energy behavior with the symmetric Kondo model. Whereas

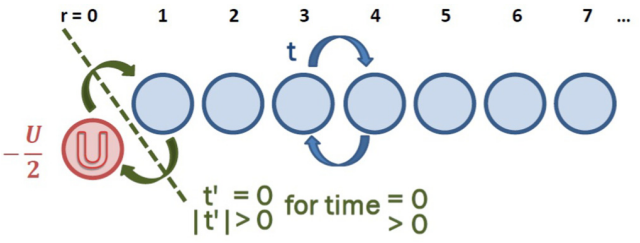

FIG. 1. (Color online) The model consists of a fermionic impurity with local Coulomb repulsion U, which is coupled to a one-dimensional half-filled tight-binding chain in a particle-hole symmetric fashion. At time $\tau = 0$ [54] we switch on the tunneling t' and study the evolution of the spin and charge correlation functions, $S(r,\tau)$ and $C(r,\tau)$.

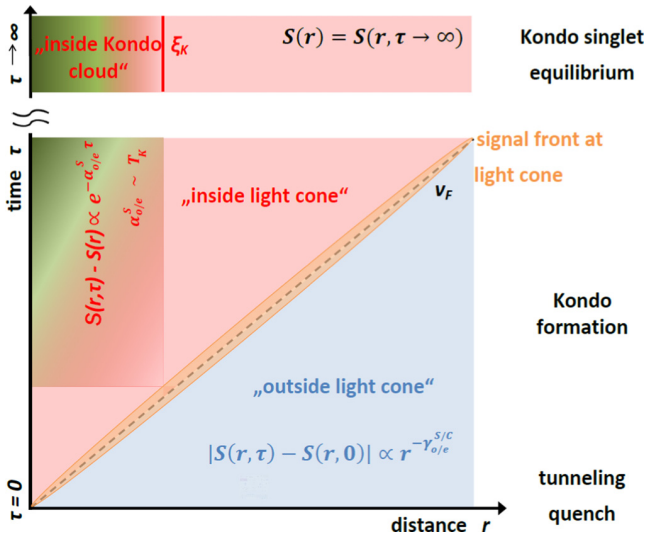

FIG. 2. (Color online) Schematic summary of results of this paper. The time evolution of the spin correlation function $S(r,\tau)$ exhibits three characteristic regions in space and time. These are divided by (i) a major signal following the quench, which propagates at the lattice Fermi velocity v_F and defines a light cone (dashed line), and (ii) the spread of the Kondo spin screening cloud. Region 1 (green) lies inside the light cone and inside the Kondo screening cloud. Here Kondo correlations develop on two characteristic time scales. The main structure of the Kondo singlet correlations is formed rapidly, at v_F. Then these correlations approach their equilibrium values exponentially slowly in time for $\tau \to \infty$, with an exponent $\alpha^S_{\text{o/e}}$ that is proportional to the Kondo temperature T_K. Region 2 (red) lies inside the light cone but outside the Kondo screening cloud. Here the spin correlations decay as a power law in space [53]. In region 3 (blue), which lies outside the light cone and outside the Kondo screening cloud, the correlation function at odd/even distances decays as a power law $\propto r^{-\gamma^{S/C}_{\text{o/e}}}$ in space with exponents that are independent of time and interaction strength.

in the Kondo model, only spin interactions survive and charge fluctuations are treated on an effective level [64], we take them into account explicitly. To our knowledge, our study is the first one analyzing the nonequilibrium properties of the screening length in the interacting SIAM.

Our results are summarized in Fig. 2, which also serves as a guiding map for this work. We identify a major signal following the quench, which propagates with the lattice Fermi velocity v_F and defines a light cone for the propagation of information [55–57,65–69]. Inside the light cone the time-evolved correlation functions converge to their equilibrium counterparts which exhibit the Kondo length scale. We find that Kondo correlations develop on two characteristic time scales. The main structure of the Kondo singlet is formed rapidly at v_F. These correlations approach their equilibrium values exponentially in time, defining a dynamic energy scale $\alpha^S_{\text{o/e}}$, which is proportional to the Kondo temperature T_K. Outside the light cone, we find that correlation functions at odd/even distances decay as a power law $\propto r^{-\gamma^{S/C}_{\text{o/e}}}$ in space, with exponents which are independent of time and interaction strength.

The structure of this paper is as follows: We summarize the specific model used in Sec. II. We define the Kondo singlet in Sec. III, present our numerical approach in Sec. IV, and provide an overview of the equilibrium situation in Sec. V. We start our presentation of nonequilibrium phenomena in Sec. VI, where we discuss the evolution of local observables. The main findings of this work are available in Sec. VII. There we discuss the nonequilibrium formation of the Kondo screening cloud in Sec. VII A. The situation outside the light cone is presented in Sec. VII B. The quality of our numerical data is assessed in Appendix A.

II. MODEL

We study a lattice realization of the SIAM [58],

$$\hat{\mathcal{H}}_{\mathrm{SIAM}} = \hat{\mathcal{H}}_{\mathrm{imp}} + \hat{\mathcal{H}}_{\mathrm{tunn}} + \hat{\mathcal{H}}_{\mathrm{res}}, \tag{1}$$

which consists of a single fermionic spin-$\frac{1}{2}$ impurity coupled via a standard hopping term to a reservoir of noninteracting tight-binding fermions (see Fig. 1). In particular, we consider a particle-hole symmetric impurity with on-site interaction U:

$$\hat{\mathcal{H}}_{\mathrm{imp}} = -\frac{U}{2}\sum_{\sigma} f_\sigma^\dagger f_\sigma + U\,\hat{n}_{f\uparrow}\hat{n}_{f\downarrow}. \tag{2}$$

The electronic annihilation (creation) operators f_σ ($f_\sigma^\dagger$) obey the usual anticommutation relations with spin $\sigma = \{\uparrow,\downarrow\}$, and $\hat{n}_{f\sigma} = f_\sigma^\dagger f_\sigma$ is the particle number operator [70]. The impurity is coupled via a tunneling term,

$$\hat{\mathcal{H}}_{\mathrm{tunn}} = -t'\sum_{\sigma}(c_{1\sigma}^\dagger f_\sigma + f_\sigma^\dagger c_{1\sigma}),$$

to a one-dimensional tight-binding chain,

$$\hat{\mathcal{H}}_{\mathrm{res}} = -t\sum_{\sigma}\sum_{i=1}^{L-2}(c_{i\sigma}^\dagger c_{i+1\sigma} + c_{i+1\sigma}^\dagger c_{i\sigma}),$$

such that the overall system, including the impurity, is of length L. We always take the reservoir FS $\hat{\mathcal{H}}_{\mathrm{res}}$ half-filled. For large L, the reservoir mimics a semi-infinite one-dimensional tight-binding reservoir [71] with a semicircular density of states at the first site and bandwidth $D = 4t$ [72]. Studies of finite-size effects are available in Refs. [33,37,45], and [73–76]. The hopping parameter of the reservoir t is taken to be unity, and its coupling to the impurity $t' = 0.3162t$ combine to an equilibrium Anderson width [1] of $\Delta \equiv \pi\, t'^2\, \rho_{\mathrm{reservoir}}(0) = \frac{t'^2}{t} \approx 0.1\,t$, where $\rho_{\mathrm{reservoir}}(\omega)$ denotes the density of states of the reservoir.

At equilibrium, many characteristics of the SIAM are known, although it poses a difficult interacting problem. Seminal results for the ground-state and thermodynamic properties of the SIAM at equilibrium are available from perturbation theory [77–80], renormalization group [81–84], and the Bethe ansatz (BA) [85–87]. The Hirsch-Fye QMC [48,88] and the continuous-time QMC [89] accurately describe the imaginary time dynamics. Further, some physical results can be inferred from the Kondo Hamiltonian, which is related to the SIAM by the Schrieffer-Wolff transformation, to obtain its low-energy realization, in which charge fluctuations are integrated out [64,81].

III. THE KONDO SINGLET

at equilibrium, the SIAM features a characteristic length scale which, for finite interaction strength, is the Kondo length scale and is expected to correspond to the size of the singlet screening cloud. This length scale is defined as $\xi_K \equiv \frac{v_F}{T_K}$ [28,41,49,90–92]; i.e., it is proportional to the Fermi velocity $v_F \approx 2t$ and the inverse Kondo temperature $\frac{1}{T_K}$ [1,86,87]. T_K can be extracted from many observables; most intuitive is the definition as the temperature at which the local moment becomes quenched, i.e., when the impurity entropy goes from ln(2), indicating the local moment regime, to ln(1), indicating the singlet state [93]. A scale proportional to T_K is also available from the zero-temperature self-energy [94] or from the width of the Kondo resonance in the spectral function [95]. An analytic expression for T_K, as obtained from the spin susceptibility, is available for the SIAM at particle-hole symmetry in the wide band limit with a linear dispersion [96] by the BA [85–87]: $T_K^{\mathrm{BA}} = \sqrt{\Delta U}\, e^{-\frac{\pi}{16\Delta}U}$. The Kondo singlet, therefore, is exponentially large in the interaction strength U:

$$\xi_K^{\mathrm{BA}} \approx \frac{2t}{\sqrt{\Delta U}} e^{\frac{\pi}{16\Delta}U}. \tag{3}$$

For typical Kondo materials, like dilute magnetic impurities in free electron metals [97], one finds $v_F \approx 10^6$ m/s and $T_K \approx 1$ K valid, for example, in gold with dilute iron impurities [98]. Thus, the screening length becomes macroscopic, $\xi_K \approx 1\,\mu$m [49].

Here, we extract the screening length scale ξ_K directly from correlation functions, and not via the Kondo temperature. The spin correlation function is defined as

$$S(r,\tau) = \langle \hat{\mathbf{S}}_0 \cdot \hat{\mathbf{S}}_r \rangle(\tau), \tag{4}$$

where $\hat{\mathbf{S}}_r = (\hat{S}_r^x, \hat{S}_r^y, \hat{S}_r^z)$ [99] and r denotes the distance from the impurity in units of the lattice spacing (see Fig. 1). Due to the oscillations of S, it is convenient to distinguish between the spin correlation function for odd $[S_{\mathrm{o}}(r,\tau)]$ and that for even $[S_{\mathrm{e}}(r,\tau)]$ distances.

Length scales can be extracted from the crossover in the functional dependence of $S_{\mathrm{o}}(r,\tau)$ or via determining zeros or minima in $S_{\mathrm{e}}(r,\tau)$ [49,50,53]. Its charge analog is defined as [100]

$$C(r,\tau) = \sum_{\sigma\sigma'}\langle \hat{n}_{0\sigma}\hat{n}_{r\sigma'}\rangle(\tau). \tag{5}$$

Correlation functions without a time argument, $S(r)$ and $C(r)$, refer to the ground state of the equilibrium system, Eq. (1), i.e., an impurity coupled to the free electron reservoir. Steady-state correlation functions are indicated with $\tau \to \infty$. Later we show that in this limit the time-dependent correlation functions converge to the equilibrium correlations, $S(r,\tau\to\infty) = S(r)$, as expected from the fact that the quench is intensive. An intuitive measure which quantifies how much of the singlet correlations is contained inside a distance r is the integrated spin correlation function,

$$\Sigma(r,\tau) = \sum_{r'=0}^{r} S(r',\tau). \tag{6}$$

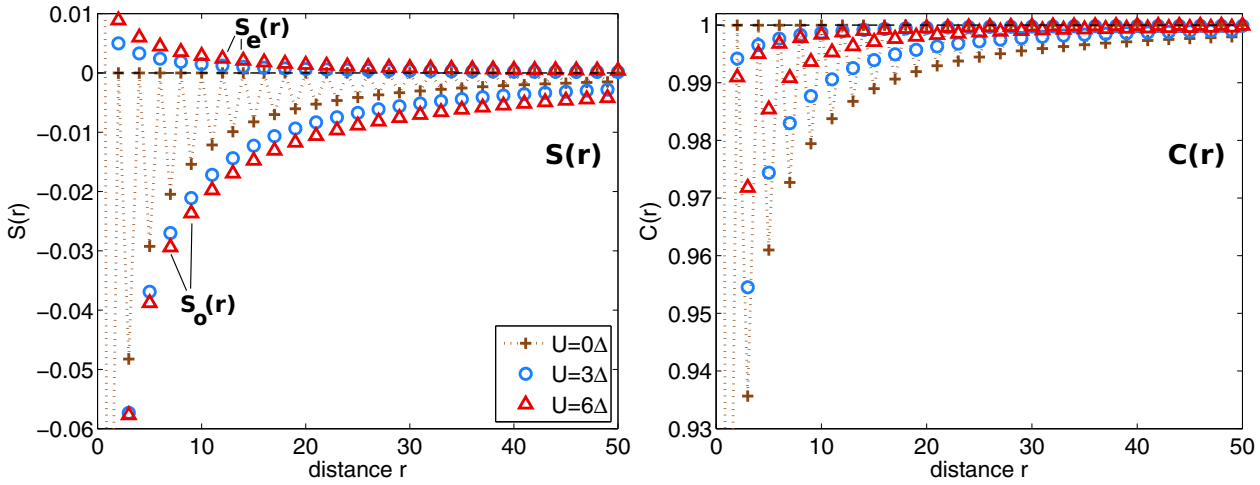

FIG. 3. (Color online) Equilibrium correlation functions. The equilibrium correlation functions for spin, $S(r)$ [left; Eq. (4)], and charge, $C(r)$ [right; Eq. (5)], are shown for short distances from the impurity r. The correlation functions at even [odd] distances, $S_e(r)$ [$S_o(r)$], are indicated explicitly in the left panel. The key is valid for both panels: data for the noninteracting system [(brown) crosses] are compared to data for interaction strengths of $U = 3\,\Delta$ [(blue) circles] and $U = 6\,\Delta$ [(red) triangles]. The alternating behavior, present for all data sets, is indicated by the dotted line in the $U = 0$ data.

As discussed below and in Refs. [48] and [52], the screening length ξ_k can be extracted from $\Sigma(r,\tau)$ by defining it as the length scale at which a certain fraction f (here we use $f = 95\%$) of the correlation lies inside a given distance; i.e.,

$$\Sigma(\xi_k,\tau) = (1-f)\Sigma(0,\tau). \tag{7}$$

IV. METHOD

Here we outline how the correlation functions, Eq. (4) and Eq. (5), are evaluated. We start with a short discussion of the noninteracting system in equilibrium. In this case we find

$$S^{U=0}(r) = \langle \hat{m}_0\rangle\langle \hat{m}_r\rangle + \frac{1}{4}\sum_\sigma \langle c^\dagger_{0\sigma}c_{r\sigma}\rangle(3\delta_{0r} - \langle c^\dagger_{r\sigma}c_{0\sigma}\rangle - 2\langle c^\dagger_{r\bar\sigma}c_{0\bar\sigma}\rangle) \tag{8}$$

$$= \tfrac{3}{2}\langle c^\dagger_0 c_r\rangle(\delta_{0r} - \langle c^\dagger_r c_0\rangle), \tag{9}$$

where $\langle \hat{m}_r\rangle = \frac{1}{2}\langle \hat{n}_{r\uparrow} - \hat{n}_{r\downarrow}\rangle$, and the last result holds for the unpolarized case. Here, $c^\dagger_r/c_r$ denote operators for any one of the spin directions $\sigma = \{\uparrow, \downarrow\}$. The opposite spin direction is denoted $\bar\sigma = -\sigma$. For $U = 0$ at equilibrium [48]

$$C^{U=0}(r) = S^{U=0}(r) + \sum_\sigma \langle \hat{n}_{r\sigma}\rangle. \tag{10}$$

In the particle-hole symmetric and non-spin-polarized case the asymptotic limits can be analytically evaluated, using results of Ghosh *et al.* in Ref. [53], to be

$$|S^{U=0}(r)| = \frac{3}{\pi^2}\frac{\Delta}{v_F}\begin{cases}\left(r\frac{\Delta}{v_F}\right)^{-2} & \text{for } r\frac{\Delta}{v_F}\to\infty,\\ \left[\gamma+\ln\left(r\frac{\Delta}{v_F}\right)\right]^2 & \text{for } r\frac{\Delta}{v_F}\to 0^+\end{cases} \tag{11}$$

for odd r, with $\gamma \approx 0.577\,216$ the Euler-Mascheroni constant. The correlation function becomes 0 for even distances r. The behavior of the spin correlation function exhibits a crossover at distance $\xi^{U=0} \approx \frac{v_F}{\Delta}$, which defines a length scale in the noninteracting system.

We obtain both $S(r,\tau)$ and $C(r,\tau)$ for zero temperature from computer simulations using matrix product state [63] techniques. First, to study ground-state correlations, we employ the DMRG [59–61] on a system of length L, which is typically $\leqslant$ 500 sites. Second, to study the dynamic formation of the Kondo singlet, we start from a decoupled system in the state $|\Psi\rangle = |\uparrow\rangle_{\text{impurity}} \otimes |\text{FS}\rangle_{\text{reservoir}}$, with a non-spin-polarized half-filled FS, at time $\tau = 0$, and then switch on the tunneling term $t' = 0.3162t$ for times $\tau > 0$. The evolution in real time is obtained from TEBD [62].

Matrix-product-state-based time evolution has proven to be a highly accurate method to evaluate the properties of one-dimensional strongly interacting quantum systems out of equilibrium [102–114]. The combination DMRG and TEBD is quasiexact as long as the quantum entanglement stays tractable. It has been shown that the main limitation arises due to the growth of entanglement after the quench [103,115], which ultimately restricts the available simulation time. Furthermore, since we are interested in the physics resulting from an infinite bath, the maximum available simulation time is restricted by reflections at the lattice boundary and therefore by the finite spatial extent of the system. We have been able to reliably evolve the system long enough to reach a local steady state for all presented data sets. We have checked the convergence of our correlation functions carefully by (i) making comparisons to exact data in the $U = 0$ system, (ii) systematically studying the dependence on the TEBD matrix dimension χ for finite U, and (iii) carefully analyzing the entanglement entropy. These analyses as well as details of the numerical approach and parameters are provided in Appendix A.

V. EQUILIBRIUM

We start our discussion by presenting the equilibrium spin $[S(r)]$ and charge $[C(r)]$ correlation functions. $S(r)$ was first

studied by Iishi [41], and $C(r)$ by Grüner *et al.* [42,43], who determined the basic spatial dependence and properties. Seminal QMC data [48] have been extended with the use of the NRG [49,50] and recently also the DMRG [52]. Here we summarize the most important findings, relevant for the subsequent discussion, and we provide details specific to the finite-size model and numerical method used. In particular, we identify a length scale in the equilibrium spin correlation function and show later that our nonequilibrium correlation functions converge to the equilibrium correlation function for long times τ.

As shown in Fig. 3, both $S(r)$ and $C(r)$ exhibit an oscillating behavior, $\propto \sin(k_F r)$. Since the system is half-filled, the Fermi wave vector is $k_F = \frac{\pi}{2}$ and the oscillation period is $r = 2$ sites. We first discuss the spin correlations for $U = 0$ using Eq. (9). In this case we find $S^{U=0}(0) = \frac{3}{2}\langle \hat{n}_{0\uparrow}\rangle(1 - \langle \hat{n}_{0\uparrow}\rangle) = \frac{3}{8}$. Furthermore, $S^{U=0}(r)$ vanishes for even distances r, which follows from general properties of tight-binding fermions [116]. The odd-r correlations $S_o(r)$ are negative and therefore antiferromagnetic with respect to the impurity. For $U > 0$, $S_o(r)$ stays negative and increases in magnitude [117]. At the same time, the spin correlation function for even distances $S_e(r)$ gradually develops ferromagnetic correlations at short distances, while it is antiferromagnetic at longer distances. On the one hand, it is the antiferromagnetic component which reflects the screening cloud and signals the formation of the singlet ground state. On the other hand, the ferromagnetic component can be attributed to Coulomb repulsion of opposite spins [48]. Neither the period nor the phase of the oscillations is changed by the presence of interactions [48].

The charge correlation for $U = 0$ is linked to the spin correlation via Eq. (10). There is oscillatory behavior between even and odd sites. For even sites the correlation function is unity, while for odd sites it increases monotonically towards unity. For finite interaction strengths we observe a suppression of these Friedel-like oscillations [118] with increasing U [119]. At even distances the charge correlations show behavior similar to that of the odd channel, however, of a smaller magnitude. The suppression due to the interaction can be traced back to the change in the impurity spectral weight, which develops a narrow Kondo resonance with a width proportional to T_K at the Fermi energy [42,43].

While at $U = 0$ the characteristic length scale is $\xi^{U=0} \propto \frac{v_F}{\Delta}$, for finite U, long-range correlations develop, which change the behavior at a distance $\xi_K \propto \frac{v_F}{T_K}$. This crossover, characterizing the size of the Kondo spin compensation cloud, is visible in the spin correlation function $S(r)$. Figure 4 (top) shows that the antiferromagnetic spin compensation is visible in the spin correlation function at odd distances, $S_o(r)$. $S_o(r)$ changes from a logarithmic dependence at small $r\frac{\Delta}{v_F}$ to a power-law behavior at large $r\frac{\Delta}{v_F}$ [see Eq. (11)] [53,120]. We note that this is different from the Kondo model, where the behavior is $S(r) \propto r^{-d}$ for $r < \xi_K$ to $S(r) \propto r^{-(d+1)}$ for $r > \xi_K$, with d being the dimensionality of the conduction electron reservoir [49,50].

The crossover is difficult to extract directly from numerical data for $S_o(r)$ since very large system sizes and small Δ are required to reach the low-$r\frac{\Delta}{v_F}$ limit. We nevertheless found two ways to obtain an estimate for the crossover scale. First,

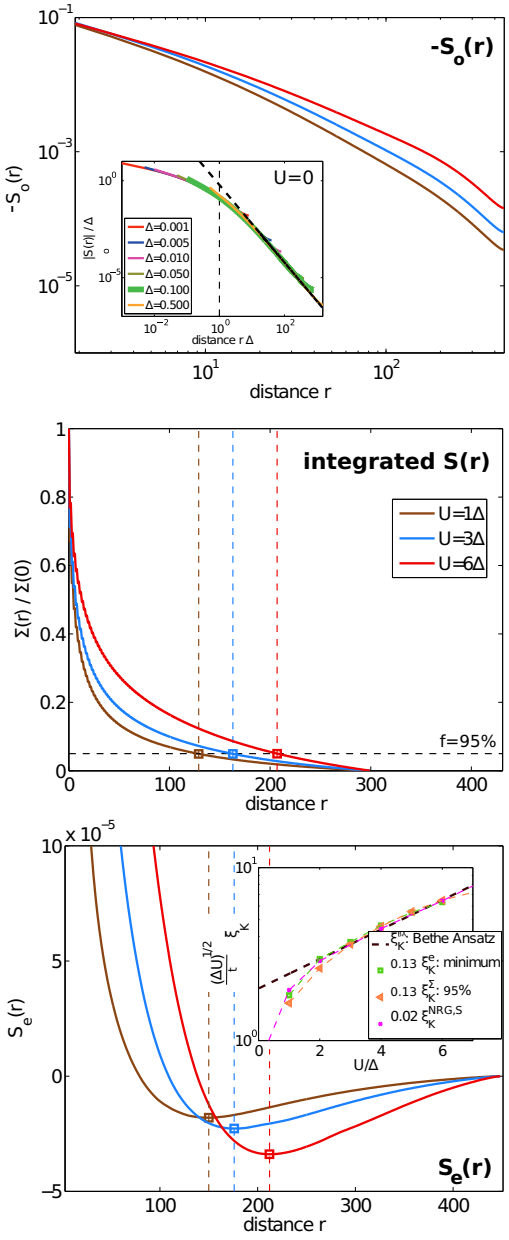

FIG. 4. (Color online) Extraction of the equilibrium screening length ξ_K. Results are shown for $U = 1\Delta$ (brown line) $U = 3\Delta$ (blue line), and $U = 6\Delta$ (red line). Top: Spin correlation function for odd distances, $S_o(r)$ (solid line), which displays a crossover between two behaviours at small and large r. This is particularly obvious in the $U = 0$ results, shown in the inset. There, $S^{U=0}(r)$ displays the asymptotic behavior given in Eq. (11). The large-r behavior is shown by the dashed black line. Our interacting matrix product state calculations are determined for $\Delta = 0.1$, which corresponds to the thickest (green) line in this plot for $U = 0$. Middle: Integrated correlation function $\Sigma(r)$ of Eq. (6). Dashed vertical lines indicate the distances ξ_K^Σ inside which 95% of the singlet cloud is contained, which we use to estimate the screening length. Bottom: Spin correlation function for even distances, $S_e(r)$. The position ξ_K^e of the minima (circles and dashed vertical lines) is used as the alternative definition for ξ_K. Inset: These ξ_K^e [(green) squares] and ξ_K^Σ [(orange) triangles]. As reference data we show the BA result and data obtained from an NRG calculation [101]; see text.

a screening length scale can be extracted from the integrated correlation function $\Sigma(r)$ [see Fig. 4 (middle)]. Similarly to Refs. [48] and [52], here we denote ξ_K^{Σ} the distance at which 95% of the singlet correlations are covered, i.e., by Eq. (7). Second, we extract a length scale ξ_K^{e} from the spin correlation function at even distances $S_{\mathrm{e}}(r)$, which, for finite U, contains both a ferromagnetic component at short distances and the decaying antiferromagnetic one at large distances. As shown in Fig. 4 (bottom) the function $S_{\mathrm{e}}(r)$ displays a 0 and a minimum and is fit well by a Morse potential [121]. We take the position of the minimum as a measure for the crossover scale ξ_K^{e}. The numerical results obtained with these two crossover scales agree very well and they also agree qualitatively with that obtained by locating the crossover length between $r^{-1.4}$ and $r^{-(1+1.4)}$ behavior in the $S_{\mathrm{o}}(r)$ data, which can be estimated from Fig. 4 (top).

In the inset in Fig. 4 (bottom) we show that our two estimates, ξ_K^{Σ} and ξ_K^{e}, agree well with established results for the equilibrium screening length. An analytical result, ξ_K^{BA} [Eq. (3)], for the screening length is available via its relation to the Kondo temperature, which can be obtained from the BA in the wide-band limit by calculating the static spin susceptibility, Eq. (3). A second benchmark is provided by accurate numerical data from the NRG [101,122], where $T_K^{\mathrm{NRG},\mathcal{S}}$ is defined as the temperature at which the impurity entropy reaches $\mathcal{S} = \frac{\ln(2)}{2}$ [123]. However, while the large-U behavior is universal for all these definitions, the small-U expression, as well as the overall coefficient, depends on the specific observable from which it is extracted (spin susceptibility, entropy, etc.). Our data, ξ_K^{Σ} and ξ_K^{e}, agree well with the NRG result, $\xi_K^{\mathrm{NRG},\mathcal{S}}$; they are all compatible with a simple exponential growth in U,

$$\xi_K \propto e^{\frac{\pi}{16\Delta}U}. \tag{12}$$

For $U > 2\,\Delta$ this agrees with the BA prediction, Eq. (3), which features an additional factor of $\sqrt{\Delta U}$. We note that for $U \leqslant 2\,\Delta$ no well-defined local moment has formed [52]; i.e., U is too small for the system to develop a pronounced local moment regime in between the low- and the high-temperature limit. Our data also compare very well with those presented in an extensive study of length scales in the SIAM on a finite lattice in equilibrium in Ref. [52].

These results indicate that the method presented here is reliable in producing unbiased correlation functions in equilibrium which exhibit the characteristic features of a Kondo screening cloud. The cloud is well contained within the numerically tractable lattice size $L \leqslant 500$ for $U \leqslant 6\Delta$ (see Appendix A). Therefore, we focus our calculations on $U \leqslant 6\Delta$ when discussing the time-dependent correlation functions.

VI. TIME EVOLUTION OF LOCAL OBSERVABLES

Before beginning the discussion of the temporal evolution of spatial correlations we present the time evolution of the local observables with a focus on the impurity site. At time $\tau = 0$ we start with a spin-↑ particle at the impurity and a non-spin-polarized half-filled FS: $|\Psi\rangle = |\uparrow\rangle_{\mathrm{impurity}} \otimes |\mathrm{FS}\rangle_{\mathrm{reservoir}}$. For the connected equilibrium system in the thermodynamic limit we expect a uniform and non-spin-polarized density that is $\langle n_{0\uparrow}\rangle(\tau \to \infty) = 0.5$, $\langle n_{0\downarrow}\rangle(\infty) = 0.5$, $\langle n_0\rangle(\infty) = 1$, and $\langle S_0^z\rangle(\infty) = 0$. The impurity double occupation in a noninteracting system or in the high-temperature limit is $\langle n_{0\uparrow} n_{0\downarrow}\rangle^{U=0}(\infty) = 0.25$ [124]. For finite interaction strength the evolution is nontrivial.

Figure 5(a) shows the expectation values of the spin-z projection $\langle S_r^z\rangle(\tau) = \frac{1}{2}(\langle n_{r\uparrow}\rangle(\tau) - \langle n_{r\downarrow}\rangle(\tau))$. Due to particle-hole symmetry, the total charge density $\langle n_r\rangle(\tau)$ is unity.

Indeed we find that, following the hybridization quench, the excess spin-↑ on the impurity is transported away. This happens essentially at the Fermi velocity $v_F \approx 2t$, as shown by the major signal in Fig. 5(a).

The resulting missing spin-↑ density is exactly compensated by the spin-↓ density due to particle-hole symmetry. This compensation takes place simultaneously and completely symmetrically in both spin channels as is evident from the spin-↑ and spin-↓ currents shown in the inset in Fig. 5(a). The time integral over the spin current reveals that half a particle is transferred in or out of the impurity in a time of the order of $\approx 3\Delta^{-1}$ for $U = 3\Delta$.

Figure 5(b) shows the local evolution of expectation values as a function of the time and interaction strength. All expectation values converge to their respective, exactly known, equilibrium values as noted above. The time-evolved double occupancy also converges to the equilibrium results obtained by DMRG. This indicates that our time evolution is accurate and unbiased, at least for large times. For more convergence checks and uncertainty estimates we refer the interested reader to Appendix A.

At a certain distance r from the impurity, a resulting signal arrives at $\tau \approx \frac{r}{v_F}$. This signal is oscillating and strongly damped in time [see Fig. 5(b)]. With increasing interaction strength U, the initial spike becomes dampened in amplitude, but the oscillating tail gains weight. The signal at $r = 40$ in the double occupancy has the same structure on a scale of 10^{-3} around its equilibrium value.

In the following we consider the temporal decay of the spin-z density at the impurity in detail. Previous studies using the time-dependent NRG for the SIAM [125] and analytical calculations at the Toulouse point of the anisotropic Kondo model [126] found that the initial dynamics of $\langle S_{\mathrm{o}}^z\rangle(\tau)$ is governed by a fast time scale, $\propto \frac{1}{\Delta}$, while the eventual relaxation exhibits a long time scale, $\propto \frac{1}{T_K}$, governed by Kondo physics. These results were confirmed by bold-line QMC simulations [127] on the SIAM, which showed these two time scales collapsing into one for an applied bias voltage.

From our data we find that, as expected, the spin-z density at $U = 0$ decays in a single-exponential manner,

$$\langle S^{z,U=0}(r=0,\tau)\rangle = (0.561 \pm 0.001)e^{-2(1.060\pm0.002)\tau\Delta} + (0.0001 \pm 0.0001);$$

hence it features the fast hopping time scale $\mathcal{T}_{U=0} \propto \frac{1}{\Delta}$. For finite U, a double-exponential decay develops:

$$\langle S^z(r=0,\tau)\rangle = c_1 e^{-G_1\tau\Delta} + c_2 e^{-G_2\tau\Delta}. \tag{13}$$

In Figs. 5(c) and 5(d) we show the results of this data analysis with respect to the interaction strength U in the available range of $U \in [1,6]$. We identify one fast, exponential decay, $G_2 \approx 2(1.4 \pm 0.2)$, yielding a U-independent time scale $\mathcal{T}_{\mathrm{fast}} \propto \frac{1}{\Delta}$

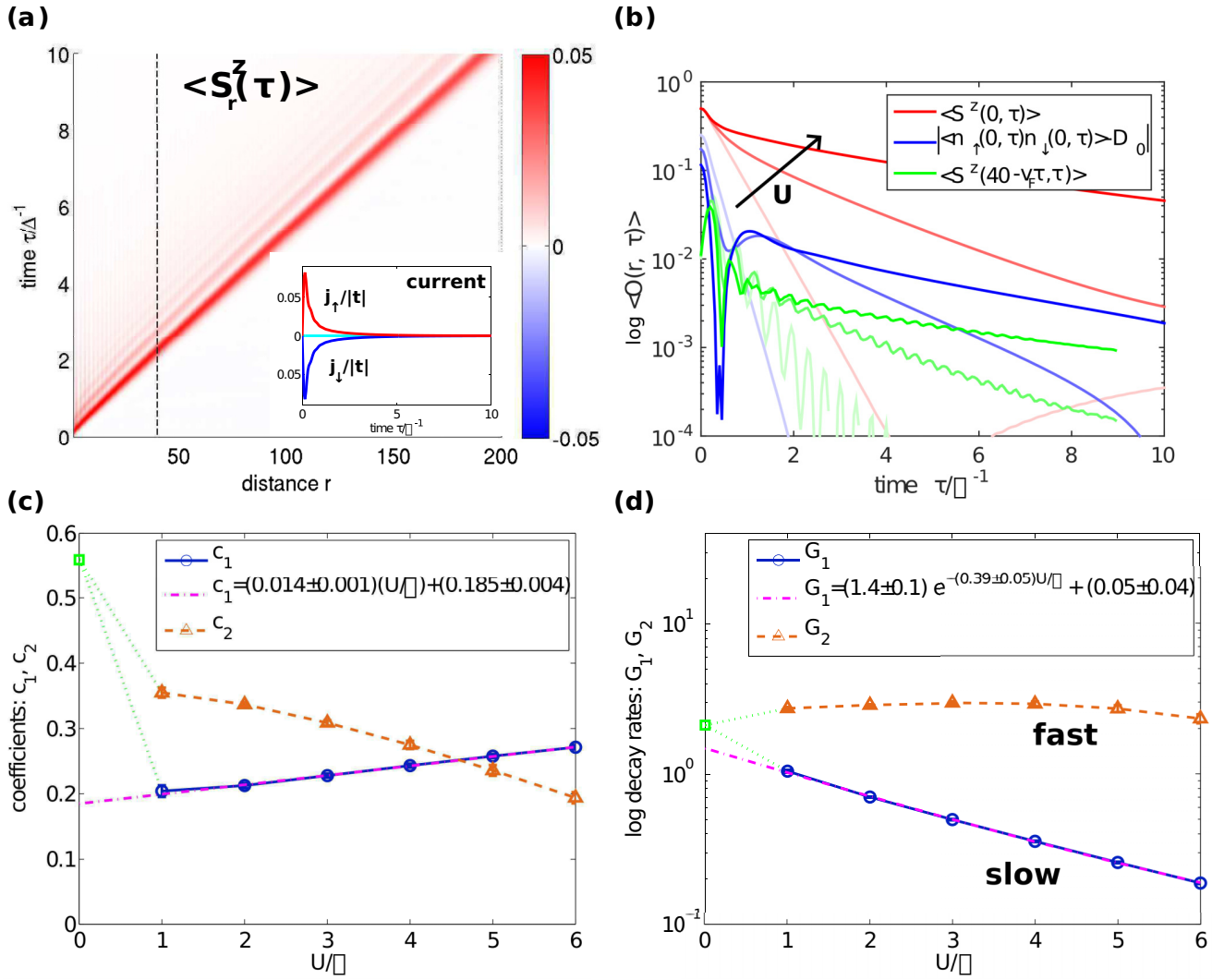

FIG. 5. (Color online) Time evolution of local expectation values. (a) Evolution of the spin-z density $\langle S^z_r(\tau)\rangle$ as a function of the distance r and time τ. We plot data for $U = 3\Delta$ and the color axes are cut off below the maximum for better visibility of fine structures. The vertical black line indicates a cut at distance $r = 40$. Inset: Time-dependent spin current [115] $\langle j_\sigma(\tau)\rangle = i\,\pi\,t'\langle f^\dagger_\sigma c_{1\sigma} - c^\dagger_{1\sigma} f_\sigma\rangle$ at the bond next to the impurity, $j_\uparrow(\tau)$ (red line) and $j_\downarrow(\tau)$ (blue line), and the total current $j(\tau)$ (cyan line). (b) Local spin-z density at the impurity site $r = 0$ and at $r = 40$ as a function of time. Note that the $r = 40$ data are shifted such that the light cone coincides with the origin. From the local double occupancy at the impurity site $r = 0$ we subtracted the equilibrium values $D_0(U) = \{0.25, 0.1745, 0.1153\}$ for $U = \{0, 3, 6\}\Delta$ as obtained by DMRG. All data are plotted for three interaction strengths, $U = \{0, 3, 6\}\Delta$, from lighter to darker color, as indicated by the black arrow. (c) Fit coefficients $c_{1/2}$ of the double-exponential fit of the decay of $\langle S^z(r,\tau)\rangle$ to its equilibrium value as a function of U [cf. Eq. (13)]. The magenta line indicates a linear fit to the coefficient of the slow component c_1. (d) Decay rates $G_{1/2}$ of the double-exponential fit of the decay of S^z to its equilibrium value as a function of U. The magenta line indicates an exponential fit to the decay rate of the slow component G_1. The single-exponential behavior at $U = 0\,\Delta$ is indicated in green.

similar to $\mathcal{T}_{U=0}$. The corresponding coefficient c_2 decreases in magnitude with increasing U. In contrast, the more interesting slow exponential decay G_1 has a coefficient c_1 which becomes more and more prominent with increasing U. In particular, the coefficient c_1 exhibits a linear behavior in U:

$$c_1(U) = (0.014 \pm 0.01)\frac{U}{\Delta} + (0.185 \pm 0.004).$$

The slow decay rate G_1 is exponentially small in U:

$$G_1(U) = (1.4 \pm 0.1)e^{-2(0.19\pm0.02)\frac{U}{\Delta}} + (0.05 \pm 0.04).$$

This implies that the Kondo physics manifests itself in the local dynamic observable $\langle S^z_0\rangle(\tau)$ in the form of a slow time constant, $\mathcal{T}_{\text{slow}} \propto e^{2(0.19\pm0.02)\frac{U}{\Delta}}$, which shows the same U behavior as the Kondo temperature [cf. Eq. (12)].

The double occupancy $\langle n_{0\uparrow} n_{0\downarrow}\rangle(\tau)$ converges to its equilibrium value with the same dominant slow decay (within numerical uncertainty) as observed in the spin-z density for finite U. At $U = 0$ the fast decay rate is twice the rate observed in the spin-z density at $U = 0$.

Performing the same analysis for distances r away from the impurity that considers $\langle S^z_r\rangle(\tau)$, we again observe the same

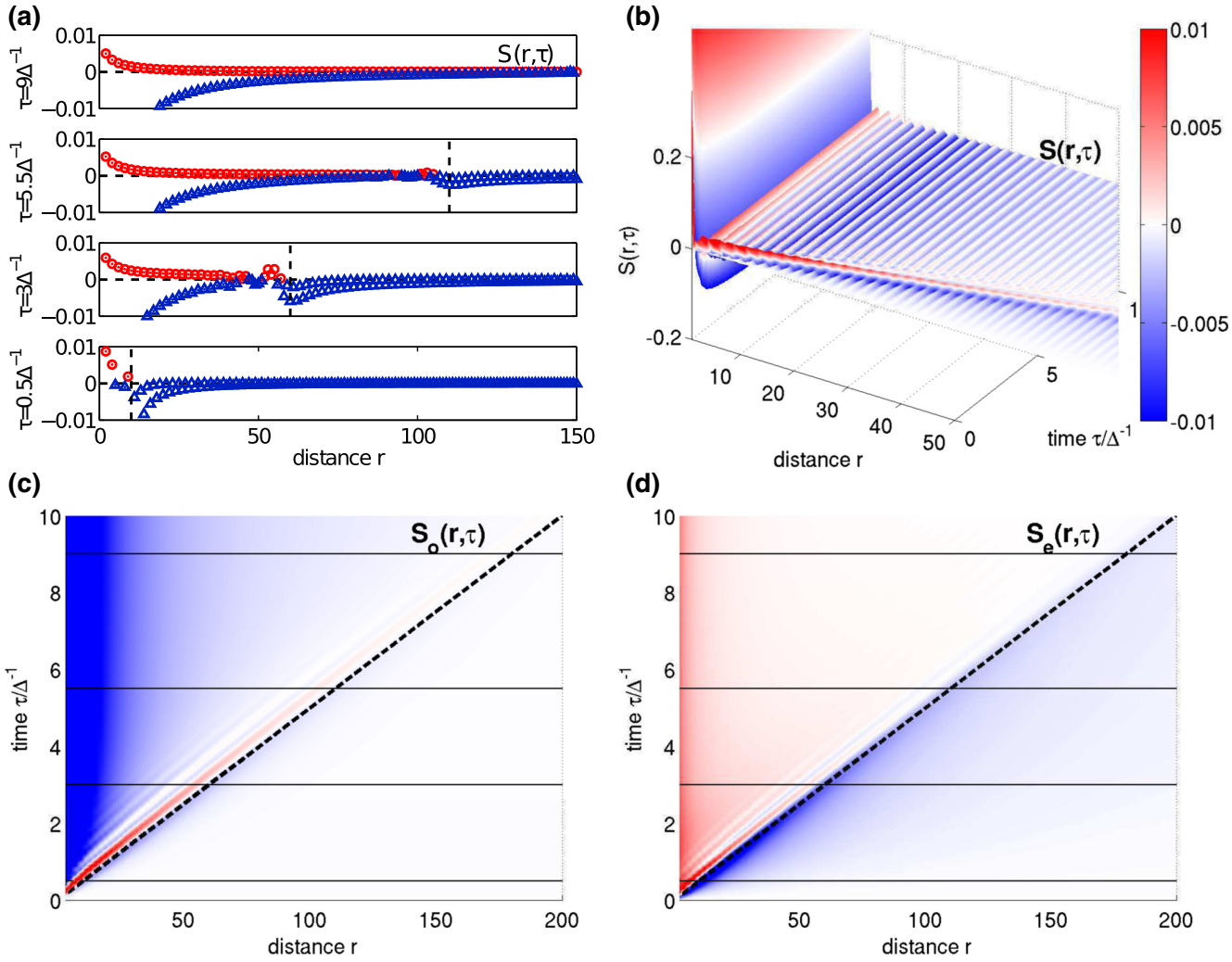

FIG. 6. (Color online) Overall profile of the space-time evolution of the spin correlation function $S(r,\tau)$, Eq. (4). (a) $S(r,\tau)$ as a function of distance r for four times: from bottom to top, $\tau = 0.5\Delta^{-1}$, $\tau = 3\Delta^{-1}$, $\tau = 5.5\Delta^{-1}$, and $\tau = 9\Delta^{-1}$. The ferromagnetic contribution is shown as (red) circles, while antiferromagnetic components are represented by (blue) triangles. Dashed horizontal black lines indicate the zeros. Far behind the signal wake the antiferromagnetic component coincides with $S_o(r,\tau)$ and the ferromagnetic component with $S_e(r,\tau)$. The signal front (light cone), traveling at speed $v_F \approx 2t$, is indicated as the dashed vertical black line. In all panels the signal at very small distances, which is of order unity, has been cut off for better visibility. (b) Three-dimensional visualization of $S(r,\tau)$. The color bar in (b) is also valid for (c) and (d). (c) Spin correlation function at odd distances: $|S_o(r,\tau)|$ (top view). (d) Spin correlation function at even distances: $|S_e(r,\tau)|$ (top view). (c, d) Horizontal black lines indicate times at which data are presented in (a). The light cone defined by v_F is represented by the thick dashed black line. All data shown are for $U = 3\Delta$.

decay as at the impurity site within the fit uncertainty [see Fig. 5(b)]. This supports the quasiparticle picture introduced in Ref. [56], which translates the physics at the impurity via emission of spin-dependent quasiparticles to a given distance r.

VII. TIME EVOLUTION OF THE SCREENING CLOUD

A very interesting question is how the spatial structure of the Kondo screening cloud develops, i.e., whether and how it is approached in a nonequilibrium time evolution starting from an initial state without Kondo physics. The question was recently first studied in pioneering work on the case of an exactly solvable model, namely, the anisotropic Kondo model at the Toulouse point [55,56,128]. A complementary numeric study using the time-dependent NRG [57] was performed shortly afterward on the isotropic Kondo model, extending and confirming the analytical results from the Toulouse limit.

Let us now investigate the formation of spatial correlations $S(r,\tau)$ [Eq. (4)] and $C(r,\tau)$ [Eq. (5)] after switching on the tunneling between the Anderson impurity and the reservoir electrons. We first focus on the major characteristics of $S(r,\tau)$, displayed in Fig. 6. At time $\tau = 0$ the initial configuration is a product state $|\Psi(\tau = 0)\rangle = |\uparrow\rangle_{\text{impurity}} \otimes |\text{FS}\rangle_{\text{reservoir}}$. Using Eq. (8), we find at the impurity $S^{U=0}(r = 0,\tau = 0) = \frac{3}{4}\langle\hat{n}_0\rangle - \frac{3}{2}\langle\hat{n}_{0\uparrow}\rangle\langle\hat{n}_{0\downarrow}\rangle = 0.75$, where $\hat{n}_0 = \sum_\sigma \hat{n}_{0\sigma}$ since we have $\langle\hat{n}_{0\uparrow}\rangle = 1$ and $\langle\hat{n}_{0\downarrow}\rangle = 0$.

After the quench in the hybridization t', we observe a strong signal in $S(r,\tau)$, traveling at the Fermi velocity $v_F \approx 2t$, which

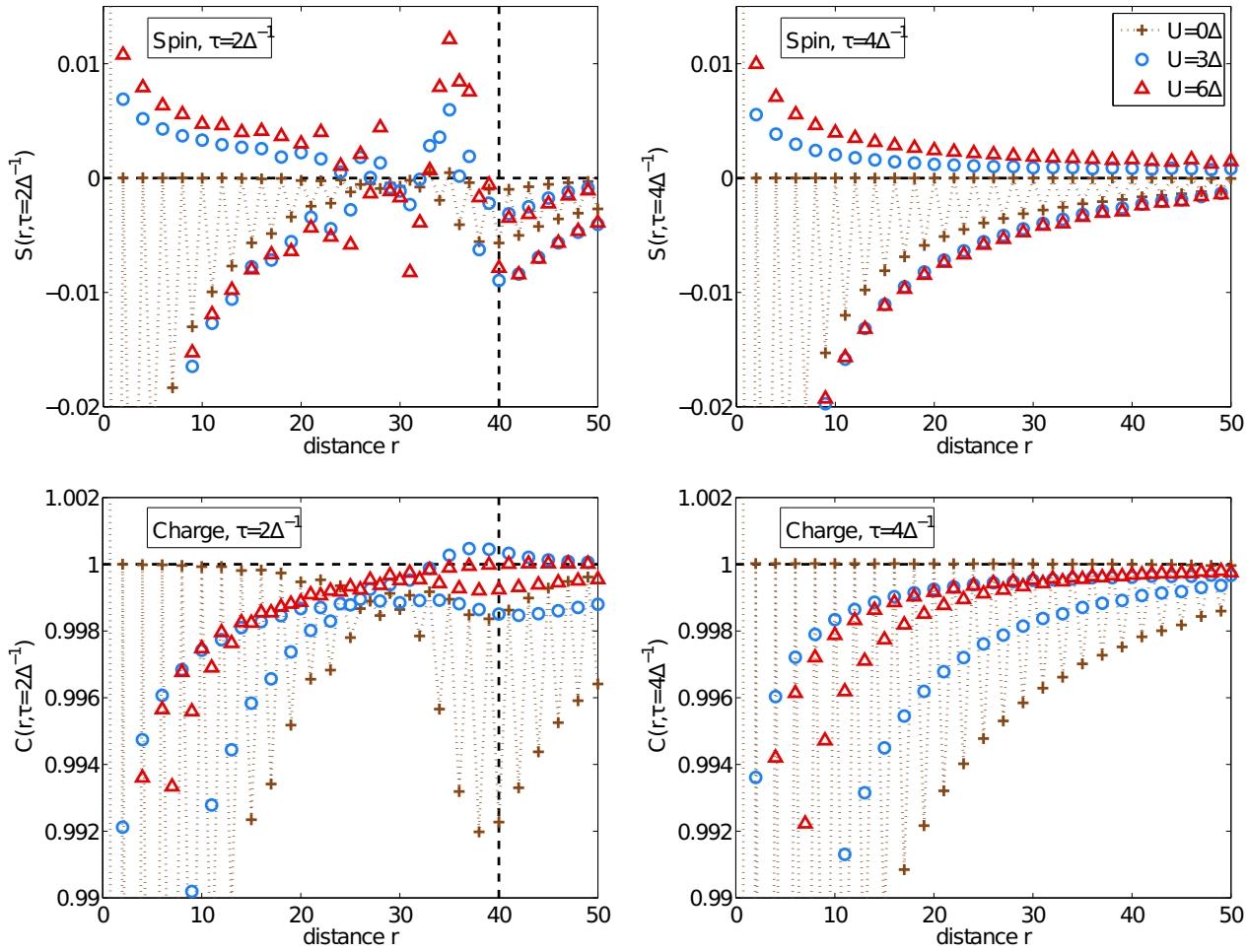

FIG. 7. (Color online) Detail of the time-evolved correlation functions. $S(r,\tau)$ (bottom) and $[C(r,\tau)]$ (top) for $\tau = 2\Delta^{-1}$ (left column) and $\tau = 4\Delta^{-1}$ (right column). The signal front, traveling at speed $v_F \approx 2t$, is indicated as the dashed vertical black line. Results are shown for different values of U as indicated in the key, which is valid for all panels. The alternating behavior is indicated by the dotted line in the $U = 0$ data.

defines a light cone. It has been attributed to the propagation of quasiparticles in Ref. [56]. The propagating signal front divides the space time into two regions: (i) a region at large times and small distances, where the correlation function is directly affected by the impurity and Kondo correlations develop; and (ii) a region at small times and large distances, where small structures from the quench are observed. In Sec. VII A and Sec. VII B we discuss the detailed behavior of the correlation functions within these two regions. The signal front itself carries a large chaotic disturbance in its wake and a small monotonic perturbation ahead of it.

As discussed below in detail, the time-evolved data $S(r,\tau)$ converge to the equilibrium correlation functions $S(r)$ within the light cone. Already a look at the almost-vertical structures in Figs. 6(c) and 6(d) for times $\tau \geqslant 8\Delta^{-1}$ and a comparison of the line plots for $\tau = 6.5\Delta^{-1}$ and $\tau = 9\Delta^{-1}$ for small distances r hint at the convergence to a local steady state within the light cone.

Figure 6(d) reveals that, as expected from the equilibrium state, a ferromagnetic correlation develops for even distances r in $S_e(r,\tau)$ within the light cone for finite U, while outside the light cone this correlation function is always antiferromagnetic. As shown in Figs. 6(a) and 6(c), the wake behind the light cone carries a ferromagnetic signal also at odd distances r that is in the otherwise antiferromagnetic $S_o(r,\tau)$ for all U. We interpret this signal as remnant information of the spin which occupied the impurity at $\tau = 0$ before the quench. Following the signal wake, all characteristic features of the equilibrium correlation function $S(r)$ develop quickly on a qualitative level. Far behind the signal wake the antiferromagnetic component coincides with $S_o(r,\tau)$, and the ferromagnetic component with $S_e(r,\tau)$.

A closer look, as provided in Fig. 7, reveals that the nonequilibrium correlation functions gradually develop the characteristic features of the equilibrium correlation functions $S(r)$ and $C(r)$ for $r < v_F\tau$. As a precursor of the equilibrium structure, the spin correlation function $S(r,\tau)$ develops the oscillatory behavior of its equilibrium counterpart inside the light cone. That is, it oscillates from an antiferromagnetic correlation at odd distances r to a ferromagnetic correlation at even r for finite U or to 0 at $U = 0$. This structure of the phase and period of these oscillations in space is fixed over time inside the light cone. However, the light cone induces a phase shift of π in the nodal structure of the correlation function. We

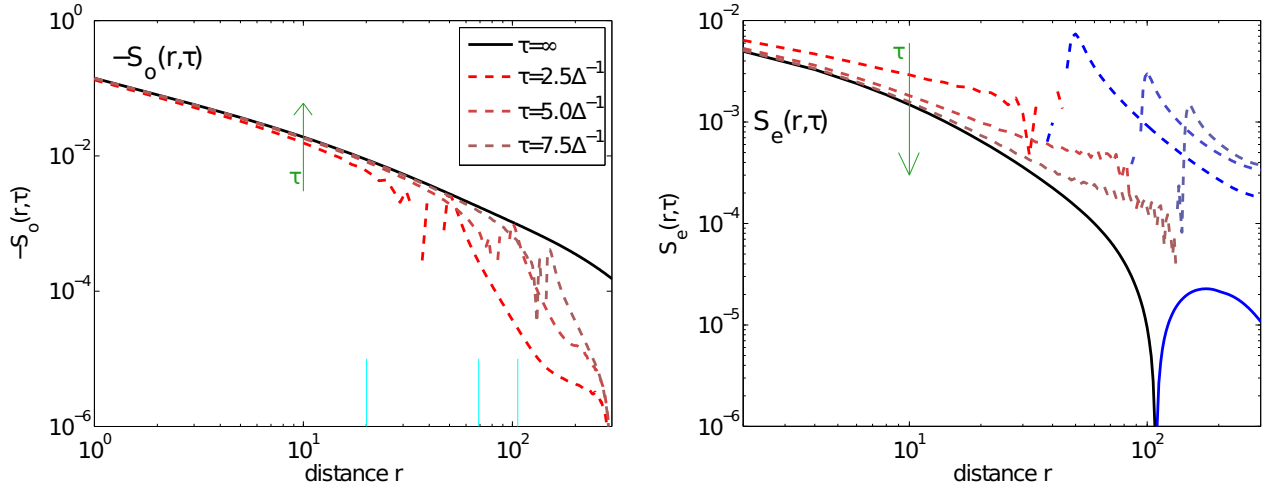

FIG. 8. (Color online) Convergence of the nonequilibrium data to the equilibrium results inside the light cone. Spin correlation functions $S(r,\tau)$ at odd, $S_{\mathrm{o}}(r,\tau)$ (left), and even, $S_{\mathrm{e}}(r,\tau)$ (right), distances are depicted as a function of the distance r for three times—$\tau = 2.5\Delta^{-1}$, $\tau = 5\Delta^{-1}$, and $\tau = 7.5\Delta^{-1}$—in a log-log fashion (dashed lines). We plot $-S_{\mathrm{o}}(r,\tau)$ since it is almost entirely negative, while $S_{\mathrm{e}}(r,\tau)$ is positive inside the light cone and negative outside (see Fig. 6). Blue lines represent $|S_{\mathrm{e}}(r,\tau)|$ in regions where $S_{\mathrm{e}}(r,\tau)$ is negative. The key depicted in the left panel is valid for both panels. Green arrows mark the direction of increasing time τ. Data from the equilibrium simulation are plotted in solid black and referred to as $\tau = \infty$ in the key. The vertical cyan lines in the left panel mark those distances at which cuts through the data as a function of τ are presented in Fig. 9. All data shown are for $U = 3\Delta$.

attribute this phase shift to the initial state of the FS. It takes place across the broad signal behind the light cone visible at around $r \approx 30$ in Fig. 7. As a function of U the same behavior is present inside the light cone as in equilibrium, apart from the chaotic disturbance at the light cone. The qualitative functional form of the correlation functions develops quickly in the wake of the light cone. However, its amplitude overshoots the expected equilibrium value slightly and then gradually decays to it at a much slower time scale (see discussion in Sec. VII A).

The charge correlation function $C(r,\tau)$ gradually develops reduced Friedel-like oscillations with increasing U, as observed at equilibrium. We find $C(r,\tau) < 1$ except at distances $r < 3$ and in the vicinity of the signal front.

In the following we investigate in detail the interplay of characteristic time and length scales and their dependence on the interaction strength.

A. Inside the light cone

Next we discuss the spin correlation function $S(r,\tau)$ inside the light cone. Figure 8 shows the convergence of $S_{\mathrm{o}}(r,\tau)$ and $S_{\mathrm{e}}(r,\tau)$ to their equilibrium $S_{\mathrm{o}}(r)$ and $S_{\mathrm{e}}(r)$ values for large times in detail. For large times the odd component is antiferromagnetic, while the even component exhibits a sign change from ferromagnetic at small distances to antiferromagnetic at large distances (blue curves) as discussed in the equilibrium results. The vanishing ferromagnetic component represents a related measure for the extent of a screening cloud [48].

In the following we identify a time scale at which large correlations with the impurity develop inside the light cone, i.e., for distances $r \leqslant v_F\tau$ (see Fig. 2). In Fig. 9 (left) we show the difference between the time-dependent spin correlation function and the equilibrium result: $\Delta S_{\mathrm{o/e}}(r,\tau) = |S_{\mathrm{o/e}}(r,\tau) - S_{\mathrm{o/e}}(r)|$. This quantity exhibits contributions from the traveling signal, which show up in the form of large spikes at times $\tau \approx \frac{r}{v_F}$. We first focus on the convergence in time at fixed distances r. For times beyond the signal wake $\tau \propto \frac{r}{v_F}$, the qualitative structure of correlations has established itself; i.e., Kondo correlations have reached the given distance r. We find that soon after the signal wake $S(r,\tau)$ converges to the equilibrium result exponentially in time,

$$\Delta S_{\mathrm{o/e}}(r,\tau) \propto e^{-\tau\Delta\cdot\Gamma^{S}_{\mathrm{o/e}}(r,U)}$$

[see Fig. 9(a), inset]. Note that this implies that the curves move "as a whole." We determine $\Gamma^{S}_{\mathrm{o/e}}$ by a single-exponential fit in time of $\Delta S_{\mathrm{o/e}}(r,\tau)$, successively for distances $r \in [40,120]$. We observe that $\Gamma^{S}_{\mathrm{o/e}}(r,U)$ is only weakly dependent on r, with odd distances r being especially stable [see Fig. 9(b)], while Γ^{S}_{e} has larger uncertainties and some drift at large r. The uncertainty increases slightly with distance r, which is also due to the smaller available fit intervals in τ. A two-exponential decay as in Sec. VI, featuring also a fast time scale $\propto \frac{1}{\Delta}$ and independent of U, might be present in the data but cannot be identified due to the presence of the signal at the light cone, which overshadows this fast decay. In general, the fit quality improves with increasing U. Details on the data analysis and uncertainty estimates are provided in Appendix B.

In order to condense this information we consider a mean value,

$$\Gamma^{S}_{\mathrm{o/e}}(U) := \frac{1}{N_r}\sum_{r=40(41)}^{120}\Gamma^{S}_{\mathrm{o/e}}(r,U),$$

with N_r the number of distances in the respective odd or even interval [see Fig. 9(b)].

Our first main result is that $\Gamma^{S}_{\mathrm{o/e}}(U)$ shows exponential behavior in U, like the Kondo scale, Eq. (12):

$$\Gamma^{S}_{\mathrm{o/e}}(U) \propto e^{-\alpha^{S}_{\mathrm{o/e}}\frac{U}{\Delta}}. \tag{14}$$

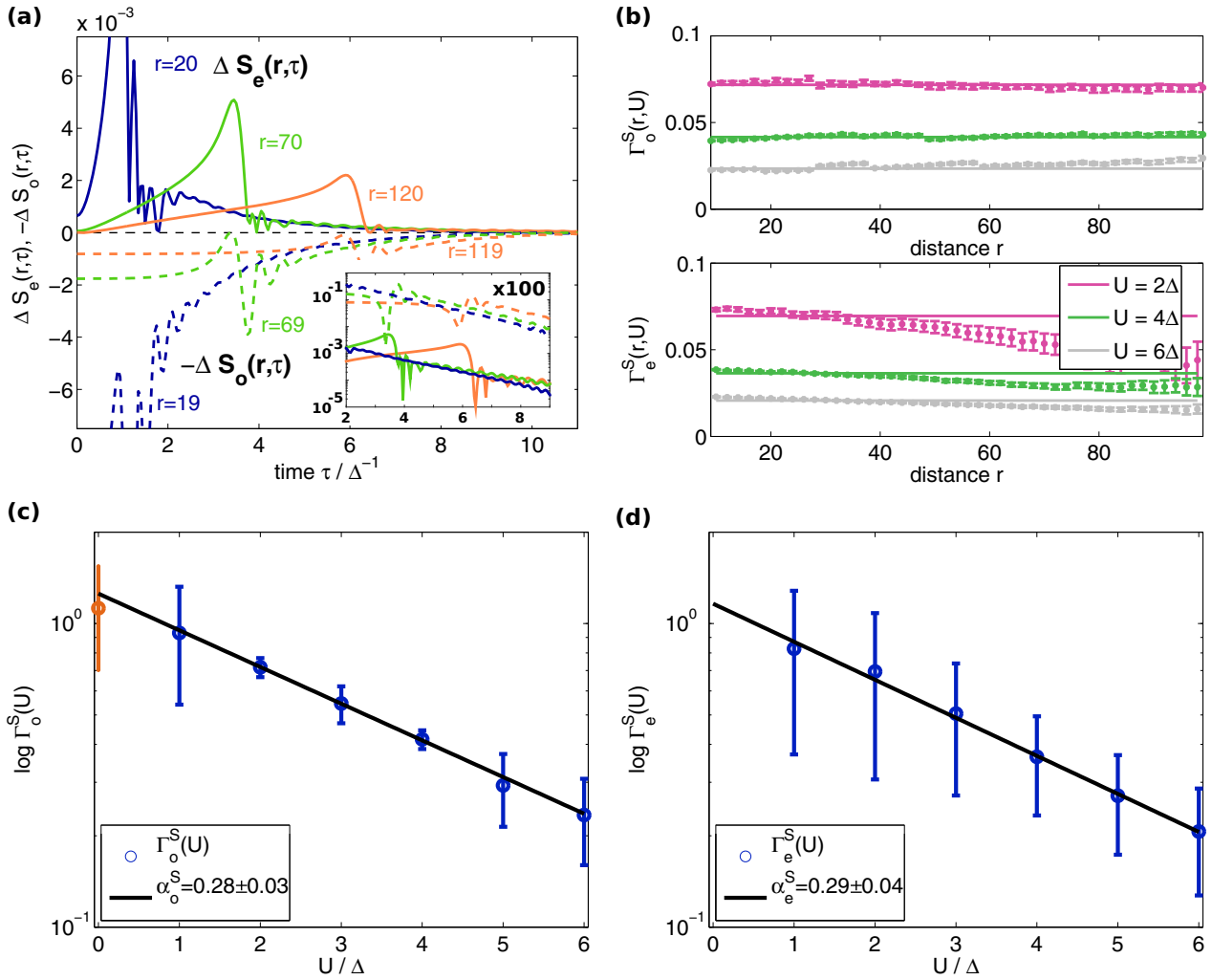

FIG. 9. (Color online) Identification of a dynamic time scale in the exponential convergence to equilibrium inside the light cone. (a) Deviation of the time-dependent spin correlation function from the equilibrium spin correlation function at even (solid lines) and odd (dashed lines) distances $\Delta S_{e/o}(r,\tau)$ as a function of time τ for three distances: $r = 20/19$ (blue lines), $r = 70/69$ (green lines), and $r = 120/119$ (orange lines). For better visibility we show $-\Delta S_o(r,\tau)$. The signal changes behavior at the light cone at $\tau \approx \frac{r}{v_F}$ which is visible as a large hump. The region inside the light cone is to the right of this hump. The semilogarithmic zoom to this region in the inset shows exponential convergence. To separate the curves of the even and the odd components in the inset, data for odd distances are multiplied by a factor of 100. Data shown are for $U = 3\Delta$. (b) Extracted decay rates $\Gamma^S_{e/o}(r,U)$ as a function of distance r for three values of interaction strength: $U = \{2,4,6\}\Delta$. (c, d) Spatially averaged exponential decays at odd (c) and even (d) distances $\Gamma^S_{o/e}(U)$ as a function of the interaction strength U (circles). The dynamic scale $\alpha^S_o = 0.28 \pm 0.03$ and $\alpha^S_e = 0.29 \pm 0.04$, Eq. (14) (solid black line), is extracted via a single-exponential fit of the respective data where only data points for $U \geqslant 1\Delta$ are considered (blue circles) and data for $U < 1\Delta$ are excluded (orange circles). For details of the fits see Appendix B.

Figures 9(c) and 9(d) show the fit in U to Eq. (14) where we find $\alpha^S_o = (0.28 \pm 0.03)$ and $\alpha^S_e = (0.29 \pm 0.04)$, which is similar to the BA result in the wide-band limit for the Kondo temperature, $T_K^{\mathrm{BA}} \propto e^{-\alpha_{\mathrm{BA}} \frac{U}{\Delta}}$, $\alpha_{\mathrm{BA}} = 0.196$ [compare Eq. (3)]. The deviation of the effective exponent $\alpha^S_{o/e}$ from α_{BA} may be due to the fact that it is particularly difficult to reach the common asymptotic limit in space and in time for large U. Note that $\langle S(0,\tau)\rangle\langle S(r,\tau)\rangle \ll S(r,\tau)$, thus the connected correlation function displays essentially the same behavior as $S(r,\tau)$.

We conclude that the formation of Kondo correlations inside the light cone is a process which involves two major time scales. The first time scale is fast and determined by the lattice Fermi velocity v_F, which defines the light cone and develops qualitatively correct correlations in $S(r,\tau)$ and $C(r,\tau)$. The second time scale is slow and depends exponentially on U. This process sets in after the qualitatively correct correlations have built up with v_F and renormalizes the correlation functions, which then converge at an exponential rate, Eq. (14), $\alpha^S_{o/e} \propto T_K$, to the equilibrium result.

The SIAM is related to its low-energy realization, the antiferromagnetic, symmetric Kondo model via the Schrieffer Wolf transformation [64], which effectively integrates out charge fluctuations. The two models share common features in their low-energy behavior, most prominently the Kondo scale T_K. Note, however, that the correlation functions of the two models have very different spatial structures in general.

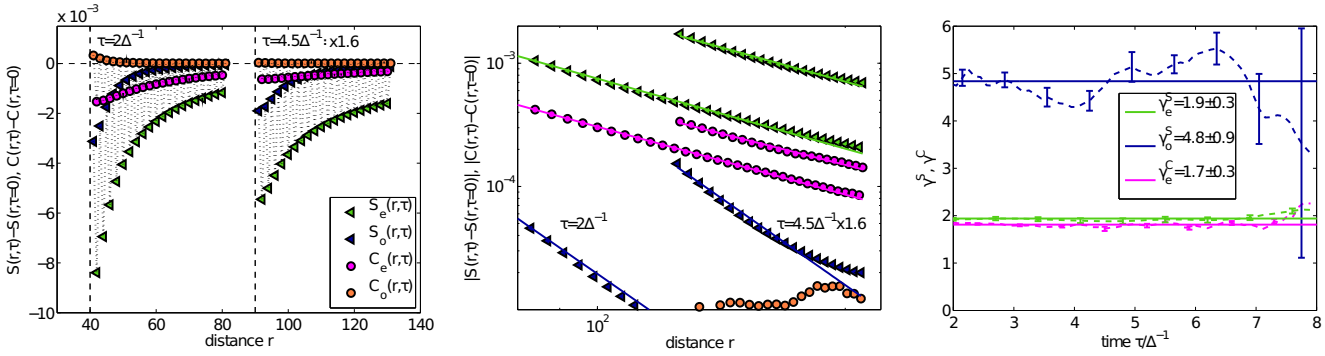

FIG. 10. (Color online) Correlations outside the light cone. Left: $S(r,\tau)$ (blue, green triangles) and $C(r,\tau)$ (orange, magenta circles) outside the light cone with their $\tau = 0$ values subtracted and resolved by even and odd distances r. Data are depicted as a function of r for two times: $\tau = 2\Delta^{-1}$ and $\tau = 4.5\Delta^{-1}$. Note that we only display data in the vicinity of the light cone (dashed vertical black lines). For reasons of representation only, data at $\tau = 4.5\Delta^{-1}$ are scaled by a factor of 1.6. Middle: Modulus of the data in the left panel plotted in a double-logarithmic representation. The key in the left panel is also valid. Straight lines represent power-law fits. Right: The extracted power-law coefficients $\gamma^S_{e/o}$ (dashed blue/green lines) and γ^C_e (dashed orange line) are plotted as a function of the time τ. Error bars, shown for some data points only, are estimated from the nonlinear fit presented in the middle panel and its susceptibility to changing the fit intervals. Solid horizontal lines indicate weighted time and interaction-strength averages: $\gamma^S_e = 1.9 \pm 0.3$, $\gamma^S_o = 4.8 \pm 0.9$, and $\gamma^C_e = 1.7 \pm 0.3$. Data in all three panels are for $U = 3\Delta$.

It is therefore interesting to compare our results to recently obtained ones for the Kondo model. In Ref. [57] Lechtenberg *et al.* studied a coupling quench in the symmetric Kondo model using the time-dependent NRG as well as second-order perturbation theory. Similarly to our results for the SIAM, they found that in the Kondo model spin correlations develop rather rapidly, on the scale of the Fermi velocity. In the linear response to a magnetic field, at equilibrium they observed another, slower time scale similar to $\frac{1}{T_K}$. Our results unambiguously and quantitatively identify this common slower scale $\frac{1}{T_K}$ beyond linear response, directly from the nonequilibrium time evolution of correlation functions.

Charge correlations in equilibrium do not exhibit Kondo physics. We observe that the charge-time-dependent correlation functions $C(r,\tau)$ do exhibit qualitatively the same convergence to equilibrium as the spin correlations $S(r,\tau)$, that is, with a time constant exponentially large in U (not shown). The same analysis as for the spin using Eq. (14) yields respective coefficients for the charge correlation function $\alpha^C_{o/e} \approx (0.3 \pm 0.1)$. That is, the exponent is the same as for the spin, albeit with a larger uncertainty. We attribute this to the resolution of the spin in the correlators present in $C(r,\tau)$. Note that this is true neither for the local density, which does not show such a scale, nor for the mean-field result, $C^{\mathrm{mf}}(r,\tau) \propto 1$.

B. Outside the light cone

For distances $r > v_F\tau$, i.e., outside the light cone (see Fig. 2), we find decaying correlation functions $S(r,\tau)$ and $C(r,\tau)$ as a function of r (see Fig. 10). As before, both spin and charge correlation functions show alternating behavior from site to site. The overall magnitude of both correlation functions decreases over time and the charge correlation function is of a smaller magnitude than the spin correlation function for all except very early times. To identify the correlations generated by the quench, we subtract the initial correlation $S(r,\tau = 0)$ and $C(r,\tau = 0)$ from the time-dependent data.

The second main result of this work is that correlations outside the light cone are power law suppressed,

$$|S(r,\tau) - S(r,0)| \propto r^{-\gamma^S_{o/e}}, \quad |C(r,\tau) - C(r,0)| \propto r^{-\gamma^C_e}, \quad (15)$$

with slightly time-dependent exponents $\gamma^S_{o/e}$ and γ^C_e. Due to the finite size of the system, we only have a limited set of data available to extract the asymptotic decay outside the light cone. We start the extraction of power-law exponents at distances $r_s = v_F\tau + 35$ to avoid spurious contributions from the light cone and end it at $r_e = L - 70$ to avoid a bias originating from the boundary at $L = 450$. From the separate fits for odd/even distances we obtain $\gamma^S_o \approx 1.9 \pm 0.3$ and $\gamma^S_e \approx 4.8 \pm 0.9$. The charge correlation function exhibits a power-law decay $\gamma^C_e \approx 1.7 \pm 0.3$ for the odd component, while the even component's behavior cannot be identified within our numerical accuracy due to the small magnitude of the correlations. The fit has been performed in the same fashion as presented in Appendix B but here we estimate the uncertainty in the γ's from the fluctuations of the respective γ upon changing the start (r_s) and end point (r_e) of the fit. Within this uncertainty, the values are independent of U and τ.

Considering the fact that extracting exponents from numerical data is challenging, our results agree quite well with two recent studies of similar models exhibiting comparable low-energy physics. First, in Ref. [56] Medvedyeva *et al.* obtained time-dependent correlation functions at the Toulouse point of the anisotropic Kondo model with a linear dispersion. In an analytic calculation in several limits, neglecting Friedel oscillations, they showed that outside the light cone the commutator spin-z correlation function $\langle[\hat{S}^z_0\hat{S}^z_r(\tau)]_-\rangle$, which is related to the linear response to a perturbation, vanishes. For the anticommutator, which is proportional to our $S(r,\tau)$ [see Eq. (4)], however, they obtained a power-law decay r^{-2} at zero temperature (see Eq. 27 in their work). They found the initial entanglement in the reservoir FS to be responsible for the power-law decay of the anticommutator correlation function.

Moreover, second-order perturbation theory results [57] suggest that initial correlations of the FS transfer to the time-dependent correlations outside the light cone. Here again a r^{-2} power-law decay outside the light cone was obtained, this time for the isotropic Kondo model with antiferromagnetic coupling J. Our study of the symmetric SIAM finds an r^{-2} decay for $S_{\mathrm{o}}(r,\tau)$ outside the light cone, which we attribute to the same structures of the electronic reservoir in the three studies. We are not aware of any previous reports of even-distance decay exponents $\gamma_{\mathrm{e}}^{S} \propto r^{-5}$.

VIII. CONCLUSIONS

We studied the time-dependent formation of the spin screening cloud in the SIAM. Starting from an unentangled state we switched on the impurity-reservoir hybridization and followed the subsequent dynamics in real time. We used the DMRG to obtain ground states and TEBD to obtain spin and charge correlation functions. From these correlation functions we obtained characteristic time and length scales. Our results agree with previous calculations at equilibrium and, for local observables, out of equilibrium. We found that the nonequilibrium correlation functions converge to the equilibrium results for long times.

In the time-dependent data, we identified a linear spreading of signals traveling at the lattice Fermi velocity, which has been referred to as a light cone in recent literature on the buildup of a screening cloud at the Toulouse point of the anisotropic Kondo model [55,56]. We observed a ferromagnetic response in the wake of the signal at the light cone. While Refs. [55] and [56] identified the Kondo temperature as an inverse time scale in the anisotropic Kondo model outside the light cone, for the symmetric Kondo model it was observed as a time scale in an equilibrium linear response calculation to a magnetic perturbation following an initial fast decay [57]. We observe directly from the nonequilibrium time evolution of correlation functions that, in the SIAM too, the structure of the correlation functions inside the light cone emerges on two time scales. The qualitative core of the correlation functions develops rapidly, at the lattice Fermi velocity. This includes the phase and period of oscillations as well as fixed ferromagnetic and antiferromagnetic domains. These correlations then reach their equilibrium values exponentially slowly in time, defining a dynamic rate which has the same exponential U dependence as the Kondo temperature.

Outside the light cone, we find a power-law decay of the correlation functions $\propto r^{-\gamma_{\mathrm{o/e}}^{S/C}}$, with essentially interaction-strength- and time-independent exponents, Eq. (15). In addition to the r^{-2} decay also observed in the Kondo model [55–57], we find a decay $\propto r^{-5}$.

Our results could be experimentally verified in one-dimensional optical lattices featuring two fermionic species. By monitoring the evolution of the spin correlations in time, our findings provide the basis for extracting information about the dynamic scale and, therefore, indirectly about the Kondo screening cloud dynamics as well as the system parameters.

Possible future extensions to this work include the study of the inverse process. Starting from a coupled impurity-reservoir system and investigating the Kondo destruction after switching the hybridization to 0 would allow study of the time-reversed situation. It would also be very interesting to study the effects of a bias voltage on the Kondo screening process using a two-terminal setup as in Ref. [115]. Further interesting extensions involve the study of conduction bands with singularities or testing of implications of the nonequilibrium fluctuation-dissipation theorem. Also, calculations away from particle-hole symmetry or with applied magnetic fields are feasible.

ACKNOWLEDGMENTS

We gratefully acknowledge fruitful discussion with Sabine Andergassen, Masud Haque, Fabian Heidrich-Meisner, Kerstin T. Oppelt, and Shreyoshi Ghosh. We thank Rok Žitko for providing the NRG LJUBLJANA code [101]. This work was partly supported by Austrian Science Fund (FWF) Grant No. P24081-N16 and SFB-ViCoM projects F04103 and F04104 as well as NaWi Graz. M.N. thanks the Forschungszentrum Jülich, in particular, the Autumn School for Correlated Electrons, for hospitality.

APPENDIX A: NUMERICAL DETAILS

In this Appendix we specify details about our numerical analysis carried out via the DMRG [59,60] and TEBD, [62] and we present the DMRG and TEBD parameters used. In addition, we discuss finite-size effects and the convergence as a function of auxiliary parameters specific to the numerical method applied, as well as the stability of the real-time evolution. Our numerical implementation of the DMRG and TEBD is flexible, is parallelized, and exploits two Abelian symmetries: particle number $\hat{N}$ and spin projection $\hat{S}^{z}$. To find ground states we use the two-site DMRG algorithm with successive single-site DMRG steps. The time evolution is based on a second-order Suzuki-Trotter decomposition of the propagator [61,63].

After extensive studies of the dependence of our results on auxiliary system parameters we found converged results for a Trotter time step of $\delta\tau = 0.05t^{-1}$. We used DMRG and TEBD matrix dimensions of $\chi = 2000$ states and always started the DMRG optimization from a half-filled system in the canonical ensemble where alternating up and down spins are chosen as the seed. A detailed discussion is available in Ref. [115] in the context of previous work.

Figure 11 shows the equilibrium DMRG calculation of the correlation functions. The influence of the finiteness of the lattice is twofold:

(i) The equilibrium spin correlation function $S(r)$ displays an even-odd effect as a function of the total system size L: While for even L, $S_{\mathrm{o}}(r)$ converges from above to its $L \to \infty$ value, for odd L it converges from below. $S_{\mathrm{e}}(r)$ converges in the opposite way. For odd L an extra spin-$\uparrow$ gives a spurious total magnetization. For the equilibrium simulations, in the main part of the paper, we have chosen $L = 450$, since it supports a half-filled and non-spin-polarized system. The spin correlation function at $r \leqslant 150$ is converged, as can be seen in Fig. 11 by comparing the $L = 450$ and $L = 300$ results. Larger distances are influenced by L because $S(r)$ is a nonlocal quantity. Nevertheless, even for larger distances, no qualitative differences are observed between the $L = 450$ and the $L = 300$ data. When performing the time evolution we use $L_{\mathrm{equilibrium}} + 1$ lattice sites, including the impurity, so

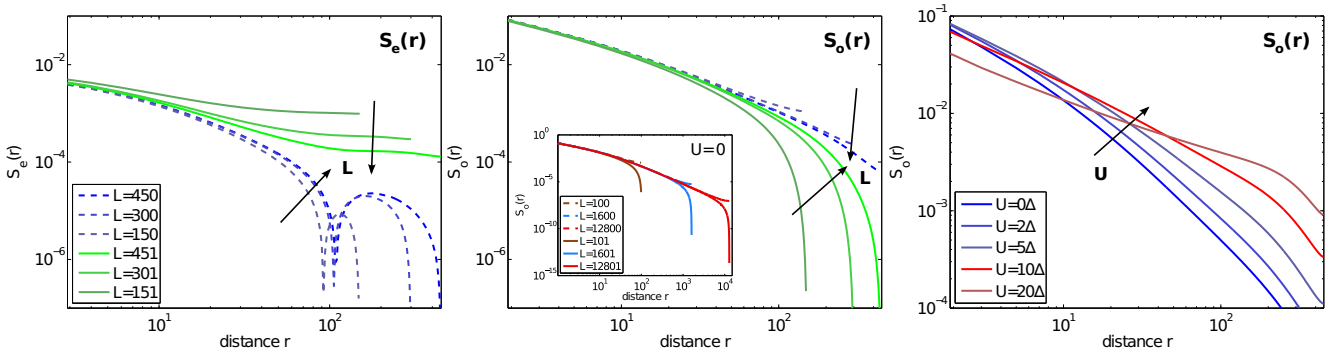

FIG. 11. (Color online) Finite-size analysis and the imposed limits on interaction strength. Finite-size effects in the equilibrium spin correlation function at even $[S_e(r)$; left] and at odd $[S_o(r)$; middle] distances. For each one, we compare even total lattice sizes $L = \{150,300,450\}$ (blue lines) to odd $L = \{151,301,451\}$ (green lines). The key in the left panel is valid for both the left and the middle panels. Both panels show data for $U = 3\,\Delta$. Inset (middle): Evolution with U for a total system size of $L = 450$. Right: Evolution of $S_o(r)$ with increasing interaction strength $U = \{0,2,5,10,20\}\Delta$ for $L = 450$. The correlation becomes qualitatively wrong if U is too large for a given L.

that the reservoir is nonmagnetized and half-filled. With this choice the correlation functions of the equilibrium and the nonequilibrium simulations become comparable.

(ii) The size of the Kondo screening cloud becomes exponentially large in U. It is therefore important to identify the characteristics of finite-size effects with increasing U. In Fig. 11 (right) we plot data with increasing U for fixed L and study the behavior of $S_o(r)$. From $U = 0$ to $U = 6\Delta$ the correlation function follows a monotonic trend and qualitatively the same behavior. However, the curves for $U = 10\Delta$ and $U = 20\Delta$ are qualitatively different. This indicates that these values of U are too large for the given L, as expected from the size of ξ_K^{BA}, which becomes of the order of $L \approx 200$ sites here [see Eq. (3)]. In the present work we therefore restrict ourselves to values of $U \leqslant 6\Delta$.

Next we show that our time evolution yields a controlled accuracy using a DMRG/TEBD matrix dimension of $\chi = 2000$. The bipartite entanglement $\omega(i,\tau) = -\mathrm{tr}[\hat{\rho}_{\mathrm{L/R}}(\tau)\ln(\hat{\rho}_{\mathrm{L/R}}(\tau))]$ [63] provides an estimate of the time when TEBD becomes unreliable for a fixed χ. This is signaled by a sharp increase in ω. Here $\hat{\rho}_{\mathrm{L/R}}$ denotes the reduced density matrix to the left (L) or to the right (R) of a lattice bipartition at bond i. Figure 12 (left) shows the entanglement increase, which turns out to mostly affect the region next to the impurity and the major propagating signal at $r = v_F\tau$. In our simulations we find that $\chi = 2000$ is sufficient to account for the additionally generated entanglement, which is not much larger than in the equilibrium case. In addition, we investigate the direct influence of increasing χ on the interacting spin correlation function $S_\chi(r,\tau)$ by comparing results using $\chi = 2000$ with results obtained at a smaller χ. Figure 12 (middle) shows the modulus of the deviation $|S_{2000}(r,\tau) - S_\chi(r,\tau)|$. We calculate this deviation at each point in space r and time τ and for $U = \{0,1,2,3,4,5,6\}\Delta$. The deviation fluctuates over space

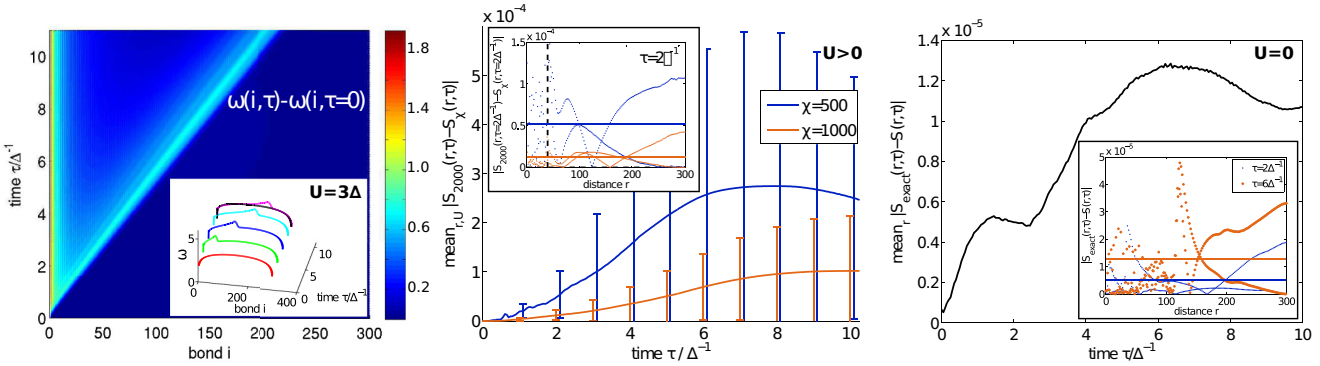

FIG. 12. (Color online) Quality of the DMRG and TEBD data. Left: Bond- and time-resolved entanglement entropy $\omega(i,\tau)$. We subtracted the $\omega(i,\tau = 0)$ data to highlight changes caused by the time evolution. Inset: Cuts through the $\omega(i,\tau)$ raw data at constant times. The black line is the result of a corresponding equilibrium simulation. The area hidden by the inset is homogeneously dark blue, which corresponds to $\omega(i,\tau) - \omega(i,\tau = 0) \equiv 0$. Data shown is for $U = 3\Delta$. Middle: Convergence of the interacting spin correlation function with increasing TEBD matrix dimension χ. Modulus of the residuals $|S_{2000}(r,\tau) - S_\chi(r,\tau)|$, benchmarking the quality of the time evolution with increasing TEBD matrix dimension χ. We show results comparing $\chi = 2000$ with $\chi = 500$ (blue lines) and $\chi = 2000$ with $\chi = 1000$ (orange lines). We show the residuals averaged over distance and interaction strength as a function of time τ. Inset: Spatially resolved residuals plotted at time $\tau = 2\Delta^{-1}$ and for $U = 3\Delta$. Right: Comparison of the noninteracting spin correlation function as obtained by TEBD, $S(r,\tau)$, and the noninteracting spin correlation as obtained exactly, $S_{\mathrm{exact}}(r,\tau)$. Spatially averaged absolute distance. Inset: Spatial resolution for two times, $\tau = \{2,6\}\Delta^{-1}$. Note that each blue (orange) line belongs to one data set only, which is alternating.

with systematic signatures at the light cone and beyond it, while the interior of the light cone looks chaotic. The results are almost independent of U. We find that the space r and interaction U averaged deviation grows over time and becomes of the order of $O(5\times10^{-4})$ for $\chi=500$ and $O(1\times10^{-4})$ for $\chi=1000$ within the reachable simulation time. Furthermore, for $U=0$ we compare the correlation functions obtained via TEBD with the numerically exact ones [Eq. (8)] in Fig. 12 (right). As one can see, the maximum deviation occurs at the boundary far from the impurity, with a maximum error of $\approx1\times10^{-5}$.

We conclude that for simulations of nonlocal correlation functions within the DMRG and TEBD in the SIAM the major limiting factor is the computation time $T\propto L(\chi)^3$. This is due to the large matrix dimensions χ needed to achieve accurate results and is, furthermore, complicated by the fact that the SIAM exhibits exponentially long correlation lengths, which require large lattice sizes L. The accuracy can be controlled by benchmarking against exactly known $U=0$ data and, for finite U, by increasing the TEBD matrix dimension χ. Furthermore, all the scales extracted in the text, $\alpha^S_{\mathrm{o/e}}$ and $\gamma_{\mathrm{C/S_{o/e}}}$ are retrieved from two subtracted correlation functions, in which we expect errors to further compensate.

APPENDIX B: EXTRACTION OF THE DYNAMIC ENERGY SCALE

In the following we provide details of the data analysis of the dynamic scale $\alpha_{\mathrm{o/e}}$ as discussed in Sec. VII A, which is valid for both even and odd distances. First, we obtain the time dependence of the spin correlation function by performing a nonlinear fit in time τ to the spin correlation function for fixed distances r and given interaction U: $\Delta S(\tau|r,U)$ (see Sec. VII A), using $f(\boldsymbol{\phi}=(c_1,\Gamma(r,U)),\tau)=c_1e^{-\Gamma(r,U)\tau}$ with two fit parameters $\boldsymbol{\phi}$. The data are single exponential plus oscillations and exhibit an eventual systematic bias close to the lattice border and due to the signal front at the light cone. For each r we manually choose intervals $[\tau_s(r,U),\tau_e(r,U)]$ for the fit in time in order to minimize these influences. Typically we choose fit intervals which start $r_s\approx10$ sites behind the light cone and extend up to $r_e\approx250$ for large U. For small U the data become noise before this r_e is reached and we adjust the end points accordingly. We estimate the fit uncertainty $\Delta\Gamma(r,U)$ by $\Delta\phi_i\approx\sqrt{C_{ii}}$, where $\mathbf{C}=(\mathbf{J}^\dagger\mathbf{J})\eta^2$ is the estimated covariance, $\mathbf{J}=\frac{\partial f(\boldsymbol{\phi},\tau_i)}{\partial\alpha_j}$ is the fit Jacobian, and $\eta^2=\frac{\mathbf{r}^T\mathbf{r}}{N_\tau(r,U)-p}$ is the mean square error defined by the residuals $r_i=\Delta S(\tau_i|r,U)-f(\boldsymbol{\phi},\tau_i)$ on $N_\tau(r,U)$ data points in time $\Delta S(\tau_i|r,U)$. These estimates are consistent with those obtained from fluctuations upon changing $\tau_s(r,U)$ and $\tau_e(r,U)$. Second, we condense the r dependence by averaging $\Gamma(r,U)$ over distances r. We make use of a Bayesian approach with Gaussian error statistics. We obtain the weighted mean value $\Gamma(U)=\frac{1}{P}\sum_r\frac{1}{\Delta\Gamma(r,U)^2}\Gamma(r_i,U)$ with $P=\sum_r\frac{1}{\Delta\Gamma(r,U)^2}$ and a weighted error estimate $\Delta\Gamma(U)=\frac{1}{\sqrt{P}}$, where the weights are obtained from $\Delta\Gamma(r,U)$. Third, we obtain the U dependence of the exponent considering data for $\Gamma(U)$ for $N(U)=6$ data points at $U=\{1,2,3,4,5,6\}\Delta$. The data $\Gamma(U)$ can be fitted very well by a single exponential in U: $\Gamma(U)=c_2e^{-\alpha U}$. The same scheme as in the first step is used to estimate the uncertainty $\Delta\Gamma$. We assume correlated data, i.e., $\eta^2=\frac{\mathbf{r}^T\mathbf{r}}{\widetilde{N}_{\mathrm{eff}}}$, with $\widetilde{N}_{\mathrm{eff}}\approx\frac{N(U)-p}{2N_{\mathrm{corr}}}\approx\frac{6-2}{2\times6}$, which enlarges the uncertainty by a factor of $\sqrt{3}$ compared to the naive value.

[1] A. C. Hewson, *The Kondo Problem to Heavy Fermions* (Cambridge University Press, Cambridge, 1997).

[2] J. Friedel, On some electrical and magnetic properties of metallic solid solutions, Can. J. Phys. **34**, 1190 (1956).

[3] A. M. Clogston, B. T. Matthias, M. Peter, H. J. Williams, E. Corenzwit, and R. C. Sherwood, Local magnetic moment associated with an iron atom dissolved in various transition metal alloys, Phys. Rev. **125**, 541 (1962).

[4] J. Kondo, Resistance minimum in dilute magnetic alloys, Prog. Theor. Phys. **32**, 37 (1964).

[5] P. Nozières, A "fermi-liquid" description of the Kondo problem at low temperatures, J. Low Temp. Phys. **17**, 31 (1974).

[6] D. Goldhaber-Gordon, J. Göres, M. A. Kastner, H. Shtrikman, D. Mahalu, and U. Meirav, From the Kondo regime to the mixed-valence regime in a single-electron transistor, Phys. Rev. Lett. **81**, 5225 (1998).

[7] S. M. Cronenwett, T. H. Oosterkamp, and L. P. Kouwenhoven, A tunable Kondo effect in quantum dots, Science **281**, 540 (1998).

[8] F. Simmel, R. H. Blick, J. P. Kotthaus, W. Wegscheider, and M. Bichler, Anomalous Kondo effect in a quantum dot at nonzero bias, Phys. Rev. Lett. **83**, 804 (1999).

[9] W. G. van der Wiel, S. De Franceschi, T. Fujisawa, J. M. Elzerman, S. Tarucha, and L. P. Kouwenhoven, The Kondo effect in the unitary limit, Science **289**, 2105 (2000).

[10] W. G. van der Wiel, S. De Franceschi, J. M. Elzerman, T. Fujisawa, S. Tarucha, and L. P. Kouwenhoven, Electron transport through double quantum dots, Rev. Mod. Phys. **75**, 1 (2002).

[11] S. De Franceschi, R. Hanson, W. G. van der Wiel, J. M. Elzerman, J. J. Wijpkema, T. Fujisawa, S. Tarucha, and L. P. Kouwenhoven, Out-of-equilibrium Kondo effect in a mesoscopic device, Phys. Rev. Lett. **89**, 156801 (2002).

[12] A. V. Kretinin, H. Shtrikman, and D. Mahalu, Universal line shape of the Kondo zero-bias anomaly in a quantum dot, Phys. Rev. B **85**, 201301 (2012).

[13] S. J. Chorley, M. R. Galpin, F. W. Jayatilaka, C. G. Smith, D. E. Logan, and M. R. Buitelaar, Tunable Kondo physics in a carbon nanotube double quantum dot, Phys. Rev. Lett. **109**, 156804 (2012).

[14] W. Liang, M. P. Shores, M. Bockrath, J. R. Long, and H. Park, Kondo resonance in a single-molecule transistor, Nature **417**, 725 (2002).

[15] V. Madhavan, W. Chen, T. Jamneala, M. F. Crommie, and N. S. Wingreen, Tunneling into a single magnetic atom: Spectroscopic evidence of the Kondo resonance, Science **280**, 567 (1998).
[16] W. Brenig and K. Schönhammer, On the theory of chemisorption, Z. Phys. **267**, 201 (1974).
[17] J.-H. Chen, L. Li, W. G. Cullen, E. D. Williams, and M. S. Fuhrer, Tunable Kondo effect in graphene with defects, Nat. Phys. **7**, 535 (2011).
[18] A. Georges, G. Kotliar, W. Krauth, and M. J. Rozenberg, The local impurity self consistent approximation (LISA) to strongly correlated fermion systems and the limit of infinite dimensions, Rev. Mod. Phys. **68**, 13 (1996).
[19] D. Vollhardt, Dynamical mean-field theory of electronic correlations in models and materials, in *Lecture Notes on the Physics of Strongly Correlated Systems*, Vol. 1297 of AIP Conf. Proc., edited by A. Avella and F. Mancini (American Institute of Physics, New York, 2010), pp. 339–403.
[20] W. Metzner and D. Vollhardt, Correlated lattice fermions in $d = \infty$ dimensions, Phys. Rev. Lett. **62**, 324 (1989).
[21] P. Nozières, Impuretés magnétiques et effet Kondo, Ann. Phys. Fr. **10**, 19 (1985).
[22] P. Nozières, Some comments on Kondo lattices and the Mott transition, Eur. Phys. J. B Condens. Matter Complex Syst. **6**, 447 (1998).
[23] S. Doniach, Phase diagram for the Kondo lattice, in *Valence Instabilities and Related Narrow-Band Phenomena*, edited by R. Parks (Springer, New York, 1977), pp. 169–176.
[24] S. Doniach, The Kondo lattice and weak antiferromagnetism, Physica B+C **91**, 231 (1977).
[25] M. A. Ruderman and C. Kittel, Indirect exchange coupling of nuclear magnetic moments by conduction electrons, Phys. Rev. **96**, 99 (1954).
[26] T. Kasuya, A theory of metallic ferro- and antiferromagnetism on Zener's model, Prog. Theor. Phys. **16**, 45 (1956).
[27] K. Yosida, Magnetic properties of Cu-Mn alloys, Phys. Rev. **106**, 893 (1957).
[28] I. Affleck, The Kondo screening cloud: What it is and how to observe it, in *Perspectives of Mesoscopic Physics* (World Scientific, Singapore, 2009), Chap. 1.
[29] I. Affleck, The Kondo screening cloud, in *Strongly Correlated Fermions and Bosons in Low-Dimensional Disordered Systems*, edited by I. V. Lerner, B. L. Althschuler, V. I. Fal'ko, and T. Giamarchi (Springer, Berlin, 2001).
[30] W. D. Knight, Nuclear magnetic resonance shift in metals, Phys. Rev. **76**, 1259 (1949).
[31] C. H. Townes, C. Herring, and W. D. Knight, The effect of electronic paramagnetism on nuclear magnetic resonance frequencies in metals, Phys. Rev. **77**, 852 (1950).
[32] W. D. Knight, *Solid State Physics*, Vol. 2, edited by F. Seitz and D. Turnbull (Academic Press, New York, 1956), p. 93.
[33] T. Hand, J. Kroha, and H. Monien, Spin correlations and finite-size effects in the one-dimensional Kondo box, Phys. Rev. Lett. **97**, 136604 (2006).
[34] G. Binnig and H. Rohrer, Scanning tunneling microscopy, IBM J. Res. Dev. **30**, 355 (1986).
[35] H. Prüser, M. Wenderoth, P. E. Dargel, A. Weismann, R. Peters, T. Pruschke, and R. G. Ulbrich, Long-range Kondo signature of a single magnetic impurity, Nature Phys. **7**, 203 (2011).
[36] I. Affleck, L. Borda, and H. Saleur, Friedel oscillations and the Kondo screening cloud, Phys. Rev. B **77**, 180404 (2008).
[37] I. Affleck and P. Simon, Detecting the Kondo screening cloud around a quantum dot, Phys. Rev. Lett. **86**, 2854 (2001).
[38] R. G. Pereira, N. Laflorencie, I. Affleck, and B. I. Halperin, Kondo screening cloud and charge staircase in one-dimensional mesoscopic devices, Phys. Rev. B **77**, 125327 (2008).
[39] J. Park, S.-S. B. Lee, Y. Oreg, and H.-S. Sim, How to directly measure a Kondo clouds length, Phys. Rev. Lett. **110**, 246603 (2013).
[40] H. C. Manoharan, C. P. Lutz, and D. M. Eigler, Quantum mirages formed by coherent projection of electronic structure, Nature **403**, 512 (2000).
[41] H. Ishii, Spin correlation in dilute magnetic alloys, J. Low Temp. Phys. **32**, 457 (1978).
[42] F. Mezei and G. Grüner, Theory of anomalous charge oscillation around resonant scattering impurities, Phys. Rev. Lett. **29**, 1465 (1972).
[43] V. Zlatic and G. Grüner, Preasymptotic charge oscillations around 3d impurities in aluminium, J. Phys. (Paris) Lett. **38**, 87 (1977).
[44] V. Barzykin and I. Affleck, The Kondo screening cloud: What can we learn from perturbation theory? Phys. Rev. Lett. **76**, 4959 (1996).
[45] E. S. Sørensen and I. Affleck, Scaling theory of the Kondo screening cloud, Phys. Rev. B **53**, 9153 (1996).
[46] E. S. Sørensen and I. Affleck, Kondo screening cloud around a quantum dot: Large-scale numerical results, Phys. Rev. Lett. **94**, 086601 (2005).
[47] S. Costamagna, C. J. Gazza, M. E. Torio, and J. A. Riera, Anderson impurity in the one-dimensional Hubbard model for finite-size systems, Phys. Rev. B **74**, 195103 (2006).
[48] J. E. Gubernatis, J. E. Hirsch, and D. J. Scalapino, Spin and charge correlations around an Anderson magnetic impurity, Phys. Rev. B **35**, 8478 (1987).
[49] L. Borda, Kondo screening cloud in a one-dimensional wire: Numerical renormalization group study, Phys. Rev. B **75**, 041307 (2007).
[50] L. Borda, M. Garst, and J. Kroha, Kondo cloud and spin-spin correlations around a partially screened magnetic impurity, Phys. Rev. B **79**, 100408 (2009).
[51] C. A. Büsser, G. B. Martins, L. Costa Ribeiro, E. Vernek, E. V. Anda, and E. Dagotto, Numerical analysis of the spatial range of the Kondo effect, Phys. Rev. B **81**, 045111 (2010).
[52] A. Holzner, I. P. McCulloch, U. Schollwöck, J. von Delft, and F. Heidrich-Meisner, Kondo screening cloud in the single-impurity Anderson model: A density matrix renormalization group study, Phys. Rev. B **80**, 205114 (2009).
[53] S. Ghosh, P. Ribeiro, and M. Haque, Real-space structure of the impurity screening cloud in the resonant level model, J. Stat. Mech.: Theory Exp. (2014) P04011.
[54] We denote real time τ.
[55] A. Hoffmann, Spatiotemporal formation of the Kondo cloud, Ph.D. thesis, Ludwig Maximilians Universitat Munchen, 2012.
[56] M. Medvedyeva, A. Hoffmann, and S. Kehrein, Spatiotemporal buildup of the Kondo screening cloud, Phys. Rev. B **88**, 094306 (2013).
[57] B. Lechtenberg and F. B. Anders, Spatial and temporal propagation of Kondo correlations, Phys. Rev. B **90**, 045117 (2014).

[58] P. W. Anderson, Localized magnetic states in metals, Phys. Rev. **124**, 41 (1961).

[59] S. R. White, Density matrix formulation for quantum renormalization groups, Phys. Rev. Lett. **69**, 2863 (1992).

[60] S. R. White, Density-matrix algorithms for quantum renormalization groups, Phys. Rev. B **48**, 10345 (1993).

[61] U. Schollwöck, The density-matrix renormalization group, Rev. Mod. Phys. **77**, 259 (2005).

[62] G. Vidal, Efficient simulation of one-dimensional quantum many-body systems, Phys. Rev. Lett. **93**, 040502 (2004).

[63] U. Schollwöck, The density-matrix renormalization group in the age of matrix product states, Ann. Phys. (Spec. Issue) **326**, 96 (2011).

[64] J. R. Schrieffer and P. A. Wolff, Relation between the Anderson and Kondo hamiltonians, Phys. Rev. **149**, 491 (1966).

[65] E. H. Lieb and D. W. Robinson, The finite group velocity of quantum spin systems, Commun. Math. Phys. **28**, 251 (1972).

[66] S. Bravyi, M. B. Hastings, and F. Verstraete, Lieb-Robinson bounds and the generation of correlations and topological quantum order, Phys. Rev. Lett. **97**, 050401 (2006).

[67] B. Nachtergaele and R. Sims, Lieb-Robinson bounds and the exponential clustering theorem, Commun. Math. Phys. **265**, 119 (2006).

[68] N. Schuch, S. K. Harrison, T. J. Osborne, and J. Eisert, Information propagation for interacting-particle systems, Phys. Rev. A **84**, 032309 (2011).

[69] M. Hastings, *Quantum Theory from Small to Large Scales* (Oxford University Press, New York, 2012), Chap. 1.

[70] We denote all operators with a hat, $\hat{O}$, except for elementary fermion annihilation/creation operators: $c/c^\dagger$.

[71] E. N. Economou, *Green's Functions in Quantum Physics*, 3rd ed. (Springer, Berlin, 2010).

[72] The retarded single-particle Green's function of a reservoir with a semicircular density of states reads $G^R(\omega) = \frac{\omega-\epsilon}{2t^2} - i\sqrt{\frac{4t^2-(w-\epsilon)^2}{2t^2}}$, where ϵ denotes the reservoir on-site energy.

[73] W. B. Thimm, J. Kroha, and J. von Delft, Kondo box: A magnetic impurity in an ultrasmall metallic grain, Phys. Rev. Lett. **82**, 2143 (1999).

[74] P. Simon and I. Affleck, Kondo screening cloud effects in mesoscopic devices, Phys. Rev. B **68**, 115304 (2003).

[75] A. Schwabe, D. Gütersloh, and M. Potthoff, Competition between Kondo screening and indirect magnetic exchange in a quantum box, Phys. Rev. Lett. **109**, 257202 (2012).

[76] I. Titvinidze and M. Potthoff, Boundary and finite-size effects in the competition between indirect magnetic exchange and Kondo screening, J. Korean Phys. Soc. **62**, 1434 (2013).

[77] K. Yosida and K. Yamada, Perturbation expansion for the Anderson hamiltonian, Prog. Theor. Phys. Suppl. **46**, 244 (1970).

[78] K. Yamada, Perturbation expansion for the Anderson hamiltonian. II, Prog. Theor. Phys. **53**, 970 (1975).

[79] K. Yosida and K. Yamada, Perturbation expansion for the Anderson hamiltonian. III, Prog. Theor. Phys. **53**, 1286 (1975).

[80] K. Yamada, Perturbation expansion for the Anderson hamiltonian. IV, Prog. Theor. Phys. **54**, 316 (1975).

[81] P. W. Anderson, A poor man's derivation of scaling laws for the Kondo problem, J. Phys. C **3**, 2436 (1970).

[82] K. G. Wilson, The renormalization group: Critical phenomena and the Kondo problem, Rev. Mod. Phys. **47**, 773 (1975).

[83] H. R. Krishna-murthy, J. W. Wilkins, and K. G. Wilson, Renormalization-group approach to the Anderson model of dilute magnetic alloys. I. Static properties for the symmetric case, Phys. Rev. B **21**, 1003 (1980).

[84] R. Bulla, T. A. Costi, and T. Pruschke, Numerical renormalization group method for quantum impurity systems, Rev. Mod. Phys. **80**, 395 (2008).

[85] H. Bethe, Zur theorie der metalle, Z. Phys. **71**, 205 (1931).

[86] P. B. Wiegmann and A. M. Tsvelick, Exact solution of the Anderson model: I, J. Phys. C **16**, 2281 (1983).

[87] A. M. Tsvelick and P. B. Wiegmann, Exact solution of the Anderson model. II. Thermodynamic properties at finite temperatures, J. Phys. C **16**, 2321 (1983).

[88] J. E. Hirsch and R. M. Fye, Monte Carlo method for magnetic impurities in metals, Phys. Rev. Lett. **56**, 2521 (1986).

[89] E. Gull, A. J. Millis, A. I. Lichtenstein, A. N. Rubtsov, M. Troyer, and P. Werner, Continuous-time Monte Carlo methods for quantum impurity models, Rev. Mod. Phys. **83**, 349 (2011).

[90] F. D. M. Haldane, Theory of the atomic limit of the Anderson model. I. Perturbation expansions re-examined, J. Phys. C **11**, 5015 (1978).

[91] V. Barzykin and I. Affleck, Screening cloud in the k-channel Kondo model: Perturbative and large-k results, Phys. Rev. B **57**, 432 (1998).

[92] R. Žitko, J. Bonča, A. Ramšak, and T. Rejec, Kondo effect in triple quantum dots, Phys. Rev. B **73**, 153307 (2006).

[93] T. Pruschke, Landau's fermi liquid concept to the extreme: The physics of heavy fermions, AIP Conf. Proc. **1485**, 78 (2012).

[94] C. Karrasch, R. Hedden, R. Peters, T. Pruschke, K. Schnhammer, and V. Meden, A finite-frequency functional renormalization group approach to the single impurity Anderson model, J. Phys.: Condens. Matter **20**, 345205 (2008).

[95] P. Coleman, Local moment physics in heavy electron systems, AIP Conf. Proc. **629**, 79 (2002).

[96] In the wide-band limit a featureless (constant) electronic density of states of the reservoirs is assumed which has a bandwidth much larger than the characteristic energy scales of the system coupled to the reservoir. The retarded single-particle Green's function is then given by $G^R(\omega) = -\frac{1}{2W}\ln(\frac{\omega-W}{\omega+W})$, where W is the half-bandwidth.

[97] N. W. Ashcroft and N. D. Mermin, *Solid State Physics*, 1st ed. (Cengage Learning, Singapore, 1976).

[98] R. J. Barton and J. F. Kos, The Kondo temperature of gold, Solid State Commun. **27**, 661 (1978).

[99] Note that although our Hamiltonian is spin rotation invariant, in our system $S(r,\tau) \neq 3\langle \hat{S}_0^z \hat{S}_r^z \rangle(\tau)$ since our initial state is not spin rotation invariant.

[100] Here we also consider the disconnected contribution to the charge correlation function in order to make comparisons to Ref. [48].

[101] R. Žitko, NRG LJUBLJANA (open source numerical renormalization-group code), V2.3.20 (2013); http://nrgljubljana.ijs.si/

[102] E. Boulat, H. Saleur, and P. Schmitteckert, Twofold advance in the theoretical understanding of far-from-equilibrium properties of interacting nanostructures, Phys. Rev. Lett. **101**, 140601 (2008).

[103] F. Heidrich-Meisner, A. E. Feiguin, and E. Dagotto, Real-time simulations of nonequilibrium transport in the single-impurity Anderson model, Phys. Rev. B **79**, 235336 (2009).

[104] P. Schmitteckert, Nonequilibrium electron transport using the density matrix renormalization group method, Phys. Rev. B **70**, 121302 (2004).

[105] K. A. Al-Hassanieh, A. E. Feiguin, J. A. Riera, C. A. Büsser, and E. Dagotto, Adaptive time-dependent density-matrix renormalization-group technique for calculating the conductance of strongly correlated nanostructures, Phys. Rev. B **73**, 195304 (2006).

[106] F. Heidrich-Meisner, I. González, K. A. Al-Hassanieh, A. E. Feiguin, M. J. Rozenberg, and E. Dagotto, Nonequilibrium electronic transport in a one-dimensional Mott insulator, Phys. Rev. B **82**, 205110 (2010).

[107] M. Žnidarič, Spin transport in a one-dimensional anisotropic Heisenberg model, Phys. Rev. Lett. **106**, 220601 (2011).

[108] S. Jesenko and M. Žnidarič, Finite-temperature magnetization transport of the one-dimensional anisotropic Heisenberg model, Phys. Rev. B **84**, 174438 (2011).

[109] F. Heidrich-Meisner, G. B. Martins, C. A. Büsser, K. A. Al-Hassanieh, A. E. Feiguin, G. Chiappe, E. V. Anda, and E. Dagotto, Transport through quantum dots: A combined DMRG and embedded-cluster approximation study, Eur. Phys. J. B **67**, 527 (2009).

[110] S. Kirino, T. Fujii, J. Zhao, and K. Ueda, Time-dependent DMRG study on quantum dot under a finite bias voltage, J. Phys. Soc. Jpn. **77**, 084704 (2008).

[111] S. Kirino and K. Ueda, Nonequilibrium current in the one dimensional Hubbard model at half-filling, J. Phys. Soc. Jpn. **79**, 093710 (2010).

[112] M. A. Cazalilla and J. B. Marston, Time-dependent density-matrix renormalization group: A systematic method for the study of quantum many-body out-of-equilibrium systems, Phys. Rev. Lett. **88**, 256403 (2002).

[113] H. G. Luo, T. Xiang, and X. Q. Wang, Comment on "Time-dependent density-matrix renormalization group: A systematic method for the study of quantum many-body out-of-equilibrium systems", Phys. Rev. Lett. **91**, 049701 (2003).

[114] M. A. Cazalilla and J. B. Marston, Cazalilla and Marston reply:, Phys. Rev. Lett. **91**, 049702 (2003).

[115] M. Nuss, M. Ganahl, H. G. Evertz, E. Arrigoni, and W. von der Linden, Steady-state and quench-dependent relaxation of a quantum dot coupled to one-dimensional leads, Phys. Rev. B **88**, 045132 (2013).

[116] E. H. Lieb, M. Loss, and R. J. McCann, Uniform density theorem for the Hubbard model , J. Math. Phys. **34**, 891 (1993).

[117] A nonmonotonic behavior of the magnitude of the spin correlation function $S(r)$ with increasing U has been reported for small U [48]. Our data points in U are not dense enough to comment on this aspect. Our results suggest a monotonic dependence.

[118] P. Fulde, *Electron Correlations in Molecules and Solids*, 3rd ed. (Springer, Berlin, 2013).

[119] In Ref. [48] it was observed that $C(r)$ exhibits a suppression $r \ll \frac{v_F}{T_K}$, which gradually recovers to the full Friedel value at large distances. We cannot comment on the full recovery due to our limited system sizes.

[120] While the asymptotic limits of Eq. (11) are obtained for $U = 0$, it is argued in Ref. [53] that they stay valid in the interacting system.

[121] H. Haken and H. C. Wolf, *Atom- und Quantenphysik: Einfhrung in die experimentellen und theoretischen Grundlagen*, 8th ed. (Springer, Berlin, 2004).

[122] R. Žitko, Adaptive logarithmic discretization for numerical renormalization group methods, Comput. Phys. Commun. **180**, 1271 (2009).

[123] Making use of the NRG LJUBLJANA code [101] we studied the model as presented in the text by calculating the impurity thermodynamics. We used a Z discretization scheme, $Nz = 7$ points for z averaging, and a cutoff $\Lambda = 1.8$. The presented results are converged in all auxiliary numerical parameters.

[124] A. Dirks, S. Schmitt, J. E. Han, F. Anders, P. Werner, and T. Pruschke, Double occupancy and magnetic susceptibility of the Anderson impurity model out of equilibrium, Europhys. Lett. **102**, 37011 (2013).

[125] F. B. Anders and A. Schiller, Real-time dynamics in quantum-impurity systems: A time-dependent numerical renormalization-group approach, Phys. Rev. Lett. **95**, 196801 (2005).

[126] D. Lobaskin and S. Kehrein, Crossover from nonequilibrium to equilibrium behavior in the time-dependent Kondo model, Phys. Rev. B **71**, 193303 (2005).

[127] G. Cohen, E. Gull, D. R. Reichman, A. J. Millis, and E. Rabani, Numerically exact long-time magnetization dynamics at the nonequilibrium Kondo crossover of the Anderson impurity model, Phys. Rev. B **87**, 195108 (2013).

[128] The Toulouse point of the anisotropic Kondo model maps via bosonization and refermionization [129] and a special choice of parameters to a noninteracting resonant level model [130].

[129] J. von Delft and H. Schoeller, Bosonization for beginners – refermionization for experts, Ann. Physik **7**, 225 (1998).

[130] G. Toulouse, Infinite-U Anderson Hamiltonian for dilute alloys, Phys. Rev. B **2**, 270 (1970).

5.4. Variational cluster approach to the single-impurity Anderson model

5.4.1. Preamble

This part of our work has been published in PHYSICAL REVIEW B 85, 235107 (2012) [357] and is also available as a preprint on arXiv:1110.4533. Reproduced with permission from PHYSICAL REVIEW B 85, 235107 (2012), doi:10.1103/PhysRevB.85.235107. Copyright 2012, the American Physical Society.

This paper is the first step to a series of publications on steady-state quantum cluster methods, see Sec. 5.5, Sec. 5.6, Sec. 5.7, Sec. 5.8 and Sec. 5.10. Before studying the steady-state generalizations of CPT and VCA, this work serves as a benchmark in equilibrium. The basic developments of these quantum cluster methods are outlined in Sec. 3.3.1 and Sec. 3.3.2. Although the SIAM is the simplest model of a molecular or nano-scopic junction, obtaining faithful results turns out to be far from trivial and highly accurate methods are necessary as also discussed in Sec. 3.1 and the time evolution sections Sec. 5.2 and Sec. 5.3. Physical applications are discussed in Ch. 2. In particular these physical aspects are vital to understand correlation phenomena as discussed in Sec. 5.1 and Sec. 5.9. In this work we discuss results obtained by an alternative, self-consistent formulation of VCA as required in the nonequilibrium setting for stsVCA and compare results to the conventional VCA based on the stationary points of the grand potential. We furthermore explore the capabilities of these methods to treat strongly inhomogeneous systems as needed for the description across nano-scopic devices or molecular junctions. By benchmarking CPT and VCA data versus established ED, NRG, DMRG and CT-QMC results, we were able to show that CPT and VCA are capable of yielding reasonably accurate results in equilibrium. These results are for the spectral function, the Friedel sum rule, the static spin susceptibility, the Kondo temperature, the grand potential and the self-energy. This data provides the basis for the development of the stsCPT and the stsVCA. The contents of this publication are advancements of work that has been done in MN's preceding diploma thesis [329]. In this publication we found that stsVCA yields the correct scaling of the Kondo temperature, that is exponential in interaction-strength, however with an underestimated exponent. Later during the writing of this thesis we found an optimization scheme for non-interacting baths which yields even the correct exponent, see App. G.

This study is authored by Martin Nuss (MN) and co-authored by MN's supervisor Enrico Arrigoni (EA), Markus Aichhorn (MA) and MN's supervisor Wolfgang von der Linden (WL). This research was to a large and significant extent conducted by MN under the supervision of WL and EA. The work was initiated by EA and WL who provided guidance and expertise throughout the whole working period. The self-consistent VCA was proposed by EA and WL, developed by MN, EA and WL and implemented on the computer infrastructure by MN. MN also adapted the CPT method to the SIAM and wrote the according computer code. The idea to apply the method to study a single quantum dot was proposed by WL and EA while MN conducted literature research on this topic. WL, EA and MN independently worked out the expressions for the grand potential for reference systems of infinite size. MN tested the computer code, conducted the numerical calculations and studied various implementations of variational parameters. MN prepared, collected, interpreted, analyzed and visualized the results and set them in context with recent literature. MN wrote the first version of the manuscript. MA provided expertise, guidance and data for the CT-QMC calculations as well as the TRIQS computer code [1]. WL conducted the analytical expansion of the self-energy for high Matsubara frequencies. MN introduced the calculations with a symmetry breaking field. MN wrote the first version of the manuscript. All authors participated equally in discussing the results and revising the text of the manuscript.

Robert Peters provided his DMRG and NRG data shown in Fig. 3 and to Christoph Karrasch provided his FRG and NRG data shown in Figs. 5, 13, and 15. We discussed our results with Kurt Schönhammer, Thomas Pruschke, Michael Knap, Piet Dargel, Olivier Parcollet and Michel Ferrero.

5.4.2. Manuscript

PHYSICAL REVIEW B **85**, 235107 (2012)

Variational cluster approach to the single-impurity Anderson model

Martin Nuss,* Enrico Arrigoni, Markus Aichhorn, and Wolfgang von der Linden
Institute of Theoretical and Computational Physics, Graz University of Technology, 8010 Graz, Austria
(Received 20 November 2011; revised manuscript received 19 March 2012; published 5 June 2012)

We study the single-impurity Anderson model by means of cluster perturbation theory and the variational cluster approach (VCA). An expression for the VCA grand potential for a system in a noninteracting bath is presented. Results for the single-particle dynamics in different parameter regimes are shown to be in good agreement with established renormalization group results. We aim at a broad and comprehensive overview of the capabilities and shortcomings of the methods. We address the question as to what extent the elusive low-energy properties of the model are reproducible within the framework of VCA. These are furthermore benchmarked against continuous-time quantum Monte Carlo calculations. We also discuss results obtained by an alternative, i.e., self-consistent formulation of VCA, which was introduced recently in the context of nonequilibrium systems.

DOI: 10.1103/PhysRevB.85.235107 PACS number(s): 71.27.+a, 71.10.−w, 71.15.−m, 72.15.Qm

I. INTRODUCTION

In recent years, both the applications for strongly correlated quantum impurity models and the number of successful approaches to harvest their physical results have grown enormously. Those models were introduced to describe the effects of magnetic transition-metal impurities immersed in metallic hosts.[1,2] Originally, they were derived to capture remarkable physical properties such as the resistance minimum[3,4] at a specific temperature scale T_K (Ref. 5) or the anomalous magnetic susceptibility and specific heat of such materials. Today, a whole realm of applications for quantum impurity models has opened. They describe the physics of quantum dots and wires[6–8] as well as molecular electronics.[9] Applications range from nanoelectronics all the way to quantum information processing.[10] Their properties are essential for today's technological applications in single-electron transistors[11] exhibiting the Coulomb blockade effect[12] or in devices dominated by Ruderman-Kittel-Kasuya-Yosida (RKKY) interaction.[13–15] The behavior of various magnetic phenomena and the fascinating branch of heavy-fermion physics is described by strongly correlated quantum impurity models.[16,17] Recent studies have shown that the remarkable material graphene exhibits Kondo physics,[18] which may be investigated theoretically by virtue of quantum impurity models. These models have further been applied to understand the adsorption of atoms onto surfaces.[19–21] In addition, they are of theoretical importance as solvable models of quantum field theories.[22,23] A renewed interest in understanding and calculating dynamic quantities of these models was created with the advent of dynamical mean-field theory (DMFT).[24–26] In the foundations of this theory, quantum impurity models have to be solved as an auxiliary problem.

A wide range of methods and approximations have been suggested for the solution of quantum impurity models. They, however, prove to be a very delicate subject because standard perturbative approaches diverge.[5] Prominent methods to gain physical conclusions include a self-consistent perturbative expansion[27] and Bethe ansatz techniques[28] for one-dimensional problems. The low-energy physics is very well described by numerical renormalization group[29] (NRG) and in some limits also by functional renormalization group[30,31] (FRG) and density matrix renormalization group[32–34] (DMRG). There is a range of slave-particle methods[35,36] available as well as methods based on Hubbard's X-operator technique[37,38] and calculations using variational wave functions.[21] Valuable physical insight has been gained by using equation-of-motion techniques applying different approximation schemes.[39] For moderate system sizes, the Hirsch-Fye quantum Monte Carlo[41] (QMC) algorithm has proven to achieve good results. In the past years, different approaches to continuous-time QMC (Ref. 40) have been applied very successfully to solve quantum impurity models especially in application with DMFT. In this context, exact diagonalization (ED) methods have been explored to solve small systems.[42]

As of today, some limits of quantum impurity models are understood with great precision, but there appear several gaps to be bridged. The low-energy properties of these models are reproduced very well by renormalization-group-based approaches (i.e., NRG). These approaches in general have trouble to capture the high-energy parts of the spectrum. The same may be said about QMC methods, which if applicable yield dynamic quantities in imaginary time. The analytic continuation to the real energy axis is ill conditioned. Spectra obtained by, for example, the maximum-entropy method[43,44] have a large uncertainty for higher energies. Exact diagonalization methods, in principle, grant access to low- as well as high-energy parts of the spectrum at the same time. Due to the prohibitively large Hilbert space, however, only small systems (about 10 to 20 sites) may be treated with this method, the low-energy behavior of which is expected to deviate from the one of the infinite lattice significantly. Nevertheless, the advantage consists in the fact that the spectral properties may be determined directly on the real energy axis. Aside from the issue of the low-energy scale, also the flexibility to adapt to various impurity configurations and geometries is limited in many methods. NRG has been successfully applied only to the one and two impurity cases so far. QMC approaches may suffer from the sign problem for more complex multiband models.[40] The region of large interaction strength is naturally difficult to treat in standard perturbative/diagrammatic approaches (i.e., diagrammatic perturbation theory or FRG).

In this work, we test cluster perturbation theory[45,46] (CPT) and the variational cluster approach[47–49] (VCA) on the

single-impurity Anderson model.[1] The great flexibility and versatility of CPT/VCA allows for obtaining approximate single-particle dynamic quantities and static expectation values in all parameter regions of any lattice impurity model with local interactions. However, these many-body cluster methods can not be expected to describe the low-energy excitations as accurately as specifically tailored methods do. It is, however, interesting to see whether the correct low-energy behavior may be reproduced at least to some extent. CPT as well as VCA bare several advantages:[50] (i) They yield spectra directly on the real axis and (ii) also the high-energy incoherent part of the dynamics becomes available. (iii) They are applicable in all parameter regions and also at high interaction strengths. (iv) They have the advantage of comparatively low computational cost for a required resolution. Our main goal in studying the well-understood single impurity is to benchmark CPT/VCA for future application to the not-so-well-understood case of multiband impurity models in various spatial geometries. This paper also sets the foundations for a future extension to nonequilibrium problems.

The text is organized as follows. The single-impurity Anderson model is introduced in Sec. II. A short review on CPT and VCA in this context is given in Sec. III. A self-consistent formulation of VCA previously introduced in the context of nonequilibrium problems[51] is presented in Sec. III 1. Some remarks about the choice of variational parameters are provided in Sec. III 2. In Sec. IV, we discuss the grand potential Ω for infinite fermionic systems in relation with the VCA. Results for the single-particle dynamics of the SIAM are provided in Sec. V. In this section, also the quality of the low-energy Kondo physics is compared to benchmarking results from NRG, DMRG, CT-QMC, Hartree-Fock, and Bethe ansatz calculations. Finally, we summarize and conclude our findings in Sec. VI.

II. SINGLE-IMPURITY ANDERSON MODEL

We consider the single-impurity Anderson model[1] (SIAM) in real space, in one dimension:

$$\hat{\mathcal{H}}_{\mathrm{SIAM}} = \hat{\mathcal{H}}_{\mathrm{conduction}} + \hat{\mathcal{H}}_{\mathrm{impurity}} + \hat{\mathcal{H}}_{\mathrm{hybridization}}. \tag{1}$$

A tight-binding band of noninteracting s electrons with nearest-neighbor $\langle i, j\rangle$ hopping is described by

$$\hat{\mathcal{H}}^{N_s}_{\mathrm{conduction}} = \epsilon_s \sum_{i=1}^{N_s}\sum_{\sigma} c^{\dagger}_{i\sigma}\, c_{i\sigma} - t \sum_{\langle i,\, j\rangle\, \sigma} c^{\dagger}_{i\sigma}\, c_{j\sigma}, \tag{2}$$

where ϵ_s is the onsite energy of the particles, t is the overlap integral between nearest-neighbor orbitals, and $i, j \in \{1, \ldots, N_s\}$ where N_s is eventually taken to be infinity. The operators $c^{\dagger}_{i\sigma}$ and $c_{i\sigma}$, respectively, create and annihilate electrons in orbital i with spin σ. The impurity Hamiltonian consists of a single f orbital with local Coulomb repulsion U:

$$\hat{\mathcal{H}}_{\mathrm{impurity}} = \epsilon_f \sum_{\sigma} f^{\dagger}_{\sigma}\, f_{\sigma} + U\, \hat{n}^{f}_{\uparrow}\, \hat{n}^{f}_{\downarrow}, \tag{3}$$

with $f^{\dagger}_{\sigma}$ creating an electron with spin σ and onsite energy ϵ_f located at the impurity. The particle number operator is defined as $\hat{n}^{f}_{\sigma} = f^{\dagger}_{\sigma}\, f_{\sigma}$. Finally, the coupling between a noninteracting

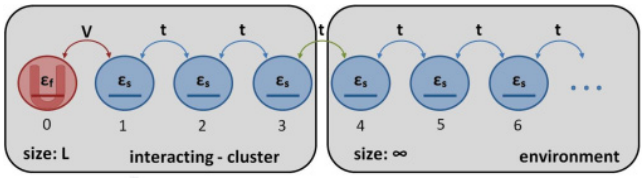

FIG. 1. (Color online) Illustration of the single-impurity Anderson model. The model consists of a semi-infinite chain of noninteracting s orbitals with nearest-neighbor hopping t and onsite energy ϵ_s. The impurity f orbital is subjected to a local onsite energy ϵ_f and local Coulomb interaction U and is hybridized with one of the s orbitals (here, the one at the beginning of the chain) via a hybridization matrix element V. This maps the impurity f orbital onto site 0 and the impurity s orbital onto site 1 in this geometry, and the rest of the conduction-band s-electron orbitals are mapped onto sites 2 to ∞. The semi-infinite noninteracting chain is truncated at some site L. This decomposes the model into two clusters: an interacting cluster of variable size including the interacting impurity f orbital and a semi-infinite chain of noninteracting s orbitals. In CPT/VCA, these decomposed systems are coupled via a hopping element t.

s orbital and the impurity f orbital is given by

$$\hat{\mathcal{H}}_{\mathrm{hybridization}} = -V \sum_{\sigma} c^{\dagger}_{1\sigma}\, f_{\sigma} + f^{\dagger}_{\sigma}\, c_{1\sigma}, \tag{4}$$

where V is the hybridization matrix element between the s and the f orbitals of the impurity atom (see Fig. 1 for illustration).

We have set the chemical potential μ to the center (ϵ_s) of the conduction-electron density of states and choose $\mu = \epsilon_s = 0$. The resonance width Δ is defined as

$$\Delta \equiv \pi\, V^2\, \rho_s(0) = \frac{V^2}{t}. \tag{5}$$

For the model defined in Eq. (2), the local density of states of the conduction electrons $\rho_s(0)$ is given by $\rho_s(0) = \frac{1}{\pi t}$. In the forthcoming discussion, we refer to the particle-hole symmetric case when we furthermore set $\epsilon_f = -\frac{U}{2}$. All calculations are performed with $t = 1$ and $V = 0.3162$, which yields $\Delta = 0.1$. All reported results, except for the CT-QMC data in Sec. V F, are for zero temperature.

III. CLUSTER PERTURBATION THEORY/VARIATIONAL CLUSTER APPROACH

A handle on dynamic single-particle correlations and expectation values is given by the single-particle Green's function $G^{\sigma\sigma'}_{ij}(\omega)$, which we calculate within cluster perturbation theory[45,46] as well as the variational cluster approach.[47] CPT and VCA have been previously applied *inter alia* to the fermionic Hubbard model and VCA also with great success to bosonic systems[52–54] with broken-symmetry phases. The groundwork of VCA lies within cluster perturbation theory, which is a cluster extension of strong-coupling perturbation theory, valid to first order in the intercluster hopping. The main result of CPT is that the Green's function of the physical system G (which we call full Green's function throughout this text) may be obtained by a Dyson-type equation in matrix form

$$\mathrm{G}^{-1} = \mathrm{g}^{-1} - \mathrm{T}. \tag{6}$$

Here, g denotes the Green's function of a cluster which comes about by tiling the lattice of the physical system into smaller, numerically exactly solvable patches. This tiling is done by removing the hoppings between sites connecting such clusters. Therefore, the matrix $\mathrm{T} = \mathrm{g}_0^{-1} - \mathrm{G}_0^{-1}$ contains all single-particle terms connecting clusters (i.e., the intercluster hopping which will be referred to as $\mathrm{T}_{\mathrm{inter}}$ below). The subscript zero denotes the noninteracting Green's function. To apply this approach to the SIAM, we start by splitting the physical model under consideration [Eq. (1)] into appropriate pieces. Here, we consider a cluster decomposition consisting of two parts. One part, consisting of a cluster of size L, which contains the interacting impurity f orbital

$$\hat{\mathcal{H}}_{\mathrm{interacting}} = \hat{\mathcal{H}}^{L-1}_{\mathrm{conduction}} + \hat{\mathcal{H}}_{\mathrm{impurity}} + \hat{\mathcal{H}}_{\mathrm{hybridization}}, \quad (7)$$

and a second, infinitely large part, the environment, which contains the rest of the conduction band

$$\hat{\mathcal{H}}_{\mathrm{environment}} = \hat{\mathcal{H}}^{\infty}_{\mathrm{conduction}}. \quad (8)$$

The original Hamiltonian Eq. (1), defined on the semi-infinite lattice, may now be rewritten as

$$\hat{\mathcal{H}}_{\mathrm{SIAM}} = \hat{\mathcal{H}}_{\mathrm{interacting}} + \hat{\mathcal{H}}_{\mathrm{environment}} + \mathrm{T}_{\mathrm{inter}}. \quad (9)$$

Here, $\mathrm{T}_{\mathrm{inter}}$ is the part of T describing the hopping from the interacting cluster to environment "cluster," which is the only term not included in the two clusters. For the SIAM, the two bare Green's functions $\mathrm{g}_{\mathrm{interacting}}$ and $\mathrm{g}_{\mathrm{env}}$ {which correspond to $\hat{\mathcal{H}}_{\mathrm{interacting}}$ [Eq. (7)] and $\hat{\mathcal{H}}_{\mathrm{environment}}$ [Eq. (8)]} needed for Eq. (6) may be evaluated separately. This is a bit different from the usual application of CPT to translationally invariant systems which normally leads to a single cluster having discrete spectra, embedded in a superlattice. Therefore, the application of CPT to this problem does obviously not suffer from issues arising due to periodization prescriptions for the Green's function or self-energy.[50] We are dealing with two fundamentally different clusters, where one has a discrete [interacting cluster, Eq. (7)] and the other a continuous spectrum [environment, Eq. (8)]. Due to the continuous spectrum of the environment, a numerically favorable representation of the Green's function of the physical system G in terms of the Lehmann representation (see, for example, Ref. 55) is not possible. For evaluating quantities from the Green's function G, one therefore has to use a direct numerical integration, which works best on the Matsubara axis.

The cluster Green's function $\mathrm{g}_{\mathrm{interacting}}$ is determined by exact diagonalization of Eq. (7). We apply the Lanczos algorithm[56] to find the ground state and a band Lanczos method to obtain the Green's function. The band Lanczos method is initialized with a set of all annihilation and creation operators under consideration applied to the ground state. Thereby, we obtain the so-called Q matrices,[57] which are used to calculate the Green's function

$$\mathrm{g}^{\sigma\sigma'}_{\mathrm{interacting},ij}(\omega) = \sum_{\alpha}\left(\sum_{\gamma} Q^{\sigma}_{i\gamma}\frac{1}{\omega-\lambda_\gamma}Q^{\sigma'\dagger}_{j\gamma}\right)_{\alpha},$$

$$Q^{\sigma\dagger}_{i\gamma} = \begin{cases} \frac{1}{\sqrt{d}}\langle\gamma|\hat{c}^{\sigma\dagger}_i|\Psi_0\rangle & \text{particle part,} \\ \frac{1}{\sqrt{d}}\langle\Psi_0|\hat{c}^{\sigma\dagger}_i|\gamma\rangle & \text{hole part,} \end{cases}$$

$$\lambda_\gamma = \begin{cases} \omega_\gamma - \omega_0 & \text{particle part,} \\ \omega_0 - \omega_\gamma & \text{hole part.} \end{cases}$$

Essentially, this is the Lehmann representation for zero-temperature Green's functions. The sum over α denotes a sum over a possibly d-fold degenerate set of ground states. The sum over γ is over a set of orthonormal basis states having one particle more than the ground state (particle part) and one particle less than the ground state (hole part).

The Green's function of the environment $\mathrm{g}_{\mathrm{env}}$ is given analytically by the Green's function of a semi-infinite tight-binding chain[58]

$$\begin{aligned} \mathrm{g}_{\mathrm{env},i,j}(\omega) &= \upsilon_{0,i-j}(\omega) - \upsilon_{0,i+j}(\omega), \\ \upsilon_{i,j}(\omega) &= \frac{-i\ \mathrm{sign}[\mathrm{Im}(\omega)]}{\sqrt{4|t|^2-(\omega-\epsilon_s)^2}}\left(-\frac{\omega-\epsilon_s}{2|t|}\right. \\ &\quad \left. + i\ \mathrm{sign}[\mathrm{Im}(\omega)]\sqrt{1-\left(\frac{\omega-\epsilon_s}{2|t|}\right)^2}\right)^{|i-j|}, \end{aligned} \quad (10)$$

where $\upsilon_{i,j}$ is the retarded/advanced Green's function of the infinite tight-binding chain if the infinitesimal imaginary part (0^+) of ω is positive/negative.

VCA, the variational extension of CPT, is based on the self-energy functional approach (SFA).[48,49] In the SFA, one considers the Legendre-transformed Luttinger-Ward[59] functional $F[\Sigma]$, which is a universal functional of the self-energy, i.e., it does not depend on G_0. F generates the Green's function, i.e.,

$$\beta\frac{\delta F[\Sigma]}{\delta\Sigma} = -\mathrm{G}[\Sigma], \quad (11)$$

where β denotes the inverse temperature. Introducing the (nonuniversal) self-energy functional

$$\Omega[\Sigma,\mathrm{G}_0] = F[\Sigma] - \mathrm{Tr}\ln\left[\left(-\mathrm{G}_0^{-1}+\Sigma\right)\mathrm{G}_\infty\right] \quad (12)$$

(see Ref. 53 for a definition of G_∞), one recovers Dyson's equation at its stationary point:

$$\beta\frac{\delta\Omega[\Sigma,\mathrm{G}_0]}{\delta\Sigma} = -\mathrm{G}[\Sigma] + \left(\mathrm{G}_0^{-1}-\Sigma\right)^{-1} \stackrel{!}{=} 0. \quad (13)$$

Equation (13) is an equation for the physical self-energy Σ given the Luttinger-Ward functional $F[\Sigma]$ and the free Green's function G_0. The trace Tr is short for $\mathrm{Tr} \equiv \frac{1}{\beta}\sum_{\omega_n}\mathrm{tr}$, the sum is over fermionic Matsubara frequencies, and the small form trace tr denotes a sum over lattice sites and spin. The idea is that, due to its universality, $F[\Sigma]$ (and thus $\Omega[\Sigma,\mathrm{G}_0]$) can be evaluated exactly by exploiting a different system (so-called "reference system") which differs from the physical system by single-particle terms only. This reference system $\hat{\mathcal{H}}'$ is simpler, and thus exactly solvable. It is defined on a cluster tiling of the original lattice and has the same interaction as the original system $\hat{\mathcal{H}}$. The VCA reference system is chosen to be a cluster

decomposition of the original lattice, as the one introduced for CPT above. Comparing Eq. (12) for the full and the reference systems yields

$$\Omega[\Sigma,G_0] = \Omega'[\Sigma,g_0] + \mathrm{Tr}\,\ln\left[-\left(g_0^{-1}-\Sigma\right)\right] - \mathrm{Tr}\,\ln\left[-\left(G_0^{-1}-\Sigma\right)\right], \quad (14)$$

where lowercase g denotes Green's functions of the reference system. Thus, the SFA/VCA approximation consists in solving Eq. (13) in a restricted range of self-energies Σ, i.e., those produced by the reference system. In this way, the space of allowed Σ is spanned by the set of single-particle parameters of the reference system x'. This means that the functional $\Omega[\Sigma,G_0]$ [Eq. (14)] becomes a function of those parameters:

$$\Omega(\mathsf{x}') = \Omega'(\mathsf{x}') + \mathrm{Tr}\,\ln[-G(\mathsf{x}')] - \mathrm{Tr}\,\ln[-g(\mathsf{x}')]. \quad (15)$$

The stationarity condition determining the physical parameters (13) is then given by

$$\nabla_{\mathsf{x}'}\Omega(\mathsf{x}') \stackrel{!}{=} 0. \quad (16)$$

The Green's function of the physical system is obtained by the CPT relation (6). The matrix $T = g_0^{-1} - G_0^{-1}$ [Eq. (6)] in VCA contains all single-particle terms not included in the reference system (i.e., T_{inter}) as well as, in addition, the deviation introduced by VCA, $\Delta\mathsf{x} \equiv \mathsf{x}' - \mathsf{x}$ of the single-particle parameters of the reference system x' with respect to those of the original system x. In the following, we fully adopt the zero-temperature formalism, in which according expressions for the grand potential and related quantities may be readily evaluated.

1. Alternative: Self-consistent VCA

In Ref. 51, we explored an alternative version of VCA whereby the variational parameters x' were determined by a suitable self-consistent criterion, instead of looking for the stationary point of the grand potential Ω [Eq. (16)]. This alternative approach was introduced to treat systems out of equilibrium, although it can equally be adopted in equilibrium. The advantage of this approach is that the solution of a self-consistent equation is numerically easier than the search for a saddle point. The idea of this self-consistent approach is to use a reference system which resembles the full system best.

The strategy is to find those values x' for the set of parameters of the reference system which let the expectation values of their corresponding single-particle operators $\langle\hat{O}\rangle_{\mathrm{cluster},\mathsf{x}'}$ coincide with those of the full system $\langle\hat{O}\rangle_{\mathrm{CPT},\mathsf{x},\mathsf{x}'}$. Here, the angle brackets denote expectation values in the cluster and the full system coupled by CPT or VCA, respectively. Consider the onsite energies ϵ_f' and ϵ_s' as variational parameters. We will look for those cluster parameters ϵ_f' and ϵ_s', which fulfill the relations

$$\begin{aligned} \left\langle\hat{n}_\sigma^f\right\rangle_{\mathrm{cluster},\epsilon_f',\epsilon_s'} &\stackrel{!}{=} \left\langle\hat{n}_\sigma^f\right\rangle_{\mathrm{CPT},\epsilon_f,\epsilon_s,\epsilon_f',\epsilon_s'}, \\ \sum_i^{L-1}\left\langle\hat{n}_\sigma^i\right\rangle_{\mathrm{cluster},\epsilon_f',\epsilon_s'} &\stackrel{!}{=} \sum_i^{L-1}\left\langle\hat{n}_\sigma^i\right\rangle_{\mathrm{CPT},\epsilon_f,\epsilon_s,\epsilon_f',\epsilon_s'}. \end{aligned} \quad (17)$$

The sum is over all noninteracting sites included in the cluster. This amounts to solving a system of nonlinear equations in each step of the self-consistency cycle. In general, it is possible to vary each single-particle parameter individually. For reasons of keeping the numerics tractable, we use one ϵ_s' only, which we take to be the same for each orbital in the chain. Extension to a larger number of ϵ_s' is straightforward. To fix this parameter, we require the average particle density on the noninteracting sites to fulfill the condition (17). This corresponds to the condition presented in Ref. 51 [see Eq. (13) therein]. In some situations (see the following), we will alternatively consider the hybridization matrix element V' and the intracluster hopping t' as variational parameters, and proceed in an analogous way. Specifically, the particle number expectation values in Eq. (17) are replaced by hopping expectation values. Again, for t' we use a single variational parameter for hopping between all uncorrelated sites and fix it by requiring the mean value of hopping in the cluster and the full system to coincide. A discussion of this self-consistency condition in connection with (cluster) DMFT is given in Ref. 51. We use an improved multidimensional Newton-Raphson algorithm to find the roots of the system (17). In some parameter regions, no solution is found.

A comparison between results obtained via the usual SFA, i.e., as stationary points of the grand potential Ω, which we will now refer to as VCA_Ω, to those obtained by the above-mentioned self-consistent condition ($\mathrm{VCA}_{\mathrm{SC}}$) will be given in the results section (Sec. V).

2. Choice of variational parameters

In VCA, one can, in principle, optimize all possible single-particle parameters which are present in the original model, as well as additional ones. By adding bath sites not present in the original model, one includes dynamical contributions to the cluster Green's function.[48] The numerical difficulty increases with the number of variational parameters. For the $\mathrm{VCA}_{\mathrm{SC}}$ case, a multidimensional root-finding algorithm has to be adopted. For the VCA_Ω case, a saddle point in many dimensions has to be located. Since the allowed set of variational parameters limits the search space for the self-energies, one will find a solution in this restricted space only. It is therefore desirable to vary as many single-particle quantities as possible. A balance has to be found between a large space of available self-energies and numerically feasible multidimensional algorithms. Many works have addressed the question of which parameters are the most important to vary and how the choice of variational parameters will influence or limit the results.[50] As discussed in Refs. 60 and 61, it is important to include an overall chemical potential as a variational parameter in order to preserve thermodynamic consistency. As a compromise, we will take two variational parameters $\mathsf{x} = \{\epsilon_f,\epsilon_s\}$, which cover the overall chemical potential. Note that this amounts to shifting an overall onsite energy in the whole cluster plus an extra independent shift at the correlated site. For the variation of onsite energies, we observe the grand potential Ω to be maximal at the stationary point, which is in agreement with results for other models. Further parameters in the SIAM are the hopping t and the hybridization V. As discussed, for example, in Ref. 62, the variation of hopping parameters is not straightforward. For the VCA_Ω approach, we observe a maximum of Ω at $\Delta V =$

$-V$ in the center of two symmetric stationary points. The two symmetrically lying minima are equivalent due to the fact that the self-energy is an even power of V. As one tunes the parameters away from particle-hole symmetry, this stationary point is lost in the crossover region from the Kondo plateau to a doubly or unoccupied impurity (see Sec. V C). In this parameter region, the hopping t and hybridization V are probably not appropriate to be used as variational parameters within VCA_Ω.

In the following, we always choose the set $\mathsf{x} = \{V\}$ or $\mathsf{x} = \{V,t\}$ for calculations at particle-hole symmetry, which also includes $\{\epsilon_f,\epsilon_s\}$, since the variation of onsite energies will always yield zero deviations from the physical parameters and thus reproduce the CPT result here. For all other parameter regions, it is sufficient to consider $\mathsf{x} = \{\epsilon_f,\epsilon_s\}$ as variational parameters.

IV. GRAND POTENTIAL FOR REFERENCE SYSTEMS OF INFINITE SIZE

The reference system consists of two parts: a finite interacting system and a noninteracting system of infinite size, the environment. $\Omega'(\mathsf{x}')$ is given by the sum of the grand potentials of the interacting cluster ($\Omega'_{\mathrm{interacting}}$) and of the environment (Ω'_{env}) {which correspond to $\hat{\mathcal{H}}_{\mathrm{interacting}}$ [Eq. (7)] and $\hat{\mathcal{H}}_{\mathrm{environment}}$ [Eq. (8)]}. Here, we outline how to determine the grand potential for such kinds of reference systems. For the Green's function G within the CPT/VCA approximation, the Dyson equation is given in Eq. (6). The Green's function and T have the block structure

$$\mathrm{G} = \begin{pmatrix} \mathrm{G}_{cc} & \mathrm{G}_{ce} \\ \mathrm{G}_{ec} & \mathrm{G}_{ee} \end{pmatrix}, \quad \mathrm{T} = \begin{pmatrix} \mathrm{T}_{cc} & \mathrm{T}_{ce} \\ \mathrm{T}_{ec} & 0 \end{pmatrix}.$$

Up to this point, all matrices involving environment indices have infinite size. As far as the Green's function itself is concerned, this is no problem as we are primarily interested in G_{cc} for which the Dyson equation reduces to

$$\begin{aligned} \mathrm{G}_{cc} &= \mathrm{g}_{cc} + \mathrm{g}_{cc}\mathrm{T}_{cc}\mathrm{G}_{cc} + \mathrm{g}_{cc}\mathrm{T}_{ce}\mathrm{G}_{ec}, \\ \mathrm{G}_{ec} &= \mathrm{g}_{ee}\mathrm{T}_{ec}\mathrm{G}_{cc}, \end{aligned}$$

and therefore

$$\mathrm{G}_{cc} = \mathrm{g}_{cc} + \mathrm{g}_{cc}\tilde{\Sigma}_{cc}\mathrm{G}_{cc}, \quad \tilde{\Sigma}_{cc} := \mathrm{T}_{cc} + \mathrm{T}_{ce}\mathrm{g}_{ee}\mathrm{T}_{ec}.$$

A bit more tedious is the elimination of the explicit dependence on the environment part of G, as far as the grand potential, Eq. (15), is concerned. We start out from a form of the grand potential functional given by Sénéchal:[50]

$$\Delta\Omega := \Omega - \Omega' = -\mathrm{Tr}\,\ln(\mathbb{1} - \mathrm{Tg}). \tag{18}$$

In Appendix A, it is shown that $\Delta\Omega$ can be expressed solely in terms of cluster quantities

$$\Delta\Omega = -\mathrm{Tr}\,\ln(\mathbb{1}_{cc} - \tilde{\Sigma}_{cc}\mathrm{g}_{cc}). \tag{19}$$

Along the lines outlined in Ref. 50, the resulting integral can be regularized and expressed as

$$\begin{aligned} \Omega - \Omega'_{\mathrm{env}} = {} & \Omega'_{\mathrm{interacting}} + \mathrm{tr}(\mathrm{T}) - \frac{1}{\pi}\sum_\sigma \int_0^\infty d\omega \\ & \times \ln\left|\det\left(\mathbb{1}_{cc} - \tilde{\Sigma}^\sigma_{cc}(i\omega)\mathrm{g}^\sigma_{cc}(i\omega)\right)\right|. \end{aligned} \tag{20}$$

The quantities Ω' are the grand potentials of the uncoupled reference system. The constant infinite contribution Ω'_{env} is absorbed into the definition of Ω. It plays no further role as it does not depend on the variational parameters. This integral may be evaluated as suggested in Ref. 50 by integrating from 0 to Λ_1, from Λ_1 to Λ_2, and from Λ_2 to ∞. Λ_1 and Λ_2 represent two characteristic scales in the problem (for example, the smallest/largest eigenvalue of the Hamiltonian matrix). For the last part of the integral, a substitution $\tilde{\omega} = \frac{1}{\omega}$ is performed. We use an adaptive Gauss Legendre integrator for the evaluation.

V. RESULTS

We have evaluated several benchmarking dynamic quantities of the SIAM. In the following, results for the impurity density of states will be presented and compared to ED, NRG, and DMRG data. We will elaborate on the strengths and weaknesses of the methods as well as the comparison of CPT to VCA. Furthermore, we will discuss the relation between $\mathrm{VCA}_{\mathrm{SC}}$, where the variational parameters are determined self-consistently via Eq. (17) and VCA_Ω, where the variational parameters are defined at the stationary point of the grand potential. We will show that the Kondo resonance is reproduced within the framework of CPT/VCA and that the variational results fulfill certain analytic relations such as the Friedel sum rule [Eq. (23)]. The method will be shown to provide reasonably accurate results in a wide range of parameter regimes of the model. Low-energy properties related to the Kondo temperature T_K will be discussed in context with renormalization group results. The imaginary frequency Green's function and self-energy will be compared to CT-QMC results.

A. Even-odd effect: Choice of the impurity position

CPT/VCA rely on the Green's function of an interacting cluster of size L which is obtained by exact diagonalization. Due to this fact, it is unavoidable that some effects of the finite-size cluster influence the solution of the full system (except in the case of vanishing interaction strength, i.e., $U = 0$.) Therefore, suitable clusters have to be chosen on a basis of physical results. Some aspects of this are discussed by Balzer *et al.*[60] in the context of DMFT and VCA and by Hand *et al.*[63] in the context of DMRG. In this work, we consider interacting clusters of even size only. For these systems, the ground state does in general not suffer from spin degeneracy. Furthermore, the spatial position of the impurity is important. This can be inferred from the bath's density of states, which vanishes for $\omega = 0$ at every second site. It may also be seen in the structure of the ground state, for which the size of the degenerate sectors alternates with the geometrical size of the cluster. Throughout this work, we position the impurity f orbital at the beginning of the infinite chain, although essentially the same results are achieved by attaching it to an s orbital at site two, four, etc., inside the chain.

B. Spectral properties

The single-particle spectral function A_{ii}^{σ} is obtained from the retarded Green's function $G_{ii}^{\sigma,\mathrm{ret}}$ (see, e.g., Ref. 64):

$$A_{ii}^{\sigma}(\omega) = -\frac{1}{\pi}\,\mathrm{Im}\big[G_{ii}^{\sigma,\mathrm{ret}}(\omega)\big]. \tag{21}$$

The diagonal element at the impurity f orbital $A_{ff}^{\sigma}(\omega)$ describes the impurity density of states $\rho_f^{\sigma}(\omega)$. A physical property of the SIAM, which poses a challenge to numerical methods, is the Kondo-Abrikosov-Suhl resonance often referred to as the Kondo peak.[4] It arises in the parameter regime where the magnetic moment of the impurity is screened by the conduction electrons to form a singlet state.[65] The particle-hole symmetric model lies in the center of this Kondo region. This quasiparticle excitation is, for example, not captured in mean-field approaches. With increasing interaction strength U, the numerical solution becomes increasingly challenging.

In this section, we elaborate on the results for the density of states in the particle-hole symmetric case. A comparison of the local single-particle spectral function at the impurity f orbital as obtained by exact diagonalization and VCA_{Ω} is shown in Fig. 2. The ED result is for a 10-site system with open boundary conditions. The VCA_{Ω} result is for an infinite reference system, where the interacting part of the reference system was taken to be of size $L = 10$. An ED treatment of a finite-size SIAM can not reproduce the low-energy resonance at zero energy in the single-particle spectral function (see also Appendix B). It consists, in the particle-hole symmetric case, for an even number of sites (and open boundary conditions), of symmetrically lying excitations which shift closer to zero for increasing system size and represent a large energy scale. For an odd number of sites, a pole in the local single-particle Green's function of the impurity f orbtial will be present at $\omega = 0$. CPT as well as VCA are able to reproduce finite spectral weight at $\omega = 0$ (even for $0^+ \to 0$) since these methods are

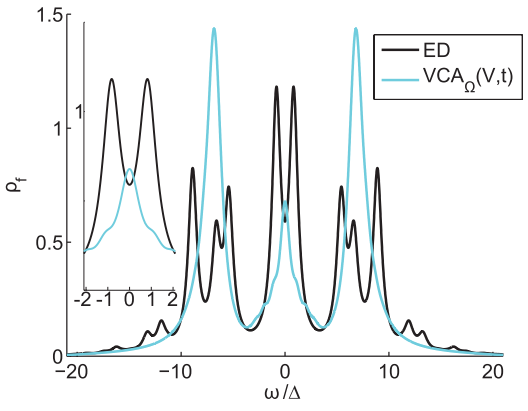

FIG. 2. (Color online) Comparison of the local single-particle spectral function at the impurity f orbital at particle-hole symmetry as obtained by exact diagonalization (ED) of a 10-site chain (black line) and VCA_{Ω} (cyan line). VCA_{Ω} was used with two variational parameters: the hopping t and the hybridization V considering a length of the interacting part of the reference system of $L = 10$. All data shown are for an interaction strength of $U/\Delta = 12$. All results have been obtained for a large numerical broadening $0^+ = 0.05$. The inset shows a zoom to the low-energy region.

formulated for an infinite system. The finite-size structure in the high-energy incoherent part of the spectrum, owing from the excitations of the interacting part of the reference system, is strongly reduced in VCA_{Ω}.

Results for the single-particle spectral function (21) of the impurity f orbital are shown in Fig. 3 for four different interaction strengths $U/\Delta = 4$, 8, 12, and 20. As a reference, the spectra obtained with NRG and DMRG from Peters[34] are plotted. Renormalization group approaches such as NRG are especially suited to reproduce the low-energy quasiparticle excitations of this model and therefore serve as a reference for our data. The spectra of Peters were obtained for a flat conduction electron density of states, which was mapped by linear discretization in energy space onto the corresponding orbitals of a semi-infinite chain. Our model is based on a semicircular density of states of the conduction electrons. The low-energy part of the spectra is comparable because we have chosen the only relevant parameter for the low-energy part of the spectrum: Δ accordingly. This parameter fully determines the influence of the conduction electrons on the impurity f orbital for low energies and therefore the low-energy part of the spectrum. The high-energy part of the spectrum may deviate slightly and is not directly comparable, but yields a crude reference. In addition, we have chosen here a very large numerical broadening of $0^+ = 0.05$ for reasons of comparison only. This value was used in the DMRG calculations and is needed there to obtain spectra using the correction vector method. This influences the width and the height of the Kondo resonance, located at $\omega = 0$. The CPT spectral weight at $\omega = 0$ appears too broad in the plot in comparison with the NRG result. This is only partly due to a large numerical broadening. Due to the nature of the CPT method, we can not expect it to reproduce the low-energy spectrum as well as RG calculations do. The height of the Kondo resonance appears too small in this figure because of the large 0^+. It converges with $0^+ \to 10^{-6}$ to the result predicted by scattering theory (see Fig. 5 and Sec. V C). The high-energy incoherent parts of the spectrum located at $\omega \approx -\epsilon_f$ and $\omega \approx -\epsilon_f + U$ develop more and more with increasing length of the interacting part of the reference system L. A comparison of the center of gravity of the high-energy incoherent part of the spectrum of the $L = 14$ site CPT result and the 50-site DMRG result is in reasonable agreement. There are spurious structures in the spectral density, originating from the cluster Green's function of the finite system, preventing continuous spectra to form. We would like to note that the accurate determination of the Green's function of the reference system is of prime importance. An inaccuracy in pole positions or pole weights for very small but nonvanishing weights will yield spurious artifacts in the spectra in the vicinity of $\omega = 0$.

To improve on the result of CPT, we considered the hopping matrix element t and the hybridization matrix element V as variational parameters. The parameters used for the evaluation of the reference system were determined with two different methods. VCA_{Ω} results are depicted in the plot for a length of the interacting cluster of $L = 10$. As shown in the figure, this method strongly reduces the finite-size peaks in the high-energy incoherent part of the spectrum. The width of that part of the spectrum is reproduced correctly for high values of U where the full width at half maximum (FWHM) within VCA

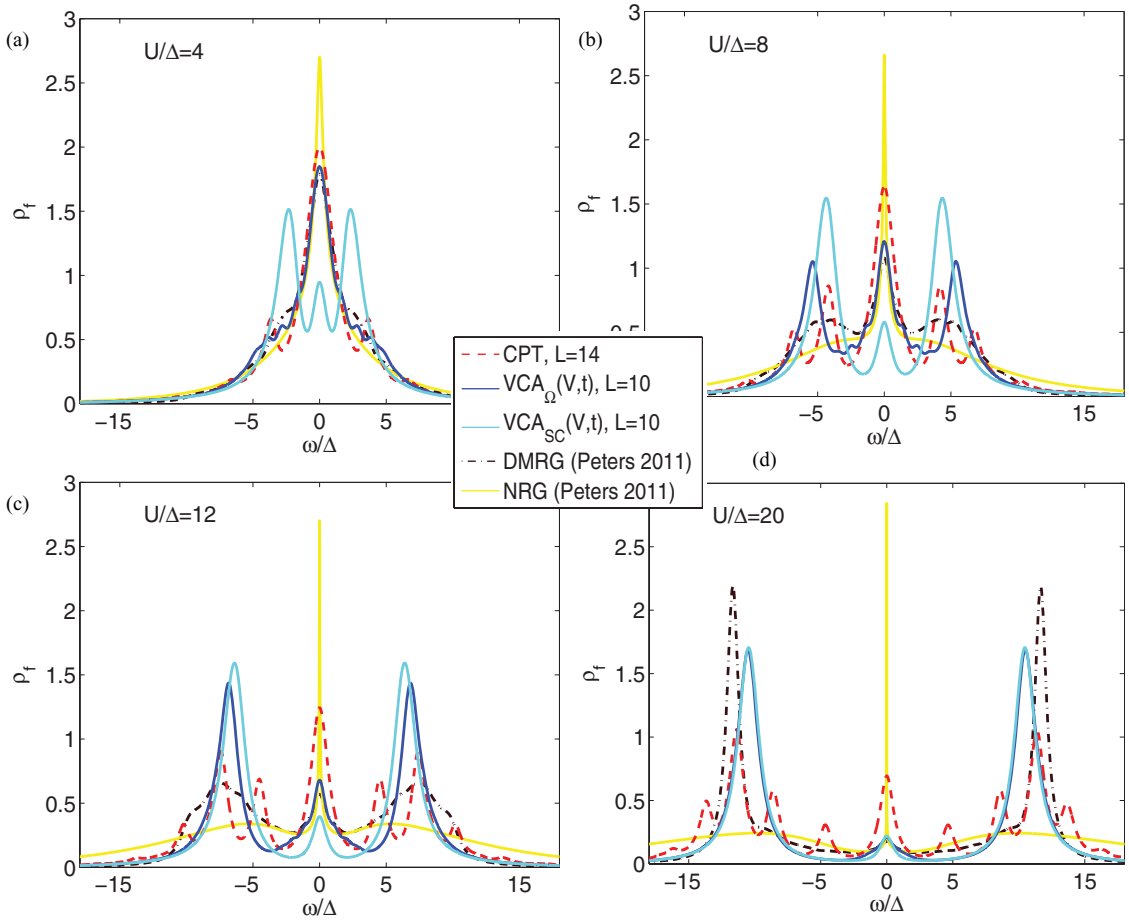

FIG. 3. (Color online) Single-particle spectral function at the impurity f orbital at particle-hole symmetry for different interaction strengths U. The interaction strengths shown are $U/\Delta = 4$ in the upper left figure (a), $U/\Delta = 8$ in the upper right figure (b), $U/\Delta = 12$ in the lower right figure (c), and $U/\Delta = 20$ in the lower right figure (d). Each plot shows the results obtained by CPT for a length of the interacting part of the reference system of $L = 14$ (dashed red line), VCA_Ω with two variational parameters: the hopping t and the hybridization V, which are determined by the stationary point of the grand potential Ω at a length of the interacting part of the reference system of $L = 10$ (blue line), $\mathrm{VCA}_{\mathrm{SC}}$ with the same variational parameters determined self-consistently at a length of the interacting part of the reference system of $L = 10$ (cyan line). All results have been obtained for a large numerical broadening $0^+ = 0.05$. As a reference, the NRG and DMRG results of Peters (Ref. 34) are plotted in yellow and dashed-dotted dark brown lines, respectively.

is given by $\approx 1.9\Delta$. This comes very close to the expected 2Δ (Refs. 21 and 66) of the high-energy atomic excitations. VCA improves the spectral properties of the Kondo resonance with respect to CPT, bringing it closer to the 50-site DMRG result. The data obtained using the self-consistent VCA approach $\mathrm{VCA}_{\mathrm{SC}}$ agree very well with the result based on VCA_Ω on the position of the spectral features. The respective weight, however, disagrees for low values of interaction strength U, which is due to the different values predicted for the variational parameters by the two procedures. One should note that the two broad Lorentzian high-energy peaks (in VCA_Ω as well as $\mathrm{VCA}_{\mathrm{SC}}$) consist of many excitations which will be revealed upon repeating this calculation with smaller 0^+.

A spatially resolved image of the spectral function, calculated with CPT, for the parameter set used in Fig. 3(c) is shown in Fig. 4. The qualitative picture would be the same in VCA; merely, the structures are slightly shifted. This view reveals how the perturbation, introduced by the impurity, is fading away slowly in an alternating fashion. At every second site away from the impurity, a dip at $\omega = 0$ is present, which is usually referred to as Fano dip.

A more detailed look on the spectral region of the Kondo resonance is provided in Fig. 5. The CPT/VCA_Ω data are compared to NRG and FRG data as well as results obtained from a restricted Hartree-Fock calculation from Karrasch *et al.*[31] The CPT/VCA results are plotted for lengths of the interacting part of the reference system $L = 2$, 4, 6, 8,and 10 for two different sets of parameters. The results for higher L are always located towards the center of the figure. The results corresponding to the resonance at $\omega = 0$ were obtained for the particle-hole symmetric model. For this set of parameters, we used the hybridization V as a variational parameter. The second peak shown centered around $\omega/\Delta \approx 0.8$ corresponds to a parameter set right at the border of the Kondo region. The variational parameters used away from particle-hole symmetry are $\mathbf{x} = \{\epsilon_f, \epsilon_s\}$. One can see that the CPT result is not converged for the $L = 10$ site interacting clusters yet. In contrast, the VCA_Ω result seems to converge much faster.

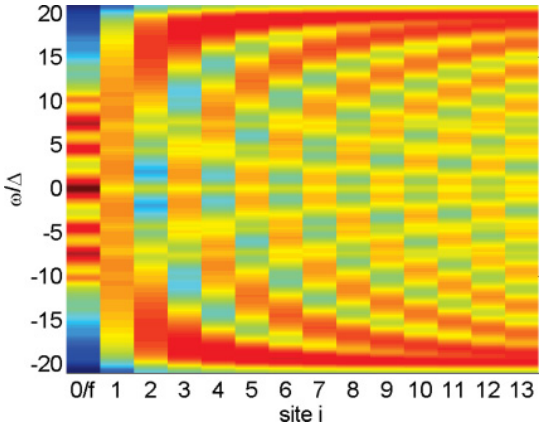

FIG. 4. (Color online) The local density of states [Eq. (21)] is shown resolved in real space. The spectrum was obtained using CPT on a $L = 14$ site interacting cluster. The impurity parameters were $U/\Delta = 12$, $\epsilon_f/\Delta = -6$, and the numerical broadening was set to $0^+ = 0.05$. The spectrum shown in Fig. 3(c) corresponds to the data shown for the impurity f orbital located at site 0 in the plot. The density plot is shown with a logarithmically scaled coloring from blue indicating zero to red indicating high values.

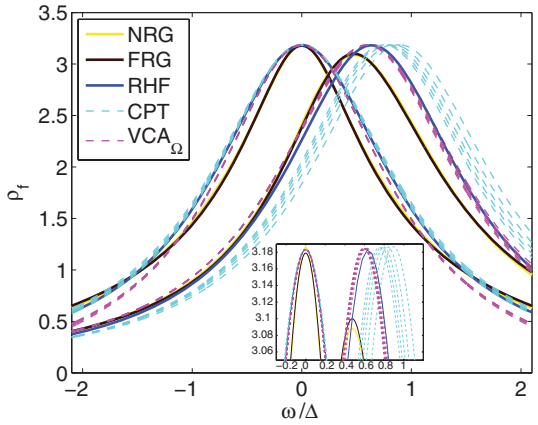

FIG. 5. (Color online) Magnification of the Kondo resonance in the density of states of the impurity f orbital. Shown are calculations for two different sets of parameters. The resonance at $\omega = 0$ corresponds to the particle-hole symmetric model: $U/\Delta = 20$, $\epsilon_f/\Delta = -10$, while the resonance away from zero corresponds to a set of parameters right at the edge of the Kondo region: $U/\Delta = 20$, $\epsilon_f/\Delta = 0$. For comparison, we show NRG (yellow line) and FRG (dark brown line) data as well as results obtained from a restricted Hartree-Fock calculation (blue line) from Karrasch *et al.* (Ref. 31). (The NRG results are partially hidden by the FRG results.) The CPT result (cyan line) is shown for lengths of the interacting part of the reference system $L = 2$, 4, 6, 8, and 10. Results for higher L are always located towards the center of the plot. In the particle-hole symmetric case, VCA$_\Omega$ (magenta line) was performed with variational parameters $\mathsf{x} = \{V\}$ for $L = 2$, 4, 6, 8,and 10. Away from particle-hole symmetry, VCA$_\Omega$ was performed with variational parameters $\mathsf{x} = \{\epsilon_f, \epsilon_s\}$ for the same lengths of the interacting part of the reference system L. For the CPT/VCA calculations, a numerical broadening of $0^+ = 10^{-6}$ was used. The inset shows a zoom to the top region of the peaks.

Although in the plot it looks like the VCA result does not improve much upon a restricted Hartree-Fock calculation, we will show in the following that CPT/VCA yields results in all parameter regimes of the SIAM which can not be reproduced within a mean-field treatment.

The variational parameters obtained for the two sets of parameters shown in Fig. 5 are presented in Fig. 6. In addition to the VCA$_\Omega$ parameters, which were used for the results above, the variational parameters obtained in VCA$_{\mathrm{SC}}$ are also depicted. We plotted the difference of the parameter of the reference system x' to the physical parameter x: $\Delta\mathsf{x}$. All deviations $\Delta\mathsf{x}$ appear to converge to zero with increasing length L of the interacting part of the reference system. Notice that the self-consistent approach always leads to a $\Delta\mathsf{x}$ of greater magnitude with respect to VCA$_\Omega$. Remarkably, the spectra obtained by VCA$_\Omega$ and VCA$_{\mathrm{SC}}$ for the parameter set $\mathsf{x} = \{\epsilon_f, \epsilon_s\}$ are in very good agreement even though the variational parameters are rather different. The most striking difference is that the self-consistent approach yields a negative $\Delta\epsilon_f$, while the Ω-based VCA yields a positive $\Delta\epsilon_f$. This is, however, compensated by the different $\Delta\epsilon_s$. Using the hybridization V as a variational parameter, the ΔV obtained by VCA$_\Omega$ and VCA$_{\mathrm{SC}}$ agree rather well. Remarkably, the resulting density of states is very different, which shows that the calculation is extremely sensitive to this parameter.

The low computational effort of CPT/VCA proves advantageous for calculating spectra. The VCA procedure (for a 12-site interacting cluster) usually converges in minutes to hours on a standard workstation PC, while more demanding numerical methods often need days to a week to converge. Furthermore, the spectra are exactly determined from the Lehmann representation, and no ill-posed analytical continuation is required in comparison to methods working in imaginary time or imaginary frequency space. To our knowledge, the most accurate spectra available for this model so far are published in Ref. 67.

Overall, one may conclude that CPT, VCA$_\Omega$, and VCA$_{\mathrm{SC}}$ reproduce a Kondo resonance, which fulfills the Friedel sum rule [Eq. (23)] for $0^+ \to 10^{-6}$. The VCA results improve drastically upon the CPT data, which may be seen in a much faster convergence in L and a suppression of finite-size effects, especially in the high-energy part of the spectrum, which in addition has the expected width within VCA. VCA$_\Omega$ and VCA$_{\mathrm{SC}}$ agree rather well on the position of the spectral features. However, they assign very different spectral weight to them at low values of interaction strength U.

C. Impurity density of states and occupation

The occupation of the impurity f orbital is given at $T = 0$ by

$$\langle n_\sigma^f \rangle = \frac{1}{2} + \frac{1}{\pi} \int_0^\infty d\omega \, \mathrm{Re}\big[\mathrm{G}_{ff}^\sigma(i\omega)\big]. \tag{22}$$

This integral may be evaluated from the imaginary frequency Green's function, which in turn is directly accessible within CPT/VCA.

To see whether CPT/VCA are good approximations in all parameter regions of the SIAM, we vary the onsite energy of the impurity ϵ_f at fixed interaction strength U. The local impurity density of states at the chemical potential ($\omega = \mu =$

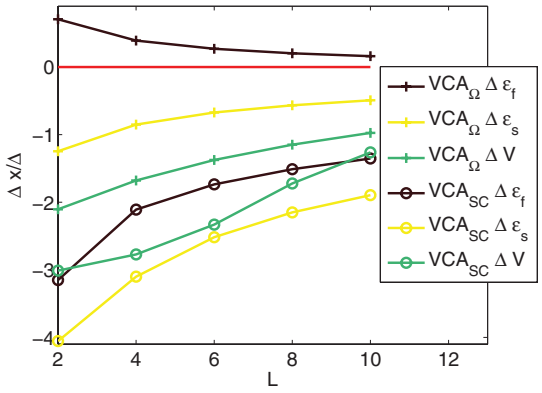

FIG. 6. (Color online) Evolution of the variational parameters for the data shown in Fig. 5. Shown is the difference of the parameters of the reference system $\mathbf{x}'$ to the physical parameter $\mathbf{x}$: $\Delta\mathbf{x} = \mathbf{x}' - \mathbf{x}$. Parameters obtained by VCA$_\Omega$ (crosses) are compared to those obtained by VCA$_{SC}$ (circles). The variational parameters $\Delta\epsilon_f$ (dark brown line) and $\Delta\epsilon_s$ (yellow line) correspond to the calculation away from particle-hole symmetry in Fig. 5, while the parameter ΔV (olive line) corresponds to the calculation at particle-hole symmetry. Lines are only guides to the eye.

0) and the impurity occupation number are plotted for various lengths of the interacting part of the reference system $L = 2, 4, 6,$ and 8 for the same model parameters. The VCA$_\Omega$ result is shown in Fig. 7, a VCA$_{SC}$ calculation in Fig. 8, and the CPT data in Fig. 9.

We start out by discussing the VCA$_\Omega$ result (Fig. 7). The variational parameters $\mathbf{x}$ used within VCA$_\Omega$ are the onsite

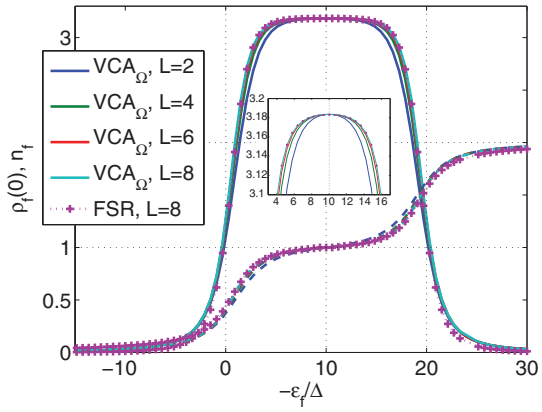

FIG. 7. (Color online) Density of states of the impurity f orbital (solid lines) obtained via VCA$_\Omega$ at $\omega = 0$ and average occupation of the impurity (dashed lines) for different lengths of the interacting part of the reference system $L = 2, 4, 6,$ and 8 (blue, green, red, and cyan lines) as a function of the impurity onsite energy ϵ_f. The Coulomb interaction U is kept constant at $U/\Delta = 20$. The numerical broadening used is $0^+ = 10^{-6}$. The set of single-particle parameters considered for variation within VCA$_\Omega$ is $\mathbf{x} = \{\epsilon_f, \epsilon_s\}$. Note that here the point $\epsilon_f = -\frac{U}{2}$ corresponds to the particle-hole symmetric case. The Friedel sum rule [Eq. (23)] was applied to the $L = 8$ result (dotted violet line). It is fulfilled to a very good approximation in the Kondo region and far outside of it. Small deviations from the Friedel sum rule arise at the crossover region to an empty or doubly occupied impurity. The inset shows a zoom to the Kondo plateau.

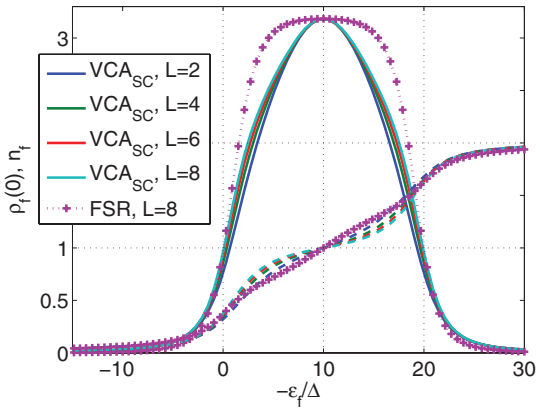

FIG. 8. (Color online) Density of states of the impurity f orbital (solid lines) obtained via VCA$_{SC}$ at $\omega = 0$ and average occupation of the impurity (dashed lines) for different lengths of the interacting part of the reference system $L = 2, 4, 6,$ and 8 (blue, green, red, and cyan lines) as a function of the impurity onsite energy ϵ_f. The Coulomb interaction U is kept constant at $U/\Delta = 20$. The numerical broadening used is $0^+ = 10^{-6}$. The set of single-particle parameters considered for variation within VCA$_{SC}$ is $\mathbf{x} = \{\epsilon_f\}$. Note that here the point $\epsilon_f = -\frac{U}{2}$ corresponds to the particle-hole symmetric case. The Friedel sum rule [Eq. (23)] was applied to the $L = 8$ result (dotted violet line). It is fulfilled in a region of $n_f \lesssim 0.4$ and $n_f \gtrsim 1.6$.

energy of the impurity ϵ_f and the onsite energies of the uncorrelated cluster sites ϵ_s. The density of states $\rho_f(0)$ display a pronounced plateau which is related to the existence of a quasiparticle peak (Kondo resonance) pinned at the chemical potential. The parameter regions leading to an empty ($-\epsilon_f < 0$) or to a doubly occupied ($-\epsilon_f > U$) impurity do not

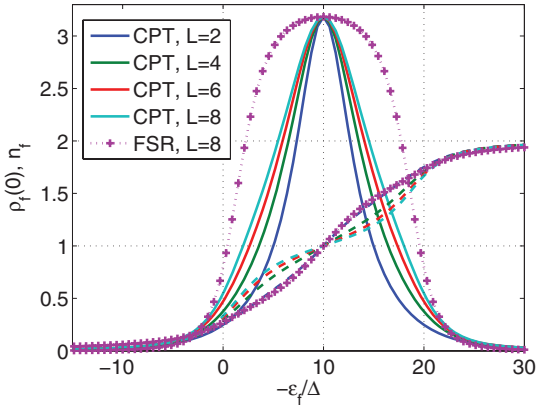

FIG. 9. (Color online) Density of states of the impurity f orbital (solid lines) obtained via CPT at $\omega = 0$ and average occupation of the impurity (dashed lines) for different lengths of the interacting part of the reference system $L = 2, 4, 6,$ and 8 (blue, green, red, and cyan lines) as a function of the impurity onsite energy ϵ_f. The Coulomb interaction U is kept constant at $U/\Delta = 20$. The numerical broadening used is $0^+ = 10^{-6}$. Note that here the point $\epsilon_f = -\frac{U}{2}$ corresponds to the particle-hole symmetric case. The Friedel sum rule [Eq. (23)] was applied to the $L = 8$ result (dotted violet line). It is drastically violated. However, the results are far from converged for the small lengths of the interacting part of the reference system considered here.

show a pinning of the Kondo resonance at the Fermi energy, as expected. In the half-filled region which lies in-between, virtual spin fluctuations lead to a pronounced quasiparticle peak at the chemical potential. We observe that the result converges with increasing length of the interacting part of the reference system L to the physically expected result. Due to the variational parameters considered, the deviations of the results as a function of L are rather small as compared to CPT, where the results change significantly with increasing size of the reference system (see Fig. 9). We expect CPT calculations in the empty or doubly occupied regions to converge rather fast (within a few sites), while calculations in the Kondo regime, and particularly in the crossover region, may fully converge only at very large (i.e., exponentially) sizes of the reference system.[63] This is inferred from the spin-spin correlation function in the cluster which is observed to decay sufficiently fast outside the Kondo plateau (i.e., it is effectively zero at the boundary of the cluster) but shows long-range correlations inside the plateau. The $\mathrm{VCA_{SC}}$ results are obtained with one variational parameter $\mathsf{x} = \{\epsilon_f\}$. The reason for not using $\mathsf{x} = \{\epsilon_f, \epsilon_s\}$ again is that the result is almost the same as that obtained with VCA_Ω (see Fig. 7). However, in some (small) parameter regions, the numerical evaluation becomes difficult. The $\mathrm{VCA_{SC}}$ data shown in Fig. 8 show a clear improvement as compared to CPT but does not reach the quality of the VCA_Ω result in terms of convergence in system size.

The Friedel sum rule[5,68,69] (FSR) provides an exact relation between the extra states induced below the Fermi energy by a scattering center and the scattering phase shift. It also holds true for interacting systems. This gives a relation between the f-orbital occupation $\langle n^f \rangle$, and the density of states at the Fermi energy:

$$\rho_f(0) = \frac{1}{\pi \Delta} \sin^2\left(\frac{\pi \langle n^f \rangle}{2}\right). \tag{23}$$

In our case, the mean occupation in the Kondo regime is $\langle n^f \rangle \approx 1$. Since both the occupancy of the f orbital and the magnitude of the local density of states at the Fermi energy can be evaluated independently, we can check the validity of the Friedel sum rule in our approximation. Results are shown in Fig. 7 applied to the $L = 8$ site VCA_Ω data. The VCA_Ω results fulfill the Friedel sum rule almost in the whole Kondo region. At the crossover to an empty or doubly occupied impurity, the Friedel sum rule is not fulfilled exactly any more but approximated very well. Further outside, the agreement is again excellent. The variational parameters of VCA are crucial to fulfill the Friedel sum rule as can be seen from a CPT calculation (Fig. 9), which violates it in all parameter regions. It appears that VCA_Ω with variational parameters $\mathsf{x} = \{\epsilon_f, \epsilon_s\}$ naturally drives the system to fulfill this condition. The $\mathrm{VCA_{SC}}$ result (Fig. 8) violates the sum rule too. This is not a feature of $\mathrm{VCA_{SC}}$ in general, but has to do rather with the choice of variational parameters, which was just $\mathsf{x} = \{\epsilon_f\}$ in this case. The $\mathrm{VCA_{SC}}$ result for two variational parameters $\mathsf{x} = \{\epsilon_f, \epsilon_s\}$ looks qualitatively like the respective VCA_Ω result.

Scanning the interaction strength U at fixed impurity onsite energy ϵ_f confirms the presence of the Kondo behavior. Shown in Fig. 10 are results obtained with VCA_Ω using the same variational parameters $\mathsf{x} = \{\epsilon_f, \epsilon_s\}$ as above. In the weakly

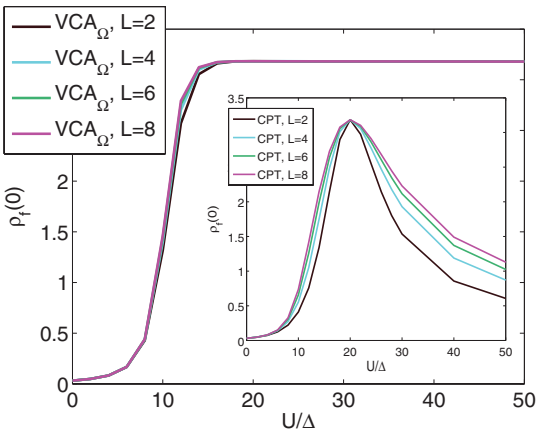

FIG. 10. (Color online) Density of states of the impurity f orbital at $\omega = 0$ for different lengths of the interacting part of the reference system $L = 2$, 4, 6, and 8 (dark brown, cyan, olive, and magenta lines) as a function of the interaction strength U. The impurity onsite energy ϵ_f is kept constant at $\epsilon_f/\Delta = -10$. The numerical broadening is chosen to be $0^+ = 10^{-6}$. The set of single-particle parameters considered for variation within VCA_Ω is $\mathsf{x} = \{\epsilon_f, \epsilon_s\}$. The inset shows the CPT results.

correlated part ($U/\Delta \lesssim 5$), the density of states at the chemical potential is low. The intermediate region ($5 \lesssim U/\Delta \lesssim 15$) signals the crossover to the Kondo regime. For larger U, the Kondo regime is reached with an impurity occupation of $\langle n^f \rangle \approx 1$, which may be inferred from the Friedel sum rule. In the inset of the figure, the CPT results for the same lengths of the interacting part of the reference system L are shown. The CPT results are by far not converged for the interacting cluster sizes considered here. This emphasizes the importance of the variational parameters.

Our results in Figs. 7 and 10 agree very well with those of calculations based on X-operator technique exercised by Lobo *et al.*[38] In their work, a strong-coupling perturbation theory is applied starting from the Anderson molecule as a basis and using the Friedel sum rule as a condition to fix the position of an infinitely narrow conduction band.

Analytic considerations (see Appendix B) allow insight into the behavior of the Friedel sum rule in ED, CPT, and VCA. There, it is shown that ED always has to violate the Friedel sum rule, while CPT always fulfills it in the particle-hole symmetric case. This comes about in the first place because the height of the Kondo resonance at $\omega = 0$ does not depend on the self-energy. A pinning of the Kondo resonance, however, can only be achieved via the improved self-energy contributions obtained within VCA.

The results of this section clearly show that VCA is able to capture the basic physics of the SIAM in every parameter region. The improvement obtained by going over from CPT to VCA is crucial to fulfill exact analytic relations. Moreover, we have shown that CPT/VCA is clearly superior to ED calculations. VCA is, even at small L, capable of fulfilling the FSR also away from particle-hole symmetry due to a pinning of the Kondo resonance at the Fermi energy. This pinning can be attributed to the better approximation of the self-energy of VCA with respect to CPT.

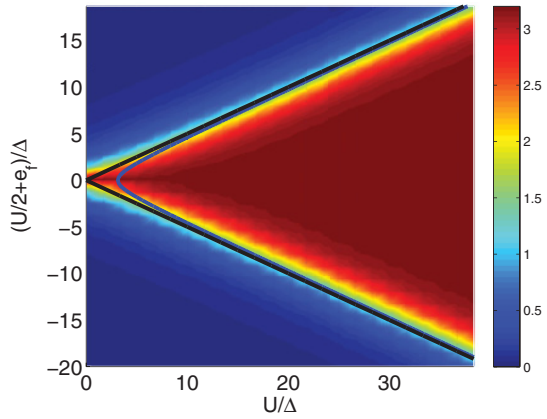

FIG. 11. (Color online) In this plot, a "phase diagram" of the SIAM is shown. The quantity on the z axis is the density of states in the impurity ρ_f at $\omega = 0$ (i.e., the height of the Kondo resonance). The results are obtained with VCA$_\Omega$ for a set of variational parameters $\mathbf{x} = \{\epsilon_f, \epsilon_s\}$, $L = 6$, and $0^+ = 10^{-6}$. The black line indicates the different regions obtained from an atomic-limit calculation. In the right cone, local moments are to be expected. While in the upper region, the impurity is expected to be empty and in the lower half to be doubly occupied. The blue curve shows the onset of a spurious magnetic state as obtained by a mean-field treatment (see text).

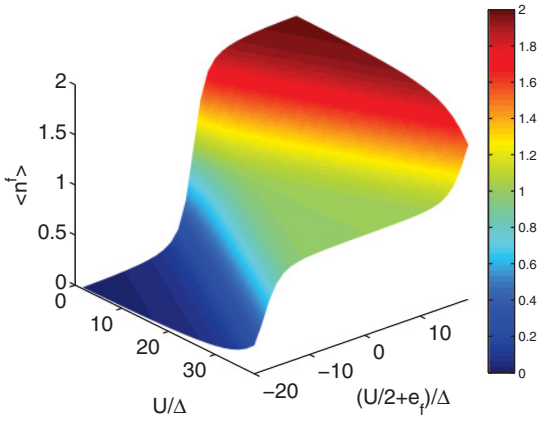

FIG. 12. (Color online) Average particle density in the impurity $\langle n^f \rangle$ as a function of U and ϵ_f for the same parameters as in Fig. 11.

D. Crossover diagram

To delve into the CPT/VCA results for the whole parameter range of the SIAM, a "phase diagram" is presented in this section. This should be understood to be a mere scan of the parameters U and ϵ_f because the model does not undergo a phase transition. The density of states of the impurity at the chemical potential $\rho_f(0)$ is shown in Fig. 11 in a density plot. This figure essentially shows the height of the Kondo resonance as a function of interaction strength and onsite energy of the impurity. The different regimes of the SIAM, as obtained by an atomic-limit calculation, are indicated as black lines. These lines divide the physics into regions where the impurity is doubly, singly, or not occupied. In the singly occupied region ($\frac{U}{2} > |\epsilon_f + \frac{U}{2}|$), local moments and their screening are expected to appear. This region, which bestrides the cone enclosed by black lines, is the region where Kondo physics may take place within this approximation. The parameter regions where the impurity is empty or doubly occupied lie above and below this cone. More sophisticated methods will lead to a smearing out of the border of these regions and introduce a crossover area with competing effects. A boundary expected between a single resonance and a spurious local moment behavior where the single resonance is split into two for spin up and spin down, respectively, is obtained by mean-field theory.[65] In the mean-field approach, the density-density interaction of the impurity Hamiltonian is replaced by a spin-dependent density exposed to the mean contribution of the other spins' density. The mean-field boundary is then obtained by replacing the mean-field parameters $\langle n^f_\uparrow \rangle$ and $\langle n^f_\downarrow \rangle$ by the particle number n and magnetization m. Setting the magnetization to $m = 0^+$ in the self-consistent equations yields the implicit result $U_c = \pi\Delta[1 + \cot(\pi \frac{\langle n_f \rangle}{2})^2]$ and $\epsilon_{f,c} = \Delta\{\cot(\pi \frac{\langle n_f \rangle}{2}) + \frac{\pi}{2}(1 - \langle n_f \rangle)[1 + \cot(\pi \frac{\langle n_f \rangle}{2})^2]\}$. The plot shows that the Kondo plateau is reproduced very well by VCA$_\Omega$. The results appear almost converged for lengths $L \approx 6$ of the interacting part of the reference system. Increasing L yields better results in the crossover region. Results obtained by means of CPT do not reproduce the Kondo plateau very well for small L.

The average impurity occupation for the same parameter region is shown in Fig. 12. The result obtained with VCA$_\Omega$ clearly shows the Kondo plateau where the impurity is singly occupied. The parameter regions of a doubly occupied or empty impurity lead to a density of states in the impurity which is zero at the chemical potential (compare to Fig. 11).

The results of this section have been obtained using VCA$_\Omega$ with variational parameters $\mathbf{x} = \{\epsilon_f, \epsilon_s\}$. It should be noted that using only $\mathbf{x} = \{\epsilon_f\}$ already yields good results. As mentioned in Sec. V C, CPT needs very large values L to yield the same quality of the results as VCA does with much smaller values of L.

E. Low-energy properties, Kondo temperature

In this section, we examine the low-energy properties of the symmetric SIAM. In the strong-coupling limit, a single scale, the Kondo temperature T_K, governs the low-energy physics.[5] The Kondo temperature T_K is known from Bethe ansatz results for the particle-hole symmetric SIAM (Refs. 70 and 71)

$$T_K = \sqrt{\frac{\Delta U}{2}}\, e^{-\gamma \frac{\pi}{8\Delta} U}, \quad \gamma = 1. \tag{24}$$

This scale, which is inversely proportional to the spin-flip rate of the impurity, divides the physics of the SIAM into two regions: a local moment behavior of the impurity, where the spin is free, and a low-temperature region where the local spin and the conduction electrons become entangled and form a singlet state.[72]

Quantities which depend inversely on T_K are the effective mass m^* and the static spin susceptibility χ_m. The Kondo temperature may furthermore be extracted from the width or weight of the Kondo resonance in the local density of states of the impurity f orbital. We investigate and compare the results for the scale T_K obtained from the direct determination of T_K (from the FWHM and the spectral weight of the Kondo

resonance) and the inverse quantities m^* and χ_m. We find that the results of all four measurements turn out to yield the correct qualitative behavior in VCA_Ω . However, in a region where the dependence of T_K is exponentially dependent on the interaction strength U, the exponential prefactor is not predicted correctly. Therefore, we introduce a scaling factor γ [Eq. (24)], which turns out to be the same for all four ways of determining T_K. In particular, this factor is independent of the set of model parameters used. The scaling factor may be calculated semianalytically for a reference system consisting of a two-site interacting cluster and the semi-infinite environment within VCA_Ω and $\mathrm{VCA}_{\mathrm{SC}}$ ($\mathbf{x} = \{V\}$). The calculation for VCA_Ω leads to an integral expression for the stationary point of the grand potential Ω with respect to ΔV from which the optimal ΔV can be obtained numerically (see Appendix C). The Kondo scale may be determined from the so-obtained values of $V'(U) = \Delta V(U) + V$ by

$$T_K(U) \propto \left(\frac{V'(U)}{U}\right)^2. \tag{25}$$

This leads to a perfect exponential behavior as defined in Eq. (24) with

$$\gamma = 0.6511.$$

The issue of obtaining an exponential scale but not the correct exponent for the functional dependence on U is common to various approximate methods [for example, variational wave functions where the issue was cured by introducing an extended ansatz by Schönhammer,[73] saddle-point approximations of a functional integral approach,[74] or FRG (Ref. 75)]. A faint analogy may be drawn here to Gutzwiller approximation, where an exponential energy scale in U arises by a renormalized hybridization parameter V,[76] which is also the case for VCA_Ω.

The self-consistent calculation for $\mathrm{VCA}_{\mathrm{SC}}$ also leads to an integral expression for the determination of ΔV. This expression is obtained by requiring the expectation values of the hopping from the impurity f orbital to the neighboring site in the reference system to be the same as the expectation value in the physical system. This procedure does not yield an exponential scale in U. The optimal cluster parameter V' shows spurious behavior as a function of U. We conclude that $\mathrm{VCA}_{\mathrm{SC}}$ with $\mathbf{x} = \{V\}$ can not reproduce the low-energy properties of the SIAM even qualitatively, while VCA_Ω yields the correct behavior apart from an exponential factor.

1. *Effective mass–quasiparticle renormalization*

The effective mass m^* is defined as the quasiparticle renormalization[31]

$$\begin{aligned}\frac{m^*(U)}{m^*(0)} &= 1 - \left.\frac{d\left[\mathrm{Im}\Sigma^\sigma_{ff}(i\omega,U)\right]}{d\,\omega}\right|_{\omega=0^+} \\ &= \left.\frac{d\left[\mathrm{Im}G^\sigma_{ff}(i\omega,U)\right]}{d\,\omega}\right|_{\omega=0^+} \\ &\quad\times\left(\left.\frac{d\left[\mathrm{Im}G^\sigma_{ff}(i\omega,0)\right]}{d\,\omega}\right|_{\omega=0^+}\right)^{-1},\end{aligned} \tag{26}$$

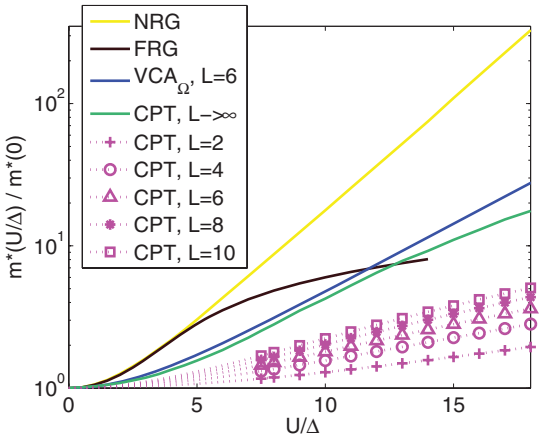

FIG. 13. (Color online) Effective mass m^* of the Kondo resonance [Eq. (26)] as a function of interaction strength U. We plot CPT results for lengths of the interacting part of the reference system $L = 2$, 4, 6, 8, and 10 (magenta), the $L \to \infty$ extrapolated CPT result (olive line), as well as VCA_Ω results (blue line). The data points for the CPT resulting in the low-U region are not shown to avoid messing up the plot. The variational parameter used for the VCA_Ω result was $\mathbf{x} = \{V\}$. The VCA_Ω data were obtained for $L = 6$. For CPT as well as VCA_Ω, we used a numerical broadening of $0^+ = 10^{-6}$. For comparison, the results obtained by NRG (yellow line) and FRG (dark brown line) are shown (Ref. 31).

where we introduced the dependence on the interaction strength U explicitly. In the Kondo regime, this quantity becomes inversely proportional to the Kondo temperature.

We want to answer the question as to whether the Kondo scale is approximately captured by CPT/VCA or not. Therefore, we compare the functional form and the exponent obtained from the effective mass and the analytic result for T_K [Eq. (24)]. The result for the effective mass obtained within VCA_Ω is shown in Fig. 13. The variational parameter used was $\mathbf{x} = \{V\}$. The functional form is reproduced well by VCA_Ω (i.e., it starts out quadratically and goes over to an exponential behavior in the Kondo region). However, the exponent $(\frac{\pi}{8\Delta})$ is not reproduced correctly. VCA_Ω yields a lower exponent of $\approx(\gamma\frac{\pi}{8\Delta})$. The factor γ is defined in Appendix C, determined from a semianalytical calculation of T_K within VCA_Ω . This additional factor is the same for all initial parameters (within the Kondo regime), it is particularly independent of Δ. If plotted over a scaled U axis $U' = \frac{1}{\gamma}U$, the VCA_Ω result would lie on top of the NRG data. However, using larger sizes of the interacting part of the reference system does not lead to much better results regarding γ. It is to be expected that a significant improvement can only be obtained using exponentially large L. The CPT result shows a very different convergence behavior in L, which is rather slow.

An attempt was made to extrapolate the CPT data to $L \to \infty$ by a simple $\frac{1}{L}$ scaling. It is interesting to observe that this extrapolated curve coincides nicely with the VCA result ($L = 6$) in the low-U region. However, we expect this extrapolation based on small L to be insufficient to capture the exponential scaling of the data in L. Note that since in CPT the self-energy is taken from the cluster, the CPT results for the effective mass coincide with ED results for systems of size L.

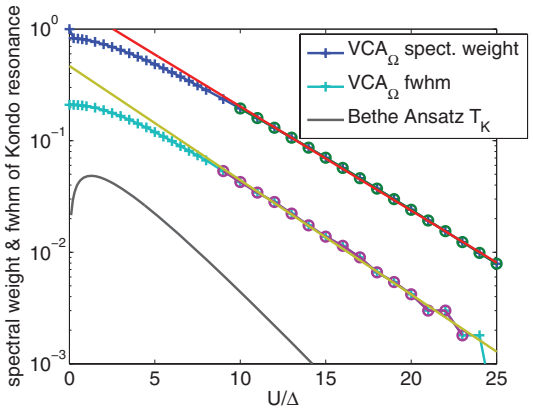

FIG. 14. (Color online) VCA_Ω results for the spectral weight (blue) and full width at half maximum (olive) of the Kondo resonance as a function of interaction strength U. The variational parameter used was $\mathbf{x} = \{V\}$. A length of the interacting part of the reference system of $L = 6$ sites and a numerical broadening of $0^+ = 10^{-6}$ were used for this calculation. Data points marked with a circle were used for the fit of the exponential function in the Kondo region. The black line shows the Kondo temperature T_K as obtained by Bethe ansatz calculations [Eq. (24)].

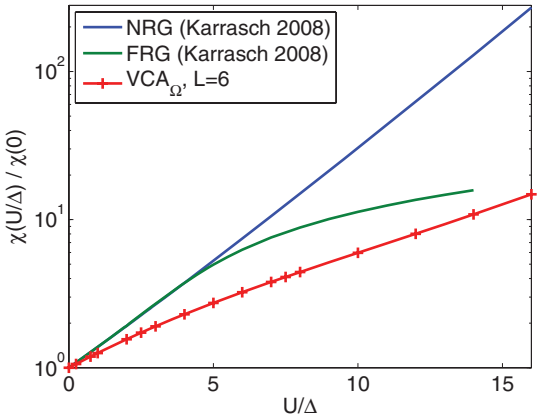

FIG. 15. (Color online) The static spin susceptibility χ_m [Eq. (27)] is shown as a function of interaction strength U. The variational parameter used was $\mathbf{x} = \{V\}$. The data were obtained for $L = 6$ sites and $0^+ = 10^{-6}$. For comparison, the results obtained by NRG (blue line) and FRG (green line) are shown (Ref. 31).

2. *Kondo spectral weight and half width*

Since the height of the Kondo resonance is fixed by the Friedel sum rule (23), the width and the weight (area) of the peak are proportional to the Kondo temperature T_K. Obtaining the spectral weight or FWHM of the Kondo resonance from the spectrum introduces a large uncertainty. Nevertheless, we made an attempt to get an idea of the behavior of T_K. We fixed the spectral weight by the first minimum to the left and to the right of the central peak (see also Ref. 63). In general, the effective mass and static spin susceptibility will yield more reliable results, but it is instructive to compare these four ways of determining T_K.

Shown in Fig. 14 is the evolution of the spectral weight and the FWHM of the Kondo resonance with increasing interaction strength U. The data were acquired using VCA_Ω with a variational parameter $\mathbf{x} = \{V\}$ for the particle-hole symmetric SIAM. Within the uncertainty, the same exponential behavior for the Kondo temperature T_K is obtained as by calculating the effective mass in VCA_Ω.

3. *Static spin susceptibility*

The static spin susceptibility χ_m is given by the linear response to an applied magnetic field B in the z direction:

$$\chi_m(U) = -\left.\frac{d(\langle n^f_\uparrow\rangle - \langle n^f_\downarrow\rangle)}{d\,B}\right|_{B=0}. \tag{27}$$

In the Kondo regime, this quantity too becomes inversely proportional to the Kondo temperature. For the calculations in this section, we introduce an additional spin-dependent term in the impurity Hamiltonian [Eq. (3)]

$$\hat{\mathcal{H}}_{\mathrm{magnetic}} = \sum_\sigma \sigma \frac{B}{2} f^\dagger_\sigma f_\sigma. \tag{28}$$

The static spin susceptibility χ_m as obtained with VCA_Ω is shown in Fig. 15. The variational parameter used was $\mathbf{x} = \{V\}$. As a reference, the results of NRG and FRG (Ref. 31) are shown. The behavior of the VCA result is good for small interaction strength U. The VCA result shown for $L = 6$ appears already converged while the CPT result would require much larger systems.

We would like to highlight that VCA_Ω reproduces an energy scale T_K. Results from direct calculation of T_K, calculation of the effective mass m^*, and the static spin susceptibility χ_m yield the correct functional form, but not the right exponent.

F. Benchmarking CPT/VCA against continuous-time quantum Monte Carlo

In this section, we compare CPT/VCA results to QMC data. We obtained the Monte Carlo results using the continuous-time quantum Monte Carlo (CT-QMC) code of the TRIQS (Ref. 77) toolkit and its implementation of the hybridization expansion (CT-HYB) (Ref. 78) algorithm using Legendre polynomials.[79] This method enables access to very low temperatures and is especially suited to obtain low-energy properties.[40] The CT-QMC data provide statistically exact and reliable results to test our data.

All CT-QMC calculations were done for a single-impurity orbital at $U = 0.8$ and $\epsilon_f = -0.4$. We used a semicircular hybridization function with half bandwidth $D = 2$ and $V = 0.3162$. This setup corresponds to the same model under investigation here. The value for the interaction strength $U = 0.8$ was chosen because of the relatively low expected Kondo temperature of $\beta_K = T_K^{-1} \approx 100$. For all calculations, 1.2×10^9 MC updates where conducted, with a sweep size of 100 updates, plus a 10% thermalization period.

To ensure that the Kondo resonance is correctly reproduced by CT-QMC, we evaluated the Matsubara Green's function for various values of inverse temperature β. The height of the Kondo resonance is given by the Friedel sum rule [Eq. (23)] to be $\mathrm{Im}[G_{ff}(i\omega_n = 0)] = -10$ for the parameters used here ($\Delta = 0.1$). To obtain $\mathrm{Im}[G_{ff}(i\omega_n = 0)]$, we extrapolate twice,

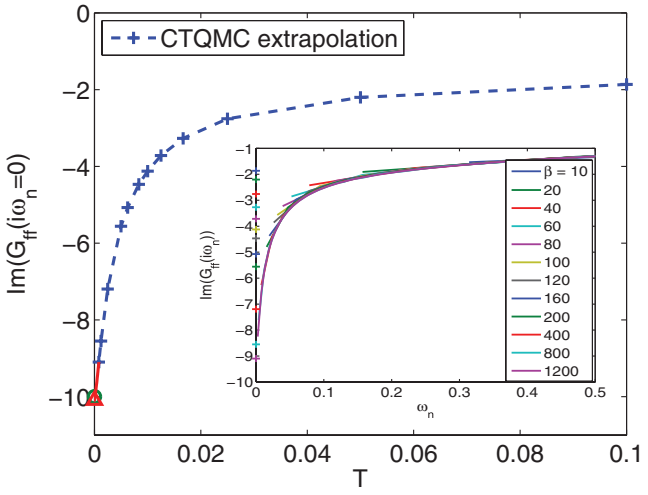

FIG. 16. (Color online) CT-QMC result for the imaginary part of the impurity Green's function extrapolated to $i\omega_n = 0$. An extrapolation to zero temperature is attempted, which yields a good agreement with the result predicted by the Friedel sum rule (green circle) within the uncertainty (red triangle). The inset shows the imaginary part of the impurity Green's function for various β (see legend) and the extrapolated points at $i\omega_n = 0$.

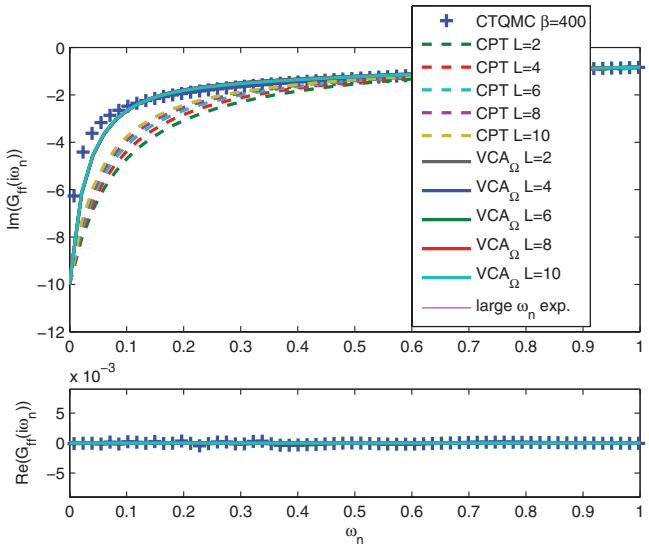

FIG. 17. (Color online) Comparison of the Matsubara impurity Green's function $G_{ff}(i\omega_n)$ obtained by CT-QMC ($\beta = 400$), CPT, and VCA$_\Omega$. The CPT/VCA results were obtained for $L =$ 2, 4, 6, 8,and 10. The real part shown in the lower part of the figure is zero. The Friedel sum rule prediction of $\mathrm{Im}[G_{ff}(i\omega_n = 0)] = -10$ is fulfilled by all methods. The legend of this figure serves as well as legend for Figs. 18 and 19. That is why the last entry {large $i\omega_n$ exp. [see Eq. (29)]} is displayed in the legend but is missing in the graph of this figure.

first in $i\omega_n \to 0$ for each β, then we use these results and extrapolate to $T \to 0$. The extrapolation to $i\omega_n \to 0$ is done linearly using the first two Matsubara frequencies. The imaginary part of $G_{ff}(i\omega_n)$ and the extrapolated value to $i\omega_n \to 0$ are shown in the inset of Fig. 16 for $\beta \in [10,1200]$. Those extrapolated values are plotted as a function of temperature (Fig. 16). These data points are then extrapolated to $T \to 0$ using a fit by a rational model function. The result clearly shows the onset of the Kondo resonance when the temperature is lowered below the Kondo temperature T_K. The extrapolation to $T = 0$ shows very good agreement $\{\mathrm{Im}[G_{ff}(i\omega_n = 0)] \approx -10.1\}$ with the result expected from the Friedel sum rule within the uncertainty. It is important to note that the CT-QMC results converge very nicely in β. Although for higher β, lower Matsubara frequencies become available, the overall shape of the Green's function does not change significantly.

Therefore, we may compare the $T = 0$ CPT/VCA results for the Green's function and self-energy to the CT-QMC data. The Matsubara Green's functions of the impurity f orbital $G_{ff}(i\omega_n)$ obtained by CT-QMC ($\beta = 400$), CPT, and VCA are shown in Fig. 17. We use $\beta = 400$ as a compromise between low temperatures and still reliable CT-QMC results (within manageable computation time). The $\beta = 400$ result was obtained using 65 Legendre coefficients. A detailed analysis has shown that this number is sufficient to get high-frequency moments of the self-energy Σ accurately. The VCA$_\Omega$ results were obtained with one variational parameter $\mathsf{x} = \{V\}$ for $U =$ 0.8, $\Delta = 0.1$, and $0^+ = 10^{-6}$ in the particle-hole symmetric case. For the CPT calculation, we used the same parameters. For both methods, we considered lengths of the interacting part of the reference system of $L = 2$, 4, 6, 8,and 10. The VCA result lies near the CT-QMC data but underestimates the slope of the curve at low $i\omega_n$. The VCA result provides a huge improvement upon CPT for the lengths of the interacting part of the reference system shown here. The real part of $G_{ff}(i\omega_n)$ is exactly zero within CPT/VCA, as it is supposed to be. Note that the value of $G_{ff}(i\omega_n = 0)$ which is fixed by the Friedel sum rule is exactly reproduced within CPT and VCA for the particle-hole symmetric case. The same is shown for the self-energy of the impurity f orbital $\Sigma_{ff}(i\omega_n)$ in Fig. 19. From the imaginary part of $\Sigma_{ff}(i\omega_n)$, one can infer the convergence of the CPT/VCA result with larger length of

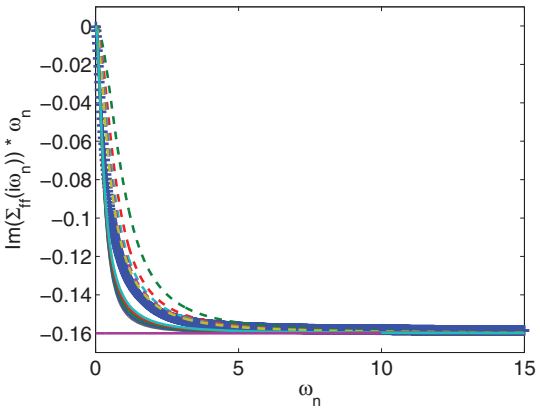

FIG. 18. (Color online) Comparison of the self-energy of the impurity $\Sigma_{ff}(i\omega_n)$ times energy ω_n obtained by CT-QMC ($\beta =$ 400), CPT, and VCA$_\Omega$. The CPT/VCA results were obtained for $L = 2$, 4, 6, 8,and 10. CPT as well as VCA$_\Omega$ become exact for high Matsubara frequencies. An expansion of $\Sigma(i\omega_n)$ for large $i\omega_n$ [Eq. (29)] is additionally shown [straight line at $-(\frac{U}{2})^2$]. The legend for this figure is the same as for Fig. 17 and is displayed there.

the interacting part of the reference system L. The real part of the self-energy $\{\mathrm{Re}[\Sigma_{ff}(i\omega_n)] = \mu = -e_f = \frac{U}{2} = 0.4\}$ is again exactly reproduced within CPT/VCA.

In the following, we discuss the self-energy $\Sigma(i\omega_n)$ for the two interesting cases of very-low and very-high Matsubara frequency. We start out by conducting an expansion of the self-energy $\Sigma(z)$ for high Matsubara frequencies ($z = i\omega_n \to \infty$), which shall be outlined here briefly. The self-energy matrix is defined by

$$\Sigma(z) = \mathrm{G}_0^{-1} - \mathrm{G}^{-1} = z - \mathrm{T} - \mathrm{G}^{-1}.$$

Here, T is the one-particle part of the Hamiltonian. In the particle-hole symmetric case considered here, it contains all the hoppings as well as the onsite energy of the impurity $\epsilon_f = -\frac{U}{2}$. We conduct a series expansion in powers of z^{-1} of $\Sigma(z)$. Apart from the real constant T_{ii}, all z-dependent terms of $\Sigma_{ii}(z)$ are antisymmetric in z. Therefore, even powers in $z^{\pm 2l}$, $l > 0$ vanish. Expanding the Green's function $\mathrm{G}(z)$ yields, for the self-energy $\Sigma(z)$,

$$\Sigma(z) = -\mathrm{T} - z\sum_{m=1}^{\infty}(-1)^m X^m,$$

$$X = \sum_{n=1}^{\infty} z^{-n} C_n,$$

$$(C_n)_{ij} = \langle\Psi_0|\, a_i(\Delta\hat{\mathcal{H}})^n a_j^\dagger\,|\Psi_0\rangle + (-1)^n\langle\Psi_0|\, a_j^\dagger(\Delta\hat{\mathcal{H}})^n a_i|\Psi_0\rangle\,,$$

where $\Delta\hat{\mathcal{H}} = \hat{\mathcal{H}} - \omega_0$ and ω_0 is the ground-state energy of $\hat{\mathcal{H}}$. Collecting powers of z yields a cumulantlike expansion for the self-energy $\Sigma(z)$:

$$\Sigma(z) = \sum_{n=1}^{\infty} z^{-n}\,\Sigma_n, \quad \text{where}$$

$$\Sigma_0 = -T + C_1 \quad \text{and} \quad \Sigma_1 = C_2 - C_1^2\,.$$

Here, we consider the zeroth and first order in z^{-1} only and obtain, for $\Sigma(i\omega_n)$,

$$\Sigma_{ff}(i\omega_n) = \frac{U}{2} - \frac{i}{\omega}\left(\frac{U}{2}\right)^2 + \mathcal{O}\left(\frac{1}{i\omega_n}\right)^3, \qquad (29)$$

where the self-energy at the impurity f orbital Σ_{ff} is the only nonvanishing matrix element of Σ_{ij}. This result is plotted as a reference in Fig. 19. Due to the nature of the CPT/VCA approximation, these methods always yield the exact self-energy for high Matsubara frequency as shown in Fig. 18.

The low-energy properties examined in the previous section depend basically on the slope of the Matsubara Green's function at $(i\omega_n) = 0^+$. The results shown in Figs. 17 and 19 show that this slope is underestimated by CPT/VCA in comparison to CT-QMC, at least at the small lengths of the interacting part of the reference system available.

The above results suggest a possible application of VCA as an impurity solver for zero-temperature DMFT. The results would not suffer from a bath truncation error as in exact diagonalization-based DMFT. A big advantage would be the low demand on computational power of VCA as well as the approximate reproduction of the main features of the local density of states (i.e., Kondo resonance and high-energy incoherent part of the spectrum).

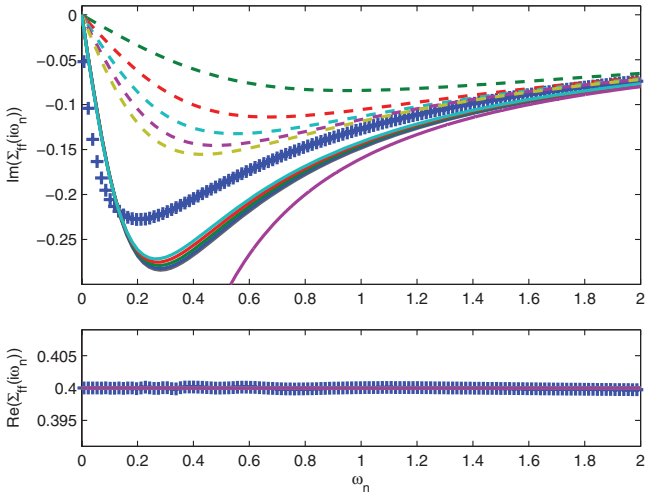

FIG. 19. (Color online) Comparison of the imaginary part of the self-energy of the impurity $\mathrm{Im}[\Sigma_{ff}(i\omega_n)]$ obtained by CT-QMC ($\beta = 400$), CPT, and VCA_Ω. The CPT/VCA results were obtained for $L = 2$, 4, 6, 8,and 10. An expansion of $\Sigma(i\omega_n)$ for large $i\omega_n$ [Eq. (29)] is shown in addition (magenta line which diverges at zero). CPT/VCA always reproduces the exact self-energy for high Matsubara frequencies. The legend for this figure is the same as for Fig. 17 and is displayed there.

G. Introducing a symmetry-breaking field

We explore the possibility to improve the VCA results achieved by varying the internal single-particle parameters of the model by introducing a symmetry-breaking "spin-flip field" at the impurity f orbital. The term added to the impurity

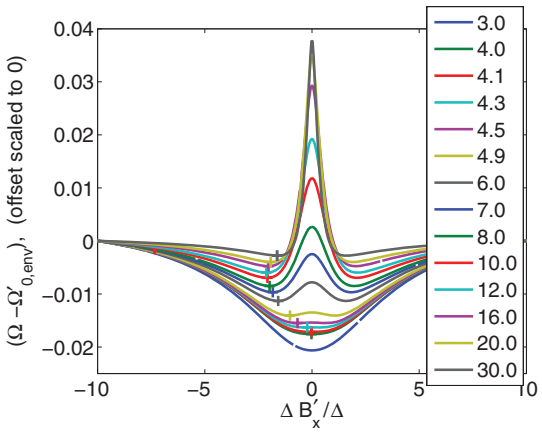

FIG. 20. (Color online) Grand potential $\Omega - \Omega'_{0,\mathrm{env}}$ [Eq. (20)] as a function of the interaction strength U/Δ (see legend). The data were obtained by studying a $L = 4$ site interacting cluster coupled to a semi-infinite lead. The numerical broadening used was $0^+ = 10^{-6}$. The crosses indicate the respective minimum of the grand potential. There exists a critical $U_c/\Delta \approx 4.3$ above which a finite B'_x is preferred by the system.

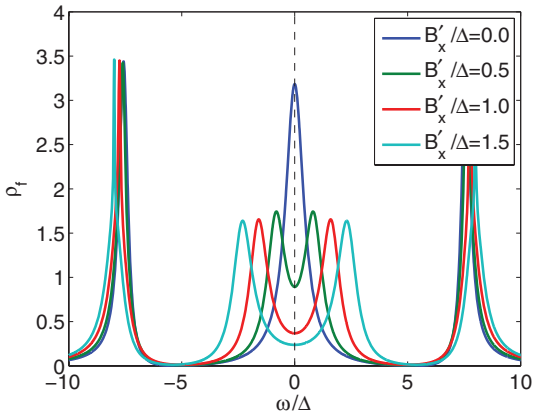

FIG. 21. (Color online) The splitting of the Kondo resonance caused by an applied magnetic field in the x direction is shown for different values of the auxiliary field B'_x. The plots were obtained using VCA (i.e., the physical field B_x is always zero). Instead of taking the parameter B'_x at the stationary point of the grand potential (this value would be $B'_x/\Delta \approx 1.9$ for the parameters used), we explicitly plug in a fixed value for B'_x. The length of the interacting part of the reference system used was $L = 6$ for the model parameters $U/\Delta = 12$. The numerical broadening used was $0^+ = 10^{-6}$.

Hamiltonian (3),

$$\hat{\mathcal{H}}_{\text{flip}} = B_x\,(f^\dagger_\uparrow f_\downarrow + f^\dagger_\downarrow f_\uparrow), \tag{30}$$

explicitly breaks the conservation of spin in the cluster solution. We are interested in the model with a physical parameter $B_x = 0$ so this variable may only attain a finite value as a variational parameter B'_x in the reference system. We investigate the particle-hole symmetric model at $V = 0.3162$ and $t = 1$. Our findings indicate that any finite value of B'_x splits the Kondo resonance and has thus to be discarded on physical grounds for the system under investigation.

While this prevents the application of this field to improve the VCA results, it gives very nice insight in the physics of the SIAM as described by CPT/VCA. We find that a critical interaction strength U_c depending on the length of the interacting part of the reference system exists, which separates solutions which would prefer a finite B'_x from those which would prefer $B'_x = 0$. The critical interaction strength for $L = 4$ is given by $U_c/\Delta \approx 4.3$. The grand potential $\Omega - \Omega'_{0,\text{env}}$ is plotted for various interaction strengths U in Fig. 20. For an analogous calculation for $L = 6$ site interacting clusters, a value of $U_c/\Delta \approx 4.1$ is achieved. The mean-field result would yield a critical interaction strength $U_c/\Delta = \pi$ for the parameters used here. We interpret this value as a signature of the onset of local moment behavior. The values for U_c are of course not to be taken literally, they depend very much on the finite size of the cluster under investigation.

The splitting of the Kondo resonance caused by a nonzero variational field B'_x is shown in Fig. 21. The value of $U/\Delta = 12$ used for this calculation lies in the region above U_c where the system prefers a nonzero field B'_x.

VI. CONCLUSIONS

In this work, we have applied the variational cluster approach (VCA) to the single-impurity Anderson model. We devised a cluster tiling applicable to this nontranslationally invariant model, which leads to a cluster with a discrete spectrum and an environment having a continuous spectrum. We have derived an expression for the change of the grand potential originating from the coupling of the impurity to the semi-infinite bath.

We have compared results for the single-particle dynamics to data obtained by exact diagonalization and cluster perturbation theory (CPT). We found that the variational extension made by the VCA is vital for a good reproduction of the expected behavior of the SIAM. The CPT/VCA spectra both yield a Kondo resonance in the impurity density of states with the correct height as predicted by the Friedel sum rule. A close look at the Kondo resonance shows that the VCA is able to reproduce the resonance and the functional behavior for the Kondo temperature in a remarkable way. The Kondo temperature is expected to show exponential behavior in interaction strength in the Kondo regime. VCA yielding an exponential behavior, however, tends to underestimate the exponent. Comparison of dynamic quantities to continuous-time quantum Monte Carlo solidifies the origins of this behavior. The high-energy incoherent part of the spectrum shows strong finite-size effects within CPT which are partly removed by virtue of the VCA. VCA furthermore reproduces the expected position and width of the high-energy part of the spectrum. For the asymmetric model, the Friedel sum rule is fulfilled in all parameter regions implying that the Kondo resonance is pinned at the chemical potential in the Kondo region. In addition, a self-consistent formulation of the VCA, previously introduced in the context of nonequilibrium problems,[51] was explored. Results obtained by the self-consistent approach show agreement with results obtained by VCA based on the grand potential for the density of states of the impurity f orbital. Thereby the positions of the spectral features agree very well with the traditional VCA result, while the spectral weight distribution may deviate especially for small values of interaction strength. Comparison to results obtained from Bethe ansatz, renormalization group approaches, and data obtained from X-Operator based calculations show reasonable agreement for all quantities investigated.

In conclusion, while there are certainly more accurate methods to deal with a single-quantum-impurity model,[23] especially at low energies, our work shows that VCA is a flexible and versatile method which provides reasonably accurate results with modest computational resources. Here, the VCA self-consistency condition proves to be crucial. This allows us to obtain the same accuracy that CPT would provide with a much larger, inaccessible, interacting cluster size. One of the advantages is the flexibility of the method, i.e., it is straightforward to extend it to many impurities, nonequilibrium problems,[51] etc. In the spirit of NRG,[29] one could improve on the present results by carrying out an appropriate unitary transformation on the bath such that the bath hoppings decay with increasing distance from the impurity. In this work, we do not include such an improvement and choose a constant hopping sequence [Eq. (2)] since our

goal is to benchmark VCA/CPT only. Nevertheless, a hybrid approach combining NRG and VCA would be an interesting extension of this work.

ACKNOWLEDGMENTS

We are grateful to R. Peters for providing his DMRG and NRG data shown in Fig. 3 and to C. Karrasch for providing his FRG and NRG data shown in Figs. 5, 13, and 15. M.N. thanks K. Schönhammer, T. Pruschke, M. Knap, and P. Dargel for fruitful discussions. We thank O. Parcollet and M. Ferrero for important, critical feedback concerning the convergence of our CT-QMC data. We made use of the CT-QMC code of the TRIQS (Ref. 77) toolkit. This work is partly supported by the Austrian Science Fund (FWF) P18551-N16. M.N. acknowledges financial support by the Förderungsstipendium of the TU Graz.

APPENDIX A: GRAND POTENTIAL

Here, we outline the proof of Eq. (19). We start out from Eq. (18), i.e.,

$$\Delta\Omega = -\mathrm{Tr}\,\ln(\mathbb{1} - \mathrm{Tg}).$$

Taylor expansion yields

$$\Delta\Omega = \sum_{n=1}^{\infty} \frac{1}{n} \{\mathrm{Tr}\,[(\mathrm{Tg})^n]_{cc} + \mathrm{Tr}\,[(\mathrm{Tg})^n]_{ee}\}. \tag{A1}$$

Due to $\mathrm{T}_{ee} = 0$, each term g_{ee} in the first trace occurs only in the form

$$\tilde{\mathrm{g}}_{cc} := \mathrm{T}_{ce}\mathrm{g}_{ee}\mathrm{T}_{ec}.$$

The expressions in the second part of Eq. (A1) can be modified by a cyclic permutation of the factors in the argument of the trace

$$\mathrm{Tr}\,(\mathrm{T}_{ec}\mathrm{g}_{cc}\ldots\mathrm{T}_{ce}\mathrm{g}_{ee}) = \mathrm{Tr}\,(\mathrm{g}_{cc}\ldots\mathrm{T}_{ce}\mathrm{g}_{ee}\mathrm{T}_{ec}),$$

in which g_{ee} again only occurs in the dressed form $\tilde{\mathrm{g}}_{cc}$. If we replace all occurrences of $\mathrm{T}_{ce}\mathrm{g}_{ee}\mathrm{T}_{ec}$ by $\tilde{\mathrm{g}}_{cc}$, then there are no matrices T_{ce} and T_{ec}, respectively, left. Hence, we can as well introduce in Eq. (18) the following replacements:

$$\mathrm{g}_{ee} \to \tilde{\mathrm{g}}_{cc}, \quad \mathrm{T}_{ce} \to \mathbb{1}_{cc}, \quad \mathrm{T}_{ec} \to \mathbb{1}_{cc}, \quad \mathbb{1} \to \mathbb{1}_{cc},$$

as it leads in the series expansion to the same expressions. The argument in Eq. (18) then assumes the form

$$\mathbb{1} - \mathrm{Tg} = \mathbb{1} - \begin{pmatrix} \mathrm{T}_{cc} & \mathbb{1}_{cc} \\ \mathbb{1}_{cc} & 0_{cc} \end{pmatrix}\begin{pmatrix} \mathrm{g}_{cc} & 0_{cc} \\ 0_{cc} & \tilde{\mathrm{g}}_{cc} \end{pmatrix} = \begin{pmatrix} b & -\tilde{\mathrm{g}}_{cc} \\ -\mathrm{g}_{cc} & \mathbb{1} \end{pmatrix},$$

with the abbreviation $b := \mathbb{1} - \mathrm{T}_{cc}\mathrm{g}_{cc}$. Prompted by the Schur complement, the matrix can be factorized into upper and lower triangular block matrices

$$\begin{pmatrix} b & -\tilde{\mathrm{g}}_{cc} \\ -\mathrm{g}_{cc} & \mathbb{1} \end{pmatrix} = \begin{pmatrix} b & 0 \\ -\mathrm{g}_{cc} & \mathbb{1} - \mathrm{g}_{cc}b^{-1}\tilde{\mathrm{g}}_{cc} \end{pmatrix}\begin{pmatrix} \mathbb{1} & -b^{-1}\tilde{\mathrm{g}}_{cc} \\ 0 & \mathbb{1} \end{pmatrix},$$

such that the determinant is easily computed since the determinant of the second matrix is 1 and the determinant of the first matrix is simply the product of the determinants of the diagonal blocks, resulting in

$$\begin{aligned} \det\begin{pmatrix} b & -\tilde{\mathrm{g}}_{cc} \\ -\mathrm{g}_{cc} & \mathbb{1} \end{pmatrix} &= \det(b)\det\left(\mathbb{1} - b^{-1}\tilde{\mathrm{g}}_{cc}\mathrm{g}_{cc}\right) \\ &= \det(b - \tilde{\mathrm{g}}_{cc}\mathrm{g}_{cc}) \\ &= \det(\mathbb{1} - (\mathrm{T}_{cc} + \mathrm{T}_{ce}\mathrm{g}_{ee}\mathrm{T}_{ec})\mathrm{g}_{cc}). \end{aligned}$$

The final result for Eq. (18) reads as

$$\Delta\Omega = -\mathrm{Tr}\,\ln(\mathbb{1}_{cc} - \tilde{\Sigma}_{cc}\mathrm{g}_{cc}).$$

APPENDIX B: BEHAVIOR OF THE FRIEDEL SUM RULE WITHIN ED, CPT, AND VCA

It is possible to gain a somewhat deeper understanding of the behavior of the FSR within ED/CPT/VCA by considering the local Green's function at the impurity f orbital

$$\mathrm{G}_{ff}(z) = [z - \epsilon_f - \Gamma(z) - \Sigma(z)]^{-1}, \tag{B1}$$

where $\Gamma(z)$ is the contribution due to the single-particle terms of the hybridization and $\Sigma(z)$ the self-energy due to the local interaction (for details, see Appendix C). In the following, we consider the particle-hole symmetric case. We are interested in the behavior of the retarded Green's function $\mathrm{G}^{\mathrm{ret}}_{ff}(\omega) = \mathrm{G}_{ff}(\omega + i0^+)$ at the Fermi energy ($\omega = 0$), which we investigate by taking the limit on the Matsubara axis $\mathrm{G}^{\mathrm{ret}}_{ff}(0) = \lim_{\nu\to 0^+} \mathrm{G}_{ff}(i\nu)$. We expand the self-energy $\Sigma(i\nu)$ up to linear order in ν and rewrite the expression using the definition of the effective quasiparticle mass m^* [see Eq. (26)] as

$$\begin{aligned} \Sigma(i\nu) &\approx -\epsilon_f + i\mathrm{Im}[\Sigma(0)] + i\nu\left.\frac{\partial \mathrm{Im}[\Sigma(i\nu)]}{\partial(i\nu)}\right|_{0^+} + i\mathcal{O}[(i\nu)^2] \\ &\approx -\epsilon_f + i\nu(1 - m^*). \end{aligned}$$

Inserting into Eq. (B1), we obtain

$$\begin{aligned} \mathrm{G}^{\mathrm{ret}}_{ff}(0) &= \lim_{\nu\to 0^+} \mathrm{G}_{ff}(i\nu) \\ &= \lim_{\nu\to 0^+} (i\{m^*\nu - \mathrm{Im}[\Gamma(i\nu)]\} - \mathrm{Re}[\Gamma(i\nu)])^{-1}. \end{aligned} \tag{B2}$$

We will now investigate two separate, general cases of an ED and a CPT/VCA treatment of the Green's function. From Eq. (B2), it is easy to see that the remnant m^* of the impurity self-energy and therefore the self-energy itself does not contribute to the Friedel sum rule. In outlining how to notice this, we simultaneously show that a discrete spectrum of the conduction band (as obtained for example in ED) will not fulfill the Friedel sum rule. Consider an arbitrary discrete spectrum of the conduction electrons with hybridization

$$\Gamma(i\nu) = V^2 \sum_{\mu} \frac{\alpha_\mu}{i\nu - \omega_\mu},$$

with excitation energies ω_μ. Splitting into real and imaginary parts and inserting into Eq. (B2) gives

$$\begin{aligned} &\mathrm{Im}\left[\mathrm{G}^{\mathrm{ret}}_{ff}(0)\right] \\ &= \lim_{\nu\to 0^+} \frac{-(m^* + V^2A(\nu))\nu}{(m^{*2} + 2m^*V^2A(\nu) + V^4A(\nu)^2)\nu^2 + V^4B(\nu)^2}, \end{aligned}$$

$$A(\nu) = \sum_\mu \alpha_\mu \frac{1}{\omega_\mu^2 + \nu^2}, \quad B(\nu) = \sum_\mu \alpha_\mu \frac{\omega_\mu}{\omega_\mu^2 + \nu^2}.$$

Upon neglecting the weak dependence of $A(\nu)$ and $B(\nu)$ on ν, one obtains, in this case, in the limit $\nu \to 0$: $\mathrm{Im}[\mathrm{G}^{\mathrm{ret}}_{ff}(0)] \to 0$ if all $\omega_\mu \neq 0$ or $\mathrm{Im}[\mathrm{G}^{\mathrm{ret}}_{ff}(0)] \to -\infty$ if any $\omega_\mu = 0$. We would like to further illustrate this for the specific model considered in this work (i.e., an impurity coupled to a semi-infinite chain with open boundary conditions)

$$\mathcal{H} = -V(c_f^\dagger c_0 + c_0^\dagger c_f) - t\sum_{i=0}^{L-1}(c_i^\dagger c_{i+1} + c_{i+1}^\dagger c_i),$$

where we suppressed spin indices. We obtain by using the equation of motion for the local impurity f-orbital Green's function

$$\begin{aligned}\omega\,\mathrm{G}_{ff}(\omega) &= \omega\,\langle\langle c_f; c_f^\dagger\rangle\rangle \\ &= \langle[c_f, c_f^\dagger]_+\rangle - \langle\langle[c_f,\mathcal{H}]_-; c_f^\dagger\rangle\rangle\end{aligned}$$

for an even number of sites (including the impurity)

$$\mathrm{Im}[\Gamma_{\mathrm{even}}(i\nu)] = -\frac{V^2}{\nu}\,R_L(\nu,t),$$

and for an odd number of sites

$$\mathrm{Im}[\Gamma_{\mathrm{odd}}(i\nu)] = -V^2\nu\,R_L(\nu,t),$$

where $R_L(\nu,t)$ is a rational function which is well behaved upon taking the limit $\nu \to 0^+$ [i.e., it approaches a constant $\lim_{\nu\to 0^+} R_L(\nu,t) = f_L(t)$] and the real part is always zero. Upon inserting into Eq. (B2), one can easily verify that for an even number of sites, this yields zero spectral weight at the Fermi energy, while for an odd number of sites it yields $-\infty$ (i.e., there is a pole exactly at $\omega = 0$). Therefore, the ED results alternate with even/odd system size between $\rho_f^{\mathrm{even}}(0) = 0$ and $\rho_f^{\mathrm{odd}}(0) = \infty$. This result shows that the FSR is always violated in ED because a finite value of the impurity density of states at the Fermi energy may only be obtained using an artificial numerical broadening. It furthermore shows that all terms involving m^* go to zero and can not contribute to the sum rule.

Now we turn to the case of CPT/VCA, where the conduction electron hybridization takes the form [see Eq. (10)]

$$\Gamma(i\nu) = i\,\frac{V^2}{2t^2}\,(\nu - \sqrt{4t^2+\nu^2})$$

for the model considered in Eq. (1) (i.e., a semicircular density of states of the conduction electrons). The CPT/VCA Green's function of the physical system is then given upon insertion of this Γ into Eq. (B2):

$$\mathrm{Im}\big[\mathrm{G}^{\mathrm{ret}}_{ff}(0)\big] = \lim_{\nu\to 0^+}\frac{-1}{(m^* - \frac{V^2}{2t^2})\nu + \frac{V^2}{2t^2}\sqrt{4t^2+\nu^2}},$$

which yields upon expansion of the square root up to linear order in ν

$$\mathrm{Im}\big[\mathrm{G}^{\mathrm{ret}}_{ff}(0)\big] = \lim_{\nu\to 0^+}\frac{-1}{(m^* - \frac{V^2}{2t^2} + \frac{1}{4t})\nu + \frac{V^2}{t}},$$

and when the limit $\nu \to 0$ is taken

$$\mathrm{Im}\big[\mathrm{G}^{\mathrm{ret}}_{ff}(0)\big] = -\frac{t}{V^2} = -\frac{1}{\Delta},$$

which is exactly the value predicted by the FSR [Eq. (23)]:

$$\mathrm{Im}\big[\mathrm{G}^{\mathrm{ret}}_{ff}(0)\big] = -\pi\,\frac{1}{\pi\Delta}\,\sin\left(\frac{\pi}{2}\right)^2 = -\frac{1}{\Delta}.$$

This result is independent of the size of the reference system. Away from particle-hole symmetry (occupation of the f orbital not one), the calculation becomes more tedious. The numerical VCA calculations, however, show that a pinning of the Kondo resonance at the Fermi energy is obtained in contrast to CPT at small L.

APPENDIX C: SEMIANALYTICAL EXPRESSIONS FOR VCA OF THE TWO-SITE PROBLEM

To gain a better understanding of the behavior of the low-energy properties of the SIAM, we solve a small system semianalytically. We obtain the scaling of the Kondo temperature T_K with interaction strength U within VCA_Ω as well as $\mathrm{VCA}_{\mathrm{SC}}$. A reference system consisting of a two-site cluster and an infinite environment is used.

The Kondo scale will be determined from the effective mass [Eq. (26)] using the self-energy of a two-site cluster [Eq. (C3)], which leads to

$$m^*(U) = 1 + \frac{1}{36}\left(\frac{U}{V'}\right)^2. \tag{C1}$$

The Kondo scale T_K is inversely proportional to $m^*(U)$ [Eq. (25)]. Therefore, within this approximation, the behavior of the optimal cluster parameter V' governs the low-energy physics.

To determine the optimal hopping V', the Green's function of the reference system g is calculated as

$$\mathrm{g}^{-1}(z) = \begin{pmatrix} z-\Sigma'(z) & V' & 0 \\ V' & z & 0 \\ 0 & 0 & \mathrm{G}'^{-1}_{ee}(z)\end{pmatrix}.$$

The CPT/VCA Green's function G,

$$\mathrm{G}^{-1}(z) = \begin{pmatrix} z-\Sigma'(z) & V & 0 \\ V & z & t \\ 0 & t & \mathrm{G}'^{-1}_{ee}(z)\end{pmatrix},$$

is obtained by Eq. (6) using

$$\mathrm{T} = \begin{pmatrix} 0 & \Delta V & 0 \\ \Delta V & 0 & -t \\ 0 & -t & 0\end{pmatrix}.$$

Here, $\mathrm{G}_{11} = \mathrm{G}_{ff}$ [Eq. (C2)] corresponds to the impurity f orbital, $\mathrm{G}_{22} = \mathrm{G}_{ss}$ the second site in the interacting part of the reference system, and $\mathrm{G}_{33} = \mathrm{G}_{ee}$ [Eq. (10)] the semi-infinite environment. The cluster parameter V' is given by the physical parameter V plus the variation ΔV. Note that in here we work with the reduced expressions for Ω and G justified in Appendix A. Schönhammer and Brenig calculated the Green's function of the correlated orbital for this model perturbatively and showed that their expression becomes exact in the limit of vanishing bandwidth.[21] This is exactly the case considered here, where the impurity f orbital is coupled to a single noninteracting site providing a bath with vanishing bandwidth.

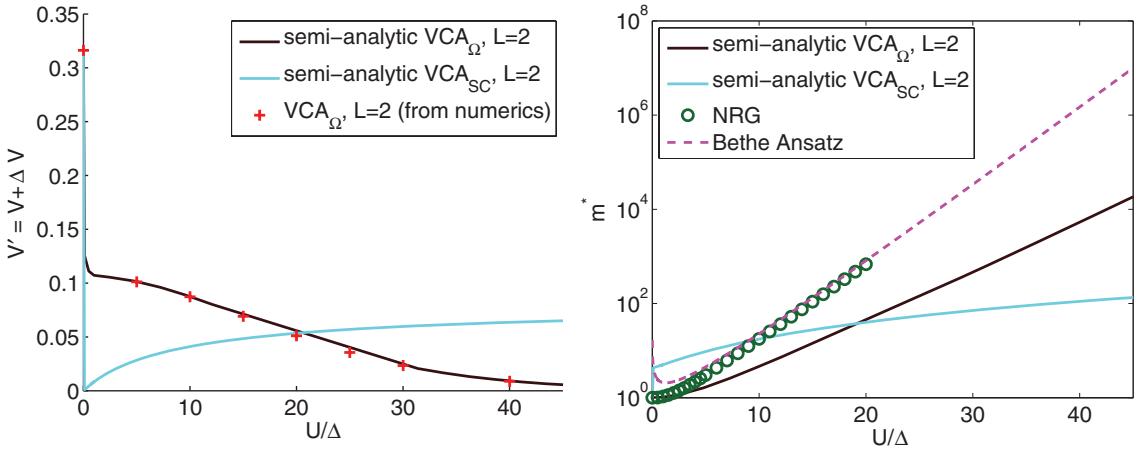

FIG. 22. (Color online) Left: Optimal parameter V' of the reference system as obtained by the semianalytical equations for VCA$_\Omega$ [Eq. (C4)] and VCA$_{SC}$ [Eq. (C5)]. As a reference, the $L = 2$ data of our numerical simulation are shown too. Right: The effective mass [Eq. (C1)] obtained by the optimized parameter V' of the reference system (see left figure). Additionally shown are the Bethe ansatz (Ref. 5) [Eq. (24)] and NRG (Ref. 31) result as a reference.

They obtained

$$g_{ff}(z) = \frac{1}{z - \Gamma'(z) - \Sigma'(z)}, \tag{C2}$$

where the hybridization $\Gamma'(z)$ in our case is given by

$$\Gamma'(z) = \frac{V'^2}{z},$$

and the self-energy $\Sigma'(z)$ is given by

$$\Sigma'(z) = \frac{\frac{U^2}{4}}{z - 9\Gamma'(z)}. \tag{C3}$$

From this, all elements of the cluster Green's function may be obtained by the equation-of-motion technique.

To be able to calculate the grand potential Ω, the ground-state energy of the interacting part of the reference system ω_0' needs to be obtained (which can be done, for example, by diagonalization of the Hamiltonian matrix or by an integral over the Green's function):

$$\omega_0' = -\tfrac{1}{4}(U + \sqrt{U^2 + 64V'^2}).$$

Using the expression for the CPT/VCA Green's function g and the ground-state energy and taking the derivative of the grand potential (20) with respect to ΔV, one is able to obtain an integral expression, which allows us to determine V' within VCA$_\Omega$:

$$\begin{aligned}\frac{d\,\Omega(\Delta V)}{d\,(\Delta V)} = {} & \nabla_{\Delta V}\omega_0'(\Delta V) - \frac{1}{\pi}\int_0^\infty d\omega \\ & \times \mathrm{Re}\{\mathrm{tr}\big[[\mathbb{1} - \mathrm{T}(\Delta V)\mathrm{g}(i\omega,\Delta V)]^{-1} \\ & \times ([\nabla_{\Delta V}\mathrm{T}(\Delta V)\mathrm{g}(i\omega,\Delta V)] \\ & + [\mathrm{T}(\Delta V)\nabla_{\Delta V}\mathrm{g}(i\omega,\Delta V)])\big]\} \stackrel{!}{=} 0. \end{aligned} \tag{C4}$$

The resulting $V'(U)$ is shown in Fig. 22 (left) and is used to calculate the effective mass [Eq. (C1)] shown right in the figure. The effective mass shows exponential behavior, but the exponent does not match the Bethe ansatz result as discussed in Sec. V E.

Next, we attempt to obtain the VCA$_{SC}$ solution for the two-site problem. The only variational parameter is V and therefore we determine the expectation value of $\sum_\sigma \langle f_\sigma^\dagger c_{1\sigma}\rangle$ self-consistently. Here, 1 denotes the impurity's s orbital. Since we are considering a spin-symmetric model, we sum over both spin directions and denote this expectation value as $\langle f^\dagger c\rangle$ in the following. The hopping expectation value is given by

$$\langle f^\dagger c\rangle = -\frac{2}{\pi}\int_0^\infty d\omega\, \mathrm{G}_{fc}(i\omega).$$

Evaluation of this expectation value in the cluster yields

$$\begin{aligned}&\langle f^\dagger c\rangle_{\text{cluster}} \\ &\quad = -\frac{2}{\pi}\int_0^\infty d\omega \\ &\qquad \times \frac{4(\Delta V + V)[9(\Delta V + V)^2 + w^2]}{36(\Delta V + V)^4 + [U^2 + 40(\Delta V + V)^2]w^2 + 4w^4}.\end{aligned}$$

Evaluation of this expectation value in the total system gives

$$\begin{aligned}\langle f^\dagger c\rangle_{\text{CPT}} = {} & -\frac{2}{\pi}\int_0^\infty d\omega \\ & \times \frac{8V}{8V^2 + \frac{w[U^2+36(\Delta V+V)^2+4w^2](w+\sqrt{4t^2+w^2})}{9(\Delta V+V)^2+w^2}}.\end{aligned}$$

Upon requiring the two expectation values to coincide

$$\langle f^\dagger c\rangle_{\text{cluster}} \stackrel{!}{=} \langle f^\dagger c\rangle_{\text{CPT}}, \tag{C5}$$

the optimal value of ΔV is obtained numerically. The resulting $V'(U)$ is plotted in Fig. 22 (left) and is used to calculate the effective mass [Eq. (C1)] shown right in the figure. The effective mass does not show exponential behavior in VCA$_{SC}$.

*martin.nuss@student.tugraz.at

[1] P. W. Anderson, Phys. Rev. **124**, 41 (1961).
[2] J. Friedel, Can. J. Phys. **34**, 1190 (1956).
[3] A. M. Clogston, B. T. Matthias, M. Peter, H. J. Williams, E. Corenzwit, and R. C. Sherwood, Phys. Rev. **125**, 541 (1962).
[4] J. Kondo, Prog. Theor. Phys. **32**, 37 (1964).
[5] A. C. Hewson, *The Kondo Problem to Heavy Fermions* (Cambridge University Press, Cambridge, UK, 1997).
[6] Y. Meir, N. S. Wingreen, and P. A. Lee, Phys. Rev. Lett. **66**, 3048 (1991).
[7] Y. Meir, N. S. Wingreen, and P. A. Lee, Phys. Rev. Lett. **70**, 2601 (1993).
[8] A. P. Jauho, N. S. Wingreen, and Y. Meir, Phys. Rev. B **50**, 5528 (1994).
[9] R. Hanson, L. P. Kouwenhoven, J. R. Petta, S. Tarucha, and L. M. K. Vandersypen, Rev. Mod. Phys. **79**, 1217 (2007).
[10] D. Loss and D. P. DiVincenzo, Phys. Rev. A **57**, 120 (1998).
[11] M. Kastner and D. Goldhaber-Gordon, Solid State Commun. **119**, 245 (2001).
[12] L. L. Sohn, G. Schön, and L. P. Kouwenhoven, *Mesoscopic Electron Transport,* 1st ed. (Springer, Netherlands, 2009).
[13] M. A. Ruderman and C. Kittel, Phys. Rev. **96**, 99 (1954).
[14] T. Kasuya, Prog. Theor. Phys. **16**, 45 (1956).
[15] K. Yosida, Phys. Rev. **106**, 893 (1957).
[16] F. Steglich, J. Aarts, C. D. Bredl, W. Lieke, D. Meschede, W. Franz, and H. Schäfer, Phys. Rev. Lett. **43**, 1892 (1979).
[17] P. Coleman, *Handbook of Magnetism and Advanced Magnetic Materials*, edited by Helmut Kronmuller and Stuart Parkin, Vol. 1 (John Wiley and Sons, New York, 2007), pp. 95–148.
[18] J. Chen, L. Li, W. G. Cullen, E. D. Williams, and M. S. Fuhrer, Nat. Phys. **7**, 535 (2011).
[19] R. Brako and D. M. Newns, J. Phys. C: Solid State Phys. **14**, 3065 (1981).
[20] D. C. Langreth and P. Nordlander, Phys. Rev. B **43**, 2541 (1991).
[21] W. Brenig and K. Schönhammer, Z. Phys. **267**, 201 (1974).
[22] K. G. Wilson, Rev. Mod. Phys. **47**, 773 (1975).
[23] I. Affleck, arXiv:0809.3474.
[24] A. Georges, G. Kotliar, W. Krauth, and M. J. Rozenberg, Rev. Mod. Phys. **68**, 13 (1996).
[25] G. Kotliar, S. Y. Savrasov, K. Haule, V. S. Oudovenko, O. Parcollet, and C. A. Marianetti, Rev. Mod. Phys. **78**, 865 (2006).
[26] K. Held, I. A. Nekrasov, G. Keller, V. Eyert, N. Blümer, A. K. McMahan, R. T. Scalettar, T. Pruschke, V. I. Anisimov, and D. Vollhardt, Phys. Status Solidi **243**, 2599 (2006).
[27] K. Yamada and K. Yosida, Prog. Theor. Phys. **53**, 1286 (1975).
[28] H. Bethe, Z. Phys. **71**, 205 (1931).
[29] R. Bulla, T. A. Costi, and T. Pruschke, Rev. Mod. Phys. **80**, 395 (2008).
[30] R. Hedden, V. Meden, T. Pruschke, and K. Schönhammer, J. Phys.: Condens. Matter **16**, 5279 (2004).
[31] C. Karrasch, R. Hedden, R. Peters, T. Pruschke, K. Schönhammer, and V. Meden, J. Phys.: Condens. Matter **20**, 345205 (2008).
[32] S. Nishimoto and E. Jeckelmann, J. Phys.: Condens. Matter **16**, 613 (2004).
[33] S. Nishimoto, F. Gebhard, and E. Jeckelmann, Phys. B (Amsterdam) **378–380**, 283 (2006).
[34] R. Peters, Phys. Rev. B **84**, 075139 (2011).
[35] S. Florens and A. Georges, Phys. Rev. B **70**, 035114 (2004).
[36] P. Coleman, Phys. Rev. B **29**, 3035 (1984).
[37] J. Hubbard, Proc. R. Soc. London A **276**, 238 (1963).
[38] T. Lobo, M. S. Figueira, and M. E. Foglio, Nanotechnology **21**, 274007 (2010).
[39] H. Haug and A. Jauho, *Quantum Kinetics in Transport and Optics of Semiconductors*, 2nd ed. (Springer, Berlin, 1996).
[40] E. Gull, A. J. Millis, A. I. Lichtenstein, A. N. Rubtsov, M. Troyer, and P. Werner, Rev. Mod. Phys. **83**, 349 (2011).
[41] J. E. Hirsch and R. M. Fye, Phys. Rev. Lett. **56**, 2521 (1986).
[42] M. Caffarel and W. Krauth, Phys. Rev. Lett. **72**, 1545 (1994).
[43] S. Gull and G. Daniell, Nature (London) **272**, 686 (1978).
[44] J. Skilling, in *Maximum Entropy and Bayesian Methods*, edited by J. Skilling (Kluwer Academic, Dordrecht, 1989), pp. 45–52.
[45] C. Gros and R. Valentí, Phys. Rev. B **48**, 418 (1993).
[46] D. Sénéchal, D. Perez, and M. Pioro-Ladriére, Phys. Rev. Lett. **84**, 522 (2000).
[47] M. Potthoff, M. Aichhorn, and C. Dahnken, Phys. Rev. Lett. **91**, 206402 (2003).
[48] M. Potthoff, Eur. Phys. J. B **32**, 429 (2003).
[49] M. Potthoff, Eur. Phys. J. B **36**, 335 (2003).
[50] D. Sénéchal, arXiv:0806.2690.
[51] M. Knap, W. von der Linden, and E. Arrigoni, Phys. Rev. B **84**, 115145 (2011).
[52] W. Koller and N. Dupuis, J. Phys.: Condens. Matter **18**, 9525 (2006).
[53] E. Arrigoni, M. Knap, and W. von der Linden, Phys. Rev. B **84**, 014535 (2011).
[54] M. Knap, E. Arrigoni, and W. von der Linden, Phys. Rev. B **83**, 134507 (2011).
[55] M. Knap, E. Arrigoni, and W. von der Linden, Phys. Rev. B **81**, 024301 (2010).
[56] C. Lanczos, J. Res. Natl. Bur. Stand. (US) **45**, 255 (1951).
[57] M. G. Zacher, R. Eder, E. Arrigoni, and W. Hanke, Phys. Rev. B **65**, 045109 (2002).
[58] E. N. Economou, *Green's Functions in Quantum Physics*, 3rd ed. (Springer, Berlin, 2010).
[59] J. M. Luttinger and J. C. Ward, Phys. Rev. **118**, 1417 (1960).
[60] M. Balzer, W. Hanke, and M. Potthoff, Phys. Rev. B **77**, 045133 (2008).
[61] M. Aichhorn, E. Arrigoni, M. Potthoff, and W. Hanke, Phys. Rev. B **74**, 024508 (2006).
[62] M. Knap, E. Arrigoni, and W. von der Linden, Phys. Rev. B **81**, 235122 (2010).
[63] T. Hand, J. Kroha, and H. Monien, Phys. Rev. Lett. **97**, 136604 (2006).
[64] J. W. Negele and H. Orland, *Quantum Many-Particle Systems* (Westview Press, Boulder, CO, 1998).
[65] P. Coleman, AIP Conf. Proc. **629**, 79 (2002).
[66] O. Gunnarsson and K. Schönhammer, Handb. Phys. Chem. Rare Earths **10**, 103 (1987).
[67] R. Zitko and T. Pruschke, Phys. Rev. B **79**, 085106 (2009).
[68] J. S. Langer and V. Ambegaokar, Phys. Rev. **121**, 1090 (1961).
[69] D. C. Langreth, Phys. Rev. **150**, 516 (1966).
[70] V. A. Fateev and P. B. Wiegmann, Phys. Lett. A **81**, 179 (1981).
[71] N. Kawakami and A. Okiji, Phys. Lett. A **86**, 483 (1981).
[72] P. Fulde, *Electron Correlations in Molecules and Solids*, 3rd ed. (Springer, Berlin, 2003).

[73]K. Schönhammer, Phys. Rev. B **13**, 4336 (1976).
[74]G. Kotliar and A. E. Ruckenstein, Phys. Rev. Lett. **57**, 1362 (1986).
[75]S. Andergassen, T. Enss, C. Karrasch, and V. Meden, in *Quantum Magnetism*, edited by B. Barbara, Y. Imry, G. Sawatzky, and P. C. E. Stamp (Springer, Berlin, 2008).
[76]H. Tsunetsugu, M. Sigrist, and K. Ueda, Rev. Mod. Phys. **69**, 809 (1997).
[77]M. Ferrero and O. Parcollet [http://ipht.cea.fr/triqs].
[78]P. Werner and A. J. Millis, Phys. Rev. B **74**, 155107 (2006).
[79]L. Boehnke, H. Hafermann, M. Ferrero, F. Lechermann, and O. Parcollet, Phys. Rev. B **84**, 075145 (2011).

5.5. Non-linear transport through a strongly correlated quantum dot

5.5.1. Preamble

This part of our work has been published in AIP Conf. Proc. 1485, 302 (2012) [63]. Reproduced with permission from AIP Conf. Proc. 1485, 302 (2012), doi: 10.1063/1.4755830. Copyright 2012, AIP Publishing LLC.

This is the first of two papers in which we develop and apply the steady-state quantum cluster methods stsCPT and stsVCA to a single quantum dot under bias voltage, see also the paper in Sec. 5.5. The basic physical effects in such a device are collected in Sec. 3.1 and applications in Ch. 2. The principles of the stsCPT and stsVCA are outlined in Sec. 3.3.1 and Sec. 3.3.2. We discussed the time evolution of this model in Sec. 5.2 and Sec. 5.3. We find the variational feedback introduced in the stsVCA reference state, Sec. 5.4 to be crucial for an accurate description of nonequilibrium correlation phenomena. In particular the stsCPT and the stsVCA are found to yield the correct linear-response current and stsVCA is found to exhibit a linear splitting of the Kondo resonance with bias voltage, see Sec. 5.6 for details. This work provides the basis for the application of stsCPT and stsVCA to more complicated, multi-orbital models in Sec. 5.7, Sec. 5.8. Further aspects of the SIAM are explored in Sec. 5.1, Sec. 5.9 and Sec. 5.10. The contents of this publication are advancements of preliminary data reported in MN's preceding diploma thesis [329].

This paper is authored by Martin Nuss (MN) and co-authored by MN's supervisors Enrico Arrigoni (EA) and Wolfgang von der Linden (WL). This research was to a large and significant extent conducted by MN under the supervision of WL and EA. The work was initiated by EA and WL. The stsVCA was proposed by EA and WL and developed by MN, EA and WL. The idea to apply the method to study a single quantum dot was proposed by WL and EA. MN wrote the stsCPT and stsVCA computer codes, tested them, conducted the calculations and studied various implementations of variational parameters. MN prepared, collected, interpreted, analyzed and visualized the results and set them in context with recent literature. MN wrote the first version of the manuscript. All authors participated equally in discussing the results and revising the text of the manuscript. EA and WL provided guidance throughout the work. We discussed our results with Michael Knap.

5.5.2. Manuscript

Non-linear transport through a strongly correlated quantum dot

Martin Nuss, Enrico Arrigoni, and Wolfgang von der Linden

Citation: AIP Conf. Proc. **1485**, 302 (2012); doi: 10.1063/1.4755830
View online: http://dx.doi.org/10.1063/1.4755830
View Table of Contents: http://proceedings.aip.org/dbt/dbt.jsp?KEY=APCPCS&Volume=1485&Issue=1
Published by the American Institute of Physics.

Non-linear transport through a strongly correlated quantum dot

Martin Nuss, Enrico Arrigoni and Wolfgang von der Linden

Institute of Theoretical and Computational Physics, TU Graz, 8010 Graz, Austria

Abstract. We study non-equilibrium properties of a strongly correlated quantum dot system, represented by the single impurity Anderson model, by means of the recently introduced non-equilibrium variational cluster approach [1]. We focus on the steady-state current density and non-equilibrium density of states in a parameter region of high interaction strength in the particle-hole symmetric case, which lies in the center of the Kondo regime. The bias dependent current density shows a gradually developing two peak structure with increasing interaction strength. It agrees with the linear response result in the low bias region and vanishes as expected at high bias due to a vanishing band overlap. The non-equilibrium density of states exhibits a linear splitting of the Kondo resonance with applied bias voltage. We compare results obtained via non-equilibrium variational cluster approach with non-equilibrium cluster perturbation theory.

Keywords: non-equilibrium theory, strongly-correlated systems, many-body cluster methods
PACS: 73.63.Kv, 73.23.-b, 72.10.Fk, 71.15.-m

INTRODUCTION

Experiments with nano-scale electronics [2] brought tremendous new insights into the physics of non-equilibrium phenomena in a fundamental quantum mechanical context. Understanding these phenomena on a theoretical level represents a challenge until today and valuable, new insights are still to be expected. Building upon general results [3, 4], qualitative descriptions of strongly interacting non-equilibrium systems are notoriously difficult to obtain because it is expected, that such systems remain in the strong coupling regime also at high bias voltages [5]. The combination of true many-body problems and a non-equilibrium situation usually refrains from a standard perturbative treatment in many interesting parameter regions. In addition, the need for energy relaxation and/or particle dissipation mechanisms sets a difficult environment for many theoretical approaches. In recent years promising concepts have been developed including the scattering Bethe Ansatz [6] or the effective equilibrium formulation in terms of scattering operators [7]. Due to the complexity of the problem, numerical calculations are appealing. Various established many-body methods have been extended to the non-equilibrium case over the past decade. Among them one can quote the non-equilibrium functional renormalization group [8, 9], quantum Monte Carlo [10], dual-fermion approaches [11] and many more. Using time dependent density matrix renormalization group it is possible to gain insight into quasi-stationary state behavior [12].
In this work, the non-equilibrium variational cluster approach is used to evaluate dynamic non-equilibrium quantities in the steady-state.

Lectures on the Physics of Strongly Correlated Systems XVI
AIP Conf. Proc. 1485, 302-306 (2012); doi: 10.1063/1.4755830

MODEL AND METHOD

We consider a model for a single quantum dot represented by the one dimensional single impurity Anderson model (SIAM) [13] in real space

$$\hat{\mathscr{H}} = \sum_{\alpha=L/R} \sum_{\sigma} \left(\varepsilon^{\alpha} \sum_{i=0}^{\infty} c_{i\sigma}^{\alpha\dagger} c_{i\sigma}^{\alpha} - t \sum_{\langle i,j \rangle} c_{i\sigma}^{\alpha\dagger} c_{j\sigma}^{\alpha} \right) + \varepsilon_f \sum_{\sigma} f_{\sigma}^{\dagger} f_{\sigma} + U \hat{n}_{\uparrow}^{f} \hat{n}_{\downarrow}^{f} - V \sum_{\alpha=L/R} \sum_{\sigma} \left(c_{0\sigma}^{\alpha\dagger} f_{\sigma} + f_{\sigma}^{\dagger} c_{0\sigma}^{\alpha} \right) . \quad (1)$$

Non-interacting left and right (L/R) leads are represented by tight binding bands with a nearest-neighbor hopping t. The lead on-site energies are denoted by $\varepsilon^{L/R}$. The operators $c_{i\sigma}^{\alpha\dagger}$ and $c_{i\sigma}^{\alpha}$, respectively, create and annihilate electrons in lead α on site i with spin σ. The dot Hamiltonian consists of a single orbital with local Coulomb repulsion U. The operator $f_{\sigma}^{\dagger}$ creates an electron with spin σ and on-site (gate-) energy ε_f located at the dot. Finally the symmetric tunneling between the non-interacting leads and the dot is given by V. In this work we adopt units in which $\hbar, e$, as well as the inter-lead hopping t are equal to 1. The lead-dot tunneling is fixed to $V = 0.3162$ which leads to an Anderson width of $\Delta \equiv \pi V^2 \rho_{\text{lead}}(0) = \frac{V^2}{t} = 0.1$. In the following, we investigate the particle-hole symmetric model ($\varepsilon_f = -\frac{U}{2}$) in the zero temperature case.

Non-equilibrium variational cluster approach (nVCA) was recently introduced in [1]. This method provides an approximation for the non-equilibrium single-particle Green's function in the usual Keldysh representation $\widetilde{\mathrm{G}}$ containing retarded (G^R), advanced (G^A), and Keldysh (G^K) Green's functions, which in this case are matrices in site/spin space. Similarly to equilibrium VCA [14] one first computes the Green's function $\widetilde{\mathrm{G}}'(z)$ of a numerically exactly solvable reference system $\hat{\mathscr{H}}'$ with single-particle parameters x' to be later determined self-consistently (see [1] eq. (13) therein). In our case, the reference system consists in three disconnected regions: a central region of total length L containing the dot and, possibly, a certain number of lead sites, and the two remaining parts of the two semi-infinite leads.

The approximation to the Green's function of the entire system is then given by the CPT [15] expression

$$\widetilde{\mathrm{G}}^{-1}(z) = \widetilde{\mathrm{G}}'^{-1}(z) - \mathrm{T},$$

where T is a matrix which describes the single-particle "difference" Hamiltonian $\hat{\mathscr{H}} - \hat{\mathscr{H}}'$. This consists of single-particle terms connecting the three regions, as well as corrections of the possibly varied single-particle parameters $\Delta\mathsf{x} = \mathsf{x}' - \mathsf{x}$. For $\Delta\mathsf{x} = 0$ we recover plain non-equilibrium cluster perturbation theory (nCPT) [16].

In the present non-equilibrium variational cluster approach we will present results obtained by using a single variational parameter $\Delta t = t' - t$ which is taken to be the same for all the hoppings t including the tunneling V. The self-consistency condition then amounts in requiring that the sum of all expectation values of the hoppings and the lead-dot tunneling in the reference system coincides with the respective expectation value of

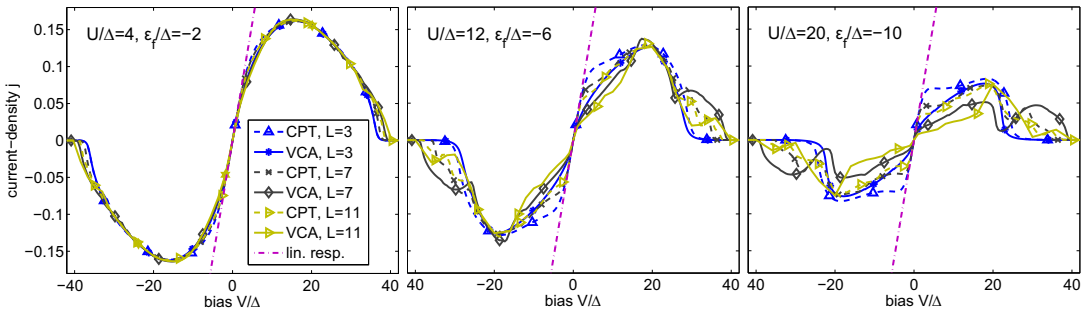

FIGURE 1. Non-equilibrium steady-state current density as a function of bias voltage. Results are obtained for $L = 3, 7$ and 11, respectively. For each L, the nCPT result is compared with the corresponding nVCA data. The plots from left to right show data for increasing interaction strengths $\frac{U}{\Delta} = 4, 12$ and 20. These results are for a singly-occupied dot: $\varepsilon_f = -\frac{U}{2}$ in the center of the Kondo region. For comparison, the corresponding linear-response results are also shown.

the entire system described by $\hat{\mathscr{H}}$. In this way, the self-energy of the reference system produces a self-consistent feedback of the non-equilibrium situation and the reference system is made as similar as possible to the entire one. The choice of this particular variational parameter is motivated by results obtained for simulations in equilibrium [17], see also [1]. The central region, consisting of the dot plus an equal amount of orbitals from the left and right lead, is solved exactly and its Green's function computed by means of the Band Lanczos method. In the spirit of CPT we expect to improve our results by enlarging the central interacting region, i. e. increasing L. The Green's functions of the remaining parts of the left and right leads are readily evaluated analytically. The VCA approximation, thus, consists of replacing the self-energy of the exact system with the self-energy Σ' of the reference system.

In the following, we consider reference systems with $L = 3, 7$ and 11-sites, which correspond to symmetric central regions. A bias voltage V_{bias} is applied in a symmetric manner by setting the on-site energies as well as the chemical potentials of the left and right leads to $\varepsilon^L = \mu^L = -\varepsilon^R = -\mu^R = \frac{V_{bias}}{2}$.
The current density is obtained via the Keldysh part of the Green's function

$$j_{ij}^{\sigma} = \frac{t_{ij}}{2} \sum_{\sigma} \int_{-\infty}^{+\infty} \frac{d\omega}{2\pi} \Re\mathrm{e} \left(\mathrm{G}_{ij}^{K\sigma}(w) - \mathrm{G}_{ji}^{K\sigma}(w) \right) , \tag{2}$$

where i and j are nearest-neighbor sites. The non-equilibrium (local) density of states (nLDOS) of the dot is given by the retarded part of its local Green's function: $\rho_f^{\sigma}(\omega) = -\frac{1}{\pi} \Im\mathrm{m} \left(\mathrm{G}_{ff}^{R\sigma}(\omega) \right)$.

RESULTS FOR THE STEADY-STATE

The current density eq. (2) (for both spin channels) is examined here for different values of interaction strength $\frac{U}{\Delta} = 4, 12$ and 20. The current density was measured between the left lead and the first site of the central region and it was checked that

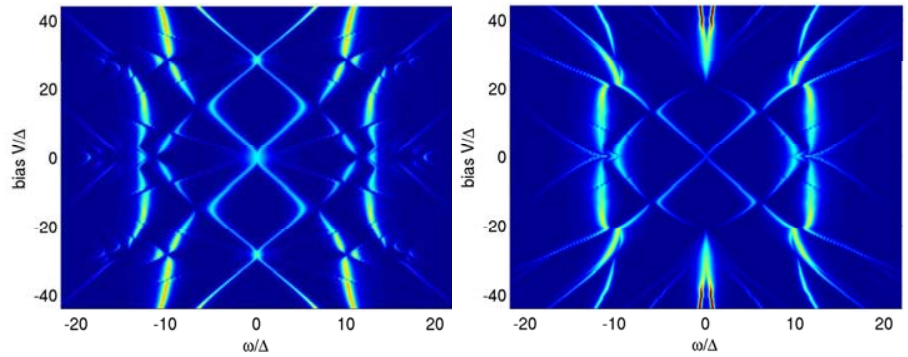

FIGURE 2. Non-equilibrium local density of states in the dot as a function of applied bias voltage. Results were obtained for a interaction strength of $\frac{U}{\Delta} = 20$ within nCPT (left) and within nVCA (right) and $L = 7$. The spectral function sum rule $\int_{-\infty}^{\infty} d\omega \, \rho_f^{\sigma}(\omega) = 1$ is fulfilled for each applied bias voltage.

the continuity equation is fulfilled. nCPT/nVCA results for the current density are compared for different sizes of the central region of the reference system (see fig. 1). All results become exact in the linear response limit for small bias voltages: $j_{\text{low}} = \frac{e^2}{\pi\hbar} V_{bias}$. The current density in the linear response regime is furthermore independent of the interaction strength U in the Kondo regime. This is due to the fact that nVCA fulfills the Friedel sum rule in equilibrium [17]. The trivial limit of high bias voltages where the lead-bands stop overlapping (here at $V_{\text{bias}}/\Delta = 40$) is reproduced exactly as well, yielding $j_{\text{high}} = 0$. In those cases, where the current density goes to zero before reaching this bias voltage, the vanishing of the current density is due to correlation effects in the dot. It is interesting to observe, that nVCA always departs sooner from the linear response behavior than nCPT with increasing interaction strength U. This is to be expected due to an exponential thinning of the Kondo resonance with increasing U [18]. For smaller interaction strengths (see for example $U/\Delta = 4$), the nCPT/nVCA results for different cluster sizes almost coincide. For large interaction strength (see for example $U/\Delta = 20$) they depart from each other, respecting the low/high bias voltage limits. The maximum current density decreases monotonically with interaction strength U. The most interesting region lies at intermediate to high bias voltages for large interaction strength U. A pronounced two-peak structure seems to evolve for the nVCA $L > 3$ results with increasing interaction strength U which may be explained considering the nLDOS. The nLDOS in the dot is shown in fig. 2 for a large interaction strength of $U/\Delta = 20$ and $L = 7$ (corresponding to the steady-state current in fig. 1 (right)). It is plotted in a density plot as a function of energy ω (horizontal) and applied bias voltage (vertical). A splitting of the Kondo resonance, which resides at the Fermi energy ($\varepsilon_F = 0$) for zero bias, is observed in both nCPT (left) and nVCA (right). A linear splitting and slight broadening of the Kondo resonance with increasing bias voltage is observed in nVCA. By inspecting the nLDOS, we find that the position ω_{K} of the split Kondo resonance depends on the interaction strength U: $\omega_{\text{K}} = \pm\frac{U}{4t} V_{\text{bias}}$ for $V_{\text{bias}} < 2t$ and $\omega_{\text{K}} = \pm\frac{U}{2}$ for $V_{\text{bias}} > 2t$. This expected linear form of the splitting is not present within nCPT. For high voltages these split peaks merge with the Hubbard bands and saturate. In this region a new excitation at low energy forms for sizes of the central

part of the reference systems $L > 3$. This additional peak in the nLDOS has a dominant contribution of the total weight and is responsible for the two-peak structure in the steady-state current density (see fig. 1). Because this effect is present for $L > 3$ we conclude that it is not due to a finite size effect but the current density may exhibit a non-monotonic multi-peak behavior as a function of bias voltage in a quantum dot.

CONCLUSIONS

We have calculated the steady-state current density and non-equilibrium density of states for a single quantum dot coupled to leads, modeled by the single impurity Anderson model, by means of the nVCA. The method is, in principle, applicable at arbitrary interaction strengths and bias voltages. We observe a non-monotonic, two peak, behavior of the steady-state current density for high values of interaction strength. A linear splitting of the equilibrium Kondo resonance with increasing bias voltage is predicted within the nVCA. The nCPT/nVCA result may be systematically improved by considering larger sizes of the interacting part of the reference system and/or more variational parameters in the case of nVCA. nVCA is comparatively fast and easily extendable to multi-orbital dots in any geometry or dimension. It is capable of producing results for large interaction strengths and high bias voltages. The self-consistent feedback included in nVCA is responsible for the superiority with respect to nCPT and proves to be a crucial ingredient.

ACKNOWLEDGMENTS

This work was partly supported by the Austrian Science Fund (FWF) P24081-N16. We acknowledge fruitful discussion with Michael Knap.

REFERENCES

1. M. Knap, W. von der Linden, and E. Arrigoni, *Phys. Rev. B* **84**, 115145 (2011).
2. S. M. Cronenwett, *Science* **281**, 540–544 (1998).
3. Y. Meir, N. S. Wingreen, and P. A. Lee, *Phys. Rev. Lett.* **66**, 3048 (1991).
4. A.-P. Jauho, N. S. Wingreen, and Y. Meir, *Phys. Rev. B* **50**, 5528 (1994).
5. P. Coleman, C. Hooley, and O. Parcollet, *Phy. Rev. Lett.* **86**, 4088–4091 (2001).
6. P. Mehta, and N. Andrei, *Phys. Rev. Lett.* **96**, 216802 (2006).
7. S. Hershfield, *Phys. Rev.* **70**, 2134–2137 (1993).
8. T. Kloss, and P. Kopietz, *Phys. Rev. B* **83**, 205118 (2010).
9. S. G. Jakobs, M. Pletyukhov, and H. Schoeller, *Phys. Rev. B* **81**, 195109 (2010).
10. J. E. Han, and R. J. Heary, *Phys. Rev. Lett.* **99**, 236808 (2007).
11. C. Jung, A. Lieder, Brener, and etal., *Annalen der Physik* **524**, 49–61 (2010).
12. F. Heidrich-Meisner, I. González, K. Al-Hassanieh, and etal., *Phys. Rev. B* **82**, 1–11 (2010).
13. P. W. Anderson, *Phys. Rev.* **124**, 41 (1961).
14. M. Potthoff, M. Aichhorn, and C. Dahnken, *Phys. Rev. Lett.* **91**, 206402 (2003).
15. C. Gros, and R. Valenti, *Phys. Rev. B* **48**, 418 (1993).
16. M. Balzer, and M. Potthoff, *Phys. Rev. B* **83**, 195132 (2011).
17. M. Nuss, E. Arrigoni, M. Aichhorn, and W. von der Linden, *arXiv:1110.4533* (2011).
18. P. Dutt, J. Koch, J. Han, and K. Le Hur, *Annals of Physics* **326**, 2963–2999 (2011).

5.6. Steady-state spectra, current, and stability diagram of a quantum dot: A nonequilibrium variational cluster approach

5.6.1. Preamble

This part of our work has been published in PHYSICAL REVIEW B 86, 245119 (2012) [62] and is also available as a preprint on arXiv:1207.5641. Reproduced with permission from PHYSICAL REVIEW B 85, 235107 (2012), doi:10.1103/PhysRevB.85.235107 under Creative Commons Attribution 3.0 License.

The purpose of this study is to thoroughly analyse the performance of stsVCA for the SIAM, see Sec. 3.1. The equilibrium properties of the SIAM are analyzed in Sec. 5.4 and a first look at the steady-state characteristics is provided in Sec. 5.5. Applications of the model are discussed in Ch. 2. The stsVCA is outlined in Sec. 3.3.1 and Sec. 3.3.2. In a detailed benchmark versus a quasi-exact real time evolution DMRG+TEBD, see also Sec. 5.2, we find stsVCA to yield accurate results for the steady-state current for low to intermediate bias voltages. We discuss in detail the self-consistent feedback mechanism of stsVCA. Numerically obtained stability diagrams compare very well to experimental data [64]. The linear splitting of the Kondo resonance is analyzed in detail. This work provides the basis for the application of stsCPT and stsVCA to more complicated, multi-orbital models in Sec. 5.7, Sec. 5.8. The physics of the SIAM is discussed further in Sec. 5.1, Sec. 5.3, Sec. 5.9 and Sec. 5.10.

This work is authored by Martin Nuss (MN) and co-authored by Christoph Heil (CH), Martin Ganahl (MG), Michael Knap (MK), Hans Gerd Evertz (HE) as well as by MN's supervisors Enrico Arrigoni (EA) and Wolfgang von der Linden (WL). This research was to a large and significant extent conducted by MN under the supervision of WL and EA. The work was initiated by EA and WL. The stsVCA was proposed by EA and WL, developed by EA, WL, MK and MN and implemented by MN. The idea to apply the method to study a single quantum dot was proposed by WL and EA. MN wrote the CPT and VCA computer codes, tested the methods, conducted the calculations and studied various implementations of variational parameters. MN prepared, collected, interpreted, analyzed and visualized the results and set them in context with recent literature. MG and HE provided expertise, guidance and a computer code for the DMRG+TEBD calculations. MN adapted this code and conducted calculations for the SIAM. CH implemented an alternative version of the stsVCA based on the grand potential [269]. MN wrote the first version of the manuscript. All authors participated equally in discussing the results and revising the text of the manuscript. EA, WL and MK provided guidance and expertise throughout the work. We gratefully acknowledge fruitful discussions with Sabine Andergassen. We thank Phillipp Werner for providing his CT-QMC data.

5.6.2. Manuscript

Steady-state spectra, current, and stability diagram of a quantum dot: A nonequilibrium variational cluster approach

Martin Nuss,* Christoph Heil, Martin Ganahl, Michael Knap, Hans Gerd Evertz, Enrico Arrigoni, and Wolfgang von der Linden
Institute of Theoretical and Computational Physics, Graz University of Technology, 8010 Graz, Austria
(Received 27 July 2012; published 19 December 2012)

We calculate steady-state properties of a strongly correlated quantum dot under voltage bias by means of nonequilibrium cluster perturbation theory and the nonequilibrium variational cluster approach, respectively. Results for the steady-state current are benchmarked against data from accurate matrix product state based time evolution. We show that for low to medium interaction strength, nonequilibrium cluster perturbation theory already yields good results, while for higher interaction strength the self-consistent feedback of the nonequilibrium variational cluster approach significantly enhances the accuracy. We report the current-voltage characteristics for different interaction strengths. Furthermore we investigate the nonequilibrium local density of states of the quantum dot and illustrate that within the variational approach a linear splitting and broadening of the Kondo resonance is predicted which depends on interaction strength. Calculations with applied gate voltage, away from particle-hole symmetry, reveal that the maximum current is reached at the crossover from the Kondo regime to the doubly occupied or empty quantum dot. Obtained stability diagrams compare very well to recent experimental data [A. V. Kretinin *et al.*, Phys. Rev. B **84**, 245316 (2011)].

DOI: 10.1103/PhysRevB.86.245119 PACS number(s): 73.63.Kv, 73.23.−b, 72.15.Qm, 71.15.−m

I. INTRODUCTION

The understanding of nonequilibrium phenomena in strongly correlated many-body systems may reveal previously unknown fundamental aspects of physics as well as prove crucial for the development of technical applications in the fields of nano or molecular electronics. Currently, combined insight of experiments on nanodevices[1–3] and results from artificial quantum simulators (see, e.g., Refs. 4–8) are capable of providing coherent insight into the nonequilibrium behavior of the quantum world. These experiments provide both a challenge for theoretical concepts as well as an accurate check for theoretical results. Both nanodevices and condensed matter simulators are often described remarkably well by interacting model Hamiltonians which are in general not exactly solvable.

Here we focus on a model of a single quantum dot, the single-impurity Anderson model (SIAM).[9] This model, incorporating spin and charge fluctuations as well as Kondo correlations, has been studied as an idealized realization of an interacting system by a wide array of techniques in equilibrium [for an overview see, e.g., Hewson (Ref. 10)]. The model we use here is applicable to generic single quantum dot systems including effects of a finite lead bandwidth.

However, the evaluation of dynamic quantities of strongly correlated quantum many-body systems out of equilibrium poses a notoriously difficult problem. A particular challenge for the SIAM is that it is expected to remain in a strong-coupling regime, even under the influence of a bias voltage.[11] Additional challenges are posed by the need for particle and/or energy dissipation mechanisms. Techniques which allow the calculation of physical quantities beyond the linear response regime are quite restrictive up to now and no full understanding of the nonequilibrium dynamics or the steady state under bias are available for the SIAM, apart from some special cases.[13–15] Nevertheless, controlled results have been obtained with the analytical Bethe ansatz for some physical quantities in the interacting resonant level model[16] and for the SIAM.[17] Perturbative calculations[18,19] as well as noncrossing approximation studies[20,21] extend early fundamental work on the nonequilibrium problem[22–25] and the impurity out of equilibrium.[26–28] Depending on the setup of parameters and model details, insight may be gained by semiclassical methods[29] or master equation approaches.[30] Recently, moreover, several techniques, which have proven very successful in the equilibrium theory, have been extended to the nonequilibrium case. Among them are many-body cluster methods,[31,32] renormalization group (RG) approaches,[33–39] flow equation methods,[40,41] real-time path-integral calculations,[42] out-of-equilibrium noncrossing approximation (NCA),[94] generalized slave-boson methods,[12,96] diagrammatic quantum Monte Carlo (QMC),[43–45] or QMC methods based on a complex chemical potential.[46–49] The Gutzwiller approximation has been generalized to the time-dependent case[50] and so has numerical renormalization group (NRG)[51–54] where however some issues with the use of Wilson chains in nonequilibrium systems have been pointed out by Rosch.[55] Dual-fermion approaches[56] have been proposed as well as superoperator techniques.[57,58] Some recent work attempts to compare several of these theories[59–61] and shed light on the critical issue of time scales involved.[62] Finally, some results for the SIAM are available[63] from numerically exact time evolution by a combination of density matrix renormalization group (DMRG)[64] and successive time evolution via time-dependent DMRG (tDMRG).[63,65–67] They are currently limited to small bias voltages and moderate interaction strengths.

In the present paper we explore the capabilities of nonequilibrium cluster perturbation theory (nCPT)[31] and benchmark the nonequilibrium variational cluster approach (nVCA)[32]

on the SIAM. We obtain the full current-voltage characteristics which we compare to results from a very accurate time evolution by means of time evolving block decimation (TEBD)[68] and QMC.[43] We also comment on the comparison to other results obtained by tDMRG,[69] perturbation theory,[18] and FRG.[34] Because of good agreement with these data, we then proceed to evaluate the single-particle spectrum of the quantum dot in the steady state. Since this is a dynamic quantity, it is even harder to obtain for most numerical methods. We find a linear splitting of the Kondo resonance[85,86] which depends on the interaction strength. Detailed results for the particle-hole symmetric model where Kondo correlations dominate are presented and supplemented by data in the whole parameter space including an applied gate voltage. We highlight the crucial edge which nVCA gains over nCPT via its self-consistent feedback.

Both many-body cluster techniques, nCPT and nVCA, are based on the well-established equilibrium counterparts cluster perturbation theory (CPT)[70,71] and the variational cluster approach (VCA).[72,73] They make use of the nonequilibrium Keldysh-Schwinger Green's function technique.[74–76] The present paper extends and benchmarks the ideas for adapting VCA to nonequilibrium situations introduced in Ref. 32. We attempt to give a comprehensive overview of the current capabilities and shortcomings of nCPT and nVCA for the application to steady-state problems of strongly correlated systems. The SIAM provides an excellent probing ground for our purposes as a model where the effects of correlations are crucial. It is however still relatively simple which permits systematic study and some results are available which allow for comparison. Reasonable results for the SIAM in equilibrium have been obtained previously by CPT as well as VCA.[77] Both cluster methods are approximate but they yield fairly reliable results and are therefore interesting due to their great flexibility and versatility. They are computationally not very demanding and allow in principle treating a wide range of fermionic/bosonic lattice Hamiltonians out of equilibrium. Possible extensions include electronic multiband or multiorbital systems in one, two, or three dimensions also including phonons.

This paper is organized as follows: In Sec. II we sketch the SIAM and describe the setup used. We proceed by outlining nCPT (Sec. III A) and nVCA (Sec. III B). In Sec. IV A, a comparison of steady-state currents as obtained by nCPT, nVCA, DMRG, and successive TEBD[78] and QMC[43] is presented. The nonequilibrium local density of states (nLDOS) is examined in Sec. IV B. Finally effects of an applied gate voltage on the steady-state current are studied in Sec. IV C.

II. MODEL OF A SINGLE QUANTUM DOT

We model the setup, consisting of a single correlated quantum dot in between two metallic leads, by a single-site Hubbard model embedded in a one-dimensional infinite tight-binding chain. The Hamiltonian of this single-impurity Anderson model (SIAM)[9] reads (see Fig. 1)

$$\hat{\mathcal{H}} = \hat{\mathcal{H}}_{\text{dot}} + \hat{\mathcal{H}}_{\text{lead}} + \hat{\mathcal{H}}_{\text{coup}}, \tag{1a}$$

$$\hat{\mathcal{H}}_{\text{dot}} = \epsilon_f \sum_{\sigma} f_\sigma^\dagger f_\sigma + U\, \hat{n}_\uparrow^f \hat{n}_\downarrow^f, \tag{1b}$$

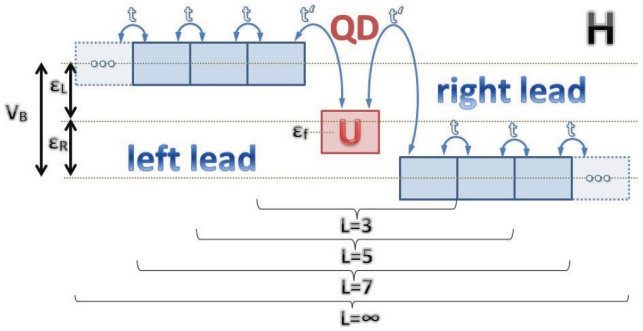

FIG. 1. (Color online) Illustration of the SIAM as prepared for use within nCPT and nVCA. An interacting quantum dot (QD) is located in the middle of two noninteracting electronic leads. In order to employ the cluster approaches, the system is divided into three pieces, a left part, a right part, and a central region of length L, which includes the quantum dot as well as parts of left and right leads.

$$\hat{\mathcal{H}}_{\text{lead}} = \sum_{\alpha,\sigma} \left(\epsilon_\alpha \sum_{i=0}^{\infty} c_{i\alpha\sigma}^\dagger\, c_{i\alpha\sigma} - t \sum_{\langle i,\, j\rangle} c_{i\alpha\sigma}^\dagger\, c_{j\alpha\sigma} \right), \tag{1c}$$

$$\hat{\mathcal{H}}_{\text{coup}} = -t' \sum_{\alpha,\sigma} (c_{0\alpha\sigma}^\dagger\, f_\sigma + f_\sigma^\dagger\, c_{0\alpha\sigma}). \tag{1d}$$

The electronic annihilation (creation) operators $c_{i\alpha\sigma}, f_\sigma$ ($c_{i\alpha\sigma}^\dagger, f_\sigma^\dagger$) obey the usual anticommutation relations with spin $\sigma = \{\uparrow, \downarrow\}$ and annihilate (create) electrons in the left or right lead $\alpha = \{L, R\}$ or the quantum dot, respectively. The particle number operator of the quantum dot is defined by $\hat{n}_\sigma^f = f_\sigma^\dagger f_\sigma$. U represents the on-site Hubbard repulsion. The single-particle energy of the quantum dot $\epsilon_f = -\frac{U}{2} + V_G$ is composed of a gate voltage V_G and a shift by $-\frac{U}{2}$ [Eq. (1b)], such that the particle-hole symmetric point is reached when the gate voltage vanishes and the bias is applied in an antisymmetric fashion as described below. Noninteracting left and right leads are described by tight-binding chains with a nearest-neighbor hopping t [Eq. (1c)]. The lead on-site energies are denoted by $\epsilon_{L/R}$. A bias voltage V_B may be applied to the system in an antisymmetric fashion by setting $\epsilon_L = \mu_L = -\epsilon_R = -\mu_R = \frac{V_B}{2}$, where $\mu_{L/R}$ denote the chemical potentials of the decoupled leads ($t' = 0$). Finally, the symmetric tunneling between the noninteracting leads and the quantum dot is denoted by t' [Eq. (1d)]. In this work we adopt units in which $\hbar, e$, as well as the interlead hopping t are equal to 1. The lead-dot tunneling is fixed to $t' = 0.3162$ throughout this paper, which implies an Anderson width of $\Delta \equiv \pi\, t'^2\, \rho_{\text{lead}}(0) = \frac{t'^2}{t} \approx 0.1$. This choice of parameters furthermore implies an effective lead bandwidth of $D = 40\Delta$. For higher bias voltages we therefore include additional effects due to finite bandwidth and band shape as compared to the often used wide-band limit. The prefactor for the current is then given by $j_0 = \frac{2|e|t}{\hbar}$. In the following, we always consider the zero-temperature case.

III. METHODS

All information needed to evaluate expectation values in the steady state of an interacting fermionic lattice Hamiltonian

is contained in a single object, the single-particle Green's function in Keldysh space $\widetilde{\mathrm{G}}$ [Eq. (A1)] (for details see Appendix A). Evaluating this object is in general impossible to do exactly but a handle on $\widetilde{\mathrm{G}}$ is given by nCPT and nVCA. These approximations are to be discussed in the following.

A. Nonequilibrium cluster perturbation theory

The idea of nCPT is to split an (infinitely) large system $\hat{\mathcal{H}}$ for times $\tau < \tau_0$ into a set of small decoupled clusters (described by the Hamiltonian $\hat{h}$), for which the single-particle Green's functions can be determined exactly, by numerical means

$$\hat{\mathcal{H}} = \hat{h} + \theta(\tau - \tau_0)\,\hat{\mathrm{T}}.$$

At time τ_0 the coupling of the individual subsystems $\hat{\mathrm{T}} = \hat{\mathcal{H}} - \hat{h}$ is switched on and the solution for the single-particle Green's function of the total system can be obtained by the CPT equation[70] in Keldysh-, site- and spin-space

$$\widetilde{\mathrm{G}}^{-1} = \widetilde{\mathrm{g}}^{-1} - \hat{\mathrm{T}} \otimes \tilde{\mathbb{1}}, \tag{2}$$

where $\widetilde{\mathrm{G}}/\widetilde{\mathrm{g}}$ denote the single-particle Green's function in Keldysh space of the total system/split systems. The unit matrix in Keldysh space is denoted by $\tilde{\mathbb{1}}$. Equation (2) is a strong-coupling perturbation theory result and holds up to first order in the intercluster hopping $\hat{\mathrm{T}}$, as far as the self-energy is concerned. As a consequence, the self-energy $\Sigma_{\hat{\mathcal{H}}}$ of the total system is approximated by the self-energy of the initial system $\Sigma_{\hat{h}}$. This implies that nCPT/nVCA become exact in the noninteracting limit, since in this case, the self-energy of the total system agrees with that of the initial system, which are both zero. The results of nCPT and nVCA converge towards the exact results with increasing cluster size.

In the present paper we illustrate this approach for the SIAM out of equilibrium. We start out by splitting the infinite chain [Eq. (1a)] into three parts: (i) an interacting central region of length L consisting of the interacting site (the quantum dot) as well as an equal amount of sites of the left and the right leads, (ii) a semi-infinite, noninteracting left region consisting of the remaining part of the left lead, and (iii) a semi-infinite, noninteracting right region consisting of the remaining part of the right lead (see Fig. 1). To proceed, the single-particle Green's functions in Keldysh space have to be determined exactly for those three systems. Results for the left and right part are available analytically by the retarded Green's function of a semi-infinite tight-binding chain[82]

$$\mathrm{g}^{L/R}_{i,j}(\omega) = \upsilon^{L/R}_{0,i-j}(\omega) - \upsilon^{L/R}_{0,i+j}(\omega), \tag{3}$$

$$\upsilon^{L/R}_{i,j}(\omega) = \frac{-\imath}{\sqrt{4|t|^2 - (\omega - \epsilon^{L/R})^2}} \left[-\frac{\omega - \epsilon^{L/R}}{2|t|} + \imath \sqrt{1 - \left(\frac{\omega - \epsilon^{L/R}}{2|t|} \right)^2} \right]^{|i-j|}, \tag{4}$$

where $\upsilon_{i,j}$ is the retarded Green's function of the infinite tight-binding chain. The single-particle Green's function of the central interacting region can be determined in the Q-matrix formalism by the Band-Lanczos algorithm (see Refs. 77 and 83). The advanced component can always be obtained by the relation $\mathrm{G}^A = (\mathrm{G}^R)^\dagger$. Before coupling the three subsystems at time $\tau = \tau_0$, each of them is in equilibrium at different chemical potentials $\mu_{L/R/C}$. Therefore we may evaluate the corresponding Keldysh components by the relation[84]

$$\mathrm{G}^K(\omega,\mu) = [\mathrm{G}^R(\omega) - \mathrm{G}^A(\omega)][1 - 2\,p_{\mathrm{FD}}(\omega,\mu)], \tag{5}$$

where p_{FD} denotes the Fermi-Dirac distribution function at inverse temperature β: $p_{\mathrm{FD}} = 1/(1 + e^{\beta(\omega-\mu)})$. In the zero-temperature limit, $[1 - 2\,p_{\mathrm{FD}}(\omega,\mu)]$ may be reexpressed as $\mathrm{sign}(\omega - \mu)$. This is the only expression in which the chemical potential μ enters. It is crucial that this relation does not hold in a nonequilibrium situation any longer. The Hermitian part of $\mathrm{G}^K(\omega,\mu)$ is zero in equilibrium. The imaginary part consists of contributions due to delta peaks for finite-size systems like the central regions. The operator $\hat{\mathrm{T}}$ just contains the two hopping terms from the left to the central and from the central to the right region. At time τ_0, the hopping processes between these three regions are switched on and the steady-state single-particle Green's function $\widetilde{\mathrm{G}}$ is determined using nCPT, Eq. (2). As in the equilibrium case, the CPT results can be improved by the variational cluster approach, in which the single-particle part of the initial system is suitably modified. In the following a variational extension (nVCA) of the scheme described above will be presented following Ref. 32.

B. Nonequilibrium variational cluster approach

The idea of enlarging the size of the central region in nCPT is to find a better approximation for the starting point of perturbation theory. As pointed out before, in CPT the self-energy of the total system is approximated by that of the decoupled system. By increasing the size of the central region, the self-energy of the decoupled system converges gradually towards that of the total system. In nVCA an even more suitable initial system is chosen. This can be achieved by making use of the fact that the decomposition of $\hat{\mathcal{H}}$ into clusters $\hat{h}$ and intercluster parts $\hat{\mathrm{T}}$ is not unique. We are free to add single-particle operators $\hat{\Delta}(\mathsf{x})$, which depend linearly on parameters x, to the initial Hamiltonian $\hat{h}$, provided we subtract them again from $\hat{\mathrm{T}}$:

$$\hat{\mathcal{H}} = [\hat{h} + \hat{\Delta}(\mathsf{x})] + \theta(\tau - \tau_0)\,[\hat{\mathrm{T}} - \hat{\Delta}(\mathsf{x})].$$

Here,

$$\hat{\Delta}(\mathsf{x}) = \sum_l \mathsf{x}_l\,\hat{\Delta}_l,$$

where $\hat{\Delta}_l$ is quadratic in the fermion operators. This parametrized single-particle field introduces additional freedom in the starting guess for perturbation theory and can be used for a self-consistent feedback on the clusters. The system described by $[\hat{h} + \hat{\Delta}(\mathsf{x})]$, usually referred to as reference system in the context of VCA, has the same structure as in equilibrium VCA. The condition to fix the single-particle parameters x, however, is different in nVCA and VCA. Equilibrium VCA is based on the self-energy functional approach (SFA)[87,88] and provides a variational principle for the generalized grand potential functional, which is not well defined in the context of nonequilibrium systems any longer. An alternative criterion for fixing the variational parameters x was introduced in Ref. 32 and compared to the traditional VCA criterion in Ref. 77. It is based on the idea of starting from a system which is as similar as possible to the total,

original system in terms of physically observable quantities. We demand the expectation values of the operators $\hat{\Delta}_l$ to coincide in the initial (reference) system and the steady state of the total system; i.e.,

$$\langle \hat{\Delta}_l \rangle_{\mathrm{g}} \stackrel{!}{=} \langle \hat{\Delta}_l \rangle_{\mathrm{G}}.$$

For example, adding variational freedom in the on-site energy of the quantum dot, corresponding to $\Delta = \mathsf{x}_{\epsilon_f} \hat{n}^f_\sigma$, yields the self-consistency condition: $\langle \hat{n}^f_\sigma \rangle_{\mathrm{g}} \stackrel{!}{=} \langle \hat{n}^f_\sigma \rangle_{\mathrm{G}}$. From a more conceptual point of view, it is interesting that these self-consistency conditions follow from the condition[32]

$$\int_{-\infty}^{\infty} \frac{d\omega}{2\pi} \mathrm{tr} \left\{ \widetilde{\tau}_1 \frac{\partial (\widetilde{\mathrm{g}}_0)^{-1}}{\partial \mathsf{x}'} (\widetilde{\mathrm{g}} - \widetilde{\mathrm{G}}) \right\} = 0, \tag{6}$$

which is closely related to the stationarity condition of the generalized grand potential functional Ω in the equilibrium approach.[89] Here $\widetilde{\tau}_1 = \left(\begin{smallmatrix} 0 & \mathbb{1} \\ \mathbb{1} & 0 \end{smallmatrix}\right)$ is a Pauli matrix in Keldysh space and the subscript zero denotes noninteracting Green's functions. From the numerical point of view, one has to find the roots of an n-dimensional set of nonlinear equations (where n is the number of variational parameters x).

Like in first-order Dirac perturbation theory, the influence of the perturbation increases with time [perturbations introduced due to the coupling with hopping elements t at τ_0 are proportional to $t(\tau - \tau_0)$ since we are considering first-order perturbation theory] and one might argue that nCPT is bound to fail in the long-time, steady-state limit, even for small couplings between the clusters.[31] This argument cannot be true in general, as nCPT yields exact results in the case of noninteracting particles, although the initial decoupled systems are far from the steady-state behavior.

The initial system in nCPT is independent of the nonequilibrium situation and this shortcoming is improved to some extent within nVCA, where the information about the applied bias voltage is self-consistently fed back to the initial reference system. As we will see in this paper, there are circumstances under which nCPT already yields reasonable results. In general, however, we observe that nVCA represents a significant improvement over nCPT. This implies, on the one hand, that under steady-state conditions, the self-energy in the central cluster is significantly modified when going from nCPT to nVCA. On the other hand, it indicates that the steady-state situation can be mimicked in an equilibrium system by the auxiliary one-particle terms, determined self-consistently. A point for improvement of this approach is to modify the self-energy so that it is a genuine nonequilibrium one. Details on the nVCA procedure and the particular choice of variational parameters are provided in Appendix B.

IV. RESULTS

In the following we compare nCPT and nVCA data for the steady-state current with TEBD[68] and QMC[43] results in the particle-hole symmetric model. We elaborate on the nonequilibrium density of states and finally discuss results for the steady-state current away from particle-hole symmetry by applying a gate voltage. Earlier preliminary results obtained for the SIAM out of equilibrium by nCPT and nVCA are available in Refs. 92 and 93.

A. Steady-state current

Here we investigate the steady-state current-voltage characteristics of the particle-hole symmetric SIAM. In this parameter region, Kondo correlations are especially important. All nCPT and nVCA results are for an infinite system using a self-energy based on an $L \leqslant 11$ site interacting reference system. Although the length of Kondo correlations scales exponentially in interaction strength, it has been shown in Ref. 77 that the VCA approximation, similarly to other approximate methods such as FRG or Gutzwiller wave functions, is capable of retaining qualitatively most features of the ongoing Kondo physics, although, possibly, with renormalized scales. The steady-state current can be evaluated on any link either within the central region or between the central and the neighboring regions, since we find that the continuity equation is fulfilled within at least 10^{-6} relative to the steady-state current amplitude. We note again that in the noninteracting case nCPT as well as nVCA become exact so we do not show these data explicitly.

Results obtained by Eq. (A2) for the nCPT case are shown in the left column of Fig. 2 for various values of the interaction strength U. The linear response result $j_{\mathrm{lin}} = 2\,G_0 V_B$, where G_0 is the conductance quantum, is fulfilled within nCPT (and nVCA) in the very low bias region. This is because these methods fulfill the Friedel sum rule in equilibrium.[77] Actually, nCPT tends to stay in the linear response regime longer than nVCA and therefore overestimates the current for low (but not very low) bias voltages. We model the leads by one-dimensional tight-binding chains, yielding a semicircular density of states [Eq. (4)] of bandwidth $D = 40\Delta$. This implies a vanishing current in the high bias limit at $V_B = 40\Delta$, due to nonoverlapping lead density of states. This limit again is trivially fulfilled within nCPT and nVCA. Note that in a wide-band limit the current curves would approach a constant roughly at their respective maxima in the data shown.

For comparison, numerically exact results[68] as obtained by a real-time evolution with TEBD are also indicated in Fig. 2. Note that the TEBD data are obtained from the steady-state plateau in the time dependence of the current. At small and medium bias, the current converges well and the TEBD results provide an accurate benchmark. At higher bias, convergence is low, but the TEBD data still provide a reasonably reliable upper bound for the steady-state current.

In the intermediate bias region it is interesting to investigate the behavior of nCPT with increasing size of the central region L. As can be seen from the plots, for any interaction strength increasing L yields monotonically improving results. While for low interaction strength $U = 4\Delta$ the nCPT results almost coincide with the TEBD data, greater deviations arise at higher interaction strengths. For very large interaction strength (see for example $U = 20\Delta$), the lengths of the central region L considered here are not sufficient. At high bias voltage some spurious finite-size effects of the reference system are visible in the form of peaks in the steady-state current.

Next we would like to discuss the performance of nVCA. An illustration is shown in the middle column of Fig. 2. Here we compare nCPT and nVCA$_T$ for $L = 3,7$, and 11 again for increasing interaction strengths $U/\Delta = 4,8,12$, and 20. We

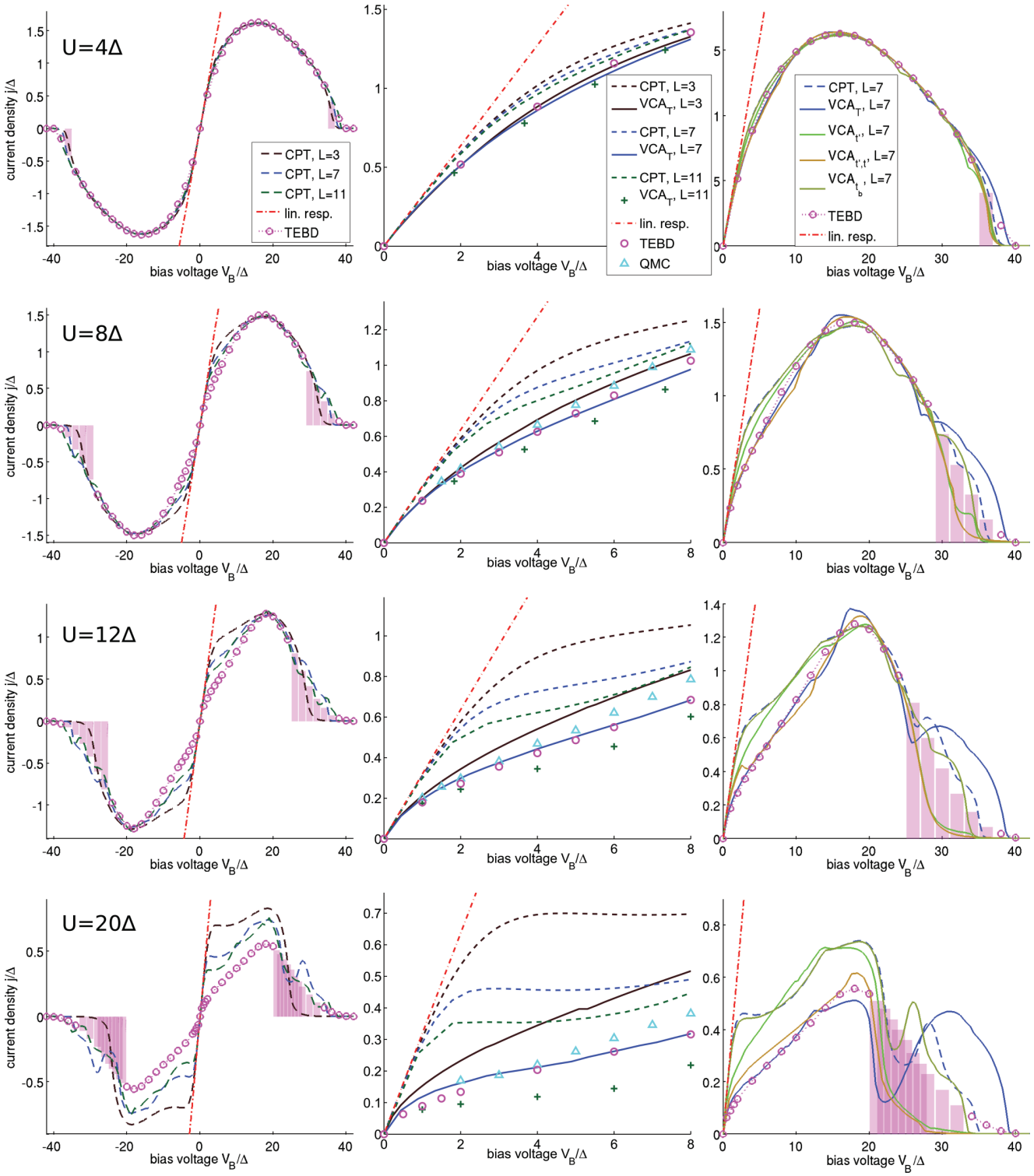

FIG. 2. (Color online) Steady-state current-voltage characteristics in the particle-hole symmetric case ($V_G = 0$). Results are shown for small to large interaction strength: $U = 4\Delta$ (top row), $U = 8\Delta$ (second row), $U = 12\Delta$ (third row), and $U = 20\Delta$ (bottom row). The first column contains the full current-voltage characteristics as obtained with nCPT for $L = 3,7$, and 11. As benchmarks, accurate TEBD results (Ref. 68) and the linear response result $j_{\text{lin}} = 2\,G_0\,V_B$ are depicted as well. In some bias regions, only an upper bound can be obtained by TEBD. This upper limit is depicted as a magenta bar. In the second column a close-up of the low bias region is presented. Here we compare nCPT ($L = 3,7$, and 11), nVCA$_T$ ($L = 3,7$, and 11) with TEBD data as well as QMC results (Ref. 43). Note that the QMC data have been obtained in a wide-band limit. The third column contains results obtained for $L = 7$ for various sets of nVCA variational parameters: nCPT, nVCA$_T$, nVCA$_{t'}$, nVCA$_{t,t'}$, nVCA$_{t_b}$. Legends are displayed once in the top row for the respective column.

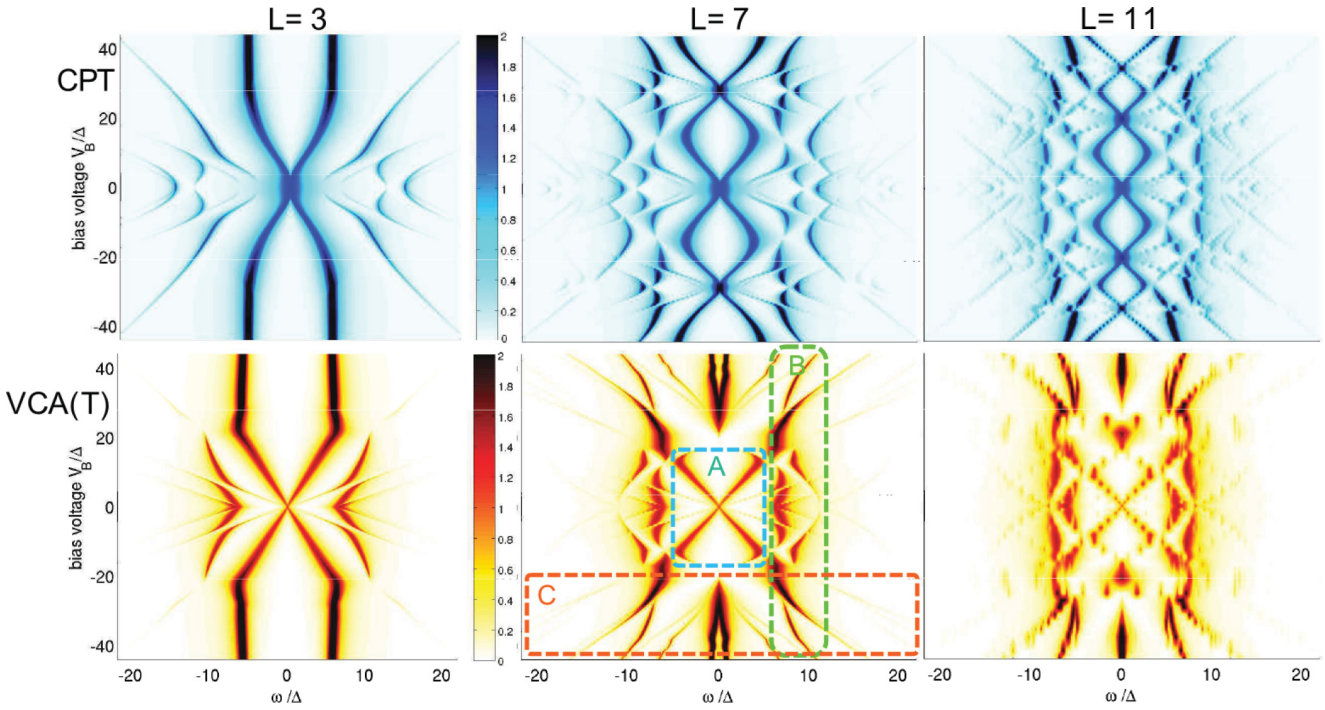

FIG. 3. (Color online) Nonequilibrium local density of states of the quantum dot ρ_f as a function of energy ω and bias voltage V_B in the particle-hole symmetric case ($V_G = 0$). Region A represents the experimentally most interesting region where no effects of the lead bands come into play and one observes a splitting of the equilibrium Kondo resonance. Region B is dominated by high-energy incoherent excitations which are expected to form continuous Hubbard bands in the thermodynamic limit. In region C, the lead density of states becomes relevant, causing a new low-energy resonance for $L \geqslant 7$. Data are depicted for $U = 12\Delta$ and an artificial numerical broadening of $0^+ = 0.05$. nCPT results are shown in the first row for system sizes of $L = 3$ (left), $L = 7$ (middle), and $L = 11$ (right). The second row displays the corresponding nVCA$_T$ data. For reasons of visualization the color scale is cut off at $\rho_{\max} = 2$. Note that a horizontal line through the center of each plot at $V = 0$ corresponds to the equilibrium density of states. The spectral function sum rule Eq. (A3) is fulfilled for each applied bias voltage. The $L = 11$ results are noisy as fewer data points have been obtained.

show a zoom to the low bias region where benchmarking data from other techniques such as TEBD data,[68] tDMRG,[69] FRG,[34] and QMC data obtained by Werner *et al.*[43] in the wide-band limit are available. One aspect to note immediately is that nVCA, like TEBD, departs sooner than nCPT from the linear response data, which is due to the better reproduction of the Kondo resonance within nVCA. The thinning of this narrow resonance at zero bias with increasing interaction strength is responsible for the departure from the linear response result.[57] Since the Kondo resonance is better accounted for in nVCA, the curves leave the linear response data sooner than the respective nCPT results. The TEBD data[68] and QMC data obtained by Werner *et al.*[43] in the wide-band limit are also plotted and serve as a benchmark up to $V_B \approx 5\Delta$ before effects of a different lead density of states become important. Curves obtained by tDMRG[69]/FRG[34] are not shown but lie basically on top of the TEBD/QMC data. Early data from perturbation theory[18] are known to have some additional spurious bumps in the low bias region. The improvement due to the variational feedback in nVCA becomes clear by comparing to the nCPT results for the same L, especially at higher interaction strengths.

The right column of Fig. 2 shows a comparison of the performance of different variational parameters considered within nVCA for $L = 7$. For small interaction strength all nVCA parameter sets work equally well. With increasing interaction strength, however, the different variational parameters predict a different behavior of the steady-state current. It should be noted here that some parameters like the ones used in nVCA$_{t_b}$ cause almost no deviation from the nCPT result while others improve it appreciably, such as nVCA$_T$. It predicts a two-peak structure in the high bias voltage regime, which however is not observed directly in the TEBD benchmark data. No final conclusion can be drawn about the behavior of the current in this bias regime because TEBD can only predict upper bounds for the steady-state current there. The position of the dip in the steady-state current is at $V_B = U$ for all interaction strengths. We note that this is where the bare level position of the quantum dot $\epsilon_f = -\frac{U}{2}$ is about to stop overlapping with one of the lead density of states (while still overlapping with the other). The calculation for two independent variational parameters (nVCA$_{t,t'}$) yields results similar to those for nVCA$_T$ in the lower bias region but goes to zero quickly for high bias voltages and does not show a dip.

On the whole, one may say that the self-consistent feedback implemented within nVCA provides a significant improvement over the nCPT results. This has been already observed in Ref. 77. However, there this result was deduced from the convergence of results with increasing cluster size and not with a benchmark comparison with alternative numerical methods. For low interaction strengths $U \lesssim 4\Delta$, bare nCPT already performs very well (independent of L) while for

larger interaction strengths the variational improvement of nVCA becomes important. Motivated by the success of nVCA for the steady-state current, we proceed by evaluating the nonequilibrium local density of states of the quantum dot.

B. Nonequilibrium local density of states

The nLDOS in the quantum dot $\rho_f(\omega)$ as obtained by nCPT and nVCA$_T$ is depicted in Fig. 3 for three sizes of the central part of the reference system: $L = 3,7$, and 11 and a large interaction strength of $U/\Delta = 12$ [corresponding to the steady-state current in Fig. 2 (third row)]. We plot the nLDOS in a density plot as a function of energy ω (horizontal) and applied bias voltage (vertical). The equilibrium result, consisting of a thin Kondo resonance at the Fermi energy ($\epsilon_F = 0$ here) and two broad incoherent peaks located at $\approx \pm\frac{U}{2}$ with a width of $\approx 2\Delta$, can be inferred from a horizontal cut at $V_B = 0$. For finite bias voltage, a splitting of the Kondo resonance is observed in both nCPT (top row) and nVCA$_T$ (bottom row). It is well known that the noncrossing approximation (NCA) predicts a splitting of the Kondo resonance into two under voltage bias and that within second-order perturbation theory the resonance is not split but suppressed only.[18] A linear splitting and slight broadening of the Kondo resonance with increasing bias voltage is proposed, e.g., in Ref. 94. Intuitively it is expected that the split Kondo resonances pin at the chemical potentials of the leads. Several other methods yield a splitting with different features: real-time diagrammatic[95] and scaling methods[97] as well as the equation-of-motion technique.[20,21,98–101] Within fourth-order perturbation theory the Kondo resonance splits into two, which are located near the chemical potentials of the two leads.[18] In experiments on nanodevices a linear splitting of the Kondo resonance has been observed.[85,86] Such a linear splitting is also predicted by nVCA (see Fig. 4), while nCPT yields a splitting which shows a roughly quadratic dependence on V_B. In addition within nVCA one observes an interaction-dependent splitting (see Fig. 5). In contrast to the prediction of Ref. 94 we do not however observe a simple pinning of the Kondo resonance at the chemical potentials of the leads. Our results indicate that

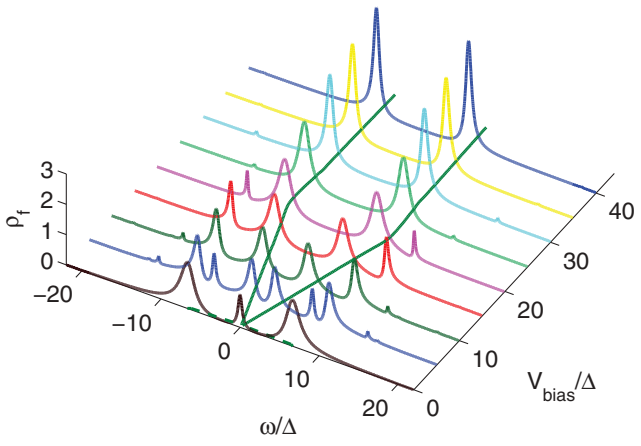

FIG. 4. (Color online) Nonequilibrium local density of states of the interacting quantum dot. Data are shown for $U = 12\Delta$ and an artificial numerical broadening of $0^+ = 0.05$. Results are obtained by nVCA$_T$ with $L = 3$.

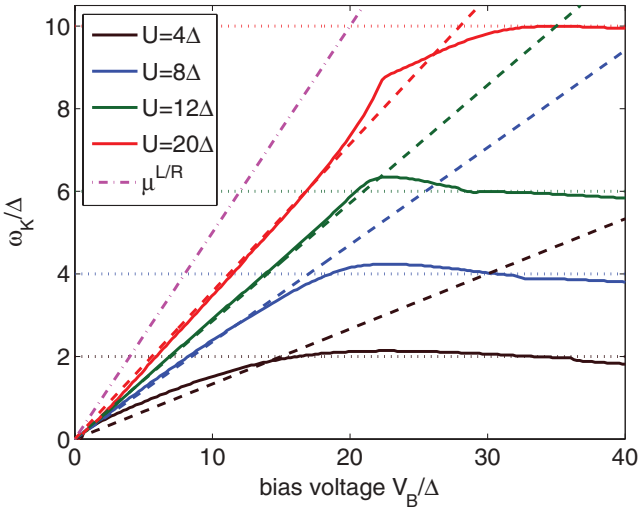

FIG. 5. (Color online) Interaction-dependent splitting of the Kondo resonance at ω_K under bias. Data shown are for different interaction strengths $U = 4,8,12$, and 20Δ (solid lines). The resonance merges with the incoherent high-energy spectrum (Hubbard bands), located at $\omega_H \approx \pm\frac{U}{2}$ (dotted lines) at a certain bias voltage $V_m \approx 15,17,21$, and 28 respectively. These values have been obtained by the linear fits (indicated as dashed lines). If the Kondo resonance would pin at the chemical potential of the leads ω_K, the linear behavior indicated as $\mu_{L/R}$ (dash-dotted line) would follow.

the position ω_K of the split Kondo resonance depends on the interaction strength U: $\omega_K = \pm\frac{U}{2V_m}V_B$ for $V_B \leqslant V_m$ and $\omega_K = \pm\frac{U}{2}$ for $V_B \geqslant V_m$ (see Fig. 5). Here V_m is the voltage where the Kondo resonance merges with the high-energy part of the spectrum located at $\omega_H \approx \pm\frac{U}{2}$: $V_m = 15,17,21$, and $28\,\Delta$ for $U = 4,8,12$, and $20\,\Delta$. The U-dependent values of V_m have been determined from the respective linear fit to the data.

For high voltages, these split peaks merge with the Hubbard bands and saturate, which has also been observed in fourth-order perturbation theory calculations.[18] In this bias region a new low-energy excitation is observed for $L > 3$ within nVCA$_T$. This additional peak in the nLDOS has a dominant contribution to the total weight and is responsible for the two-peak structure observed in the nVCA$_T$ steady-state current (see Fig. 2).

C. Finite gate voltage: Steady-state current and stability diagram

It is interesting to investigate the steady-state current away from the particle-hole symmetric point and the region where Kondo correlations are present. In this section the current through the quantum dot under bias is analyzed as a function of an applied gate voltage V_G and applied bias voltage V_B at fixed interaction strength U. Results are presented for $L = 3$. In this case no two-peak structure has been found in the nVCA$_T$ current in Fig. 2, which is corroborated by Fig. 3 (bottom left). The dependence of the current on the gate and bias voltage as obtained by nCPT and nVCA$_T$ is depicted in Fig. 6 for interaction strengths $U/\Delta = 4$ and $U/\Delta = 20$. First we discuss the so-called stability diagram (differential conductance as a function of bias and gate voltage) which is

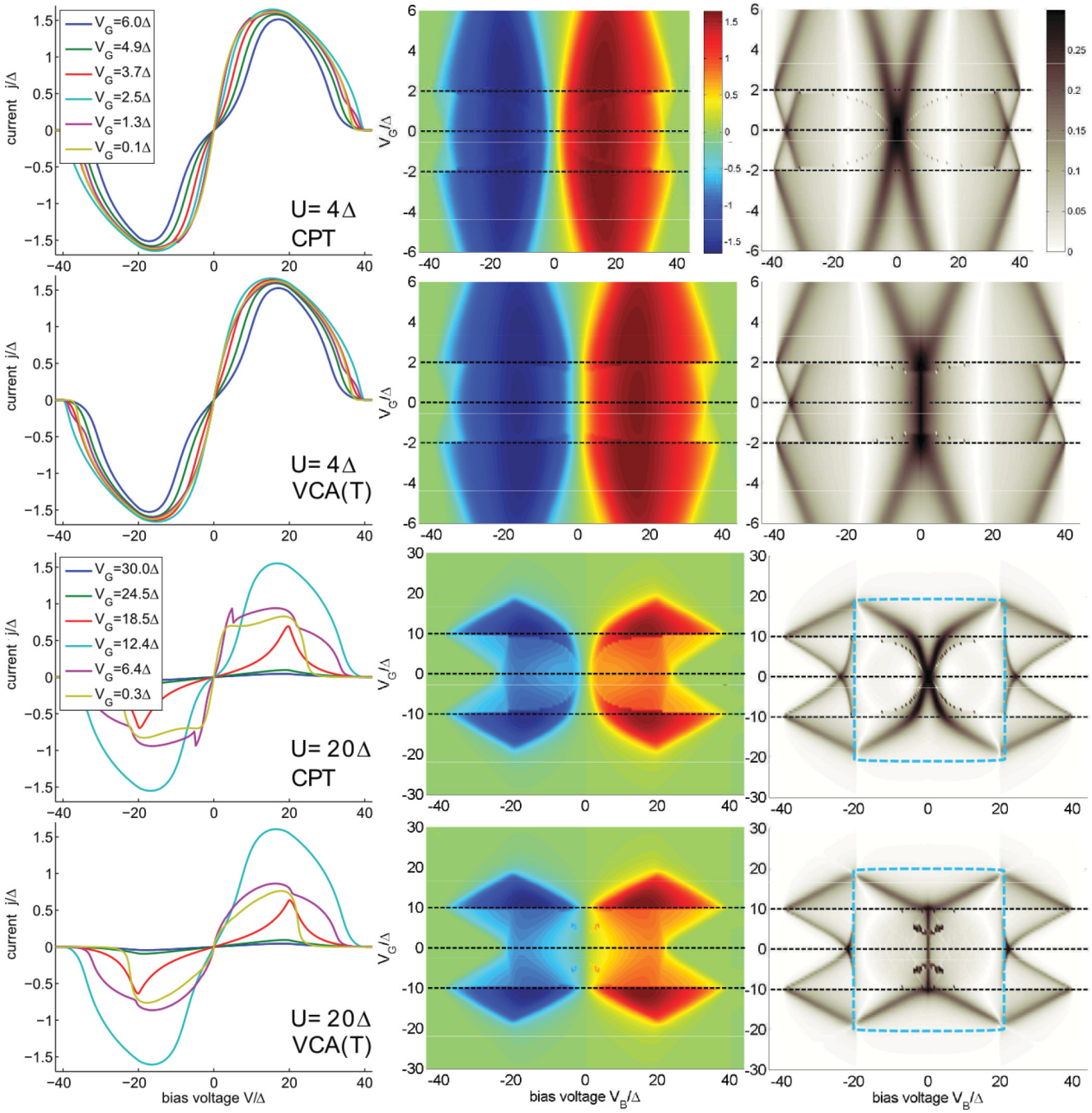

FIG. 6. (Color online) Stability diagram and steady-state current as a function of bias voltage V_B and gate voltage V_G. In the first column, the steady-state current is shown as a function of bias voltage for various gate voltages. The second column contains a density plot of the steady-state current in the full V_B/V_G parameter space. In the third column a similar density plot is shown for the differential conductance $G = \frac{dI}{dV_B}$ (stability diagram). The four rows depict results obtained by nCPT for $U = 4\Delta$, nVCA$_T$ for $U = 4\Delta$, nCPT for $U = 20\Delta$, and nVCA$_T$ for $U = 20\Delta$. The squares in the two stability diagrams bottom right mark the experimentally most interesting region. In the nVCA$_T$ result, the Kondo region (vertical line in the center) is reproduced extremely well, as are the Coulomb blockade regions ($\propto V_B$) above and below. For comparison to recent experimental data see Ref. 2 (Fig. 5 therein). Effects at higher bias voltage arise from the finite bandwidth used here and are typically not seen in experiment.

shown in the third column of Fig. 6. The dashed squares mark the region which is typically accessed experimentally. In the nVCA$_T$ result, the Kondo region (vertical line in the center) is reproduced extremely well, as are the Coulomb blockade regions ($\propto V_B$) above and below. Our data compare very well to recent experimental data of Ref. 2 (Fig. 5 therein). Effects at higher bias voltage arise from the finite bandwidth used here and are typically not seen in experiment.

The steady-state current as a function of bias and gate voltage is shown in the first and second column of Fig. 6.

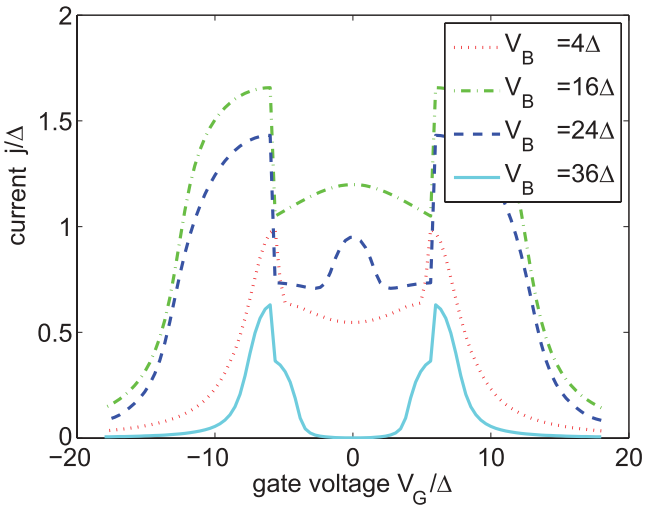

FIG. 7. (Color online) Dependence of the steady-state current on gate voltage V_G. The largest steady-state current is obtained in a parameter regime which crosses from the Kondo plateau to the doubly occupied or empty quantum dot. Data as obtained by nVCA$_T$ ($L = 3$) are presented for an interaction strength of $U/\Delta = 12$.

It is interesting to observe that the largest current is obtained exactly at the crossover points from the Kondo to the empty or doubly occupied quantum dot (these regions are marked by black-dashed lines in middle and right panel of Fig. 6). This aspect can be seen more clearly in Fig. 7, where the current is plotted as a function of gate voltage. For $U = 4\Delta$ there is not much difference between the nCPT and nVCA results as can be inferred from Fig. 6. For $U = 20\Delta$, however, we see that the feedback mechanism in VCA has a significant impact and leads to smoother j-V_B curves due to suppression of finite-size effects originating from the reference system. The sharp jumps at the crossover point in Fig. 7 originate from abrupt changes of the particle number in the ground state of the central cluster $L = 3$. We expect that this step smoothens with increasing L.

Concerning the reliability of the methods used, our data suggest that outside the parameter region where Kondo correlations dominate the single occupied quantum dot (in between the horizontal dashed black lines in Fig. 6) nCPT and nVCA perform almost equally well. Results are significantly easier to obtain outside the Kondo plateau (which was mentioned before, e.g., in Ref. 77 within exact diagonalization/CPT/VCA or in Ref. 63 within DMRG). Thereby the convergence within system size is greatly enhanced with respect to the Kondo region and very accurate results may be obtained already with small systems. Therefore, we may argue that for the steady-state of the SIAM, nCPT and nVCA perform quite well outside the Kondo region for any interaction strength as well as in the Kondo region for small interaction strengths. On the other hand, in the Kondo region nVCA outperforms nCPT for higher interaction strengths.

V. CONCLUSIONS

We have presented results for the steady state of the single-impurity Anderson model. We have applied nonequilibrium cluster perturbation theory and its variational extension, the nonequilibrium variational cluster approach, to this model for a single quantum dot under bias. Both methods make use of the Keldysh Green's function formalism and are capable of working in the thermodynamic limit which is necessary to account for particle and energy dissipation mechanisms.

Results for the particle-hole symmetric model, which is dominated by Kondo correlations, have been compared to time evolving block decimation and quantum Monte Carlo. At low values of interaction strength they show excellent agreement already for nonequilibrium cluster perturbation theory. For higher values of interaction strength, the self-consistency implemented within the nonequilibrium variational cluster approach proves crucial in order to obtain reasonable results. Both methods coincide with the low bias linear response data for the steady-state current. Both methods furthermore become exact in the noninteracting limit.

The nonequilibrium local density of states of the quantum dot exhibits a linear and interaction dependent splitting of the bias voltage within the nonequilibrium variational cluster approach which is not visible in the nonequilibrium cluster perturbation theory. At a certain (interaction dependent) bias voltage we find that this split Kondo resonance merges with the high-energy incoherent part of the spectrum.

When applying a gate voltage and thereby leaving the Kondo regime, calculations become a lot easier and nonequilibrium cluster perturbation theory and the nonequilibrium variational cluster approach appear to perform very well, which can be inferred from the convergence of our data. The highest current amplitude is obtained at the crossover from the Kondo to the empty or doubly occupied quantum dot. Experimental stability diagrams are reproduced very well within the variational approach. They show a clear Kondo regime and a Coulomb blockade region.

We may conclude that the nonequilibrium variational cluster approach is a promising method for the evaluation of steady-state quantities of strongly correlated model systems. Dynamic quantities become available in the whole complex plane and, in principle, any fermionic or bosonic lattice model may be treated including multiband or multiorbital systems. It is both fast and versatile and in principle all parameter regimes of the model are accessible. Subjects for further investigation are the self-consistency criterion, which is not unique, as well as the use of different variational parameters and an optimized out-of-equilibrium variational principle.

ACKNOWLEDGMENTS

We gratefully acknowledge fruitful discussions with S. Andergassen and thank P. Werner for providing his continuous time QMC data. This work was partly supported by the Austrian Science Fund (FWF) P24081-N16 and ViCoM subprojects F04103 and F04104. Some of the numerical calculations have been conducted at the Vienna Scientific Cluster (VSC-I&II).

APPENDIX A: GREEN'S FUNCTIONS, NOTATION, AND OBSERVABLES

Upon introducing the basic notation we follow standard literature (see, e.g., Ref. 79). The nonequilibrium single-particle properties are provided by the single-particle Green's

function in the 2×2 Keldysh space (denoted by tildes)

$$\widetilde{\mathrm{G}} = \begin{pmatrix} \mathrm{G}^R & \mathrm{G}^K \\ 0 & \mathrm{G}^A \end{pmatrix}, \tag{A1}$$

where $\mathrm{G}^{R/A/K}$ are again matrices in site/spin space and functions of two time coordinates.[79] R denotes the retarded, A the advanced, and K the Keldysh component of the single-particle Green's function which for (nonrelativistic) fermions read

$$\begin{aligned}
\mathrm{G}^R_{ij}(\tau_1 - \tau_2) &= \imath\theta(\tau_1 - \tau_2)\langle[c_i(\tau_1), c_j^\dagger(\tau_2)]\rangle, \\
\mathrm{G}^A_{ij}(\tau_1 - \tau_2) &= -\imath\theta(\tau_2 - \tau_1)\langle[c_i(\tau_1), c_j^\dagger(\tau_2)]\rangle, \\
\mathrm{G}^K_{ij}(\tau_1 - \tau_2) &= -\imath\langle c_i^\dagger(\tau_1)c_j(\tau_2) + c_i(\tau_1)c_j^\dagger(\tau_2)\rangle,
\end{aligned}$$

where i, j denote site as well as spin, τ_1, τ_2 real time, and $[\hat{A}, \hat{B}] = \hat{A}\hat{B} - \hat{B}\hat{A}$ the standard commutator. Note that in the following we consider the spin symmetric model [see Eq. (1a)] and therefore suppress spin indices. In the formulas for the current we therefore include an additional factor of two. The handy matrix relations $\mathrm{G}^A(\tau_1 - \tau_2) = (\mathrm{G}^R)^\dagger(\tau_2 - \tau_1)$ and $\mathrm{G}^K(\tau_1 - \tau_2) = -(\mathrm{G}^K)^\dagger(\tau_2 - \tau_1)$ follow from the definitions.

Our goal is to investigate the steady state in which the system becomes time-translationally invariant. Therefore we may Fourier-transform to the energy domain and evaluate single-particle steady-state expectation values

$$\langle c_i^\dagger c_j\rangle = \frac{\delta_{ij}}{2} + \frac{1}{2}\int_{-\infty}^{\infty}\frac{d\omega}{2\pi}\Im\mathrm{m}\,\mathrm{G}^K_{ij}(\omega).$$

The steady-state current through site m can be evaluated[80,81] by the time derivative of the total particle number to the left of this site

$$j = \langle\dot{\hat{N}}_M(t)\rangle, \quad \hat{N}_M = \sum_{i=-\infty}^{m-1}\hat{n}_i.$$

This expression for the current may be rewritten in terms of the Keldysh component of the single-particle Green's function

$$j_{i\,i+1} = t_{i\,i+1}\int_{-\infty}^{\infty}\frac{d\omega}{2\pi}\Re\mathrm{e}\big(\mathrm{G}^K_{i\,i+1}(\omega) - \mathrm{G}^K_{i+1\,i}(\omega)\big), \tag{A2}$$

where $t_{i\,i+1}$ is assumed to be real. The nonequilibrium density of states at site i is given by

$$\rho_i(\omega) = -\frac{1}{\pi}\Im\mathrm{m}\,\mathrm{G}^R_{ii}(\omega),$$

which has to fulfill the spectral sum rule

$$1 \stackrel{!}{=} \int_{-\infty}^{\infty}\rho_i(\omega) \quad \forall i. \tag{A3}$$

APPENDIX B: DETAILS ON THE nVCA PROCEDURE

In this paper we compare nCPT with nVCA for different auxiliary one-particle terms $\hat{\Delta}(\mathsf{x})$. In agreement with our previous experience, that the variational hopping parameters are crucial for the physics in the Kondo regime,[77] we observe that it suffices to consider only hopping processes inside the central region of the reference system. The most general form of the auxiliary one-particle term considered in this work reads

$$\begin{aligned}
\hat{\Delta}(\mathsf{x}_t, \mathsf{x}_{t'}, \mathsf{x}_{t_b}) = \mathsf{x}_{t'}\sum_{\alpha,\sigma}(c^\dagger_{0\alpha\sigma}\,f_\sigma + \mathrm{H.c.}) \\
+ \mathsf{x}_t\sum_{\alpha,\sigma}\sum_{i=1}^{\ell-1}(c^\dagger_{i\alpha\sigma}\,c_{i-1\alpha\sigma} + \mathrm{H.c.}) \\
+ \mathsf{x}_{t_b}\sum_{\alpha,\sigma}(c^\dagger_{\ell\alpha\sigma}\,c_{\ell-1\alpha\sigma} + \mathrm{H.c.}),
\end{aligned}$$

where $\ell \equiv (L-3)/2$. It contains three different hopping processes. The first term describes the hopping processes to and out of the quantum dot. The second term contains nearest-neighbor hopping processes between the lead sites of the central region except the border one. The last hopping process involves the nearest-neighbor sites at the boundary of the central region. In the sequel, we consider the following cases: (nVCA$_T$) with $\mathsf{x}_{t'} = \mathsf{x}_t = \mathsf{x}_{t_b}$, (nVCA$_{t,t'}$) with $\mathsf{x}_{t_b} = 0$, (nVCA$_{t'}$) with $\mathsf{x}_t = \mathsf{x}_{t_b} = 0$, and (nVCA$_{t_b}$) with $\mathsf{x}_t = \mathsf{x}_{t'} = 0$.

A bias voltage V_B is applied in an antisymmetric manner by setting the on-site energies as well as the chemical potentials of the left and right leads to $\epsilon_L = \mu_L = -\epsilon_R = -\mu_R = \frac{V_B}{2}$. Note that the sites of the leads which are incorporated in the central region of the reference system are also subjected to these on-site energies. All calculations are done for sizes of the central region of $L = 3, 7$, and 11 sites, which corresponds to symmetric central regions. We note that $L = 5, 9$ suffer from a finite-size gap which closes with increasing L. This gap arises due to an even amount of sites to the left as well as to the right of the quantum dot. We do not consider even L since this would correspond to an unequal amount of sites of the left and right lead in the central region. Thereby, the geometric symmetry of the problem would be spoiled and the application of a bias voltage which respects particle-hole symmetry would not be possible.

In order to reduce finite-size effects of the calculated quantities and to make an extrapolation to infinite central cluster sizes easier we scrutinized the idea of averaging over boundary conditions as outlined in Ref. 90 or Ref. 91. In CPT/VCA one has the freedom to add single-particle terms to $\hat{h}$ and subtract them again in $\hat{\mathrm{T}}$. Therefore we may add hopping terms which connect the first and last site of the central cluster and which have an arbitrary phase. The spectral function of the impurity site for a central region with complex periodic boundary conditions is in general no longer particle-hole symmetric, which makes it necessary to average $\widetilde{G}_\phi(\omega)$ over ϕ to retain the symmetry.

The result, however, was disappointing as the expected faster convergence towards the thermodynamic limit has not been confirmed. In this work we do not consider the long-range part of the Coulomb interaction which leads to additional charging effects in real devices.

*martin.nuss@student.tugraz.at

[1] D. Goldhaber-Gordon, J. Göres, M. Kastner, H. Shtrikman, D. Mahalu, and U. Meirav, Phys. Rev. Lett. **81**, 5225 (1998).

[2] A. V. Kretinin, H. Shtrikman, D. Goldhaber-Gordon, M. Hanl, A. Weichselbaum, J. von Delft, T. Costi, and D. Mahalu, Phys. Rev. B **84**, 245316 (2011).

[3] A. V. Kretinin, H. Shtrikman, and D. Mahalu, Phys. Rev. B **85**, 201301(R) (2012).
[4] J.-P. Brantut, J. Meineke, D. S. S. Krinner, and T. Esslinger, arXiv:1203.1927.
[5] U. Schneider, L. Hackermuller, J. P. Ronzheimer, S. Will, S. Braun, T. Best, I. Bloch, E. Demler, S. Mandt, D. Rasch *et al.*, Nat. Phys. **8**, 213 (2012).
[6] S. Trotzky, P. Cheinet, S. Fölling, M. Feld, U. Schnorrberger, A. M. Rey, A. Polkovnikov, E. A. Demler, M. D. Lukin, and I. Bloch, Science **319**, 295 (2008).
[7] N. Strohmaier, D. Greif, R. Jördens, L. Tarruell, H. Moritz, T. Esslinger, R. Sensarma, D. Pekker, E. Altman, and E. Demler, Phys. Rev. Lett. **104**, 080401 (2010).
[8] M. Greiner, O. Mandel, T. W. Hänsch, and I. Bloch, Nature (London) **419**, 51 (2002).
[9] P. W. Anderson, Phys. Rev. **124**, 41 (1961).
[10] A. C. Hewson, *The Kondo Problem to Heavy Fermions* (Cambridge University Press, Cambridge, 1997).
[11] P. Coleman, C. Hooley, and O. Parcollet, Phys. Rev. Lett. **86**, 4088 (2001).
[12] R. Aguado and D. C. Langreth, Phys. Rev. Lett. **85**, 1946 (2000).
[13] F. Lesage and H. Saleur, Phys. Rev. Lett. **80**, 4370 (1998).
[14] A. Schiller and S. Hershfield, Phys. Rev. B **62**, R16271 (2000).
[15] A. Komnik, Phys. Rev. B **79**, 245102 (2009).
[16] P. Mehta and N. Andrei, Phys. Rev. Lett. **96**, 216802 (2006).
[17] R. M. Konik, H. Saleur, and A. W. W. Ludwig, Phys. Rev. Lett. **87**, 236801 (2001).
[18] T. Fujii and K. Ueda, Phys. Rev. B **68**, 155310 (2003).
[19] S. Hershfield, J. H. Davies, and J. W. Wilkins, Phys. Rev. Lett. **67**, 3720 (1991).
[20] Y. Meir, N. S. Wingreen, and P. A. Lee, Phys. Rev. Lett. **70**, 2601 (1993).
[21] N. S. Wingreen and Y. Meir, Phys. Rev. B **49**, 11040 (1994).
[22] Y. Meir, N. S. Wingreen, and P. A. Lee, Phys. Rev. Lett. **66**, 3048 (1991).
[23] Y. Meir and N. S. Wingreen, Phys. Rev. Lett. **68**, 2512 (1992).
[24] Y. Meir, N. S. Wingreen, and P. A. Lee, Phys. Rev. Lett. **70**, 2601 (1993).
[25] A.-P. Jauho, N. S. Wingreen, and Y. Meir, Phys. Rev. B **50**, 5528 (1994).
[26] T. K. Ng and P. A. Lee, Phys. Rev. Lett. **61**, 1768 (1988).
[27] R. Aguado, G. Platero, C. Tejedor, and R. Lopez, Physica B **258**, 256 (1998).
[28] A. Kaminski, Yu. V. Nazarov, and L. I. Glazman, Phys. Rev. B **62**, 8154 (2000).
[29] K. Richter, *Semiclassical Theory of Mesoscopic Quantum Systems* (Springer, Berlin, 1999).
[30] C. Timm, Phys. Rev. B **77**, 195416 (2008).
[31] M. Balzer and M. Potthoff, Phys. Rev. B **83**, 195132 (2011).
[32] M. Knap, W. von der Linden, and E. Arrigoni, Phys. Rev. B **84**, 115145 (2011).
[33] V. Meden, S. Andergassen, T. Enss, H. Schoeller, and K. Schönhammer, New J. Phys. **10**, 045012 (2008).
[34] S. G. Jakobs, M. Pletyukhov, and H. Schoeller, Phys. Rev. B **81**, 195109 (2010).
[35] B. Doyon and N. Andrei, Phys. Rev. B **73**, 245326 (2006).
[36] H. Schoeller and J. König, Phys. Rev. Lett. **84**, 3686 (2000).
[37] A. Rosch, J. Kroha, and P. Wölfle, Phys. Rev. Lett. **87**, 156802 (2001).
[38] R. Gezzi, T. Pruschke, and V. Meden, Phys. Rev. B **75**, 045324 (2007).
[39] S. G. Jakobs, V. Meden, and H. Schoeller, Phys. Rev. Lett. **99**, 150603 (2007).
[40] P. Wang and S. Kehrein, Phys. Rev. B **82**, 125124 (2010).
[41] S. Kehrein, Phys. Rev. Lett. **95**, 056602 (2005).
[42] S. Weiss, J. Eckel, M. Thorwart, and R. Egger, Phys. Rev. B **77**, 195316 (2008).
[43] P. Werner, T. Oka, M. Eckstein, and A. J. Millis, Phys. Rev. B **81**, 035108 (2010).
[44] P. Werner, T. Oka, and A. J. Millis, Phys. Rev. B **79**, 035320 (2009).
[45] M. Schiró and M. Fabrizio, Phys. Rev. B **79**, 153302 (2009).
[46] J. E. Han and R. J. Heary, Phys. Rev. Lett. **99**, 236808 (2007).
[47] A. Dirks, P. Werner, M. Jarrell, and T. Pruschke, J. Phys.: Conf. Ser. **273**, 012150 (2011).
[48] J. E. Han, A. Dirks, and T. Pruschke, Phys. Rev. B **86**, 155130 (2012).
[49] A. Dirks, J. E. Han, M. Jarrell, and T. Pruschke, arXiv:1205.1817.
[50] M. Fabrizio, arXiv:1204.2175.
[51] F. B. Anders, Phys. Rev. Lett. **101**, 066804 (2008).
[52] F. B. Anders and A. Schiller, Phys. Rev. Lett. **95**, 196801 (2005).
[53] F. B. Anders and A. Schiller, Phys. Rev. B **74**, 245113 (2006).
[54] D. Roosen, M. R. Wegewijs, and W. Hofstetter, Phys. Rev. Lett. **100**, 087201 (2008).
[55] A. Rosch, Eur. Phys. J. B **85**, 6 (2012).
[56] C. Jung, A. Lieder, S. Brener *et al.*, Ann. Phys. **524**, 49 (2010).
[57] P. Dutt, J. Koch, J. Han, and K. Le Hur, Ann. Phys. **326**, 2963 (2011).
[58] E. Mu, C. J. Bolech, and S. Kirchner, arXiv:1111.4076.
[59] S. Andergassen, V. Meden, H. Schoeller, J. Splettstoesser, and M. R. Wegewijs, Nanotechnology **21**, 272001 (2010).
[60] J. Eckel, F. Heidrich-Meisner, S. G. Jakobs, M. Thorwart, M. Pletyukhov, and R. Egger, New J. Phys. **12**, 043042 (2010).
[61] A. M. Uimonen, E. Khosravi, A. Stan, G. Stefanucci, S. Kurth, R. van Leeuwen, and E. K. U. Gross, Phys. Rev. B **84**, 115103 (2011).
[62] L. D. Contreras-Pulido, J. Splettstoesser, M. Governale, J. König, and M. Büttiker, Phys. Rev. B **85**, 075301 (2012).
[63] F. Heidrich-Meisner, I. González, K. Al-Hassanieh, A. E. Feiguin, M. Rozenberg, and E. Dagotto, Phys. Rev. B **82**, 1 (2010).
[64] S. R. White, Phys. Rev. B **48**, 10345 (1993).
[65] K. A. Al-Hassanieh, A. E. Feiguin, J. A. Riera, C. A. Büsser, and E. Dagotto, Phys. Rev. B **73**, 195304 (2006).
[66] L. G. G. V. Dias da Silva, F. Heidrich-Meisner, A. E. Feiguin, C. A. Büsser, G. B. Martins, E. V. Anda, and E. Dagotto, Phys. Rev. B **78**, 195317 (2008).
[67] G. Schneider and P. Schmitteckert, arXiv:cond-mat/0601389.
[68] M. Nuss, M. Ganahl, H. G. Evertz, E. Arrigoni, and W. Von der Linden (unpublished).
[69] F. Heidrich-Meisner, A. E. Feiguin, and E. Dagotto, Phys. Rev. B **79**, 235336 (2009).
[70] C. Gros and R. Valenti, Phys. Rev. B **48**, 418 (1993).
[71] D. Sénéchal, D. Perez, and M. Pioro-Ladriére, Phys. Rev. Lett. **84**, 522 (2000).
[72] M. Potthoff, M. Aichhorn, and C. Dahnken, Phys. Rev. Lett. **91**, 206402 (2003).
[73] M. Potthoff, in *Strongly Correlated Systems*, edited by A. Avella and F. Mancini, Springer Series in Solid-State Sciences Vol. 171 (Springer, Berlin, Heidelberg, 2012), Chap. 10, pp. 303–339.
[74] L. V. Keldysh, Zh. Eksp. Teor. Fiz. **47**, 1515 (1965).

[75]R. P. Feynman and F. L. Vernon Jr., Ann. Phys. **24**, 118 (1963).
[76]J. Schwinger, J. Math. Phys. **2**, 407 (1961).
[77]M. Nuss, E. Arrigoni, M. Aichhorn, and W. von der Linden, Phys. Rev. B **85**, 235107 (2012).
[78]G. Vidal, Phys. Rev. Lett. **93**, 040502 (2004).
[79]J. Rammer and H. Smith, Rev. Mod. Phys. **58**, 323 (1986).
[80]H. Haug and A. Jauho, *Quantum Kinetics in Transport and Optics of Semiconductors*, 2nd ed. (Springer-Verlag GmbH, Berlin, 1996).
[81]A. Jauho (unpublished).
[82]E. N. Economou, *Green's Functions in Quantum Physics*, 3rd ed. (Springer, Berlin, 2010).
[83]M. G. Zacher, R. Eder, E. Arrigoni, and W. Hanke, Phys. Rev. B **65**, 045109 (2002).
[84]J. W. Negele and H. Orland, *Quantum Many-Particle Systems* (Westview Press, Boulder, CO, 1998).
[85]R. Leturcq, L. Schmid, K. Ensslin, Y. Meir, D. C. Driscoll, and A. C. Gossard, Phys. Rev. Lett. **95**, 126603 (2005).
[86]S. De Franceschi, R. Hanson, W. G. van der Wiel, J. M. Elzerman, J. J. Wijpkema, T. Fujisawa, S. Tarucha, and L. P. Kouwenhoven, Phys. Rev. Lett. **89**, 156801 (2002).
[87]M. Potthoff, Eur. Phys. J. B **32**, 429 (2003).
[88]M. Potthoff, Eur. Phys. J. B **36**, 335 (2003).
[89]D. Sénéchal, arXiv:0806.2690.
[90]J. T. Gammel, D. K. Campbell, and E. Y. Loh Jr., arXiv:cond–mat/9209026.
[91]E. Loh and D. Campbell, Synth. Met. **27**, A499 (1988).
[92]M. Nuss, Ph.D. thesis, TU Graz, 2011.
[93]M. Nuss, E. Arrigoni, and W. von der Linden, AIP Conf. Proc. **1485**, 302 (2012).
[94]E. Lebanon and A. Schiller, Phys. Rev. B **65**, 035308 (2001).
[95]J. König, J. Schmid, H. Schoeller, and G. Schön, Phys. Rev. B **54**, 16820 (1996).
[96]S. Smirnov and M. Grifoni, Phys. Rev. B **84**, 125303 (2011).
[97]A. Rosch, J. Paaske, J. Kroha, and P. Wölfle, Phys. Rev. Lett. **90**, 076804 (2003).
[98]K. Yosida and K. Yamada, Prog. Theor. Phys. Suppl. **46**, 244 (1970).
[99]K. Yamada, Prog. Theor. Phys. **53**, 970 (1975).
[100]K. Yosida and K. Yamada, Prog. Theor. Phys. **53**, 1286 (1975).
[101]K. Yamada, Prog. Theor. Phys. **54**, 316 (1975).

5.7. Effects of electronic correlations and magnetic field on a molecular ring out-of-equilibrium

5.7.1. Preamble

This part of our work has been published in PHYSICAL REVIEW B 89, 155139 (2014) [65] and is also available as a preprint on arXiv:1307.7530.

With this paper we turn our attention to steady-state transport across molecular junctions as introduced in Sec. 2.2. Recent developments in this field are discussed in Sec. 2.1 and Sec. 2.2. Molecular junctions may exhibit pronounced correlations effects due to confined geometries and appropriate methods are needed for the accurate description of electronic transport. The stsCPT as introduced in Sec. 3.3.1, was shown to yield good results for the SIAM in Sec. 5.4, Sec. 5.5, Sec. 5.6 and Sec. 5.10 and is here generalized to multi orbital interacting systems. In this work we adapt the stsCPT to study transport across molecular ring junctions in magnetic fields. We obtain the current-voltage characteristics and the interaction renormalized charge distribution and magnetization in the steady-state. We find that stsCPT is superior to QME approaches because it accurately takes into account lead induced broadening effects. However interaction induced blocking effects cannot be captured which led us to the development of a new reference state in meCPT, see Sec. 5.8.

This article is authored by Martin Nuss (MN) and co-authored by MN's supervisors Wolfgang von der Linden (WL) and Enrico Arrigoni (EA). This research was to a large and significant extent conducted by MN under the supervision of WL and EA. WL and EA suggested to apply the stsCPT to study transport across a molecular ring junction under magnetic fields. WL and EA provided guidance and expertise through all steps of the working process. MN, EA and WL developed the stsCPT scheme for magnetic fields. MN developed the computer code, tested it and did parameter studies. MN ran the computer simulations. MN prepared, collected, interpreted, analyzed and visualized the results and set them in context with recent literature. MN conducted the literature research and wrote the first version of the manuscript. All authors contributed equally to discussing the results and revising the manuscript. We discussed our results with Karin Zojer, Dmitry A. Ryndyk, and Max Sorantin.

5.7.2. Manuscript

Effects of electronic correlations and magnetic field on a molecular ring out of equilibrium

Martin Nuss,* Wolfgang von der Linden, and Enrico Arrigoni
Institute of Theoretical and Computational Physics, Graz University of Technology, 8010 Graz, Austria
(Received 31 July 2013; revised manuscript received 18 March 2014; published 29 April 2014)

We study the effects of electron-electron interactions on the steady-state characteristics of a hexagonal molecular ring in a magnetic field as a model for a benzene molecular junction. The system is driven out of equilibrium by applying a bias voltage across two metallic leads. We employ a model Hamiltonian approach to evaluate the effects of on-site as well as nearest-neighbor density-density–type interactions in a physically relevant parameter regime. Results for the steady-state current, charge density, and magnetization in three different junction setups (para, meta, and ortho) are presented. Our findings indicate that interactions beyond the mean-field level renormalize voltage thresholds as well as current plateaus. Electron-electron interactions lead to substantial charge redistribution as compared to the mean-field results. We identify a strong response of the circular current on the electronic structure of the metallic leads. Our results are obtained by steady-state cluster perturbation theory, a systematically improvable approximation to study interacting molecular junctions out of equilibrium, even in magnetic fields. Within this framework, general expressions for the current, charge density, and magnetization in the steady state are derived. The method is flexible and fast and can straightforwardly be applied to effective models as obtained from *ab initio* calculations.

DOI: 10.1103/PhysRevB.89.155139 PACS number(s): 71.27.+a, 71.15.−m, 73.63.Kv

I. INTRODUCTION

Miniaturization as a performance-enhancing concept in microelectronics may be advanced by the introduction of nanoscale molecular devices in what is today known as the concept of molecular electronics [1]. Recent years fostered fascinating advances in experimental control of fabrication [2], assembling [3], as well as contacting [4,5] on a molecular level. These achievements in combination with ever-improving measurement techniques [6] lead to a plethora of important insights into the basic mechanisms of electrical transport across molecular junctions [7]. Understanding these transport characteristics is a major focus of today's experimental as well as theoretical ventures and establishes the very basis for possible future device engineering.

A relevant and still relatively simple molecular junction is comprised of a ring-shaped molecule in between two metallic leads. For the particular molecule we have in mind the aromatic complex benzene (C_6H_6). Such setups have been realized using the mechanically controllable break junction technique (MCBJ) [5] and are stable on time scales required for transport experiments. Measurement of the transport characteristics has been achieved for benzene bound by thiol anchor groups to gold electrodes [8–10], as well as for benzene directly connected to platinum leads [11]. These experiments typically grant access to the current-voltage characteristics, conductance, higher derivatives of the current, or shot noise, albeit often in a statistical way [9]. It is likely that molecular ring junctions will find technological applications in the foreseeable future in the form of single-electron transistors [12,13], in quantum interference (QI) based electronics [14], or as data storage devices [15]. Naturally such junctions are dominated by quantum mechanical effects in an out-of-equilibrium context, which promotes predicting the outcome of experiments to a highly nontrivial theoretical task.

For benzene-based molecular junctions, general understanding of the noninteracting device is available in literature [16,17]. Electronic transport in π-conjugated systems is special due to QI effects [18,19]. Magnetic fields add to the rich Aharonov-Bohm physics [20,21] of quantum ring structures by inducing, for example, persistent currents [22]. Electronic correlations are important [23] due to the confined geometry and have been recently studied in equilibrium and linear response using the Hirsch-Fye quantum monte carlo (QMC) method [24], as well as dynamical mean-field theory (DMFT) [24,25]. While the basic features of QI effects can be understood from noninteracting calculations, the interplay of QI and electronic correlations can become nontrivial [26–30]. The remarkable property of negative differential conductance has been reported and explained in devices considering electron-electron interactions [27,31] using generalized master equation approaches. In addition, Green's function techniques have been applied within various approximations, especially within a combination with *ab initio* techniques [32]. In gated devices even nonperturbative many-body features like the Kondo effect [33] have been reported [3,4,30,34,35].

Investigating transport characteristics for molecular junctions out of equilibrium [5,36] is a very active field in modern theoretical physics. Although much progress has been made lately [37–40], reproducing experiments [10,41] in a qualitative and quantitative way remains an elusive goal. In going beyond semiclassical treatment [42] and combining nonequilibrium Green's function (NEGF) methods [43] with density functional theory (DFT) [44,45], much effort is devoted to the study of molecular junctions in a combined DFT+NEGF scheme [46–56]. Such *ab initio* approaches can be considered today's gold standard for weakly correlated molecular junction calculations. However, they tend

*martin.nuss@tugraz.at

to overestimate currents in comparison to highly accurate data [57] of experiments, especially in interesting cases of low device-lead coupling [58]. This overestimation can often be attributed to too simplistic treatment of electron-electron interactions [59,60]. In the worst case, when many-body interaction effects beyond mean field become important, these methods might even predict nonphysical results such as low conductivity when the device would really show transparent conduction due to many-body effects [61].

Therefore it is desirable to extend these techniques with methods to tackle the effects of strong correlations in an out-of-equilibrium context [57,62–67]. Many-body effects of electron-electron interaction can be studied by making use of simplified model Hamiltonians. By using a model-based approach, however, results may strongly depend on the model parameters, which are usually notoriously difficult to estimate. For benzene, physically relevant interaction parameters have been obtained in literature by fitting experimental spectra [68,69] which provide the basis for many theoretical works [26,27]. Such parametrizations are typically not unique, since considering different interaction matrix elements may yield again a good agreement with a specific set of experimental data but might promote very different physical mechanisms. Another approach, yielding model parameters, is to determine them in an *ab initio* way from first-principles calculations [70,71]. Again, these parameters are subject to changes due to screening effects, when the molecular device is finally coupled to leads or embedded in an environment [72,73].

In this work we study the many-body effects of electron-electron interaction beyond mean field in the steady state (sts) of a ring-shaped molecular junction under voltage bias in a magnetic field. A simple Pariser-Parr-Pople model [74,75] description for the atomic carbon p_z orbitals is employed for a charge-neutral device coupled to two metallic leads. We address the question of how electron-electron interactions influence device properties in a magnetic field and identify their fingerprints. We do so by assessing naturally important quantities for molecular junctions, which are sts observables under applied bias voltage. We focus on studying the dependence of the sts currents, sts charge density, as well as sts magnetization on electron-electron interactions and a magnetic field, as well as their dependence on device-lead coupling. The purpose of this work is to concentrate on the qualitative effects of electronic correlations, rather than seeking quantitative agreement with experiments. A detailed, quantitative comparison to experiments would of course require the inclusion of additional electronic bands, mechanical vibrations, as well as charging and temperature effects. On the other hand, correlation effects would be very difficult to treat at a comparable level of accuracy in such a rich model. In this work we focus on the interaction effect on the most simple model for a benzene junction to identify basic mechanisms. However, the presented approach can easily be generalized to include anchor groups or specific lead geometry.

To solve the interacting system out of equilibrium, we use cluster perturbation theory [76–78], which amounts to treating the intercluster hopping within first-order strong coupling perturbation theory. This approach is, in principle, refinable by considering larger cluster sizes. Here, we target directly the sts, which is formulated in the framework of sts cluster perturbation theory (stsCPT). We work out general expressions for the sts density matrix and all bond currents in presence of a magnetic field in terms of stsCPT single-particle Green's functions. This framework provides a flexible, versatile, and easy to use method for evaluating sts observables for interacting molecular junctions out of equilibrium in magnetic fields. It can easily be generalized to other junctions and can straightforwardly be combined with *ab initio* calculations.

Our results indicate that while properties of the electronic structure of the bare device, including symmetry considerations and degeneracies, have a dominant influence [27] on the sts behavior, electron-electron interactions effectively renormalize conduction characteristics like threshold voltages and plateau currents in magnetic fields. We find that the sts charge density becomes strongly renormalized beyond mean field and identify signals in the sts magnetization. This paves the way for an even more sound and trustworthy interpretation of results from sophisticated *ab initio*-based methods, as well as model-based calculations at fixed model parameters. Furthermore, we reexamine effects introduced by magnetic fields in context with electron-electron interactions, lead-induced broadening, as well as lead electronic structure.

This paper is organized as follows. We present the theoretical model in Sec. II and introduce the formalism for our calculations in Sec. III. We outline how to systematically improve results obtained with the presented method and compare obtained data with existing calculations in Sec. III D. Results for the sts currents, sts charge density, and sts magnetization are provided in Sec. IV.

II. MODEL

We consider the effect of electron-electron interactions on the electric transport through a benzenelike aromatic molecular ring. A simple starting point is provided by a tight-binding approach for the molecule coupled to the left and right metallic leads [see Fig. 1 (top)]:

$$\hat{\mathcal{H}} = \hat{\mathcal{H}}_{\text{ring}} + \hat{\mathcal{H}}^{L}_{\text{lead}} + \hat{\mathcal{H}}^{R}_{\text{lead}} + \hat{\mathcal{H}}_{\text{ring-leads}}\,. \tag{1}$$

The benzene ring is modelled by considering one atomic p_z orbital $\phi_{i\sigma}$ per carbon atom, yielding a six-atomic-orbital Pariser-Parr-Pople [74,75] [(extended) Hubbard [79]] Hamiltonian,

$$\begin{aligned}\hat{\mathcal{H}}_{\text{ring}} = \sum_{\sigma}\Bigg[&\left(\epsilon_d + \sigma\frac{B}{2} - \frac{U}{2} - 2W\right)\sum_{i=1}^{6}\hat{n}_{i\sigma} \\ &+ t_d\sum_{i}^{6}\left(e^{i\Phi(B)}d^{\dagger}_{i\sigma}d_{i+1\sigma} + e^{-i\Phi(B)}d^{\dagger}_{i+1\sigma}d_{i\sigma}\right)\Bigg] \\ &+ U\sum_{i=1}^{6}\hat{n}_{i\uparrow}\hat{n}_{i\downarrow} + W\sum_{\sigma\sigma'}\sum_{\langle ij\rangle}\hat{n}_{i\sigma}\hat{n}_{j\sigma'}\,,\end{aligned} \tag{2}$$

where $i,j \in [1,6]$ enumerates the six ring orbitals in a clockwise fashion. The six nearest-neighbor bonds are denoted $\langle ij\rangle$. Elementary fermionic operators $d_{i\sigma}/d^{\dagger}_{i\sigma}$ annihilate/create an electron on the ring orbital $\phi_{i\sigma}$ with spin $\sigma = \{\uparrow,\downarrow\}$, and

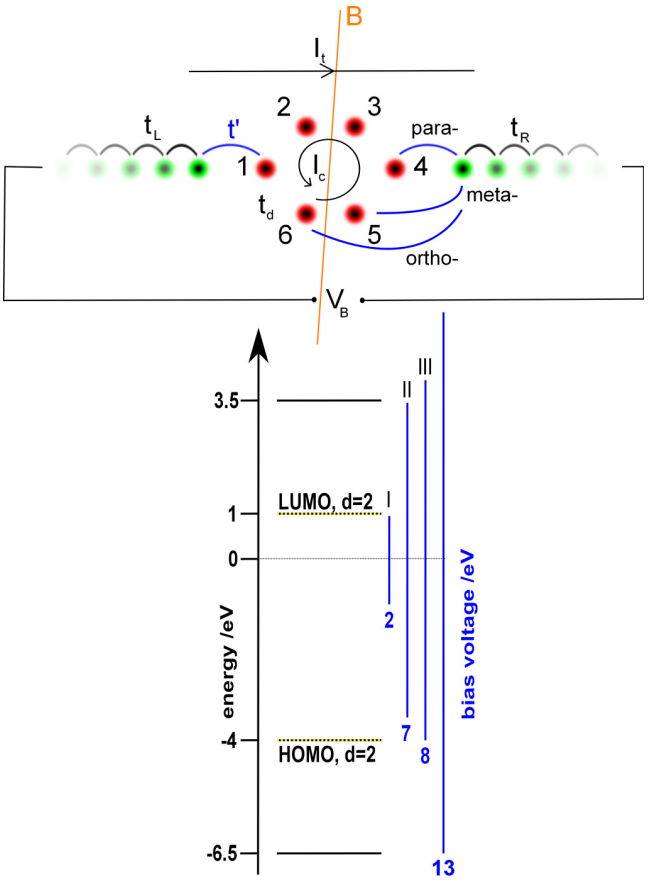

FIG. 1. (Color online) (Top) Illustration of the device setup: A planar molecular ring is connected to two metallic reservoirs. The setup is placed in a perpendicular magnetic field B. A bias voltage V_B is applied between the left and right lead. (Bottom) Bare single-particle energy levels of the noninteracting, disconnected molecule. Bias voltages required for the specific levels to contribute to transport are indicated on the right. The HOMO as well as the LUMO are doubly degenerate ($d = 2$) for $B = 0$.

the particle number operator is defined in the usual way as $\hat{n}_{i\sigma} = d^\dagger_{i\sigma} d_{i\sigma}$.

The on-site energy of the ring orbitals is comprised of the bare on-site energy $\epsilon_d = -1.5\,\text{eV}$ [80] (with respect to the leads), a Zeeman term $\sigma \frac{B}{2}$, and a correction canceling the mean-field contribution of the on-site interaction U and the nearest-neighbor density-density interaction W: $-\frac{U}{2} - 2W$. Literature [68,69] provides an optimal parametrization for Eq. (2) when not connected to leads. Fitting to excitation spectra [81], the authors of Ref. [68] find that benzene is best described by a nearest-neighbor overlap integral of $t_d \approx -2.5$ eV and an on-site interaction of $U \approx 10$ eV [82]. Such a model is frequently used in literature [26,27], along with approaches where the interaction parameters are determined in an *ab initio* way from first-principles calculations [70,71]. We expect the values of U and W to be substantially reduced when the molecule is connected to the leads due to screening from the band electrons [72,73]. Therefore we set in the following $t_d = -2.5$ eV and discuss values of $U \leqslant 9$ eV as well as $W \leqslant 3$ eV.

We consider the effects of a magnetic field B which is applied perpendicular to the plane spanned by the molecular ring. This is described by a Peierls phase [83] $\Phi(B)$ as well as by a Zeeman term.

For simplicity, we model the right ($\alpha = R$) and left ($\alpha = L$) leads by semi-infinite tight-binding chains,

$$\hat{\mathcal{H}}^\alpha_{\text{lead}} = \sum_\sigma \left[\left(\epsilon_\alpha \pm \frac{V_B}{2} \right) \sum_{i=1}^{\infty} \hat{n}_{i\alpha\sigma} + t_\alpha \sum_{\langle ij \rangle} c^\dagger_{i\alpha\sigma} c_{j\alpha\sigma} \right], \quad (3)$$

where the fermionic operators in the lead orbitals $c_{i\alpha\sigma}/c^\dagger_{i\alpha\sigma}$ are defined in a standard way. The resulting semicircular electronic density of states (DOS) is centered around the leads' on-site energy ϵ_α, which is fixed to zero for zero bias. Application of a bias voltage V_B is done by shifting the lead's chemical potential (strictly speaking, at infinity) and on-site energies to $\epsilon_\alpha = \mu_\alpha = \mp \frac{V_B}{2}$, so that the leads are kept half-filled. We use a large lead nearest-neighbor hopping $t_\alpha = -6.0$ eV (independent of α), which implies a quite large bandwidth $D = 24$ eV, so that most of our results are comparable to the wide-band limit [80,84]. We will also discuss and compare to differently shaped lead DOS when effects on the sts properties are to be expected.

The coupling between the ring and the leads is described by a single-particle hopping t' to the left and right lead. The leads are connected to the molecule in the so-called para(1,4), meta(1,5), or ortho(1,6) configuration. Here the two numbers in the braces label the ring position at which the (left, right) lead is attached, denoted $(1, x \in \{4,5,6\})$ in the following:

$$\hat{\mathcal{H}}_{\text{ring-leads}} = \sum_\sigma \left[t' \left(d^\dagger_{1\sigma} c_{1L\sigma} + c^\dagger_{1L\sigma} d_{1\sigma} \right) + t' \left(d^\dagger_{x\sigma} c_{1R\sigma} + c^\dagger_{1R\sigma} d_{x\sigma} \right) \right]. \quad (4)$$

This molecular-lead setup provides a good description of, e.g., two widely used experimental techniques: scanning tunneling microscopy (STM) [6] or MCBJ [8]. Then the STM tip/substrate material or break junction material enters in $\hat{\mathcal{H}}_{\text{lead}}$ through the DOS, while $\hat{\mathcal{H}}_{\text{ring-leads}}$ describes the tunneling from the molecule into the experimental device. In most of the present work, we focus on a typically small value for the molecule-lead coupling of $t' = -0.05$ eV [16], which enhances both the effects of electronic correlations and of the magnetic field. This leads to a level broadening of the order of $\Gamma \propto \pi t'^2 \text{DOS}_{\text{leads}}(\omega = 0) \approx \frac{t'^2}{|t|} \approx 10^{-4}$ eV. To study the effects of this lead-induced broadening, we also present results for larger t'.

For the sake of simplicity we neglect the effects of mechanical vibrations. The coupling of the electronic degrees of freedom to vibrations can lead to a renormalization of conductance thresholds as well as current plateaus as discussed in Ref. [85] and will be addressed in more detail in future work [86]. Furthermore, we do not discuss charging effects due to the connection of the leads.

III. METHOD

We aim at calculating sts properties of an interacting molecular device. Here we focus on the current between each bond as well as the charge distribution and magnetization.

We consider two currents of special interest: (i) the total transmission current j_t and (ii) the circular current j_c. In the presence of a bias-induced transmission current, the two ring directions carry different currents. This leads, in principle, to an ambiguity in the definitions of the circular current. However, as discussed by Rai *et al.* [80], the most natural expression is the one which is directly related to the current-induced magnetic flux through the ring. According to Biot-Savart's formula [87], this is given by the average current obtained by weighting the current flowing through each segment by its length. In our case, in which there are two contacts dividing two ring segments $i = 1,2$ of lengths L_i (in units of the lattice constant), in which currents $\bar{j}_i$ flow (say, clockwise), we have

$$j_c = \frac{(\bar{j}_1 L_1 + \bar{j}_2 L_2)}{6}. \tag{5}$$

In this work, we consider couplings to the leads in para: $L_1 = 3, L_2 = 3$, meta: $L_1 = 4, L_2 = 2$, and ortho: $L_1 = 5, L_2 = 1$ configuration [see Fig. 1 (top)].

The total transmission current is given by

$$j_t = \bar{j}_2 - \bar{j}_1 ,$$

which equals the inflow as well as the outflow at the bonds connecting the leads to the ring by virtue of the continuity equation.

The sts charge distribution $\langle n \rangle$ and magnetization $\langle m \rangle$ can be obtained from the sts single-particle density matrix D^σ_{ij}, which also encodes all information about the sts current.

A. Nonequilibrium Green's functions

One way of obtaining the sts density matrix is by making use of nonequilibrium Green's functions in the Keldysh-Schwinger [88–90] formalism,

$$\widetilde{G} = \begin{pmatrix} G^R & G^K \\ 0 & G^A \end{pmatrix},$$

where $G^{R/A/K}$ are matrices in orbital/spin space and functions of two time coordinates τ [91]. R denotes the retarded, A the advanced, and K the Keldysh component of the single-particle Green's function in Keldysh space $\widetilde{G}$. Since we focus on the sts, time translation invariance applies and we can express the Green's functions in frequency space ω.

The sts density matrix D^σ_{ij} is obtained from the sts Green's function $\widetilde{G}(\omega)$ in matrix notation:

$$D^\sigma_{ij} = \frac{\delta_{ij}}{2} - \frac{i}{2}\int_{-\infty}^{\infty} \frac{d\omega}{2\pi} G^{K\sigma}_{ij}(\omega). \tag{6}$$

The sts current through orbital i in the presence of a magnetic field B can be obtained by the time derivative of the total particle number of orbitals on either side of i [92]. In terms of equal time [93] correlation functions, one can express the current by Keldysh Green's functions $G^K = G^< + G^>$ in a symmetrized way $j^\sigma_{i,i+1} = \frac{e}{2\hbar}(t_{i,i+1\sigma} G^{K\sigma}_{i,i+1}(\tau,\tau) - t_{i+1,i\sigma} G^{K\sigma}_{i+1,i}(\tau,\tau))$.

Generalizing the notation to arbitrary indices and keeping in mind that a definition of current only makes sense for nearest-neighbor orbitals, an expression in terms of the sts density matrix D becomes available:

$$\begin{aligned} j^\sigma_{ij} &= \frac{e}{2\hbar}\left(h^\sigma_{ij}\int_{-\infty}^{\infty}\frac{d\omega}{2\pi}G^{K\sigma}_{ij}(\omega) - h^\sigma_{ji}\int_{-\infty}^{\infty}\frac{d\omega}{2\pi}G^{K\sigma}_{ji}(\omega)\right) \\ &= \frac{ie}{\hbar}\left(h^\sigma_{ij}D^\sigma_{ij} - h^\sigma_{ji}D^\sigma_{ji}\right), \end{aligned}$$

where h^σ_{ij} denotes the single-particle part of $\hat{\mathcal{H}}$ [Eq. (1)] in the orbital/spin basis. The expression is purely real because D and h are Hermitian.

Since we are concerned with electron-electron interactions, evaluating the needed Green's functions $\widetilde{G}$ is not possible in general.

B. Steady-state cluster perturbation theory

We employ stsCPT [76,94,95] as outlined in Refs. [77] and [78] to construct an approximate solution for $\widetilde{G}(\omega)$ in the sts.

Within this approach, the thermodynamically large system Eq. (1) is split into individually, exactly solvable parts at time $\tau \to -\infty$. The single-particle Green's function $\widetilde{g}(\omega)$ for each of these parts (clusters) is obtained by analytic or numeric means. The coupling between these parts is switched on at a later time τ_0 using the intercluster (perturbation) matrix T, which holds the couplings between the disconnected parts. The sts Green's function of the full system in the stsCPT [94,95] approximation is given by

$$\widetilde{G}(\omega)^{-1} = \widetilde{g}(\omega)^{-1} - \widetilde{\mathbb{1}} \otimes T , \tag{7}$$

where $\widetilde{\mathbb{1}}$ is the identity in Keldysh space. We use lower case g for the single-particle Green's function of the initially decoupled equilibrium system, while upper case G denote the sts Green's functions of the fully coupled system. The stsCPT approximation made here is to replace the self-energy Σ_G of the full system by the self-energy Σ_g of the cluster. This amounts to a first-order strong coupling perturbation theory in intercluster terms T. The appealing aspect of this approximation is that it becomes exact in each one of three different limits: (i) for $T = 0$, (ii) for $U = 0$, or, in principle, (iii) for an infinite cluster.

In our case, the system at $\tau \to -\infty$ thus consists of the molecular ring $\hat{\mathcal{H}}_{\text{ring}}$ [Eq. (2)], disconnected from the two leads $\hat{\mathcal{H}}^\alpha_{\text{lead}}$ [Eq. (3)], i.e., $t' = 0$. One can compute the retarded single-particle Green's function g^R of the interacting ring by a standard Lanczos approach, [96,97] and that of the noninteracting leads analytically [98,99]. The advanced component is available by the identity $g^A = (g^R)^\dagger$. The Keldysh component g^K of the initial systems, which are separately in equilibrium, can by obtained by the relation [100]

$$g^K(\omega) = [g^R(\omega) - g^A(\omega)][1 - 2p_{\text{FD}}(\omega,\mu,\beta)], \tag{8}$$

where $p_{\text{FD}}(\omega,\mu,\beta) = \frac{1}{e^{\beta(\omega-\mu)}+1}$ is the Fermi-Dirac distribution function, β denotes the inverse temperature, and μ the chemical potential.

The state of the molecular device at $\tau \to -\infty$ is half-filled and unpolarized for all parameters under discussion in this work. While, in principle, the sts results should not depend on the initial state of the finite-size central part, the approximate nature of the calculation leads to some dependencies on the

initial temperature and chemical potential of the central region in the presence of interactions. In general, we take the zero temperature ground state as a starting ($\tau \to -\infty$) point, which leads to very good results in most cases. There are some exceptions, in particular when degenerate states are involved. Therefore blocking effects as discussed in [26,27] cannot be observed within our approach. However, these are expected to occur for $B = 0$ up to very small fields only [27], since B breaks the degeneracy responsible for these effects.

It is sufficient to calculate two 6×6 matrix Green's functions for the central molecule (six orbitals times spin) and four scalar Green's functions representing the contacting orbital of the two leads (times spin). Making use of Eq. (7), these three initial systems are perturbatively connected by the coupling Hamiltonian [Eq. (4)] in the single-particle basis to obtain the sts single-particle Green's function in Keldysh space $\widetilde{G}(\omega)$.

C. Evaluation of steady-state observables

Using the $\widetilde{G}(\omega)$ obtained via stsCPT, we rewrite the expression for the sts density matrix Eq. (6) in the corresponding language,

$$D^{\sigma}_{ij} = \frac{i}{2}\int_{-\infty}^{\infty}\frac{d\omega}{2\pi}\left[G^{R\sigma}_{in}(\omega)P^{\sigma}_{nj}(\omega) - P^{\sigma}_{in}(\omega)G^{R\sigma *}_{jn}(\omega)\right] + \frac{i}{2}\int_{-\infty}^{\infty}\frac{d\omega}{2\pi}\left[G^{R\sigma}_{in}(\omega)([P^{\sigma}(\omega),T^{\sigma}]_{-})_{nm}G^{R\sigma *}_{jm}(\omega)\right], \tag{9}$$

where $[A,B]_{-}$ denotes the standard commutator, and Einstein's summation convention is implicit. The occupation matrix $P^{\sigma}(\omega)$ corresponds to the second part of Eq. (8) and is diagonal: $P^{\sigma}_{ij}(\omega) = 2\delta_{ij}\, p_{\mathrm{FD}}(\omega,\mu_i,\beta_i)$, where μ_i, β_i are the chemical potential and inverse temperature of site i at $\tau \to -\infty$. This expression is used to evaluate all sts observables as defined in Sec. III A.

The integrals in Eq. (9) are nonzero only between $\mu_{\min}$ and $\mu_{\max}$, which is due to the P dependence and renders the numerical evaluation of Eq. (9) much more favorable than directly evaluating Eq. (6). For a numerical evaluation, a high-precision adaptive integration scheme is necessary [101], especially when it comes to resolving small differences in bond currents as induced by magnetic fields [see Eq. (5)].

D. Quality of the stsCPT approximation and systematic improvements

In the following we assess the quality of the stsCPT approximation and discuss systematic improvements for the treatment of correlations. Upon testing we found these improvements to be unimportant for this particular setup. They can, however, be be of considerable importance in systems exhibiting a more complicated quantum mechanical ground state [78].

As discussed above, one can, in principle, systematically improve results by enlarging the central region to include a certain number of orbitals of the leads in addition to the molecular ring. This means that at $\tau \to -\infty$ the system is disconnected at some bond t of the lead's chain. This sets much higher computational demands because the Hilbert space of the interacting part of the system grows exponentially in system size. In order to assess the accuracy of our results, we have investigated the convergence by adding one to three sites of each lead to the molecule and found negligible deviations in the sts results. This also allows us to conclude that data presented in this work are accurate and no serious error is being made due to the above-mentioned approximations. Other expansions in the framework of Keldysh perturbation theory are discussed in Ref. [28] in this context.

Another way of improving the approximation for the self-energy is to include a self-consistent feedback within the nonequilibrium variational cluster approach [77,78]. We find this to be a major improvement for "gapless"systems. In this work we consider a system which has a large highest-occupied to lowest-unoccupied molecular orbital gap (HOMO-LUMO, respectively), and we found the improvements introduced by the self-consistency to be less important. Therefore, in this work we are restricted to the nonvariational stsCPT. Moreover, we limit ourselves to zero temperatures, although finite temperatures are easily accessed.

IV. RESULTS AND DISCUSSION

We present results for the sts properties of para-, meta-, and ortho-connected benzene. We start by discussing lead-induced broadening effects on the interacting ring within stsCPT for a broad range of molecule lead coupling strengths. Then we focus on the interesting case of small molecular lead coupling, where the effects of a magnetic field B and electron-electron interactions become important. The current-voltage characteristics of the total transmission current j_t and the circular current j_c are presented, including a discussion of effects induced by the shape of the leads' DOS. We identify the behavior of threshold voltages V_T and maximum reachable currents. A detailed view on the highly interesting bias region of high variation in the current (around V_T) will be provided, identifying the effects of electron-electron interactions on the current signal shapes. Finally, we examine the sts particle density $\langle n\rangle$ and magnetization $\langle m\rangle$ in the device.

We note that the presented method becomes exact in the noninteracting limit $(U,W) \to 0$ and therefore has to agree with results for the noninteracting device presented by Rai *et al.* [16,17], obtained by calculations based on the Landauer formula [102] (not shown). We go beyond their detailed description in terms of transmission coefficients and QI effects by discussing effects of electron-electron interaction and by adding a Zeeman term to the discussion of the magnetic field. As discussed above, our approach may become unreliable in the presence of degeneracies in transport states, which occur in this model for $B = 0$ (see Sec. III B). Therefore we do not observe the current blocking state which has been reported [26,27] in asymmetrically connected junctions at finite bias voltage for $U > 0$ and $B = 0$.

A. Lead-induced broadening

Lead-induced broadening is obviously important for not-too-small values of the molecule-lead coupling t', as we show in Fig. 2 (top). On the other hand, there are important broadening effects even for small t', such as the ledge in the

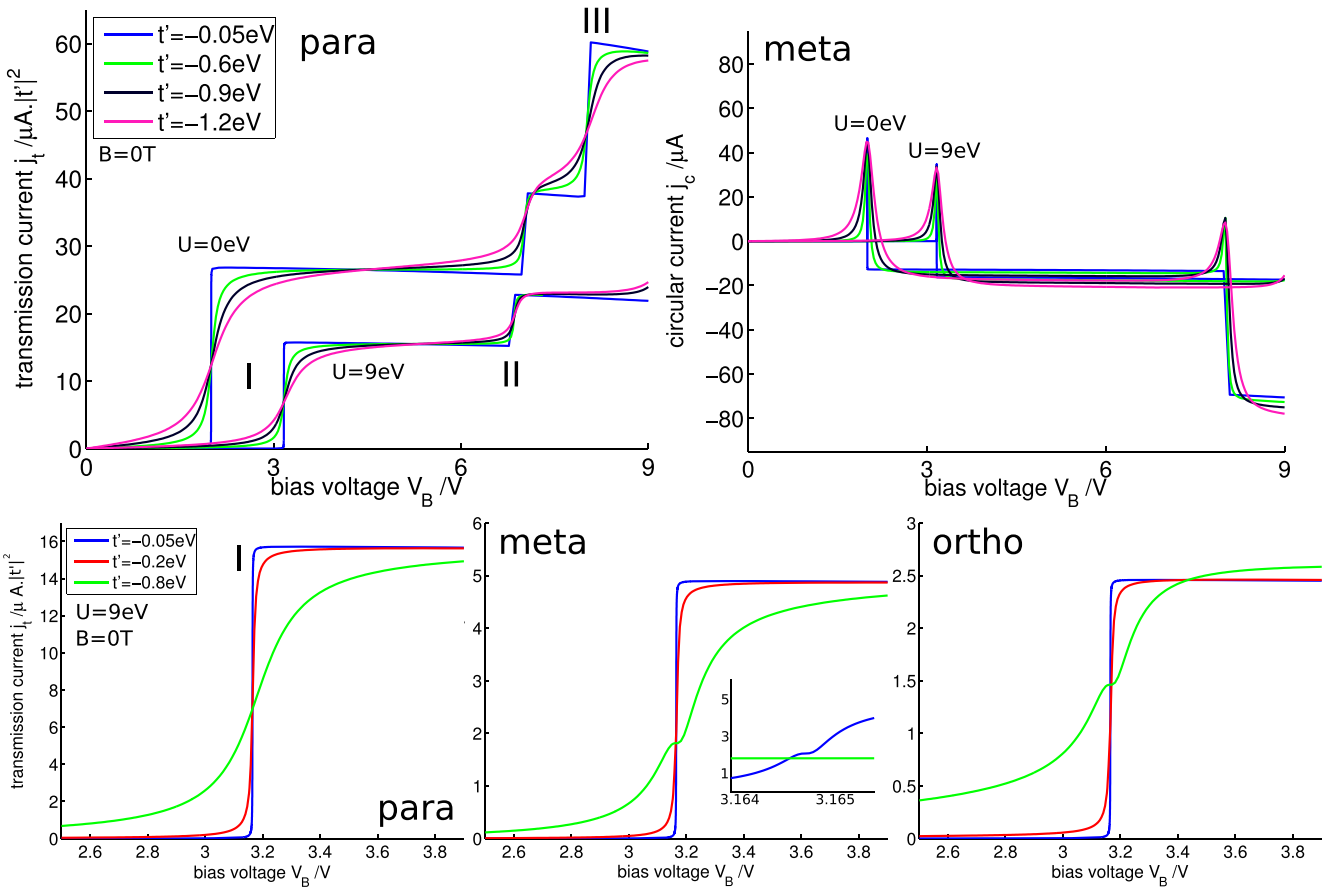

FIG. 2. (Color online) (Top row) In the left panel, the total transmission current j_t for molecule-lead couplings of $t' = -0.05$ eV (blue), $t' = -0.6$ eV (green), $t' = -0.9$ eV (black), and $t' = -1.2$ eV (magenta) is shown for para-connected benzene. In the right panel the circular current j_c is shown for the same parameters. In each panel we visualize results for the noninteracting device and for an on-site interaction strength of $U = 9$ eV. (Bottom row) The total transmission current j_t for molecule-lead couplings of $t' = -0.05$ eV (blue), $t' = -0.2$ eV (red), and $t' = -0.8$ eV (green) is shown for para-(left), meta-(center), and ortho-(right) connected benzene in the vicinity of the first threshold voltage. Data shown are for an on-site interaction strength of $U = 9$ eV in the zero-field setup. The zoom in the central figure shows the ledge for $t' = 0.05$ eV in detail. Note that the vertical axis of the transmission current data is scaled by a factor of $\frac{1}{|t'|^2}$.

transmission current visible in Fig. 2 (bottom) for the meta and ortho setup, which is absent in the para case [103]. It is clear that an accurate treatment of broadening effects is highly desirable, even more so when electron-electron interactions come into play. We find that the total transmission current scales with $|t'|^2$, while the circular current does not show a clear scaling as a function of t'.

A technique commonly employed in the field of molecular electronics is based on generalized master equations [26,27]. Lead-induced broadening is in general difficult to take into account accurately within such methods. stsCPT is able to capture broadening effects even in the interacting molecule, thus rendering stsCPT an interesting, complementary approach to the generalized master equation technique.

Note that we did not discuss the effects of a magnetic field here since they are fully washed away by the large t' (for reasonable fields on the order of a few Tesla). Effects of electronic correlations become increasingly important for smaller t'. For these two reasons, in the rest of this work we focus on $t' = -0.05$ eV because we aim at studying the interplay of a correlated device in a magnetic field.

B. Field-dependent current-voltage characteristics

To ease navigation in the rest of the text, we provide a bird's eye view on the current-voltage characteristics in a large voltage regime $V_B = [0,9]$ V in Fig. 3. Here, effects of the finite bandwidth on the transmission current are still small. Since the magnetic field induces a very small energy scale in comparison with the on-site, hopping, and interaction energies in the Hamiltonian [Eq. (1)], we will be zooming into regions $V_B = \pm 0.001$ V around selected voltage points. We note that the absolute position on the bias axis strongly depends on the bare molecule-lead potential difference ($\epsilon_d = -1.5$ eV) which governs the first threshold voltage.

We start out by comparing the total transmission current j_t and the circular current j_c of para-, meta-, and ortho-connected benzene for the noninteracting case, as well as for $U = 9$ eV, with and without magnetic field B. j_t shows multiple threshold voltages V_T in a plateaulike structure for all three device setups. At exactly these thresholds, a signal spike in j_c is observed. Those signals in j_c are of considerable magnitude, which are tens of microamperes, as compared to j_t, which is on the order of tens of nanoamperes, the latter being

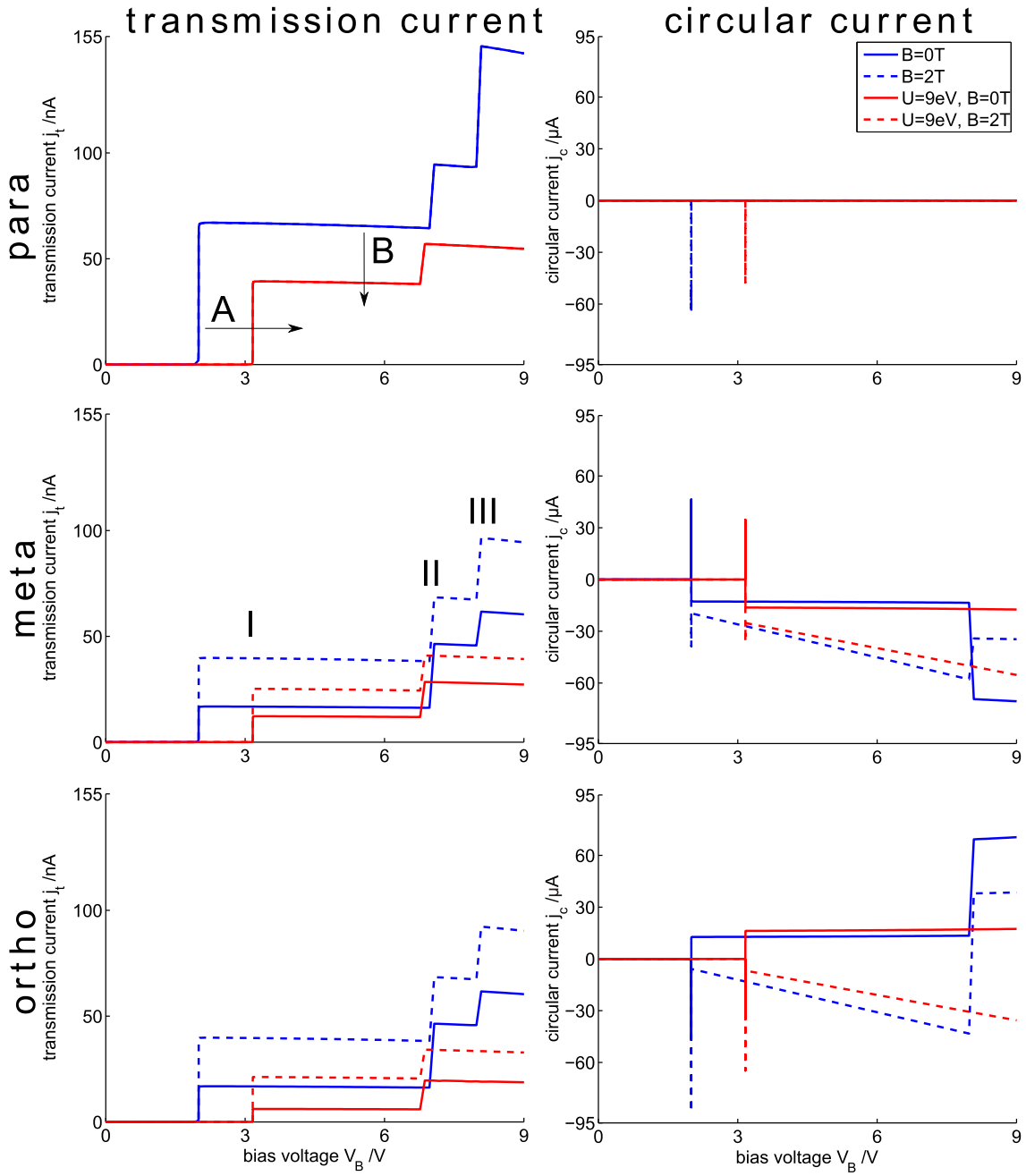

FIG. 3. (Color online) Current-voltage characteristics of para-(top), meta-(center), and ortho-(bottom) connected benzene. We plot the total transmission current j_t/nA in the left and the ring current $j_c/\mu A$ in the right column. For every device setup, data for the noninteracting case (blue) is shown in comparison to results for an on-site interaction strength of $U = 9$ eV. We compare data for the zero-field case (solid lines) to curves obtained for a magnetic field of $B = 2$ T (dash-dotted lines).

mainly determined by the molecule-lead coupling t'. Such thresholds in j_t and large signals in j_c seem to be a generic feature of molecular ring devices [104–106] and can be associated with nearly degenerate pairs of states with opposite angular momentum whose contribution to the net current is rendered small by destructive interference [80]. We discuss the interaction dependence of the threshold voltages V_T in detail in Sec. IV D. Here we note that one effect of electron-electron interaction is to shift the conduction thresholds V_T (see A in Fig. 3). Notice that this is a pure correlation effect, since the mean-field contribution has already been subtracted.

The magnitude of the plateaus in j_t is fixed by the amount of current which can be carried by the molecular level starting to participate in transport at the corresponding V_T. Due to symmetry, j_t in the para device is quite a bit higher than in the corresponding meta or ortho devices, the latter two being comparable. In particular, we find that the plateau current magnitudes are the same in the noninteracting meta and ortho devices but not when interactions are present (see also Sec. IV E). The transmission current of the para setup is independent of the magnetic field, while in the meta and ortho device, j_t grows until it seems to saturate, at least for

the magnetic field magnitudes discussed in this work (see Sec. IV E). Increasing on-site interaction U or density-density nearest-neighbor interaction W (not shown) always decreases the total transmission current (see B in Fig. 3, discussion in Sec. IV E).

The spikes in j_c at V_T (which are split by the Zeeman field, see Sec. IV F) are of considerable magnitude, which is tens of microamperes. Similarly to j_t, increasing on-site interaction U or nearest-neighbor density-density interaction W reduces the magnitude of these signals. In the para device the ring currents exactly cancel for $B = 0$ T due to device symmetry, while in the other two setups circular currents are also present in the field-free system. Upon increasing the magnitude of the magnetic field, all currents show saturation (see Sec. IV E). Note that for half-filled systems in the large U limit [107] the current is unaffected by magnetic flux because electron motion becomes severely hindered [22].

We find that effects of electron-electron interactions (shifting of conduction thresholds and decreasing plateau currents in j_t and signal currents in j_c) are smooth and do not depend on the specific type of interaction (on-site or nearest-neighbor density-density).

C. Effects originating from the electronic structure of the leads

Instead of the often imposed wide-band DOS of the leads, we use a semicircular lead DOS with a large bandwidth ($t = -6$ eV). As expected, our setup mimics a wide-band limit regarding j_t for low bias voltages where only a small bending down of the current can be observed due to the negative curvature at $\omega = 0$ eV of the leads' DOS [see Fig. 3 (left)].

However, it turns out that j_c is highly sensitive to even slight variations in the leads' DOS. Let us first discuss the behavior of j_c in detail. In the para setup, the magnetic field induces peaks in j_c at V_T, while in between it falls back to plateaus in the nanoampere range. In the meta and ortho setup, also at zero field, a finite ring current exists which can be amplified or suppressed by the magnetic flux, depending on its direction according to Lenz's law [87]. These two setups show a behavior of j_c which is different from the para case. Without magnetic field, j_c shows plateaus ($\propto V_B^2$) in the microampere range between the peaks. When a magnetic field is imposed, the two conducting states of the molecule at $k = \pm\frac{2\pi}{3}$ and energy $\omega \approx 1$ eV split up [see Fig. 1 (bottom)]. In our setup j_c shows a linear growth between the signals starting at the first threshold voltage. This large effect can be traced back to different occupation of the $k = \pm\frac{2\pi}{3}$ states. Calculations for a constant lead DOS do not show this linear increase in circular current. Instead, constant plateaus (and therefore a moderate imbalance in the population of the $k = \pm\frac{2\pi}{3}$ states) are obtained. These plateaus have a magnitude which j_c acquires for the semicircular DOS right after V_T. The crucial parameter here is the curvature of the lead DOS, which in the end amplifies the population imbalance and renders it bias dependent. For a semicircular DOS, the coupling of the two levels at $\omega \approx 1$ eV to the high-bias and low-bias lead is of different magnitude (effectively Γ becomes different for the two leads), and this difference grows linearly with increasing bias voltage. To our knowledge, this effect has not been discussed before and is probably difficult to observe experimentally, especially since it strongly depends on the features of the DOS of the leads. Moreover, electron-electron interaction does not play a role here. However, if a suitable system can be constructed, bias voltage could be used to linearly tune the circular current over a significant current magnitude.

D. Current signal position

The transmission current-voltage characteristics consist of plateaus with steep jumps between them [see Fig. 4 (left)]. These signal positions at threshold voltages V_T are independent of the setup used (para, meta, or ortho connection) and furthermore, are independent of the magnetic field B [108]. We plot data for meta-connected benzene for $B = 1$ T as a representative in Fig. 4 (left). The width of the current

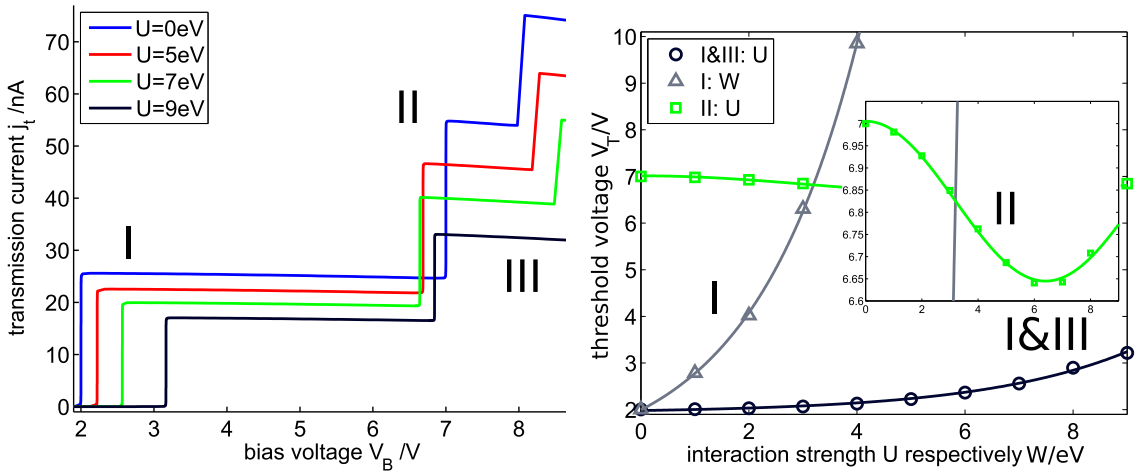

FIG. 4. (Color online) (Left) Total transmission current j_t as a function of bias voltage V_B for various interaction strengths U. We illustrate data for meta-connected benzene and a magnetic field of $B = 1$ T. (Right) Threshold voltage V_T at which the signal in the circular current j_c and inflection point in the transmission current j_t occurs in regions I, II, and III (symbols).

signals is $\approx 10^{-3}$ eV (see Sec. IV F) due to the small lead-ring coupling t'.

For the noninteracting disconnected ring without magnetic field [Eq. (2)], the single-particle energy levels are located at $\epsilon_k = \epsilon_d + 2t_d \cos(k) = \{-6.5, -4, -4, 1, 1, 3.5\}$ eV for $k = \frac{2\pi n}{6}$ and $n \in [-2,3]$, which leads to a ground-state energy in the nonpolarized half-filled case of $\omega_0 = -29$ eV, with dynamics governed by a HOMO-LUMO gap [109] of $\Delta = 5$ eV [see Fig. 1 (bottom)]. Based on this energetic structure, one expects signals in the current at bias voltages of $V_B \approx (2\times$ electronic level position), i.e., at $\approx 2, 7, 8$, and 13 V. This is confirmed by our data (see Fig. 3).

In the interacting device one can still interpret our data in terms of the single-particle excitations of the molecular system obtained from exact diagonalization of the molecular Hamiltonian [Eq. (2)]. Comparing the HOMO-LUMO gap $\Delta(U,W)$ to the data for the sts current (see Fig. 4), one finds a linear relation between the gap and the threshold voltage $V_T^{\mathrm{I}} = \Delta - 3$ eV. Note that the constant depends on the position of the molecular on-site energy with respect to the leads, but the effects of interactions in Δ are universal for weakly coupled charge-neutral devices. From our data we find a change in the HOMO-LUMO gap due to interactions beyond mean field $\Delta(U)[\mathrm{eV}] = 5[\mathrm{eV}] + (0.02 \pm 0.01)\, e^{(0.43\pm0.03)U[\mathrm{eV}]}$. The jump to plateau III exhibits the same dependence on U as the jump to plateau I but located at a different position: $V_T^{\mathrm{III}} = \Delta + 3$ eV. Interestingly enough, these two thresholds are monotonic in interaction strength but the threshold II in between is not. It shows a strongly nonmonotonic behavior [see Fig. 4 (right)].

The functional dependence of the thresholds on on-site U is the same as for nearest-neighbor density-density interactions W (not shown). It is clear that the HOMO-LUMO gap grows much quicker with increasing W than with increasing U.

We conclude that the voltage thresholds in the parameter regime of the device under study, which consists of (i) small molecule-lead coupling $t' \ll t_d \ll t$ and (ii) a charge-neutral setting, are perturbatively accessible and can even be inferred to a high degree of accuracy from the single-particle spectrum of the isolated device. However, our results show that they can be subjected to nonmonotonic behavior as a function of interaction strength.

E. Current signal magnitude

We now turn to the analysis of the maximum current $j_t^{\max}$ in the vicinity (± 0.1 V) of the first threshold voltage V_T^{I}.

As noted before, the para setup does not show a magnetic field dependence in this channel for fixed interaction parameters due to device symmetry [thick black line, stars in Fig. 5 (left)]. In the meta and ortho devices, we find that the maximum current increases as a function of magnetic field $|B|$ until saturation for the considered range of magnetic field strength for all bias voltages [see Fig. 5 (right)].

Note that the eigenstates of the disconnected, noninteracting molecule in a magnetic field are $\epsilon_{n_\sigma} = \epsilon_d + \sigma\frac{B}{2} + 2t_d \cos[\frac{2\pi n_\sigma}{L} + \Phi(B)]$, with $n_\sigma \in [-2,3]$. The inherent circular current driven by the magnetic field is given by $j_c^{\mathrm{inh}} = -\frac{e\hbar 2\pi}{m_e 6^2}\sum_{n_{\mathrm{occ},\sigma}} n_\sigma$. From this expression it is clear that in this case the circular current magnitude is bounded from above because the magnetic field just redistributes occupied momenta of compact states. This analysis holds for all finite-size quantum ring devices, but not for the corresponding one-dimensional field theory [110].

Depending on interaction strength U, we find that the maximum transmission current is monotonically decreasing (roughly $\propto$ const. $- U^2$) in all device setups [see Fig. 5 (left)]. The same effect is observed for nearest-neighbor density-density interactions W (not shown). The maximum transmission currents of the meta and ortho device are identical in the noninteracting device but start to differ when interactions are turned on.

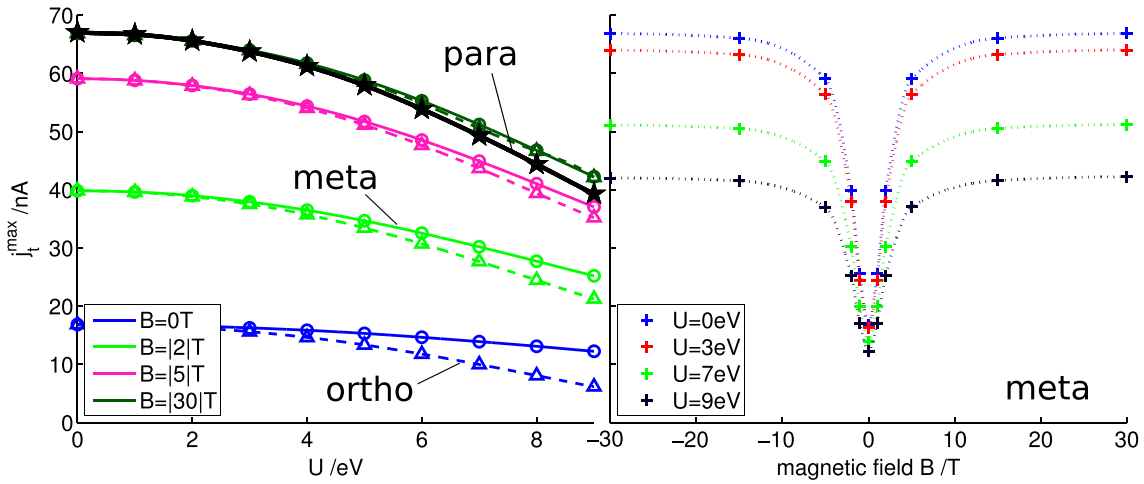

FIG. 5. (Color online) Maximal total transmission current $j_t^{\max}$ in the vicinity of the first threshold voltage (I). (Left) As a function of on-site interaction strength U for the meta (solid, circles) and ortho (dashed, triangles) device. For the para setup (thick black line, stars), it is independent of B as a function of U. (Right) The same quantity showing saturation as a function of B for various values of on-site interaction strength U in the meta device.

F. Current signal

A zoom-in to the signal in the sts currents at the position of their respective first threshold voltages (I) is provided in Fig. 6. We compare the currents for the noninteracting system with those of on-site interaction strength $U = 9$ eV. We observe similar signal shapes for all values of interaction strength (U, W). These signals are, however, shifted in bias depending on the electron-electron interaction parameters (U, W) and the signal magnitude is decreased. In Fig. 6 we compare the signals of the noninteracting and interacting setups whereby the horizontal axis has been shifted in order for the threshold voltages to coincide.

The total transmission current j_t does not depend on the direction of the magnetic field in the para setup. The magnitude of the plateaus is, however, increased with increasing $|B|$ in the meta and ortho setup, while staying on the field-free value in the para setup. The effects of the Zeeman term are visible in j_t due to a splitting $\propto |B|$ of the transition to the next plateau into two subplateaus around the transition points V_T.

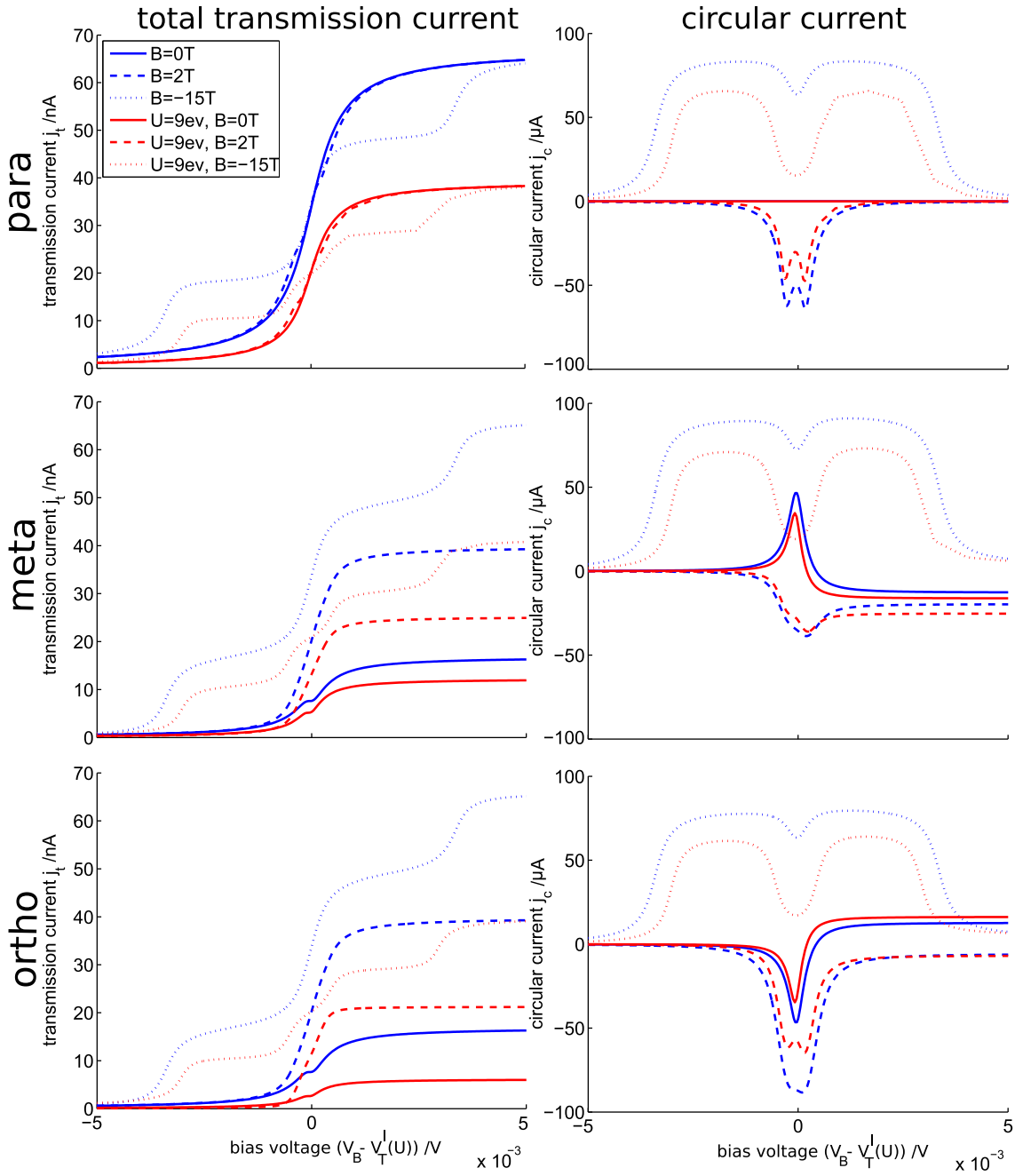

FIG. 6. (Color online) Total transmission current signal j_t (left column) and ring current signal j_s (right column) as a function of bias voltage V_B. From top to bottom we compare the current signal in the para-, meta-, and ortho-connected device for the noninteracting case $U = 0$ eV (blue) to an on-site interaction strength of $U = 9$ eV (red). We show data for zero field $B = 0$ T (solid), a field of $B = 2$ T (dashed), as well as $B = 15$ T(dotted). The signals have been shifted from their respective first threshold voltage (I) on top of each other to $V_B = 0$.

The circular currents j_c in the para setup depends on B in a symmetric way, i.e., reversing the direction of B reverses just the sign of j_c. The meta and ortho setups show a different magnitude in the circular current for the same $|B|$ due to inherent circular currents which are either amplified by the magnetic field or suppressed, depending on its alignment. The Zeeman splitting introduces a double-peak structure around V_T which is proportional to the magnetic field magnitude $|B|$. This splitting is introduced in a symmetric fashion around V_T. The circular currents j_c grow with increasing magnetic field until a saturation is reached. Besides the decrease in circular current magnitude, we observe a more pronounced Zeeman splitting with increasing interaction strength.

We again find a generic dependence on interactions beyond mean field, i.e., using on-site or nearest-neighbor density-density interaction, which might even permit extracting interaction parameters for model Hamiltonians by carrying out transport measurements and fitting the position and height of sts currents at threshold voltages.

G. Steady-state local charge density

The sts charge density is shown in Fig. 7 for all three device setups for an interaction strength of $U = 9$ eV and a magnetic field of $B = 2\,\mathrm{T}$ as an example for its generic behavior. It exhibits features at the same threshold voltages as the sts current, where it either decreases or increases in a plateaulike fashion. In the para setup [Fig. 7 (left)] we observe an increased charge density at the orbitals at which the leads are connected and a strongly reduced charge density in the other orbitals of the molecule due to interactions, i.e., for the noninteracting molecule all densities would start at one. The sts charge density of the meta and ortho setups [Fig. 7 (right)] are symmetry related. They show the same sts charge density, except for the fact that two orbitals exchange their respective charge density each.

The suppression of occupation is most pronounced in the orbitals in the "interior" of the molecule, respecting symmetry. These are orbitals 2,3,5,6 in the para device, orbitals 3,6 in the meta device, and orbitals 2,5 in the ortho device.

For smaller interaction strength, the overall shape of the curves does not change. However, we find that in all setups, for on-site interaction strengths $U \leqslant 5$ eV, all local densities are 1 in the low-bias regime up to the first threshold voltage, $\Delta n = 0$, and depend on the interaction strength beyond that point. For interaction strength $U \geqslant 6$ eV, Δn depends on interaction also in the low-bias region.

We note that for increasing molecule-lead coupling t', the magnitude of the sts local charge density stays the same but the transitions become washed out (not shown). Furthermore, with increasing bias voltage as well as in the vicinity of the threshold voltages, a splitting of the degenerate orbitals occurs.

The main effect of interactions beyond mean field is to suppress the sts charge density respecting the symmetry of the isolated molecule. Such substantial charge redistribution in sts transport due to interactions is an important effect to be considered when discussing results from self-consistent DFT+NEGF calculations.

H. Steady-state magnetization

In our calculations a Zeeman term is included. Therefore the magnetic field induces a sts magnetization in the vicinity of the threshold voltages V_T. We consider just the paramagnetic (spin) contribution, since it is the dominant term. In Fig. 8, we show data for all three device setups in the vicinity of the first voltage threshold (I) for the interacting case. Increasing the magnetic field turns the resonancelike structure in j_c around V_T into a structure which consists of two maxima on the positive

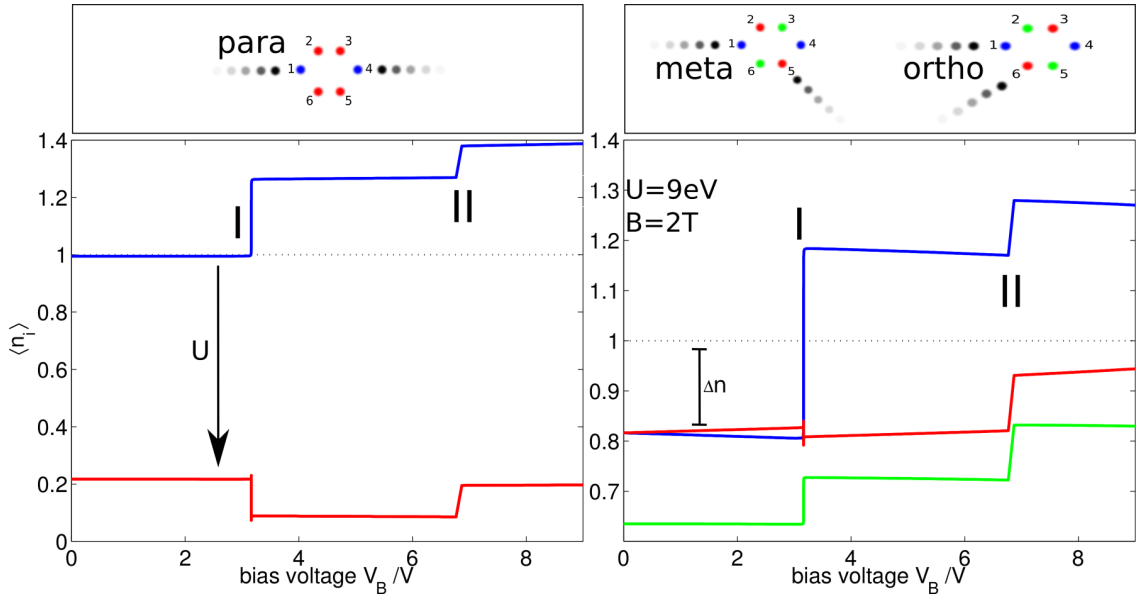

FIG. 7. (Color online) Ss local charge density of the para-connected device (left) as well as the meta-, and ortho-connected devices (right). We show data for a device with on-site interaction of $U = 9$ eV in a magnetic field of $B = 2$ T. The drawings of the device at the top serve as a legend for the line colors to identify the respective orbitals. Δn denotes the shift of the local density away from $\langle n_i \rangle = 1$ in the low-bias region.

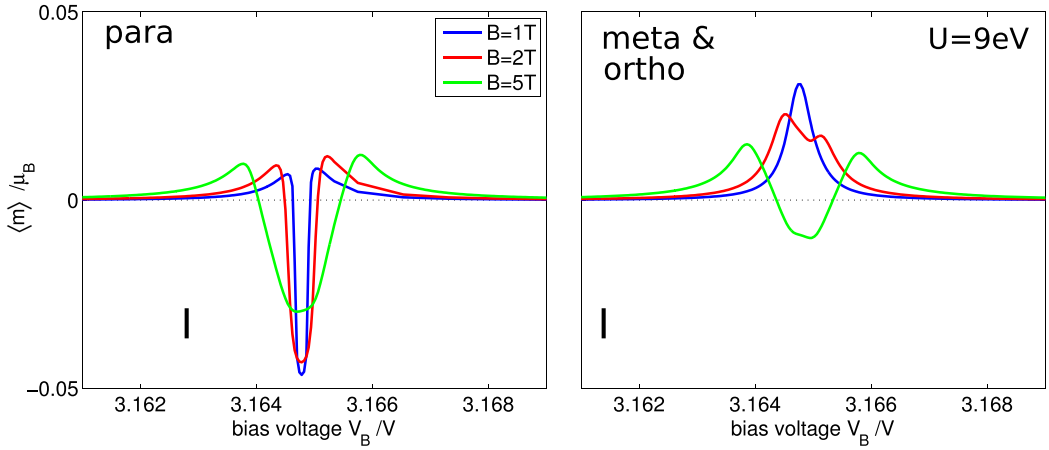

FIG. 8. (Color online) Signals in the sts magnetization of the device due to the Zeeman effect. We compare the effects of magnetic fields of $B = 1$ T (blue), $B = 2$ T (red), and $B = 5$ T (green) for a device with an on-site interaction of 9 eV.

and one on the negative axis in between. The effect of changing the direction of the magnetic field while keeping $|B|$ constant is to mirror the sts magnetization curves around the x axis (not shown). Without interactions the effect is quite similar and only of slightly different magnitude.

We find that the sts magnetization is a highly sensitive quantity as a function of bias voltage (in the submillivolt regime) in the region around V_T where it is possible to alter the direction as well as the magnitude of the magnetization by $\approx \pm 10^{-2}/\mu_B$.

V. CONCLUSIONS

We study effects of electron-electron interactions in a benzenelike ring-shaped molecule, subject to a finite bias voltage induced by two metallic leads, as a function of an applied magnetic field. We make use of a Hubbard-type-model–based description of such a device in the charge-neutral regime. Using steady-state cluster perturbation theory, observables have been computed for para, meta, as well as ortho setups.

Results for the total transmission current and circular current as well as the steady-state charge distribution and magnetization have been presented. By studying physically relevant regimes of electron-electron interactions in addition to an applied magnetic field, we describe the effects of electron-electron interactions on the steady state beyond the mean-field level. We found that these are to shift voltage thresholds and to decrease the magnitude of currents. Additionally, interactions lead to deviating currents in the meta and ortho setup which were comparable in the noninteracting system. The steady-state charge distribution becomes strongly renormalized by interactions respecting the symmetry of the isolated molecule. Due to the Zeeman effect, we obtain a steady-state magnetization which is highly sensitive to bias voltage.

Our results may help to validate model calculations at fixed interaction parameters and contribute to the understanding of sophisticated *ab initio*–based transport calculations. They might even contribute to designing empirical formulas for junction engineering. Our results indicate that the main effect of interactions is to renormalize voltage thresholds and current magnitudes. Care has to be taken in discussing symmetry relations of meta- and ortho-connected devices. Furthermore, we showed that the charge density is sensitive to electron-electron interactions and becomes strongly renormalized with every additional electronic level contributing to transport. This fact has to be accounted for in self-consistent approaches. We find that insights into the relevant interaction parameters, as well as their magnitude, could be extracted from transport measurements, provided the on-site potential of the molecule with respect to the leads is known.

We presented general expressions for steady-state observables in the language of steady-state cluster perturbation theory. The presented formalism is flexible and simple to apply to a broad range of molecular junctions. Its approximate nature is systematically improvable, and the method does work in all parameter regimes. The method is especially interesting in parameter regimes which exhibit extremely high time scales, rendering approaches based on time evolution not feasible, and when lead-induced broadening effects become important, which renders generalized master equation techniques difficult. The presented approach is, however, unable to capture interaction-mediated interference effects, such as current blocking in asymmetrically connected junctions, when degeneracies in transport channels are present. This can be overcome by a more elaborate construction of the "starting" ($\tau \to -\infty$) cluster state. Work along these lines is in progress.

ACKNOWLEDGMENTS

We gratefully acknowledge fruitful discussions with Karin Zojer, Dmitry A. Ryndyk, and Max Sorantin. This work was partly supported by the Austrian Science Fund (FWF, No. P24081-N16) as well as SFB-ViCoM (Projects No. F04103 and No. F04104). M.N. thanks the MPI-PKS Dresden, particularly Masud Haque and the QSOE13, for hospitality.

[1] G. Cuniberti, G. Fagas, and K. Richter, *Introducing Molecular Electronics* (Springer, New York, 2005).

[2] R. H. M. Smit, Y. Noat, C. Untiedt, N. D. Lang, M. C. van Hemert, and J. M. van Ruitenbeek, Nature (London) **419**, 906 (2002).

[3] J. Park, A. N. Pasupathy, J. I. Goldsmith, C. Chang, Y. Yaish, J. R. Petta, M. Rinkoski, J. P. Sethna, H. D. Abruna, P. L. McEuen *et al.*, Nature (London) **417**, 722 (2002).

[4] W. Liang, M. P. Shores, M. Bockrath, J. R. Long, and H. Park, Nature (London) **417**, 725 (2002).

[5] N. Agrait, A. L. Yeyati, and J. M. van Ruitenbeek, Phys. Rep. **377**, 81 (2003).

[6] L. Venkataraman, J. E. Klare, C. Nuckolls, M. S. Hybertsen, and M. L. Steigerwald, Nature (London) **442**, 904 (2006).

[7] A. Nitzan and M. A. Ratner, Science **300**, 1384 (2003).

[8] M. A. Reed, C. Zhou, C. J. Muller, T. P. Burgin, and J. M. Tour, Science **278**, 252 (1997).

[9] E. Lörtscher, H. B. Weber, and H. Riel, Phys. Rev. Lett. **98**, 176807 (2007).

[10] J. C. Cuevas and E. Scheer, *Molecular Electronics: An Introduction to Theory and Experiment*, 1st ed. (World Scientific, Singapore, 2010).

[11] M. Kiguchi, O. Tal, S. Wohlthat, F. Pauly, M. Krieger, D. Djukic, J. C. Cuevas, and J. M. van Ruitenbeek, Phys. Rev. Lett. **101**, 046801 (2008).

[12] H. Song, Y. Kim, Y. H. Jang, H. Jeong, M. A. Reed, and T. Lee, Nature (London) **462**, 1039 (2009).

[13] A. A. Kocherzhenko, L. D. A. Siebbeles, and F. C. Grozema, J. Phys. Chem. Lett. **2**, 1753 (2011).

[14] S.-H. Ke, W. Yang, and H. U. Baranger, Nano Letters **8**, 3257 (2008).

[15] R. Stadler, M. Forshaw, and C. Joachim, Nanotechnology **14**, 138 (2003).

[16] D. Rai, O. Hod, and A. Nitzan, Phys. Rev. B **85**, 155440 (2012).

[17] D. Rai, O. Hod, and A. Nitzan, J. Phys. Chem. Lett. **2**, 2118 (2011).

[18] G. C. Solomon, D. Q. Andrews, T. Hansen, R. H. Goldsmith, M. R. Wasielewski, R. P. Van Duyne, and M. A. Ratner, J. Chem. Phys. **129**, 054701 (2008).

[19] T. Markussen, R. Stadler, and K. S. Thygesen, Nano Letters **10**, 4260 (2010).

[20] Y. Aharonov and D. Bohm, Phys. Rev. **115**, 485 (1959).

[21] Y. Aharonov and D. Bohm, Phys. Rev. **123**, 1511 (1961).

[22] S. Viefers, P. Koskinen, P. S. Deo, and M. Manninen, Phys. E (Amsterdam, Neth.) **21**, 1 (2004).

[23] J. P. Bergfield, G. C. Solomon, C. A. Stafford, and M. A. Ratner, Nano Lett. **11**, 2759 (2011).

[24] A. Valli, Ph.D. thesis, Vienna University of Technology, 2013.

[25] A. Valli, G. Sangiovanni, A. Toschi, and K. Held, Phys. Rev. B **86**, 115418 (2012).

[26] G. Begemann, D. Darau, A. Donarini, and M. Grifoni, Phys. Rev. B **77**, 201406 (2008).

[27] D. Darau, G. Begemann, A. Donarini, and M. Grifoni, Phys. Rev. B **79**, 235404 (2009).

[28] J. P. Bergfield and C. A. Stafford, Phys. Rev. B **79**, 245125 (2009).

[29] J. P. Bergfield and C. A. Stafford, Nano Lett. **9**, 3072 (2009).

[30] D. Bohr and P. Schmitteckert, Ann. Phys. **524**, 199 (2012).

[31] M. Leijnse, W. Sun, M. Brondsted Nielsen, P. Hedegard, and K. Flensberg, J. Chem. Phys. **134**, 104107 (2011).

[32] D. A. Ryndyk, J. Bundesmann, M.-H. Liu, and K. Richter, Phys. Rev. B **86**, 195425 (2012).

[33] A. C. Hewson, *The Kondo Problem to Heavy Fermions* (Cambridge University Press, Cambridge, UK, 1997).

[34] L. H. Yu, Z. K. Keane, J. W. Ciszek, L. Cheng, J. M. Tour, T. Baruah, M. R. Pederson, and D. Natelson, Phys. Rev. Lett. **95**, 256803 (2005).

[35] L. Tosi, P. Roura-Bas, and A. A. Aligia, J. Phys.: Condens. Matter **24**, 365301 (2012).

[36] R. J. Nichols, W. Haiss, S. J. Higgins, E. Leary, S. Martin, and D. Bethell, Phys. Chem. Chem. Phys. **12**, 2801 (2010).

[37] S. Datta, *Quantum Transport: Atom to Transistor*, 2nd ed. (Cambridge University Press, Cambridge, UK, 2005).

[38] M. D. Ventra, *Electrical Transport in Nanoscale Systems* (Cambridge University Press, New York, 2008).

[39] D. K. Ferry, S. M. Goodnick, and J. Bird, *Transport in Nanostructures*, 2nd ed. (Cambridge University Press, Cambridge, UK, 2009).

[40] Y. V. Nazarov and Y. M. Blanter, *Quantum Transport: Introduction to Nanoscience* (Cambridge University Press New York, 2009).

[41] L. Venkataraman, J. E. Klare, I. W. Tam, C. Nuckolls, M. S. Hybertsen, and M. L. Steigerwald, Nano Lett. **6**, 458 (2006).

[42] K. Richter, *Semiclassical Theory of Mesoscopic Quantum Systems* (Springer, New York, 1999).

[43] C. Caroli, R. Combescot, P. Nozieres, and D. Saint-James, J. Phys. C: Solid State Phys. **4**, 916 (1971).

[44] P. Hohenberg and W. Kohn, Phys. Rev. **136**, B864 (1964).

[45] W. Kohn and L. J. Sham, Phys. Rev. **140**, A1133 (1965).

[46] T. Frederiksen, M. Paulsson, M. Brandbyge, and A.-P. Jauho, Phys. Rev. B **75**, 205413 (2007).

[47] J. Taylor, H. Guo, and J. Wang, Phys. Rev. B **63**, 245407 (2001).

[48] M. Brandbyge, J.-L. Mozos, P. Ordejón, J. Taylor, and K. Stokbro, Phys. Rev. B **65**, 165401 (2002).

[49] Y. Fujimoto and K. Hirose, Phys. Rev. B **67**, 195315 (2003).

[50] A. R. Rocha, V. M. Garcia-Suarez, S. Bailey, C. Lambert, J. Ferrer, and S. Sanvito, Phys. Rev. B **73**, 085414 (2006).

[51] A. Calzolari, N. Marzari, I. Souza, and M. Buongiorno Nardelli, Phys. Rev. B **69**, 035108 (2004).

[52] K. Thygesen and K. Jacobsen, Chem. Phys. **319**, 111 (2005).

[53] Z. Li and D. S. Kosov, J. Phys.: Condens. Matter **18**, 1347 (2006).

[54] T. M. Perrine, T. Berto, and B. D. Dunietz, J. Phys. Chem. B **112**, 16070 (2008).

[55] A. Arnold, F. Weigend, and F. Evers, J. Chem. Phys. **126**, 174101 (2007).

[56] Recently it was found that using the DFT auxiliary (Kohn-Sham) particles in Kubo linear response theory, the conductance through a benzene molecular junction is zero for all bias voltages, while a "noninteracting" description in terms of the reduced density matrix leads to conduction on the correct order of magnitude [111].

[57] A. A. Dzhioev and D. S. Kosov, J. Chem. Phys. **134**, 044121 (2011).

[58] C. Toher, A. Filippetti, S. Sanvito, and K. Burke, Phys. Rev. Lett. **95**, 146402 (2005).

[59] P. Delaney and J. C. Greer, Phys. Rev. Lett. **93**, 036805 (2004).

[60] M. Strange, I. S. Kristensen, K. S. Thygesen, and K. W. Jacobsen, J. Chem. Phys. **128**, 114714 (2008).

[61] W. Lee, N. Jean, and S. Sanvito, Phys. Rev. B **79**, 085120 (2009).

[62] R. Baer and D. Neuhauser, Chem. Phys. Lett. **374**, 459 (2003).

[63] K. S. Thygesen and A. Rubio, Phys. Rev. B **77**, 115333 (2008).

[64] P. Myöhänen, A. Stan, G. Stefanucci, and R. van Leeuwen, Phys. Rev. B **80**, 115107 (2009).

[65] C. D. Spataru, M. S. Hybertsen, S. G. Louie, and A. J. Millis, Phys. Rev. B **79**, 155110 (2009).

[66] Y. Dahnovsky, Phys. Rev. B **80**, 165305 (2009).

[67] E. Arrigoni, M. Knap, and W. von der Linden, Phys. Rev. Lett. **110**, 086403 (2013).

[68] R. J. Bursill, C. Castleton, and W. Barford, Chem. Phys. Lett. **294**, 305 (1998).

[69] B. William, *Electronic and Optical Properties of Conjugated Polymers* (Oxford University Press, Oxford, UK, 2005).

[70] M. H. Hettler, W. Wenzel, M. R. Wegewijs, and H. Schoeller, Phys. Rev. Lett. **90**, 076805 (2003).

[71] D. A. Ryndyk, A. Donarini, M. Grifoni, and K. Richter, Phys. Rev. B **88**, 085404 (2013).

[72] K. Kaasbjerg and K. Flensberg, Nano Lett. **8**, 3809 (2008).

[73] S. Kubatkin, A. Danilov, M. Hjort, J. Cornil, J.-L. Bredas, N. Stuhr-Hansen, P. Hedegard, and T. Bjornholm, Nature (London) **425**, 698 (2003).

[74] R. Pariser and R. Parr, J. Chem. Phys. **21**, 767 (1953).

[75] J. A. Pople, Trans. Faraday Soc. **49**, 1375 (1953).

[76] M. Balzer and M. Potthoff, Phys. Rev. B **83**, 195132 (2011).

[77] M. Knap, W. von der Linden, and E. Arrigoni, Phys. Rev. B **84**, 115145 (2011).

[78] M. Nuss, C. Heil, M. Ganahl, M. Knap, H. G. Evertz, E. Arrigoni, and W. von der Linden, Phys. Rev. B **86**, 245119 (2012).

[79] J. Hubbard, Proc. R. Soc. London, Ser. A **276**, 238 (1963).

[80] D. Rai, O. Hod, and A. Nitzan, J. Phys. Chem. C **114**, 20583 (2010).

[81] *National Institute for Standards and Technology, Computational Chemistry Comparison and Benchmark Data Base*, http://cccbdb.nist.gov/ (2012) [Online; accessed 28-December-2012].

[82] Bursill *et al.* [68] used an Ohno parametrization for of-diagonal interaction parameters which in our notation reads $W_{ij}[\mathrm{eV}] = \frac{U[\mathrm{eV}]}{2\sqrt{1+\frac{U[\mathrm{eV}]r_{ij}[\mathrm{A}]}{14.397}}}$ and found $U \approx 10.06\,\mathrm{eV}$. In literature often only nearest-neighbor density-density interactions are included using $W = 6\,\mathrm{eV}$ [26, 27]. Very recently it was shown that for the model under discussion it is possible to take nonlocal Coulomb interaction into account in an effective model with reduced on-site Coulomb interaction only [112]. Based on a constrained random phase approximation calculation, they found a value for the bare on-site interaction $\frac{U}{t} = 3.96$, which reduces in the model with on-site interactions only by more than a factor of 2: $\frac{U^*}{t} = 1.2$.

[83] We carry out the Peierls substitution in a standard way [16] for fields B perpendicular to the ring plane. The geometry of the ring enters through the expression $(\mathbf{r}_i \times \mathbf{r}_j) \cdot \hat{e}_z$, which is a parallelepiped consisting of one-third of the area of the full ring. Using the lattice constant of benzene $a = 1.39\,\mathrm{\AA}$ [81], one obtains nearest-neighbor hopping in the ring structure of $\tilde{t}_d = t_d\, e^{i\frac{\sqrt{3}a^2}{4}\frac{B[T]}{2.35.10^5}} = t_d\, e^{i1.2713.10^{-5}B[T]} = t_d\, e^{i\Phi(B)}$.

[84] In the wide-band limit, a featureless (constant) electronic density of states of the reservoirs is assumed which has a bandwidth much larger than the characteristic energy scales of the system coupled to the reservoir. The retarded Green's function is then given by $G^R(\omega) = -\frac{1}{2W}\ln(\frac{\omega-W}{\omega+W})$, where W is the half-bandwidth. To compare to the semicircular DOS, the intralead hopping $t_\alpha^{\mathrm{wide-band}} = \frac{t_\alpha}{4\pi}$ has to be rescaled so that the same Γ is obtained.

[85] M. Knap, E. Arrigoni, and W. von der Linden, Phys. Rev. B **88**, 054301 (2012).

[86] M. Sorantin, E. Arrigoni, and W. von der Linden (unpublished).

[87] J. D. Jackson, *Classical Electrodynamics* (Wiley, New York, 1998).

[88] J. Schwinger, J. Math. Phys. **2**, 407 (1961).

[89] R. Feynman and F. V., Jr., Ann. Phys. **24**, 118 (1963).

[90] L. Keldysh, Zh. Eksp. Teor. Fiz. **47**, 1515 (1965).

[91] J. Rammer and H. Smith, Rev. Mod. Phys. **58**, 323 (1986).

[92] H. Haug and A. Jauho, *Quantum Kinetics in Transport and Optics of Semiconductors*, 2nd ed. (Springer-Verlag GmbH, Berlin, 1996).

[93] We denote real time by τ.

[94] C. Gros and R. Valenti, Phys. Rev. B **48**, 418 (1993).

[95] D. Sénéchal, D. Perez, and M. Pioro-Ladrière, Phys. Rev. Lett. **84**, 522 (2000).

[96] C. Lanczos, J. Res. Natl. Bur. Stand. (U. S.) **45**, 255 (1951).

[97] Z. Bai, J. Demmel, J. Dongarra, A. Ruhe, and H. van der Vorst, *Templates for the Solution of Algebraic Eigenvalue Problems: A Practical Guide (Software, Environments and Tools)* (Society for Industrial and Applied Mathematics, Philadelphis, PA, 1987).

[98] E. N. Economou, *Green's Functions in Quantum Physics*, 3rd ed. (Springer, New York, 2010).

[99] M. Nuss, E. Arrigoni, M. Aichhorn, and W. von der Linden, Phys. Rev. B **85**, 235107 (2012).

[100] J. W. Negele and H. Orland, *Quantum Many-Particle Systems* (Westview Press, Boulder, CO, 1998).

[101] We use a double adaptive integration scheme CQUAD [113].

[102] R. Landauer, IBM J. Res. Dev. **1**, 223 (1957).

[103] This effect has been obtained as well in Ref. [17].

[104] S. Nakanishi and M. Tsukada, Jpn. J. Appl. Phys. **37**, L1400 (1998).

[105] S. Nakanishi and M. Tsukada, Phys. Rev. Lett. **87**, 126801 (2001).

[106] M. Ernzerhof, H. Bahmann, F. Goyer, M. Zhuang, and P. Rocheleau, J. Chem. Theory Comput. **2**, 1291 (2006).

[107] The large U limit is directly accessible by Bethe ansatz [114] or via transformation to $t\,J$ or Heisenberg Hamiltonians.

[108] Strictly speaking, the threshold voltages V_T depend on the Zeeman splitting, which is, however, a very small energy scale for reasonable magnetic fields.

[109] In this work we refer to the single-particle gap Δ as the HOMO-LUMO gap also for interacting systems $U, W \neq 0$.

[110] The corresponding field theory is exactly solvable, with eigenenergies $\epsilon_n = \frac{\hbar^2 n^2}{2m_e R^2} + V + \mu_B \sigma B - \frac{\hbar e}{2m_e} Bn + \frac{e^2 R^2}{8m_e} B^2$, where V is the electrostatic potential and R the radius of

the ring. The (angular) momentum $\hbar n$ is characterized by $n = 0, \pm 1, \pm 2, \ldots$. The circular current driven by a magnetic field is given by $j_c = \frac{eN}{2\pi R m_e}(eB - \frac{2\hbar}{R^2}\sum_{n_{\mathrm{occ},\sigma}} n_\sigma)$.

[111] P. Schmitteckert, Phys. Chem. Chem. Phys. **15**, 15845 (2013).

[112] M. Schüler, M. Rösner, T. O. Wehling, A. I. Lichtenstein, and M. I. Katsnelson, Phys. Rev. Lett. **111**, 036601 (2013).

[113] P. Gonnet, ACM Trans. Math. Softw. **37**, 26 (2010).

[114] N. Yu and M. Fowler, Phys. Rev. B **45**, 11795 (1992).

5.8. Master equation based steady-state cluster perturbation theory

5.8.1. Preamble

This part of our work is submitted to PHYSICAL REVIEW B (2015) and is available as a preprint on arXiv:1505.01683 [66].

In this work on steady-state transport across molecular junctions we generalize the stsCPT method introduced in Sec. 5.4, Sec. 5.5, Sec. 5.6, Sec. 5.7 and Sec. 5.10 to an improved reference state. The method is outlined in Sec. 3.3.3. The new starting point is a mixed state as obtained from a QME and already incorporates information about the environment. We apply the meCPT to molecular junctions in the single-electron transistor regime as discussed in Sec. 2.1 and Sec. 2.2: An electron-electron interaction based quantum diode and a triple-ring quantum dot junction. Both devices show NDC and interaction induced quantum blocking. The latter is a feature which cannot be captured in the plain stsCPT method but has been observed in QME calculations.

This work is authored by Martin Nuss (MN) and co-authored by Gerhard Dorn (GD), Antonius Dorda (AD) and MN's supervisors Enrico Arrigoni (EA) and Wolfgang von der Linden (WL). This research was to a large and significant extent conducted by MN under the supervision of WL and EA. EA suggested the meCPT method. MN, WL and EA developed the method and decided to apply it to interaction induced current blocking in molecular junctions. MN developed a multi purpose computer code, tested it and ran parameter studies. GD developed a computer code to solve the quantum master equation without the secular approximations. WL and EA provided guidance and expertise. MN ran computer simulations and conducted literature research. MN prepared, collected, interpreted, analyzed and visualized the results and set them in context with recent literature. MN wrote the first version of the manuscript. GD wrote the section on the non-secular approximation. AD provided expertise for the QME and revised the manuscript. All authors contributed in discussing the results and revising the manuscript.

5.8.2. Manuscript

Master equation based steady-state cluster perturbation theory

Martin Nuss,* Gerhard Dorn, Antonius Dorda, Wolfgang von der Linden, and Enrico Arrigoni
Institute of Theoretical and Computational Physics,
Graz University of Technology, 8010 Graz, Austria

(Dated: May 8, 2015)

A simple and efficient approximation scheme to study electronic transport characteristics of strongly correlated nano devices, molecular junctions or heterostructures out of equilibrium is provided by steady-state cluster perturbation theory. In this work, we improve the starting point of this perturbative, nonequilibrium Green's function based method. Specifically, we employ an improved unperturbed (so-called reference) state $\hat{\rho}^S$, constructed as the steady-state of a quantum master equation within the Born-Markov approximation. This resulting hybrid method inherits beneficial aspects of both, the quantum master equation as well as the nonequilibrium Green's function technique. We benchmark the new scheme on two experimentally relevant systems in the single-electron transistor regime: An electron-electron interaction based quantum diode and a triple quantum dot ring junction, which both feature negative differential conductance. The results of the new method improve significantly with respect to the plain quantum master equation treatment at modest additional computational cost.

PACS numbers: 71.15.-m, 71.27+a, 73.63.-b, 73.63.Kv

I. INTRODUCTION

Electronic transport in the realm of molecular scale junctions and devices has become a subject of intense study in recent years.[1–7] Nowadays the controlled assembly of structures[8] via electro migration,[9–17] the contacting in mechanical break-junction setups,[18–21] electronic gating[17,19,22] and measurement via scanning tunnelling microscopy[23–26] have become established tools, ultimately opening routes from elementary understanding to device engineering. Prompted by these formidable advances in experimental techniques, the characterization of transport through e.g. molecules bound by anchor groups to metal electrodes,[21,27,28] heterostructures[29,30] or nano structures on two- dimensional substrates[29,31–36] has become feasible. These constitute the foundation for future applications in electronic devices based on single electron tunnelling,[37] quantum interference effects,[38–44] spin control[45,46] or even quantum many-body effects[9,10,12,47,48] like Kondo[49] behaviour.[50–54]

Typically the electronic transport through such devices is significantly influenced by electronic correlation effects, which may become large due to the reduced effective dimensionality and/or confined geometries. This is reflected, for instance, in major discrepancies between experimental and theoretical current-voltage characteristics obtained with (uncorrelated) nonequilibrium Green's function[55–58] calculations based on *ab-initio* density functional theory states.[1,59–62] The inclusion of many-body effects in the theoretical description of fermionic systems out of equilibrium[55,63–65] is challenging and an active area of current research.[66–74] Suitable approximations need to be devised in order to solve a finite strongly correlated quantum many-body problem out of equilibrium coupled to an infinite environment. Typically, the nonequilibrium setup consists of a correlated central region (system) attached to two leads (environment).

A well-established method for treating such open quantum systems is by means of quantum master equations (Qme).[75–80] Herein, the environment-degrees of freedom are integrated out and usually incorporated in a perturbative manner. The Qme approach allows a detailed investigation of transport phenomena[45,46] and recent self-consistent extensions attempt to cure some of its long-standing limitations.[81]

In the framework of nonequilibrium Green's functions (NEGF) various schemes exist to approximately calculate the electronic self-energy of the correlated region, see e.g. Ref. 68,82–87. In cluster approaches, such as cluster perturbation theory (CPT) and its improvement, the variational cluster approach (VCA),[88] the whole system is partitioned into parts which can be treated exactly and determine the self-energy. Originally devised for strongly correlated systems in equilibrium,[89,90] both approaches have recently been extended to nonequilibrium situations in the time dependent case[91,92] as well as in the steady-state.[92,93] In previous work we applied the steady-state CPT (stsCPT) to obtain transport characteristics of heterostructures,[93] quantum dots[94–96] and molecular junctions[97,98] and obtained good results even in the challenging Kondo regime.[49,94,95]

A key issue in the CPT approach is to identify an appropriate many-body state for the disconnected correlated cluster in the central region, as a starting point of perturbation theory, the so-called reference state. Up to now, a common choice in stsCPT is to use an equilibrium state at some temperature T_S (often $T_S = 0$) and chemical potential μ_S in-between the values of the leads. Such an ad-hoc choice is clearly unsatisfactory. Furthermore, it fails to describe certain quantum interference effects in transport phenomena as for example so-called current blocking effects.[45,46,97]

The purpose of the present work is to improve on stsCPT by constructing a consistent and conceptually

more appropriate reference state, given by the steady-state reduced many-body density matrix $\hat{\rho}^S$ obtained from a Qme in the Born-Markov approximation. Within this quantum master equation based stsCPT (meCPT), the ambiguity in defining μ_S and T_S for the central region is resolved. The equilibrium case, in which μ_S and T_S coincide with those of the environment, is automatically included. In contrast to standard Qme approaches, lead induced level-broadening effects are accounted for and the noninteracting limit is reproduced exactly, as in the original stsCPT. In addition, meCPT is able to capture the previously mentioned current blocking effects, as shown below.

Other NEGF/Qme hybrid methods exist in the literature.[67,99,100] For instance, in a recent work[101,102] we have proposed a so-called auxiliary master equation (AME) approach, whereby a Lindblad equation is introduced which models the leads by a small number of bath sites plus Markovian environments. The AME is suited to address steady-state properties of single impurity problems as encountered in the framework of nonequilibrium dynamical mean field theory.[72,87,101,103–105] In contrast, the meCPT presented in this work is more appropriate to treat non-local self-energy effects which cannot be captured by single-site DMFT.

This paper is organized as follows: After defining the model Hamiltonian in Sec. II, the meCPT is introduced in detail in Sec. III. We present results obtained with the improved method for two experimentally realizable devices: i) In Sec. IV A, an electron-electron interaction based quantum diode, ii) and in Sec. IV B, a triple quantum dot ring junction which both feature negative differential conductance (NDC).

For ring systems, extensive Qme results and an explanation of the NDC in terms of quantum interference mediated blocking are available in Ref. 45,46.

II. MODEL

We consider a model of spin-$\frac{1}{2}$ fermions, having in mind the electronic degrees of freedom of a contacted nano structure, heterostructure or a molecular junction. The Hamiltonian consists of three parts:

$$\hat{\mathcal{H}} = \hat{\mathcal{H}}^S + \hat{\mathcal{H}}^E + \hat{\mathcal{H}}^{SE} . \tag{1a}$$

i) The "system" $\hat{\mathcal{H}}^S$ represents the interacting central region i.e. the nano device or molecule consisting of single-particle as well as interaction many-body terms. It is described by electronic annihilation/creation operators $f_{i\sigma}/f_{i\sigma}^\dagger$ at site $i = [1, \ldots, N_S]$ where N_S is typically small and spin $\sigma = \{\uparrow, \downarrow\}$.[106] We will specify the particular form of $\hat{\mathcal{H}}^S$ in the respective results section. ii) The "environment" Hamiltonian $\hat{\mathcal{H}}^E$ describes the two noninteracting electronic leads

$$\hat{\mathcal{H}}^E = \sum_{\lambda=1}^{2} \sum_{k\sigma} \epsilon_{\lambda k\sigma} c_{\lambda k\sigma}^\dagger c_{\lambda k\sigma} , \tag{1b}$$

where $c_{\lambda k\sigma}/c_{\lambda k\sigma}^\dagger$ denote the fermion operators of the infinite size lead λ with energies $\epsilon_{\lambda k\sigma}$ and electronic density of states (DOS) $\rho_{\lambda\sigma}(\omega) = \frac{1}{N_\lambda} \sum_k \delta(\omega - \epsilon_{\lambda k\sigma})$ where $N_\lambda \to \infty$ are the number of levels in the leads. The disconnected leads are held at constant temperatures T_λ and chemical potentials μ_λ so that the particles obey the Fermi-Dirac distribution $p_\lambda^{\mathrm{FD}}(\omega, T_\lambda, \mu_\lambda)$.[106,107] iii) Finally the system and the environment are coupled by the single-particle hopping

$$\hat{\mathcal{H}}^{SE} = \sum_{\lambda=1}^{2} \sum_{ik\sigma} \left(t'_{\lambda ik\sigma} f_{i\sigma}^\dagger c_{\lambda k\sigma} \right) + h.c. . \tag{1c}$$

III. MASTER EQUATION BASED CLUSTER PERTURBATION THEORY

Our goal is to obtain the steady-state transport characteristics of the Hamiltonian $\hat{\mathcal{H}}$, Eq. (1a) in a nonequilibrium situation induced by environment parameters like a bias voltage V_B or temperature gradient ΔT. The important step consists in evaluating the steady-state single-particle Green's function in Keldysh space $\widetilde{G}$ in the well established Keldysh-Schwinger nonequilibrium Green's function formalism.[108–110] In general $\hat{\mathcal{H}}$ is both interacting and of infinite spatial extent. Therefore explicit evaluation of $\widetilde{G}$ is prohibitive in all but the most simple cases which motivates the introduction of approximate schemes.

One such scheme is CPT,[89,90] in which one performs an expansion in a 'small' single-particle perturbation, for example the system-environment coupling $\hat{\mathcal{H}}^{SE}$ of Eq. (1c). The unperturbed Hamiltonian $\hat{\mathcal{H}}^S + \hat{\mathcal{H}}^E$ can be solved exactly. While in the noninteracting case CPT becomes exact, results obtained in the presence of interaction are approximate and depend on the reference state for the unperturbed system. A common practice within stsCPT[92,94–98] is to use a pure state given by the equilibrium ground state $|\Psi_0\rangle_S$ of the disconnected interacting system Hamiltonian $\hat{\mathcal{H}}^S$. In a nonequilibrium situation, this is still ambiguous, as it depends on an arbitrary choice of the chemical potential μ_S and/or temperature T_S for the interacting finite system.

The goal of this work is to provide an unambiguous and conceptually more rigorous criterion for the choice of the reference state for the interacting central region. Ideally, the reference state is selected such that it resembles best the situation of the coupled system, i.e. for the full Hamiltonian, Eq. (1a) in the steady-state. An appropriate choice in equilibrium is to use the grand-canonical density operator[106] $\hat{\rho}_{gc}^S$ as reference state. In this case,

T_S and μ_S are uniquely determined by the equilibrium situation. Equivalently, $\hat{\rho}^S_{gc}$ is given by the steady-state solution of a Qme in the Born-Markov approximation (see Sec. III B), when coupling the system to one thermal environment. From this viewpoint a natural extension to the nonequilibrium situation is to make use of a Qme as well in order to obtain a consistent reference state, given then by the steady-state reduced density operator of the system $\hat{\rho}^S$. In this work, a second order Born-Markov Qme is employed, which yields the correct zeroth order reduced density operator $\hat{\rho}^S$ (adjusted to $\hat{\mathcal{H}}^{SE}$).[111,112] Subsequently, $\hat{\mathcal{H}}^{SE}$ is included within the CPT approximation,[89,90] in order to obtain improved results for the Green's function and in turn for the transport observables.

In summary, the meCPT method consists of the following three main steps, analogous to a standard CPT treatment:

1. Decompose the whole system into a small interacting central region (system) and noninteracting leads of infinite size (environment), see $\hat{\mathcal{H}}^S$ and $\hat{\mathcal{H}}^E$ in Eq. (1a).

2. The *new step introduced in this work* is to solve a Qme for the system in order to obtain the reduced density operator $\hat{\rho}^S$, which serves as a reference state to calculate the cluster (retarded) Green's function[113]

$$g^R_{ij\sigma}(\tau) = -i\theta(\tau)\mathrm{tr}\left\{\hat{\rho}^S\left[f_{i\sigma}(\tau), f^\dagger_{j\sigma}\right]_+\right\}. \qquad (2)$$

3. Reintroduce the system-environment coupling $\hat{\mathcal{H}}^{SE}$ perturbatively, see Sec. III A and Eq. (4), to determine the Green's function of the coupled system.

A. Steady-state cluster perturbation theory

Here we briefly recall the main, well-established CPT concepts and equations, as this is the starting point for the formalism presented in this work. For an in depth discussion of CPT[114] and its nonequilibrium extension we refer the reader to the literature.[91,93,95,97]

The central element of stsCPT is the steady-state single-particle Green's function in Keldysh space[115]

$$\widetilde{G} = \begin{pmatrix} G^R & G^K \\ 0 & G^A \end{pmatrix}, \qquad (3)$$

where R denotes the retarded, A the advanced, and K the Keldysh component. In the present formalism, $G^{R/A/K}$ become matrices in the space of cluster sites and depend on one energy variable ω since time translational invariance applies in the steady-state.

As explained above, in order to compute $\widetilde{G}(\omega)$ within stsCPT one partitions $\hat{\mathcal{H}}$, Eq. (1a) in real space, into individually exactly solvable parts, in this case, the system $\hat{\mathcal{H}}^S$ and the environment $\hat{\mathcal{H}}^E$, which leaves the coupling Hamiltonian $\mathcal{H}^{SE}$ as a perturbation. The single-particle Green's function of the disconnected Hamiltonian is denoted by $\widetilde{g}(\omega)$, which obviously does not mix the disconnected regions. For the noninteracting environment, the respective block entries of $\widetilde{g}(\omega)$ are available analytically.[94,116] For the interacting part the respective entries of $\widetilde{g}(\omega)$ are calculated via the Lehmann representation with respect to the reference state. This can be computed e.g. based on the Band Lanczos method.[117–119]

The full steady-state Green's function in the CPT approximation is found by reintroducing the inter-cluster coupling perturbatively

$$\widetilde{G}(\omega)^{-1} = \widetilde{g}(\omega)^{-1} - \widetilde{M}; \quad M^R = M^A = M, \; M^K = 0, \qquad (4)$$

where we denote by the matrix M the single-particle Wannier representation of $\hat{\mathcal{H}}^{SE}$. CPT is equivalent to using the self-energy $\widetilde{\Sigma}$ of the disconnected Hamiltonian as an approximation to the full self-energy. Therefore, the quality of the approximation can in principle be systematically improved by adding more and more sites of the leads to the central cluster. However, in doing so the complexity for the exact solution of the central cluster grows exponentially. Independent of the reference state, this scheme becomes exact in the noninteracting limit.

B. Born-Markov equation for the reference state

In the following we outline how to obtain the reference state $\hat{\rho}^S$ by using a Born-Markov-secular (BMsme), or more generally a Born-Markov master equation (BMme).[75–80] Although this approach is standard, for completeness we present here the main aspects and notation. We loosely follow the treatment of Ref. 40,78,79.

The real time τ evolution of the full many-body density matrix $\hat{\rho}$ is given by the von-Neumann equation $\dot{\hat{\rho}} = -i\left[\hat{\mathcal{H}}, \hat{\rho}\right]_-$.[75] Typically the large size of the Hilbert space of $\hat{\mathcal{H}}$ prohibits the full solution in the interacting case. One thus considers the weak coupling limit $|\hat{\mathcal{H}}^{SE}| \ll |\hat{\mathcal{H}}^E|$ and performs a perturbation theory in terms of $|\hat{\mathcal{H}}^{SE}|$.[80,120]

In the usual way one obtains an equation for the reduced many-body density matrix of the system $\hat{\rho}^S(\tau) = \mathrm{tr}_E\{\hat{\rho}\}$ by working in the interaction picture $\hat{\rho}_I(\tau) = e^{+i(\hat{\mathcal{H}}^S+\hat{\mathcal{H}}^E)\tau}\hat{\rho}(0)e^{-i(\hat{\mathcal{H}}^S+\hat{\mathcal{H}}^E)\tau}$ with respect to the coupling Hamiltonian, Eq. (1c). One then performs three standard approximations: i) Within the Born approximation, valid to lowest order in $|\hat{\mathcal{H}}^{SE}|$, the density matrix is factorized $\hat{\rho}_I(\tau) \approx \hat{\rho}^S_I(\tau) \otimes \hat{\rho}^E_I$. Furthermore, the environment $\hat{\rho}^E_I$ is assumed to be so large that it is not affected by $|\hat{\mathcal{H}}^{SE}|$ and thus independent of time. ii) The Markov approximation implies a memory-less environment, that is, the system density matrix varies much slower in time than the decay time of the environment

correlation functions $C_{\alpha\beta}(\tau)$. Upon transforming back to the Schrödinger picture this yields the BMme, which is time-local, preserves trace and hermiticity, and depends on constant coefficients. iii) To obtain an equation of Lindblad form which also preserves positivity one typically employs the secular approximation, which averages over fast oscillating terms, yielding the BMsme.[78,121,122]

The system-environment coupling can be quite generally written in the form $\hat{\mathcal{H}}^{SE} = \sum_\alpha \hat{S}_\alpha \otimes \hat{E}_\alpha$, with $\hat{S}_\alpha = \hat{S}_\alpha^\dagger$ and $\hat{E}_\alpha = \hat{E}_\alpha^\dagger$. This hermitian form is convenient for further treatment.The tensor product form can be achieved even for fermions by a Jordan-Wigner transformation,[79] see App. B. For our coupling Hamiltonian, Eq. (1c) and particle number conserving systems, the coupling operators take the form

$$\hat{S}_{1i\sigma} = \frac{1}{\sqrt{2}}(f_{i\sigma} + f_{i\sigma}^\dagger), \hat{E}_{1\lambda i\sigma} = \frac{1}{\sqrt{2}}(c_{\lambda i\sigma} + c_{\lambda i\sigma}^\dagger) \quad (5)$$
$$\hat{S}_{2i\sigma} = \frac{i}{\sqrt{2}}(f_{i\sigma} - f_{i\sigma}^\dagger), \hat{E}_{2\lambda i\sigma} = \frac{i}{\sqrt{2}}(c_{\lambda i\sigma} - c_{\lambda i\sigma}^\dagger)\,.$$

In the energy eigenbasis of the system Hamiltonian $\hat{\mathcal{H}}^S |a\rangle = \omega_a |a\rangle$, the BMme in the Schrödinger representation reads[113]

$$\dot{\hat{\rho}}^S(\tau) = -i\left[\hat{\mathcal{H}}^S + \hat{\mathcal{H}}^{LS}, \hat{\rho}^S(\tau)\right]_- + \sum_{abcd} \Xi_{ab,cd} \left(|a\rangle\langle b|\,\hat{\rho}^S(\tau)\,|d\rangle\langle c| - \frac{1}{2}\left[\,|d\rangle\langle c|\,|a\rangle\langle b|\,, \hat{\rho}^S(\tau)\right]_+ \right), \quad (6)$$

with

$$\Xi_{ab,cd} = \sum_{\alpha\beta} \xi_{\alpha\beta}(\omega_{ba}, \omega_{dc})\,\langle a|\,\hat{S}_\beta\,|b\rangle\,\langle c|\,\hat{S}_\alpha\,|d\rangle^*\,, \quad (7)$$

where $\omega_{ba} = \omega_b - \omega_a$. The Lamb-shift Hamiltonian $\hat{\mathcal{H}}^{LS}$ and the environment functions $\xi_{\alpha\beta}(\omega_1, \omega_2)$ are defined in App. A. When employing the secular approximation, the terms in the BMsme simplify and in Eq. (7) one can replace $\xi_{\alpha\beta}(\omega_{ba}, \omega_{dc}) \to \xi_{\alpha\beta}(\omega_b - \omega_a)\delta_{\omega_b-\omega_a,\omega_d-\omega_c}$. Due to the secular approximation the BMsme can only lead to interference between degenerate states. The more general BMme also couples non-degenerate states at the cost of loosing the Lindblad structure of the Qme, see Sec. IV B and Ref. 40.

Single-particle Green's function

As discussed above, for meCPT, the Green's function $\widetilde{g}(\omega)$ of the isolated system is evaluated from the reference state $\hat{\rho}^S$. The retarded component Eq. (2) takes the explicit form

$$g^R_{ij(\sigma)}(\omega) = \sum_{abc} \rho^S_{ab} \times \left(\frac{\langle b|\,f_{i\sigma}\,|c\rangle\langle c|\,f_{j\sigma}^\dagger\,|a\rangle}{\omega + i0^+ - (\omega_c - \omega_b)} + \frac{\langle b|\,f_{j\sigma}^\dagger\,|c\rangle\langle c|\,f_{i\sigma}\,|a\rangle}{\omega + i0^+ - (\omega_a - \omega_c)} \right), \quad (8)$$

where i, j denote indices of system sites. The advanced component follows from $g^A = \left(g^R\right)^\dagger$ and the Keldysh component g^K of the finite, unperturbed system is not relevant for the CPT equation, Eq. (4). Once $\widetilde{g}$ is obtained, the full Green's function is again approximately obtained within CPT by Eq. (4). Notice that for $U = 0$, $\widetilde{G}$ is independent of the reference state, which is why stsCPT, stsVCA as well as meCPT coincide (and become exact) in the noninteracting case.

C. Numerical implementation

From a numerical point of view, the two main steps are to first obtain the reference state $\hat{\rho}^S$ by solving the Qme and then to evaluate the Green's functions using Eq. (8) and Eq. (4). For the solution of the BMme, Eq. (6) one needs to carry out the following: i) Full diagonalization of the interacting system Hamiltonian which is done in *LAPACK*, making use of the block structure in $\hat{N}$ and $\hat{S}^z$. ii) Evaluation of the coefficients of the BMme in Eq. (6), which involves coupling matrix elements $\langle a|\,\hat{S}_\alpha\,|b\rangle$ and numerical integration of the bath correlations functions, see App. A, C, for which an adaptive Gauss-Kronrod scheme is employed. iii) The steady-state $\hat{\rho}^S$ is finally obtained from the unique eigenvector with eigenvalue zero of Eq. (6), which we determine by a sparse Arnoldi diagonalization. Again, a block structure is related to $\hat{N}$ and $\hat{S}^z$. The numerical effort for the exact diagonalization scales with the size of the Hilbert space, and therefore exponentially with the system size N_S. In the second major step, the Green's function of the disconnected system is calculated by Eq. (8). Finally, the meCPT Green's function $\widetilde{G}(\omega)$ is found using Eq. (4). We outline how to evaluate observables within meCPT and the Qme in App. D.

IV. RESULTS

In this section we present results obtained from the meCPT approach. In all calculations, except the ones in Sec. IV B, the secular approximation is applied for the reference state $\hat{\rho}^S$. The main improvements of meCPT with respect to bare BMsme are i) the inclusion of lead induced broadening effects, ii) the correct $U = 0$ limit and iii) a correction for effects missed by an improper treatment of quasi degenerate states in the BMsme (see below). In comparison to the previous "standard" stsCPT, meCPT also captures current blocking effects, which are discussed in detail in Ref. 39 and Ref. 40 within a Qme treatment.

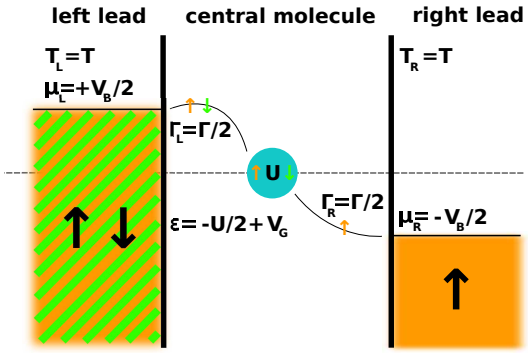

FIG. 1: (Color online) *Quantum dot diode:* Schematic representation, see Sec. IV A. Single quantum dot with Hubbard interaction U and gate voltage V_G (particle-hole symmetric at $V_G = 0$), coupled via $\Gamma_{\mathrm{L/R}} = \frac{\Gamma}{2}$ to a left and right lead. The right lead is fully polarized, i.e. only spin-↑ DOS is present. An external bias voltage V_B shifts the chemical potentials by $\mu_{\mathrm{L/R}} = \pm\frac{V_B}{2}$. The leads are in the wide band limit and at the same temperature T.

A. Quantum dot diode

We first discuss a quite simple model system: a quantum diode based on electron-electron interaction effects. Fig. 1 depicts this junction consisting of a single interacting orbital described by a Hubbard interaction and an on-site term to allow for a gate voltage V_G:[123]

$$\hat{\mathcal{H}}^S = U\left(\hat{n}^f_\uparrow - \frac{1}{2}\right)\left(\hat{n}^f_\downarrow - \frac{1}{2}\right) + V_G\sum_\sigma \hat{n}^f_\sigma\,,$$

where $\hat{n}^f_\sigma = f^\dagger_\sigma f_\sigma$. The environment Eq. (1b), consists of two spin dependent, conducting leads. We model both, the left (L) and the right (R) lead by a flat DOS with local retarded single-particle Green's function[116] $g^R_{L/R}(\omega) = -\frac{1}{2D}\ln\left(\frac{\omega+i0^+-D}{\omega+i0^++D}\right)$, with a half-bandwidth D much larger than all other energy scales in the model, mimicking a wide band limit. We keep both leads at the same temperature $T_L = T_R = T$ and at chemical potentials $\mu_L = -\mu_R = \frac{V_B}{2}$ corresponding to a symmetrically applied bias voltage V_B. The right lead is fully spin polarized, i.e. tunnelling of one spin species (↓) into the right lead is prohibited while both spin species can tunnel to the left lead. The system is coupled to the two leads via a single-particle hopping amplitude t' in $\hat{\mathcal{H}}^{SE}$, Eq. (1c) which results in a lead broadening parameter of $\Gamma^\uparrow_L = \Gamma^\downarrow_L = \Gamma^\uparrow_R = \frac{\Gamma}{2} = \pi|t'|^2\frac{1}{2D}$, Eq. (C1), and $\Gamma^\downarrow_R \equiv 0$. We use Γ without an argument for $\Gamma(\omega = 0)$ as defined in Eq. (C1). For meCPT we use $\mathcal{H}^{SE}$, see Eq. (1c), as perturbation.

Such a system could be realized in: i) A "metal - artificial atom - half-metallic ferromagnet"[124] nano structure where spin-↑ DOS is present at the Fermi energy while the respective spin-↓ DOS is zero. ii) A graphene nano structure[31,32] with ferromagnetic cobalt electrodes.[33] iii) A one dimensional optical lattice of ultra cold fermions in a quantum simulator[125] where the hopping of spin-↓ particles into the right reservoir is suppressed. For all three systems spin-↓ particles cannot reach the right lead, in the first two due to a vanishing DOS, in the third one due to a vanishing tunnelling amplitude.

We consider parameters such that the junction is operated in a single electron transistor (SET) regime,[37] i.e. temperatures above the Kondo temperature.[49] In this regime we expect an interaction induced - magnetization mediated blocking due to the fact that the system fills up with spin-↓ particles. On the one hand they cannot escape, yielding a vanishing spin-↓ current, and on the other hand they suppress the spin-↑ occupation, at finite repulsive interaction U, resulting also in a vanishing spin-↑ current.[46]

Fig. 2 (A) shows the meCPT stability diagram of the interacting system in the $V_B - V_G$ plane. When applying a particle-hole transformation for all particles, leads and system, along with $t' \to -t'$ we easily find the symmetry properties

$$j(-V_B, -V_G) = -j(V_B, V_G)\,,$$
$$\langle n^f_\sigma\rangle(-V_B, -V_G) = 1 - \langle n^f_\sigma\rangle(V_B, V_G)\,.$$

From the continuity equation it is clear that only spin-↑ steady-state current can flow which limits the maximum current to $\frac{\Gamma}{2}$. The energies ω_N of the isolated quantum dot can be labelled by the total particle number N and are for $V_G = U$ given by $\omega_0 = 0$, $\omega_1 = \frac{1}{2}U$ and $\omega_2 = 2U$. This gate voltage corresponds to the dashed line, marked by (X) in Fig. 2 (A). The corresponding energy differences $\Delta_{01} = 0.5\,U$ between the single-occupied and the empty dot and $\Delta_{12} = 1.5\,U$ between double-occupied and single-occupied dot are associated with a further transport channel opening as soon as the bias V_B reaches twice their values. The meCPT result for the current exhibits the well known Coulomb diamond[37] close to $V_B = 0$ and $V_G = 0$, where current is hindered because all system energies are far outside the transport window $\pm\frac{V_B}{2}$, see Eq. (D2). At $V_G = 0$ a current sets in at $\frac{V_B}{2} = \pm|\frac{U}{2}|$, i.e. when transport across the system's single particle level becomes allowed. The point, at which the current sets in, shifts with V_G linearly to higher bias voltages. This transition is broadened $\propto \max(\Gamma = 0.1\,U, T = 0.025\,U)$. However, not only the transport window and possible excitations in the system energies determine the current-voltage characteristics. The particular occupation of the system states may lead to more complicated effects, such as current blocking.

Our first main result is that in contrast to stsCPT the blocking is correctly reproduced in meCPT. The current blocking is visible in Fig. 2 (A) in region (Y), see also the detailed data in subplot (C1). It is asymmetric in V_B and therefore responsible for the rectifying behaviour for $|V_G| > |\frac{U}{2}|$. This feature is easily understood from the plots of the spin resolved densities in Fig. 2 (C2). In the region of interest, for positive V_B, $\langle n_\downarrow\rangle = 1$ which hinders spin-↑ particles from the left lead to enter the system, due

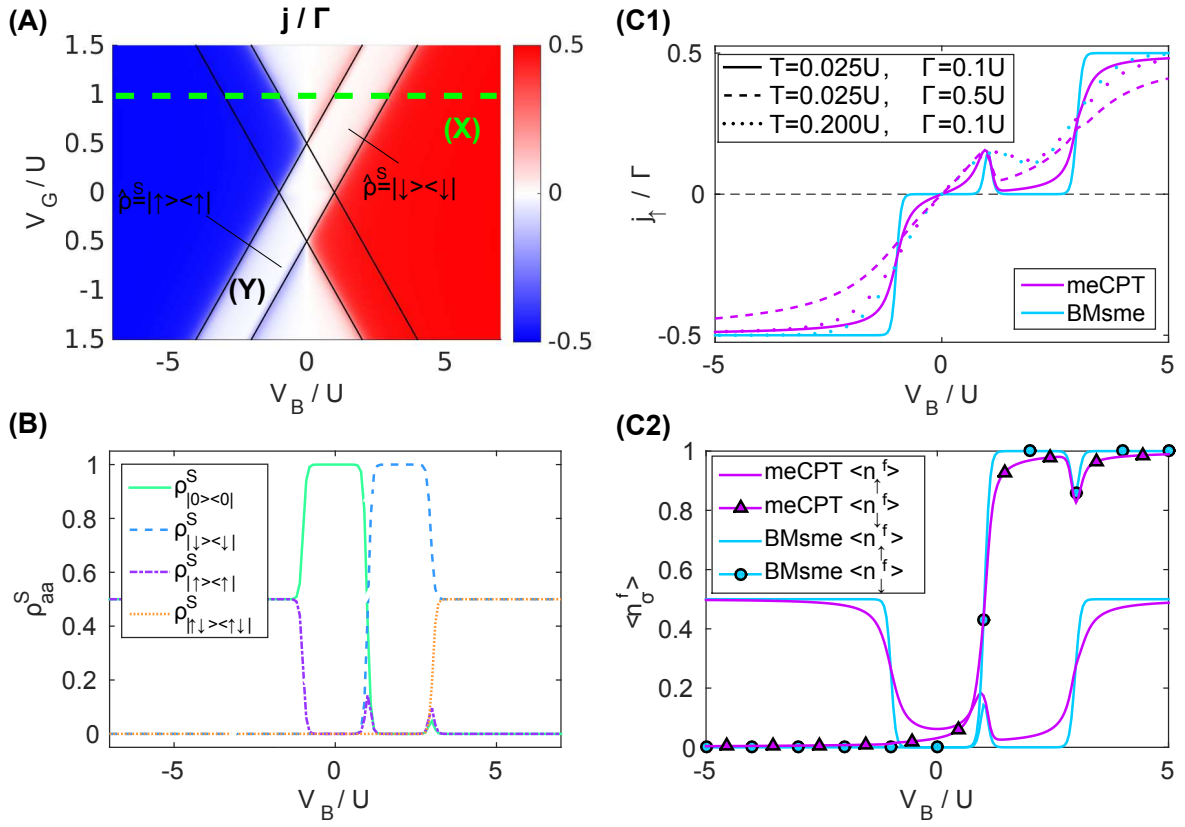

FIG. 2: (Color online) *Quantum dot diode:* **(A)** Stability diagram, based on the total current $j = \langle j_\uparrow \rangle + \langle j_\downarrow \rangle$ as a function of bias voltage V_B and gate voltage V_G, obtained within meCPT. Note that $\langle j_\downarrow \rangle \equiv 0$. Results are depicted for $T = 0.025\,U$ and $\Gamma = 0.1\,U$. (Y) marks the current blocking region. The green dashed line (X) at $V_G = U$ indicates the parameter regime for the panels (B) and (C). **(B)** Diagonal part of the reduced density matrix ρ^S_{aa} obtained by BMsme. **(C1)** Spin-↑ current $j_\uparrow$ within meCPT compared to BMsme. Solid lines are for the same parameters as line (X) in panel (A). Blue dashed and solid lines for BMsme are indistinguishable. **(C2)** Spin resolved densities $\langle n_\uparrow \rangle$ and $\langle n_\downarrow \rangle$ for the same parameters as in panel (C1), see solid lines in the legend.

to the repulsive interaction U and suppresses the current. For negative V_B, the situation is reversed. A direct computation of the current in the framework of BMsme, see App. D 2, also predicts the blocking, which is however not the case if we use stsCPT based on the zero temperature ground state $|\Psi_0\rangle_S$. The blocking is evident in Fig. 2 (B), where we observe that in the blocking regime, the reduced density is $\rho_S = |\downarrow\rangle\langle\downarrow|$. Independent of the value of $U > 0$, the blocking sets in at the same values of V_B in meCPT and BMsme. Fig. 2 (C1) shows that within BMsme this regime is entered after a U independent hump in the current while within meCPT the hump is broader and weakly U dependent. The current blocking disappears at a bias voltage $V_B \propto U$ in both methods. Immediately apparent are the much broader features in meCPT, which leads to a less pronounced effect in contrast to the total blocking predicted by BMsme. In BMsme the broadening parameter Γ enters merely as prefactor of the current, and broadening is solely induced by the temperature. This temperature induced broadening is correctly taken into account in both methods. For $T > \Gamma$ the latter dominates and the meCPT results are similar to the plain BMsme solution. A comparison of the three methods is given in Tab. I. In this simple model the blocking can be captured even by a straight forward steady-state mean-field theory in the Keldysh Green's function with self-consistently determined spin densities or in stsVCA. This is not the case for the more elaborate system studied in the next section.

TABLE I: Comparison of steady-state cluster perturbation theory (stsCPT), the Born-Markov-secular master equation (BMsme) and the quantum master equation based stsCPT (meCPT) with respect to their ability to capture temperature (T) or lead (Γ) induced level broadening, current blocking and whether the noninteracting limit is fulfilled.

method	T-broadening	Γ-broadening	blocking	$U = 0$
stsCPT	yes	yes	no	exact
BMsme	yes	no	yes	approx.
meCPT	yes	yes	yes	exact

B. Triple quantum dot

In this section we discuss a more elaborate model system: a triple quantum dot ring junction which features negative differential conductance (NDC) based on electron-electron interaction effects mediated by quantum interference due to degenerate states as outlined in detail in Ref. 45,46. Fig. 3 (A) depicts the triple quantum dot ring junction, described by the following Hubbard Hamiltonian[126]

$$\hat{\mathcal{H}}^S = \sum_{i=1}^{3} U\big(\hat{n}^f_{i\uparrow} - \frac{1}{2}\big)\big(\hat{n}^f_{i\downarrow} - \frac{1}{2}\big) + V_G \sum_{i=1}^{3}\sum_{\sigma} \hat{n}^f_{i\sigma} + t\sum_{\langle ij\rangle}\sum_{\sigma} f^\dagger_{i\sigma} f_{j\sigma}\,. \tag{9}$$

In addition to the model parameters described in Sec. IV A, a nearest-neighbour $\langle ij\rangle$ hopping t is present. The environment, Eq. (1b) and coupling, Eq. (1c) are now both symmetric in spin. Moreover, we use $\mu_L = -\mu_R = \frac{V_B}{2}$, $T = T_L = T_R$ and $\Gamma_L = \Gamma_R = \frac{\Gamma}{2} = \pi|t'|^2\frac{1}{2D}$.

Such a junction can be experimentally realized: i) Via local anodic oxidation (LAO) on a GaAs/AlGaAs heterostructure[29] which enables tunable few electron control.[30] ii) In a graphene nano structure.[31,32] Experimentally the stability diagram has been explored[34] alongside characterisation and transport measurements.[29,35,36] The negative differential conductance has been observed in a device aimed as a quantum rectifier.[127] Theoretically the study of the nonequilibrium behaviour of such a device has become an active field recently.[45,46,128–134]

We investigate transport properties for values of the parameters such that the junction is in a single electron transistor (SET) regime,[37] i.e. temperatures above the Kondo temperature.[49] In this regime we expect an interaction induced - quantum interference mediated blocking as discussed in Ref. 45,46. The rotational symmetry ensures degenerate eigenstates labelled by a quantum number of angular momentum. In situations where these degenerate states participate in the transport they provide two equivalent pathways through the system and lead to quantum interference.[45] The blocking sets in at a bias voltage, where the degenerate states start to participate in the transport. It then becomes possible that a superposition is selected which forms one state with a node at the right lead. In the long time limit this state will be fully occupied while the other one will be empty due to Coulomb repulsion, for reasons very similar to the ones discussed in the previous section.[39,40]

The steady-state charge distribution and current-voltage characteristics of the interacting triple quantum dot are presented in Fig. 3 (B, C) in a wide bias voltage window. The current, depicted in panel (C), in general increases in a stepwise manner and is fully antisymmetric with respect to the bias voltage direction. A blocking effect occurs at $V_B \approx 1.5\,|t|$ as can be observed in the BMsme and meCPT data. The previous version of stsCPT based on the pure zero temperature ground state $|\Psi_0\rangle_S$ misses this region of NDC. In contrast to the simpler model presented in the previous section, a self-consistent mean-field solution does not capture the blocking effects correctly in this more elaborate system. The BMsme solution shows many more steps in the current than the stsCPT one, which is due to transitions in the reference state $\hat{\rho}^S$ of the central region. The meCPT results in general follow these finer steps, correcting their width to incorporate also lead induced broadening effects in addition to the pure temperature broadening. As can be seen in panel (B1), meCPT predicts a large charge increase at the site connected to the high bias lead. Note that the charge density at site 2, which is connected to the right lead is simply: $\langle n_2\rangle(V_B) = \langle n_1\rangle(-V_B)$. The charge density at site 3 is symmetric with respect to the bias voltage origin.

Next we study the impact of a gate voltage on the blocking. Results obtained by meCPT are depicted as stability diagram in Fig. 4. Upon increasing $|V_G|$, the onset of the blocking shifts linearly to higher V_B (Y). We find a Coulomb diamond for $2V_G \gtrapprox V_B - |t|$ (D). Upon increasing the bias voltage out of the Coulomb diamond, see e.g. line (X), a current sets in but is promptly hindered by the blocking so that the current diminishes after a hump of width $\propto \max(T, \Gamma)$. Interestingly this device could be operated as a transistor in two fundamentally different modes. In mode (T1), at a source-drain voltage of $\approx |t|$ the current is on for a gate voltage of $V_G = 0$ and off for $V_G \approx 0.5\,|t|$ due to the Coulomb blockade. In mode (T2), at a source-drain voltage of $\approx 1.5\,|t|$ the current is off for a gate voltage of $V_G = 0$ due to quantum interference mediated blocking and on for $V_G = 0.25\,|t|$.

Next we discuss the current characteristics in the vicinity of the blocking in more detail, as well as the impact of the interaction strength U. The first row of Fig. 5 shows the total current through the device for different values of U. The blocking region shifts to lower bias voltages with increasing U. As discussed earlier, structures in the BMsme results are only broadened by temperature effects in the steady-state density (compare e.g. the width of the structures in the local density in the second row of Fig. 5), while meCPT additionally takes into account the finite life time of the quasi particles due to the coupling to the leads, given by $1/\Gamma$. This can be seen by solving Eq. (4) for the local Green's function at device sites. Especially for higher lead broadening Γ this gives rise to significant differences in the meCPT results compared to the BMsme data. From the bottom row of Fig. 5 we see that, before the blocking regime is entered, the steady-state changes from a pure $N = 2$ state to a mixed $N = 2\,/\,N = 3$ state at the hump in the current. Obviously, blocking arises because the system reaches a pure $N = 3$ state for $U = 2\,|t|$ and $U = 3\,|t|$ at $V_B \approx 1.4\,|t|$. For $U = |t|$ the current is only partially blocked, because the contribution of the $N = 2$ state is not fully suppressed. For all U-values, however, we find NDC. As far as the meCPT current is concerned, the complete blocking at higher interaction strengths, pre-

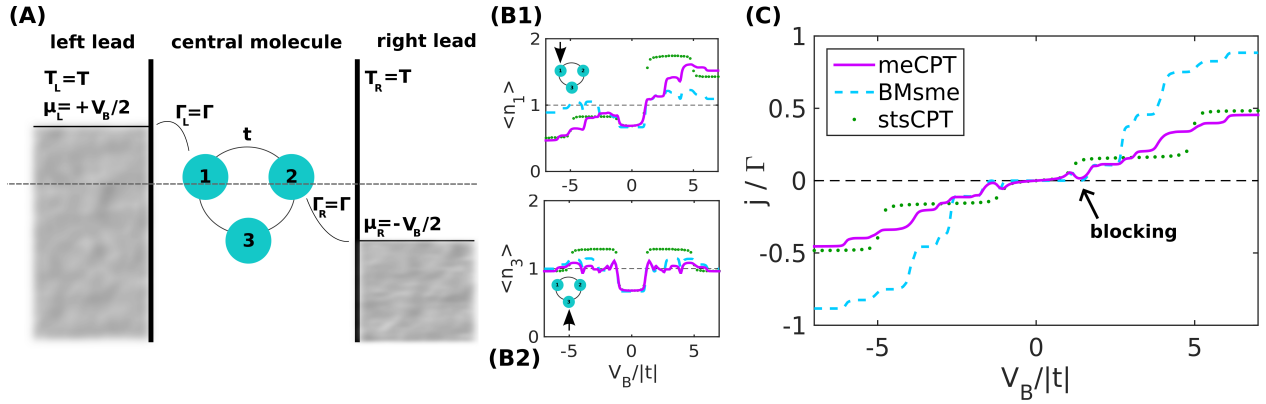

FIG. 3: (Color online) *Triple quantum dot* **(A)** Schematic representation, see Sec. IV B. System Hamiltonian as defined in Eq. (9). Site 1 couples to the left lead and site 2 to the right one, both with $\Gamma_{\mathrm{L/R}} = \frac{\Gamma}{2}$. The leads are held at the same temperature $T_{\mathrm{L/R}} = T$ and the chemical potentials $\mu_{\mathrm{L/R}} = \pm\frac{V_B}{2}$ are shifted by the bias voltage. **(B)** Local charge density $\langle n_i \rangle$ as a function of bias voltage V_B. The results are obtained by meCPT, BMsme and stsCPT, see color code of panel (C). **(C)** Total current $j = \sum_\sigma \langle j_{L1\sigma} \rangle$ into the system at site 1 as a function of bias voltage V_B. Results, shown in panels (B,C), are for $U = 2\,|t|$, $T \approx 0.02\,|t|$, $\Gamma = 0.1\,|t|$ and $V_G = 0$, corresponding to line (X) in Fig. 4.

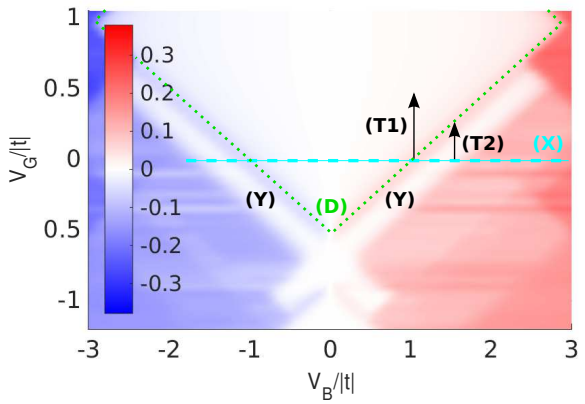

FIG. 4: (Color online) *Triple quantum dot: stability diagram.* Total current entering the system as a function of bias voltage V_B and gate voltage V_G, obtained within meCPT. The blocking region is indicated by (Y), the Coulomb diamond by (D). The two arrows (T1) and (T2) mark two device operation modes as discussed in the text. All results are for $U = 2\,|t|$, $T = 0.02\,|t|$ and $\Gamma = 0.1\,|t|$. Dashed line (X) for $V_G = 0$ marks the parameter region depicted in Fig. 3 (C).

dicted by BMsme, is reduced to a partial blocking due to the lead induced broadening effects in meCPT. Although ρ^S_{ab} changes significantly twice in the blocking region (for $U = 2$ and $U = 3$), the charge density $\langle n_i \rangle$ just increases once from $\langle n_1 \rangle \approx 0.75$ to $\langle n_1 \rangle \approx 1$.

Details of the steady-state dynamics are provided in Fig. 6. Before the blocking region is entered ($V_B = 0.4\,|t|$) the system is in a pure state with $N = 2$, which corresponds to the zero temperature ground state $|\Psi_0\rangle_S$ in the $N = 2$ sector. Here the transmission function $\mathcal{T}(\omega)$, Eq. (D3), of meCPT agrees with the one of stsCPT. A small current is obtained due to the $N = 2 \to 3$ excitation at $\omega \approx 0.55\,|t|$. Increasing the bias voltage has no influence on the reference state in stsCPT, which therefore remains in the $N = 2$ particle sector. Consequently, the transmission function in stsCPT does not change. Only the transport window increases linearly with increasing V_B. For $V_B = 1.4\,|t|$ it includes the peak at $\approx 0.7|t|$ and results in a significant increase in the current obtained in stsCPT (see stsCPT result in Fig. 3). This is in stark contrast to the BMsme current, depicted in Fig. 5, which exhibits perfect blocking for $V_B = 1.4\,|t|$. The reason for the current-blocking is that only two states, both in the $N = 3$ sector and doubly degenerate, have significant weight in ρ^S_{ab}. The meCPT solution is based on the modified density matrix and therefore the current is diminished, since the next possible excitation is at $\omega \approx 0.9\,|t|$ ($N = 2 \to 3$), which is outside the transport window $W(\omega) \approx (-0.7|t|, 0.7|t|)$, Eq. (D2). Due to the lead induced broadening of $\mathcal{T}(\omega)$ and the temperature induced broadening of the transport window, the current is however only partially blocked. For $V_B = 2.4\,|t|$ this excitation falls into the transport window and the current is no longer blocked. In this case, the state ρ^S_{ab} is a mixture of $N = 2, 3, 4$. The dominant excitation responsible for this current is again the ground state excitation at $\omega \approx 0.55\,|t|$ from $N = 2 \to 3$. This is why in this regime the stsCPT current, based on the pure two particle state is again similar to the meCPT current.

Our results on the Qme level have been checked with those presented by Begemann *et al.* in Ref. 39 and Darau *et al.* in Ref. 40 for a six orbital ring which shows similar blocking effects. Different types of blocking effects in various parameter regimes have been discussed in detail in a Qme framework also for the three orbital ring by Donarini *et al.* in Ref. 45,46.

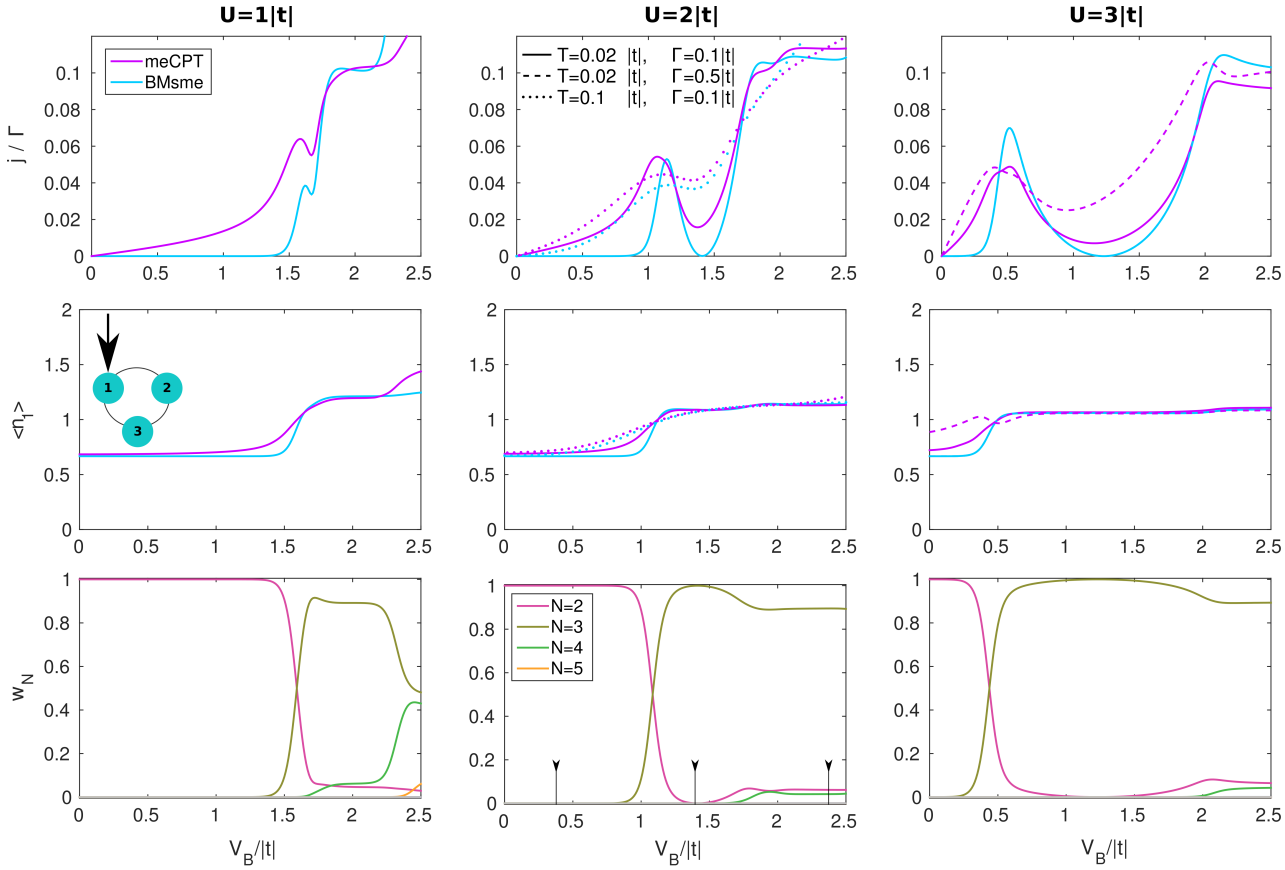

FIG. 5: (Color online) *Triple quantum dot:* Dependence of the current blocking on the interaction strength U. **(Top row)** Total current j as a function of bias voltage V_B. **(Middle row)** Charge density $\langle n_1 \rangle$ at site 1. The color code of the top row is valid. **(Bottom row)** Summed diagonal elements of the density matrix $w_N = \sum_{a \in N} \rho^S_{aa}$ per particle number N. The black markers in the mid panel ($U = 2\,|t|$) indicate for which V_B detailed results are given in Fig. 6. Solid lines in all panels are for $T = 0.02\,|t|$, $\Gamma = 0.1\,|t|$ and $V_G = 0$. Results for $T = 0.1\,|t|$ are depicted in the central panels by dotted lines and those for $\Gamma = 0.5\,|t|$ in the right panels by dashed lines.

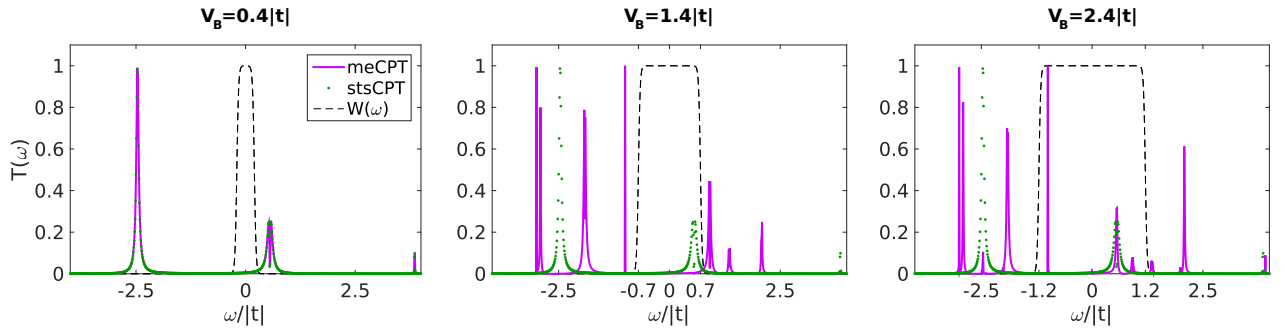

FIG. 6: (Color online) *Triple quantum dot:* Dynamic transmission function $\mathcal{T}(\omega)$, Eq. (D3), as obtained by meCPT and stsCPT. Same parameters as in Fig. 5 (bottom mid) at the three indicated bias voltages: $V_B = 0.4\,|t|$ (left), $V_B = 1.4\,|t|$ (middle) and $V_B = 2.4\,|t|$ (right). The temperature broadened transport window $W(\omega)$, Eq. (D2), is depicted as a dashed black line.

Quasi-degenerate states

Next we study the reliability of the secular approximation in the case of quasi degeneracy of the isolated energies of the system and benchmark its applicability to create a reference state for meCPT. To this end we apply a second gate voltage that couples only to the third orbital, see Fig. 3 (left), and leads to an additional term $V_{G,3}\,\hat{n}^f_3$ in the system Hamiltonian. This lifts the degeneracy of states present at $V_{G,3} = 0$ and therefore requires

a treatment within the BMme, see Ref. 40.

In the following we discuss the same parameter regime as above. In Fig. 7 we present results obtained using meCPT (solid lines) and Qme results (dashed lines) for the BMsme (A) and for the BMme (B). The meCPT results of each panel are obtained using the respective Qme. In the BMsme data a very small $|V_{G,3}|$ has a drastic effect on the current-voltage characteristics. The blocking present at $V_{G,3} = 0$ is immediately lifted by very small $|V_{G,3}|$ and the current jumps to a plateau. For larger $|V_{G,3}|$ the current stays on this plateau until further transport channels open up. This "jump" at small $|V_{G,3}|$ arises due to the improper treatment of quasi degeneracies in BMsme. MeCPT results based on BMsme show a smooth change of the current-voltage characteristics. BMme on the other hand correctly accounts for the coupling of the quasi-degenerate states and also exhibits a smooth dependence on $V_{G,3}$. For meCPT based on BMme we find qualitative similar results to meCPT based on BMsme, which emphasizes the robustness of the meCPT results in general. From this it is apparent that meCPT is capable of repairing the decoupling of quasi-degenerate states in the BMsme to some degree. However, to study blocking effects at quasi degenerate points it is of advantage to make use of the BMme in meCPT.

As discussed below in Sec. IV C, the BMme is not of Lindblad form and does not necessarily result in a positive definite reduced many-body density matrix ρ^S_{ab} in general. Using a not proper density matrix in Eq. (8) may result in non-causal Green's functions when the steady-state ρ^S_{ab} is obtained from the BMme. This can be avoided by using a modified reference state $\rho^S_{ab} \to \rho^S_{ab}\Theta(\Delta - |\omega_a - \omega_b|)$, with $\Theta(x)$ the Heaviside step function and Δ a small quantity, being e.g. $\approx 10^{-6}$, in Eq. (8), which renders the Green's functions causal. This is somewhat an ad-hoc approximation and should be seen simply as a way to explore the effects of continuously breaking degeneracy in the problem.

C. Current conservation

Finally we comment on conservation laws in meCPT. Within BMsme and BMme the current conservation (continuity equation) is always maximally violated in a sense that the current within the system is zero. This is due to the zeroth order $\hat{\rho}^S$ as discussed in App. D 2. In BMsme the inflow from the left lead into the system however always equals the outflow from the system to the right lead. Without the secular approximation the quantum master equation (BMme) is not of Lindblad form and the final many-body density matrix is not guaranteed to be positive definite.[121,122] This in turn can lead to slightly negative currents in regions where they are required to be positive by the direction of the bias voltage[78]. Furthermore, the inflow can be slightly different from the outflow.

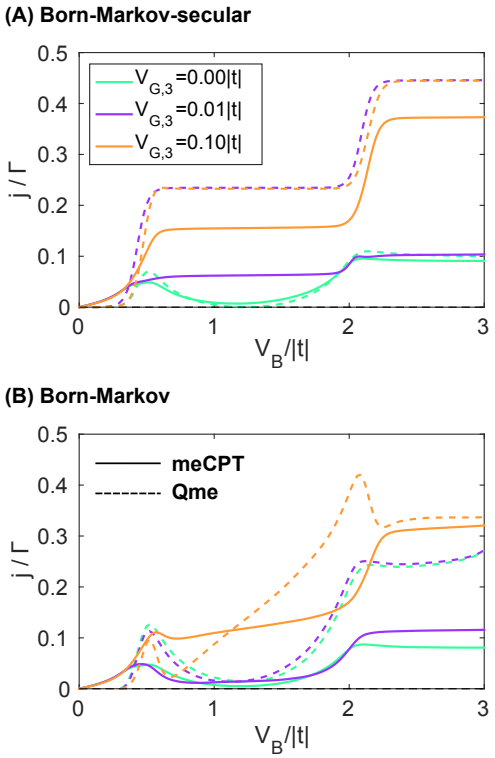

FIG. 7: (Color online) *Triple quantum dot:* Effects of lifting degeneracies in the system energies by a third gate voltage. Total current j as a function of bias voltage V_B, for three different gate voltages $V_{G,3}$ applied to site 3. Results based on the Born-Markov-secular approximation are compared with those of the Born-Markov approximation. Solid/dashed lines indicate the meCPT/BM(s)me result. All results are for $U = 3\,|t|$, $T = 0.02\,|t|$ and $\Gamma = 0.1\,|t|$.

In the noninteracting case, meCPT fully repairs the violation of the continuity equation present in the reference state. For increasing interaction strength, the violation of the continuity equation typically grows also in meCPT. In particular, the overall symmetry of the current stays intact (in our case, inflow equals outflow), while the current on bonds between interacting sites does not exactly match the current between noninteracting sites. This typically small violation of the continuity equation can be attributed to the violation of Ward identities[135,136] in the non-conserving approximation scheme of CPT.[137,138]

V. SUMMARY AND CONCLUSIONS

We improved steady-state cluster perturbation theory with an appropriate, consistent reference state. This reference state is obtained by the reduced many-body density matrix in the steady-state obtained from a quantum master equation. The resulting hybrid method inherits beneficial aspects of steady-state cluster perturbation theory as well as from the quantum master equation.

We benchmarked the new method on two experimentally realizable systems: a quantum diode and a triple quantum dot ring, which both feature negative differential conductance and interaction induced current blocking effects. meCPT is able to improve the bare quantum master equation results by a correct inclusion of lead induced level-broadening effects, and the correct noninteracting limit. In contrast to previous realizations of the steady-state cluster perturbation theory, meCPT is able to correctly predict interaction induced current blocking effects. It is well known that the secular approximation (BMsme) is not applicable to quasi degenerate problems, which is corroborated by our results for the steady-state current. However, meCPT based on the BMsme density, is able to repair most of the shortcomings of BMsme. The results are very close to those obtained by meCPT based on the density of BMme, where the quasi-degenerate states are treated consistently.

The computational effort of meCPT beyond that of the bare quantum master equation scales with the number of significant entries in the reference state density matrix but is typically small. In the presented formulation the new method is flexible and fast and therefore well suited to study nano structures, molecular junctions or heterostructures also starting from an *ab-inito* calculation.[139]

Acknowledgments

The authors acknowledge fruitful discussion with A. Rosch. This work was partly supported by the Austrian Science Fund (FWF) Grants No. P24081 and P26508 as well as SFB-ViCoM projects F04103 and F04104 and NaWi Graz. MN, GD and AD thank the Forschungszentrum Jülich, in particular the autumn school on correlated electrons, for hospitality and support.

Appendix A: Born-Markov and Pauli master equation

Here we provide the detailed expressions for the coefficients in the BMme and BMsme of Eq. (6) and discuss the equations governing the time evolution into the steady-state.

The Lamb-shift Hamiltonian is defined as $\hat{\mathcal{H}}^{LS} = \sum_{ab} \Lambda_{ab} |a\rangle \langle b|$, with

$$\Lambda_{ab} = \frac{1}{2i} \sum_{\alpha\beta} \sum_{c} \lambda_{\alpha\beta}(\omega_{bc}, \omega_{ac}) \langle c| \hat{S}_\beta |b\rangle \langle c| \hat{S}_\alpha |a\rangle^* . \tag{A1}$$

Note that $[\hat{\mathcal{H}}^{LS}, \hat{\mathcal{H}}^{S}]_- = 0$. In the secular approximation (BMsme) one can replace $\lambda_{\alpha\beta}(\omega_{bc}, \omega_{ac}) \to \lambda_{\alpha\beta}(\omega_b - \omega_c)\delta_{\omega_b,\omega_a}$. The expressions for the BMme and BMsme Eq. (6) are valid if $\left[\hat{\mathcal{H}}^E, \hat{\rho}^E\right]_- = 0$ and $\mathrm{tr}\left\{\hat{E}_\alpha \hat{\rho}^E\right\} = 0$. The environment functions $\xi_{\alpha\beta}$ and $\lambda_{\alpha\beta}$ in Eq. (A1) and Eq. (7) are determined by the time dependent environment correlation functions

$$C_{\alpha\beta}(\tau) = \mathrm{tr}\left\{\hat{E}_\alpha(\tau)\hat{E}_\beta \hat{\rho}_E\right\} , \tag{A2}$$

where the Heisenberg time evolution in the environment operators is $\hat{E}_\alpha(\tau) = e^{+i\hat{\mathcal{H}}^E\tau}\hat{E}_\alpha e^{-i\hat{\mathcal{H}}^E\tau}$.

For the BMme, $\xi_{\alpha\beta}$ and $\lambda_{\alpha\beta}$ are given by a sum of complex Laplace transforms

$$\xi_{\alpha\beta}(\omega_1, \omega_2) = \int_0^\infty d\tau\, C_{\alpha\beta}(\tau) e^{+i\omega_1\tau} + \int_{-\infty}^0 d\tau\, C_{\alpha\beta}(\tau) e^{+i\omega_2\tau} , \tag{A3}$$

$$\lambda_{\alpha\beta}(\omega_1, \omega_2) = \int_0^\infty d\tau\, C_{\alpha\beta}(\tau) e^{+i\omega_1\tau} - \int_{-\infty}^0 d\tau\, C_{\alpha\beta}(\tau) e^{+i\omega_2\tau} , \tag{A4}$$

whereas for the BMsme ($\omega_1 = \omega_2$) the expressions simplify to the full even and odd Fourier transforms[78]

$$\xi_{\alpha\beta}(\omega) = \int_{-\infty}^{\infty} d\tau\, C_{\alpha\beta}(\tau) e^{+i\omega\tau} , \tag{A5}$$

$$\lambda_{\alpha\beta}(\omega) = \int_{-\infty}^{\infty} d\tau\, \mathrm{sign}(\tau) C_{\alpha\beta}(\tau) e^{+i\omega\tau} = \frac{i}{\pi} \fint_{-\infty}^{\infty} d\omega' \frac{\xi_{\alpha\beta}(\omega')}{\omega - \omega'} . \tag{A6}$$

The coupled equations for the real time evolution of the components of the reduced system many-body density matrix $\rho^S_{ab} = \langle a| \hat{\rho}^S |b\rangle$ according to the BMsme read

$$\begin{aligned} \dot{\rho}^S_{ab}(\tau) = {} & i(\omega_b - \omega_a)\rho^S_{ab}(\tau) \\ & + i \sum_c \left(\rho^S_{ac}(\tau)\Lambda_{cb} - \Lambda_{ac}\rho^S_{cb}(\tau) \right) \\ & + \sum_{cd} \left(\Xi_{ac,bd}\rho^S_{cd}(\tau) - \frac{1}{2}\Xi_{cd,ca}\rho^S_{db}(\tau) \right. \\ & \left. - \frac{1}{2}\Xi_{cb,cd}\rho^S_{ad}(\tau) \right) . \end{aligned} \tag{A7}$$

The equations simplify further for system Hamiltonians $\hat{\mathcal{H}}^S$ with non-degenerate eigenenergies ω_a. Then the diagonal components $\phi_a = \rho^S_{aa}$ decouple from the off-diagonals and one recovers the Pauli master equation for classical probabilities

$$\dot{\phi}_a(\tau) = \sum_c \left(\Xi_{ac}\phi_c(\tau) - \Xi_{ca}\phi_a(\tau) \right) , \tag{A8}$$

with simplified coefficients

$$\Xi_{ab} := \Xi_{ab,ab} = \sum_{\alpha\beta} \xi_{\alpha\beta}(\omega_b - \omega_a) \langle a| \hat{S}_\beta |b\rangle \langle a| \hat{S}_\alpha |b\rangle^* .$$

In this case the dynamics of the decoupled off-diagonal terms ($a \neq b$) is given by

$$\dot{\rho}^S_{ab}(\tau) = \Bigg(i(\omega_b + \Lambda_b - \omega_a - \Lambda_a) - \frac{1}{2}\sum_c \Big(\Xi_{ca} + \Xi_{cb}\Big)\Bigg)\rho^S_{ab}(\tau)\,,$$

where the simplified Lamb shift terms are

$$\Lambda_a := \Lambda_{aa} = \frac{1}{2i}\sum_{\alpha\beta}\sum_c \lambda_{\alpha\beta}(\omega_a - \omega_c)\,\langle c|\,\hat{S}_\beta\,|a\rangle\,\langle c|\,\hat{S}_\alpha\,|a\rangle^*\,.$$

Appendix B: Hermitian tensor product form of the coupling Hamiltonian

For the BMsme (see Sec. III B) it is necessary to bring the fermionic system-environment coupling Hamiltonian, Eq. (1c) to a hermitian tensor product form, which requires $[\hat{S}_\alpha, \hat{E}_\alpha]_- = 0$. For the fermionic operators in Eq. (1c) we however have $[f^\dagger_{i\sigma}, c_{\lambda k\sigma}]_- = 2f^\dagger_{i\sigma}c_{\lambda k\sigma}$. A solution is provided in Ref. 79 by performing a Jordan-Wigner transformation[140] on the system and environment operators

$$\begin{aligned} f_{i\sigma} &= \prod_\sigma \left(\xi^z_1 \otimes \ldots \otimes \xi^z_{i-1}\xi^-_i \mathbb{1}_{i+1} \otimes \ldots \otimes \mathbb{1}_{L_S}\right)_{S,\sigma} \\ &\quad \otimes \prod_\lambda \left(\mathbb{1}_1 \otimes \ldots \otimes \mathbb{1}_{L_E}\right)_{E,\lambda\sigma}\,, \\ c_{\lambda j\sigma} &= \prod_\sigma \left(\xi^z_1 \otimes \ldots \otimes \xi^z_{L_S}\right)_{S,\sigma} \otimes \\ &\quad \prod_\lambda \left(\eta^z_1 \otimes \ldots \otimes \eta^z_{j-1}\eta^-_j \mathbb{1}_{j+1} \otimes \ldots \otimes \mathbb{1}_{L_E}\right)_{E,\lambda\sigma}\,, \end{aligned}$$

where ξ_i and η_j denote local spin-$\frac{1}{2}$ degrees of freedom at the system and environment sites respectively and the overall ordering of operators is important. L_S/L_E denote the size of the system / environment. Reordering Eq. (1c) we find $\hat{\mathcal{H}}^{SE}_\lambda = \sum_{ij\sigma} t'_{\lambda ij\sigma} f^\dagger_{i\sigma}c_{\lambda j\sigma} - t'^*_{\lambda ij\sigma} f_{i\sigma}c^\dagger_{\lambda j\sigma}$, where the minus sign arises due to the fermionic anti-commutator. Plugging in the Jordan-Wigner transformed operators leads to

$$\begin{aligned} \hat{\mathcal{H}}^{SE}_\lambda &= \sum_{ij\sigma}\Bigg(t'_{\lambda ij\sigma}\Big[\xi^+_i \otimes \\ &\quad [-\xi^z_{i+1} \otimes \ldots \otimes \xi^z_{L_S} \otimes \eta^z_1 \otimes \ldots \otimes \eta^z_{j-1}] \otimes \eta^-_j\Big]_{\sigma\lambda} + t'^*_{\lambda ij\sigma} \\ &\quad \Big[\xi^-_i \otimes [-\xi^z_{i+1} \otimes \ldots \otimes \xi^z_{L_S} \otimes \eta^z_1 \otimes \ldots \otimes \eta^z_{j-1}] \otimes \eta^+_j\Big]_{\sigma\lambda}\Bigg) \\ &= \sum_i \left(\bar{f}^\dagger_i \otimes \bar{c}_i + \bar{f}_i \otimes \bar{c}^\dagger_i\right)\,, \end{aligned}$$

where in the last line we have defined new operators

$$\begin{aligned} \bar{f}_{i\sigma} &= \left[\xi^-_i \otimes [-\xi^z_{i+1} \otimes \ldots \otimes \xi^z_{L_S}]\right]_\sigma\,, \\ \bar{f}^\dagger_{i\sigma} &= \left[[-\xi^z_{i+1} \otimes \ldots \otimes \xi^z_{L_S}] \otimes \xi^+_i\right]_\sigma\,, \\ \bar{c}_{\lambda i\sigma} &= \sum_j t'_{\lambda ij\sigma}\left[[\eta^z_1 \otimes \ldots \otimes \eta^z_{j-1}] \otimes \eta^-_j\right]_{\lambda\sigma}\,, \\ \bar{c}^\dagger_{\lambda i\sigma} &= \sum_j t'^*_{\lambda ij\sigma}\left[\eta^+_j \otimes [\eta^z_1 \otimes \ldots \otimes \eta^z_{j-1}]\right]_{\lambda\sigma}\,. \end{aligned}$$

Note that the phase operator $\hat{P}_{i(j\lambda)\sigma} = \left[-\xi^z_{i+1} \otimes \ldots \otimes \xi^z_{L_S} \otimes [\eta^z_1 \otimes \ldots \otimes \eta^z_{j-1}]_\lambda\right]_\sigma = (-1)^{1+\sum_{\lambda'}\sum_{m=i+1}^{L_S}\hat{n}_m + \hat{N}_{j\lambda'}}$ counts the particles between system site i and environment site j for spin σ depending on the ordering of the environments λ. It is straight forward to show that the bar operators fulfil fermionic anti-commutation rules. Furthermore $[\bar{f}_{i\sigma}, \bar{c}_{\lambda i\sigma}]_- = 0$, which allows us to write the coupling Hamiltonian in a tensor product form. Note that in general $[\bar{f}_{i\sigma}, \bar{c}_{\lambda' j\sigma}]_- \neq 0$ for $i \neq j$ which is however not relevant for the coupling Hamiltonian where only the same i couple.

The new operators in hermitian form are given in Eq. (5) by replacing $c \to \bar{c}$ and $f \to \bar{f}$. Next we show, by examining the BMsme, that in most cases the additional phase operator in $\bar{c}$ drops out of the calculations and we are even allowed to use the original f and c operators instead of the barred ones. The operators $\bar{c}$ only enter the equations in the environment correlation functions $C_{\alpha\beta}(\tau)$ as defined in Eq. (A2). Plugging in the barred operators we obtain for normal systems which preserve particle number

$$C_{\alpha\beta}(\tau) \propto \mathrm{tr}\left\{e^{+i\hat{\mathcal{H}}^E\tau} f^\dagger_{\lambda j\sigma} e^{-i\hat{\mathcal{H}}^E\tau}\hat{P}^2_{i(j\lambda)\sigma}c_{\lambda j\sigma}\hat{\rho}^E\right\}\,,$$

with $\hat{P}^2_{ij} = \mathbb{1}$, where we required that $[\hat{\mathcal{H}}^E, \hat{P}_{ij}]_- = 0$. The dropping out of the phase operators implies that for normal systems where the disconnected environments conserve particle number we can omit the Jordan-Wigner transformation and do all calculations as is with the original environment creation/annihilation operators in hermitian form.

Appendix C: Bath correlation functions

In the wide band limit, analytical expressions for the bath correlation functions are available in Ref. 39. For arbitrary environment DOS, explicit evaluation of the environment correlation functions becomes convenient for hermitian couplings, Eq. (5) as outlined in App. B.[78] Essentially the environment functions can all be obtained via integrals of the environment DOS $\rho(\omega)$. Care has to be taken when going to very low temperatures and solving the integrals with finite precision arithmetic to avoid underflow errors.

The time dependent environment correlation functions $C_{\alpha\beta}(\tau)$, Eq. (A2) become

$$C_{11}(\tau) = C_{22}(\tau) = \frac{1}{4\pi}\sum_{\lambda\sigma}\int_{-\infty}^{\infty} d\nu\,\Gamma_{\lambda\sigma}(\nu) \times\left(e^{-i\nu\tau} + 2ip_{\rm FD}(\nu,T_\lambda,\mu_\lambda)\sin(\nu\tau)\right),$$

$$C_{12}(\tau) = -C_{21}(\tau) = \frac{i}{4\pi}\sum_{\lambda\sigma}\int_{-\infty}^{\infty} d\nu\,\Gamma_{\lambda\sigma}(\nu) \times\left(-e^{-i\nu\tau} + 2p_{\rm FD}(\nu,T_\lambda,\mu_\lambda)\cos(\nu\tau)\right),$$

where $C_{\alpha\beta}(\tau) = C^\dagger_{\beta\alpha}(-\tau)$ and the coefficient

$$\Gamma_{\lambda\sigma}(\nu) = 2\pi|t'_{\lambda\sigma}|^2\sum_k \delta(\nu-\omega_{\lambda k\sigma}), \tag{C1}$$

is proportional to the lead DOS.

For the BMsme, the respective full even Fourier transforms $\xi_{\alpha\beta}(\omega)$, Eq. (A5) we find

$$\xi_{11}(\omega) = \xi_{22}(\omega) = \frac{1}{2}\sum_{\lambda\sigma}\Gamma_{\lambda\sigma}(-\omega)p_{\rm FD}(-\omega,\beta_\lambda,\mu_\lambda) + \Gamma_{\lambda\sigma}(\omega)\overline{p}_{\rm FD}(\omega,T_\lambda,\mu_\lambda),$$

$$\xi_{12}(\omega) = -\xi_{21}(\omega) = \frac{i}{2}\sum_{\lambda\sigma}\Gamma_{\lambda\sigma}(-\omega)p_{\rm FD}(-\omega,\beta_\lambda,\mu_\lambda) - \Gamma_{\lambda\sigma}(\omega)\overline{p}_{\rm FD}(\omega,T_\lambda,\mu_\lambda),$$

where $\overline{p}_{\rm FD}(\omega,T,\mu) = 1 - p_{\rm FD}(\omega,T,\mu)$.

The odd Fourier transforms $\lambda_{\alpha\beta}(\omega)$, Eq. (A6) are given by

$$\lambda_{11}(\omega) = \lambda_{22}(\omega) = \frac{i}{2\pi}\sum_{\lambda\sigma}\fint_{-\infty}^{\infty} d\nu\Gamma_{\lambda\sigma}(\nu)\left(\frac{p_{\rm FD}(\nu,\beta_\lambda,\mu_\lambda)}{\nu+\omega} - \frac{\overline{p}_{\rm FD}(\nu,\beta_\lambda,\mu_\lambda)}{\nu-\omega}\right),$$

$$\lambda_{12}(\omega) = -\lambda_{21}(\omega) = -\frac{1}{2\pi}\sum_{\lambda\sigma}\fint_{-\infty}^{\infty} d\nu\Gamma_{\lambda\sigma}(\nu)\left(\frac{p_{\rm FD}(\nu,\beta_\lambda,\mu_\lambda)}{\nu+\omega} + \frac{\overline{p}_{\rm FD}(\nu,\beta_\lambda,\mu_\lambda)}{\nu-\omega}\right).$$

Appendix D: Evaluation of steady-state observables

1. Steady-state cluster perturbation theory

Within meCPT single-particle observables are available by integration of $\widetilde{G}(\omega)$, Eq. (4). Its easy to show that the single-particle density matrix $\kappa_{ij\sigma} = \frac{\delta_{ij}}{2} - \frac{i}{2}\int_{-\infty}^{\infty}\frac{d\omega}{2\pi}G^K_{ij\sigma}(\omega)$ can be expressed in terms of the retarded CPT Green's function

$$\kappa_{ij\sigma} = \frac{\delta_{ij}}{2} - \frac{i}{2}\int_{-\infty}^{\infty}\frac{d\omega}{2\pi}\Big(G^R_{in\sigma}(\omega)P_{nj\sigma}(\omega) - P_{in\sigma}(\omega)(G^R_{jn\sigma}(\omega))^* + G^R_{in\sigma}(\omega)\left([P_\sigma(\omega),M_\sigma]_-\right)_{nm}(G^R_{jm\sigma}(\omega))^*\Big),$$

where M_σ is the inter-cluster perturbation defined in Eq. (4). Here we use the Einstein summation convention, the last line holds within CPT and $P_{ij\sigma}(\omega) = \delta_{ij}(1-2p_{\rm FD}(\omega,T_i,\mu_{i\sigma}))$.

From the real part of the single-particle density-matrix we read off the site occupation $\langle n_i\rangle = \sum_\sigma \kappa_{ii\sigma}$ the spin resolved occupations $\langle n_{i\sigma}\rangle = \kappa_{ii\sigma}$ and the magnetization $\langle m_i\rangle = \frac{1}{2}(\kappa_{ii\uparrow} - \kappa_{ii\downarrow})$.

The current $\langle j_{\langle ij\rangle}\rangle$ between nearest-neighbour sites $\langle ij\rangle$ is related to the imaginary part of $\kappa_{ij\sigma}$ and reads in symmetrized form

$$\langle j_{\langle ij\rangle}\rangle = \frac{e}{2\hbar}\left(h_{ij\sigma}\kappa_{ij\sigma} - h_{ji\sigma}\kappa_{ji\sigma}\right),$$

which is of Meir-Wingreen form[82] and $h_{ij\sigma}$ is the single-particle Hamiltonian.

Equivalently, the transmission current between two environments $\lambda = 1, 2$ can be evaluated in the Landauer-Büttiker form[55,65,98]

$$\langle j_{1/2}\rangle = \frac{e}{\hbar}\int_{-\infty}^{\infty}\frac{d\omega}{2\pi}W(\omega)\mathrm{tr}\left\{\mathcal{T}(\omega)\right\}, \tag{D1}$$

with the transport window

$$W(\omega) = p_{\rm FD}(\omega,T_1,\mu_1) - p_{\rm FD}(\omega,T_2,\mu_2), \tag{D2}$$

and where the transmission function

$$\mathcal{T}(\omega) = G^R(\omega)\Gamma_1(\omega)\left(G^R(\omega)\right)^\dagger\Gamma_2(\omega), \tag{D3}$$

is given in terms of $G^R(\omega) = \left((g^R(\omega))^{-1} - (\widetilde{\Sigma}_1 + \widetilde{\Sigma}_2)\right)^{-1}$ with the lead broadening functions of lead λ projected onto the system sites i,j is $\widetilde{\Sigma}_{\lambda ij} = M_{i\lambda}g^R_{\lambda\lambda}M_{\lambda j}$ and $\Gamma_\lambda = -2\Im\mathrm{m}\left(\widetilde{\Sigma}_\lambda\right)$, compare also Eq. (C1).

2. Born-Markov master equation

Within the Qme, basic single-particle observables are available in terms of the reduced system many-body density matrix $\hat{\rho}^S$. The single-particle density matrix κ reads

$$\kappa_{ij\sigma} = \mathrm{tr}\left(f^\dagger_{i\sigma}f_{j\sigma}\hat{\rho}^S\right) = \sum_{ab}\langle b|\,f^\dagger_{i\sigma}f_{j\sigma}\,|a\rangle\,\rho^S_{ab}, \tag{D4}$$

where a and b denote eigenstates of the system Hamiltonian. Note that within the BMme/BMsme $\kappa_{ij\sigma}$ is purely real and therefore does predict zero current.

However, an expression for the current to reservoir λ can be found by making use of the operator of total system charge $\hat{Q}$ and total system particle number $\hat{N}$, where q denotes the charge of one carrier

$$\sum_{\lambda} j^{\lambda}(\tau) = \frac{d}{d\tau}\langle \hat{Q}(\tau)\rangle = q\,\mathrm{tr}\left(\hat{N}\dot{\hat{\rho}}^{S}(\tau)\right) .$$

Taking $\dot{\hat{\rho}}^{S}(\tau)$ from the Qme we obtain

$$j^{\lambda} = q\sum_{abc}\left(n_c - \frac{1}{2}n_b - \frac{1}{2}n_a\right)\Xi^{\lambda}_{ca,cb}\Big)\rho^{S}_{ab}\,,$$

and for non-degenerate systems, in the Pauli limit we find from the BMsme

$$j^{\lambda}_{\text{non-deg}} = q\sum_{ab}(n_a - n_b)\,\Xi^{\lambda}_{ab}\phi_b\,.$$

* martin.nuss@tugraz.at

[1] G. Cuniberti, G. Fagas, and K. Richter, *Introducing Molecular Electronics* (Springer, 2005), ISBN 3540279946.
[2] A. Nitzan and M. A. Ratner, Science **300**, 1384 (2003).
[3] N. Agrait, A. L. Yeyati, and J. M. van Ruitenbeek, Physics Reports **377**, 81 (2003).
[4] J. C. Cuevas and E. Scheer, *Molecular Electronics: An Introduction to Theory and Experiment* (World Scientific Publishing Company, 2010), 1st ed., ISBN 9814282588.
[5] Y. V. Nazarov and Y. M. Blanter, *Quantum Transport: Introduction to Nanoscience* (Cambridge University Press New York, 2009), ISBN 0521832462.
[6] M. D. Ventra, *Electrical Transport in Nanoscale Systems* (Cambridge University Press, New York, 2008), ISBN 0521896347.
[7] D. K. Ferry, S. M. Goodnick, and J. Bird, *Transport in Nanostructures* (Cambridge University Press, 2009), 2nd ed., ISBN 0521877482.
[8] L. Grill, M. Dyer, L. Lafferentz, M. Persson, M. V. Peters, and S. Hecht, Nat Nano **2**, 687 (2007).
[9] J. Park, A. N. Pasupathy, J. I. Goldsmith, C. Chang, Y. Yaish, J. R. Petta, M. Rinkoski, J. P. Sethna, H. D. Abruna, P. L. McEuen, et al., Nature **417**, 722 (2002).
[10] W. Liang, M. P. Shores, M. Bockrath, J. R. Long, and H. Park, Nature **417**, 725 (2002).
[11] S. Kubatkin, A. Danilov, M. Hjort, J. Cornil, J.-L. Bredas, N. Stuhr-Hansen, P. Hedegard, and T. Bjornholm, Nature **425**, 698 (2003).
[12] L. H. Yu, Z. K. Keane, J. W. Ciszek, L. Cheng, J. M. Tour, T. Baruah, M. R. Pederson, and D. Natelson, Phys. Rev. Lett. **95**, 256803 (2005).
[13] D.-H. Chae, J. F. Berry, S. Jung, F. A. Cotton, C. A. Murillo, and Z. Yao, Nano Letters **6**, 165 (2006).
[14] M. Poot, E. Osorio, K. O'Neill, J. M. Thijssen, D. Vanmaekelbergh, C. A. van Walree, L. W. Jenneskens, and H. S. J. van der Zant, Nano Letters **6**, 1031 (2006).
[15] H. B. Heersche, Z. de Groot, J. A. Folk, H. S. J. van der Zant, C. Romeike, M. R. Wegewijs, L. Zobbi, D. Barreca, E. Tondello, and A. Cornia, Phys. Rev. Lett. **96**, 206801 (2006).
[16] E. Osorio, K. O'Neill, N. Stuhr-Hansen, O. Nielsen, T. Bjrnholm, and H. vanderZant, Advanced Materials **19**, 281 (2007).
[17] A. Danilov, S. Kubatkin, S. Kafanov, P. Hedegrd, N. Stuhr-Hansen, K. Moth-Poulsen, and T. Bjrnholm, Nano Letters **8**, 1 (2008).
[18] R. H. M. Smit, Y. Noat, C. Untiedt, N. D. Lang, M. C. van Hemert, and J. M. van Ruitenbeek, Nature **419**, 906 (2002).
[19] A. R. Champagne, A. N. Pasupathy, and D. C. Ralph, Nano Letters **5**, 305 (2005).
[20] E. Lörtscher, H. B. Weber, and H. Riel, Phys. Rev. Lett. **98**, 176807 (2007).
[21] M. Kiguchi, O. Tal, S. Wohlthat, F. Pauly, M. Krieger, D. Djukic, J. C. Cuevas, and J. M. van Ruitenbeek, Phys. Rev. Lett. **101**, 046801 (2008).
[22] D. I. Gittins, D. Bethell, D. J. Schiffrin, and R. J. Nichols, Nature **408**, 67 (2000).
[23] Xiao, Xu, and N. J. Tao, Nano Letters **4**, 267 (2004).
[24] J. Repp, G. Meyer, S. M. Stojković, A. Gourdon, and C. Joachim, Phys. Rev. Lett. **94**, 026803 (2005).
[25] L. Venkataraman, J. E. Klare, C. Nuckolls, M. S. Hybertsen, and M. L. Steigerwald, Nature **442**, 904 (2006).
[26] M. Koch, F. Ample, C. Joachim, and L. Grill, Nat Nano **7**, 713 (2012).
[27] M. A. Reed, C. Zhou, C. J. Muller, T. P. Burgin, and J. M. Tour, Science **278**, 252 (1997).
[28] E. Lörtscher, H. B. Weber, and H. Riel, Phys. Rev. Lett. **98**, 176807 (2007).
[29] M. C. Rogge and R. J. Haug, Phys. Rev. B **78**, 153310 (2008).
[30] L. Gaudreau, A. Kam, G. Granger, S. A. Studenikin, P. Zawadzki, and A. S. Sachrajda, Applied Physics Letters **95**, 193101 (2009).
[31] F. Molitor, S. Drscher, J. Gttinger, A. Jacobsen, C. Stampfer, T. Ihn, and K. Ensslin, Applied Physics Letters **94**, 222107 (2009).
[32] J. Eroms and D. Weiss, New Journal of Physics **11**, 095021 (2009).
[33] N. Tombros, C. Jozsa, M. Popinciuc, H. T. Jonkman, and B. J. van Wees, Nature **448**, 571 (2007).
[34] L. Gaudreau, S. A. Studenikin, A. S. Sachrajda, P. Zawadzki, A. Kam, J. Lapointe, M. Korkusinski, and P. Hawrylak, Phys. Rev. Lett. **97**, 036807 (2006).
[35] L. Gaudreau, A. S. Sachrajda, S. Studenikin, A. Kam,

F. Delgado, Y. P. Shim, M. Korkusinski, and P. Hawrylak, Phys. Rev. B **80**, 075415 (2009).
[36] G. Austing, C. Payette, G. Yu, J. Gupta, G. Aers, S. Nair, S. Amaha, and S. Tarucha, Japanese Journal of Applied Physics **49**, 04DJ03 (2010).
[37] L. Kouwenhoven, C. Marcus, P. McEuen, S. Tarucha, R. Westervelt, and N. Wingreen, Kluwer Series, Proceedings of the NATO Advanced Study Institute on Mesoscopic Electron Transport **E345**, 105 (1997).
[38] B. William, *Electronic and Optical Properties of Conjugated Polymers* (Oxford University Press, 2005), ISBN 0198526806.
[39] G. Begemann, D. Darau, A. Donarini, and M. Grifoni, Phys. Rev. B **77**, 201406 (2008).
[40] D. Darau, G. Begemann, A. Donarini, and M. Grifoni, Phys. Rev. B **79**, 235404 (2009).
[41] D. M. Cardamone, C. A. Stafford, and S. Mazumdar, Nano Letters **6**, 2422 (2006).
[42] A. Gagliardi, G. C. Solomon, A. Pecchia, T. Frauenheim, A. Di Carlo, N. S. Hush, and J. R. Reimers, Phys. Rev. B **75**, 174306 (2007).
[43] Z. Qian, R. Li, X. Zhao, S. Hou, and S. Sanvito, Phys. Rev. B **78**, 113301 (2008).
[44] S.-H. Ke, W. Yang, and H. U. Baranger, Nano Letters **8**, 3257 (2008).
[45] A. Donarini, G. Begemann, and M. Grifoni, Nano Letters **9**, 2897 (2009).
[46] A. Donarini, G. Begemann, and M. Grifoni, Phys. Rev. B **82**, 125451 (2010).
[47] N. Roch, S. Florens, V. Bouchiat, W. Wernsdorfer, and F. Balestro, Nature **453**, 633 (2008).
[48] D. Lobaskin and S. Kehrein, Phys. Rev. B **71**, 193303 (2005).
[49] A. C. Hewson, *The Kondo Problem to Heavy Fermions* (Cambridge University Press, 1997), ISBN 0521599474.
[50] D. Goldhaber-Gordon, J. Göres, M. A. Kastner, H. Shtrikman, D. Mahalu, and U. Meirav, Phys. Rev. Lett. **81**, 5225 (1998).
[51] S. De Franceschi, R. Hanson, W. G. van der Wiel, J. M. Elzerman, J. J. Wijpkema, T. Fujisawa, S. Tarucha, and L. P. Kouwenhoven, Phys. Rev. Lett. **89**, 156801 (2002).
[52] R. Leturcq, L. Schmid, K. Ensslin, Y. Meir, D. C. Driscoll, and A. C. Gossard, Phys. Rev. Lett. **95**, 126603 (2005).
[53] A. V. Kretinin, H. Shtrikman, D. Goldhaber-Gordon, M. Hanl, A. Weichselbaum, J. von Delft, T. Costi, and D. Mahalu, Phys. Rev. B **84**, 245316 (2011).
[54] A. V. Kretinin, H. Shtrikman, and D. Mahalu, Phys. Rev. B **85**, 201301 (2012).
[55] H. Haug and A. Jauho, *Quantum Kinetics in Transport and Optics of Semiconductors* (Springer-Verlag GmbH, 1996), 2nd ed., ISBN 3540616020.
[56] P. Myöhänen, A. Stan, G. Stefanucci, and R. van Leeuwen, Phys. Rev. B **80**, 115107 (2009).
[57] J.-S. Wang, B. Agarwalla, H. Li, and J. Thingna, Frontiers of Physics **9**, 673 (2014).
[58] T. Kubis and P. Vogl, Journal of Computational Electronics **6**, 183 (2007).
[59] P. Delaney and J. C. Greer, Phys. Rev. Lett. **93**, 036805 (2004).
[60] M. Strange, I. S. Kristensen, K. S. Thygesen, and K. W. Jacobsen, J. Chem. Phys. **128**, 114714 (2008).
[61] J. Chen, K. S. Thygesen, and K. W. Jacobsen, Phys. Rev. B **85**, 155140 (2012).
[62] M. Strange and K. S. Thygesen, Beilstein Journal of Nanotechnology **2**, 746 (2011).
[63] D. A. Ryndyk, R. Gutiérrez, B. Song, and G. Cuniberti, in *Energy Transfer Dynamics in Biomaterial Systems*, edited by I. Burghardt, V. May, D. A. Micha, and E. R. Bittner (Springer Berlin Heidelberg, Berlin, Heidelberg, 2009), vol. 93, pp. 213–335, ISBN 978-3-642-02305-7, 978-3-642-02306-4.
[64] K. Richter, *Semiclassical Theory of Mesoscopic Quantum Systems* (Springer, 1999), ISBN 3540665668.
[65] S. Datta, *Quantum Transport: Atom to Transistor* (Cambridge University Press, 2005), 2nd ed., ISBN 0521631459.
[66] S. Andergassen, V. Meden, H. Schoeller, J. Splettstoesser, and M. R. Wegewijs, Nanotechnology **21**, 272001 (2010).
[67] H. Schoeller, Eur. Phys. J. Special Topics **168**, 179 (2009).
[68] A. Rosch, J. Paaske, J. Kroha, and P. Wölfle, J. Phys. Soc. Jpn. **74**, 118 (2005).
[69] A. Hackl and S. Kehrein, Journal of Physics: Condensed Matter **21**, 015601 (2009).
[70] J. Eckel, F. Heidrich-Meisner, S. G. Jakobs, M. Thorwart, M. Pletyukhov, and R. Egger, New. J. Phys. **12**, 043042 (2010).
[71] J. F. Rentrop, S. G. Jakobs, and V. Meden, Journal of Physics A: Mathematical and Theoretical **48**, 145002 (2015).
[72] H. Aoki, N. Tsuji, M. Eckstein, M. Kollar, T. Oka, and P. Werner, Rev. Mod. Phys. **86**, 779 (2014).
[73] U. Schollwöck, Annals of Physics **326**, 96 (2011), january 2011 Special Issue.
[74] F. B. Anders, Phys. Rev. Lett. **101**, 066804 (2008).
[75] H.-P. Breuer and F. Petruccione, *The Theory of Open Quantum Systems* (Oxford University Press, 2002), ISBN 0198520638.
[76] H. J. Carmichael, *An Open Systems Approach to Quantum Optics: Lectures Presented at the Universite Libre De Bruxelles October 28 to November 4, 1991 (Lecture Notes in Physics New Series M)* (Springer-Verlag, 1993), ISBN 0387566341.
[77] H. J. Carmichael, *Statistical Methods in Quantum Optics 1: Master Equations and Fokker-Planck Equations* (Springer, 2010), ISBN 3642081339.
[78] G. Schaller, *Non-Equilibrium Master Equations* (2014).
[79] G. Schaller, *Open Quantum Systems Far from Equilibrium* (Springer, Cham ; New York, 2014), auflage: 2014 ed., ISBN 9783319038766.
[80] C. Cohen-Tannoudji, J. Dupont-Roc, and G. Grynberg, *Atom-Photon Interactions: Basic Processes and Applications* (Wiley-VCH, 1998), ISBN 0471293369.
[81] J. Jin, J. Li, Y. Liu, X.-Q. Li, and Y. Yan, The Journal of Chemical Physics **140**, 244111 (2014).
[82] Y. Meir and N. S. Wingreen, Phys. Rev. Lett. **68**, 2512 (1992).
[83] H. Schoeller and G. Schön, Phys. Rev. B **50**, 18436 (1994).
[84] M. Eckstein, A. Hackl, S. Kehrein, M. Kollar, M. Moeckel, P. Werner, and F. Wolf, The European Physical Journal - Special Topics **180**, 217 (2009).
[85] R. Gezzi, T. Pruschke, and V. Meden, Phys. Rev. B **75**, 045324 (2007).
[86] S. G. Jakobs, V. Meden, and H. Schoeller, Phys. Rev. Lett. **99**, 150603 (2007).
[87] J. K. Freericks, V. M. Turkowski, and V. Zlatić, Phys. Rev. Lett. **97**, 266408 (2006).
[88] M. Potthoff, M. Aichhorn, and C. Dahnken, Phys. Rev. Lett. **91**, 206402 (2003).
[89] C. Gros and R. Valenti, Phys. Rev. B **48**, 418 (1993).

[90] Sénéchal, D. Perez, and M. Pioro-Ladriére, Phys. Rev. Lett. **84**, 522 (2000).
[91] M. Balzer and M. Potthoff, Phys. Rev. B **83**, 195132 (2011).
[92] F. Hofmann, M. Eckstein, E. Arrigoni, and M. Potthoff, Phys. Rev. B **88**, 165124 (2013).
[93] M. Knap, W. von der Linden, and E. Arrigoni, Phys. Rev. B **84**, 115145 (2011).
[94] M. Nuss, E. Arrigoni, M. Aichhorn, and W. von der Linden, Phys. Rev. B **85**, 235107 (2012).
[95] M. Nuss, C. Heil, M. Ganahl, M. Knap, H. G. Evertz, E. Arrigoni, and W. von der Linden, Phys. Rev. B **86**, 245119 (2012).
[96] M. Nuss, E. Arrigoni, and W. von der Linden, AIP Conference Proceedings **1485**, 302 (2012).
[97] M. Nuss, W. von der Linden, and E. Arrigoni, Phys. Rev. B **89**, 155139 (2014).
[98] M. Knap, E. Arrigoni, and W. von der Linden, Phys. Rev. B **88**, 054301 (2013).
[99] A. A. Dzhioev and D. S. Kosov, Journal of Physics: Condensed Matter **24**, 225304 (2012).
[100] A. A. Dzhioev and D. S. Kosov, Journal of Physics A: Mathematical and Theoretical **48**, 015004 (2015).
[101] E. Arrigoni, M. Knap, and W. von der Linden, Phys. Rev. Lett. **110**, 086403 (2013).
[102] A. Dorda, M. Nuss, W. von der Linden, and E. Arrigoni, Phys. Rev. B **89**, 165105 (2014).
[103] A. Georges, G. Kotliar, W. Krauth, and M. J. Rozenberg, Rev. Mod. Phys. **68**, 13 (1996).
[104] W. Metzner and D. Vollhardt, Phys. Rev. Lett. **62**, 324 (1989).
[105] P. Schmidt and H. Monien, arXiv:cond-mat/0202046.
[106] J. W. Negele and H. Orland, *Quantum Many-particle Systems* (Westview Press, 1998), ISBN 0738200522.
[107] Throughout this paper we use $\hbar = k_B \equiv 1$.
[108] J. Schwinger, J.Math. Phys. **2**, 407 (1961).
[109] R. Feynman and F. V. Jr., Ann. Phys. **24**, 118 (1963).
[110] L. Keldysh, Zh. Eksp. Teor. Fiz. **47**, 1515 (1965).
[111] C. H. Fleming and N. I. Cummings, Phys. Rev. E **83**, 031117 (2011).
[112] T. Mori and S. Miyashita, Journal of the Physical Society of Japan **77**, 124005 (2008).
[113] $[\hat{a}, \hat{b}]_{\pm} = \hat{a}\hat{b} \pm \hat{b}\hat{a}$ denotes the anti-commutator and commutator, respectively.
[114] D. Sénéchal, arXiv:0806.2690 (2009).
[115] J. Rammer and H. Smith, Rev. Mod. Phys. **58**, 323 (1986).
[116] E. N. Economou, *Green's Functions in Quantum Physics* (Springer, 2010), 3rd ed., ISBN 3642066917.
[117] Z. Bai, J. Demmel, J. Dongarra, A. Ruhe, and H. van der Vorst, *Templates for the Solution of Algebraic Eigenvalue Problems: A Practical Guide (Software, Environments and Tools)* (Society for Industrial and Applied Mathematics, 1987), ISBN 0898714710.
[118] W. H. Press, S. A. Teukolsky, W. T. Vetterling, and B. P. Flannery, *Numerical Recipes 3rd Edition: The Art of Scientific Computing* (Cambridge University Press, 2007), 3rd ed., ISBN 0521880688.
[119] Assuming that the interacting part is small enough to be treated exactly, otherwise it has to be decomposed into sub partitions again.
[120] We denote the largest energy scale or parameter of $\hat{\mathcal{H}}$ as $|\hat{\mathcal{H}}|$.
[121] R. S. Whitney, Journal of Physics A: Mathematical and Theoretical **41**, 175304 (2008).
[122] Y. Yan, F. Shuang, R. Xu, J. Cheng, X.-Q. Li, C. Yang, and H. Zhang, The Journal of Chemical Physics **113**, 2068 (2000).
[123] P. W. Anderson, Phys. Rev. **124**, 41 (1961).
[124] M. I. Katsnelson, V. Y. Irkhin, L. Chioncel, A. I. Lichtenstein, and R. A. de Groot, Rev. Mod. Phys. **80**, 315 (2008).
[125] I. Bloch, J. Dalibard, and W. Zwerger, Rev. Mod. Phys. **80**, 885 (2008).
[126] J. Hubbard, Proc. R. Soc. Lond. A **276**, 238 (1963).
[127] A. Vidan, R. M. Westervelt, M. Stopa, M. Hanson, and A. C. Gossard, Applied Physics Letters **85**, 3602 (2004).
[128] F. Delgado, Y.-P. Shim, M. Korkusinski, L. Gaudreau, S. A. Studenikin, A. S. Sachrajda, and P. Hawrylak, Phys. Rev. Lett. **101**, 226810 (2008).
[129] W. Gong, Y. Zheng, and T. L, Applied Physics Letters **92**, 042104 (2008).
[130] T. Kostyrko and B. R. Bułka, Phys. Rev. B **79**, 075310 (2009).
[131] Y.-P. Shim, F. Delgado, and P. Hawrylak, Phys. Rev. B **80**, 115305 (2009).
[132] C. Pöltl, C. Emary, and T. Brandes, Phys. Rev. B **80**, 115313 (2009).
[133] C. Emary, Phys. Rev. B **76**, 245319 (2007).
[134] M. Busl, R. Sánchez, and G. Platero, Phys. Rev. B **81**, 121306 (2010).
[135] J. C. Ward, Phys. Rev. **78**, 182 (1950).
[136] S. Engelsberg and J. R. Schrieffer, Phys. Rev. **131**, 993 (1963).
[137] G. Baym and L. P. Kadanoff, Phys. Rev. **124**, 287 (1961).
[138] G. Baym, Phys. Rev. **127**, 1391 (1962).
[139] D. A. Ryndyk, A. Donarini, M. Grifoni, and K. Richter, Phys. Rev. B **88**, 085404 (2013).
[140] P. Jordan and E. Wigner, Zeitschrift für Physik **47**, 631 (1928).

5.9. Auxiliary master equation approach to nonequilibrium correlated impurities

5.9.1. Preamble

This part of our work has been published in PHYSICAL REVIEW B 89, 165105 (2014) [69] and is also available as a preprint on arXiv:1312.4586. Reproduced with permission from PHYSICAL REVIEW B 89, 165105 (2014), doi:10.1103/PhysRevB.89.165105 under Creative Commons Attribution 3.0 License.

The AMEA has been developed in [68] and is applied to the SIAM under bias voltage in this work. An introduction to the SIAM is available in Sec. 3.1 and some of its applications are discussed in Ch. 2. An overview of the AMEA method is provided in Sec. 3.4. So far we discussed a perturbative treatment of the steady-state in terms of NEGF. In contrast, this steady-state NEGF approach sets up an auxiliary system described by a Lindblad master equation which is mapped to the physical system using the hybridization function in Keldysh space. We obtain results for the current-voltage characteristics and compare them to previous results of Sec. 5.4, Sec. 5.4, Sec. 5.4, Sec. 5.5, Sec. 5.6, Sec. 5.2, Sec. 5.3 and Sec. 5.10. The splitting of the Kondo resonance is studied in detail. The method is well suited as a future impurity solver for steady-state DMFT, see also Sec. 5.1.

This study is authored by Antonius Dorda (AD) and co-authored by Martin Nuss (MN) as well as by MN's supervisors Wolfgang von der Linden (WL) and Enrico Arrigoni (EA). EA, Michael Knap and WL introduced the auxiliary master equation approach in [68]. AD, MN, EA and WL further developed the method. MN and AD worked on the formal part of nonequilibrium Green's functions in the Lindblad formalism. MN, AD and EA independently worked out expressions and relations for the non-interacting case. MN studied in detail the non-interacting situation in the NEGF. AD wrote a computer code to solve interacting systems and implemented the auxiliary master equation approach. AD analyzed and collected the data. AD, MN and EA wrote the first version of the manuscript. All authors contributed in writing and revising the manuscript as well as discussing the results. We discussed our results with with Achim Rosch, Walter Hofstetter, Sebastian Diehl, Michael Knap, Daniel Rost and Frauke Schwarz.

5.9.2. Manuscript

PHYSICAL REVIEW B **89**, 165105 (2014)

Auxiliary master equation approach to nonequilibrium correlated impurities

Antonius Dorda,* Martin Nuss, Wolfgang von der Linden, and Enrico Arrigoni
Institute of Theoretical and Computational Physics, Graz University of Technology, 8010 Graz, Austria
(Received 23 December 2013; published 7 April 2014)

We present a numerical method for the study of correlated quantum impurity problems out of equilibrium, which is particularly suited to address steady-state properties within dynamical mean field theory. The approach, recently introduced by Arrigoni *et al*. [Phys. Rev. Lett. **110**, 086403 (2013)], is based upon a mapping of the original impurity problem onto an auxiliary open quantum system, consisting of the interacting impurity coupled to bath sites as well as to a Markovian environment. The dynamics of the auxiliary system is governed by a Lindblad master equation whose parameters are used to optimize the mapping. The accuracy of the results can be readily estimated and systematically improved by increasing the number of auxiliary bath sites, or by introducing a linear correction. Here, we focus on a detailed discussion of the proposed approach including technical remarks. To solve for the Green's functions of the auxiliary impurity problem, a non-Hermitian Lanczos diagonalization is applied. As a benchmark, results for the steady-state current-voltage characteristics of the single-impurity Anderson model are presented. Furthermore, the bias dependence of the single-particle spectral function and the splitting of the Kondo resonance are discussed. In its present form, the method is fast, efficient, and features a controlled accuracy.

DOI: 10.1103/PhysRevB.89.165105 PACS number(s): 71.15.−m, 71.27.+a, 73.63.Kv, 73.23.−b

I. INTRODUCTION

Correlated systems out of equilibrium have recently attracted increasing interest due to the significant progress in a number of related experimental fields. Advances in microscopic control and manipulation of quantum mechanical many-body systems within quantum optics [1] and ultracold quantum gases, for example in optical lattices [2–6], have long reached high accuracy and versatility. Ultrafast laser spectroscopy [7,8] offers the possibility to explore and understand electronic dynamics in unprecedented detail. Experiments in condensed matter nanotechnology [9], spintronics [10], molecular junctions [11–16], and quantum wires or quantum dots [17,18] are able to reveal effects of the interference of few microscopic quantum states. The nonequilibrium nature of such experiments does not only offer a new route to explore fundamental aspects of quantum physics, such as nonequilibrium quantum phase transitions [19], the interplay between quantum entanglement, dissipation, and decoherence [20], or the pathway to thermalization [21,22], but also suggests the possibility of exciting future applications [11,23].

Addressing the dynamics of correlated quantum systems poses a major challenge to theoretical endeavors. In this respect, quantum impurity models help improving our understanding of fermionic many-body systems. In particular, the single-impurity Anderson model (SIAM) [24], which was originally devised to study magnetic impurities in metallic hosts [25,26], has become an important tool in many areas of condensed matter physics [27,28]. Most prominently, it features nonperturbative many-body physics which manifest in the Kondo effect [29]. It provides the backbone for all calculations within dynamical mean field theory (DMFT) [28,30], a technique which allows us to understand the properties of a broad range of correlated systems and becomes exact in the limit of infinite dimensions [31]. The basic physical properties of the SIAM in equilibrium are quite well understood [29] thanks to the pioneering work from Kondo [32], renormalization group [33], as well as perturbation theory (PT) [34–37] and the mapping to its low-energy realization, the Kondo model [38].

The SIAM out of equilibrium provides a description for several physical processes such as, for example, nonlinear transport through quantum dots [17,39], correlated molecules [13,14,40–42], or the influence of adsorbed atoms on surfaces or bulk transport [43]. As in the equilibrium case, the solution of the SIAM constitutes the bottleneck of nonequilibrium DMFT [44–51] calculations. Therefore, accurate and efficient methods to obtain dynamical correlation functions of impurity models out of equilibrium are required in order to describe time-resolved experiments on strongly correlated compounds [7,8] and to understand their steady-state transport characteristics [23].

However, nonequilibrium correlated impurity models still pose an exciting challenge to theory. Our work addresses this issue with special emphasis on the steady state. But, before introducing this work in Sec. I, we briefly review previous approaches. In recent times, a number of computational techniques have been devised to handle the SIAM out of equilibrium. Among them are scattering-state Bethe ansatz (BA) [52], scattering-state NRG (SNRG) [53–55], noncrossing approximation studies [56,57], fourth-order Keldysh PT [58], other perturbative methods [59,60] in combination with the renormalization group (RG) [61–65], iterative summation of real-time path integrals [66], time-dependent NRG [67], flow equation techniques [68,69], the time-dependent density matrix RG (DMRG) [70–75] applied to the SIAM [76,77], nonequilibrium cluster PT (CPT) [78], the nonequilibrium variational cluster approach (VCA) [79,80], dual fermions

*dorda@tugraz.at

[81], the functional RG (fRG) [82,83], diagrammatic quantum Monte Carlo (QMC) [84,85], continuous time QMC (CT-QMC) calculations on an auxiliary system with an imaginary bias [86–90], superoperator techniques [91,92], many-body PT and time-dependent density functional theory [93], generalized slave-boson methods [94], real-time RG (rtRG) [95], time-dependent Gutzwiller mean field calculations [96], and generalized master equation approaches [97]. Comparisons of the results of some of these methods are available in literature [77,98,99] and time scales have been discussed in Ref. [100].

Despite this large number of approaches, only a limited number of them is applicable to nonequilibrium DMFT, and very few are still accurate for large times in steady state. Beyond the quadratic action for the Falicof-Kimball model [46,101,102], iterated PT (IPT) [45], numerical renormalization group (NRG) [48], real-time QMC [48,103], the noncrossing approximation (NCA) [104,105], and recently Hamiltonian-based impurity solvers [106] have been applied in the time-dependent case. Some of the above approaches, such as QMC [49] and DMRG [73], are very accurate in addressing the short- and medium-time dynamics, but in some cases the accuracy decreases at long times and a steady state can not be reliably identified. Some other methods are perturbative and/or valid only in certain parameter regions or for restricted models. RG approaches (e.g., [61]) are certainly more appropriate to identify the low-energy behavior.

This work

In this paper, we discuss a method, first proposed in [51], which addresses the correlated impurity problem out of equilibrium, and is particularly efficient for the steady state. The accuracy of the results is *controlled* as it can be directly estimated by analyzing the bath hybridization function (details following). Here, we extend, test, and provide details of this approach and its implementation. The basic idea is to map the impurity problem onto an auxiliary open system, consisting of a small number of bath sites coupled to the interacting impurity and, additionally, to a so-called Markovian environment [107]. The parameters of this auxiliary open quantum system are obtained by optimization in order to represent the original impurity problem as accurately as possible. The auxiliary system dynamics are governed by a Lindblad master equation which is solved exactly with the non-Hermitian Lanczos method. The crucial point is that the overall accuracy of the method is thus solely determined by how well the auxiliary system reproduces the original one. This can be, in principle, improved by increasing the number of auxiliary bath sites.

In this study, we provide convincing benchmarks for the steady-state properties of the SIAM coupled to two metallic leads under bias voltage. We include a discussion of convergence as a function of the number of bath sites and present a scheme to estimate the error and partially correct for it. In its presented form, the method is fast, efficient, and is directly applicable to steady-state dynamical mean field theory [51] for which previously suggested methods are less reliable. Extending the method to treat time-dependent properties and multiorbital systems is possible, in principle, however with a much heavier computational effort.

The paper is organized as follows: In Sec. II A, the SIAM under bias voltage is introduced. In Sec. II B, we introduce nonequilibrium Green's functions and in Secs. II C and II D, we outline the auxiliary master equation approach where we also focus on details of our particular implementation. Results for the steady state, including the equilibrium situation, are presented in Sec. III. This includes the steady-state current-voltage characteristics which we compare with exact results from matrix product state (MPS) time evolution [77] as well as data for the spectral function under bias which we compare with nonequilibrium NRG [54]. We conclude and give an outlook in Sec. IV.

II. AUXILIARY MASTER EQUATION APPROACH

As discussed above, the method is particularly suited to deal with nonequilibrium steady-state properties caused by different temperatures and/or chemical potential in the leads of a correlated quantum impurity system. As such, it can be readily used as impurity solver for nonequilibrium DMFT [46,51]. Here, we illustrate its application to the fermionic SIAM with two leads having different chemical potentials, and, in principle, different temperatures.

A. Nonequilibrium single-impurity Anderson model

We consider a single Anderson impurity coupled to electronic leads under bias voltage [see Fig. 1(a)]

$$\hat{\mathcal{H}} = \hat{\mathcal{H}}_{\text{imp}} + \hat{\mathcal{H}}_{\text{res}} + \hat{\mathcal{H}}_{\text{coup}}. \tag{1}$$

The impurity orbital features charge as well as spin degrees of freedom and is subject to a local Coulomb repulsion U:

$$\hat{\mathcal{H}}_{\text{imp}} = \epsilon_f \sum_\sigma f_\sigma^\dagger f_\sigma + U\, \hat{n}_\uparrow^f \hat{n}_\downarrow^f.$$

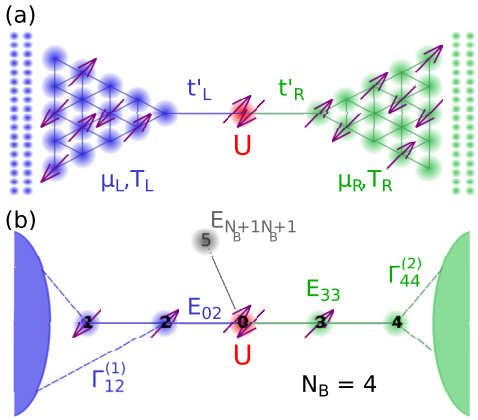

FIG. 1. (Color online) (a) Sketch of the quantum impurity model (1) consisting of an impurity with interaction U coupled via hybridizations t'_λ to noninteracting leads at chemical potential μ_λ and temperature T_λ, $\lambda \in \{L, R\}$. (b) Illustration of the auxiliary open quantum system [Eq. (10a)] with single-particle parameters $E_{\mu\nu}$ and Lindblad dissipators $\Gamma^\kappa_{\mu\nu}$ consisting of the impurity at site $f = 0$, N_B bath sites ($N_B = 4$ in the plot), as well as a Markovian environment (shaded areas). When evaluating linear corrections (see Appendix C), an additional site $N_B + 1$ is used.

Here, $f_\sigma^\dagger/f_\sigma$ denote fermionic creation/annihilation operators for the impurity orbital with spin $\sigma \in \{\uparrow,\downarrow\}$, respectively. The particle-number operator is defined in the usual way $\hat{n}_\sigma^f = f_\sigma^\dagger f_\sigma$ and the impurity onsite potential is $\epsilon_f = (V_G - \frac{U}{2})$, with gate voltage $V_G = 0$ at particle-hole symmetry. The impurity is coupled to two noninteracting electronic leads $\lambda \in \{L,R\}$ with dispersion $\epsilon_{\lambda k}$:

$$\hat{\mathcal{H}}_{\rm res} = \sum_{\lambda k\sigma} (\epsilon_\lambda + \epsilon_{\lambda k})\, c_{k\lambda\sigma}^\dagger\, c_{k\lambda\sigma}.$$

The effect of a bias voltage ϕ is to shift the chemical potential and the onsite energies of the two leads by $\epsilon_\lambda = \pm\frac{\phi}{2}$, respectively. For the energies $\epsilon_{\lambda k}$ of the leads we will consider two cases.

(i) Two tight-binding semi-infinite chains with nearest-neighbor hopping t, corresponding to a semicircular electronic density of states (DOS): In this case, the boundary retarded single-particle Green's function of the two uncoupled leads is given by [108–110]

$$g_\lambda^R(\omega) = g_{{\rm SC},\lambda}^R(\omega) = \frac{\omega-\epsilon_\lambda}{2t^2} - i\frac{\sqrt{4t^2-(\omega-\epsilon_\lambda)^2}}{2t^2}, \qquad (2)$$

with a bandwidth of $D_{\rm SC} = 4\,t$.

(ii) A constant DOS with a bandwidth $D_{\rm WB} = \pi\, t$ results in boundary Green's functions [109]

$$g_\lambda^R(\omega) = g_{{\rm WB},\lambda}^R(\omega) = -\frac{1}{D_{\rm WB}} \ln\left(\frac{\omega-\epsilon_\lambda-\frac{D_{\rm WB}}{2}}{\omega-\epsilon_\lambda+\frac{D_{\rm WB}}{2}}\right). \qquad (3)$$

The choice $D_{\rm WB} = \pi\, t$ makes sure that the DOS at $\omega = 0$ of both lead types coincide. The leads are coupled to the impurity orbital by

$$\hat{\mathcal{H}}_{\rm coup} = \sum_{\lambda\sigma} t'_\lambda \frac{1}{\sqrt{N_k}} \sum_k (c_{k\lambda\sigma}^\dagger\, f_\sigma + f_\sigma^\dagger\, c_{k\lambda\sigma}),$$

where we take the same hybridization $t'_\lambda = -0.3162\,t$ for both leads, and $N_k \to \infty$ is the number of k points. Expressions presented below are valid for arbitrary temperatures, although we will show results for zero temperature only, which is numerically the most unfavorable case [111]. The setup chosen here represents by no means a limitation of the method and extensions to more complicated situations, such as nonsymmetric couplings, off particle-hole symmetry, etc., are straightforward.

B. Steady-state nonequilibrium Green's functions

We are interested in the steady-state behavior under bias voltage of the model described by Eq. (1). We assume that such a steady state exists and is unique [112]. We denote the single-particle Green's function of the impurity in the nonequilibrium Green's function (Keldysh) formalism by [113–117]

$$\underline{G}(\omega) = \begin{pmatrix} G^R(\omega) & G^K(\omega) \\ 0 & G^A(\omega) \end{pmatrix}. \qquad (4)$$

Fourier transformation to energy ω is possible since in the steady state the system becomes time translationally invariant. In that case, the memory of the initial condition has been fully washed away, so there is no contribution from the Matsubara branch [118]. We will use an underline $\underline{\ldots}$ to denote two-point functions with the Keldysh matrix structure as in Eq. (4).

The Green's function of the correlated impurity can be expressed via Dyson's equation

$$\underline{G}^{-1}(\omega) = \underline{G}_0^{-1}(\omega) - \underline{\Sigma}(\omega), \qquad (5)$$

where $\underline{\Sigma}(\omega)$ is the impurity self-energy. The noninteracting impurity Green's function $\underline{G}_0(\omega)$ can be written in the form

$$\underline{G}_0^{-1}(\omega) = \underline{g}_0^{-1}(\omega) - \underline{\Delta}(\omega), \qquad (6)$$

$\underline{g}_0(\omega)$ being the noninteracting Green's function of the disconnected impurity [108], and

$$\underline{\Delta}(\omega) = \sum_\lambda {t'_\lambda}^2\, \underline{g}_\lambda(\omega) \qquad (7)$$

is the hybridization function of the leads (a 2×2 Keldysh object, in contrast to the equilibrium case, where it is convenient to work in Matsubara space). We define an equilibrium Anderson width [29] for each lead $\Delta_0 \equiv -\frac{1}{2}\,{\rm Im}[\underline{\Delta}^R(\omega = 0)] = \frac{t'^2_\lambda}{t} \approx 0.1\,t$. In the following, we will use Δ_0 as a unit of energy and in addition we choose $\hbar = e = 1$.

The boundary Green's functions $\underline{g}_\lambda$ of each disconnected lead is determined by (a) its retarded component g_λ^R [either Eqs. (2) or (3)], (b) its advanced component $g_\lambda^A = g_\lambda^{R*}$, and (c) its Keldysh component, which satisfies the fluctuation dissipation theorem

$$g_\lambda^K(\omega) = 2i\,[1 - 2p_{\rm F}(\omega-\mu_\lambda)]\,{\rm Im}\big[g_\lambda^R(\omega)\big] \qquad (8)$$

since the disconnected leads are in equilibrium. Here, $p_{\rm F}(\omega-\mu_\lambda)$ is the Fermi distribution with chemical potential μ_λ. For the noninteracting isolated impurity, one can take $(g_0^{-1})^R = \omega - \epsilon_f$ and $(g_0^{-1})^K = 0$ since infinitesimals 0^+ can be neglected after coupling to the leads (unless there are bound states). As usual, the presence of the interaction U makes the solution of the problem impurity plus leads a major challenge both in equilibrium as well as out of equilibrium, which we plan to address in this paper.

Similarly to the equilibrium case, the action of the leads on the impurity is completely determined by the hybridization function $\underline{\Delta}(\omega)$, *independently of how the leads are represented in detail*. In other words, if one constructs a different configuration of leads (e.g., with more leads with different temperatures, DOS, etc.), which has the same $\underline{\Delta}(\omega)$, i.e. the same $\Delta^R(\omega)$ and $\Delta^K(\omega)$ as Eq. (7), then the resulting local properties of the interacting impurity, e.g., the Green's function $\underline{G}(\omega)$ are the same. This holds provided the leads contain *noninteracting* fermions only.

The approach we suggested in Ref. [51] precisely exploits this property. The idea is to replace the impurity plus leads system [Eq. (1)] by an auxiliary one which reproduces $\underline{\Delta}(\omega)$ as accurately as possible, and at the same time can be solved exactly by numerical methods, such as Lanczos exact diagonalization. Details on the construction of the auxiliary impurity system are given in the following.

The self-energy $\underline{\Sigma}_{\rm aux}(\omega)$ of the auxiliary system, obtained by exact diagonalization, is used in analogy to DMFT [28,119]

as an approximation to the physical self-energy of the original impurity system. Inserting $\underline{\Sigma}(\omega) \approx \underline{\Sigma}_{\rm aux}(\omega)$ into Eqs. (5) and (6), together with the exact hybridization function $\underline{\Delta}(\omega)$ yields an approximation for the physical Green's function. From this, observables such as the current or the spectral function are then calculated. We emphasize that the accuracy of this approximation can be controlled by the difference between the $\underline{\Delta}_{\rm aux}(\omega)$ of the auxiliary system and the physical one $\underline{\Delta}(\omega)$, and that this can be, in principle, systematically improved, as discussed below.

C. Auxiliary open quantum system

The idea presented here is strongly related to the exact diagonalization (ED) approach for the DMFT impurity problem in *equilibrium* [28,119]. Here, the infinite leads are replaced by a small number of bath sites, whose parameters are optimized by fitting the hybridization function in Matsubara space. The reduced system of bath sites plus impurity is then solved by Lanczos ED [120]. This approach can not be straightforwardly extended to the nonequilibrium steady-state case for several reasons: (i) since the small bath is finite, its time dependence is (quasi)periodic, i.e., no steady state is reached, (ii) there is no Matsubara representation out of equilibrium [121], thus, one is forced to use real energies but (iii) in this case $\mathrm{Im}[\Delta^R_{\rm aux}(\omega)]$ of the small bath consists of δ peaks and can hardly be fitted to a smooth $\Delta^R(\omega)$. The solution we suggested in Ref. [51] consists in additionally coupling the small bath to a Markovian environment, which makes it effectively "infinitely large," and solves problems (i) and (iii) above. Specifically, we replace the impurity plus leads model [Eq. (1)] by an auxiliary *open* quantum system consisting of the impurity plus a small number of bath sites, which in turn are coupled to a Markovian environment.

The dynamics of the system (consisting of bath sites and impurity), including the effect of the Markovian environment is expressed in terms of the Lindblad quantum master equation which controls the time dependence of its reduced density operator $\hat{\rho}$ [107,122]:

$$\dot{\hat{\rho}} = \hat{\hat{\mathcal{L}}}\hat{\rho}. \tag{9}$$

The Lindblad superoperator [123]

$$\hat{\hat{\mathcal{L}}} = \hat{\hat{\mathcal{L}}}_H + \hat{\hat{\mathcal{L}}}_D \tag{10a}$$

consists of a unitary contribution

$$\hat{\hat{\mathcal{L}}}_H\hat{\rho} = -i[\hat{\mathcal{H}}_{\rm aux},\hat{\rho}],$$

as well as a nonunitary, dissipative term originating from the coupling to the Markovian environment

$$\hat{\hat{\mathcal{L}}}_D\hat{\rho} \equiv 2\sum_{\mu\nu=0}^{N_B}\sum_{\sigma}\left[\Gamma^{(1)}_{\nu\mu}\left(d_{\mu\sigma}\hat{\rho}\,d^\dagger_{\nu\sigma} - \frac{1}{2}\{\hat{\rho},d^\dagger_{\nu\sigma}d_{\mu\sigma}\}\right) + \Gamma^{(2)}_{\nu\mu}\left(d^\dagger_{\nu\sigma}\hat{\rho}\,d_{\mu\sigma} - \frac{1}{2}\{\hat{\rho},d_{\mu\sigma}d^\dagger_{\nu\sigma}\}\right)\right], \tag{10b}$$

where $[\hat{A},\hat{B}]$ and $\{\hat{A},\hat{B}\}$ denote the commutator and anticommutator, respectively. The unitary time evolution is generated by the Hamiltonian

$$\hat{\mathcal{H}}_{\rm aux} = \sum_{\mu\nu=0}^{N_B}\sum_{\sigma}E_{\mu\nu}d^\dagger_{\mu\sigma}d_{\nu\sigma} + Ud^\dagger_{f\uparrow}d_{f\uparrow}d^\dagger_{f\downarrow}d_{f\downarrow}, \tag{11}$$

describing a fermionic "chain" ($E_{\mu\nu}$ is nonzero only for onsite and nearest-neighbor terms). It is convenient to choose the interacting impurity at site $f = 0$ and N_B auxiliary bath sites at $\mu,\nu = 1,\ldots,N_B$ (see Fig. 1(b)). As usual, $d^\dagger_{\mu\sigma}/d_{\mu\sigma}$ create/annihilate the corresponding auxiliary particles. The quadratic form of the dissipator [Eq. (10b)] corresponds to a noninteracting Markovian environment. The dissipation matrices $\Gamma^{(\kappa)}_{\mu\nu}$, $\kappa \in \{1,2\}$, are Hermitian and positive semidefinite [122]. The advantage of replacing the impurity problem by the auxiliary one described by Eqs. (9)–(11), is that for a small number of bath sites the dynamics of the interacting auxiliary system can be solved exactly by diagonalization of the superoperator $\hat{\hat{\mathcal{L}}}$ in the space of many-body density operators (see Sec. II D 2).

Intuitively, one can consider the effective system as a truncation of the original chain described by Eq. (1), whereby the Markovian environment compensates for the missing "pieces." However, this would still be a crude approximation and, in addition, it would not be clear how to introduce the chemical potential in the Markovian environment (except for weak coupling). Our strategy, similarly to the equilibrium case, consists in simply using the parameters of the auxiliary system in order to provide an optimal fit to the bath spectral function $\underline{\Delta}(\omega)$. The parameters for the fit are, in principle, $E_{\mu\nu}$ and $\Gamma^{(\kappa)}_{\mu\nu}$. However, one should consider that there is a certain redundancy. In other words, several combinations of parameters lead to the same $\underline{\Delta}(\omega)$. For example, it is well known in equilibrium that in the case of the $E_{\mu\nu}$ one can restrict to diagonal and nearest-neighbor terms only [124].

The accuracy of the results will be directly related to the accuracy of the fit to $\underline{\Delta}(\omega)$, and this is expected to increase rapidly with the number of fit parameters, which obviously increases with N_B. On the other hand, also the computational complexity necessary to exactly diagonalize the interacting auxiliary system increases exponentially with N_B. The fit does not present a major numerical difficulty, as the determination of the hybridization functions of both the original model [Eq. (7)], as well as the one of the auxiliary system $\underline{\Delta}_{\rm aux}(\omega)$ described by the Lindblad equation (10) require the evaluation of $\underline{G}_0$ [cf. (6)], i.e., the solution of a *noninteracting* problem.

The fit is obtained by minimizing the cost function

$$\chi\left(E_{\mu\nu},\Gamma^{(\kappa)}_{\mu\nu}\right) = \sum_{\alpha\in\{R,K\}}\int_{-\infty}^{\infty}d\omega\,W^\alpha(\omega) \times \left|\Delta^\alpha(\omega) - \Delta^\alpha_{\rm aux}\left(\omega;E_{\mu\nu},\Gamma^{(\kappa)}_{\mu\nu}\right)\right|^n \tag{12}$$

with respect to the parameters of the auxiliary system. The advanced component does not need to be considered as $\Delta^A = \Delta^{R*}$. Of course, as in ED-based DMFT, there exists an ambiguity which is related to the choice of the weight function $W^\alpha(\omega)$, which also sets the integral boundaries. This uncertainty is clearly reduced upon increasing N_B.

Depending on the expected physics, it might be useful to adopt an energy-dependent weight function. This could be

used, for example, to describe the physics around the chemical potentials more accurately.

Once the auxiliary system is defined in terms of $E_{\mu\nu}$ and $\Gamma^{(\kappa)}_{\mu\nu}$, the corresponding interacting nonequilibrium problem (10) can be solved by an exact diagonalization of the non-Hermitian superoperator $\hat{\hat{\mathcal{L}}}$ within the space of many-body density operators. The dimension of this space is equal to the square of the dimension of the many-body Hilbert space, and thus it grows exponentially as a function of N_B. Therefore, for $N_B \geqslant 4$, a non-Hermitian Lanczos treatment must be used. The solution of the noninteracting Lindblad problem is nonstandard (see, e.g., Ref. [125]), and a method particularly suited for the present approach is discussed in Sec. II D 1.

D. Green's functions of the auxiliary Lindblad problem

In this section, we present expressions for the Green's functions of the auxiliary system. Specifically, we will derive an analytic expression for the noninteracting Green's functions in Sec. II D 1, and illustrate the numerical procedure to determine the interacting ones in Sec. II D 2. The derivations make largely use of the formalism of [126] (see also [127]). For an alternative appealing approach to the noninteracting case, see also Ref. [125]. All Green's functions discussed in Sec. II D are the ones of the auxiliary system, which are different from the physical ones for $N_B < \infty$.

The dynamics of the auxiliary open quantum system described by the superoperator $\hat{\hat{\mathcal{L}}}$ [Eq. (10)] can be recast in an elegant way as a standard operator problem in an augmented fermion Fock space with twice as many sites [125–128]. Specifically, one introduces "tilde" operators $\tilde{d}_\mu/\tilde{d}^\dagger_\mu$ together with the original ones $d_\mu/d^\dagger_\mu$ [129]. Introducing the so-called left vacuum

$$|I\rangle = \sum_S (-i)^{N_S} |S\rangle \otimes |\tilde{S}\rangle , \tag{13}$$

where $|S\rangle$ are many-body states of the original Fock space, $|\tilde{S}\rangle$ the corresponding ones of the tilde space [126], and N_S the number of particles in S. The nonequilibrium density operator can be written as a state vector in this augmented space

$$|\rho(t)\rangle\rangle \equiv \hat{\rho}(t)\,|I\rangle . \tag{14}$$

The Lindblad equation is rewritten in a Schrödinger-type fashion [123,126]

$$\frac{d}{dt}\,|\rho(t)\rangle\rangle = \hat{\mathcal{L}}\,|\rho(t)\rangle\rangle , \tag{15}$$

where now $\hat{\mathcal{L}}$ is an ordinary *operator* in the augmented space. $\hat{\mathcal{L}} = \hat{\mathcal{L}}_0 + \hat{\mathcal{L}}_I$ is conveniently represented in terms of the operators of the augmented space in a vector notation [129]:

$$\boldsymbol{d}^\dagger = \left(d^\dagger_0, \ldots, d^\dagger_{N_B}, \tilde{d}_0, \ldots \tilde{d}_{N_B}\right).$$

Its noninteracting part $\mathcal{L}_0$ reads in the augmented space [123,126] as

$$i\hat{\mathcal{L}}_0 = \sum_\sigma (\boldsymbol{d}^\dagger \boldsymbol{h} \boldsymbol{d} - \mathrm{Tr}(\boldsymbol{E} + i\boldsymbol{\Lambda})), \tag{16}$$

where Tr denotes the matrix trace and the matrix $\boldsymbol{h}$ is given by

$$\boldsymbol{h} = \begin{pmatrix} \boldsymbol{E} + i\boldsymbol{\Omega} & 2\boldsymbol{\Gamma}^{(2)} \\ -2\boldsymbol{\Gamma}^{(1)} & \boldsymbol{E} - i\boldsymbol{\Omega} \end{pmatrix}, \tag{17}$$

with

$$\boldsymbol{\Lambda} = (\boldsymbol{\Gamma}^{(2)} + \boldsymbol{\Gamma}^{(1)}), \quad \boldsymbol{\Omega} = (\boldsymbol{\Gamma}^{(2)} - \boldsymbol{\Gamma}^{(1)}).$$

Its interacting part has the form [126]

$$i\mathcal{L}_I = U d^\dagger_{f\uparrow} d_{f\uparrow} d^\dagger_{f\downarrow} d_{f\downarrow} - U \tilde{d}^\dagger_{f\uparrow} \tilde{d}_{f\uparrow} \tilde{d}^\dagger_{f\downarrow} \tilde{d}_{f\downarrow}.$$

In this auxiliary open system, dynamic two-time correlation functions for two operators $\hat{A}$ and $\hat{B}$ of the system can be expressed as

$$\begin{aligned} iG_{BA}(t_2,t_1) &\equiv \langle \hat{B}_{\mathcal{U}}(t_2)\hat{A}_{\mathcal{U}}(t_1)\rangle \\ &= \mathrm{tr}_{\mathcal{U}}(\hat{B}_{\mathcal{U}}(t_2)\hat{A}_{\mathcal{U}}(t_1)\hat{\rho}_{\mathcal{U}}) = \mathrm{tr}\left(\hat{B}\,\hat{A}_{t_1,t_2-t_1}\right), \end{aligned} \tag{18}$$

where $\hat{\rho}_{\mathcal{U}}$ is the density operator of the "universe" $\mathcal{U}$ composed of the system and Markovian environment, tr is the trace over the system degrees of freedom, tr_E the one over the environment, $\mathrm{tr}_{\mathcal{U}} = \mathrm{tr} \otimes \mathrm{tr}_E$ the one over the universe, $\hat{O}_{\mathcal{U}}(\ldots)$ denotes the unitary time evolution of an operator $\hat{O}$ according to the Hamiltonian of the universe $\hat{\mathcal{H}}_{\mathcal{U}}$. Here [107],

$$\hat{A}_{t_1,t} \equiv \mathrm{tr}_E(e^{-i\hat{\mathcal{H}}_{\mathcal{U}}t}\,\hat{A}\hat{\rho}_{\mathcal{U}}(t_1)e^{+i\hat{\mathcal{H}}_{\mathcal{U}}t}). \tag{19}$$

Notice that the time evolution of $\hat{\rho}_{\mathcal{U}}(t)$, as well as the one in Eq. (19), are *opposite with respect to the Heisenberg time evolution of operators*. This is the convention for density operators. For $t = t_2 - t_1 > 0$ one can use the quantum regression theorem [107] which holds under the same assumptions as for Eq. (9). It states that

$$\frac{d}{dt}\hat{A}_{t_1,t} = \hat{\hat{\mathcal{L}}}\hat{A}_{t_1,t}. \tag{20}$$

In the augmented space, in the same way as for (14) and (15), one can associate the operator (19) with the state vector $|A_{t_1,t}\rangle\rangle = \hat{A}_{t_1,t}\,|I\rangle$. For this vector, (20) translates into

$$\frac{d}{dt}\left|A_{t_1,t}\right\rangle\rangle = \hat{\mathcal{L}}\left|A_{t_1,t}\right\rangle\rangle . \tag{21}$$

Considering its initial value (time $t = 0$)

$$\left|A_{t_1,0}\right\rangle\rangle = \hat{A}\,|\rho(t_1)\rangle\rangle ,$$

the solution of (21) reads as

$$\left|A_{t_1,t}\right\rangle\rangle = e^{\hat{\mathcal{L}}t}\hat{A}\,|\rho(t_1)\rangle\rangle . \tag{22}$$

Therefore, we have for the correlation function (18) for $t_2 > t_1$, which we denote as $G^+_{BA}(t_2,t_1)$:

$$iG^+_{BA}(t_2,t_1) = \langle I|\hat{B}e^{\hat{\mathcal{L}}(t_2-t_1)}\hat{A}|\rho(t_1)\rangle\rangle = \langle I|\hat{B}(t_2-t_1)\hat{A}|\rho(t_1)\rangle\rangle,$$

where

$$\hat{B}(t) := e^{-\hat{\mathcal{L}}t}\hat{B}e^{\hat{\mathcal{L}}t} \tag{23}$$

is the non-Hermitian time evolution of the operator $\hat{B}$, and we have exploited the relation [126] $\langle I|\,\hat{\mathcal{L}} = 0$. For the steady-state correlation function, which depends on $t = t_2 - t_1$, we have

$$iG^+_{BA}(t) = \langle I|\,\hat{B}(t)\hat{A}\,|\rho_\infty\rangle\rangle , \tag{24}$$

where $\hat{\rho}_\infty$ is the steady-state density operator. Since the quantum regression theorem only propagates forward in time, for $t < 0$ one has to take the complex conjugate of Eq. (18), which gives for the $t < 0$ steady-state correlation function denoted as G^-_{BA}

$$iG^-_{BA}(t) = -iG^+_{A^\dagger B^\dagger}(-t)^* = \langle I|\,\hat{A}^\dagger(-t)\hat{B}^\dagger\,|\rho_\infty\rangle^* . \quad (25)$$

Using (24), the steady-state greater Green's function for times $t > 0$ reads as [130]

$$\begin{aligned} G^{>+}_{\mu\nu}(t) &\equiv -i\theta(t)\,\langle d_\mu(t+t_1)d^\dagger_\nu(t_1)\rangle_{t1\to\infty} \\ &= -i\theta(t)\;\langle I|\,d_\mu(t)d^\dagger_\nu\,|\rho_\infty\rangle\,. \end{aligned} \quad (26)$$

We can use (24) also for the lesser Green's function, however, for [130] $t < 0$,

$$\begin{aligned} G^{<+}_{\mu\nu}(t) &\equiv i\theta(-t)\,\langle d^\dagger_\nu(t_1)d_\mu(t+t_1)\rangle_{t1\to\infty} \\ &= i\theta(-t)\;\langle I|\,d^\dagger_\nu(-t)d_\mu\,|\rho_\infty\rangle\,. \end{aligned}$$

For the opposite sign of t, we can use (25), so that for both Green's functions one has [123,130]

$$\boldsymbol{G}^{\gtrless -}(t) = -\boldsymbol{G}^{\gtrless +}(-t)^\dagger. \quad (27)$$

For the Fourier-transformed Green's function, defined, with abuse of notation as

$$\boldsymbol{G}^{\gtrless\pm}(\omega) = \int dt\, e^{i\omega t}\boldsymbol{G}^{\gtrless\pm}(t)\,, \quad (28)$$

relation (27) translates into

$$\boldsymbol{G}^{\gtrless -}(\omega) = -\boldsymbol{G}^{\gtrless +}(\omega)^\dagger. \quad (29)$$

We need the retarded and the Keldysh Green's functions

$$\begin{aligned} \boldsymbol{G}^R &= \boldsymbol{G}^{>+} - \boldsymbol{G}^{<-} = \boldsymbol{G}^{>+} + \boldsymbol{G}^{<+\dagger}, \\ \boldsymbol{G}^K &= \boldsymbol{G}^{>+} + \boldsymbol{G}^{<-} + \boldsymbol{G}^{>-} + \boldsymbol{G}^{<+} = \boldsymbol{G}^{>+} + \boldsymbol{G}^{<+} - \text{H.c.}, \end{aligned} \quad (30)$$

whereby both relations hold for the time-dependent as well as for the Fourier-transformed ones.

1. Noninteracting case

To solve the noninteracting Lindblad problem described by (16), one first diagonalizes the non-Hermitian matrix [126] $\boldsymbol{h}$ in Eq. (17):

$$\boldsymbol{\varepsilon} = \boldsymbol{V}^{-1}\boldsymbol{h}\boldsymbol{V}, \quad (31)$$

where $\boldsymbol{\varepsilon}$ is a diagonal matrix of eigenvalues ε_μ. The noninteracting Lindbladian (16) can then be written as

$$i\hat{\mathcal{L}}_0 = \bar{\boldsymbol{\xi}}\,\boldsymbol{\varepsilon}\,\boldsymbol{\xi} + \eta$$

in terms of the normal modes

$$\boldsymbol{\xi} = \boldsymbol{V}^{-1}\boldsymbol{d}, \quad \bar{\boldsymbol{\xi}} = \boldsymbol{d}^\dagger\boldsymbol{V}, \quad (32)$$

and a constant η. The normal modes still obey canonical anticommutation rules

$$\{\xi_\mu, \bar{\xi}_\nu\} = \delta_{\mu\nu}, \quad (33)$$

but are not mutually Hermitian conjugate.

The steady state $|\rho_\infty\rangle$ obeys the equation

$$\hat{\mathcal{L}}\,|\rho_\infty\rangle = 0.$$

Let us now consider the time evolution (22) of a state initially consisting of the normal mode operators applied to the steady-state density matrix

$$e^{\hat{\mathcal{L}}_0 t}\xi_\mu\,|\rho_\infty\rangle = e^{\hat{\mathcal{L}}_0 t}\xi_\mu e^{-\hat{\mathcal{L}}_0 t}\,|\rho_\infty\rangle = e^{i\varepsilon_\mu t}\xi_\mu\,|\rho_\infty\rangle\,.$$

If $\mathrm{Im}(\varepsilon_\mu) < 0$, this term diverges exponentially in the long-time limit, which would be in contradiction to the fact that $|\rho_\infty\rangle$ is a steady state, unless the state created by ξ_μ is zero. Therefore, we must have

$$\xi_\mu\,|\rho_\infty\rangle = 0 \quad \text{for } \mathrm{Im}(\varepsilon_\mu) < 0. \quad (34a)$$

Similarly, we must have

$$\bar{\xi}_\mu\,|\rho_\infty\rangle = 0 \quad \text{for } \mathrm{Im}(\varepsilon_\mu) > 0. \quad (34b)$$

These equations, thus, define the steady state as a kind of "Fermi sea." In addition, by requiring that expectation values of the form

$$\langle I|\,\xi_\mu(t)\bar{\xi}_\nu\,|\rho\rangle$$

do not diverge for large t, we obtain that

$$\langle I|\,\xi_\mu = 0 \quad \text{for } \mathrm{Im}(\varepsilon_\mu) > 0, \quad (34c)$$

$$\langle I|\,\bar{\xi}_\mu = 0 \quad \text{for } \mathrm{Im}(\varepsilon_\mu) < 0. \quad (34d)$$

From (34d) it follows that an expectation value of the form $\langle I|\,\bar{\xi}_\mu\xi_\nu\,|\rho_\infty\rangle$ vanishes for the case $\mathrm{Im}(\varepsilon_\mu) < 0$. For $\mathrm{Im}(\varepsilon_\mu) > 0$ we make use of the anticommutation rules (33) together with (34b) and the fact that [126] $\langle I|\rho_\infty\rangle = \mathrm{tr}\,\rho_\infty = 1$ and arrive at

$$\langle I|\,\bar{\xi}_\mu\xi_\nu\,|\rho_\infty\rangle = D_{\mu\nu},$$

where the matrix

$$D_{\mu\nu} = \delta_{\mu\nu}\,\theta[\mathrm{Im}(\varepsilon_\mu)].$$

Similarly,

$$\langle I|\,\xi_\mu\bar{\xi}_\nu\,|\rho_\infty\rangle = \bar{D}_{\mu\nu} \equiv \delta_{\mu\nu} - D_{\mu\nu}.$$

The expression for the steady-state correlation functions of the eigenmodes $\boldsymbol{\xi}$ of $\hat{\mathcal{L}}_0$ can be now evaluated by considering that, due to the anticommutation rules, the Heisenberg time evolution (23) gives

$$\xi_\mu(t) = e^{-i\varepsilon_\mu t}\,\xi_\mu, \quad \bar{\xi}_\mu(t) = e^{i\varepsilon_\mu t}\,\bar{\xi}_\mu.$$

Thus,

$$\langle I|\,\xi_\mu(t)\bar{\xi}_\nu\,|\rho_\infty\rangle = e^{-i\varepsilon_\mu t}\,\langle I|\,\xi_\mu\bar{\xi}_\nu\,|\rho_\infty\rangle = e^{-i\varepsilon_\mu t}D_{\mu\nu}.$$

In this way, the greater Green's function for $t > 0$ becomes

$$\begin{aligned} iG^{>+}_{0\mu\nu}(t) &= \langle I|\,d_\mu(t)d^\dagger_\nu\,|\rho_\infty\rangle \\ &= \sum_\varsigma V_{\mu\varsigma}e^{-i\varepsilon_\varsigma t}\bar{D}_{\varsigma\varsigma}(V^{-1})_{\varsigma\nu} \\ &= (\boldsymbol{V}e^{-i\boldsymbol{\varepsilon}t}\bar{\boldsymbol{D}}\boldsymbol{V}^{-1})_{\mu\nu}, \end{aligned} \quad (35)$$

where we have used (32). The Green's functions are defined with operators $d_\mu/d^\dagger_\mu$ in the original Fock space, so that it is sufficient to know the first $N_B + 1$ rows (columns) of $\boldsymbol{V}$ ($\boldsymbol{V}^{-1}$). For this purpose we introduce

$$\boldsymbol{U} = \boldsymbol{T}\boldsymbol{V}, \quad \boldsymbol{U}^{(-1)} = \boldsymbol{V}^{-1}\boldsymbol{T}^\dagger,$$

whereby $\boldsymbol{T}$ is a $(N_B+1)\times(2N_B+2)$ matrix, which in block form reads as $\boldsymbol{T}=(\mathbb{1}\quad \boldsymbol{0})$. Notice that $\boldsymbol{U}^{-1}\neq\boldsymbol{U}^{(-1)}$. With this, the Fourier transform (28) of (35) is given by [131]

$$\boldsymbol{G}_0^{>+}(\omega)=\left(\boldsymbol{U}\frac{\bar{\boldsymbol{D}}}{\omega-\boldsymbol{\varepsilon}}\boldsymbol{U}^{(-1)}\right), \tag{36}$$

and $G^{>-}_{0\mu\nu}(\omega)$ is obtained with the help of (29). Similarly, the lesser Green's function for $t<0$

$$\begin{aligned} iG^{<+}_{0\mu\nu}(t) &= -\langle I|d_\nu^\dagger d_\mu(t)\,|\rho_\infty\rangle \\ &= -\sum_\varsigma V_{\mu\varsigma}e^{-i\varepsilon_\varsigma t}D_{\varsigma\varsigma}(V^{-1})_{\varsigma\nu} \\ &= -(\boldsymbol{U}e^{-i\boldsymbol{\varepsilon}t}\boldsymbol{D}\boldsymbol{U}^{(-1)})_{\mu\nu}, \end{aligned}$$

with the Fourier transform

$$\boldsymbol{G}_0^{<+}(\omega)=\left(\boldsymbol{U}\frac{\boldsymbol{D}}{\omega-\boldsymbol{\varepsilon}}\boldsymbol{U}^{(-1)}\right), \tag{37}$$

and $\boldsymbol{G}_0^{<-}(\omega)$ is obtained from (29). Using (30) together with (36) and (37), we get

$$\boldsymbol{G}_0^R(\omega)=\boldsymbol{U}\frac{\bar{\boldsymbol{D}}}{\omega-\boldsymbol{\varepsilon}}\boldsymbol{U}^{(-1)}+\left(\boldsymbol{U}\frac{\boldsymbol{D}}{\omega-\boldsymbol{\varepsilon}}\boldsymbol{U}^{(-1)}\right)^\dagger, \tag{38}$$

and for the Keldysh Green's function using also (29)

$$\begin{aligned} \boldsymbol{G}_0^K(\omega) &= \boldsymbol{U}\left(\frac{\bar{\boldsymbol{D}}}{\omega-\boldsymbol{\varepsilon}}+\frac{\boldsymbol{D}}{\omega-\boldsymbol{\varepsilon}}\right)\boldsymbol{U}^{(-1)}-\text{H.c.} \\ &= \boldsymbol{U}\left(\frac{1}{\omega-\boldsymbol{\varepsilon}}\right)\boldsymbol{U}^{(-1)}-\text{H.c.} \end{aligned} \tag{39}$$

In principle, one could just carry out the diagonalization (31) and then evaluate (38) and (39) numerically, which is a rather lightweight task. However, it is possible to obtain a (partially) analytical expression for the Green's functions. Indeed, a lengthy but straightforward calculation yields for the retarded one

$$\boldsymbol{G}_0^R(\omega)=(\omega-\boldsymbol{E}+i\boldsymbol{\Lambda})^{-1}. \tag{40}$$

Similarly, for the Keldysh component of the inverse Green's function, we obtain

$$\left(\underline{\boldsymbol{G}_{\boldsymbol{0}}^{-1}}\right)^K\equiv-\boldsymbol{G}_0^{R-1}\boldsymbol{G}_0^K\boldsymbol{G}_0^{A-1}=-2i\boldsymbol{\Omega}. \tag{41}$$

To sum up, (40) and (41) are the main results of this section. To evaluate $\underline{\Delta}_{\text{aux}}(\omega)$, one then uses (6), whereby one should consider that the matrix $\underline{G}_0$ in Keldysh space is just the *local one*, i.e., in terms of the components local at the impurity G^R_{0ff} and G^K_{0ff}:

$$\underline{G}_0\equiv\begin{pmatrix} G^R_{0ff} & G^K_{0ff}\\ 0 & G^A_{0ff}\end{pmatrix}.$$

In turn, G^K_{0ff}, the ff component of $\boldsymbol{G}_0^K$, has to be obtained from (41) by the well-known expression [116] $\boldsymbol{G}_0^K=-\boldsymbol{G}_0^R(\underline{\boldsymbol{G}_{\boldsymbol{0}}^{-1}})^K\boldsymbol{G}_0^A$.

2. *Interacting case*

The next step consists in solving the interacting auxiliary Lindblad problem described by (10a) in order to determine the Green's function and the self-energy at the impurity site. This is done by Lanczos exact diagonalization within the many-body augmented Fock space.

First, the steady state $|\rho_\infty\rangle$ has to be determined as the right-sided eigenstate of the Lindblad operator $\hat{\mathcal{L}}$ with eigenvalue $l_0=0$. For convenience, we introduce

$$\hat{L}=i\hat{\mathcal{L}}, \tag{42}$$

which is a kind of non-Hermitian Hamiltonian with complex eigenvalues ℓ. The dimension of the Hilbert space can be reduced by exploiting symmetries similar to the equilibrium case. The conservation of the particle number per spin $\hat{N}_\sigma$ is replaced here by the conservation of $\hat{N}_\sigma-\hat{\tilde{N}}_\sigma$ [51]. The steady state lies in the sector $N_\sigma-\tilde{N}_\sigma=0$.

Starting from Eq. (26), the steady-state greater Green's function of the impurity reads as in a non-Hermitian Lehmann representation, for $t>0$,

$$G^{>+}_{\mu\nu}(t)=-i\sum_n e^{-i\ell_n^{(+1)}t}\,\langle I|\,d_\mu\,\big|R_n^{(+1)}\big\rangle\big\langle L_n^{(+1)}\big|\,d_\nu^\dagger\,|\rho_\infty\rangle\,,$$

where the identity $\sum_n|R_n^{(+1)}\rangle\langle L_n^{(+1)}|$ in the sector $N_\sigma-\tilde{N}_\sigma=+1$ has been inserted, in terms of right ($|R_n^{(+1)}\rangle$) and left ($\langle L_n^{(+1)}|$) eigenstates of $\hat{L}$ with eigenvalues $\ell_n^{(+1)}$, and $|I\rangle$ is the left vacuum (13). Its Fourier transform reads as

$$\begin{aligned} G^{>}_{\mu\nu}(\omega) &= \sum_n\frac{1}{\omega-\ell_n^{(+1)}}\,\langle I|\,d_\mu\,\big|R_n^{(+1)}\big\rangle\big\langle L_n^{(+1)}\big|\,d_\nu^\dagger\,|\rho_\infty\rangle \\ &\quad-\sum_n\frac{1}{\omega-\ell_n^{(+1)*}}\big(\,\langle I|\,d_\nu\,\big|R_n^{(+1)}\big\rangle\big\langle L_n^{(+1)}\big|\,d_\mu^\dagger\,|\rho_\infty\rangle\,\big)^*. \end{aligned} \tag{43}$$

The analogous expression for the lesser Green's function $G^{<}_{\mu\nu}(\omega)$ is obtained by inserting a complete set of eigenstates in the $N_\sigma-\tilde{N}_\sigma=-1$ sector and exchanging the elementary operators accordingly. $G^K_{\mu\nu}(\omega)$ and $G^R_{\mu\nu}(\omega)$ are obtained using Eq. (30) [see also (29)].

For a small number of bath sites $N_B\leqslant 3$, the dimension of the augmented Fock space is still moderate, and eigenvalues and eigenvectors can be determined by full diagonalization. For $N_B\geqslant 4$, a non-Hermitian Lanczos procedure has to be carried out. Especially extracting the steady state is not an easy task since it lies in the center of the spectrum. Details of our numerical procedure are given in Appendix A.

Once the interacting and noninteracting Green's functions of the auxiliary system at the impurity site $\underline{G}(\omega)$ and $\underline{G}_0(\omega)$, respectively, are determined, the corresponding self-energy is obtained via Dyson's equation in Keldysh space [Eq. (5)]. The individual components are explicitly [51]

$$\begin{aligned} \Sigma^R(\omega) &= 1/G_0^R(\omega)-1/G^R(\omega), \\ \Sigma^K(\omega) &= -G_0^K(\omega)\big/\big|G_0^R(\omega)\big|^2+G^K(\omega)/|G^R(\omega)|^2. \end{aligned}$$

As discussed in Sec. II B, this is used in the Dyson equation (5) for the physical Green's function.

III. RESULTS

In this section, results for the steady-state properties of a symmetric, correlated Anderson impurity coupled to two

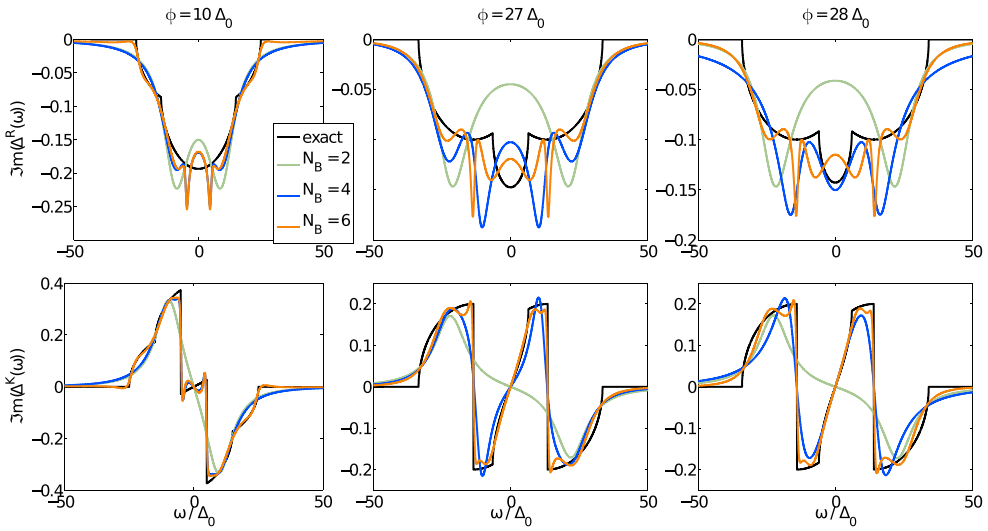

FIG. 2. (Color online) Comparison of $\mathrm{Im}[\Delta^{\alpha}(\omega)]$ from (7) (black) with $\mathrm{Im}[\underline{\Delta}^{\alpha}_{\mathrm{aux}}(\omega)]$ at the absolute minimum of the cost function (12) for auxiliary system sizes $N_B = 2,4$, and 6 bath sites (green, blue, and orange, respectively), and $\alpha = R$ (top) and K (bottom). Results are shown for tight-binding leads (2) and (8) with $t = 10\,\Delta_0$, and three different bias voltages $\phi \in \{10,27,28\}\,\Delta_0$ from left to right.

metallic leads under bias voltage are provided. We assess the validity of the proposed method by discussing the fit of the hybridization function and outline how uncertainties are estimated. Results for the current voltage characteristics and the nonequilibrium spectral function are presented and compared with data from time-evolving block decimation (TEBD) [77] and SNRG [54] calculations, respectively. The effect of a linear correction of the calculated Green's functions is illustrated.

A. Hybridization functions

The optimal representation of the exact bath $\underline{\Delta}(\omega)$ by the auxiliary one $\underline{\Delta}_{\mathrm{aux}}(\omega)$ is obtained by minimizing the cost function (12). In practice, this is done by employing a quasi-Newton line search [132,133]. In particular, we chose an equal weighting of the retarded and the Keldysh component $W^R(\omega) = W^K(\omega) = \Theta(\omega_c - |\omega|)$. After finding our results to be robust upon different values for the cutoff ω_c, as well as upon using different norms ($n = 1,2$) in Eq. (12), we finally choose $\omega_c = 50\,\Delta_0$ and consider imaginary parts $\{\mathrm{Im}[\Delta^{\alpha}(\omega) - \Delta^{\alpha}_{\mathrm{aux}}(\omega)]\}^2$ in the cost function only. This is justified since $\Delta^K_{\mathrm{aux}}(\omega)$ is purely imaginary and the real part of $\Delta^R_{\mathrm{aux}}(\omega)$ is connected to its imaginary part via the Kramers-Kronig relations [134]. The asymptotic behavior of $\Delta^R_{\mathrm{aux}}(\omega)$ is determined by Λ_{ff} whereas the one of $\Delta^K_{\mathrm{aux}}(\omega)$ by Ω_{ff}. Therefore, the correct asymptotic limit $\lim_{\omega\to\pm\infty}\underline{\Delta}_{\mathrm{aux}}(\omega) = \underline{0}$ is guaranteed by taking $\Gamma^{(1)}_{ff} = \Gamma^{(2)}_{ff} = 0$, which results in $\Gamma^{(\kappa)}_{\mu f} = \Gamma^{(\kappa)}_{f\mu} = 0$ due to the requirement of semipositive definiteness of $\Gamma^{(\kappa)}_{\mu\nu}$. Particle-hole symmetry allows for a further reduction of the auxiliary system parameters [135].

In this work, we use an even number of auxiliary bath sites $N_B = 2,4$, and 6 in a linear setup [see Fig. 1(b)] with an equal number to the left and to the right of the impurity (only Fig. 6 displays one calculation for an odd number of bath sites). In Fig. 2, the obtained auxiliary hybridization functions are compared with the exact ones for various bias voltages. We find a quick convergence as a function of N_B, which degrades for large bias voltage ϕ. The Fermi steps at the chemical potentials in $\Delta^K_{\mathrm{aux}}(\omega)$ can not be properly resolved in the case of $N_B = 2$. Especially in the case of $\phi = 10\,\Delta_0$ the auxiliary hybridization functions for $N_B = 6$ as well as for $N_B = 4$ agree fairly well with the exact one and capture all essential features, in particular the Fermi steps. The auxiliary bath develops spurious oscillations in $\Delta^R_{\mathrm{aux}}(\omega)$ at the energies of the Fermi levels of the contacts. Here, the discrepancy with $\Delta^R(\omega)$ is considerable in magnitude, but extends over small ω intervals, thus inducing only small errors in the self-energies.

When following the absolute minimum of the cost function (12) as a function of some external parameter, such as, e.g., the bias voltage ϕ, spurious discontinuities appear due to the fact that local minima cross each other. This occurs for large bias voltages and large U, and/or small N_B, for which the approach is more challenging. An example for such a situation is shown in Fig. 2 for the case $N_B = 4$, when comparing the hybridization functions just before and after such a crossing, i.e., for $\phi = 27\,\Delta_0$ and $28\,\Delta_0$. Even though the changes in the exact hybridization function are only minor, $\underline{\Delta}_{\mathrm{aux}}(\omega)$ displays a considerable difference. The influence of this spurious effect on observable quantities is shown in Fig. 3 (right panel, orange circles) for a different parameter set of $N_B = 6$ at around $\phi_c = 33\,\Delta_0$. The artificial discontinuity in the current is caused by the shift of spectral weight in $\underline{\Delta}_{\mathrm{aux}}(\omega)$.

To deal with these discontinuities, we adopt a scheme which is suitable for obtaining a continuous dependence of observables on external parameters and, in addition, allows us to estimate their uncertainties (see Fig. 3). We first identify a set of local minima of the cost function (12), obtained by a series of minimum searches starting with random initial values. These local minima are then used to calculate an average and variance of physical quantities, such as the current. We consider the distribution of local minima with a Boltzmann weight associated with an artificial "temperature," whereby the value of the cost function (12) is the associated

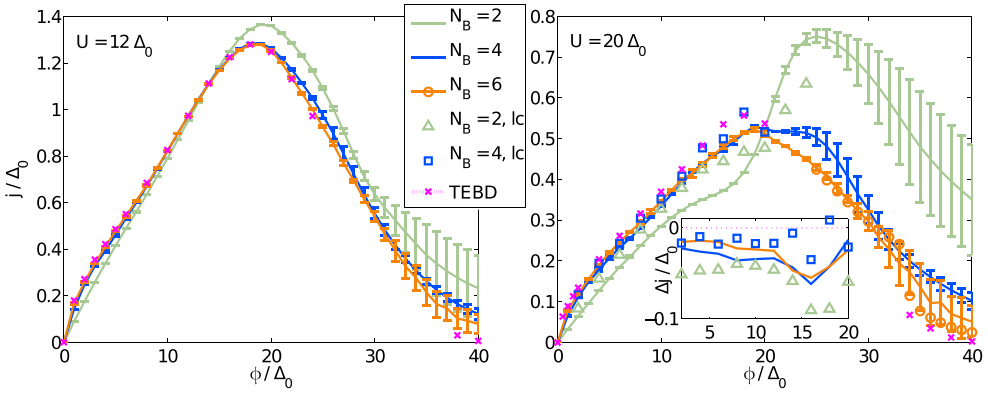

FIG. 3. (Color online) Current j vs voltage ϕ for the model (1) with tight-binding leads and onsite interaction $U = 12\,\Delta_0$ (left) and $U = 20\,\Delta_0$ (right). Results for three different auxiliary systems with $N_B \in \{2,4,6\}$ are displayed and compared with reference data from TEBD (magenta dotted and $\times$) [77]. We plot the averaged mean values connected by lines together with error bars determined according to Sec. III A and Appendix B. The additional data marks for $U = 20\,\Delta_0$ are as follows: The circles for $N_B = 6$ display $j(\phi)$ when considering the absolute minimum in the fit (12). $N_B = 2$,lc and $N_B = 4$,lc present the results of a linear correction of the current values of the absolute minima as described in Appendix C. The inset displays the difference Δj of the calculated currents to the TEBD results.

"energy." This artificial temperature for the Boltzmann weight is chosen in such a way that the averaged spectral weight of the hybridization function as a function of ϕ is as smooth as possible. Details are outlined in Appendix B. A possible pitfall, however, is that physical discontinuities, i.e., real phase transitions could be overlooked. It is thus compulsory to additionally investigate the results for the absolute minima and for different bath setups carefully. This approach has a certain degree of arbitrariness. However, we point out that it only affects regions with large error bars in Fig. 3, i.e., large ϕ and large U for which also other techniques are less accurate.

B. Current-voltage characteristics

After evaluating the interacting impurity Green's function of the physical system according to (5) with the self-energy evaluated in Sec. II D, we are able to determine the steady-state current. This is done with the help of the Meir-Wingreen expression [116,136,137] in its symmetrized form, where we have already summed over spin

$$j = i\int_{-\infty}^{\infty}\frac{d\omega}{2\pi}([\gamma_L(\omega)-\gamma_R(\omega)]G^{<}(\omega) + [p_{\mathrm{F},L}(\omega)\gamma_L(\omega)-p_{\mathrm{F},R}(\omega)\gamma_R(\omega)][G^R(\omega)-G^A(\omega)]), \tag{45}$$

$\gamma_\lambda(\omega) = -2|t'_\lambda|^2\mathrm{Im}[g^R_\lambda(\omega)]$ are the "lead self-energies" and $p_{\mathrm{F},\lambda}(\omega) = p_{\mathrm{F}}(\omega-\mu_\lambda)$ denotes the Fermi distribution of lead λ with chemical potential μ_λ.

To quantify the accuracy of the method, we compare the results for the current-voltage characteristics with quasiexact reference data from TEBD [77]. We find very good agreement for interaction strength $U < 12\,\Delta_0$. Since in this paper we want to benchmark the approach in "difficult" parameter regimes, in the following, we will discuss $U \gtrsim 12\Delta_0$ only. In Fig. 3 we display data for $U = 12\,\Delta_0$ and $20\,\Delta_0$. The data points and error bars shown are obtained by using the averaging scheme as described in Appendix B. For the universal physics at small and medium bias voltages $\phi \lesssim 20\,\Delta_0$, the current as a function of the auxiliary system size ($N_B \in \{2,4,6\}$) converges rapidly to the expected result. The convergence is even monotonic in a broad region of the parameter space. The zero-bias response is linear for all N_B and approaches the results expected from the Friedel sum rule [29] $j(\phi = 0^+) = 2\frac{e^2}{h}\phi$ quickly for increasing N_B. For $U = 12\,\Delta_0$ already the $N_B \gtrsim 4$ results yield a good reproduction of the current in this bias regime. For $U = 20\,\Delta_0$ and $\phi \gtrsim 20\,\Delta_0$, a larger difference between the $N_B = 4$ and 6 results is observed. Notice that also other available methods do not yield a satisfactory result in this parameter regime. In the lead-dependent high-bias regime, the fit becomes more challenging and large variances appear in the calculated quantities. This indicates the presence of many competing local minima with similar values for the cost function whose value tends to increase with increasing ϕ. For $\phi \geqslant 40\,\Delta_0$, the densities of states of the left and the right contacts do not overlap anymore and the current has to vanish. This limit can not be exactly reproduced by the proposed approach due to spurious long-range Lorentzian tails present in the auxiliary Markovian environment. Nevertheless, $j(\phi = 40\,\Delta_0)$ approaches zero as one increases the number of bath sites. This holds true for quantities obtained at the absolute minimum of the cost function as well as for averaged ones.

To extrapolate our results to larger N_B, a scheme for linear corrections is discussed in Appendix C. Data for $N_B = 2$,lc and 4,lc, whereby "lc" denotes "linear correction," is shown in Fig. 3. For large $U = 20\,\Delta_0$ and small- to medium-bias voltages $\phi \lesssim 20\,\Delta_0$, a solid improvement towards the TEBD reference values is observed (see inset Fig. 3). Correction ratios r (see Appendix C) close to one indicate a good applicability of the linear correction scheme. We find on average $r \approx 0.75$ for $\phi \lesssim 20\,\Delta_0$ ($N_B = 2$,lc and 4,lc). In the high-bias regime, however, the linear correction can not be applied with large magnitude and r drops below 0.5 for $N_B = 2$,lc. Nevertheless, the calculation of the effective, auxiliary hybridization function $\underline{\Delta}_{\mathrm{aux},r}(\omega)$ as described in Appendix C successfully avoids an "overcorrection" of the current values and automatically allows one to estimate the reliability of the results.

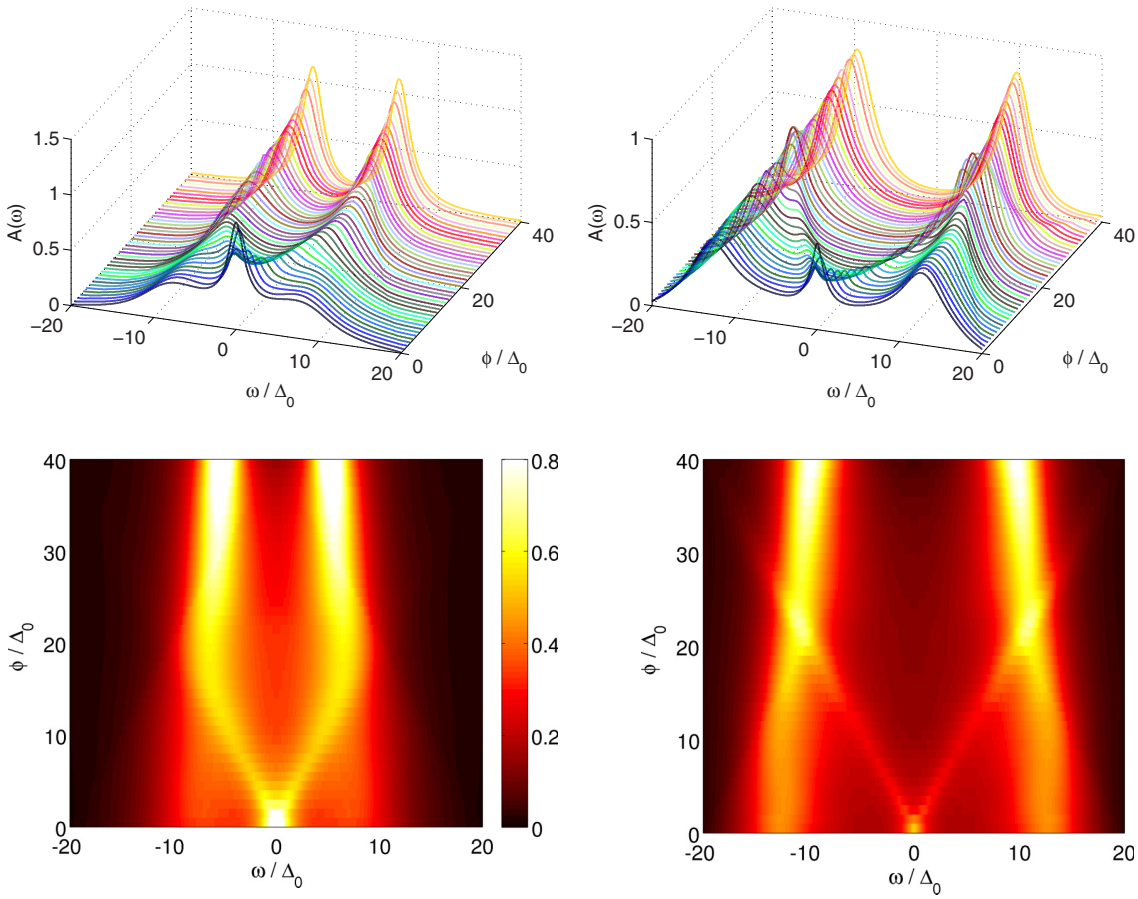

FIG. 4. (Color online) Single-particle spectral function at the impurity evaluated for $N_B = 6$, different bias voltages ϕ, and $U = 12\,\Delta_0$ (left) and $U = 20\,\Delta_0$ (right). Data are obtained according to Sec. III A and Appendix B. Other parameters are as in Fig. 3.

Judging from the larger uncertainty from the averaging procedure and the strong effects of the linear corrections, we conclude that the high-bias regime is more sensitive to the details of the fitted, auxiliary hybridization function. The universal low- and medium-bias regimes are, however, very well reproduced even with a small number of auxiliary bath sites.

C. Nonequilibrium spectral function

The bias-dependent single-particle spectral function is evaluated from the physical steady-state Green's function of the impurity $A(\omega) = -\frac{1}{\pi}\mathrm{Im}[G^R(\omega)]$. Results obtained using $N_B = 6$ for $U = 12\,\Delta_0$ and $20\,\Delta_0$ are presented for the whole bias range of interest in Fig. 4. Data for $N_B = 4$ are similar, but here the Kondo physics can not be reproduced as accurately as in the case of $N_B = 6$. Our approach does preserve the local charge density $\langle n_f \rangle = \sum_\sigma \frac{1}{2} + \frac{1}{2}\int_{-\infty}^{\infty} \frac{d\omega}{2\pi}\mathrm{Im}[G^K(\omega)] = 1$ and magnetization $\langle m_f \rangle = 0$ as well as the spectral sum rule [138].

The presented method reproduces qualitatively correctly also the equilibrium physics at $\phi = 0$ since $A(\omega)$ displays a Kondo resonance at $\omega = 0$ and two Hubbard satellites at the approximate positions $\omega \approx \pm U/2$. This renders the application to equilibrium DMFT problems an interesting perspective. The width and magnitude of the Kondo resonance are discussed in comparison with (S)NRG data in Sec. III C 1.

Upon increasing the bias voltage, the Kondo resonance splits up and two excitations are observed at the energies of the Fermi levels of the leads [78,139,140]. For $U = 12\,\Delta_0$, the splitted resonances merge into the Hubbard bands at approximately $\phi \approx 15\,\Delta_0$ and can not be clearly identified thereafter. In contrast, in the case of $U = 20\,\Delta_0$, the resonances overlap with the Hubbard satellites and can still be observed in the spectrum $A(\omega)$ at higher voltages. Calculations with increasing U in the high-bias regime $\phi \approx 40\,\Delta_0$ have shown the consistency of this effect and that a minimum value of $U \approx 15\,\Delta_0$ is needed in order for the resonances at the Fermi energies to be perceptible after having crossed the Hubbard bands.

1. Comparison with scattering states numerical renormalization group

We compare the computed spectral functions with results obtained by means of SNRG [53]. For this purpose, we use a flat DOS [Eq. (3)] for the leads, as in Ref. [53]. Focusing on the low-bias regime and $N_B = 6$, the obtained spectral functions are depicted in Fig. 5. Compared with SNRG, our results do not achieve the same accuracy in the low-energy domain, i.e., in the vicinity of $\omega \approx 0$. However, our data provide a better resolution at higher energies. When inspecting the Kondo peak in the equilibrium case $\phi = 0$, our results do not fully fulfill the Friedel sum rule [29,141,142]. Depending on parameters,

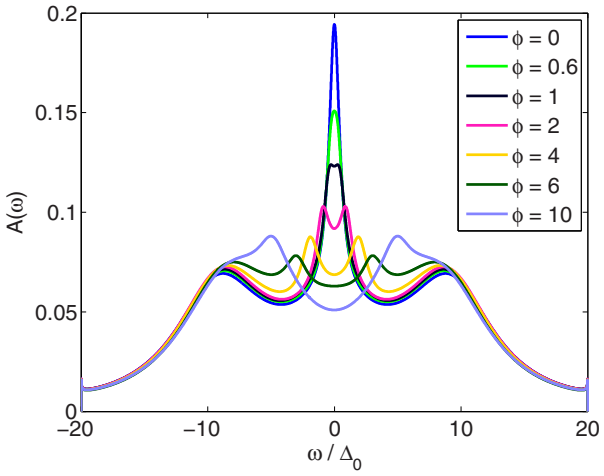

FIG. 5. (Color online) Single-particle spectral function for a constant DOS of the leads (3), with $D_{\mathrm{WB}} = 20\,\Delta_0$ and $U = 16\,\Delta_0$ and different bias voltages ϕ (in units of Δ_0). Results are obtained for $N_B = 6$ and at the absolute minimum of Eq. (12). For a comparison with SNRG [53] [Fig. 2(a) therein], note that their $\Gamma = 2\,\Delta_0$.

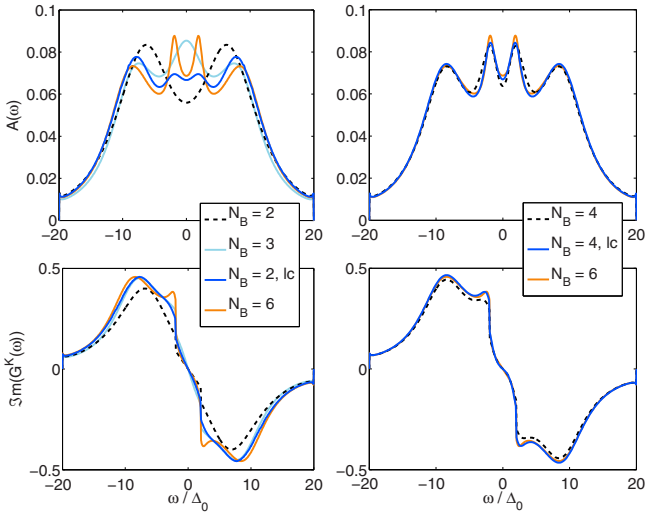

FIG. 6. (Color online) Effects of the linear corrections of the Green's functions according to Apendix C (solid blue lines). The dashed lines indicate the uncorrected $\underline{G}(\omega)$ with the same N_B, while solid orange and light blue lines display results for larger N_B for comparison. Results are shown for a constant lead DOS [Eq. (3)] with $D_{\mathrm{WB}} = 20\,\Delta_0$, $U = 16\,\Delta_0$, and $\phi = 4\,\Delta_0$.

the height of the Kondo resonance is underestimated. This is due to the fact that the imaginary part of the self-energy at $\omega = 0$ has a small finite value which is due to the Lorentzian tails of the Markovian environment.

The resolution does not suffice to tell whether a two- or a three-peak structure is present for very low-bias voltages $\phi \lesssim 2\,\Delta_0$. Nevertheless, one can say that the higher-bias regime $\phi > 4\,\Delta_0$ is resolved more accurately and one is able to clearly distinguish the excitations at the Fermi energies of the contacts from the Hubbard satellites. The observed linear splitting is consistent with experiments on nanodevices [139,140]. Within second-order Keldysh PT [58] and QMC results [143], the resonance does not split but is suppressed only. In fourth order and in NCA it splits into two, which are located near the chemical potentials of the two leads [58]. Other methods yield a splitting with features slightly different in details: real-time diagrammatics [144], VCA [78], imaginary potential QMC [90], or scaling methods [145]. Overall, a good qualitative agreement with the SNRG results is achieved which underlines the reliability of the calculated spectral functions.

2. *Linear correction of Green's functions*

Here, we consider the effect of a linear correction of the Green's functions, as outlined in Appendix C. In the left panels (right panels) of Fig. 6, we show data for $N_B = 2$ ($N_B = 4$) including linear corrections ($r = 1$) for a high interaction strength in the low-bias regime. We benchmark to data obtained using $N_B = 6$ without corrections.

For $N_B = 2$ without linear corrections, the spectral function of the auxiliary system does not feature excitations at the Fermi energies of the contacts ($\omega = \pm 2\,\Delta_0$), which are present in the $N_B = 6$ data. Also, the spectra appear washed out. The linearly corrected result, however, features not only the two resonances at the appropriate energies, but also the shoulders present in the reference data. Again, in the Keldysh Green's function a large correction towards the more accurate $N_B = 6$ results is observed. To highlight the fact that the improvement of the linear correction is not only due to the inclusion of one additional bath site, also a calculation for an auxiliary system with $N_B = 3$ is shown. Evidently, the $N_B = 3$ spectral function exhibits a large weight at low frequencies, but the resolution is rather low and only a single, smeared out peak at $\omega = 0\,\Delta_0$ is observed. It clearly does not account for the splitting of the Kondo resonance.

For $N_B = 4$, a similar enhancement is found. Clearly, the size of the corrections is much smaller. Especially in the Keldysh component, the Green's function for $N_B = 6$ and for the corrected $N_B = 4$ system nearly coincide. In general, the difference between the $N_B = 6$ and the $N_B = 4$ calculations (raw and corrected) is quite small, so that the presented spectral functions in Fig. 5 for larger values of $\phi \lesssim 12\,\Delta_0$ can be assumed to be quite accurate.

Overall, the linear correction enables a vast improvement in the universal low- and medium-bias regimes for all U, which becomes especially important for large U. For large-bias voltages, when lead band effects become prominent, the linear correction is more challenging (see also Sec. III B).

IV. CONCLUSIONS

We have presented a numerical approach to study correlated quantum impurity problems out of equilibrium [51]. The auxiliary master equation approach presented here is based on a mapping of the original Hamiltonian to an auxiliary open quantum system consisting of the interacting impurity coupled to bath sites as well as to a Markovian environment. The dynamics of the auxiliary open system is controlled by a Lindblad master equation. Its parameters are determined by a fit to the impurity-environment hybridization function.

This has many similarities to the procedure used for the exact-diagonalization dynamical mean field theory impurity solver, but has the advantage that one can work directly with real frequencies, which is mandatory for nonequilibrium systems.

We have illustrated how the accuracy of the results can be estimated, and systematically improved by increasing the number of auxiliary bath sites. A scheme to introduce linear corrections has been devised. We presented in detail how the nonequilibrium Green's functions of the correlated open quantum system are obtained by making use of non-Hermitian Lanczos diagonalization in a superoperator space. These techniques make the whole method fast and efficient as well as particularly suited as an impurity solver for steady-state dynamical mean field theory [51].

In this work, we have applied the approach to the single-impurity Anderson model, which is one of the paradigmatic quantum impurity models. We have analyzed in detail the systematic improvement of the current-voltage characteristics as a function of the number of auxiliary bath sites. Already for four auxiliary bath sites, results show a rather good agreement with quasiexact data from time-evolving block decimation [77] in the low- and medium-bias regimes. In the high-bias regime, the current deviates from the expected result with increasing interaction strength. However, we have shown how to estimate the reliability of the data from the deviation of the hybridization functions and how results can be corrected to linear order in this deviation. The impurity spectral function obtained in our calculation features a linear splitting of the Kondo resonance as a function of bias voltage. Good agreement with data from scattering-state numerical renormalization group [53] was found.

Applications of the presented method to multiorbital correlated impurities or correlated clusters is in principle straightforward, although numerically more demanding. Such systems are themselves of interest as models for transport through molecular or nanoscopic objects and as solvers for nonequilibrium cluster dynamical mean field theory. In this case, a larger number of auxiliary sites might be necessary to obtain a good representation of the various hybridization functions. For this situation, one should use numerically more efficient methods to solve for larger correlated open quantum systems, such as matrix product states and density matrix renormalization group, possibly combined with stochastic wave-function approaches [146–148], sparse polynomial space [149,150], or configuration interaction approaches [151]. A more accurate determination of low energy, and possibly critical properties, might be achieved by a combination with renormalization group iteration schemes, similar to the numerical renormalization group. Work along these lines is in progress.

Although we have presented results for the steady state, where the method is most efficient, also extensions to time-dependent phenomena provide an interesting and feasible perspective. While other approaches, such as time-dependent density matrix renormalization group [73] or quantum Monte Carlo [49] are certainly more accurate at short times, the present approach could be used to estimate directly slowly decaying modes by inspecting the behavior of the low-lying spectrum of the Lindblad operator.

ACKNOWLEDGMENTS

We acknowledge discussions with A. Rosch, W. Hofstetter, S. Diehl, M. Knap, D. Rost, and F. Schwarz. A.D. and M.N. thank the Forschungszentrum Jülich, in particular the autumn school on correlated electrons, for hospitality and support. This work was supported by the Austrian Science Fund (FWF), Grants No. P24081-N16 and No. P26508-N20, as well as SfB-ViCoM Project No. F04103.

APPENDIX A: NUMERICAL CALCULATION OF THE AUXILIARY INTERACTING GREEN'S FUNCTION

In this section, we present details of the numerical evaluation of the auxiliary Green's function, as described in Sec. II D 2. We focus on large Hilbert spaces for which a sparse-matrix approach is mandatory. To determine the steady state, which is the right-sided eigenstate of $\hat{L}$ with eigenvalue zero, one can make use of a shift-and-invert Arnoldi procedure [152–155]. The spectrum of $\hat{L}$ [Eq. (42)] has the property that $\mathrm{Im}(\ell_n) < 0$ for all eigenvalues ℓ_n (except the steady state $\ell_0 = 0$). Therefore, given a small shift $s > 0$, the eigenvector of $(\hat{L} - is\hat{\mathbb{1}})^{-1}$ with the largest eigenvalue is the steady state. Since $\hat{L}$ is non-Hermitian, the three-term recurrence of the ordinary Lanczos scheme [120] does not apply, and one has to resort to an Arnoldi scheme instead. To construct the corresponding Krylov space, a system of equations $(\hat{L} - is\hat{\mathbb{1}})\,|\tilde{\phi}_{n+1}\rangle = |\phi_n\rangle$ has to be solved in each step. For the problem at hand, we found that this can be done most efficiently by combining a stabilized biconjugate gradient method with an incomplete LU decomposition as preconditioner [156,157]. Despite using sparse-matrix methods, the memory requirements of this approach are rather high compared to the schemes presented below.

A second possible route to determine the steady state $|\rho_\infty\rangle$ is to perform an explicit time evolution. For unitary time evolutions, a well-established method relies on the Lanczos scheme to construct an approximate time evolution operator [158]. Such an approach can be adapted to the nonunitary case by using a two-sided Lanczos scheme (see below), or also by employing an Arnoldi procedure [155]. Since $\hat{L}$ is non-Hermitian, one can equally well use a simpler backward or forward Euler scheme [133] to discretize the nonunitary time evolution operator. These approaches may not yield a highly accurate time evolution of $|\rho(t)\rangle$, but can nevertheless determine the steady state within a moderate number of steps. As for the shift-and-invert approach above, to solve the implicit update of $|\rho(t_{n+1})\rangle$ at time step t_n in the case of the backward Euler, a biconjugate gradient routine has proven to be effective. For the forward time integration, a Runge-Kutta method of second order is sufficient, with the great advantage that only matrix-vector multiplications are needed, which reduces memory requirements. In practice, for the considered cases it was found that for not too large systems ($N_B < 6$), the shift-and-invert Arnoldi procedure is best suited, whereas a forward time integration is advantageous for the case $N_B = 6$.

Once the steady state is determined, Green's functions can be effectively calculated by employing a two-sided Lanczos scheme [152,159–163]. We therefore express the right- and

left-sided eigenvectors of $\hat{L}$ in Eq. (43) in a Krylov space basis

$$|R_n\rangle = \sum_k U_{kn} \left|\phi_R^k\right\rangle, \quad \langle L_n| = \sum_k (U^{-1})_{nk} \left\langle\phi_L^k\right|.$$

Here, we have omitted the $N_\sigma - \tilde{N}_\sigma$ symmetry sector index for the sake of clarity. The biorthogonal Lanczos vectors

$$\left\langle\phi_L^k\middle|\phi_R^{k'}\right\rangle = \delta_{kk'}$$

are determined by the three-term recurrence

$$\left|\phi_R^{n+1}\right\rangle = \frac{1}{c_{n+1}}\left(\hat{L}\left|\phi_R^n\right\rangle - e_n\left|\phi_R^n\right\rangle - k_n\left|\phi_R^{n-1}\right\rangle\right),$$

$$\left\langle\phi_L^{n+1}\right| = \frac{1}{c_{n+1}^*}\left(\left\langle\phi_L^n\right|\hat{L} - e_n\left\langle\phi_L^n\right| - k_n^*\left\langle\phi_L^{n-1}\right|\right),$$

with

$$e_n = \left\langle\phi_L^n\right|\hat{L}\left|\phi_R^n\right\rangle,$$

$$k_n = \left\langle\phi_L^{n-1}\right|\hat{L}\left|\phi_R^n\right\rangle = \left(\left\langle\phi_L^n\right|\hat{L}\left|\phi_R^{n-1}\right\rangle\right)^*,$$

and a normalization constant c_n such that $\langle\phi_L^n|\phi_R^n\rangle = 1$. One has a certain degree of freedom in the choice of c_n and k_n due to the relation $k_n^* = c_n$, which is fulfilled, for example, by $k_n = k_n^* = c_n$.

In the Krylov basis, $\hat{L}$ takes on a tridiagonal form $T_{nm} = \langle\phi_L^n|\hat{L}|\phi_R^m\rangle$ with the matrix elements $T_{nn} = e_n$, $T_{n-1n} = k_n$, and $T_{nn-1} = k_n^*$. When $n+1$ becomes as large as the degree of the minimal polynomial of $\hat{L}$, the eigenvalues and eigenvectors of T represent those of $\hat{L}$ [152,160]. If one truncates the Krylov basis, this statement holds still approximately true, especially for the largest eigenvalues in magnitude. Analogous to the Hermitian case [164], an exponential convergence of the eigenspectrum of T towards the one of $\hat{L}$ is observed, which is of particular importance for the calculation of Green's functions. A peculiarity of the two-sided Lanczos scheme is that not every Krylov subspace guarantees that $\mathrm{Im}(\ell_n) < 0$ for all eigenvalues ℓ_n of T. In order to obtain the appropriate pole structure for the estimated Green's functions, one has to check $\mathrm{Im}(\ell_n) < 0$ together with convergence criteria. In cases in which $\mathrm{Im}(\ell_n) < 0$ can not be fulfilled exactly, it has to be ensured at least that the corresponding weights of these eigenvalues are negligible.

For the calculation of the Green's functions needed here it is convenient to choose appropriate initial vectors, which are in the case of the greater Green's function (43)

$$\left|\phi_R^0\right\rangle = \frac{1}{c_0}(d_f^\dagger|\rho_\infty\rangle), \quad \left\langle\phi_L^0\right| = \frac{1}{c_0^*}(\langle I|\, d_f).$$

When denoting by ℓ_n and $U_{k,n}$ the eigenvalues and right-sided eigenvectors of T, respectively, Eq. (43) can be cast into the form

$$\begin{aligned} G^>(\omega) &= \sum_{n,k,k'} \frac{U_{kn}U_{nk'}^{-1}}{\omega - \ell_n}\langle I|\, d_f\left|\phi_R^k\right\rangle\left\langle\phi_L^{k'}\right| d_f^\dagger|\rho_\infty\rangle \\ &\quad - \sum_{n,k,k'} \frac{\left(U_{kn}U_{nk'}^{-1}\right)^*}{\omega - \ell_n^*}\left(\langle I|d_f\left|\phi_R^k\right\rangle\left\langle\phi_L^{k'}\right| d_f^\dagger|\rho_\infty\rangle\right)^* \\ &= |c_0|^2\sum_n \frac{U_{0n}U_{n0}^{-1}}{\omega - \ell_n} - |c_0|^2\sum_n \frac{\left(U_{0n}U_{n0}^{-1}\right)^*}{\omega - \ell_n^*}. \end{aligned}$$

APPENDIX B: AVERAGING SCHEME FOR MULTIPLE LOCAL MINIMA

This section contains details on the approach we used to determine the artificial "temperature" for the Boltzmann weights as described in Sec. III A. We consider the situation that a set of local minima for which Eq. (12) becomes stationary is known. Let us specify by $\mathbf{a}_y(\phi)$ the vector of parameters $\{E_{\mu\nu}, \Gamma_{\mu\nu}^{(\kappa)}\}_y$ corresponding to one certain local minimum for a set of model parameters, labeled by y. In order to quantify the spectral weight distribution of the corresponding hybridization function $\underline{\Delta}_{\mathrm{aux}}[\omega; \mathbf{a}_y(\phi)]$, we define

$$m_2^R[\mathbf{a}_y(\phi)] = \int_{-\omega_c}^{\omega_c} \mathrm{Im}\left\{\Delta_{\mathrm{aux}}^R[\omega; \mathbf{a}_y(\phi)]\right\}\omega^2 d\omega,$$

$$m_3^K[\mathbf{a}_y(\phi)] = \int_{-\omega_c}^{\omega_c} \mathrm{Im}\left\{\Delta_{\mathrm{aux}}^K[\omega; \mathbf{a}_y(\phi)]\right\}\omega^3 d\omega,$$

which are similar to the second and third moments of Δ_{aux}^R and Δ_{aux}^K, respectively. For the Keldysh component, a definition analogous to the first moment would yield the desired information as well but the choice above has been found to be more sensitive to details of Δ_{aux}^K. The value of the corresponding cost function $\chi[\mathbf{a}_y(\phi)]$ of the yth minimum is used as an artificial "energy" and enables one to define weights when making use of Boltzmann's statistic

$$P_y(\phi, \beta) = \frac{1}{Z}e^{-\beta\chi[\mathbf{a}_y(\phi)]},$$

where we introduced an artificial "temperature" β^{-1}. For each bias voltage separately, we are then able to calculate averaged quantities

$$\overline{m_2^R}(\phi, \beta) = \sum_y P_y(\phi, \beta) m_2^R[\mathbf{a}_y(\phi)],$$

as well as $\overline{m_3^K}(\phi, \beta)$ and $\overline{\chi}(\phi, \beta)$ in an analogous manner. The quantities $\overline{m_2^R}(\phi, \beta)$ and $\overline{m_3^K}(\phi, \beta)$ provide an estimate of the center of the spectral weight for the averaged set of hybridization functions for each bias voltage ϕ.

Our goal is that these quantities vary in a smooth way when changing the bias voltage. To achieve this, we employ a minimum curvature scheme [133], meaning that we optimize the function

$$\begin{aligned} v_c(\beta) = \int_0^{\phi_{\max}} \Bigg\{ & w^R\left|\frac{\partial^2}{\partial\phi^2}\overline{m_2^R}(\phi, \beta)\right|^2 + w^K\left|\frac{\partial^2}{\partial\phi^2}\overline{m_3^K}(\phi, \beta)\right|^2 \\ & + w^\chi\left|\frac{\partial^2}{\partial\phi^2}\overline{\chi}(\phi, \beta)\right|^2\Bigg\} d\phi, \end{aligned}$$

with respect to β. This determines the optimal artificial temperature, which ensures that the averaged cost function as well as the averaged spectral weight are as smooth functions of ϕ as possible, given the set of calculated minima $\{\mathbf{a}_y(\phi)\}$. As in many optimization problems, an arbitrariness exists in the definition of the quantities $\overline{m_2^R}(\phi, \beta)$ and $\overline{m_3^K}(\phi, \beta)$, as well as in choosing the values of the weights w^R, w^K, and w^χ. In our case, all of the weights were chosen to be equal to one in units of t.

An improvement of the results, to a certain degree at least, could be expected when making use of extensions like a

bias dependent $\beta(\phi)$. This has not been considered in this work since already a single variable β provided quite smooth observables. As mentioned in the main text, in any case, it is obligatory to examine besides the averaged results also the ones for the absolute minima and/or for different averaging schemes, in order to avoid that physical discontinuities are averaged out. We stress that this approach has to be taken with due care since it is in some aspects arbitrary. However, it is useful to give an estimate of the error of the calculation, and can certainly identify regions in parameter space where the error is negligibly small.

APPENDIX C: LINEAR CORRECTIONS

In this section, we present a scheme to correct physical quantities up to linear order in the difference [165]

$$\underline{D}(\omega) = \underline{\Delta}_{ex}(\omega) - \underline{\Delta}_{\text{aux}}(\omega)$$

between the auxiliary and the exact hybridization functions. Although $\underline{D}(\omega)$ decreases rapidly with increasing number of auxiliary bath sites N_B, the size of the Hilbert space also increases exponentially with N_B. This poses a clear limit to the maximum value of N_B.

The idea is based on the fact that each physical quantity $O[\underline{\Delta}]$ is a functional of $\underline{\Delta}(\omega)$. Its exact value is, thus, obtained as $O[\underline{\Delta}_{ex}]$. For a finite N_B there will always be a nonzero value of $\underline{D}(\omega)$ at some energies, so we will always obtain an approximate value $O[\underline{\Delta}_{\text{aux}}]$. A linear correction can be obtained by evaluating numerically the functional derivative of $O[\underline{\Delta}]$. Strictly speaking, considering that only $\text{Im}[\Delta^R(\omega)]$ and $\text{Im}[\Delta^K(\omega)]$ are independent functions, O is a functional $O[\text{Im}(\Delta^R),\text{Im}(\Delta^K)]$. Suppose one knows the functional derivatives

$$\frac{\delta O[\underline{\Delta}]}{\delta\,\text{Im}[\Delta^\alpha(\omega)]}, \quad \alpha \in \{R,K\}$$

then to linear order in $\underline{D}(\omega)$

$$\begin{aligned} O[\underline{\Delta}_{ex}] \approx\, & O[\underline{\Delta}_{\text{aux}}] \\ & + r \sum_{\alpha\in\{R,K\}} \int \frac{\delta O[\underline{\Delta}]}{\delta\,\text{Im}[\Delta^\alpha(\omega_0)]}\bigg|_{\underline{\Delta}=\underline{\Delta}_{\text{aux}}} \text{Im}[D^\alpha(\omega_0)]\, d\omega_0 \\ & + \mathcal{O}(\underline{D}^2), \end{aligned} \tag{C1}$$

with $r = 1$.

We evaluate the functional derivative numerically in the following way. One first evaluates $O[\underline{\Delta}_{\text{aux}}]$ at the optimum $\underline{\Delta}_{\text{aux}}(\omega)$. Then, O is evaluated at a "shifted" $\text{Im}[\Delta^\alpha(\omega)]$, obtained by adding a delta function peaked around a certain energy ω_0:

$$\delta_{\omega_0}(\omega) \equiv \delta(\omega - \omega_0),$$

multiplied by a small coefficient ϵ. The functional derivatives are then approximated linearly, by making use of the equations

$$\begin{aligned} & \frac{\delta O[\underline{\Delta}]}{\delta\,\text{Im}[\Delta^R(\omega_0)]} \pm 2\frac{\delta O[\underline{\Delta}]}{\delta\,\text{Im}[\Delta^K(\omega_0)]} \\ & \approx \frac{1}{\epsilon}\big(O[\text{Im}(\Delta^R),\text{Im}(\Delta^K)] \\ & \quad - O[\text{Im}(\Delta^R) - \epsilon\delta_{\omega_0},\text{Im}(\Delta^K) \mp 2\epsilon\delta_{\omega_0}]\big), \end{aligned} \tag{C2}$$

which become exact in the $\epsilon \to 0$ limit.

A (quasi)delta-peak correction $\epsilon\delta_{\omega_0}$ to $\Delta^\alpha(\omega)$ can be obtained by attaching an additional bath site $(N_B + 1)$ with onsite energy $E_{N_B+1,N_B+1} = \omega_0$ directly to the impurity site with a hopping $E_{N_B+1,f} = \sqrt{\epsilon/\pi}$. The sum of $\Gamma^{(1)}_{N_B+1,N_B+1}$ and $\Gamma^{(2)}_{N_B+1,N_B+1}$ is proportional to the width of δ_{ω_0} and, thus, should be taken as small as possible. In practice, one uses a discretization of the integration over ω_0 in Eq. (C1) and the width of the delta peaks has to be adjusted accordingly. Setting one of the components $\Gamma^\kappa_{N_B+1,N_B+1}$ to zero yields a peak in the Keldysh component with a coefficient $\pm 2\epsilon$, respectively, as used in Eq. (C2).

Notice that the functional derivative (C2) amounts to carrying out two many-body calculations for each point ω_0 on a system with $N_B + 1$ bath sites. However, it is not necessary to repeat the calculation for each physical quantity of interest. In the linearly corrected current values presented in Sec. III B, a ω_0 mesh of 200 points was used, whereby this number is likely to be reduced when optimizing the method.

Strictly speaking, the coefficient r in Eq. (C1) should be 1. However, for cases in which the linear correction is not small, this could produce an "overcorrection." In order to avoid this, we introduce a smaller ratio r which is determined as follows: We evaluate the corrected self-energy at each ω via Eq. (C1) and $O = \underline{\Sigma}(\omega)$ with some value of $r < 1$ and denote it $\underline{\Sigma}_r(\omega)$. We do the same for the Green's function of the auxiliary system and denote it $\underline{G}_r(\omega)$. Using Eqs. (5) and (6), we now have an estimate of an effective r-dependent auxiliary hybridization function of the linearly corrected system via

$$\underline{\Delta}_{\text{aux},r}(\omega) \equiv \underline{g}_0^{-1}(\omega) - \underline{G}_r^{-1}(\omega) - \underline{\Sigma}_r(\omega).$$

In principle, for $r = 1$ this gives $\underline{\Delta}_{ex}(\omega)$ up to $\mathcal{O}(\underline{D}^2)$. In practice, for finite $\underline{D}(\omega)$, one can introduce a cost function $\chi(r)$ analogous to Eq. (12) to minimize the difference $|\underline{\Delta}_{\text{aux},r}(\omega) - \underline{\Delta}_{ex}(\omega)|$ as a function of r. We checked that for the case in which the linear correction is a good approximation, the minimum occurs at $r = 1$. If the minimum of $\chi(r)$ is situated at some value $r_{\min} < 1$, then one corrects also other physical quantities according to Eq. (C1) with the same $r = r_{\min}$.

Alternatively to the correction (C1) discussed above, one can use the numerical functional derivative evaluated via Eq. (C2) in order to estimate the sensitivity of the value of O with respect to variations of $\text{Im}[\Delta^\alpha_{\text{aux}}(\omega)]$ as a function of ω and α. This is of use, in a second step, to adjust the weight function $W^\alpha(\omega)$ in Eq. (12), so that more sensitive ω regions acquire a larger weight.

[1] M. Hartmann, F. Brandão, and M. Plenio, Laser Photonics Rev. **2**, 527 (2008).

[2] M. Raizen, C. Salomon, and Q. Niu, Phys. Today **50**(7), 30 (1997).

[3] D. Jaksch, C. Bruder, J. I. Cirac, C. W. Gardiner, and P. Zoller, Phys. Rev. Lett. **81**, 3108 (1998).
[4] M. Greiner, O. Mandel, T. Esslinger, T. W. Hänsch, and I. Bloch, Nature (London) **415**, 39 (2002).
[5] S. Trotzky, P. Cheinet, S. Fölling, M. Feld, U. Schnorrberger, A. M. Rey, A. Polkovnikov, E. A. Demler, M. D. Lukin, and I. Bloch, Science **319**, 295 (2008).
[6] U. Schneider, L. Hackermuller, J. P. Ronzheimer, S. Will, S. Braun, T. Best, I. Bloch, E. Demler, S. Mandt, D. Rasch *et al.*, Nat. Phys. **8**, 213 (2012).
[7] S. Iwai, M. Ono, A. Maeda, H. Matsuzaki, H. Kishida, H. Okamoto, and Y. Tokura, Phys. Rev. Lett. **91**, 057401 (2003).
[8] A. Cavalleri, T. Dekorsy, H. H. W. Chong, J. C. Kieffer, and R. W. Schoenlein, Phys. Rev. B **70**, 161102 (2004).
[9] L. L. Bonilla and H. T. Grahn, Rep. Prog. Phys. **68**, 577 (2005).
[10] I. Zutic, J. Fabian, and S. D. Sarma, Rev. Mod. Phys. **76**, 323 (2004).
[11] G. Cuniberti, G. Fagas, and K. Richter, *Introducing Molecular Electronics* (Springer, Berlin, 2005).
[12] R. H. M. Smit, Y. Noat, C. Untiedt, N. D. Lang, M. C. van Hemert, and J. M. van Ruitenbeek, Nature (London) **419**, 906 (2002).
[13] J. Park, A. N. Pasupathy, J. I. Goldsmith, C. Chang, Y. Yaish, J. R. Petta, M. Rinkoski, J. P. Sethna, H. D. Abruna, P. L. McEuen *et al.*, Nature (London) **417**, 722 (2002).
[14] W. Liang, M. P. Shores, M. Bockrath, J. R. Long, and H. Park, Nature (London) **417**, 725 (2002).
[15] N. Agrait, A. L. Yeyati, and J. M. van Ruitenbeek, Phys. Rep. **377**, 81 (2003).
[16] L. Venkataraman, J. E. Klare, C. Nuckolls, M. S. Hybertsen, and M. L. Steigerwald, Nature (London) **442**, 904 (2006).
[17] D. Goldhaber-Gordon, J. Göres, M. A. Kastner, H. Shtrikman, D. Mahalu, and U. Meirav, Phys. Rev. Lett. **81**, 5225 (1998).
[18] A. V. Kretinin, H. Shtrikman, and D. Mahalu, Phys. Rev. B **85**, 201301 (2012).
[19] A. Mitra, S. Takei, Y. B. Kim, and A. J. Millis, Phys. Rev. Lett. **97**, 236808 (2006).
[20] A. J. Leggett, S. Chakravarty, A. T. Dorsey, M. P. A. Fisher, A. Garg, and W. Zwerger, Rev. Mod. Phys. **59**, 1 (1987).
[21] M. A. Cazalilla, Phys. Rev. Lett. **97**, 156403 (2006).
[22] M. Rigol, V. Dunjko, and M. Olshanii, Nature (London) **452**, 854 (2008).
[23] A. Nitzan and M. A. Ratner, Science **300**, 1384 (2003).
[24] P. W. Anderson, Phys. Rev. **124**, 41 (1961).
[25] J. Friedel, Can. J. Phys. **34**, 1190 (1956).
[26] A. M. Clogston, B. T. Matthias, M. Peter, H. J. Williams, E. Corenzwit, and R. C. Sherwood, Phys. Rev. **125**, 541 (1962).
[27] W. Brenig and K. Schönhammer, Z. Phys. **267**, 201 (1974).
[28] A. Georges, G. Kotliar, W. Krauth, and M. J. Rozenberg, Rev. Mod. Phys. **68**, 13 (1996).
[29] A. Cyril, *The Kondo Problem to Heavy Fermions* (Cambridge University Press, Cambridge, UK, 1997).
[30] D. Vollhardt, in *Lecture Notes on the Physics of Strongly Correlated Systems*, Vol. 1297 of *AIP Conference Proceedings*, edited by A. Avella and F. Mancini (AIP, New York, 2010), p. 339.
[31] W. Metzner and D. Vollhardt, Phys. Rev. Lett. **62**, 324 (1989).
[32] J. Kondo, Prog. Theor. Phys. **32**, 37 (1964).
[33] P. W. Anderson, J. Phys. C: Solid State Phys. **3**, 2436 (1970).
[34] K. Yosida and K. Yamada, Prog. Theor. Phys. Suppl. **46**, 244 (1970).
[35] K. Yamada, Prog. Theor. Phys. **53**, 970 (1975).
[36] K. Yosida and K. Yamada, Prog. Theor. Phys. **53**, 1286 (1975).
[37] K. Yamada, Prog. Theor. Phys. **54**, 316 (1975).
[38] J. R. Schrieffer and P. A. Wolff, Phys. Rev. **149**, 491 (1966).
[39] S. Y. Müller, M. Pletyukhov, D. Schuricht, and S. Andergassen, Phys. Rev. B **87**, 245115 (2013).
[40] D. Bohr and P. Schmitteckert, Ann. Phys. (NY) **524**, 199 (2012).
[41] L. H. Yu, Z. K. Keane, J. W. Ciszek, L. Cheng, J. M. Tour, T. Baruah, M. R. Pederson, and D. Natelson, Phys. Rev. Lett. **95**, 256803 (2005).
[42] L. Tosi, P. Roura-Bas, and A. A. Aligia, J. Phys.: Condens. Matter **24**, 365301 (2012).
[43] H. Prüser, M. Wenderoth, P. E. Dargel, A. Weismann, R. Peters, T. Pruschke, and R. G. Ulbrich, Nat. Phys. **7**, 203 (2011).
[44] H. Aoki, N. Tsuji, M. Eckstein, M. Kollar, T. Oka, and W. Philipp, arXiv:1310.5329.
[45] P. Schmidt and H. Monien, arXiv:cond-mat/0202046.
[46] J. K. Freericks, V. M. Turkowski, and V. Zlatić, Phys. Rev. Lett. **97**, 266408 (2006).
[47] J. K. Freericks, Phys. Rev. B **77**, 075109 (2008).
[48] A. V. Joura, J. K. Freericks, and T. Pruschke, Phys. Rev. Lett. **101**, 196401 (2008).
[49] M. Eckstein, M. Kollar, and P. Werner, Phys. Rev. Lett. **103**, 056403 (2009).
[50] S. Okamoto, Phys. Rev. B **76**, 035105 (2007).
[51] E. Arrigoni, M. Knap, and W. von der Linden, Phys. Rev. Lett. **110**, 086403 (2013).
[52] P. Mehta and N. Andrei, Phys. Rev. Lett. **96**, 216802 (2006).
[53] F. B. Anders, Phys. Rev. Lett. **101**, 066804 (2008).
[54] F. B. Anders and S. Schmitt, J. Phys.: Conf. Ser. **220**, 012021 (2010).
[55] A. Rosch, Eur. Phys. J. B **85**, 6 (2012).
[56] Y. Meir, N. S. Wingreen, and P. A. Lee, Phys. Rev. Lett. **70**, 2601 (1993).
[57] N. S. Wingreen and Y. Meir, Phys. Rev. B **49**, 11040 (1994).
[58] T. Fujii and K. Ueda, Phys. Rev. B **68**, 155310 (2003).
[59] H. Schoeller and G. Schön, Phys. Rev. B **50**, 18436 (1994).
[60] S. Hershfield, J. H. Davies, and J. W. Wilkins, Phys. Rev. Lett. **67**, 3720 (1991).
[61] H. Schoeller, Eur. Phys. J.: Spec. Top. **168**, 179 (2009).
[62] A. Rosch, J. Paaske, J. Kroha, and P. Wölfle, J. Phys. Soc. Jpn. **74**, 118 (2005).
[63] F. B. Anders and A. Schiller, Phys. Rev. B **74**, 245113 (2006).
[64] D. Roosen, M. R. Wegewijs, and W. Hofstetter, Phys. Rev. Lett. **100**, 087201 (2008).
[65] B. Doyon and N. Andrei, Phys. Rev. B **73**, 245326 (2006).
[66] S. Weiss, J. Eckel, M. Thorwart, and R. Egger, Phys. Rev. B **77**, 195316 (2008).
[67] F. B. Anders and A. Schiller, Phys. Rev. Lett. **95**, 196801 (2005).
[68] M. Moeckel and S. Kehrein, Phys. Rev. Lett. **100**, 175702 (2008).
[69] S. Kehrein, Phys. Rev. Lett. **95**, 056602 (2005).
[70] G. Vidal, Phys. Rev. Lett. **93**, 040502 (2004).
[71] S. R. White, Phys. Rev. B **48**, 10345 (1993).

[72] A. J. Daley, C. Kollath, U. Schollwöck, and G. Vidal, J. Stat. Mech. (2004) P04005.

[73] S. R. White and A. E. Feiguin, Phys. Rev. Lett. **93**, 076401 (2004).

[74] U. Schollwoeck, Ann. Phys. (NY) **326**, 96 (2011).

[75] P. Schmitteckert, Phys. Rev. B **70**, 121302 (2004).

[76] F. Heidrich-Meisner, A. E. Feiguin, and E. Dagotto, Phys. Rev. B **79**, 235336 (2009).

[77] M. Nuss, M. Ganahl, H. G. Evertz, E. Arrigoni, and W. von der Linden, Phys. Rev. B **88**, 045132 (2013).

[78] M. Nuss, C. Heil, M. Ganahl, M. Knap, H. G. Evertz, E. Arrigoni, and W. von der Linden, Phys. Rev. B **86**, 245119 (2012).

[79] M. Knap, W. von der Linden, and E. Arrigoni, Phys. Rev. B **84**, 115145 (2011).

[80] F. Hofmann, M. Eckstein, E. Arrigoni, and M. Potthoff, Phys. Rev. B **88**, 165124 (2013).

[81] C. Jung, A. Lieder, S. Brener, H. Hafermann, B. Baxevanis, A. Chudnovskiy, A. Rubtsov, M. Katsnelson, and A. Lichtenstein, Ann. Phys. (NY) **524**, 49 (2012).

[82] R. Gezzi, T. Pruschke, and V. Meden, Phys. Rev. B **75**, 045324 (2007).

[83] S. G. Jakobs, V. Meden, and H. Schoeller, Phys. Rev. Lett. **99**, 150603 (2007).

[84] P. Werner, T. Oka, M. Eckstein, and A. J. Millis, Phys. Rev. B **81**, 035108 (2010).

[85] G. Cohen, E. Gull, D. R. Reichman, and A. J. Millis, arXiv:1310.4151.

[86] J. E. Han, Phys. Rev. B **73**, 125319 (2006).

[87] J. E. Han and R. J. Heary, Phys. Rev. Lett. **99**, 236808 (2007).

[88] A. Dirks, P. Werner, M. Jarrell, and T. Pruschke, Phys. Rev. E **82**, 026701 (2010).

[89] J. E. Han, A. Dirks, and T. Pruschke, Phys. Rev. B **86**, 155130 (2012).

[90] A. Dirks, J. E. Han, M. Jarrell, and T. Pruschke, Phys. Rev. B **87**, 235140 (2013).

[91] P. Dutt, J. Koch, J. Han, and K. Le Hur, Ann. Phys. (NY) **326**, 2963 (2011).

[92] E. Muñoz, C. J. Bolech, and S. Kirchner, Phys. Rev. Lett. **110**, 016601 (2013).

[93] A. M. Uimonen, E. Khosravi, A. Stan, G. Stefanucci, S. Kurth, R. van Leeuwen, and E. K. U. Gross, Phys. Rev. B **84**, 115103 (2011).

[94] S. Smirnov and M. Grifoni, Phys. Rev. B **84**, 125303 (2011).

[95] H. Schoeller and J. König, Phys. Rev. Lett. **84**, 3686 (2000).

[96] M. Schiro and M. Fabrizio, Phys. Rev. Lett. **105**, 076401 (2010).

[97] C. Timm, Phys. Rev. B **77**, 195416 (2008).

[98] J. Eckel, F. Heidrich-Meisner, S. G. Jakobs, M. Thorwart, M. Pletyukhov, and R. Egger, New J. Phys. **12**, 043042 (2010).

[99] S. Andergassen, V. Meden, H. Schoeller, J. Splettstoesser, and M. R. Wegewijs, Nanotechnology **21**, 272001 (2010).

[100] L. D. Contreras-Pulido, J. Splettstoesser, M. Governale, J. König, and M. Büttiker, Phys. Rev. B **85**, 075301 (2012).

[101] L. M. Falicov and J. C. Kimball, Phys. Rev. Lett. **22**, 997 (1969).

[102] M. Eckstein and M. Kollar, Phys. Rev. Lett. **100**, 120404 (2008).

[103] M. Eckstein, M. Kollar, and P. Werner, Phys. Rev. B **81**, 115131 (2010).

[104] S. Okamoto, Phys. Rev. Lett. **101**, 116807 (2008).

[105] C. Aron, G. Kotliar, and C. Weber, Phys. Rev. Lett. **108**, 086401 (2012).

[106] C. Gramsch, K. Balzer, M. Eckstein, and M. Kollar, Phys. Rev. B **88**, 235106 (2013).

[107] H. J. Carmichael, *Statistical Methods in Quantum Optics: Master Equations and Fokker-Planck Equations*, Vol. 1 of Texts and Monographs in Physics (Springer, Singapore, 2002).

[108] In our convention, lowercase g denotes Green's functions of the system where the impurity is disconnected from the reservoirs, while capital G denotes Green's functions of the connected system.

[109] Conventions for branch cuts are such that g^R is causal.

[110] E. N. Economou, *Green's Functions in Quantum Physics* (Springer, Heidelberg, 2006).

[111] Note that in the present formalism, temperature would enter through the hybridization function $\Delta^K(\omega)$ only.

[112] This is in general true unless the system has bound states.

[113] L. P. Kadanoff and G. Baym, *Quantum Statistical Mechanics: Green's Function Methods in Equilibrium and Nonequilibrium Problems* (Addison-Wesley, Redwood City, CA, 1962).

[114] J. Schwinger, J. Math. Phys. **2**, 407 (1961).

[115] L. V. Keldysh, Zh. Eksp. Teor. Fiz. **47**, 1515 (1965) [JETP **20**, 1018 (1965)].

[116] H. Haug and A.-P. Jauho, *Quantum Kinetics in Transport and Optics of Semiconductors* (Springer, Heidelberg, 1998).

[117] J. Rammer and H. Smith, Rev. Mod. Phys. **58**, 323 (1986).

[118] A. Kamenev, *Field Theory of Non-Equilibrium Systems* (Cambridge University Press, Cambridge, 2011).

[119] M. Caffarel and W. Krauth, Phys. Rev. Lett. **72**, 1545 (1994).

[120] C. Lanczos, J. Res. Natl. Bur. Stand. **45**, 255 (1951).

[121] See Ref. [87].

[122] H.-P. Breuer and F. Petruccione, *The Theory of Open Quantum Systems* (Oxford University Press, Oxford, England, 2009).

[123] Operators are denoted by a hat $\hat{o}$, while superoperators acting on operators are denoted by a double hat $\hat{\hat{o}}$. For elementary fermionic creation/annihilation operators, we omit the hat. Finally, we use boldface for matrices and vectors in orbital indices.

[124] Alternatively, one could use the "star" representation, in which only diagonal and $E_{f,v}$ terms are nonzero.

[125] T. Prosen, New J. Phys. **10**, 043026 (2008).

[126] A. A. Dzhioev and D. S. Kosov, J. Chem. Phys. **134**, 044121 (2011).

[127] M. Schmutz, Z. Phys. B **30**, 97 (1978).

[128] U. Harbola and S. Mukamel, Phys. Rep. **465**, 191 (2008).

[129] From now on, we will omit the spin index, unless necessary.

[130] In our convention, $G^{>+}_{\mu\nu}(t)$ and $G^{<-}_{\mu\nu}(t)$ are zero for $t < 0$, and vice versa.

[131] Notice that $\boldsymbol{D}$ commutes with $\boldsymbol{\lambda}$, so $\frac{\boldsymbol{D}}{\omega - i\boldsymbol{\lambda}}$ is well defined.

[132] D. F. Shanno, Math. Comp. **24**, 647 (1970).

[133] W. H. Press, S. A. Teukolsky, W. T. Vetterling, and B. P. Flannery, *Numerical Recipes 3rd Edition: The Art of Scientific Computing* (Cambridge University Press, Cambridge, UK, 2007).

[134] J. D. Jackson, *Classical Electrodynamics*, 2nd ed. (Wiley, New York, 1975).

[135] For the particle-hole-symmetric model, the auxiliary system onsite energies are restricted to $E_{ff} = -\frac{U}{2}$ and $E_{\mu\mu} = -E_{N_B+1-\mu,N_B+1-\mu}$ for $\mu \neq f$ as well as nearest-neighbor

$\langle \ldots \rangle$ hopping to $E_{\langle \mu\nu \rangle} = (-1)^{\mu+\nu+1} E_{\langle N_B+1-\mu, N_B+1-\nu \rangle}$ while the dissipation matrices have to fulfill $\Gamma^{(1)}_{\mu\nu} = (-1)^{\mu+\nu} \Gamma^{(2)}_{N_B+1-\mu, N_B+1-\nu}$.

[136] Y. Meir and N. S. Wingreen, Phys. Rev. Lett. **68**, 2512 (1992).

[137] A.-P. Jauho, https://nanohub.org/resources/1877.

[138] J. W. Negele and H. Orland, *Quantum Many-Particle Systems*, Vol. 68 of Frontiers in Physics (Addison-Wesley, Redwood City, Calif., 1988).

[139] S. De Franceschi, R. Hanson, W. G. van der Wiel, J. M. Elzerman, J. J. Wijpkema, T. Fujisawa, S. Tarucha, and L. P. Kouwenhoven, Phys. Rev. Lett. **89**, 156801 (2002).

[140] R. Leturcq, L. Schmid, K. Ensslin, Y. Meir, D. C. Driscoll, and A. C. Gossard, Phys. Rev. Lett. **95**, 126603 (2005).

[141] J. S. Langer and V. Ambegaokar, Phys. Rev. **121**, 1090 (1961).

[142] D. C. Langreth, Phys. Rev. **150**, 516 (1966).

[143] L. Mühlbacher, D. F. Urban, and A. Komnik, Phys. Rev. B **83**, 075107 (2011).

[144] J. König, J. Schmid, H. Schoeller, and G. Schön, Phys. Rev. B **54**, 16820 (1996).

[145] A. Rosch, J. Paaske, J. Kroha, and P. Wölfle, Phys. Rev. Lett. **90**, 076804 (2003).

[146] J. Dalibard, Y. Castin, and K. Mølmer, Phys. Rev. Lett. **68**, 580 (1992).

[147] A. J. Daley, J. M. Taylor, S. Diehl, M. Baranov, and P. Zoller, Phys. Rev. Lett. **102**, 040402 (2009).

[148] T. Prosen and M. Znidaric, J. Stat. Mech. (2009) P02035.

[149] A. Alvermann and H. Fehske, Phys. Rev. Lett. **102**, 150601 (2009).

[150] A. Weisse, G. Wellein, A. Alvermann, and H. Fehske, Rev. Mod. Phys. **78**, 275 (2006).

[151] C. D. Sherrill and H. F. Schaefer III, Adv. Quantum Chem. **34**, 143 (1999).

[152] Y. Saad, *Numerical Methods for Large Eigenvalue Problems, Revised Edition* (Society for Industrial and Applied Mathematics, Philadelphia, 2011).

[153] P. Arbenz, *Lecture Notes on Solving Large Scale Eigenvalue Problems*, http://people.inf.ethz.ch/arbenz/ewp/lnotes.html.

[154] Z. Bai, J. Demmel, J. Dongarra, A. Ruhe, and H. van der Vorst, *Templates for the Solution of Algebraic Eigenvalue Problems: A Practical Guide (Software, Environments and Tools)* (Society for Industrial and Applied Mathematics, Philadelphia, 1987).

[155] M. Knap, E. Arrigoni, W. von der Linden, and J. H. Cole, Phys. Rev. A **83**, 023821 (2011).

[156] Y. Saad, *Iterative Methods for Sparse Linear Systems*, 2nd ed. (Society for Industrial and Applied Mathematics, Philadelphia, 2003).

[157] R. Barrett, M. Berry, T. F. Chan, J. Demmel, J. Donato, J. Dongarra, V. Eijkhout, R. Pozo, C. Romine, and H. V. der Vorst, *Templates for the Solution of Linear Systems: Building Blocks for Iterative Methods*, 2nd ed. (SIAM, Philadelphia, PA, 1994).

[158] T. J. Park and J. C. Light, J. Chem. Phys. **85**, 5870 (1986).

[159] Y. B. Bazaliy, E. Demler, and S.-C. Zhang, Phys. Rev. Lett. **79**, 1921 (1997).

[160] M. H. Gutknecht, The unsymmetric Lanczos algorithms and their relations to Pade approximation, continued fractions, and the qd algorithm, http://www.math.ethz.ch/~mhg/.

[161] M. H. Gutknecht, Lanczos-type solvers for non-Hermitian linear systems, http://www.math.ethz.ch/~mhg/.

[162] R. Freund, M. Gutknecht, and N. Nachtigal, SIAM J. Sci. Comput. **14**, 137 (1993).

[163] B. N. Parlett, D. R. Taylor, and Z. A. Liu, Math. Comp. **44**, 105 (1985).

[164] H.-G. Weikert, H.-D. Meyer, L. S. Cederbaum, and F. Tarantelli, J. Chem. Phys. **104**, 7122 (1996).

[165] For the sake of clarity, we specifically introduce the subscript $_{ex}$ to denote the exact hybridization function $\underline{\Delta}_{ex}$. This will be used only in this section.

5.10. Strong electronic correlations at high bias voltage and structured electronic leads

5.10.1. Preamble

This part of our work is unpublished at the time of writing this thesis [70].

This last part of the thesis concludes the studies on the nonequilibrium behaviour of the SIAM but its arguments apply to any correlated junction in general independent of the specific model. The SIAM is introduced in Sec. 3.1 and its physical applications are outlined in Ch. 2. Aspects of its equilibrium behaviour is presented in Sec. 5.1 and Sec. 5.4, nonequilibrium temporal evolution in Sec. 5.2 and Sec. 5.3 and steady-state properties in Sec. 5.5, Sec. 5.6. In this final part we explore a regime of high bias voltages near the conduction band edge of the leads. Commonly electronic correlations are believed to be important at low bias voltages while being wiped out by an effect comparable to temperature for high bias voltages. We however find strong indications that electronic correlations may increase at high bias voltage at diminishing band overlap. Our results are based on data from real time evolution, steady-state cluster methods, the AMEA as well as QMEs, see Sec. 5.8. An overview of the methods is available in Ch. 3.

This manuscript is authored by Martin Nuss (MN) and co-authored by Antonius Dorda (AD), Martin Ganahl (MG), Hans Gerd Evertz (HE) and MN's supervisors Enrico Arrigoni (EA) and Wolfgang von der Linden (WL). The research was initiated by MN. This research was to a large and significant extent conducted by MN under the supervision of WL and EA. HE, EA and WL provided guidance and expertise throughout all phases of the work. MN developed, implemented, tested an ran all simulations in stsCPT, stsVCA, DMRG+TEBD and the QME. AD conducted the AMEA calculations. MG provided his basis MPS computer code. MG and HE provided guidance and expertise for the MPS method. MN conducted the testing and parameter studies. EA initiated the work on the QME and hinted at the charge Kondo physics. MN conducted an extensive literature research. MN prepared, collected, interpreted, analyzed and visualized the results and set them in context with recent literature. MN wrote the first version of the manuscript. All authors contributed equally in discussing our results and revising the manuscript. We discussed our results with Sabine Andergassen.

5.10.2. Manuscript

Strong electronic correlations at high bias voltage and structured electronic leads

Martin Nuss,[1,*] Antonius Dorda,[1] Martin Ganahl,[1,2] Hans Gerd Evertz,[1] Enrico Arrigoni,[1] and Wolfgang von der Linden[1]

[1] *Institute of Theoretical and Computational Physics, Graz University of Technology, 8010 Graz, Austria*
[2] *Perimeter Institute for Theoretical Physics, Waterloo, Ontario*

(Dated: June 12, 2015)

We discuss the role of electron-electron correlations at high bias voltages in transport setups which feature leads with a finite and structured electronic density of states. In nonequilibrium calculations the wide band limit, that is a featureless lead density of states at all energies is commonly applied. It is found that at high bias voltages electronic correlations are dominated by the applied bias voltage. Then the system behaves essentially free, rendering the role of the bias voltage similar to temperature or a magnetic field in equilibrium. We show, in addition, that at high bias voltage in the vicinity of the band edge of the reservoirs, electronic correlations become significantly enhanced again. This behaviour can be attributed to an effective reduction of the nonequilibrium energy scale by a reduced available state space for transport. Our results are based on a combined approach using density matrix renormalization group and time evolving block decimation for an accurate real-time evolution, the steady-state variational cluster approach and the auxiliary master equation approach for steady-state dynamics and a Born-Markov-secular quantum master equation for steady-state tomography. We discuss the enhanced correlations in the steady-state double occupancy, the charge current, the local density of states and the reduced many-body density matrix of a single correlated orbital connected to two electronic reservoirs under voltage bias. In addition we provide a possible resolution to an unresolved issue about the steady-state double occupancy of the single impurity Anderson model, which arose recently in [EPL **102**, 37011 (2013)].

PACS numbers: 73.23.-b, 73.63.Kv, 72.10.Fk, 71.27+a

I. INTRODUCTION

Correlated quantum systems out of equilibrium have become a subject of intense study with promising outlook during the last decade.[1–7] Besides realizations in nanoscopic devices[8–11] and molecular junctions[12,13] their physics can be explored using highly tunable quantum simulators[14–18] and technological applications are to be expected in the near future. Quite generally these systems consist of a microscopic subsystem of quantum degrees of freedom i.e. a molecule or nano structure which exhibits a particular kind of many-body interaction and at least two electronic leads which serve as particle and temperature reservoirs. The state of the microscopic central system can be controlled by environment parameters like a bias voltage or a temperature gradient which serve the purpose of imposing a nonequilibrium situation on the central "device". The behaviour of such low dimensional, confined quantum systems is often dominated by many-body interactions rendering their detailed understanding in nonequilibrium situations essential for future device engineering.

The effects of strong electronic correlations in quantum many-body systems out of equilibrium are a priori expected in a universal low bias regime. That is, as long as the nonequilibrium energy scale of the bias voltage V_B is small compared to an electronic coherence energy scale T^*. As a result, non trivial many-body effects like the Kondo effect or the phenomenon of negative differential resistance (NDR) are expected to be pronounced for $V_B < T^*$. For larger V_B, this environmental "perturbing" energy scale acts like a high effective temperature[19–21] T or large magnetic field[22] B which suppresses electronic correlations rendering the system effectively free. Renormalization group (RG) methods have shown that the effects of electronic correlations are indeed diminished at high bias voltages assuming a featureless wide band limit for the noninteracting lead electronic density of states (DOS).[19,20,23] That is the DOS of the left and right lead are constant for all energies, allowing in principle all states of the system within the transport window to participate in transport equally.[24]

Recently, non trivial phenomena like NDR have also been found at high bias voltages but just as a result of the reservoir DOS and not in connection with electronic correlations in the device.[25] Consider a device with two leads (L/R) of equal, finite DOS within a bandwidth of $\pm D$ and an anti-symmetrically applied bias voltage $\frac{V_B}{2} = \mu_L = \epsilon_L = -\mu_R = -\epsilon_R$, where μ is the chemical potential and ϵ is the center of the band. Then it is clear that the current will become zero when the bands of the leads stop overlapping at $V_B = 2D$. Further assume a lead DOS $\rho_{L/R}(\omega)$ which is structured as for example in a semi-circular fashion, see Fig. 1 (B):

$$\rho_{L/R}(\omega) = \frac{2}{\pi D^2} \Re\mathrm{e}\left(\sqrt{D^2 - (\omega - \epsilon_{L/R}^2)}\right). \qquad (1)$$

Then the current will continuously decrease approaching the band edge because less electronic states are available for transport. This is, the NDR occurs when the reservoir

DOS is finite and the overlap starts to diminish under an applied bias voltage.

In general one expects universal physics driven by electronic correlations at low bias voltages as proposed by RG and essentially noninteracting physics possibly influenced by trivial band effects at high bias voltages.

This work reports the theoretical observation that electronic correlations can in fact even be promoted by high bias voltages at finite lead bandwidth. We discuss a general situation in which a correlated quantum system of finite size is coupled to two electronic reservoirs of finite bandwidth under voltage bias. As the simplest possible realization we present specific results for the particular example of a single correlated orbital coupled to reservoirs with semi-circular electronic density of states to back our general arguments. We show that electronic correlations are important even at high bias voltages, if the overlap of the reservoir density of states becomes small. Our observations make it therefore essential to disentangle the trivial effects of the reservoir DOS from features arising due to electronic correlations in the device.

II. MODEL AND METHOD

We consider a symmetric single impurity Anderson model[26] (SIAM) of spin-$\frac{1}{2}$ fermions. A single electronic orbital with on-site interaction U is coupled to two noninteracting one dimensional electronic reservoirs, see Fig. 1 (A). The dynamics are governed by

$$\begin{aligned}
\hat{\mathcal{H}} &= \hat{\mathcal{H}}_{\text{corr}} + \hat{\mathcal{H}}_{\text{res}} + \hat{\mathcal{H}}_{\text{coup}} \\
\hat{\mathcal{H}}_{\text{corr}} &= -\frac{U}{2} \sum_{\sigma} f_{\sigma}^{\dagger} f_{\sigma} + U\, \hat{n}_{\uparrow}^{f} \hat{n}_{\downarrow}^{f} \\
\hat{\mathcal{H}}_{\text{res}} &= \sum_{\alpha,\sigma} \left(\pm \frac{V_B}{2} \sum_{i} c_{i\alpha\sigma}^{\dagger} c_{i\alpha\sigma} - t \sum_{\langle i,\, j \rangle} c_{i\alpha\sigma}^{\dagger} c_{j\alpha\sigma} \right) \\
\hat{\mathcal{H}}_{\text{coup}} &= -t' \sum_{\alpha} \sum_{\sigma} \left(c_{0\alpha\sigma}^{\dagger} f_{\sigma} + f_{\sigma}^{\dagger} c_{0\alpha\sigma} \right) .
\end{aligned}$$

The electronic annihilation (creation) operators $c_{i\alpha\sigma}, f_{\sigma}$ ($c_{i\alpha\sigma}^{\dagger}, f_{\sigma}^{\dagger}$) obey the usual anti-commutation relations with spin $\sigma = \{\uparrow, \downarrow\}$. The particle number operator $\hat{n}$ is defined in the usual way. When needed, we will refer to the on-site energy of the correlated orbital as ϵ_f. We choose $t = -1$ for the semi-infinite one dimensional tight binding left ($\alpha = L$) and right ($\alpha = R$) reservoirs,[27] yielding a semi-circular DOS as defined in Eq. (1). A bias voltage V_B is applied in an anti-symmetric fashion,[28,29] see Fig. 1 (B). The symmetric coupling strength $t' = 0.3162\, t$ between the correlated orbital and the two half-filled reservoir leads to an equilibrium Anderson width[30] of $\Delta \equiv \pi\, t'^2\, \rho_{\text{reservoir}}(0) = \frac{t'^2}{t} \approx 0.1\, t$. We further use $\hbar \equiv k_B \equiv 1$.

This setup implements three regimes according to bias voltage, see Fig. 1 (C): I, "low-bias" V_B is small with respect to the electronic energy T^* and only states around energy $\omega = 0$ lie inside the transport window, II, "medium- bias" V_B is larger than T^* but well below the electronic lead bandwidth $W = 2D$, states at all system energies lie inside the transport window, III, "high-bias" V_B is in the vicinity of the lead band edge and only states around energy $\omega = 0$ lie inside the transport window.

In order to evaluate the effects of electron-electron correlations at finite bias voltage we compute steady-state observables using three independent numerical approaches.

A. Static steady-state observables

We evaluate static observables in the steady-state: (i) the double occupancy which will provide us with information about the electronic correlations in terms of charge fluctuations and magnetic fluctuations in the device and (ii) the charge current which indirectly measures the electronic states of the device in the transport window. These are obtained from a quasi exact real time evolution in a matrix product state (MPS) framework[31] which has proven to be the highly accurate method of choice to evaluate static time dependent observables of one dimensional interacting quantum systems out of equilibrium.[32–44] In particular we use time evolving block decimation (TEBD)[45] after quenching the system out of equilibrium from an initial state which is obtained using density matrix renormalization group (DMRG).[46] For the DMRG, we always start from a half filled system in the canonical ensemble with total $S^z = 0$. All results are consistent among three different quenches: i) quenching the coupling from zero to t' to both leads, ii) quenching the bias voltage from zero to V_B and iii) quenching the coupling from zero to t' at the left lead only. Our numerical implementation of the TEBD makes use of a second order Suzuki-Trotter decomposition of the propagator[31], Abelian symmetries and a highly parallelized computer code. The steady-state is extracted by reaching a plateau in the time dependent observables at long times as outlined in Ref. 47. For steady-state expectation values we give error bars, which indicate three times the standard deviation of the fitted constant to the steady-state plateau in the time dependent observable. Based on extensive parameter studies for converged results we use a Trotter time step of $\delta\tau = 0.05\, t^{-1}$ and a system size of overall $L = 150$ orbitals. We dynamically adjusted the size of the TEBD matrices with a maximum of $\chi = 2000$. A detailed discussion of the method, the employed quenches as well as a study of convergence in all auxiliary method dependent parameters is available in Ref. 47.

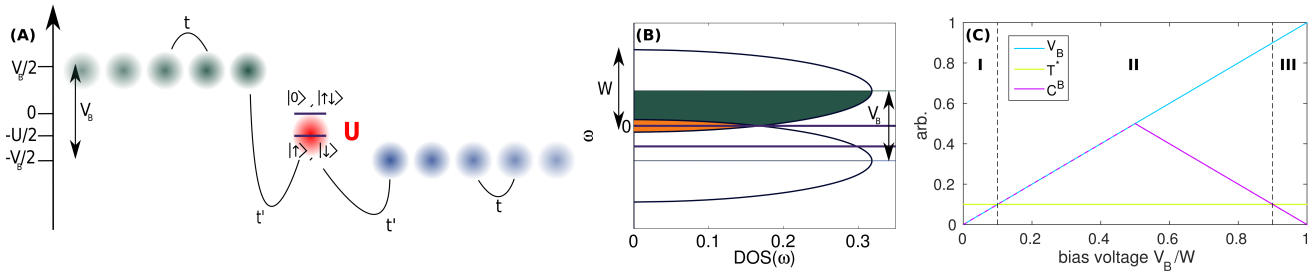

FIG. 1: (Color online) *Model, electronic leads and energy landscape.* **(A)** A single orbital with on-site electron-electron interaction U is tunnel-coupled via t' to two noninteracting one-dimensional electronic reservoirs of infinite size and bandwidth $W = 2D$ held at different chemical potential (and on-site energy) to apply a bias voltage V_B. **(B)** Reservoir DOS and respective overlap in the high bias regime, $V_B = 36\,\Delta$. The green filled region indicates the occupied electron states of the left, high bias reservoir. The orange region indicates the transport window where in addition empty states are present in the right, low bias lead. **(C)** The system features an equilibrium electronic energy scale T^* which is perturbed by the applied bias voltage V_B. The available state space for transport C_B grows and shrinks linearly with V_B. We identify three regimes: I, "low-bias" with respect to the electronic energy T^*, II, "medium- bias" above T^* and well below the electronic lead bandwidth W, III, "high-bias" in the vicinity of the lead band edge.

B. Steady-state dynamics

In order to go beyond static quantities and obtain dynamic single-particle spectra directly in the steady-state we use a nonequilibrium Green's function method: the steady-state variational cluster approach (stsVCA).[48,49] This approximate quantum many-body cluster method relies on a decomposition of the infinite lattice of system and leads into exactly solvable parts and their single-particle connections $\widetilde{T}$. The split parts are solved exactly for their respective single-particle Green's functions $\widetilde{g}(\omega)$ in Keldysh space[50] and are then perturbation connected within the first order strong coupling cluster perturbation theory:[51,52] $\widetilde{G}^{-1}(\omega) = \widetilde{g}^{-1}(\omega) - \widetilde{T}$. The steady-state $\widetilde{G}(\omega)$ is obtained within the approximation that the electronic self-energy is taken from the disconnected systems: $\widetilde{\Sigma}_{\widetilde{G}}(\omega) \stackrel{!}{=} \widetilde{\Sigma}_{\,widetildeg}(\omega)$. The variational aspect introduces self-consistently determined single-particle fields $\hat{O}$ which are optimized requiring $\langle\hat{O}\rangle_{\text{initial}} \stackrel{!}{=} \langle\hat{O}\rangle_{\text{steady-state}}$ and yield a reference state for the perturbative procedure which already incorporates information about the steady-state. In the setup under discussion we split the infinite chain into three parts, a left semi-infinite lead, a right semi-infinite lead and a central region which extends over the correlated orbital as well as three orbitals of the left and of the right lead. The left and right parts are noninteracting and their single-particle Green's functions are readily available, while the one of the interacting central part is obtained numerically exactly by a band-Lanczos method.[53] We used one variational parameter which is the nearest-neighbour hopping in the central region.[54] Details of the method are available in Ref. **?** .

To back our perturbative stsVCA results, we apply in addition the auxiliary master equation approach (AMEA)[55] to obtain steady-state spectra. Like stsVCA, AMEA is an approximate method in which the self-energy is based on a finite-size system. However, in the AMEA this auxiliary system is an open quantum system which is not obtained perturbatively but via a mapping which minimizes the "distance" to the Keldysh-space hybridization function. In a previous study, the AMEA has already proven to yield accurate results for the SIAM under voltage bias[56]. Similar to stsVCA, one has in the AMEA a controlled parameter, namely the size of the finite system specified by the number of bath sites N_B. Upon increasing N_B, the error in the hybridization function can be reduced with a rate up to exponential. Two important aspects are on the one hand, that too small system sizes result in overbroadend spectral data whereas with increasing N_B the resolution is refined and on the other hand, that one has the freedom to focus on certain energy scales in the minimization procedure. The latter is made use of here, in order to resolve especially the region around $\omega = 0$ properly and to treat the other details in the hybridization function not as accurately. To obtain the many-body solution of the auxiliary system, we do not employ an exact diagonalization as in Ref. 56, but use a solution strategy based on MPS.[57] This renders it possible to consider larger system sizes up to $N_B \approx 15$.

C. Full steady-state tomography

Finally, to gain insight in the participating states in steady-state transport, we treat the system within a Born-Markov-secular quantum master equation.[58–63] Within this perturbative framework we obtain the steady-state many-body reduced density matrix $\hat{\rho}_S$ of a system consisting of the impurity and one site of the left and the right lead each by tracing out the other bath degrees of freedom. This approach yields a quantum master equation of Lindblad form and is accurate to second order in the bath hopping t. Details of our particular implementation are available in Ref. 64.

III. RESULTS

We discuss the electronic correlations in the steady-state using numeric data for charge fluctuations, the charge current, the local density of states of the correlated orbital as well as the reduced many-body density matrix. These lead us to the conclusion that electron-electron interactions play an important role not only at low bias voltages but also at high bias voltages when the reservoir DOS is finite.

During our discussion of charge fluctuations we will take a brief detour and comment on an unresolved issues when calculating the steady-state double occupancy of the correlated orbital. Three sophisticated methods were recently shown to yield inconsistent results for this quantity.[65] Our quasi-exact data represents a fourth independent calculation which particularly supports one of the previously used methods.

A. Charge fluctuations

Electronic correlations can be deduced from the steady-state double occupancy of the correlated orbital

$$\mathcal{D} = \langle n_{f\uparrow} n_{f\downarrow} \rangle \,. \tag{2}$$

The symmetry of our setup requires impurity single-particle expectations values of $\langle n_{f\sigma}\rangle = 0.5$ which implies $\langle n_f\rangle = \langle n_{f\uparrow} + n_{f\downarrow}\rangle = 1$ and $\langle m_f\rangle = \frac{1}{2}\langle n_{f\uparrow} - n_{f\downarrow}\rangle = 0$, alongside two half-filled, non-magnetic, conducting reservoirs, which leads to $\mathcal{D} = \frac{1}{2}\left(\langle n_f^2\rangle - \langle n_f\rangle^2\right)$. Therefore, here $\mathcal{D}$ is a measure of the charge fluctuations on the correlated orbital. In the "free" system, for $U = 0$, the respective uncorrelated value is $\mathcal{D}_0 = \langle n_{f\uparrow} n_{f\downarrow}\rangle = \langle n_{f\uparrow}\rangle\langle n_{f\downarrow}\rangle = 0.25$ which is also found in the high temperature limit.[65]

Results for the steady-state double occupancy $\langle n_{f\uparrow} n_{f\downarrow}\rangle$ as obtained by DMRG + TEBD are shown in Fig. 2. In the following our intentions are two fold: At first we set our data in context with recent literature results obtained in the wide band limit. Secondly we discuss the apparent effects of electronic correlations at high bias voltages.

Results for $\mathcal{D}$, in the wide band limit at low temperatures have recently been published in Ref. 65. Their data were obtained using three state of the art out of equilibrium many-body methods: scattering-states numerical renormalization group (SNRG), the Matsubara-voltage quantum Monte-Carlo approach (MV-QMC) and real-time quantum Monte Carlo (RT-QMC). Conflicting results were found in the low to intermediate bias regime amongst these methods. Our data is obtained for zero temperature and a semi-circular DOS. A comparison to the results of Ref. 65 is however valid in the low bias regime for $V_B < 10\,\Delta$ where the lead DOS effects are negligible, compare figure 3 of Ref. 65 with our Fig. 2 (right). We find that our quasi exact DMRG + TEBD data compare best to the RT-QMC results, hinting at a large uncertainty in the double analytic continuation needed in the MV-QMC method and steady-state relaxation issues in the SNRG.[66]

The same study concludes that the double occupancy approaches the noninteracting limit $\mathcal{D}_0$ at high bias voltages, independent of interaction strength. This is expected if bias voltage roughly acts like an effective temperature as is the case in the wide band limit. Our data, for a semi-circular reservoir DOS, clearly indicate that at finite lead bandwidth the charge fluctuation do not approach this limit at high bias voltages, see Fig. 2 (left). The corresponding bias voltage in our calculation is the one at maximal lead band overlap at $V_B = 20\,\Delta$.[67] Here we observe the predicted "free" value of $\mathcal{D}_0$ at least for not too large $\frac{U}{W}$. We find that the charge fluctuations $\mathcal{D}(V_B)$ are roughly antisymmetric with respect to this point: The charge fluctuations $\mathcal{D}(V_B)$ are suppressed / enhanced with respect to $\mathcal{D}_0$ in the low bias / the high bias regime due to electronic correlations. With increasing interaction strength U this suppression /enhancement approaches its theoretical minimum $\mathcal{D} \to 0$ for $V_B \to 0$ and its maximum $\mathcal{D} \to \frac{1}{2}$ for $V_B \to W$. We conclude that the charge fluctuations in the medium-bias regime II are essentially the one of the noninteracting system in equilibrium, while in the low-bias regime I they are suppressed and in the high-bias regime III they are enhanced with respect to $\mathcal{D}_0$. Therefore we argue that reservoir DOS effects in interplay with local Coulomb repulsion can induce non trivial correlation effects at high bias voltages.

In the following we will discuss how these correlation effects influence the current voltage characteristics, a quantity which is typically measured in experiments on nanoscopic or molecular devices.

B. Charge current

Fig. 3 shows the steady-state charge current j as evaluated from the long time plateau values of the current operator

$$\hat{j} = i\,\pi\,t' \sum_{\alpha\sigma} \left(f_\sigma^\dagger\, c_{0\alpha\sigma} - c_{0\alpha\sigma}^\dagger\, f_\sigma \right) \,,$$

obtained by DMRG + TEBD. A detailed discussion of the current-voltage characteristics for this specific lead setup is available in Ref. 47 and Ref. 49.

To evaluate the effects of electron-electron interactions, we set the data of the interacting system (symbols) in context with data obtained for a resonant level model (RLM) (solid lines). The RLM constitutes the very same system but is missing the on-site interaction U and therefore electronic correlations. The level position of the resonant level model is set in accordance to the bare on-site energy of the interacting system $\epsilon_f = -\frac{U}{2}$. Based on this comparison of the current-voltage characteristics, the current can be classified into the very same three bias

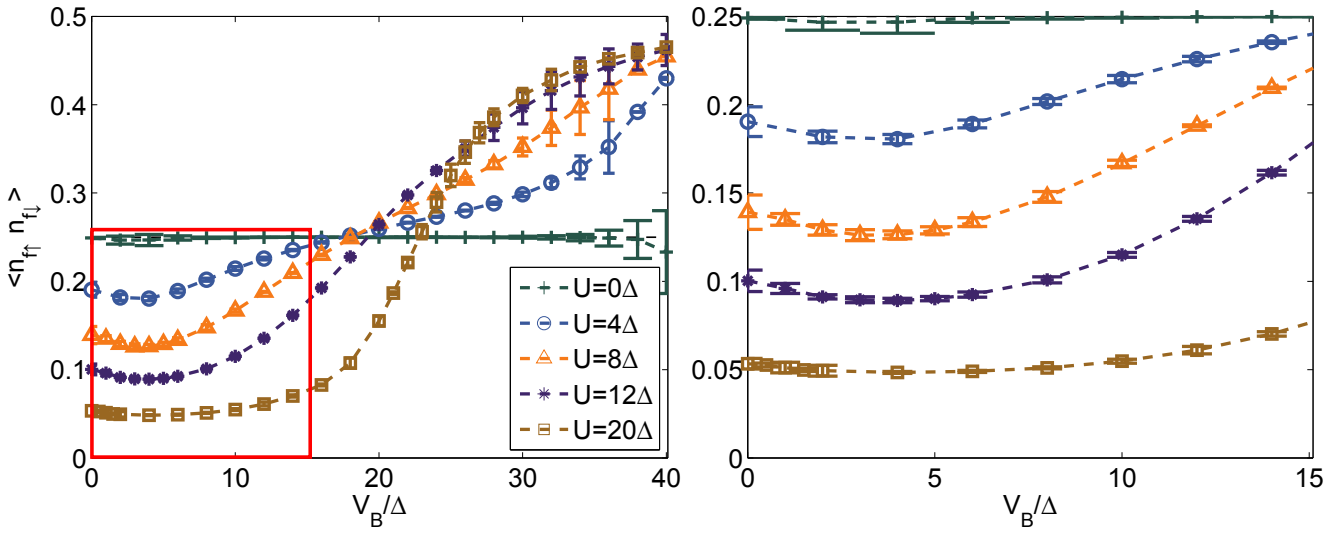

FIG. 2: (Color online) *Steady state double occupancy* of the correlated orbital $\mathcal{D} = \langle n_{f\uparrow} n_{f\downarrow} \rangle$ as a function of bias voltage V_B. We plot $\langle n_{f\uparrow} n_{f\downarrow} \rangle$ for on-site interaction strengths $U = \{4, 8, 12, 20\}\,\Delta$ as obtained by DMRG + TEBD. The right panel shows a zoom to the low bias regime indicated in red in the left part of the figure. Dashed lines are guides to the eye.

voltage regions I- III as the charge fluctuations discussed above.

In regime I, at low bias voltages the current of the interacting system j is always higher than the one of the noninteracting RLM j_0. This is related to the remnants of the equilibrium spin Kondo effect which manifest in an enhanced charge transmission set by the universal linear response conductance quantum G_0 fixed by the equilibrium Friedel sum rule. Kondo correlations become more pronounced for increasing U.[30] In the noninteracting system transport takes place across the single particle level at ϵ_f broadened by the hybridization with the leads. Therefore also the difference $j - j_0$ becomes more prominent with increasing U. In contrast the regime II of medium bias voltages is hardly influenced by the electron-electron interaction at low to intermediate interaction strength, see data for $U = 4\,\Delta$. Here the bias voltage V_B is much higher than the electronic energy scale of the system T^* and many-body effects are negligible, rendering the effects of bias voltage similar to a high temperature. In regime III, at high bias voltages, when the reservoir DOS starts to diminish we observe again an increased current for the interacting system even at low interaction strength. Similar to the low bias regime the current j is always increased in comparison to the noninteracting results j_0.

Since for high bias voltages the available transport window is quite small, an increase of current can be understood in terms of re-gained low energy spectral weight in the correlated orbital due to many-body correlations.

C. Charge spectrum

We refer to the dynamic single-particle spectral function of the correlated orbital as the local DOS (LDOS)

$$\mathrm{LDOS}(\omega) = -\frac{1}{\pi} \Im\mathrm{m}\left(G^R_{ff}(\omega)\right) ,$$

where $G^R_{ff}(\omega)$ is the retarded single-particle electron propagator in the stsVCA approximation. Results for the steady-state LDOS as obtained using stsVCA are shown in Fig. 4.

We find a linear splitting of the Kondo resonance with increasing bias voltage which persists until the resonance hits the high energy incoherent excitations (Hubbard bands). This behaviour is discussed in detail in Ref. 49. Here we focus on the high bias regime where apparently a new low energy excitation is formed carrying the majority of the spectral weight. This feature can be attributed to the self-consistent variational renormalization of the hopping in stsVCA and is not present without variational parameters.[54] The stsVCA is an approximate method and details of the result may depend on the size of the central part of the reference system as well as on the choice of variational parameters. We however found the genuine features to be robust when a renormalized hopping is considered.

The stsVCA certainly overestimates the effect of the excitation at high bias voltages due to its self-consistent character. We however find the same excitations, albeit with lower magnitude, in the AMEA. The results are depicted in Fig. 5 for different number of bath sites. We find qualitative robust results which indicate an increased spectral weight around $\omega = 0$ and a smeared out peak. For comparison the $U = 0$ result is depicted as well, for

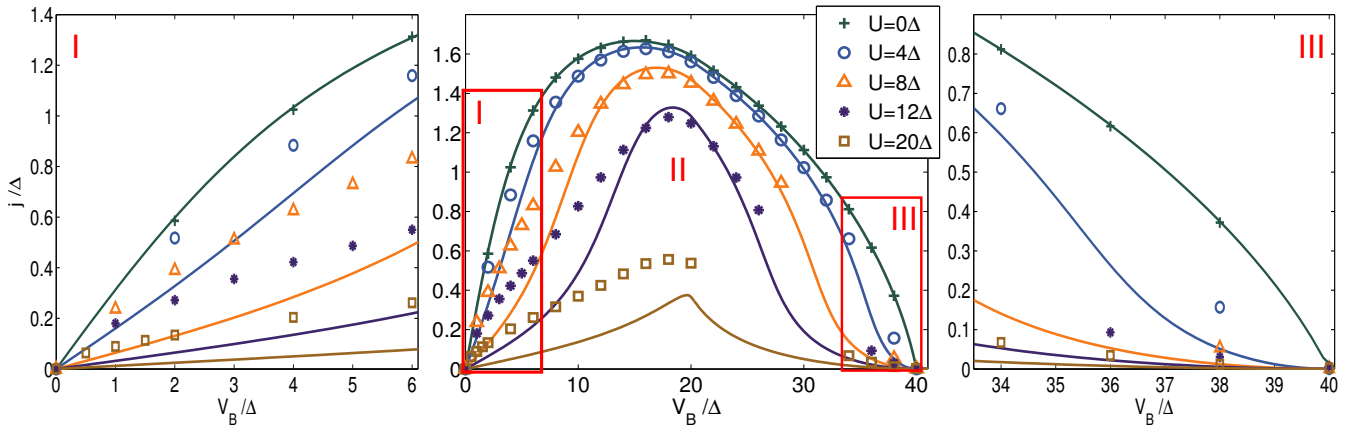

FIG. 3: (Color online) *Exact steady-state charge current* of a *noninteracting*, resonant level device with on-site potential $\epsilon_f = -\frac{U}{2}$ (solid lines) and DMRG+TEBD data for the corresponding interacting system (symbols). The parameters of these two setups are identical apart form the on-site interaction strength U missing in the *noninteracting*, resonant level model. We show five values of interaction strengths resp. on-site potentials: $\frac{U}{\Delta} = \{0, 4, 8, 12, 20\}$ resp. $\frac{\epsilon_f}{\Delta} = \{0, -2, -4, -6, -10\}$. The left/right panels show zooms to the low/high bias regime as indicated in the central part of the figure. Note the different scale on the y-axis.

the same shifted on-site energy. On has to note that already in this case a peak around $\omega = 0$ is perceptible, which is a result of the stronger hybridization of the region where the two leads overlap, see also Fig. 1. When comparing the interacting case to the $U = 0$ result, we see that a large amount of spectral weight is shifted towards zero and that the peak height at $\omega = 0$ becomes more prominent. As a consequence, the current increases, see below and compare also Fig. 3.

We attribute the increased current observed in the previous section to this newly formed low energy excitation. The current is essentially given by an integral over the transport window which convolutes the DOS of the leads with the central device.[68,69] The transmission current between the two leads can be evaluated in the Landauer-Büttiker form[70–72]

$$\langle j \rangle = \frac{e}{\hbar} \int_{-\infty}^{\infty} \frac{d\omega}{2\pi} \Big(p_{\mathrm{FD}}(\omega, \mu_L) - p_{\mathrm{FD}}(\omega, \mu_R) \Big) \mathrm{Tr} \left\{ \mathcal{T}(\omega) \right\} ,$$

where the transmission function $\mathcal{T}(\omega) = G^R(\omega)\Gamma_L(\omega) \left(G^R(\omega)\right)^\dagger \Gamma_R(\omega)$ is given in terms of $G^R(\omega) = \left((g^R(\omega))^{-1} - (\widetilde{\Sigma}_L + \widetilde{\Sigma}_R) \right)^{-1}$ with the lead broadening functions of lead α projected onto the device is $\widetilde{\Sigma}_\alpha = t' g^R_{\alpha\alpha} t'$ and $\Gamma_\alpha = -2\Im\mathrm{m}\left(\widetilde{\Sigma}_\alpha\right)$. Correlation effects at the device are incorporated in $G^R(\omega)$ which enters $\mathcal{T}(\omega)$ locally in energy. In the high bias regime the transport window which limits the current integral through the lead Fermi functions $p_{\mathrm{FD}}(\omega, \mu)$ shrinks linearly with V_B to zero as $V_B \to W$, see Fig. 1 (C). Therefore only low energy excitations of the system may contribute to the current. In an uncorrelated device with level position $\epsilon_f = -\frac{U}{2}$ only broadening assisted spectral weight contributes to transport at high bias voltage since no states of the central region lie directly within this transport energy window. In the interacting system the newly formed low energy excitations increase the transmission as a result of electronic correlations.

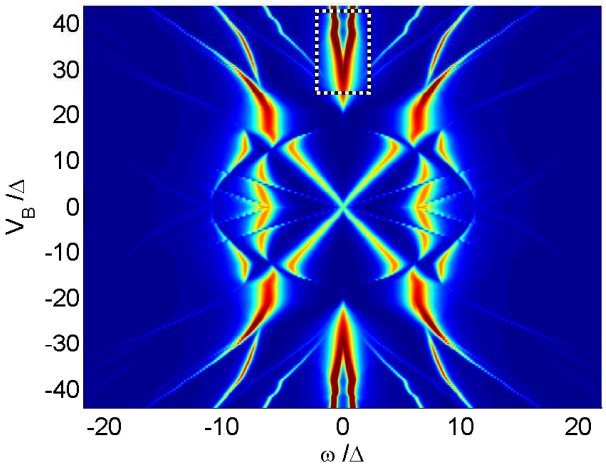

FIG. 4: (Color online) *Steady state spectral function (LDOS) of the correlated orbital.* We show data for an interaction strength of $U = 12\,\Delta$ as obtained by stsVCA on a seven site central reference system using one variational parameter which is the hopping in the central region.

IV. DISCUSSION

Next we discuss the nature of the steady-state at high bias voltages and propose a mechanism for the enhanced electronic correlations.

In our system magnetic fluctuations are directly linked to the charge fluctuations discussed above and can be

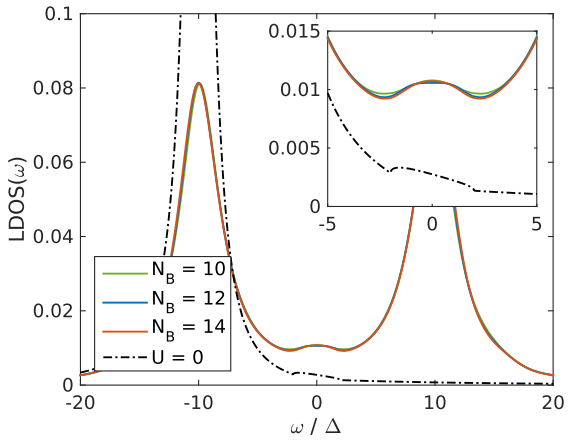

FIG. 5: (Color online) *Steady state spectral function (LDOS) of the correlated orbital.* The interaction strength is $U = 20\,\Delta$ and $V_B = 36\,\Delta$. Solid lines represent data obtained with AMEA for different number of bath sites N_B and the dash-dotted line represents the $U = 0$ result with shifted on-site energy $-10\,\Delta$.[73]

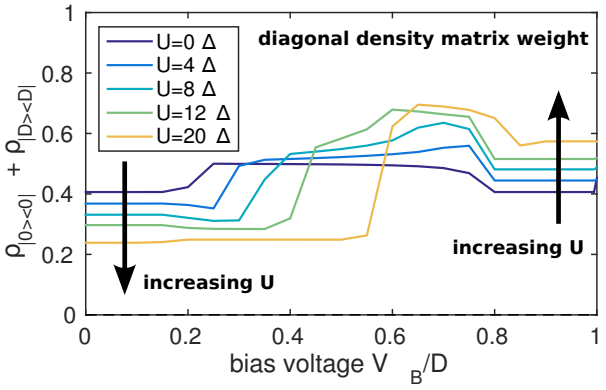

FIG. 6: (Color online) *Diagonal weight of the steady-state many-body density matrix* $\hat{\rho}$. We plot the summed weight of the density matrix diagonals where the impurity is either double occupied or empty: $\rho_{|0\rangle\langle 0|} + \rho_{|D\rangle\langle D|}$ as obtained via a quantum master equation in the Born-Markov-secular approximation at $\beta = 50$.

TABLE I: *Summary of electronic correlations according to bias voltage.*
V_B ... bias voltage: I, "low-bias" with respect to the electronic coherence energy scale T^*, II, "medium-bias" above T^* and well below the electronic lead bandwidth W, III, "high-bias" in the vicinity of the lead band edge;
correlation ... type of observed electronic correlation;
$\mathcal{D}$ ... charge fluctuations, Eq. (2);
$\mathcal{M}$ ... magnetic fluctuations, Eq. (3).

	V_B	correlation	$\mathcal{D}$	$2\mathcal{M}$
I	low	"spin"	$0 \ldots \frac{1}{4}$	$\frac{1}{2} \ldots \frac{1}{4}$
II	medium	"free"	$\frac{1}{4}$	$\frac{1}{4}$
III	high	"charge"	$\frac{1}{4} \ldots \frac{1}{2}$	$\frac{1}{4} \ldots 0$

characterized by

$$\mathcal{M} = \frac{1}{4}\langle (n_{f\uparrow} - n_{f\downarrow})^2 \rangle = \frac{1}{4}(1 - 2\mathcal{D}) \qquad (3)$$

In the free equilibrium system $\mathcal{D} = \frac{1}{4}$ we have $2\mathcal{M} = \frac{1}{4}$, see also Tab. I. As discussed above the free description applies also to the regime II of medium bias voltage in in the steady-state of our setup. In the correlated equilibrium spin Kondo state $\mathcal{D}$ decreases from $\mathcal{D} = 0.25$ at $U = 0$ to $\mathcal{D} \to 0$ for $U \to \infty$. This implies that magnetic fluctuations grow from $2\mathcal{M} = \frac{1}{4}$ at $U = 0$ to $2\mathcal{M} \to \frac{1}{2}$ for $U \to \infty$ signifying the highly fluctuating spin state. These properties are known in equilibrium[30] and our simulations show that they apply also to the low bias regime I, see Fig. 2. At high bias voltages in regime III, close to $V_B \to W$ we observe a situation vice versa as at low bias voltages. The charge fluctuations increase to $\mathcal{D} \to \frac{1}{2}$ while the magnetic fluctuations decrease to $\mathcal{M}$ *rightarrow*0. This implies that at high bias voltage the system is neither returning to its low bias spin Kondo correlations nor does it stay in the medium bias free state but approaches a new correlated state which at least in terms of spin and charge fluctuations is the "inverse" of the spin Kondo effect.

One candidate high-bias pure state compatible with the above correlations would be $|\Psi^{>}\rangle \sim \sum \left(\gamma_{\uparrow\downarrow} |\uparrow\downarrow\rangle_f - \gamma_0 |0\rangle_f\right) \otimes |L\rangle \otimes |R\rangle$. Its single-particle expectation values are $\langle n_{f\sigma}\rangle = |c_{\uparrow\downarrow}|^2$, $\langle n_f\rangle = 2|c_{\uparrow\downarrow}|^2$ and $\langle m_f\rangle = 0$, as required by symmetry. Note that this implies $|\gamma_{\uparrow\downarrow}|^2 = |\gamma_0|^2 = 0.5$. The charge fluctuations are given by $\mathcal{D} = |\gamma_{\uparrow\downarrow}|^2 = 0.5$ and the magnetic fluctuations are $\mathcal{M} = 0$, which are the values we are looking for. It is furthermore plausible, that such a state is responsible for transport in the high bias regime because the narrowing transport window contracts around $\omega = 0$. The atomic impurity states at this energy are $|0\rangle_f$ and $|\uparrow\downarrow\rangle_f$, while the singly occupied states are far outside the transport window at $\epsilon_f \approx -\frac{U}{2}$. Within a BMSme treatment, see Fig. 6 we indeed find that at high bias voltages the populations of these two device states increase with increasing correlation U. At low bias voltages on the contrary their weight decreases which signifies the growth in weight of the singly-occupied states necessary for the equilibrium spin Kondo effect. Note that the BMSme results have been obtained for a small but finite temperature of $T = 0.02\,|t|$ while all other results presented in this work are for zero temperature.

We propose that in this setup a not fully developed charge Kondo effect $|\uparrow\downarrow\rangle_L |0\rangle_f |0\rangle_R \to |0\rangle_L |0\rangle_f |\uparrow\downarrow\rangle_R$ mediated by effective pair hopping processes via the virtual state $|0\rangle_L |\uparrow\downarrow\rangle_f |0\rangle_R$ is responsible for increased charge transport.[74] The charge Kondo effect in the context of an attractive Anderson model has been explored for heavy fermion behaviour,[75] in PbTe doped with Tl impuri-

ties,[76,77] as a mechanism for large thermoelectric power in molecular quantum dots,[78] and to promote superconductivity,[79] in mesoscopic superconductors coupled to normal leads.[80]

A sound theory of a high bias charge Kondo effect does not yet exist and for a final proof a numerical nonequilibrium RG treatment at large bias voltages $V_B \approx W$ is in order. However, the effect can be easily motivated by considering the equilibrium Schrieffer-Wolff transformation[81,82] which yields the well known effective spin flip processes responsible for the equilibrium spin Kondo effect. In this transformation the fermionic degrees of freedom of the initial impurity Hamiltonian are transferred to simpler spin degrees of freedom with an effective interaction incorporating the virtual spin flips. The initial Hamiltonian can be written in block form according to its states in the $N = 1$ sector $|1\rangle = (|\uparrow\rangle\,;|\downarrow\rangle)$ and in the symmetric $N = 0/2$ sector $|X\rangle = (|0\rangle\,;|\uparrow\downarrow\rangle)$:[30]

$$\begin{bmatrix} H_{11} & H_{1X} \\ H_{X1} & H_{XX} \end{bmatrix} \begin{pmatrix} \psi_1\,|1\rangle \\ \psi_X\,|X\rangle \end{pmatrix} .$$

In the equilibrium spin Kondo effect the ground state energetically lies in the singly-occupied sector and one seeks to effectively eliminate the excited sectors $|X\rangle$ leading to the exact non-linear Schrödinger equation $\big(H_{11} + H_{1X}(\omega - H_{XX})^{-1}H_{X1}\big)\,\psi_1 \;=\; \omega\,\psi_1$. The spin Kondo Hamiltonian is then obtained by treating the second term perturbatively. In the high bias regime, the zero and doubly occupied states $|X\rangle$ lie inside the transport window and predominantly contribute to the system state. Applying the projection formalism within this block results in an equation for a charge Kondo model, which reads analogously

$$\big(H_{XX} + H_{X1}(\omega - H_{11})^{-1}H_{1X}\big)\,\psi_X = \omega\,\psi_X\,,$$

where even the arising effective terms are the same as in the spin Kondo effect with the mapping spin $\leftrightarrow$ charge: The equilibrium spin Kondo effect features a virtual spin flip between the degenerate pair $\{|\uparrow\rangle\,,|\downarrow\rangle\}$. Analogously, the high bias charge Kondo effect features a virtual double hopping process between the degenerate pair $\{|0\rangle\,,|\uparrow\downarrow\rangle\}$.

V. CONCLUSIONS

We discussed the role of electronic correlations at high bias voltage when the reservoir density of states is structured and finite and the bias voltage approaches the bandwidth. As an illustration we discuss the particular example of the steady-state of a single quantum dot connected to two leads of semicircular electronic density of states under bias voltage. We use density matrix renormalization group, time evolving block decimation, the steady-state variational cluster approach, the auxiliary master equation approach and a Born-Markov-secular quantum master equation to evaluate the steady-state double occupancy, charge current, local density of states and the reduced steady-state many-body density matrix.

In general one expects electronic correlations to impact transport characteristics at bias voltages smaller than the electronic coherence temperature. For large bias voltages it has been shown that in the wide band limit electronic correlations are dominated by the perturbing external bias. The system behaves like free and the effect of the high bias voltage is comparable to a high temperature or a high magnetic field. We do not apply the wide band limit but discuss a system which features two electronic leads with a finite and structured electronic density of states. We find that the steady-state can be classified into three regimes in bias voltage, according to the degree of electronic correlation. For low bias voltages the steady-state feels the remnants of the equilibrium spin Kondo effect. It features enhanced magnetic fluctuations and suppressed charge fluctuations. The charge current in this regime is enhanced with respect to an equivalent system without electron-electron interactions. Only states at low energies contribute to transport and their density is high due to electronic correlations. At medium bias voltages many states reside inside the transport window and we find charge and spin fluctuations comparable to those of an equilibrium noninteracting system or for the high bias steady-state in the wide band limit. The current in this regime is also comparable to the one of an equivalent noninteracting system. The finding of this work is that at high bias voltages, close to the band edge of the leads, the transport is again enhanced with respect to the noninteracting equivalent. We observe large charge fluctuations and small magnetic fluctuations in this regime. The small transport window limits the states contributing to transport again to those at low energies. These are strongly enhanced due to electronic correlations. We propose that the high bias state features the characteristics of a not fully developed charge Kondo effect.

Although our discussion is general we have presented results for a particular model system. We would like to stimulate further work in that direction by looking at different models and differently structured electronic reservoirs. In particular a renormalization group study around the point of high bias and vanishing reservoir band overlap would be desirable since here numerical approaches become difficult due to long time-scales. On the experimental side it could be challenging to find a nanoscopic system which exhibits the required features of the reservoir density of states and allows for application of a corresponding high bias voltage. We would like to point out however, that to observe the reported features one does not necessarily have to probe the band edges. It may suffice to find a structured DOS with low minima. Such an experiment could provide essential insight into electronic correlations at high bias voltage.

Acknowledgments

We gratefully acknowledge fruitful discussion with Sabine Andergassen. This work was partly supported by the Austrian Science Fund (FWF) P24081-N16, and SFB-ViCoM projects F04103 and F04104. Extensive numerical calculations have been conducted at the Vienna Scientific Cluster (VSC-I&II).

* martin.nuss@tugraz.at

[1] G. Cuniberti, G. Fagas, and K. Richter, *Introducing Molecular Electronics* (Springer, 2005), ISBN 3540279946.
[2] A. Nitzan and M. A. Ratner, Science **300**, 1384 (2003).
[3] N. Agrait, A. L. Yeyati, and J. M. van Ruitenbeek, Physics Reports **377**, 81 (2003).
[4] J. C. Cuevas and E. Scheer, *Molecular Electronics: An Introduction to Theory and Experiment* (World Scientific Publishing Company, 2010), 1st ed., ISBN 9814282588.
[5] Y. V. Nazarov and Y. M. Blanter, *Quantum Transport: Introduction to Nanoscience* (Cambridge University Press New York, 2009), ISBN 0521832462.
[6] M. D. Ventra, *Electrical Transport in Nanoscale Systems* (Cambridge University Press, New York, 2008), ISBN 0521896347.
[7] D. K. Ferry, S. M. Goodnick, and J. Bird, *Transport in Nanostructures* (Cambridge University Press, 2009), 2nd ed., ISBN 0521877482.
[8] M. A. Kastner, Rev. Mod. Phys. **64**, 849 (1992).
[9] D. Goldhaber-Gordon, H. Shtrikman, D. Mahalu, D. Abusch-Magder, U. Meirav, and M. A. Kastner, Nature **391**, 156 (1997).
[10] S. M. Cronenwett, T. H. Oosterkamp, and L. P. Kouwenhoven, Science **281**, 540 (1998).
[11] M. Pustilnik and L. Glazman, Journal of Physics: Condensed Matter **16**, R513 (2004).
[12] N. Agrait, A. L. Yeyati, and J. M. van Ruitenbeek, Physics Reports **377**, 81 (2003).
[13] R. J. Nichols, W. Haiss, S. J. Higgins, E. Leary, S. Martin, and D. Bethell, Phys. Chem. Chem. Phys. **12**, 2801 (2010).
[14] J.-P. Brantut, J. Meineke, D. S. S. Krinner, and T. Esslinger, arXiv:1203.1927 (2012).
[15] U. Schneider, L. Hackermuller, J. P. Ronzheimer, S. Will, S. Braun, T. Best, I. Bloch, E. Demler, S. Mandt, D. Rasch, et al., Nature Physics **8**, 213 (2012).
[16] S. Trotzky, P. Cheinet, S. Fölling, M. Feld, U. Schnorrberger, A. M. Rey, A. Polkovnikov, E. A. Demler, M. D. Lukin, and I. Bloch, Science **319**, 295 (2008).
[17] N. Strohmaier, D. Greif, R. Jördens, L. Tarruell, H. Moritz, T. Esslinger, R. Sensarma, D. Pekker, E. Altman, and E. Demler, Phys. Rev. Lett. **104**, 080401 (2010).
[18] M. Greiner, O. Mandel, T. W. Hänsch, and I. Bloch, Nature **419**, 51 (2002).
[19] L. Mühlbacher, D. F. Urban, and A. Komnik, Phys. Rev. B **83**, 075107 (2011).
[20] M. Pletyukhov and H. Schoeller, Phys. Rev. Lett. **108**, 260601 (2012).
[21] A. V. Kretinin, H. Shtrikman, and D. Mahalu, Phys. Rev. B **85**, 201301 (2012).
[22] A. V. Kretinin, H. Shtrikman, D. Goldhaber-Gordon, M. Hanl, A. Weichselbaum, J. von Delft, T. Costi, and D. Mahalu, Phys. Rev. B **84**, 245316 (2011).
[23] M. Pletyukhov, D. Schuricht, and H. Schoeller, Phys. Rev. Lett. **104**, 106801 (2010).
[24] Strictly speaking, the DOS $\rho_{L/R}(\omega) = -\frac{1}{\pi}\Im\mathrm{m}\left(g^R_{L/R}(\omega)\right)$ is obtained by taking the limit $D \to +\infty$ using a single-particle retarded Green's function for the left (L) and right (R) lead:[27] $g^R_{L/R}(\omega) = -\frac{1}{2D}\ln\left(\frac{\omega+i0^+-D}{\omega+i0^++D}\right)$ with half-bandwidth D. The then vanishing small DOS is compensated by a larger coupling t' of the device to the lead by keeping $\frac{t'^2}{D}$ constant.
[25] I. Bâldea and H. Köppel, Phys. Rev. B **81**, 193401 (2010).
[26] P. W. Anderson, Phys. Rev. **124**, 41 (1961).
[27] E. N. Economou, *Green's Functions in Quantum Physics* (Springer, 2010), 3rd ed., ISBN 3642066917.
[28] A. Kawabata, Reports on Progress in Physics **70**, 219 (2007).
[29] A. Kawabata, Journal of the Physical Society of Japan **65**, 30 (1996).
[30] A. C. Hewson, *The Kondo Problem to Heavy Fermions* (Cambridge University Press, 1997), ISBN 0521599474.
[31] U. Schollwöck, Annals of Physics **326**, 96 (2011), january 2011 Special Issue.
[32] E. Boulat, H. Saleur, and P. Schmitteckert, Phys. Rev. Lett. **101**, 140601 (2008).
[33] F. Heidrich-Meisner, A. E. Feiguin, and E. Dagotto, Phys. Rev. B **79**, 235336 (2009).
[34] P. Schmitteckert, Phys. Rev. B **70**, 121302 (2004).
[35] K. A. Al-Hassanieh, A. E. Feiguin, J. A. Riera, C. A. Büsser, and E. Dagotto, Phys. Rev. B **73**, 195304 (2006).
[36] F. Heidrich-Meisner, I. González, K. A. Al-Hassanieh, A. E. Feiguin, M. J. Rozenberg, and E. Dagotto, Phys. Rev. B **82**, 205110 (2010).
[37] M. Žnidarič, Phys. Rev. Lett. **106**, 220601 (2011).
[38] S. Jesenko and M. Žnidarič, Phys. Rev. B **84**, 174438 (2011).
[39] F. Heidrich-Meisner, G. B. Martins, C. A. Bsser, K. A. Al-Hassanieh, A. E. Feiguin, G. Chiappe, E. V. Anda, and E. Dagotto, The European Physical Journal B **67**, 527 (2009).
[40] S. Kirino, T. Fujii, J. Zhao, and K. Ueda, Journal of the Physical Society of Japan **77**, 084704 (2008).
[41] S. Kirino and K. Ueda, Journal of the Physical Society of Japan **79**, 093710 (2010).
[42] M. A. Cazalilla and J. B. Marston, Phys. Rev. Lett. **88**, 256403 (2002).
[43] H. G. Luo, T. Xiang, and X. Q. Wang, Phys. Rev. Lett. **91**, 049701 (2003).
[44] M. A. Cazalilla and J. B. Marston, Phys. Rev. Lett. **91**, 049702 (2003).
[45] G. Vidal, Phys. Rev. Lett. **93**, 040502 (2004).
[46] S. R. White, Phys. Rev. B **48**, 10345 (1993).
[47] M. Nuss, M. Ganahl, H. G. Evertz, E. Arrigoni, and W. von der Linden, Phys. Rev. B **88**, 045132 (2013).
[48] M. Knap, W. von der Linden, and E. Arrigoni, Phys. Rev. B **84**, 115145 (2011).
[49] M. Nuss, C. Heil, M. Ganahl, M. Knap, H. G. Evertz, E. Arrigoni, and W. von der Linden, Phys. Rev. B **86**, 245119 (2012).

[50] J. Rammer and H. Smith, Rev. Mod. Phys. **58**, 323 (1986).

[51] C. Gros and R. Valenti, Phys. Rev. B **48**, 418 (1993).

[52] Sénéchal, D. Perez, and M. Pioro-Ladriére, Phys. Rev. Lett. **84**, 522 (2000).

[53] Z. Bai, J. Demmel, J. Dongarra, A. Ruhe, and H. van der Vorst, *Templates for the Solution of Algebraic Eigenvalue Problems: A Practical Guide (Software, Environments and Tools)* (Society for Industrial and Applied Mathematics, 1987), ISBN 0898714710.

[54] M. Nuss, E. Arrigoni, M. Aichhorn, and W. von der Linden, Phys. Rev. B **85**, 235107 (2012).

[55] E. Arrigoni, M. Knap, and W. von der Linden, Phys. Rev. Lett. **110**, 086403 (2013), URL `http://link.aps.org/doi/10.1103/PhysRevLett.110.086403`.

[56] A. Dorda, M. Nuss, W. von der Linden, and E. Arrigoni, Phys. Rev. B **89**, 165105 (2014).

[57] A. Dorda, M. Ganahl, H. Evertz, W. von der Linden, and E. Arrigoni (tbp 2015), "Auxiliary master equation approach within matrix product states: Spectral properties of the nonequilibrium Anderson impurity model.".

[58] H.-P. Breuer and F. Petruccione, *The Theory of Open Quantum Systems* (Oxford University Press, 2002), ISBN 0198520638.

[59] H. J. Carmichael, *An Open Systems Approach to Quantum Optics: Lectures Presented at the Universite Libre De Bruxelles October 28 to November 4, 1991 (Lecture Notes in Physics New Series M)* (Springer-Verlag, 1993), ISBN 0387566341.

[60] H. J. Carmichael, *Statistical Methods in Quantum Optics 1: Master Equations and Fokker-Planck Equations* (Springer, 2010), ISBN 3642081339.

[61] G. Schaller, *Non-Equilibrium Master Equations* (2014).

[62] G. Schaller, *Open Quantum Systems Far from Equilibrium* (Springer, Cham ; New York, 2014), auflage: 2014 ed., ISBN 9783319038766.

[63] C. Cohen-Tannoudji, J. Dupont-Roc, and G. Grynberg, *http://www.amazon.com/Atom-Photon-Interactions-Basic-Processes-Applications/dp/0471293369* (Wiley-VCH, 1998), ISBN 0471293369.

[64] M. Nuss, G. Dorn, A. Dorda, W. von der Linden, and E. Arrigoni (2015).

[65] A. Dirks, S. Schmitt, J. E. Han, F. Anders, P. Werner, and T. Pruschke, EPL (Europhysics Letters) **102**, 37011 (2013).

[66] A. Rosch, Eur. Phys. J. B **85**, 6 (2012).

[67] A. Branschaedel, G. Schneider, and P. Schmitteckert, Annalen der Physik **522**, 657 (2010), ISSN 1521-3889.

[68] Y. Meir and N. S. Wingreen, Phys. Rev. Lett. **68**, 2512 (1992).

[69] N. S. Wingreen, A.-P. Jauho, and Y. Meir, Phys. Rev. B **48**, 8487 (1993).

[70] H. Haug and A. Jauho, *Quantum Kinetics in Transport and Optics of Semiconductors* (Springer-Verlag GmbH, 1996), 2nd ed., ISBN 3540616020.

[71] S. Datta, *Quantum Transport: Atom to Transistor* (Cambridge University Press, 2005), 2nd ed., ISBN 0521631459.

[72] M. Knap, E. Arrigoni, and W. von der Linden, Phys. Rev. B **88**, 054301 (2013).

[73] In order to focus on the low energy physics, a weighting is introduced in the fit of the hybridization function which reproduces the region $\omega \in (-10\,\Delta, 10\,\Delta)$ more accurately. Since a precise treatment of the Fermi edges is not of relevance here, $T = \Delta$ is used for fitting the Keldysh component.

[74] H. Matsuura and K. Miyake, arXiv:1209.5519 (2012).

[75] A. Taraphder and P. Coleman, Phys. Rev. Lett. **66**, 2814 (1991).

[76] Y. Matsushita, H. Bluhm, T. H. Geballe, and I. R. Fisher, Phys. Rev. Lett. **94**, 157002 (2005).

[77] T. A. Costi and V. Zlatić, Phys. Rev. Lett. **108**, 036402 (2012).

[78] S. Andergassen, T. A. Costi, and V. Zlatić, Phys. Rev. B **84**, 241107 (2011).

[79] M. Dzero and J. Schmalian, Phys. Rev. Lett. **94**, 157003 (2005).

[80] I. Garate, Phys. Rev. B **84**, 085121 (2011).

[81] J. R. Schrieffer and P. A. Wolff, Phys. Rev. **149**, 491 (1966).

[82] S. Bravyi, D. P. DiVincenzo, and D. Loss, Annals of Physics **326**, 2793 (2011), ISSN 0003-4916.

A. Extended variational cluster approach for $Li_{0.9}Mo_6O_{17}$

Here we give some additional details to the study of $Li_{0.9}Mo_6O_{17}$ presented in [41].

A.1. Crystal structure

The lattice parameters of the monoclinic crystal structure are given in Tab. A.1, the basis vectors will be denoted $\boldsymbol{u}_a, \boldsymbol{u}_b$ and $\boldsymbol{u}_c$ in the following. We predominantly work in the $b-c$ plane where a four Mo orbital unit cell is defined as

$$Mo_1 : \boldsymbol{r}_A = \begin{pmatrix} 0.9939a \\ 0.25b \\ 0.23356c \end{pmatrix}, Mo_4 : \boldsymbol{r}_C = \begin{pmatrix} 0.16635a \\ 0.25b \\ 0.9206c \end{pmatrix}, \quad Mo_1' : \boldsymbol{r}_D = \begin{pmatrix} 0.00613a \\ 0.75b \\ 0.7664c \end{pmatrix}, Mo_4' : \boldsymbol{r}_B = \begin{pmatrix} 0.8337a \\ 0.75b \\ 0.07938c \end{pmatrix}.$$

A.2. Lattice and super-lattice

The partitioning of the material's lattice γ of L^γ orbitals into clusters C of L^C orbitals introduces a super-lattice Γ of L^Γ orbitals. The original lattice γ is recovered upon attaching one cluster C at each site of the super-lattice Γ. The coordinates of the lattice may be expressed as [322]

$$\boldsymbol{r}_i^\gamma = \mathbf{r}_I^\Gamma + \boldsymbol{r}_\alpha^C \,, \quad i \to (I, \alpha) \,.$$

The L^γ reciprocal space vectors $\boldsymbol{k}^\gamma$ in the first Brillouin zone (BZ) of the original lattice BZ^γ may be expressed as

$$\boldsymbol{k}^\gamma = \boldsymbol{K} + \boldsymbol{k}^\Gamma \,,$$

where $\mathbf{K}$ belongs to both the reciprocal super-lattice Γ^{-1} and to BZ^γ while $\mathbf{k}^\Gamma$ belongs to the Brillouin zone of the super-lattice BZ^Γ.

lat. param.	a	b	c	β
Angström, degrees	12.762	5.523	9.499	90.61

Table A.1.: Effective lattice parameters for the monoclinic crystal structure. We henceforth work in the $b-c$ plane only. β is the angle between the a and c axis. From [464].

A.2.1. Orbital space lattice structure

For the two-dimensional lattice considered here, the four orbital physical unit cell $U = \{\mathcal{A}, \mathcal{B}, \mathcal{C}, \mathcal{D}\}$ and the eight orbital cluster $C = \{A, B, C, D, E, F, G, H\}$ are described by the lattice coordinates

$$\begin{aligned}
\boldsymbol{u}_{\mathcal{A}} = \boldsymbol{c}_A = \begin{pmatrix} 0 \\ 0 \end{pmatrix}, \; \boldsymbol{u}_{\mathcal{B}} = \boldsymbol{c}_B = \begin{pmatrix} a \\ 0 \end{pmatrix}, \\
\boldsymbol{u}_{\mathcal{C}} = \boldsymbol{c}_C = \begin{pmatrix} 0 \\ a_\perp \end{pmatrix}, \; \boldsymbol{u}_{\mathcal{D}} = \boldsymbol{c}_D = \begin{pmatrix} a \\ a_\perp \end{pmatrix}, \\
\boldsymbol{c}_E = \begin{pmatrix} 0 \\ a_\perp + a' \end{pmatrix}, \; \boldsymbol{c}_F = \begin{pmatrix} a \\ a_\perp + a' \end{pmatrix}, \\
\boldsymbol{c}_G = \begin{pmatrix} 0 \\ 2a_\perp + a' \end{pmatrix}, \; \boldsymbol{c}_H = \begin{pmatrix} a \\ 2a_\perp + a' \end{pmatrix},
\end{aligned}$$

where a is the lattice constant in ladder direction, $a_\perp$ the lattice constant perpendicular to the ladder direction and a' the ladder spacing.
The real space lattice vectors of the original lattice γ are then given by

$$\boldsymbol{R}_1^\gamma = \begin{pmatrix} 2a \\ 0 \end{pmatrix}, \qquad \boldsymbol{R}_2^\gamma = \begin{pmatrix} 0 \\ a_\perp + a' \end{pmatrix}, \tag{A.1}$$

The real space lattice vectors of the super lattice Γ are given by

$$\boldsymbol{R}_1^\Gamma = \begin{pmatrix} 2a \\ 0 \end{pmatrix}, \qquad \boldsymbol{R}_2^\Gamma = \begin{pmatrix} 0 \\ 2(a_\perp + a') \end{pmatrix}, \tag{A.2}$$

A.2.2. Reciprocal space lattice structure

The reciprocal space lattice vectors of the original lattice K^γ are then given by

$$\boldsymbol{K}_1^\gamma = 2\pi \begin{pmatrix} \frac{1}{2a} \\ 0 \end{pmatrix}, \qquad \boldsymbol{K}_2^\gamma = 2\pi \begin{pmatrix} 0 \\ \frac{1}{a_\perp + a'} \end{pmatrix}, \tag{A.3}$$

The reciprocal space lattice vectors of the super lattice K^Γ are given by

$$\boldsymbol{K}_1^\Gamma = 2\pi \begin{pmatrix} \frac{1}{2a} \\ 0 \end{pmatrix}, \qquad \boldsymbol{R}_2^\Gamma = 2\pi \begin{pmatrix} 0 \\ \frac{1}{2(a_\perp + a')} \end{pmatrix}. \tag{A.4}$$

A.2.3. Brillouin zone and path through reciprocal space

Within the eVCA calculation three sets of wave vectors are important. For the evaluation of the grand potential sums over the first Brillouin zone of the super-lattice Γ have to be conducted. For the evaluation of the density of states, sums over the first Brillouin zone of the original lattice γ have to be evaluated and finally to obtain spectra a suitable path through the Brillouin zone has to be chosen.

The set of reciprocal space vectors in the first Brillouin zone of the super lattice Γ is given by

$$k_x^\Gamma = -\frac{\pi}{2a} + \frac{\frac{2\pi}{2a}}{N_x^\Gamma} \times \{0, \ldots, N_x^\Gamma - 1\}$$
$$k_y^\Gamma = -\frac{\pi}{2(a_\perp + a')} + \frac{\frac{2\pi}{2(a_\perp + a')}}{N_y^\Gamma} \times \{0, \ldots, N_y^\Gamma - 1\},$$

where $N_x\Gamma$ is the number of lattice points in ladder (x) direction and $N_y\Gamma$ is the number of lattice points perpendicular to the ladder (y) direction.
The set of reciprocal space vectors in the first Brillouin zone of the original lattice γ is given by

$$k_x^\gamma = -\frac{\pi}{2a} + \frac{\frac{2\pi}{2a}}{N_x^\gamma} \times \{0, \ldots, N_x^\gamma - 1\}$$
$$k_y^\gamma = -\frac{\pi}{a_\perp + a'} + \frac{\frac{2\pi}{a_\perp + a'}}{N_y^\gamma} \times \{0, \ldots, N_y^\gamma - 1\},$$

where $N_x\gamma$ is the number of lattice points in ladder (x) direction and N_y^γ is the number of lattice points perpendicular to the ladder (y) direction. Note that $N_x^\Gamma = N_x^\gamma$ and $2N_y^\Gamma = N_y^\gamma$.
A suitable path through the first Brillouin zone is given by going from the center to the border in x direction

$$k_x^{1.\mathrm{BZ}} = [0, \frac{\pi}{2a}]$$
$$k_y^{1.\mathrm{BZ}} = 0,$$

then to the border in y direction

$$k_x^{1.\mathrm{BZ}} = \frac{\pi}{2a}$$
$$k_y^{1.\mathrm{BZ}} = [0, \frac{\pi}{a_\perp + a'}],$$

and back to the center

$$k_x^{1.\mathrm{BZ}} = [\frac{\pi}{2a}, 0]$$
$$k_y^{1.\mathrm{BZ}} = [\frac{\pi}{a_\perp + a'}, 0].$$

Since the physics is expected to be quasi one-dimensional in x direction, significant dispersion should only appear in the first part.

A.3. Cluster Green's function

As outlined in [329], if we are dealing with a translationally invariant system it is possible to obtain the ground state and single-particle Green's function of the cluster Hamiltonian $\hat{\mathcal{H}}^{\mathrm{cl}}(\boldsymbol{\varphi}, \boldsymbol{\Delta})$: $g_{ij}(z, \boldsymbol{\varphi}, \boldsymbol{\Delta})$ in the Q-Matrix formalism. Here z denotes a scalar complex energy variable and the indices $i, j \in \{1, \ldots, L\}$ cluster sites. The spectral (Lehmann) representation of the single-particle

Green's function for the zero temperature case in the energy domain is given by

$$g_{ij}^{\sigma\sigma'}(z) = \sum_{\tau}\left(\sum_{n}\frac{{}^{\tau}\langle\Psi_0|c_i^{\sigma}\ |n\rangle^{\tau}\ {}^{\tau}\langle n|c_j^{\sigma'\dagger}|\Psi_0\rangle^{\tau}}{z-(\omega_n^{\tau}-\omega_0^{\tau})}\right.$$
$$\left.-\eta\sum_{m}\frac{{}^{\tau}\langle\Psi_0|c_j^{\sigma'\dagger}|m\rangle^{\tau}\ {}^{\tau}\langle m|c_i^{\sigma}\ |\Psi_0\rangle^{\tau}}{z+(\omega_m^{\tau}-\omega_0^{\tau})}\right). \tag{A.5}$$

The sum over τ denotes a sum over a possibly d-fold degenerate set of ground states (denoted by subscript zero). We are dealing with a Hamiltonian which both conserves spin S as well as particle number N. Therefore the sums over n and m denote the subspaces with $N_0+1, S_0+\frac{1}{2}$ (particle part) and $N_0-1, S_0-\frac{1}{2}$ (hole part) particles respectively (all other matrix elements vanish identically). The index η is -1 for fermions.
This may be recast in a convenient matrix form the so-called Q-matrices [458]

$$g_{ij}^{\sigma\sigma'}(z) = \sum_{\tau}\left(\sum_{\gamma}q_{i\gamma}^{\sigma}\frac{1}{z-\lambda_\gamma}q_{j\gamma}^{\sigma'\dagger}\right)_{\tau} \tag{A.6}$$
$$q_{i\gamma}^{\sigma\dagger} = \begin{cases}\frac{1}{\sqrt{d}} < \gamma|\hat{c}_i^{\sigma\dagger}|\Psi_0 > & \text{particle part}\\ \frac{1}{\sqrt{d}} < \Psi_0|\hat{c}_i^{\sigma\dagger}|\gamma > & \text{hole part}\end{cases}$$
$$\lambda_\gamma = \begin{cases}\omega_\gamma-\omega_0 & \text{particle part}\\ \omega_0-\omega_\gamma & \text{hole part}\end{cases}.$$

To ease the notation the degeneracy index τ is suppressed on the individual quantities. The excited state energies are denoted by ω_γ. Introducing the diagonal matrix

$$\nu_{\gamma\gamma'}(z) := \frac{\delta_{\gamma\gamma'}}{z-\lambda_\gamma},$$

the cluster Green's function may be rewritten in matrix form

$$g(z) = q\,\nu(z)q^{\dagger} \tag{A.7}$$
$$[L\times L] = [L\times N_\gamma][N_\gamma\times N_\gamma][N_\gamma\times L].$$

Due to spin symmetry we define from now on all Green's functions to hold just the spin up component and use factors of two when appropriate. Here N_γ is the size of the excited state space and L the size of the cluster. It should be noted that the dimension of the Green's function is of cluster size (in general of system-size times spin multiplicity). The matrices q, containing the weights of the excitations, are of dimension $L\times N_\gamma$. The matrix $\nu(z)$ is the only dynamic quantity and is diagonal of size $N_\gamma\times N_\gamma$.

A.4. Lattice Green's function

As discussed in [329], the CPT relation to obtain the Green's function of the full system $\mathrm{G}^{-1}(z, \boldsymbol{k})$ is

$$\mathrm{G}^{-1}(z, \boldsymbol{k}) = \mathrm{g}^{-1}(z) - \mathrm{T}(\boldsymbol{k}) \,, \tag{A.8}$$

where $\mathrm{g}(z)$ is the cluster Green's function and $\mathrm{T}(\boldsymbol{k})$ is the super-lattice wavevector transform of the (single-particle) inter-cluster Hamiltonian. In Q-matrix formulation this can be rewritten

$$\mathrm{G}(z, \boldsymbol{k}) = \mathrm{q} \frac{1}{z - (\Lambda' + \mathrm{q}^\dagger \mathrm{T}(\boldsymbol{k}) \mathrm{q})} \mathrm{q}^\dagger \,,$$

where a diagonal matrix for the excitation energies λ' of the cluster

$$\Lambda'_{\gamma\gamma'} \coloneqq \lambda'_\gamma \delta_{\gamma\gamma'} \,, \tag{A.9}$$

has been introduced. To put this into an even more handy form we introduce the matrix

$$\mathrm{M}_{\boldsymbol{k}} \coloneqq \Lambda' + \mathrm{q}^\dagger \mathrm{T}(\boldsymbol{k}) \mathrm{q} \,,$$

so that the CPT Green's function is then given by

$$\mathrm{G}(z, \boldsymbol{k}) = \mathrm{q} \frac{1}{\omega - \mathrm{M}(\boldsymbol{k})} \mathrm{q}^\dagger \,. \tag{A.10}$$

Upon solving the (ω-independent) eigenvalue problem

$$\mathrm{M}_{\boldsymbol{k}} \, X_{\boldsymbol{k}} = X_{\boldsymbol{k}} \, \Lambda_{\boldsymbol{k}} \,, \tag{A.11}$$

it is possible to rewrite the fraction appearing in Eq. (A.10) as

$$\frac{1}{z - \mathrm{M}_{\boldsymbol{k}}} = X_{\boldsymbol{k}} \, (z - \Lambda_{\boldsymbol{k}})^{-1} \, X_{\boldsymbol{k}}^{-1} \,.$$

The $\Lambda_{\boldsymbol{k}}$ are diagonal matrices holding the excitation energies of the full system on the diagonal. They are the $\mathbf{k}$-dependent equivalent to the Λ' defined in Eq. (A.9) for the cluster solution. Inserting this result into Eq. (A.10) one obtains the $\boldsymbol{k}$-dependent weights $\mathrm{Q}_{\boldsymbol{k}}$ for the CPT Green's function

$$\mathrm{G}(z, \boldsymbol{k}) = \underbrace{\mathrm{q} X_{\mathbf{k}}}_{\mathrm{Q}_{\boldsymbol{k}}} \, (z - \Lambda_{\boldsymbol{k}})^{-1} \, \underbrace{X_{\boldsymbol{k}}^{-1} \mathrm{q}^\dagger}_{\mathrm{Q}_{\boldsymbol{k}}^\dagger} \,, \tag{A.12}$$

$$[L \times L] = [L \times N_\gamma][N_\gamma \times N_\gamma][N_\gamma \times L] \,.$$

A.4.1. Green's function periodization

As discussed in [329], the factorization of the total lattice into clusters breaks the translational symmetry of the lattice. This may be circumvented by a periodization prescription $\mathrm{G}_{ij} \to \mathrm{G}_{\alpha\beta}$ that provides a total Green's function $\mathrm{G}_{\alpha\beta}(z, \boldsymbol{k})$, depending only on the indices of the physical unit cell and one wave vector $\boldsymbol{k}$. The periodization prescription proposed for systems with a

single orbital unit cell in [322] reads:

$$\begin{aligned} \mathrm{G}(z,\boldsymbol{k}) &= \frac{1}{L}\sum_{\boldsymbol{r}^C,\boldsymbol{r}^{C'}}^{L} e^{-i\boldsymbol{k}\cdot\left(\boldsymbol{r}^C-\boldsymbol{r}^{C'}\right)}\,\mathrm{G}_{\boldsymbol{r}^C\boldsymbol{r}^{C'}}(z,\boldsymbol{k}) \\ &= \frac{1}{L}\sum_{i,j}^{L} e^{-i\boldsymbol{k}\cdot(\boldsymbol{c}_i-\boldsymbol{c}_j)}\,\mathrm{G}_{ij}(z,\boldsymbol{k})\,. \end{aligned}$$

The $\mathbf{c}_i$ are the cluster basis vectors. This expression may be generalized for physical unit cells consisting of more than one atom:

$$\mathrm{G}_{\alpha\beta}(z,\boldsymbol{k}) = \frac{L_{\mathrm{phys.}}}{L}\sum_{i\epsilon\alpha}\sum_{j\epsilon\beta} e^{-i\boldsymbol{k}\cdot(\boldsymbol{c}_i-\boldsymbol{c}_j)}\,\mathrm{G}_{ij}(z,\boldsymbol{k})\,,$$

where α,β denote the translationally inequivalent lattice sites of the model under consideration and $L_{\mathrm{phys.}}$ the size of the physical unit cell.

A.5. Extended variational cluster approach

We tackle the model Hamiltonian within eVCA [46, 343]. The hopping parameters are about to be produced by down folding within Wannier90 [5] from an accurate Wien-2k DFT calculation. The interactions possibly can be obtained from constraint RPA.
To proceed with eVCA it is necessary to partition the lattice into cluster $\hat{\mathcal{H}}^{\mathrm{cl}}$ and inter-cluster $\hat{\mathcal{H}}^{\mathrm{inter}}$ Hamiltonian respectively

$$\hat{\mathcal{H}} = \hat{\mathcal{H}}^{\mathrm{cl}} + \hat{\mathcal{H}}^{\mathrm{inter}}\,,$$

where only single-particle terms are allowed in the inter-cluster part. Since the model considered here also contains off diagonal Coulomb interactions, an additional mean field treatment is needed for two-particle terms which extend over the cluster boundary (see Sec. A.6). In analogy to [46] we define the cluster Hamiltonian

$$\hat{\mathcal{H}}^{\mathrm{cl}}(\boldsymbol{\Delta},\boldsymbol{\varphi}) = \hat{\mathcal{H}}_0^{\mathrm{cl}}(\boldsymbol{\Delta}) + \hat{\mathcal{H}}_1^{\mathrm{cl}} + \hat{\mathcal{H}}_{\mathrm{mf}}^{\mathrm{cl}}(\boldsymbol{\varphi})\,,$$

where the single-particle terms $\hat{\mathcal{H}}_0^{\mathrm{cl}}$ depend on the VCA variational parameters $\boldsymbol{\Delta}$, the two-particle terms are denoted $\hat{\mathcal{H}}_1^{\mathrm{cl}}$ and the mean field contributions of interactions across the cluster boundary are denoted $\hat{\mathcal{H}}_{\mathrm{mf}}^{\mathrm{cl}}$ with mean field parameters $\boldsymbol{\varphi}$. Here we choose eight-orbital clusters which are both large enough to capture the interesting features of the Hamiltonian and small enough to obtain feasible calculation times. In order to include as many of the interactions $\mathbf{V}$ already on the cluster level we choose to include two ladders with four orbitals each.

The single-particle part of the cluster Hamiltonian is given by

$$\begin{aligned} \hat{\mathcal{H}}_0^{\mathrm{cl}}(\boldsymbol{\Delta}) = (\epsilon+\Delta_\epsilon) &\sum_{j=\{A,\ldots,H\},\sigma} \hat{n}_{j,\sigma} \\ &- t\sum_{\sigma}\left(c^\dagger_{A,\sigma}c_{B,\sigma} + c^\dagger_{C,\sigma}c_{D,\sigma} + c^\dagger_{E,\sigma}c_{F,\sigma} + c^\dagger_{G,\sigma}c_{H,\sigma} + h.c.\right) \\ &- t_\perp\sum_{\sigma}\left(c^\dagger_{A,\sigma}c_{C,\sigma} + c^\dagger_{B,\sigma}c_{D,\sigma} + c^\dagger_{E,\sigma}c_{G,\sigma} + c^\dagger_{F,\sigma}c_{H,\sigma} + h.c.\right) \\ &- (t'+\Delta_{t'})\sum_{\sigma}\left(c^\dagger_{E,\sigma}c_{D,\sigma} + h.c.\right), \end{aligned} \tag{A.13}$$

where the on-site energy ϵ and the zig-zag inter ladder hopping t' are extended as a VCA variational parameter $\mathbf{\Delta} = \{\Delta_\epsilon, \Delta_{t'}\}$. We use a variational chemical potential for thermodynamic consistency and a variational inter ladder hopping to introduce freedom for natural decoupling into one-dimensional objects.

The two-particle part of the cluster Hamiltonian is given by

$$\begin{aligned}
\hat{\mathcal{H}}_1^{\mathrm{cl}} = U & \sum_{j=\{A,\ldots,H\}} \hat{n}_{j,\uparrow}\hat{n}_{j,\downarrow} \\
& + \sum_{\sigma,\sigma'} \Bigg(\\
& V \left(\hat{n}_{A,\sigma}\hat{n}_{B,\sigma'} + \hat{n}_{C,\sigma}\hat{n}_{D,\sigma'} + \hat{n}_{E,\sigma}\hat{n}_{F,\sigma'} + \hat{n}_{G,\sigma}\hat{n}_{H,\sigma'}\right) \\
& + V_\perp \left(\hat{n}_{A,\sigma}\hat{n}_{C,\sigma'} + \hat{n}_{B,\sigma}\hat{n}_{D,\sigma'} + \hat{n}_{E,\sigma}\hat{n}_{G,\sigma'} + \hat{n}_{F,\sigma}\hat{n}_{H,\sigma'}\right) \\
& + V' \left(\hat{n}_{A,\sigma}\hat{n}_{D,\sigma'} + \hat{n}_{B,\sigma}\hat{n}_{C,\sigma'} + \hat{n}_{E,\sigma}\hat{n}_{H,\sigma'} + \hat{n}_{F,\sigma}\hat{n}_{G,\sigma'}\right) \\
& + V'' \left(0\right) \\
& + V''' \left(\hat{n}_{D,\sigma}\hat{n}_{E,\sigma'}\right) \\
& + V'''' \left(\hat{n}_{C,\sigma}\hat{n}_{E,\sigma'} + \hat{n}_{D,\sigma}\hat{n}_{F,\sigma'}\right) \Bigg).
\end{aligned} \tag{A.14}$$

A.6. Mean field extension

A generic mean field part of the cluster Hamiltonian is obtained by introducing mean fields for each four-Fermi term which extends over the cluster boundary (indices a and b are located in different clusters and linked by V_{ab})

$$\begin{aligned}
\hat{\mathcal{H}}_{\mathrm{mf}} &= V_{ab} \sum_{\sigma,\sigma'} \hat{n}_{a,\sigma}\hat{n}_{b,\sigma'} \\
&= V_{ab} \left(\sum_\sigma \left(\hat{n}_{a,\sigma}\varphi_b + \hat{n}_{b,\sigma}\varphi_a\right) - \varphi_a\varphi_b \right),
\end{aligned}$$

where the order parameter is defined spin-symmetrically: $\varphi_j = \sum_\sigma \langle \hat{n}_{j,\sigma} \rangle$ and the last term in the second line stands outside of the sum. The mean field decoupling $(\hat{n}_a - \langle \hat{n}_a \rangle)(\hat{n}_b - \langle \hat{n}_b \rangle) \stackrel{!}{=} 0$ was used from the first to the second line for all spin components.

All four-Fermi terms which extend over the cluster boundary are treated within a mean field approach. Thereby $\hat{\mathcal{H}}^{\mathrm{cl}}(\boldsymbol{\varphi})$ acquires a dependence on the mean fields $\boldsymbol{\varphi}$.

Applying this decoupling scheme to eight orbital clusters we obtain

$$
\begin{aligned}
\hat{\mathcal{H}}^{\mathrm{cl}}_{\mathrm{mf}(8)} = \sum_{\sigma} \Bigg(& \hat{n}_{A,\sigma} \left(V\varphi_B + V'\varphi_D + 2V''\varphi_B + 2V'''\varphi_H + V''''\varphi_G \right) \\
& + \hat{n}_{B,\sigma} \left(V\varphi_B + V'\varphi_C + 2V''\varphi_B + V''''\varphi_H \right) \\
& + \hat{n}_{C,\sigma} \left(V\varphi_D + V'\varphi_C + 2V''\varphi_B + V''''\varphi_H \right) \\
& + \hat{n}_{D,\sigma} \left(V\varphi_C + V'\varphi_B + 2V''\varphi_C \right) \\
& + \hat{n}_{E,\sigma} \left(V\varphi_F + V'\varphi_H + 2V''\varphi_E + V'''\varphi_D \right) \\
& + \hat{n}_{F,\sigma} \left(V\varphi_E + V'\varphi_G + 2V''\varphi_F \right) \\
& + \hat{n}_{G,\sigma} \left(V\varphi_H + V'\varphi_F + 2V''\varphi_G + V''''\varphi_B \right) \\
& + \hat{n}_{H,\sigma} \left(V\varphi_G + V'\varphi_E + 2V''\varphi_H + 2V'''\varphi_B + V''''\varphi_B \right) \Bigg) \\
& - \Bigg(V \left(\varphi_B\varphi_B + \varphi_C\varphi_D + \varphi_E\varphi_F + \varphi_G\varphi_H \right) \\
& + V' \left(\varphi_B\varphi_D + \varphi_B\varphi_C + \varphi_E\varphi_H + \varphi_F\varphi_G \right) \\
& + 2V'' \left(\varphi_B^2 + \varphi_B^2 + \varphi_C^2 + \varphi_D^2 + \varphi_E^2 + \varphi_F^2 + \varphi_G^2 + \varphi_H^2 \right) \\
& + V''' \left(2\varphi_B\varphi_H + \varphi_D\varphi_E \right) \\
& + V'''' \left(\varphi_B\varphi_G + \varphi_B\varphi_H \right) \Bigg) .
\end{aligned}
$$

A.7. Grand potential of the physical system

In the situation considered here the generalized grand potential depends on the mean field parameters $\boldsymbol{\varphi}$, the VCA variational parameters $\boldsymbol{\Delta}$ and the type of mean field decoupling chosen: $\Omega^{\mathrm{mf}}(\boldsymbol{\varphi}, \boldsymbol{\Delta})$. The expression for the fermionic generalized grand potential reduces in the case of zero temperature ($\beta \to +\infty$) to

$$
\Omega^{\mathrm{mf}}(\boldsymbol{\varphi}, \boldsymbol{\Delta}) = \Omega'^{\mathrm{mf}}(\boldsymbol{\varphi}, \boldsymbol{\Delta}) - \sum_{\mathfrak{Re}\lambda'_\gamma < 0} \lambda'_\gamma + \frac{1}{N^\Gamma} \sum_{\mathfrak{Re}\lambda_\gamma(\boldsymbol{k}^\Gamma) < 0} \lambda_\gamma(\boldsymbol{k}^\Gamma) \, .
$$

The excitation energies of the cluster λ'_γ are obtained in Eq. (A.9), while the excitation energies of the total system for a given super-lattice wavevector $\boldsymbol{k}^\Gamma$ are available from the diagonalization of Eq. (A.11). Note that the last sum is over the 1st BZ of the super-lattice Γ. N^Γ is the number of points on the super-lattice Γ, i.e. the number of clusters in the total system.

The grand potential of the physical system within the eVCA approximation has to fulfil three conditions:

1. It is a minimum with respect to the mean field parameters $\boldsymbol{\varphi}$

$$
\begin{aligned}
\partial_{\boldsymbol{\varphi}} \Omega^{\mathrm{mf}}(\boldsymbol{\varphi}, \boldsymbol{\Delta}) &\stackrel{!}{=} \mathbf{0} \\
\partial^2_{\boldsymbol{\varphi}} \Omega^{\mathrm{mf}}(\boldsymbol{\varphi}, \boldsymbol{\Delta}) &\stackrel{!}{>} \mathbf{0} \, .
\end{aligned}
$$

2. It is a stationary point with respect to the VCA variational parameters $\boldsymbol{\Delta}$

$$\partial_{\boldsymbol{\Delta}} \Omega^{\mathrm{mf}}(\boldsymbol{\varphi}, \boldsymbol{\Delta}) \stackrel{!}{=} \mathbf{0}\,.$$

3. It has the lowest total energy out of the possible mean field decompositions.

It suffices to find the stationary point of the grand potential with respect to $\boldsymbol{\varphi}$ and $\boldsymbol{\Delta}$. It is automatically a minimum in the mean field parameters $\boldsymbol{\varphi}$ and an arbitrary stationary point in the VCA parameters $\boldsymbol{\Delta}$. This gives the value of the order parameters $\boldsymbol{\varphi}_{\mathrm{opt}}$ and the stationary VCA parameters $\boldsymbol{\Delta}_{\mathrm{stat}}$.

B. Pauli Matrices

The Pauli matrices are defined as [158]

$$\sigma^0 = \mathbb{1} = \begin{pmatrix} 1 & 0 \\ 0 & 1 \end{pmatrix}, \; \sigma^x = \begin{pmatrix} 0 & 1 \\ 1 & 0 \end{pmatrix}, \; \sigma^y = \begin{pmatrix} 0 & -i \\ i & 0 \end{pmatrix}, \; \sigma^z = \begin{pmatrix} 1 & 0 \\ 0 & -1 \end{pmatrix}.$$

The matrices are hermitian $\sigma^a = (\sigma^a)^\dagger$ and unitary $(\sigma^a)^{-1} = (\sigma^a)^\dagger$ and span the real Hilbert space of 2×2 complex hermitian matrices. With some algebra one derives the commutation relations

$$\begin{aligned} [\sigma^a, \sigma^b]_- &= 2i\varepsilon_{abc}\,\sigma^c \\ \{\sigma^a, \sigma^b\} &= 2\delta_{ab}\,\mathbb{1}\,, \end{aligned}$$

as well as the elementary properties

$$\begin{aligned} (\sigma^a)^2 &= \mathbb{1} \\ -i\prod_a \sigma^a &= \mathbb{1} \\ \det(\sigma^a) &= -1 \\ \mathrm{Tr}(\sigma^a) &= 0 \\ \sigma^a\sigma^b &= i\sum_c \varepsilon_{abc}\,\sigma^c + \delta_{ab}\mathbb{1}\,. \end{aligned}$$

All the respective eigenvalues are $\{-1, +1\}$. The ladder operators are defined as

$$\sigma^+ = \frac{1}{2}(\sigma^x + i\sigma^y) = \begin{pmatrix} 0 & 1 \\ 0 & 0 \end{pmatrix}, \; \sigma^- = \frac{1}{2}(\sigma^x - i\sigma^y) = \begin{pmatrix} 0 & 0 \\ 1 & 0 \end{pmatrix},$$

where $(\sigma^-)^\dagger = \sigma^+$. The commutation relations read

$$\begin{aligned} [\sigma^+, \sigma^-]_- &= \sigma^z\,, \; [\sigma^+, \sigma^+]_- = \mathbf{0}\,, \; [\sigma^-, \sigma^-]_- = \mathbf{0} \\ \{\sigma^+, \sigma^-\} &= \mathbb{1}\,, \; \{\sigma^+, \sigma^+\} = \mathbf{0}\,, \; \{\sigma^-, \sigma^-\} = \mathbf{0}\,. \end{aligned}$$

C. Heaviside step- and sign- functions

We have

$$\begin{aligned} \mathrm{sign}(-x) &= -\mathrm{sign}(x) \\ \theta(-x) &= 1 - \theta(x) \\ \mathrm{sign}(x) &= 2\theta(x) - 1\,. \end{aligned}$$

D. Jordan-Wigner transformation

The Jordan-Wigner transformation [465] consists in the mapping of a fermionic Fock space on L sites to spin operators

$$\begin{aligned} c_j &= \sigma_1^z \otimes \ldots \otimes \sigma_{j-1}^z \otimes \sigma_j^- \otimes \mathbb{1}_{j+1} \otimes \ldots \otimes \mathbb{1}_L \\ &= e^{-i\pi \hat{N}_j} \sigma_j^- \\ &= (-1)^{\hat{N}_j} \sigma_j^- \,, \end{aligned} \tag{D.1}$$

with $\hat{N}_j = \sum_{i=1}^{j-1} \hat{n}_i$, $\hat{n}_i = c_j^\dagger c_j$. Note that $e^{\pm i\pi \hat{N}_j} = e^{\pm i\pi \sum_{j=1}^{i-1} \hat{n}_j} = \prod_{j=1}^{i-1} e^{\pm i\pi \hat{n}_j} = \prod_{j=1}^{i-1} (1 - 2\hat{n}_j)$. The hermitian conjugate follows

$$\begin{aligned} c_j^\dagger &= \sigma_1^z \otimes \ldots \otimes \sigma_{j-1}^z \otimes \sigma_j^+ \otimes \mathbb{1}_{j+1} \otimes \ldots \otimes \mathbb{1}_L \\ &= \sigma_j^+ e^{+i\pi \hat{N}_j} \\ &= \sigma_j^+ (-1)^{\hat{N}_j} \,. \end{aligned}$$

Multiplication yields

$$c_j^\dagger c_j = \sigma_j^+ \sigma_j^- \,,$$

which upon making use of the matrix representation of σ^a yields

$$\sigma_j^z = 2\hat{n}_j - \mathbb{1} = (-1)^{\hat{n}_j + 1} \,,$$

since $n_j \in \{0, 1\}$. Using $\sigma^- \sigma^z = \sigma^-$, $\sigma^+ \sigma^z = -\sigma^+$ and $\sigma_i^- \sigma_j^+ + \sigma_j^+ \sigma_i^- = \delta_{ij} \mathbb{1}$ one can show that the c operators fulfil fermionic commutation relations

$$\begin{aligned} \{c_i, c_j\} &= \{c_i^\dagger, c_j^\dagger\} = \mathbf{0} \\ \{c_i, c_j^\dagger\} &= \delta_{ij} \mathbb{1} \,. \end{aligned}$$

E. Bath correlation functions

In this appendix we elaborate in detail on the bath correlations function needed in the QME treatment of molecular junctions. We start out by mapping a fermionic coupling Hamiltonian onto a tensor product form. Then we present general results for the bath correlation functions and conclude by evaluating them analytically for flat bands.

E.1. System-environment coupling

The BMsme is conveniently expressed in a specific form of the system-bath coupling Hamiltonian

$$\hat{\mathcal{H}}_c = \sum_\alpha \hat{S}_\alpha \otimes \hat{B}_\alpha \,. \tag{E.1}$$

The $\hat{S}_\alpha$ / $\hat{B}_\alpha$ act on the system / bath respectively. Firstly, the coupling Hamiltonian needs to be of tensor product form which requires $[\hat{S}_\alpha, \hat{B}_\alpha]_- = 0$ and poses an a-priory problem for fermionic operators. Secondly, the coupling operators are required to be hermitian $\hat{S}_\alpha = \hat{S}_\alpha^\dagger$, $\hat{B}_\alpha = \hat{B}_\alpha^\dagger$, which is not the case for the standard single-particle tunnelling terms. Below we will show that both issues can be resolved even for standard fermionic couplings in terms of single-particle tunnellings.

Coupling hermitization

Before that we show that it is always possible to choose hermitian coupling operators in the general case. Since $\hat{\mathcal{H}}_c = \hat{\mathcal{H}}_c^\dagger$ we may write

$$\begin{aligned}\hat{\mathcal{H}}_c &= \frac{1}{2}\left(\sum_\alpha \hat{S}'_\alpha \otimes \hat{B}'_\alpha + \sum_\alpha (\hat{S}'_\alpha \otimes \hat{B}'_\alpha)^\dagger\right) \\ &= \sum_\alpha \left(\frac{1}{\sqrt{2}}(\hat{S}'_\alpha + \hat{S}'^\dagger_\alpha) \otimes \frac{1}{\sqrt{2}}(\hat{B}'_\alpha + \hat{B}'^\dagger_\alpha) + \frac{i}{\sqrt{2}}(\hat{S}'_\alpha - \hat{S}'^\dagger_\alpha) \otimes \frac{i}{\sqrt{2}}(\hat{B}'_\alpha - \hat{B}'^\dagger_\alpha)\right).\end{aligned}$$

The hermitian coupling operators can easily be identified as the linear combinations $\hat{S}_{\alpha,1} = \frac{1}{\sqrt{2}}(\hat{S}'_\alpha + \hat{S}'^\dagger_\alpha)$, $\hat{S}_{\alpha,2} = \frac{i}{\sqrt{2}}(\hat{S}'_\alpha - \hat{S}'^\dagger_\alpha)$, $\hat{B}_{\alpha,1} = \frac{1}{\sqrt{2}}(\hat{B}'_\alpha + \hat{B}'^\dagger_\alpha)$ and $\hat{B}_{\alpha,2} = \frac{i}{\sqrt{2}}(\hat{B}'_\alpha - \hat{B}'^\dagger_\alpha)$.

Definition of a general fermionic coupling Hamiltonian

We consider the general case of a fermionic coupling Hamiltonian which consists of single-particle tunnelling events. Such a coupling applies to a broad range of systems of interest in situations where a system is electronically coupled to electronic reservoirs. The system-bath coupling then reads

$$\hat{\mathcal{H}}_c = \sum_{ik} \left(V_{ik} s_i^\dagger b_k + V_{ik}^* b_k^\dagger s_i\right) , \tag{E.2}$$

where the $s_i/s_i^\dagger$ operators annihilate / create fermions in the system with quantum number i which usually represents a compound index for orbital j and spin σ, i.e. $i = (j, \sigma)$. For the bath operators $b_k/b_k^\dagger$, the index k typically represents the bath number λ, the orbital to which the central region is coupled to j and the spin σ, i.e. $k = (\lambda, j, \sigma)$. The matrices V are the hermitian coupling strengths.

To bring the fermionic coupling Hamiltonian Eq. (E.2) to the tensor product form of hermitian couplings Eq. (E.1) we have to consider two aspects: i) we need to find a representation of Eq. (E.2) which is of tensor product structure between the system and bath degrees of freedom and ii) the respective operators have to be brought to hermitian form.

Obtaining a Tensor Product form

We first bring Eq. (E.2) to tensor product structure which requires $[\hat{S}_\alpha, \hat{B}_\alpha]_- = 0$ For the fermionic operators in Eq. (E.2) we have $[s_i^\dagger, b_k]_- = 2 s_i^\dagger b_k$. We start out by performing a Jordan-Wigner transformation on the system and bath operators [457]. Using Eq. (D.1) we find

$$
\begin{aligned}
s_i &= (\sigma_1^z \otimes \ldots \otimes \sigma_{i-1}^z \sigma_i^- \mathbb{1}_{i+1} \otimes \ldots \otimes \mathbb{1}_{L_S})_S \otimes (\mathbb{1}_1 \otimes \ldots \otimes \mathbb{1}_{L_B})_B \\
b_k &= \left(\sigma_1^z \otimes \ldots \otimes \sigma_{L_S}^z\right)_S \otimes (\tau_1^z \otimes \ldots \otimes \tau_{k-1}^z \tau_k^- \mathbb{1}_{k+1} \otimes \ldots \otimes \mathbb{1}_{L_B})_B \ ,
\end{aligned}
$$

where we have chosen an ordering system S, bath B, as indicated by the brackets. Reordering Eq. (E.2) we find

$$
\hat{\mathcal{H}}_c = \sum_{ik} \left(V_{ik} s_i^\dagger b_k - V_{ik}^* s_i b_k^\dagger \right) \ ,
$$

where the minus sign arises due to the fermionic anti-commutator. Plugging in the Jordan-Wigner transformed operators leads to

$$
\begin{aligned}
\hat{\mathcal{H}}_c = \sum_{ik} \Bigg(& V_{ik} \left[(\sigma_1^z \otimes \ldots \otimes \sigma_{i-1}^z \otimes \sigma_i^+ \otimes \mathbb{1}_{i+1} \otimes \ldots \otimes \mathbb{1}_{L_S})_S \otimes (\mathbb{1}_1 \otimes \ldots \otimes \mathbb{1}_{L_B})_B \right] \\
& \times \left[\left(\sigma_1^z \otimes \ldots \otimes \sigma_{L_S}^z\right)_S \otimes (\tau_1^z \otimes \ldots \otimes \tau_{k-1}^z \otimes \tau_k^- \otimes \mathbb{1}_{k+1} \otimes \ldots \otimes \mathbb{1}_{L_B})_B \right] \\
& + V_{ik}^* \left[(\sigma_1^z \otimes \ldots \otimes \sigma_{i-1}^z \otimes \sigma_i^- \otimes \mathbb{1}_{i+1} \otimes \ldots \otimes \mathbb{1}_{L_S})_S \otimes (\mathbb{1}_1 \otimes \ldots \otimes \mathbb{1}_{L_B})_B \right] \\
& \times \left[\left(\sigma_1^z \otimes \ldots \otimes \sigma_{L_S}^z\right)_S \otimes (\tau_1^z \otimes \ldots \otimes \tau_{k-1}^z \otimes \tau_k^+ \otimes \mathbb{1}_{k+1} \otimes \ldots \otimes \mathbb{1}_{L_B})_B \right] \Bigg) \\
= \sum_{ik} \Bigg(& V_{ik} \Big[\sigma_1^z \sigma_1^z \otimes \ldots \otimes \sigma_{i-1}^z \sigma_{i-1}^z \otimes \sigma_i^+ \sigma_i^z \otimes \mathbb{1}_{i+1} \sigma_{i+1}^z \otimes \ldots \otimes \mathbb{1}_{L_S} \sigma_{L_S}^z \\
& \otimes \mathbb{1}_1 \tau_1^z \otimes \ldots \otimes \mathbb{1}_{k-1} \tau_{k-1}^z \otimes \mathbb{1}_k \tau_k^- \otimes \mathbb{1}_{k+1} \mathbb{1}_{k+1} \otimes \ldots \otimes \mathbb{1}_{L_B} \mathbb{1}_{L_B} \Big] \\
& - V_{ik}^* \Big[\sigma_1^z \sigma_1^z \otimes \ldots \otimes \sigma_{i-1}^z \sigma_{i-1}^z \otimes \sigma_i^- \sigma_i^z \otimes \mathbb{1}_{i+1} \sigma_{i+1}^z \otimes \ldots \otimes \mathbb{1}_{L_S} \sigma_{L_S}^z \\
& \otimes \mathbb{1}_1 \tau_1^z \otimes \ldots \otimes \mathbb{1}_{k-1} \tau_{k-1}^z \otimes \mathbb{1}_k \tau_k^+ \otimes \mathbb{1}_{k+1} \mathbb{1}_{k+1} \otimes \ldots \otimes \mathbb{1}_{L_B} \mathbb{1}_{L_B} \Big] \Bigg) \\
= \sum_{ik} \Bigg(& V_{ik} \Big[[\sigma_i^+ \sigma_i^z] \otimes [\sigma_{i+1}^z \otimes \ldots \otimes \sigma_{L_S}^z \otimes \tau_1^z \otimes \ldots \otimes \tau_{k-1}^z] \otimes [\tau_k^-] \Big] \\
& - V_{ik}^* \Big[[\sigma_i^- \sigma_i^z] \otimes [\sigma_{i+1}^z \otimes \ldots \otimes \sigma_{L_S}^z \otimes \tau_1^z \otimes \ldots \otimes \tau_{k-1}^z] \otimes [\tau_k^+] \Big] \Bigg) ,
\end{aligned}
$$

where in the last line we used $(\sigma^a)^2 = \mathbb{1}$ and omitted all $\mathbb{1}$'s. Using $\sigma^-\sigma^z = \sigma^-$, and $\sigma^+\sigma^z = -\sigma^+$ we end up with

$$\begin{aligned}\hat{\mathcal{H}}_c &= \sum_{ik}\Bigg(V_{ik}\Big[\sigma_i^+ \otimes \left[-\sigma_{i+1}^z \otimes \ldots \otimes \sigma_{L_S}^z \otimes \tau_1^z \otimes \ldots \otimes \tau_{k-1}^z\right] \otimes \tau_k^-\Big] \\ &\quad + V_{ik}^*\Big[\sigma_i^- \otimes \left[-\sigma_{i+1}^z \otimes \ldots \otimes \sigma_{L_S}^z \otimes \tau_1^z \otimes \ldots \otimes \tau_{k-1}^z\right] \otimes \tau_k^+\Big]\Bigg) \\ &= \sum_i \left(\bar{s}_i^\dagger \otimes \bar{b}_i + \bar{s}_i \otimes \bar{b}_i^\dagger\right),\end{aligned}$$

where in the last line we have defined new operators

$$\begin{aligned}\bar{s}_i &= \sigma_i^- \otimes \left[-\sigma_{i+1}^z \otimes \ldots \otimes \sigma_{L_S}^z\right] \\ \bar{s}_i^\dagger &= \left[-\sigma_{i+1}^z \otimes \ldots \otimes \sigma_{L_S}^z\right] \otimes \sigma_i^+ \\ \bar{b}_i &= \sum_k V_{ik}\left[\tau_1^z \otimes \ldots \otimes \tau_{k-1}^z\right] \otimes \tau_k^- \\ \bar{b}_i^\dagger &= \sum_k V_{ik}^* \tau_k^+ \otimes \left[\tau_1^z \otimes \ldots \otimes \tau_{k-1}^z\right].\end{aligned}$$

Note that the phase operator $\hat{P}_{ik} = \left[-\sigma_{i+1}^z \otimes \ldots \otimes \sigma_{L_S}^z \otimes \tau_1^z \otimes \ldots \otimes \tau_{k-1}^z\right] = (-1)^{1+\sum_{j=i+1}^{L_S} \hat{n}_j + \hat{N}_k}$ counts the particles between system site i and bath site k. It is straight forward to show that the bar operators fulfil fermionic anti-commutation rules. Furthermore $[\bar{s}_i, \bar{b}_i]_- = 0$, which allows us to write the coupling Hamiltonian in a tensor product form. Note that in general $[\bar{s}_i, \bar{b}_j]_- \neq 0$ for $i \neq j$ which is however not relevant for the coupling Hamiltonian where only the same i couple.

Hermitization of the tensor product form

Next we need to bring the new operators to a hermitian form. This is achieved by the transformation

$$\begin{aligned}\hat{S}_{1i} &= \frac{1}{\sqrt{2}}(\bar{s}_i + \bar{s}_i^\dagger), \hat{B}_{1i} = \frac{1}{\sqrt{2}}(\bar{b}_i + \bar{b}_i^\dagger) \\ \hat{S}_{2i} &= \frac{i}{\sqrt{2}}(\bar{s}_i - \bar{s}_i^\dagger), \hat{B}_{2i} = \frac{i}{\sqrt{2}}(\bar{b}_i - \bar{b}_i^\dagger),\end{aligned} \tag{E.3}$$

which augments each index i by an auxiliary index $\in \{1, 2\}$ and leaves us with a coupling Hamiltonian of the form of Eq. (E.1).

Criteria for the use of the original fermion operators

Next we show, by examining the BMsme Eq. (3.26), that in most cases the additional phase operator in $\bar{b}$ drops out of the calculations and we are even allowed to use the original s and b operators instead of the bared ones. The operators $\bar{b}$ only enter the equations in the bath

correlation functions $C_{\alpha\beta}(\tau)$ as defined in Eq. (3.32). Plugging in the barred operators we find

$$
\begin{aligned}
C_{\alpha\beta}(\tau) &= \mathrm{Tr}\left(e^{+i\hat{\mathcal{H}}_B\tau}\hat{B}_\alpha e^{-i\hat{\mathcal{H}}_B\tau}\hat{B}_\beta\bar{\rho}_B\right) \\
&\propto \mathrm{Tr}\left(e^{+i\hat{\mathcal{H}}_B\tau}(\bar{b}_i \pm \bar{b}_i^\dagger)e^{-i\hat{\mathcal{H}}_B\tau}(\bar{b}_i \pm \bar{b}_i^\dagger)\bar{\rho}_B\right) \\
&\propto \mathrm{Tr}\left(e^{+i\hat{\mathcal{H}}_B\tau}(\sum_k V_{ik}\hat{P}_{ik}b_k \pm \sum_k V_{ik}^* b_k^\dagger \hat{P}_{ik})e^{-i\hat{\mathcal{H}}_B\tau}(\sum_q V_{iq}\hat{P}_{iq}b_q \pm \sum_q V_{iq}^* b_q^\dagger \hat{P}_{iq})\bar{\rho}_B\right) \\
&\propto \sum_{kq}\mathrm{Tr}\left(e^{+i\hat{\mathcal{H}}_B\tau}(\hat{P}_{ik}b_k \pm b_k^\dagger\hat{P}_{ik})e^{-i\hat{\mathcal{H}}_B\tau}(\hat{P}_{iq}b_q \pm b_q^\dagger\hat{P}_{iq})\bar{\rho}_B\right) \\
&\propto \begin{cases}
\propto \sum_{kq}\mathrm{Tr}\left(e^{+i\hat{\mathcal{H}}_B\tau}\hat{P}_{ik}b_k e^{-i\hat{\mathcal{H}}_B\tau}\hat{P}_{iq}b_q\bar{\rho}_B\right) \propto \langle b_k b_q\rangle = 0 \\
\propto \sum_{kq}\mathrm{Tr}\left(e^{+i\hat{\mathcal{H}}_B\tau}\hat{P}_{ik}b_k e^{-i\hat{\mathcal{H}}_B\tau}b_q^\dagger\hat{P}_{iq}\bar{\rho}_B\right) \propto \langle b_k b_q^\dagger\rangle \propto \delta_{kq} \\
\propto \sum_{kq}\mathrm{Tr}\left(e^{+i\hat{\mathcal{H}}_B\tau}b_k^\dagger\hat{P}_{ik}e^{-i\hat{\mathcal{H}}_B\tau}\hat{P}_{iq}b_q\bar{\rho}_B\right) \propto \langle b_k^\dagger b_q\rangle \propto \delta_{kq} \\
\propto \sum_{kq}\mathrm{Tr}\left(e^{+i\hat{\mathcal{H}}_B\tau}b_k^\dagger\hat{P}_{ik}e^{-i\hat{\mathcal{H}}_B\tau}b_q^\dagger\hat{P}_{iq}\bar{\rho}_B\right) \propto \langle b_k^\dagger b_q^\dagger\rangle = 0
\end{cases},
\end{aligned}
$$

where the last equality, in general, is valid for normal systems which preserve particle number. We then find

$$
\begin{aligned}
C_{\alpha\beta}(\tau) &\propto \sum_k \mathrm{Tr}\left(e^{+i\hat{\mathcal{H}}_B\tau}b_k^\dagger\hat{P}_{ik}e^{-i\hat{\mathcal{H}}_B\tau}\hat{P}_{ik}b_k\bar{\rho}_B\right) \\
&\propto \sum_k \mathrm{Tr}\left(e^{+i\hat{\mathcal{H}}_B\tau}b_k^\dagger e^{-i\hat{\mathcal{H}}_B\tau}\hat{P}_{ik}^2 b_k\bar{\rho}_B\right) \\
&= \sum_k \mathrm{Tr}\left(e^{+i\hat{\mathcal{H}}_B\tau}b_k^\dagger e^{-i\hat{\mathcal{H}}_B\tau}b_k\bar{\rho}_B\right),
\end{aligned}
$$

with $\hat{P}_{ik}^2 = \mathbb{1}$ where we required that $[\hat{\mathcal{H}}_B, \hat{P}_{ik}]_- = 0$. Therefore the dropping out of the phase operators implies that for normal systems where the disconnected baths conserve particle number we can omit the Jordan-Wigner transformation and do all calculations as is with the original bath creation/annihilation operators in hermitian form.

General Result

If the fermionic coupling Hamiltonian consist of single-particle tunnelling events, as defined in Eq. (E.2) then the coupling Hamiltonian can be written in the form of Eq. (E.1) with the coupling operators defined in Eq. (E.3). If furthermore the particle number is conserved in each individual subsystem, the barred bath operators in Eq. (E.3) can be replaced by the original fermion operators, i.e. those without the additional phase operators, since those drop out in the evaluation of the bath correlation functions, which is the only place they appear in.

Coupling of a single orbital to N_λ baths

Here we exercise the evaluation of the coupling Hamiltonian in the fermionic system Eq. (E.2) for a system consisting of a single fermionic orbital coupled to N_λ baths. Then the coupling Hamiltonian takes the form

$$
\hat{\mathcal{H}}^{SE} = \sum_{\lambda=1}^{N_\lambda} t_\lambda \left(s^\dagger b_{\lambda 0} + b_{\lambda 0}^\dagger s\right),
$$

in which the system couples to the first site 0 of lead λ with equal strength t_λ. We furthermore take the leads to be non-interacting and particle number conserving which allows us to write

$$\hat{\mathcal{H}}^{SE} = \sum_{\lambda=1}^{N_\lambda} t_\lambda \left(s^\dagger \otimes b_{\lambda 0} + s \otimes b_{\lambda 0}^\dagger \right) ,$$

i.e. for the application at hand we may omit transformation to the Jordan-Wigner bar operators. Using Eq. (E.3) we find a suitable coupling Hamiltonian

$$\begin{aligned}
\hat{\mathcal{H}}^{SE} &= \sum_{\alpha=1}^{2} \hat{S}_\alpha \otimes \hat{B}_\alpha \quad \text{with} \\
\hat{S}_1 &= \frac{1}{\sqrt{2}}(s + s^\dagger), \hat{B}_1 = \frac{1}{\sqrt{2}} \sum_\lambda t_\lambda (b_{\lambda 0} + b_{\lambda 0}^\dagger) \\
\hat{S}_2 &= \frac{i}{\sqrt{2}}(s - s^\dagger), \hat{B}_2 = \frac{i}{\sqrt{2}} \sum_\lambda t_\lambda (b_{\lambda 0} - b_{\lambda 0}^\dagger) .
\end{aligned}$$

E.2. Time dependence of the coupling operators

For the bath correlation function we have to evaluate Eq. (3.32)

$$C_{\alpha\beta}(\tau) = \mathrm{Tr}\left(\hat{B}_\alpha(\tau) \hat{B}_\beta \bar{\rho}_B \right) .$$

The Heisenberg time evolution for the first bath operators is given by

$$\begin{aligned}
\hat{B}_1(\tau) &= \frac{1}{\sqrt{2}} \sum_\lambda t'_\lambda (b_{\lambda 0} + b_{\lambda 0}^\dagger)(\tau) \\
&= \frac{1}{\sqrt{2}} \sum_\lambda t'_\lambda \sum_k (h_{\lambda k} b_{\lambda k}(\tau) + h_{\lambda k}^* b_{\lambda k}^\dagger(\tau)) \\
&= \frac{1}{\sqrt{2}} \sum_\lambda t'_\lambda \sum_k (h_{\lambda k} e^{-i\omega_{\lambda k}\tau} b_{\lambda k} + h_{\lambda k}^* e^{+i\omega_{\lambda k}\tau} b_{\lambda k}^\dagger) ,
\end{aligned}$$

where we used a transformation to the eigenmodes of the bath $b_{\lambda j} = \sum_k h_{\lambda k} e^{+ikj} b_{\lambda k}$ and $b_{\lambda j}^\dagger = \sum_k h_{\lambda k}^* e^{-ikj} b_{\lambda k}$ so $b_{\lambda 0} = \sum_k h_{\lambda k} b_{\lambda k}$ and $b_{\lambda 0}^\dagger = \sum_k h_{\lambda k}^* b_{\lambda k}$. Furthermore the time evolution of the bath operators in the eigenbasis is

$$\begin{aligned}
i\dot{b}_{\lambda k}(\tau) &= [\hat{\mathcal{H}}_B, b_{\lambda k}]_- \\
&= [\sum_{\lambda' k'} \omega_{\lambda' k'} b_{\lambda' k'}^\dagger b_{\lambda' k'}, b_{\lambda k}]_- \\
&= -b_{\lambda k} \omega_{\lambda k} ,
\end{aligned}$$

which leads to

$$\begin{aligned}
b_{\lambda k}(\tau) &= e^{-i\omega_{\lambda k}\tau} b_{\lambda k} \\
b_{\lambda k}^\dagger(\tau) &= e^{+i\omega_{\lambda k}\tau} b_{\lambda k}^\dagger
\end{aligned}$$

The time evolution for the second bath operator then is

$$\begin{aligned}\hat{B}_2(\tau) &= \frac{i}{\sqrt{2}}\sum_\lambda t'_\lambda (b_{\lambda 0} - b^\dagger_{\lambda 0})(\tau) \\ &= \frac{i}{\sqrt{2}}\sum_\lambda t'_\lambda \sum_k (h_{\lambda k} e^{-i\omega_{\lambda k}\tau} b_{\lambda k} - h^*_{\lambda k} e^{+i\omega_{\lambda k}\tau} b^\dagger_{\lambda k})\,.\end{aligned}$$

E.3. Evaluation of the correlation functions

Plugging these operators into $C_{\alpha\beta}(\tau)$ we find

$$\begin{aligned}C_{11}(\tau) &= \mathrm{Tr}\left(\hat{B}_1(\tau)\hat{B}_1\bar{\rho}_B\right) \\ &= \mathrm{Tr}\left(\left[\frac{1}{\sqrt{2}}\sum_\lambda t'_\lambda \sum_k (h_{\lambda k} e^{-i\omega_{\lambda k}\tau} b_{\lambda k} + h^*_{\lambda k} e^{+i\omega_{\lambda k}\tau} b^\dagger_{\lambda k})\right]\left[\frac{1}{\sqrt{2}}\sum_{\lambda'} t'_{\lambda'} \sum_{k'} (h_{\lambda' k'} b_{\lambda' k'} + h^*_{\lambda' k'} b^\dagger_{\lambda' k'})\right]\bar{\rho}_B\right) \\ &= \frac{1}{2}\sum_{\lambda\lambda'} t'_\lambda t'_{\lambda'} \sum_{kk'} \mathrm{Tr}\Big(\Big(\left(h_{\lambda k} h_{\lambda' k'} e^{-i\omega_{\lambda k}\tau} b_{\lambda k} b_{\lambda' k'}\right) + \left(h_{\lambda k} h^*_{\lambda' k'} e^{-i\omega_{\lambda k}\tau} b_{\lambda k} b^\dagger_{\lambda' k'}\right) \\ &+ \left(h^*_{\lambda k} h_{\lambda' k'} e^{+i\omega_{\lambda k}\tau} b^\dagger_{\lambda k} b_{\lambda' k'}\right) + \left(h^*_{\lambda k} h^*_{\lambda' k'} e^{+i\omega_{\lambda k}\tau} b^\dagger_{\lambda k} b^\dagger_{\lambda' k'}\right)\Big)\bar{\rho}_B\Big) \\ &= \frac{1}{2}\sum_{\lambda\lambda'} t'_\lambda t'_{\lambda'} \sum_{kk'}\Big(\left(h_{\lambda k} h_{\lambda' k'} e^{-i\omega_{\lambda k}\tau}\langle b_{\lambda k} b_{\lambda' k'}\rangle\right) + \left(h_{\lambda k} h^*_{\lambda' k'} e^{-i\omega_{\lambda k}\tau}\langle b_{\lambda k} b^\dagger_{\lambda' k'}\rangle\right) \\ &+ \left(h^*_{\lambda k} h_{\lambda' k'} e^{+i\omega_{\lambda k}\tau}\langle b^\dagger_{\lambda k} b_{\lambda' k'}\rangle\right) + \left(h^*_{\lambda k} h^*_{\lambda' k'} e^{+i\omega_{\lambda k}\tau}\langle b^\dagger_{\lambda k} b^\dagger_{\lambda' k'}\rangle\right)\Big),\end{aligned}$$

where in our system $\langle b_{\lambda k} b_{\lambda' k'}\rangle = 0$, $\langle b_{\lambda k} b^\dagger_{\lambda' k'}\rangle \propto \delta_{kk'}\delta_{\lambda\lambda'}$, $\langle b^\dagger_{\lambda k} b_{\lambda' k'}\rangle \propto \delta_{kk'}\delta_{\lambda\lambda'}$ and $\langle b^\dagger_{\lambda k} b^\dagger_{\lambda' k'}\rangle$. Therefore we may write

$$\begin{aligned}C_{11}(\tau) &= \frac{1}{2}\sum_\lambda t'^2_\lambda \sum_k |h_{\lambda k}|^2\Big(\left(e^{-i\omega_{\lambda k}\tau}(1 - \langle b^\dagger_{\lambda k} b_{\lambda k}\rangle)\right) + \left(e^{+i\omega_{\lambda k}\tau}\langle b^\dagger_{\lambda k} b_{\lambda k}\rangle\right)\Big) \\ &= \frac{1}{2}\sum_\lambda t'^2_\lambda \sum_k |h_{\lambda k}|^2\Big(\langle b^\dagger_{\lambda k} b_{\lambda k}\rangle\left(e^{+i\omega_{\lambda k}\tau} - e^{-i\omega_{\lambda k}\tau}\right) + e^{-i\omega_{\lambda k}\tau}\Big) \\ &= \frac{1}{2}\sum_\lambda t'^2_\lambda \sum_k |h_{\lambda k}|^2\Big(\langle \hat{n}_{\lambda k}\rangle 2i\sin(\omega_{\lambda k}\tau) + e^{-i\omega_{,\lambda k}\tau}\Big) \\ &= \frac{1}{2}\sum_\lambda t'^2_\lambda \sum_k |h_{\lambda k}|^2\Big(2ip_{\mathrm{FD}}(\omega_{\lambda k}, \beta_\lambda, \mu_\lambda)\sin(\omega_{\lambda k}\tau) + e^{-i\omega_{\lambda k}\tau}\Big),\end{aligned}$$

where

$$p_{\mathrm{FD}}(\omega, \beta, \mu) = \frac{1}{e^{\beta(\omega-\mu)} + 1}\,,$$

is the Fermi-Dirac distribution function for energy ω, inverse temperature β and chemical potential μ. Exercising the same calculation for C_{22}, we find

$$
\begin{aligned}
C_{22}(\tau) &= \mathrm{Tr}\left(\hat{B}_2(\tau)\hat{B}_2\bar{\rho}_B\right) \\
&= \mathrm{Tr}\left(\left[\frac{i}{\sqrt{2}}\sum_{\lambda} t'_{\lambda}\sum_{k}(h_{\lambda k}e^{-i\omega_{\lambda k}\tau}b_{\lambda k} - h^{*}_{\lambda k}e^{+i\omega_{\lambda k}\tau}b^{\dagger}_{\lambda k})\right]\left[\frac{i}{\sqrt{2}}\sum_{\lambda'} t_{\lambda'}(b_{\lambda' 0} - b^{\dagger}_{\lambda' 0})\right]\bar{\rho}_B\right) \\
&= -\frac{1}{2}\sum_{\lambda'\lambda} t'_{\lambda}t_{\lambda'}\sum_{k'k}\mathrm{Tr}\Big(\Big((h_{\lambda k}h_{\lambda' k'}e^{-i\omega_{\lambda k}\tau}b_{\lambda k}b_{\lambda' k'}) - (h_{\lambda k}h^{*}_{\lambda' k'}e^{-i\omega_{\lambda k}\tau}b_{\lambda k}b^{\dagger}_{\lambda' k'}) \\
&\quad - (h^{*}_{\lambda k}h_{\lambda' k'}e^{+i\omega_{\lambda k}\tau}b^{\dagger}_{\lambda k}b_{\lambda' k'}) + (h^{*}_{\lambda k}h^{*}_{\lambda' k'}e^{+i\omega_{\lambda k}\tau}b^{\dagger}_{\lambda k}b^{\dagger}_{\lambda' k'})\Big)\bar{\rho}_B\Big) \\
&= -\frac{1}{2}\sum_{\lambda'\lambda} t'_{\lambda}t_{\lambda'}\sum_{k'k}\Big((h_{\lambda k}h_{\lambda' k'}e^{-i\omega_{\lambda k}\tau}\langle b_{\lambda k}b_{\lambda' k'}\rangle) - (h_{\lambda k}h^{*}_{\lambda' k'}e^{-i\omega_{\lambda k}\tau}\langle b_{\lambda k}b^{\dagger}_{\lambda' k'}\rangle) \\
&\quad - (h^{*}_{\lambda k}h_{\lambda' k'}e^{+i\omega_{\lambda k}\tau}\langle b^{\dagger}_{\lambda k}b_{\lambda' k'}\rangle) + (h^{*}_{\lambda k}h^{*}_{\lambda' k'}e^{+i\omega_{\lambda k}\tau}\langle b^{\dagger}_{\lambda k}b^{\dagger}_{\lambda' k'}\rangle)\Big) \\
&= \frac{1}{2}\sum_{\lambda} t'^{2}_{\lambda}\sum_{k}|h_{\lambda k}|^{2}\Big((e^{-i\omega_{\lambda k}\tau}(1 - \langle b^{\dagger}_{\lambda k}b_{\lambda k}\rangle)) + (e^{+i\omega_{\lambda k}\tau}\langle b^{\dagger}_{\lambda k}b_{\lambda k}\rangle)\Big) \\
&= \frac{1}{2}\sum_{\lambda} t'^{2}_{\lambda}\sum_{k}|h_{\lambda k}|^{2}\Big(\langle b^{\dagger}_{\lambda k}b_{\lambda k}\rangle(e^{+i\omega_{\lambda k}\tau} - e^{-i\omega_{\lambda k}\tau}) + e^{-i\omega_{\lambda k}\tau}\Big) \\
&= \frac{1}{2}\sum_{\lambda} t'^{2}_{\lambda}\sum_{k}|h_{\lambda k}|^{2}\Big(\langle \hat{n}_{\lambda k}\rangle 2i\sin(\omega_{\lambda k}\tau) + e^{-i\omega_{\lambda k}\tau}\Big) \\
&= \frac{1}{2}\sum_{\lambda} t'^{2}_{\lambda}\sum_{k}|h_{\lambda k}|^{2}\Big(2ip_{\mathrm{FD}}(\omega_{\lambda k},\beta_{\lambda},\mu_{\lambda})\sin(\omega_{\lambda k}\tau) + e^{-i\omega_{\lambda k}\tau}\Big) \\
&= C_{11}(\tau)\,.
\end{aligned}
$$

For C_{12}, we find

$$
\begin{aligned}
C_{12}(\tau) &= \mathrm{Tr}\left(\hat{B}_1(\tau)\hat{B}_2\bar{\rho}_B\right) \\
&= \mathrm{Tr}\left(\left[\frac{1}{\sqrt{2}}\sum_\lambda t'_\lambda \sum_k (h_{\lambda k}e^{-i\omega_{\lambda k}\tau}b_{\lambda k} + h^*_{\lambda k}e^{+i\omega_{\lambda k}\tau}b^\dagger_{\lambda k})\right]\left[\frac{i}{\sqrt{2}}\sum_\lambda t'_\lambda \sum_k (h_{\lambda k}b_{\lambda k} - h^*_{\lambda k}b^\dagger_{\lambda k})\right]\bar{\rho}_B\right) \\
&= \frac{i}{2}\sum_{\lambda\lambda'} t'_\lambda t'_{\lambda'} \sum_{kk'} \mathrm{Tr}\Big(\Big((h_{\lambda k}h_{\lambda' k'}e^{-i\omega_{\lambda k}\tau}b_{\lambda k}b_{\lambda' k'}) - (h_{\lambda k}h^*_{\lambda' k'}e^{-i\omega_{\lambda k}\tau}b_{\lambda k}b^\dagger_{\lambda' k'}) \\
&+ (h^*_{\lambda k}h_{\lambda' k'}e^{+i\omega_{\lambda k}\tau}b^\dagger_{\lambda k}b_{\lambda' k'}) - (h^*_{\lambda k}h^*_{\lambda' k'}e^{+i\omega_{\lambda k}\tau}b^\dagger_{\lambda k}b^\dagger_{\lambda' k'})\Big)\bar{\rho}_B\Big) \\
&= \frac{i}{2}\sum_{\lambda\lambda'} t'_\lambda t'_{\lambda'} \sum_{kk'} \Big((h_{\lambda k}h_{\lambda' k'}e^{-i\omega_{\lambda k}\tau}\langle b_{\lambda k}b_{\lambda' k'}\rangle) - (h_{\lambda k}h^*_{\lambda' k'}e^{-i\omega_{\lambda k}\tau}\langle b_{\lambda k}b^\dagger_{\lambda' k'}\rangle) \\
&+ (h^*_{\lambda k}h_{\lambda' k'}e^{+i\omega_{\lambda k}\tau}\langle b^\dagger_{\lambda k}b_{\lambda' k'}\rangle) - (h^*_{\lambda k}h^*_{\lambda' k'}e^{+i\omega_{\lambda k}\tau}\langle b^\dagger_{\lambda k}b^\dagger_{\lambda' k'}\rangle)\Big) \\
&= \frac{i}{2}\sum_\lambda t'^2_\lambda \sum_k |h_{\lambda k}|^2\Big(- (e^{-i\omega_{\lambda k}\tau}(1 - \langle b^\dagger_{\lambda k}b_{\lambda k}\rangle)) + (e^{+i\omega_{\lambda k}\tau}\langle b^\dagger_{\lambda k}b_{\lambda k}\rangle)\Big) \\
&= \frac{i}{2}\sum_\lambda t'^2_\lambda \sum_k |h_{\lambda k}|^2\Big(\langle b^\dagger_{\lambda k}b_{\lambda k}\rangle(e^{+i\omega_{\lambda k}\tau} + e^{-i\omega_{\lambda k}\tau}) - e^{-i\omega_{\lambda k}\tau}\Big) \\
&= \frac{i}{2}\sum_\lambda t'^2_\lambda \sum_k |h_{\lambda k}|^2\Big(\langle b^\dagger_{\lambda k}b_{\lambda k}\rangle 2\cos(\omega_{\lambda k}\tau) - e^{-i\omega_{\lambda k}\tau}\Big) \\
&= \frac{i}{2}\sum_\lambda t'^2_\lambda \sum_k |h_{\lambda k}|^2\Big(\langle \hat{n}^\dagger_{\lambda k}\rangle 2\cos(\omega_{\lambda k}\tau) - e^{-i\omega_{\lambda k}\tau}\Big) \\
&= \frac{i}{2}\sum_\lambda t'^2_\lambda \sum_k |h_{\lambda k}|^2\Big(2p_{\mathrm{FD}}(\omega_{\lambda k},\beta_\lambda,\mu_\lambda)\cos(\omega_{\lambda k}\tau) - e^{-i\omega_{\lambda k}\tau}\Big).
\end{aligned}
$$

The evaluation for C_{21} yields

$$
\begin{aligned}
C_{21}(\tau) &= \mathrm{Tr}\left(\hat{B}_2(\tau)\hat{B}_1\bar{\rho}_B\right) \\
&= \mathrm{Tr}\Bigg(\left[\frac{i}{\sqrt{2}}\sum_\lambda t'_\lambda \sum_k (h_{\lambda k}e^{-i\omega_{\lambda k}\tau}b_{\lambda k} - h^*_{\lambda k}e^{+i\omega_{\lambda k}\tau}b^\dagger_{\lambda k})\right]\left[\frac{1}{\sqrt{2}}\sum_{\lambda'} t'_{\lambda'}\sum_{k'}(h_{\lambda' k'}b_{\lambda' k'} + h^*_{\lambda' k'}b^\dagger_{\lambda' k'})\right]\bar{\rho}_B\Bigg) \\
&= \frac{i}{2}\sum_{\lambda\lambda'} t'_\lambda t'_{\lambda'}\sum_{kk'}\mathrm{Tr}\Bigg(\Big((h_{\lambda k}h_{\lambda' k'}e^{-i\omega_{\lambda k}\tau}b_{\lambda k}b_{\lambda' k'}) + (h_{\lambda k}h^*_{\lambda' k'}e^{-i\omega_{\lambda k}\tau}b_{\lambda k}b^\dagger_{\lambda' k'}) \\
&- (h^*_{\lambda k}h_{\lambda' k'}e^{+i\omega_{\lambda k}\tau}b^\dagger_{\lambda k}b_{\lambda' k'}) - (h^*_{\lambda k}h^*_{\lambda' k'}e^{+i\omega_{\lambda k}\tau}b^\dagger_{\lambda k}b^\dagger_{\lambda' k'})\Big)\bar{\rho}_B\Bigg) \\
&= \frac{i}{2}\sum_{\lambda\lambda'} t'_\lambda t'_{\lambda'}\sum_{kk'}\Big((h_{\lambda k}h_{\lambda' k'}e^{-i\omega_{\lambda k}\tau}\langle b_{\lambda k}b_{\lambda' k'}\rangle) + (h_{\lambda k}h^*_{\lambda' k'}e^{-i\omega_{\lambda k}\tau}\langle b_{\lambda k}b^\dagger_{\lambda' k'}\rangle) \\
&- (h^*_{\lambda k}h_{\lambda' k'}e^{+i\omega_{\lambda k}\tau}\langle b^\dagger_{\lambda k}b_{\lambda' k'}\rangle) - (h^*_{\lambda k}h^*_{\lambda' k'}e^{+i\omega_{\lambda k}\tau}\langle b^\dagger_{\lambda k}b^\dagger_{\lambda' k'}\rangle)\Big) \\
&= \frac{i}{2}\sum_\lambda t'^2_\lambda \sum_k |h_{\lambda k}|^2\Big((e^{-i\omega_{\lambda k}\tau}(1 - b^\dagger_{\lambda k}\langle b_{\lambda k}\rangle)) - (e^{+i\omega_{\lambda k}\tau}\langle b^\dagger_{\lambda k}b_{\lambda k}\rangle)\Big) \\
&= \frac{i}{2}\sum_\lambda t'^2_\lambda \sum_k |h_{\lambda k}|^2\Big(\langle b^\dagger_{\lambda k}b_{\lambda k}\rangle(-e^{+i\omega_{\lambda k}\tau} - e^{-i\omega_{\lambda k}\tau}) + e^{-i\omega_{\lambda k}\tau}\Big) \\
&= \frac{i}{2}\sum_\lambda t'^2_\lambda \sum_k |h_{\lambda k}|^2\Big(-\langle b^\dagger_{\lambda k}b_{\lambda k}\rangle 2\cos(\omega_{\lambda k}\tau) + e^{-i\omega_{\lambda k}\tau}\Big) \\
&= \frac{i}{2}\sum_\lambda t'^2_\lambda \sum_k |h_{\lambda k}|^2\Big(-\langle \hat{n}_{\lambda k}\rangle 2\cos(\omega_{\lambda k}\tau) + e^{-i\omega_{\lambda k}\tau}\Big) \\
&= \frac{i}{2}\sum_\lambda t'^2_\lambda \sum \mathrm{lim}, its_k |h_{\lambda k}|^2\Big(-2p_{\mathrm{FD}}(\omega_{\lambda k},\beta_\lambda,\mu_\lambda)\cos(\omega_{\lambda k}\tau) + e^{-i\omega_{\lambda k}\tau}\Big) \\
&= -C_{12}(\tau)\,.
\end{aligned}
$$

E.4. Symmetry of the correlation functions

Symmetry requires $C_{\alpha\beta}(\tau) = C^*_{\beta\alpha}(-\tau)$. Explicitly we have

$$
\begin{aligned}
C_{11}(\tau) = C_{22}(\tau) &= \frac{1}{2}\sum_\lambda t'^2_\lambda \sum_k |h_{\lambda k}|^2\Big(2ip_{\mathrm{FD}}(\omega_{\lambda k},\beta_\lambda,\mu_\lambda)\sin(\omega_{\lambda k}\tau) + e^{-i\omega_{\lambda k}\tau}\Big) \\
C^*_{11}(-\tau) = C^*_{22}(-\tau) &= \frac{1}{2}\sum_\lambda t'^2_\lambda \sum_k |h_{\lambda k}|^2\Big(2(-i)p_{\mathrm{FD}}(\omega_{\lambda k},\beta_\lambda,\mu_\lambda)\sin(\omega_{\lambda k}(-\tau)) + e^{-(-i)\omega_{\lambda k}(-\tau)}\Big) \\
&= \frac{1}{2}\sum_\lambda t'^2_\lambda \sum_k |h_{\lambda k}|^2\Big(2ip_{\mathrm{FD}}(\omega_{\lambda k},\beta_\lambda,\mu_\lambda)\sin(\omega_{\lambda k}\tau) + e^{-i\omega_{\lambda k}\tau}\Big),
\end{aligned}
$$

and

$$
\begin{aligned}
C_{12}(\tau) &= \frac{i}{2}\sum_{\lambda} t_{\lambda}'^2 \sum_{k} |h_{\lambda k}|^2 \Big(2p_{\mathrm{FD}}(\omega_{\lambda k}, \beta_{\lambda}, \mu_{\lambda}) \cos(\omega_{\lambda k}\tau) - e^{-i\omega_{\lambda k}\tau} \Big) \\
C_{21}^{*}(-\tau) &= \frac{(-i)}{2}\sum_{\lambda} t_{\lambda}'^2 \sum_{k} |h_{\lambda k}|^2 \Big(-2p_{\mathrm{FD}}(\omega_{\lambda k}, \beta_{\lambda}, \mu_{\lambda}) \cos(\omega_{\lambda k}(-\tau)) + e^{-(-i)\omega_{\lambda k}(-\tau)} \Big) \\
&= \frac{i}{2}\sum_{\lambda} t_{\lambda}'^2 \sum_{k} |h_{\lambda k}|^2 \Big(2p_{\mathrm{FD}}(\omega_{\lambda k}, \beta_{\lambda}, \mu_{\lambda}) \cos(\omega_{\lambda k}\tau) - e^{-i\omega_{\lambda k}\tau} \Big).
\end{aligned}
$$

Therefore the symmetry requirements are met.

E.5. Energy integral representation of the correlation functions

We now switch to an energy-integral representation of the time dependent bath correlation functions $C_{\alpha\beta}(\tau)$, which will prove useful for the subsequent Fourier transformation

$$
\begin{aligned}
C_{11}(\tau) = C_{22}(\tau) &= \frac{1}{2}\sum_{\lambda} t_{\lambda}'^2 \sum_{k} |h_{\lambda k}|^2 \Big(e^{-i\omega_{\lambda k}\tau} + 2ip_{\mathrm{FD}}(\omega_{\lambda k}, \beta_{\lambda}, \mu_{\lambda}) \sin(\omega_{\lambda k}\tau) \Big) \\
&= \frac{1}{4\pi}\sum_{\lambda} \int_{-\infty}^{\infty} d\nu\, 2\pi t_{\lambda}'^2 \sum_{k} |h_{\lambda k}|^2 \delta(\nu - \omega_{\lambda k}) \Big(e^{-i\nu\tau} + 2ip_{\mathrm{FD}}(\nu, \beta_{\lambda}, \mu_{\lambda}) \sin(\nu\tau) \Big) \\
&= \frac{1}{4\pi}\sum_{\lambda} \int_{-\infty}^{\infty} d\nu\, \Gamma_{\lambda}(\nu) \Big(e^{-i\nu\tau} + 2ip_{\mathrm{FD}}(\nu, \beta_{\lambda}, \mu_{\lambda}) \sin(\nu\tau) \Big),
\end{aligned}
$$

where we defined the coupling functions to the leads, which roughly speaking is the single-particle coupling strength times the density of states of the decoupled leads $\Gamma_{\lambda}(\nu) = 2\pi t_{\lambda}'^2 \sum_{k} |h_{\lambda k}|^2 \delta(\nu - \omega_{\lambda k})$. For the off diagonal components we find

$$
\begin{aligned}
C_{12}(\tau) = -C_{21}(\tau) &= \frac{i}{2}\sum_{\lambda} t_{\lambda}'^2 \sum_{k} |h_{\lambda k}|^2 \Big(-e^{-i\omega_{\lambda k}\tau} + 2p_{\mathrm{FD}}(\omega_{\lambda k}, \beta_{\lambda}, \mu_{\lambda}) \cos(\omega_{\lambda k}\tau) \Big) \\
&= \frac{i}{4\pi}\sum_{\lambda} \int_{-\infty}^{\infty} d\nu\, 2\pi t_{\lambda}'^2 \sum_{k} |h_{\lambda k}|^2 \delta(\nu - \omega_{\lambda k}) \Big(-e^{-i\nu\tau} + 2p_{\mathrm{FD}}(\nu, \beta_{\lambda}, \mu_{\lambda}) \cos(\nu\tau) \Big) \\
&= \frac{i}{4\pi}\sum_{\lambda} \int_{-\infty}^{\infty} d\nu\, \Gamma_{\lambda}(\nu) \Big(-e^{-i\nu\tau} + 2p_{\mathrm{FD}}(\nu, \beta_{\lambda}, \mu_{\lambda}) \cos(\nu\tau) \Big)
\end{aligned}
$$

E.6. Even Fourier transform of the bath correlation functions

Next we obtain the Fourier transformed bath correlation functions

$$\xi_{\alpha\beta}(\omega) = \int_{-\infty}^{\infty} d\tau\, e^{+i\omega\tau} C_{\alpha\beta}(\tau)\,.$$

For the diagonal components we find

$$\begin{aligned}
\xi_{11}(\omega) = \xi_{22}(\omega) &= \int_{-\infty}^{\infty} d\tau\, e^{+i\omega\tau} \frac{1}{4\pi} \sum_{\lambda} \int_{-\infty}^{\infty} d\nu\, \Gamma_\lambda(\nu) \Big(e^{-i\nu\tau} + 2i p_{\mathrm{FD}}(\nu,\beta_\lambda,\mu_\lambda) \sin(\nu\tau) \Big) \\
&= \frac{1}{2} \sum_{\lambda} \int_{-\infty}^{\infty} d\nu\, \Gamma_\lambda(\nu) \frac{1}{2\pi} \int_{-\infty}^{\infty} d\tau \Big(e^{i(\omega-\nu)\tau} + p_{\mathrm{FD}}(\nu,\beta_\lambda,\mu_\lambda)(e^{+i(\omega+\nu)\tau} - e^{i(\omega-\nu)\tau}) \Big) \\
&= \frac{1}{2} \sum_{\lambda} \int_{-\infty}^{\infty} d\nu\, \Gamma_\lambda(\nu) \Big(\delta(\omega-\nu) + p_{\mathrm{FD}}(\nu,\beta_\lambda,\mu_\lambda) \left(\delta(\omega+\nu) - \delta(\omega-\nu)\right) \Big)\,,
\end{aligned}$$

where we used

$$\frac{1}{2\pi} \int_{-\infty}^{\infty} d\tau\, e^{i(\omega-\nu)\tau} = \delta(\omega-\nu)\,.$$

Defining $\bar{p}_{\mathrm{FD}}(\omega,\beta,\mu) = 1 - p_{\mathrm{FD}}(\omega,\beta,\mu)$ we end up with

$$\begin{aligned}
\xi_{11}(\omega) = \xi_{22}(\omega) &= \frac{1}{2} \sum_{\lambda} \Gamma_\lambda(\omega) + p_{\mathrm{FD}}(-\omega,\beta_\lambda,\mu_\lambda)\Gamma_\lambda(-\omega) - p_{\mathrm{FD}}(\omega,\beta_\lambda,\mu_\lambda)\Gamma_\lambda(\omega) \\
&= \frac{1}{2} \sum_{\lambda} \Gamma_\lambda(\omega)\bar{p}_{\mathrm{FD}}(\omega,\beta_\lambda,\mu_\lambda) + \Gamma_\lambda(-\omega) p_{\mathrm{FD}}(-\omega,\beta_\lambda,\mu_\lambda)\,.
\end{aligned}$$

For the Fourier transformation of the off diagonal components we find

$$\begin{aligned}
\gamma_{12}(\omega) = -\gamma_{21}(\omega) &= \int_{-\infty}^{\infty} d\tau\, e^{+i\omega\tau} \frac{i}{4\pi} \sum_{\lambda} \int_{-\infty}^{\infty} d\nu\, \Gamma_\lambda(\nu) \Big(-e^{-i\nu\tau} + 2 p_{\mathrm{FD}}(\nu,\beta_\lambda,\mu_\lambda) \cos(\nu\tau) \Big) \\
&= \frac{i}{2} \sum_{\lambda} \int_{-\infty}^{\infty} d\nu \frac{1}{2\pi} \int_{-\infty}^{\infty} d\tau\, \Gamma_\lambda(\nu) \Big(-e^{i(\omega-\nu)\tau} + p_{\mathrm{FD}}(\nu,\beta_\lambda,\mu_\lambda)(e^{i(\omega+\nu)\tau} + e^{i(\omega-\nu)\tau}) \Big) \\
&= \frac{i}{2} \sum_{\lambda} \int_{-\infty}^{\infty} d\nu\, \Gamma_\lambda(\nu) \Big(-\delta(\omega-\nu) + p_{\mathrm{FD}}(\nu,\beta_\lambda,\mu_\lambda)(\delta(\omega+\nu) + \delta(\omega-\nu)) \Big) \\
&= \frac{i}{2} \sum_{\lambda} -\Gamma_\lambda(\omega) + \Gamma_\lambda(-\omega) p_{\mathrm{FD}}(-\omega,\beta_\lambda,\mu_\lambda) + \Gamma_\lambda(\omega) p_{\mathrm{FD}}(\omega,\beta_\lambda,\mu_\lambda) \\
&= \frac{i}{2} \sum_{\lambda} \Gamma_\lambda(-\omega) p_{\mathrm{FD}}(-\omega,\beta_\lambda,\mu_\lambda) - \Gamma_\lambda(\omega)\bar{p}_{\mathrm{FD}}(\omega,\beta_\lambda,\mu_\lambda)\,.
\end{aligned}$$

E.7. Odd Fourier transform of the bath correlation functions

What is left, is to evaluate the odd Fourier transform of the time dependent correlation function Eq. (3.31). The component $\sigma_{11}(\omega)$ is given by

$$
\begin{aligned}
\lambda_{11}(\omega) = \lambda_{22}(\omega) &= \int_{-\infty}^{\infty} d\tau\, \mathrm{sign}(\tau) e^{+i\omega\tau} C_{11}(\tau) \\
&= \int_{-\infty}^{\infty} d\tau\, \mathrm{sign}(\tau) e^{+i\omega\tau} \left(\frac{1}{4\pi} \sum_{\lambda} \int_{-\infty}^{\infty} d\nu\, \Gamma_\lambda(\nu) \left(e^{-i\nu\tau} + 2i p_{\mathrm{FD}}(\nu, \beta_\lambda, \mu_\lambda) \sin(\nu\tau) \right) \right) \\
&= \frac{1}{4\pi} \sum_{\lambda} \int_{-\infty}^{\infty} d\nu\, \Gamma_\lambda(\nu) \int_{-\infty}^{\infty} d\tau\, \mathrm{sign}(\tau) e^{+i\omega\tau} \left(e^{-i\nu\tau} + 2i p_{\mathrm{FD}}(\nu, \beta_\lambda, \mu_\lambda) \sin(\nu\tau) \right) \\
&= \frac{1}{4\pi} \sum_{\lambda} \int_{-\infty}^{\infty} d\nu\, \Gamma_\lambda(\nu) \int_{-\infty}^{\infty} d\tau\, \mathrm{sign}(\tau) \left(e^{i(\omega-\nu)\tau} + p_{\mathrm{FD}}(\nu, \beta_\lambda, \mu_\lambda) \left(e^{i(\omega+\nu)\tau} - e^{i(\omega-\nu)\tau} \right) \right) \\
&= \frac{1}{4\pi} \sum_{\lambda} \int_{-\infty}^{\infty} d\nu\, \Gamma_\lambda(\nu) \left(\int_{-\infty}^{0} d\tau + \int_{0}^{\infty} d\tau \right) \mathrm{sign}(\tau) \left(\bar{p}_{\mathrm{FD}}(\nu, \beta_\lambda, \mu_\lambda) e^{i(\omega-\nu)\tau} + p_{\mathrm{FD}}(\nu, \beta_\lambda, \mu_\lambda) e^{i(\omega+\nu)\tau} \right) \\
&= \frac{1}{4\pi} \sum_{\lambda} \int_{-\infty}^{\infty} d\nu\, \Gamma_\lambda(\nu) \left(-\int_{-\infty}^{0} d\tau + \int_{0}^{\infty} d\tau \right) \left(\bar{p}_{\mathrm{FD}}(\nu, \beta_\lambda, \mu_\lambda) e^{i(\omega-\nu)\tau} + p_{\mathrm{FD}}(\nu, \beta_\lambda, \mu_\lambda) e^{i(\omega+\nu)\tau} \right) \\
&= \frac{1}{4\pi} \sum_{\lambda} \int_{-\infty}^{\infty} d\nu\, \Gamma_\lambda(\nu) \left(\int_{0}^{\infty} -d\tau' \left(\bar{p}_{\mathrm{FD}}(\nu, \beta_\lambda, \mu_\lambda) e^{-i(\omega-\nu)\tau'} + p_{\mathrm{FD}}(\nu, \beta_\lambda, \mu_\lambda) e^{-i(\omega+\nu)\tau'} \right) \right. \\
&\quad \left. + \int_{0}^{\infty} d\tau \left(\bar{p}_{\mathrm{FD}}(\nu, \beta_\lambda, \mu_\lambda) e^{i(\omega-\nu)\tau} + p_{\mathrm{FD}}(\nu, \beta_\lambda, \mu_\lambda) e^{i(\omega+\nu)\tau} \right) \right) \\
&= \frac{1}{4\pi} \sum_{\lambda} \int_{-\infty}^{\infty} d\nu\, \Gamma_\lambda(\nu) \int_{0}^{\infty} d\tau \left(\bar{p}_{\mathrm{FD}}(\nu, \beta_\lambda, \mu_\lambda) \left(e^{i(\omega-\nu)\tau} - e^{-i(\omega-\nu)\tau} \right) \right. \\
&\quad \left. + p_{\mathrm{FD}}(\nu, \beta_\lambda, \mu_\lambda) \left(e^{i(\omega+\nu)\tau} - e^{-i(\omega+\nu)\tau} \right) \right) \\
&= \frac{i}{2\pi} \sum_{\lambda} \int_{-\infty}^{\infty} d\nu\, \Gamma_\lambda(\nu) \int_{0}^{\infty} d\tau \left(\bar{p}_{\mathrm{FD}}(\nu, \beta_\lambda, \mu_\lambda) \sin((\omega-\nu)\tau) + p_{\mathrm{FD}}(\nu, \beta_\lambda, \mu_\lambda) \sin((\omega+\nu)\tau) \right) \\
&= \frac{i}{2\pi} \sum_{\lambda} \int_{-\infty}^{\infty} d\nu\, \Gamma_\lambda(\nu) \int_{0}^{\infty} d\tau \left(\bar{p}_{\mathrm{FD}}(\nu, \beta_\lambda, \mu_\lambda) \mathfrak{Im} \left(e^{(i(\omega-\nu)\tau)} \right) + p_{\mathrm{FD}}(\nu, \beta_\lambda, \mu_\lambda) \mathfrak{Im} \left(e^{(i(\omega+\nu)\tau)} \right) \right) \\
&= \frac{i}{2\pi} \sum_{\lambda} \int_{-\infty}^{\infty} d\nu\, \Gamma_\lambda(\nu) \left(\bar{p}_{\mathrm{FD}}(\nu, \beta_\lambda, \mu_\lambda) \mathfrak{Im} \left(\int_{-\infty}^{\infty} d\tau\, e^{(i(\omega-\nu)\tau)} \theta(\tau) \right) \right. \\
&\quad \left. + p_{\mathrm{FD}}(\nu, \beta_\lambda, \mu_\lambda) \mathfrak{Im} \left(\int_{-\infty}^{\infty} d\tau\, e^{(i(\omega+\nu)\tau)} \theta(\tau) \right) \right) \\
&= \frac{i}{2\pi} \sum_{\lambda} \int_{-\infty}^{\infty} d\nu\, \Gamma_\lambda(\nu) \left(\bar{p}_{\mathrm{FD}}(\nu, \beta_\lambda, \mu_\lambda) \mathfrak{Im} \left(\mathrm{pv} \frac{i}{\omega - \nu} + \pi\delta(\omega - \nu) \right) \right. \\
&\quad \left. + p_{\mathrm{FD}}(\nu, \beta_\lambda, \mu_\lambda) \mathfrak{Im} \left(\frac{i}{\omega + \nu} + \pi\delta(\omega + \nu) \right) \right) \\
&= \frac{i}{2\pi} \sum_{\lambda} \int_{-\infty}^{\infty} d\nu\, \Gamma_\lambda(\nu) \left(\bar{p}_{\mathrm{FD}}(\nu, \beta_\lambda, \mu_\lambda) \frac{1}{\omega - \nu} + p_{\mathrm{FD}}(\nu, \beta_\lambda, \mu_\lambda) \frac{1}{\omega + \nu} \right) \\
&= \frac{i}{2\pi} \sum_{\lambda} \int_{-\infty}^{\infty} d\nu\, \Gamma_\lambda(\nu) \left(p_{\mathrm{FD}}(\nu, \beta_\lambda, \mu_\lambda) \frac{1}{\nu + \omega} - \bar{p}_{\mathrm{FD}}(\nu, \beta_\lambda, \mu_\lambda) \frac{1}{\nu - \omega} \right).
\end{aligned}
$$

Another way to arrive at the same result is

$$\begin{aligned}
\lambda_{11}(\omega) = \lambda_{22}(\omega) &= \frac{i}{\pi} \fint_{-\infty}^{\infty} d\nu \frac{\gamma_{11}(\nu)}{\omega - \nu} \\
&= \frac{i}{\pi} \fint_{-\infty}^{\infty} d\nu \frac{\frac{1}{2}\sum_\lambda \Gamma_\lambda(\nu)\bar{p}_{\mathrm{FD}}(\nu,\beta_\lambda,\mu_\lambda) + \Gamma_\lambda(-\nu)p_{\mathrm{FD}}(-\nu,\beta_\lambda,\mu_\lambda)}{\omega - \nu} \\
&= \frac{i}{2\pi} \sum_\lambda \fint_{-\infty}^{\infty} d\nu \frac{1}{\omega - \nu}\Big(\Gamma_\lambda(\nu)\bar{p}_{\mathrm{FD}}(\nu,\beta_\lambda,\mu_\lambda) + \Gamma_\lambda(-\nu)p_{\mathrm{FD}}(-\nu,\beta_\lambda,\mu_\lambda)\Big) \\
&= \frac{i}{2\pi} \sum_\lambda \fint_{-\infty}^{\infty} d\nu \Big(\Gamma_\lambda(\nu)\frac{1}{\omega - \nu}\bar{p}_{\mathrm{FD}}(\nu,\beta_\lambda,\mu_\lambda) + \Gamma_\lambda(\nu)\frac{1}{\omega + \nu}p_{\mathrm{FD}}(\nu,\beta_\lambda,\mu_\lambda)\Big) \\
&= \frac{i}{2\pi} \sum_\lambda \fint_{-\infty}^{\infty} d\nu \Gamma_\lambda(\nu)\Big(\frac{p_{\mathrm{FD}}(\nu,\beta_\lambda,\mu_\lambda)}{\nu + \omega} - \frac{\bar{p}_{\mathrm{FD}}(\nu,\beta_\lambda,\mu_\lambda)}{\nu - \omega}\Big).
\end{aligned}$$

The off diagonal component is given by

$$\begin{aligned}
\lambda_{12}(\omega) = -\lambda_{21}(\omega) &= \frac{i}{\pi} \fint_{-\infty}^{\infty} d\nu \frac{\gamma_{12}(\nu)}{\omega - \nu} \\
&= \frac{i}{\pi} \fint_{-\infty}^{\infty} d\nu \frac{\frac{i}{2}\sum_\lambda \Gamma_\lambda(-\nu)p_{\mathrm{FD}}(-\nu,\beta_\lambda,\mu_\lambda) - \Gamma_\lambda(\nu)\bar{p}_{\mathrm{FD}}(\nu,\beta_\lambda,\mu_\lambda)}{\omega - \nu} \\
&= -\frac{1}{2\pi} \sum_\lambda \fint_{-\infty}^{\infty} d\nu \Big(\frac{\Gamma_\lambda(-\nu)p_{\mathrm{FD}}(-\nu,\beta_\lambda,\mu_\lambda)}{\omega - \nu} - \frac{\Gamma_\lambda(\nu)\bar{p}_{\mathrm{FD}}(\nu,\beta_\lambda,\mu_\lambda)}{\omega - \nu}\Big) \\
&= -\frac{1}{2\pi} \sum_\lambda \fint_{-\infty}^{\infty} d\nu \Gamma_\lambda(\nu)\Big(\frac{p_{\mathrm{FD}}(\nu,\beta_\lambda,\mu_\lambda)}{\omega + \nu} - \frac{\bar{p}_{\mathrm{FD}}(\nu,\beta_\lambda,\mu_\lambda)}{\omega - \nu}\Big) \\
&= -\frac{1}{2\pi} \sum_\lambda \fint_{-\infty}^{\infty} d\nu \Gamma_\lambda(\nu)\Big(\frac{p_{\mathrm{FD}}(\nu,\beta_\lambda,\mu_\lambda)}{\nu + \omega} + \frac{\bar{p}_{\mathrm{FD}}(\nu,\beta_\lambda,\mu_\lambda)}{\nu - \omega}\Big)
\end{aligned}$$

E.8. Flat band at zero temperature

E.8.1. Definition of the coupling function and particle distribution function

As the most simple case possible we consider baths which have a constant electronic density of states $\rho_\lambda = \frac{1}{2D_\lambda}$, i.e. the coupling function $\Gamma_\lambda(\omega)$ is constant within the electronic bandwidth

$\omega \in [-D_\lambda, +D_\lambda], D \in \mathcal{R} \geq 0$ at zero temperature, $T = 0$. This simplifies the coupling function to

$$\begin{aligned}\Gamma_\lambda(\omega) = \Gamma_\lambda(-\omega) &= 2\pi t_\lambda'^2 \rho_\lambda(\theta(\omega + D_\lambda) - \theta(\omega - D_\lambda)) \\ &= \frac{\pi t_\lambda'^2}{D_\lambda}(\theta(\omega + D_\lambda) - \theta(\omega - D_\lambda)) \\ &= \Gamma_\lambda(\theta(\omega + D_\lambda) - \theta(\omega - D_\lambda))\,.\end{aligned}$$

The restriction to zero temperature $\beta_\lambda \to \infty$, simplifies the Fermi-Dirac distribution to Heaviside step functions, see App. C

$$\begin{aligned}p_{\mathrm{FD}}(\omega, \beta_\lambda, \mu_\lambda) &= \theta(-\omega + \mu_\lambda) \\ \bar{p}_{\mathrm{FD}}(\omega, \beta_\lambda, \mu_\lambda) &= 1 - \theta(-\omega + \mu_\lambda) = \theta(\omega - \mu_\lambda)\,.\end{aligned}$$

E.8.2. Evaluation of the time dependent bath correlation functions

For the time dependent correlation functions we find

$$
\begin{aligned}
C_{11}(\tau) = C_{22}(\tau) &= \frac{1}{4\pi}\sum_\lambda \int_{-\infty}^{\infty} d\nu\, \Gamma_\lambda(\nu)\Big(e^{-i\nu\tau} + 2i p_{\mathrm{FD}}(\nu,\beta_\lambda,\mu_\lambda)\sin(\nu\tau)\Big) \\
&= \frac{1}{4\pi}\sum_\lambda \int_{-\infty}^{\infty} d\nu\, \Gamma_\lambda(\theta(\omega+D_\lambda)-\theta(\omega-D_\lambda))\Big(e^{-i\nu\tau} + 2i\theta(-\omega+\mu_\lambda)\sin(\nu\tau)\Big) \\
&= \frac{1}{4\pi}\sum_\lambda \Gamma_\lambda\Big(\int_{-D_\lambda}^{+D_\lambda} d\nu\, e^{-i\nu\tau} + 2i\int_{-\infty}^{+\infty} d\nu\,(\theta(\omega+D_\lambda)-\theta(\omega-D_\lambda))(1-\theta(\omega-\mu_\lambda))\sin(\nu\tau)\Big) \\
&= \frac{1}{4\pi}\sum_\lambda \Gamma_\lambda\Big(\int_{-D_\lambda}^{+D_\lambda} d\nu\, e^{-i\nu\tau} + 2i\int_{-D_\lambda}^{+D_\lambda} d\nu\,\sin(\nu\tau) \\
&\quad - 2i\int_{-\infty}^{+\infty} d\nu\,(\theta(\omega+D_\lambda)-\theta(\omega-D_\lambda))\theta(\omega-\mu_\lambda)\sin(\nu\tau)\Big) \\
&= \frac{1}{4\pi}\sum_\lambda \Gamma_\lambda\Big(\frac{1}{-i\tau}e^{-i\nu\tau}|_{-D_\lambda}^{+D_\lambda} + 2i\frac{-\cos(\nu\tau)}{\tau}|_{-D_\lambda}^{+D_\lambda} - 2i\int_{\max(-D_\lambda,\mu_\lambda)}^{+D_\lambda} d\nu\,\sin(\nu\tau)\Big) \\
&= \frac{1}{4\pi}\sum_\lambda \Gamma_\lambda\Big(\frac{1}{-i\tau}e^{-i\nu\tau}|_{-D_\lambda}^{+D_\lambda} + 2i\frac{-\cos(\nu\tau)}{\tau}|_{-D_\lambda}^{+D_\lambda} \\
&\quad + \begin{cases} -2i\frac{-\cos(\nu\tau)}{\tau}|_{\max(-D_\lambda,\mu_\lambda)}^{+D_\lambda} & \text{for } \mu_\lambda < +D_\lambda \\ 0 & \text{else} \end{cases}\Big) \\
&= \frac{1}{4\pi}\sum_\lambda \Gamma_\lambda\Big(\frac{-2i}{-i\tau}\frac{e^{-iD_\lambda\tau}-e^{+iD_\lambda\tau}}{-2i} - \frac{2i}{\tau}(\cos(+D_\lambda\tau)-\cos(-D_\lambda\tau)) \\
&\quad + \begin{cases} +\frac{2i}{\tau}(\cos(+D_\lambda\tau)-\cos(\max(-D_\lambda,\mu_\lambda)\tau)) & \text{for } \mu_\lambda < +D_\lambda \\ 0 & \text{else} \end{cases}\Big) \\
&= \frac{1}{2\pi\tau}\sum_\lambda \Gamma_\lambda\Big(\sin(D_\lambda\tau) - i\cos(+D_\lambda\tau) + i\cos(-D_\lambda\tau) \\
&\quad + \begin{cases} +i\cos(+D_\lambda\tau) - i\cos(\max(-D_\lambda,\mu_\lambda)\tau) & \text{for } \mu_\lambda < +D_\lambda \\ 0 & \text{else} \end{cases}\Big) \\
&= \frac{1}{2\pi\tau}\sum_\lambda \Gamma_\lambda\Big(\sin(D_\lambda\tau) + \begin{cases} +i\cos(+D_\lambda\tau) - i\cos(\max(-D_\lambda,\mu_\lambda)\tau) & \text{for } \mu_\lambda < +D_\lambda \\ 0 & \text{else} \end{cases}\Big) \\
&= \frac{1}{2\pi\tau}\sum_\lambda \Gamma_\lambda\Big(\begin{cases} \sin(D_\lambda\tau) & \text{for } \mu_\lambda \le -D_\lambda \\ \sin(D_\lambda\tau) + i(\cos(D_\lambda\tau)-\cos(\mu_\lambda\tau)) & \text{for } -D_\lambda < \mu_\lambda < +D_\lambda \\ \sin(D_\lambda\tau) & \text{for } \mu_\lambda \ge +D_\lambda \end{cases}\Big).
\end{aligned}
$$

As a check, rearranging the terms in a different order we obtain the same result

$$
\begin{aligned}
C_{11}(\tau) = C_{22}(\tau) &= \frac{1}{4\pi}\sum_{\lambda}\int_{-\infty}^{\infty} d\nu\,\Gamma_\lambda(\nu)\Big(e^{-i\nu\tau} + 2ip_{\mathrm{FD}}(\nu,\beta_\lambda,\mu_\lambda)\sin(\nu\tau)\Big)\\
&= \frac{1}{4\pi}\sum_{\lambda}\int_{-\infty}^{\infty} d\nu\,\Gamma_\lambda(\nu)\Big(e^{-i\nu\tau} + p_{\mathrm{FD}}(\nu,\beta_\lambda,\mu_\lambda)\left(e^{+i\nu\tau} - e^{-i\nu\tau}\right)\Big)\\
&= \frac{1}{4\pi}\sum_{\lambda}\int_{-\infty}^{\infty} d\nu\,\Gamma_\lambda(\nu)\Big(e^{-i\nu\tau}\bar{p}_{\mathrm{FD}}(\nu,\beta_\lambda,\mu_\lambda) + e^{+i\nu\tau}p_{\mathrm{FD}}(\nu,\beta_\lambda,\mu_\lambda)\Big)\\
&= \frac{1}{4\pi}\sum_{\lambda}\int_{-\infty}^{\infty} d\nu\,\Gamma_\lambda(\theta(\nu+D_\lambda)-\theta(\nu-D_\lambda))\Big(e^{-i\nu\tau}\theta(\nu-\mu_\lambda) + e^{+i\nu\tau}\theta(-\nu+\mu_\lambda)\Big)\\
&= \frac{1}{4\pi}\sum_{\lambda}\Gamma_\lambda\int_{-\infty}^{\infty} d\nu\Big((\theta(\nu+D_\lambda)-\theta(\nu-D_\lambda))\theta(-\nu+\mu_\lambda)e^{+i\nu\tau}\\
&\quad + (\theta(\nu+D_\lambda)-\theta(\nu-D_\lambda))\theta(\nu-\mu_\lambda)e^{-i\nu\tau}\Big)\\
&= \frac{1}{4\pi}\sum_{\lambda}\Gamma_\lambda\Bigg(\begin{cases}\int_{-D_\lambda}^{\min(\mu_\lambda,D_\lambda)} d\nu\, e^{+i\nu\tau} & \text{for } \mu_\lambda > -D_\lambda\\ 0 & \text{else}\end{cases}\\
&\quad + \begin{cases}\int_{\max(\mu_\lambda,-D_\lambda)}^{+D_\lambda} d\nu\, e^{-i\nu\tau} & \text{for } \mu_\lambda < +D_\lambda\\ 0 & \text{else}\end{cases}\Bigg)\\
&= \frac{1}{4\pi}\sum_{\lambda}\Gamma_\lambda\Bigg(\begin{cases}\frac{1}{i\tau}e^{+i\nu\tau}\big|_{-D_\lambda}^{\min(\mu_\lambda,D_\lambda)} & \text{for } \mu_\lambda > -D_\lambda\\ 0 & \text{else}\end{cases}\\
&\quad + \begin{cases}\frac{1}{-i\tau}e^{-i\nu\tau}\big|_{\max(\mu_\lambda,-D_\lambda)}^{+D_\lambda} & \text{for } \mu_\lambda < +D_\lambda\\ 0 & \text{else}\end{cases}\Bigg)\\
&= \frac{1}{4\pi\tau i}\sum_{\lambda}\Gamma_\lambda\Bigg(\begin{cases}e^{+i\min(\mu_\lambda,D_\lambda)\tau} - e^{-iD_\lambda\tau} & \text{for } \mu_\lambda > -D_\lambda\\ 0 & \text{else}\end{cases}\\
&\quad + \begin{cases}e^{-i\max(\mu_\lambda,-D_\lambda)\tau} - e^{-iD_\lambda\tau} & \text{for } \mu_\lambda < +D_\lambda\\ 0 & \text{else}\end{cases}\Bigg)\\
&= -\frac{i}{4\pi\tau}\sum_{\lambda}\Gamma_\lambda\Bigg(\begin{cases}e^{+iD_\lambda\tau} - e^{-iD_\lambda\tau} & \text{for } \mu_\lambda \le -D_\lambda\\ -e^{-iD_\lambda\tau} - e^{-iD_\lambda\tau} + e^{+i\mu_\lambda\tau} + e^{-i\mu_\lambda\tau} + e^{+iD_\lambda\tau} - e^{+iD_\lambda\tau} & \text{for } -D_\lambda < \mu_\lambda < +D_\lambda\\ e^{+iD_\lambda\tau} - e^{-iD_\lambda\tau} & \text{for } \mu_\lambda \ge +D_\lambda\end{cases}\Bigg)\\
&= \frac{1}{4\pi\tau}\sum_{\lambda}\Gamma_\lambda\Bigg(\begin{cases}\sin(D_\lambda\tau) & \text{for } \mu_\lambda \le -D_\lambda\\ \sin(D_\lambda\tau) + i\left(\cos(D_\lambda\tau) - \cos(\mu_\lambda\tau)\right) & \text{for } -D_\lambda < \mu_\lambda < +D_\lambda\\ \sin(D_\lambda\tau) & \text{for } \mu_\lambda \ge +D_\lambda\end{cases}\Bigg)
\end{aligned}
$$

As well as

$$
\begin{aligned}
C_{12}(\tau) = -C_{21}(\tau) &= \frac{i}{4\pi}\sum_{\lambda}\int_{-\infty}^{\infty} d\nu\,\Gamma_\lambda(\nu)\Big(-e^{-i\nu\tau}+2p_{\mathrm{FD}}(\nu,\beta_\lambda,\mu_\lambda)\cos(\nu\tau)\Big)\\
&= \frac{i}{4\pi}\sum_{\lambda}\int_{-\infty}^{\infty} d\nu\,\Gamma_\lambda(\theta(\omega+D_\lambda)-\theta(\omega-D_\lambda))\Big(-e^{-i\nu\tau}+2\theta(-\omega+\mu_\lambda)\cos(\nu\tau)\Big)\\
&= \frac{i}{4\pi}\sum_{\lambda}\Gamma_\lambda\Big(-\int_{-D_\lambda}^{+D_\lambda} d\nu\,e^{-i\nu\tau}+2\int_{-\infty}^{\infty} d\nu\,(\theta(\omega+D_\lambda)-\theta(\omega-D_\lambda))(1-\theta(-\omega+\mu_\lambda))\cos(\nu\tau)\Big)\\
&= \frac{i}{4\pi}\sum_{\lambda}\Gamma_\lambda\Big(-\int_{-D_\lambda}^{+D_\lambda} d\nu\,e^{-i\nu\tau}+2\int_{-D_\lambda}^{+D_\lambda} d\nu\,\cos(\nu\tau)\\
&\quad -2\int_{-\infty}^{\infty} d\nu\,(\theta(\omega+D_\lambda)-\theta(\omega-D_\lambda))\theta(-\omega+\mu_\lambda))\cos(\nu\tau)\Big)\\
&= \frac{i}{4\pi}\sum_{\lambda}\Gamma_\lambda\Big(-\frac{1}{-i\tau}e^{-i\nu\tau}|_{-D_\lambda}^{+D_\lambda}+\frac{2}{\tau}\sin(\nu\tau)|_{-D_\lambda}^{+D_\lambda}\\
&\quad +\begin{cases}-2\displaystyle\int_{\max(-D_\lambda,\mu_\lambda)}^{+D_\lambda} d\nu\,(\theta(\omega+D_\lambda)-\theta(\omega-D_\lambda))\theta(-\omega+\mu_\lambda))\cos(\nu\tau) & \text{for } \mu_\lambda<+D_\lambda\\ 0 & \text{else}\end{cases}\Big)\\
&= \frac{i}{4\pi}\sum_{\lambda}\Gamma_\lambda\Big(-\frac{-2i}{-i\tau}\frac{e^{-iD_\lambda\tau}-e^{+iD_\lambda\tau}}{-2i}+\frac{2}{\tau}(\sin(+D_\lambda\tau)-\sin(-D_\lambda\tau))\\
&\quad +\begin{cases}-\frac{2}{\tau}\sin(\nu\tau)|_{\max(-D_\lambda,\mu_\lambda)}^{+D_\lambda} & \text{for } \mu_\lambda<+D_\lambda\\ 0 & \text{else}\end{cases}\Big)\\
&= \frac{i}{2\pi\tau}\sum_{\lambda}\Gamma_\lambda\Big(-\sin(D_\lambda\tau)+\sin(D_\lambda\tau)+\sin(D_\lambda\tau)\\
&\quad +\begin{cases}-\sin(+D_\lambda\tau)+\sin(\max(-D_\lambda,\mu_\lambda)\tau) & \text{for } \mu_\lambda<+D_\lambda\\ 0 & \text{else}\end{cases}\Big)\\
&= \frac{i}{2\pi\tau}\sum_{\lambda}\Gamma_\lambda\Big(\sin(D_\lambda\tau)\\
&\quad +\begin{cases}-\sin(+D_\lambda\tau)+\sin(\max(-D_\lambda,\mu_\lambda)\tau) & \text{for } \mu_\lambda<+D_\lambda\\ 0 & \text{else}\end{cases}\Big)\\
&= \frac{i}{2\pi\tau}\sum_{\lambda}\Gamma_\lambda\Big(\begin{cases}\sin(D_\lambda\tau)-\sin(+D_\lambda\tau)+\sin(\max(-D_\lambda,\mu_\lambda)\tau) & \text{for } \mu_\lambda<+D_\lambda\\ \sin(D_\lambda\tau) & \text{else}\end{cases}\Big)\\
&= \frac{i}{2\pi\tau}\sum_{\lambda}\Gamma_\lambda\Big(\begin{cases}\sin(\max(-D_\lambda,\mu_\lambda)\tau) & \text{for } \mu_\lambda<+D_\lambda\\ \sin(D_\lambda\tau) & \text{else}\end{cases}\Big)\\
&= \frac{i}{2\pi\tau}\sum_{\lambda}\Gamma_\lambda\Big(\begin{cases}\sin(-D_\lambda\tau) & \text{for } \mu_\lambda\le -D_\lambda\\ \sin(\mu_\lambda\tau) & \text{for } -D_\lambda<\mu_\lambda<+D_\lambda\\ \sin(D_\lambda\tau) & \text{for } \mu_\lambda\ge +D_\lambda\end{cases}\Big).
\end{aligned}
$$

As a check we compute the terms arranged in a different way

$$
\begin{aligned}
C_{12}(\tau) = -C_{21}(\tau) &= \frac{i}{4\pi}\sum_\lambda \int_{-\infty}^{\infty} d\nu\, \Gamma_\lambda(\nu)\Big(- e^{-i\nu\tau} + 2p_{\mathrm{FD}}(\nu,\beta_\lambda,\mu_\lambda)\cos(\nu\tau)\Big) \\
&= \frac{i}{4\pi}\sum_\lambda \int_{-\infty}^{\infty} d\nu\, \Gamma_\lambda(\nu)\Big(p_{\mathrm{FD}}(\nu,\beta_\lambda,\mu_\lambda)e^{+i\nu\tau} - \bar{p}_{\mathrm{FD}}(\nu,\beta_\lambda,\mu_\lambda)e^{-i\nu\tau}\Big) \\
&= \frac{i}{4\pi}\sum_\lambda \int_{-\infty}^{\infty} d\nu\, \Gamma_\lambda(\theta(\nu+D_\lambda)-\theta(\nu-D_\lambda))\Big(e^{+i\nu\tau}\theta(-\nu+\mu_\lambda) - e^{-i\nu\tau}\theta(\nu-\mu_\lambda)\Big) \\
&= \frac{i}{4\pi}\sum_\lambda \Gamma_\lambda \int_{-\infty}^{\infty} d\nu \Big((\theta(\nu+D_\lambda)-\theta(\nu-D_\lambda))\theta(-\nu+\mu_\lambda)e^{+i\nu\tau} \\
&\quad - (\theta(\nu+D_\lambda)-\theta(\nu-D_\lambda))\theta(\nu-\mu_\lambda)e^{-i\nu\tau}\Big) \\
&= \frac{i}{4\pi}\sum_\lambda \Gamma_\lambda\Bigg(\begin{cases} \int_{-D_\lambda}^{\min(\mu_\lambda,D_\lambda)} d\nu\, e^{+i\nu\tau} & \text{for } \mu_\lambda > -D_\lambda \\ 0 & \text{else} \end{cases} \\
&\quad - \begin{cases} \int_{\max(\mu_\lambda,-D_\lambda)}^{+D_\lambda} d\nu\, e^{-i\nu\tau} & \text{for } \mu_\lambda < +D_\lambda \\ 0 & \text{else} \end{cases} \Bigg) \\
&= \frac{i}{4\pi}\sum_\lambda \Gamma_\lambda\Bigg(\begin{cases} \frac{1}{i\tau} e^{+i\nu\tau}\big|_{-D_\lambda}^{\min(\mu_\lambda,D_\lambda)} & \text{for } \mu_\lambda > -D_\lambda \\ 0 & \text{else} \end{cases} \\
&\quad - \begin{cases} \frac{1}{-i\tau} e^{-i\nu\tau}\big|_{\max(\mu_\lambda,-D_\lambda)}^{+D_\lambda} & \text{for } \mu_\lambda < +D_\lambda \\ 0 & \text{else} \end{cases} \Bigg) \\
&= \frac{1}{4\pi\tau}\sum_\lambda \Gamma_\lambda\Bigg(\begin{cases} e^{i\min(\mu_\lambda,D_\lambda)\tau} - e^{-iD_\lambda\tau} & \text{for } \mu_\lambda > -D_\lambda \\ 0 & \text{else} \end{cases} \\
&\quad + \begin{cases} -e^{-i\max(\mu_\lambda,-D_\lambda)\tau} + e^{-iD_\lambda\tau} & \text{for } \mu_\lambda < +D_\lambda \\ 0 & \text{else} \end{cases} \Bigg) \\
&= \frac{1}{4\pi\tau}\sum_\lambda \Gamma_\lambda\Bigg(\begin{cases} e^{-iD_\lambda\tau} - e^{+iD_\lambda\tau} & \text{for } \mu_\lambda \le -D_\lambda \\ e^{+i\mu_\lambda\tau} - e^{-iD_\lambda\tau} - e^{-i\mu_\lambda\tau} + e^{-iD_\lambda\tau} & \text{for } -D_\lambda < \mu_\lambda < +D_\lambda \\ e^{+iD_\lambda\tau} - e^{-iD_\lambda\tau} & \text{for } \mu_\lambda \ge +D_\lambda \end{cases} \\
&= \frac{i}{2\pi\tau}\sum_\lambda \Gamma_\lambda\Bigg(\begin{cases} \sin(-D_\lambda\tau) & \text{for } \mu_\lambda \le -D_\lambda \\ \sin(\mu_\lambda\tau) & \text{for } -D_\lambda < \mu_\lambda < +D_\lambda \\ \sin(D_\lambda\tau) & \text{for } \mu_\lambda \ge +D_\lambda \end{cases} \Bigg).
\end{aligned}
$$

E.8.3. Evaluation of the even Fourier transformed bath correlation functions

Evaluating the respective Fourier transforms via direct transformation of $C_{\alpha\beta}(\tau)$, we find

$$
\begin{aligned}
\xi_{11}(\omega) = \xi_{22}(\omega) &= \int_{-\infty}^{\infty} dt\, e^{+i\omega t} C_{11}(\tau) \\
&= \int_{-\infty}^{\infty} dt\, e^{+i\omega t} \frac{1}{2\pi\tau} \sum_{\lambda} \Gamma_\lambda \left(\begin{cases} \sin(D_\lambda \tau) & \text{for } \mu_\lambda \le -D_\lambda \\ \sin(D_\lambda \tau) + i\left(\cos(D_\lambda \tau) - \cos(\mu_\lambda \tau)\right) & \text{for } -D_\lambda < \mu_\lambda < +D_\lambda \\ \sin(D_\lambda \tau) & \text{for } \mu_\lambda \ge +D_\lambda \end{cases} \right) \\
&= \frac{1}{2\pi} \sum_{\lambda} \Gamma_\lambda \int_{-\infty}^{\infty} dt\, e^{+i\omega t} \left(\begin{cases} \frac{\sin(D_\lambda \tau)}{\tau} & \text{for } \mu_\lambda \le -D_\lambda \\ \frac{\sin(D_\lambda \tau)}{\tau} + i\left(\frac{\cos(D_\lambda \tau)}{\tau} - \frac{\cos(\mu_\lambda \tau)}{\tau}\right) & \text{for } -D_\lambda < \mu_\lambda < +D_\lambda \\ \frac{\sin(D_\lambda \tau)}{\tau} & \text{for } \mu_\lambda \ge +D_\lambda \end{cases} \right) \\
&= \frac{1}{2\pi} \sum_{\lambda} \Gamma_\lambda \Bigg(\\
&\begin{cases} \frac{\pi}{2}\left(\operatorname{sign}(\omega + D_\lambda) - \operatorname{sign}(\omega - D_\lambda)\right) & \text{for } \mu_\lambda \le -D_\lambda \\ \frac{\pi}{2}\left(\operatorname{sign}(\omega + D_\lambda) - \operatorname{sign}(\omega - D_\lambda)\right) & \\ +i\frac{i\pi}{2}\left(\left(\operatorname{sign}(\omega + D_\lambda) + \operatorname{sign}(\omega - D_\lambda) - \operatorname{sign}(\omega + \mu_\lambda) - \operatorname{sign}(\omega - \mu_\lambda)\right)\right) & \text{for } -D_\lambda < \mu_\lambda < +D_\lambda \\ \frac{\pi}{2}\left(\operatorname{sign}(\omega + D_\lambda) - \operatorname{sign}(\omega - D_\lambda)\right) & \text{for } \mu_\lambda \ge +D_\lambda \end{cases} \Bigg) \\
&= \frac{1}{4} \sum_{\lambda} \Gamma_\lambda \Bigg(\\
&\begin{cases} \operatorname{sign}(\omega + D_\lambda) - \operatorname{sign}(\omega - D_\lambda) & \text{for } \mu_\lambda \le -D_\lambda \\ \operatorname{sign}(\omega + D_\lambda) - \operatorname{sign}(\omega - D_\lambda) & \\ -\operatorname{sign}(\omega + D_\lambda) - \operatorname{sign}(\omega - D_\lambda) + \operatorname{sign}(\omega + \mu_\lambda) + \operatorname{sign}(\omega - \mu_\lambda) & \text{for } -D_\lambda < \mu_\lambda < +D_\lambda \\ \operatorname{sign}(\omega + D_\lambda) - \operatorname{sign}(\omega - D_\lambda) & \text{for } \mu_\lambda \ge +D_\lambda \end{cases} \Bigg) \\
&= \frac{1}{4} \sum_{\lambda} \Gamma_\lambda \left(\begin{cases} \operatorname{sign}(\omega + D_\lambda) - \operatorname{sign}(\omega - D_\lambda) & \text{for } \mu_\lambda \le -D_\lambda \\ -2\operatorname{sign}(\omega - D_\lambda) + \operatorname{sign}(\omega + \mu_\lambda) + \operatorname{sign}(\omega - \mu_\lambda) & \text{for } -D_\lambda < \mu_\lambda < +D_\lambda \\ \operatorname{sign}(\omega + D_\lambda) - \operatorname{sign}(\omega - D_\lambda) & \text{for } \mu_\lambda \ge +D_\lambda \end{cases} \right) \\
&= \frac{1}{2} \sum_{\lambda} \Gamma_\lambda \left(\begin{cases} \theta(\omega + D_\lambda) - \theta(\omega - D_\lambda) & \text{for } \mu_\lambda \le -D_\lambda \\ -2\theta(\omega - D_\lambda) + \theta(\omega + \mu_\lambda) + \theta(\omega - \mu_\lambda) & \text{for } -D_\lambda < \mu_\lambda < +D_\lambda \\ \theta(\omega + D_\lambda) - \theta(\omega - D_\lambda) & \text{for } \mu_\lambda \ge +D_\lambda \end{cases} \right).
\end{aligned}
$$

For the off diagonal component we obtain

$$\begin{aligned}
\xi_{12}(\omega) = -\xi_{21}(\omega) &= \int_{-\infty}^{\infty} dt\, e^{+i\omega t} C_{12}(\tau) \\
&= \int_{-\infty}^{\infty} dt\, e^{+i\omega t} \frac{i}{2\pi\tau} \sum_{\lambda} \Gamma_\lambda \left(\begin{cases} \sin(-D_\lambda \tau) & \text{for } \mu_\lambda \leq -D_\lambda \\ \sin(\mu_\lambda \tau) & \text{for } -D_\lambda < \mu_\lambda < +D_\lambda \\ \sin(D_\lambda \tau) & \text{for } \mu_\lambda \geq +D_\lambda \end{cases} \right) \\
&= \frac{i}{2\pi} \sum_{\lambda} \Gamma_\lambda \int_{-\infty}^{\infty} dt\, e^{+i\omega t} \left(\begin{cases} \frac{\sin(-D_\lambda \tau)}{\tau} & \text{for } \mu_\lambda \leq -D_\lambda \\ \frac{\sin(\mu_\lambda \tau)}{\tau} & \text{for } -D_\lambda < \mu_\lambda < +D_\lambda \\ \frac{\sin(D_\lambda \tau)}{\tau} & \text{for } \mu_\lambda \geq +D_\lambda \end{cases} \right) \\
&= \frac{i}{2\pi} \sum_{\lambda} \Gamma_\lambda \left(\begin{cases} \frac{\pi}{2} \left(\operatorname{sign}(\omega + (-D_\lambda)) - \operatorname{sign}(\omega - (-D_\lambda)) \right) & \text{for } \mu_\lambda \leq -D_\lambda \\ \frac{\pi}{2} \left(\operatorname{sign}(\omega + \mu_\lambda) - \operatorname{sign}(\omega - \mu_\lambda) \right) & \text{for } -D_\lambda < \mu_\lambda < +D_\lambda \\ \frac{\pi}{2} \left(\operatorname{sign}(\omega + D_\lambda) - \operatorname{sign}(\omega - D_\lambda) \right) & \text{for } \mu_\lambda \geq +D_\lambda \end{cases} \right) \\
&= \frac{i}{4} \sum_{\lambda} \Gamma_\lambda \left(\begin{cases} \operatorname{sign}(\omega + (-D_\lambda)) - \operatorname{sign}(\omega - (-D_\lambda)) & \text{for } \mu_\lambda \leq -D_\lambda \\ \operatorname{sign}(\omega + \mu_\lambda) - \operatorname{sign}(\omega - \mu_\lambda) & \text{for } -D_\lambda < \mu_\lambda < +D_\lambda \\ \operatorname{sign}(\omega + D_\lambda) - \operatorname{sign}(\omega - D_\lambda) & \text{for } \mu_\lambda \geq +D_\lambda \end{cases} \right) \\
&= \frac{i}{2} \sum_{\lambda} \Gamma_\lambda \left(\begin{cases} \theta(\omega + (-D_\lambda)) - \theta(\omega - (-D_\lambda)) & \text{for } \mu_\lambda \leq -D_\lambda \\ \theta(\omega + \mu_\lambda) - \theta(\omega - \mu_\lambda) & \text{for } -D_\lambda < \mu_\lambda < +D_\lambda \\ \theta(\omega + D_\lambda)\theta(\omega - D_\lambda) & \text{for } \mu_\lambda \geq +D_\lambda \end{cases} \right).
\end{aligned}$$

E.8.4. Evaluation of the odd Fourier transformed bath correlation functions

Next we evaluate the odd Fourier transform $\lambda_{\alpha\beta}(\omega)$ of the bath correlation functions via direct transformation of $C_{\alpha\beta}(\tau)$

$$\begin{aligned}
\lambda_{11}(\omega) = \lambda_{22}(\omega) &= \int_{-\infty}^{\infty} d\tau \operatorname{sign}(\tau) e^{+i\omega\tau} C_{11}(\tau) \\
&= \int_{-\infty}^{\infty} d\tau \operatorname{sign}(\tau) e^{+i\omega\tau} \frac{1}{2\pi\tau} \sum_{\lambda} \Gamma_\lambda \Big(\sin(D_\lambda \tau) + i \left(\cos(D_\lambda \tau) - \cos(\mu_\lambda \tau) \right) \Big),
\end{aligned}$$

where the first term with the sine is valid in all regions $A : \mu_\lambda \leq -D_\lambda$, $B : -D\lambda < \mu_\lambda < +D_\lambda$ and $C : \mu_\lambda \geq +D_\lambda$ while the cosine terms only appear in region B. By unwrapping the sign function

we find

$$\begin{aligned}
\lambda_{11}(\omega) = \lambda_{22}(\omega) &= \frac{1}{2\pi}\sum_\lambda \Gamma_\lambda \Bigg(\int_0^\infty d\tau - \int_{-\infty}^0 d\tau \Bigg) e^{+i\omega\tau} \frac{1}{\tau} \Bigg(\sin(D_\lambda\tau) + i\left(\cos(D_\lambda\tau) - \cos(\mu_\lambda\tau)\right) \Bigg) \\
&= \frac{1}{2\pi}\sum_\lambda \Gamma_\lambda \Bigg(\int_0^\infty d\tau\, e^{+i\omega\tau} \frac{1}{\tau} \Bigg(\sin(D_\lambda\tau) + i\left(\cos(D_\lambda\tau) - \cos(\mu_\lambda\tau)\right) \Bigg) \\
&- \int_{-\infty}^0 d\tau\, e^{+i\omega\tau} \frac{1}{\tau} \Bigg(\sin(D_\lambda\tau) + i\left(\cos(D_\lambda\tau) - \cos(\mu_\lambda\tau)\right) \Bigg) \Bigg) \\
&= \frac{1}{2\pi}\sum_\lambda \Gamma_\lambda \Bigg(\int_0^\infty d\tau\, e^{+i\omega\tau} \frac{1}{\tau} \Bigg(\sin(D_\lambda\tau) + i\left(\cos(D_\lambda\tau) - \cos(\mu_\lambda\tau)\right) \Bigg) \\
&- \int_{\infty}^0 -d\tau\, e^{-i\omega\tau} \frac{1}{-\tau} \Bigg(\sin(-D_\lambda\tau) + i\left(\cos(-D_\lambda\tau) - \cos(-\mu_\lambda\tau)\right) \Bigg) \Bigg) \\
&= \frac{1}{2\pi}\sum_\lambda \Gamma_\lambda \Bigg(\int_0^\infty d\tau\, e^{+i\omega\tau} \frac{1}{\tau} \Bigg(\sin(D_\lambda\tau) + i\left(\cos(D_\lambda\tau) - \cos(\mu_\lambda\tau)\right) \Bigg) \\
&+ \int_0^\infty d\tau\, e^{-i\omega\tau} \frac{1}{\tau} \Bigg(-\sin(D_\lambda\tau) + i\left(\cos(D_\lambda\tau) - \cos(\mu_\lambda\tau)\right) \Bigg) \Bigg) \\
&= \frac{1}{2\pi}\sum_\lambda \Gamma_\lambda \int_0^\infty \frac{d\tau}{\tau} \Bigg(\sin(D_\lambda\tau)(e^{+i\omega\tau} - e^{-i\omega\tau}) \\
&+ i\left(\cos(D_\lambda\tau) - \cos(\mu_\lambda\tau)\right)(e^{+i\omega\tau} + e^{-i\omega\tau}) \Bigg) \\
&= \frac{1}{2\pi}\sum_\lambda \Gamma_\lambda \int_0^\infty \frac{d\tau}{\tau} \Bigg(\sin(D_\lambda\tau) 2i \sin(\omega\tau) + i\left(\cos(D_\lambda\tau) - \cos(\mu_\lambda\tau)\right) 2\cos(\omega\tau) \Bigg) \\
&= \frac{i}{\pi}\sum_\lambda \Gamma_\lambda \int_0^\infty \frac{d\tau}{\tau} \Bigg(\sin(D_\lambda\tau)\sin(\omega\tau) + \left(\cos(D_\lambda\tau) - \cos(\mu_\lambda\tau)\right)\cos(\omega\tau) \Bigg),
\end{aligned}$$

where the sin sin integral converges while the separate cos cos integrals diverge at $\tau \to 0$. Therefore they have to be treated together using

$$\cos(x) - \cos(y) = 2\sin\left(\frac{y+x}{2}\right)\sin\left(\frac{y-x}{2}\right),$$

we find

$$\lambda_{11}(\omega) = \lambda_{22}(\omega) = \frac{i}{\pi}\sum_\lambda \Gamma_\lambda \int_0^\infty \frac{d\tau}{\tau} \Bigg(\sin(D_\lambda\tau)\sin(\omega\tau) + 2\sin\left(\frac{\mu_\lambda + D_\lambda}{2}\tau\right)\sin\left(\frac{\mu_\lambda - D_\lambda}{2}\tau\right)\cos(\omega\tau) \Bigg).$$

Furthermore with

$$\sin(x)\cos(y) = \frac{1}{2}\Bigg(\sin(x-y) + \sin(x+y) \Bigg),$$

we end up with

$$\begin{aligned}
\lambda_{11}(\omega) = \lambda_{22}(\omega) &= \frac{i}{\pi}\sum_{\lambda}\Gamma_{\lambda}\int_{0}^{\infty}\frac{d\tau}{\tau}\Bigg(\sin(D_{\lambda}\tau)\sin(\omega\tau) \\
&\quad + 2\sin\left(\frac{\mu_{\lambda}+D_{\lambda}}{2}\tau\right)\left(\frac{1}{2}\sin\left(\frac{\mu_{\lambda}-D_{\lambda}-2\omega}{2}\tau\right)+\sin\left(\frac{\mu_{\lambda}-D_{\lambda}+2\omega}{2}\tau\right)\right)\Bigg) \\
&= \frac{i}{\pi}\sum_{\lambda}\Gamma_{\lambda}\int_{0}^{\infty}\frac{d\tau}{\tau}\Bigg(\sin(D_{\lambda}\tau)\sin(\omega\tau) \\
&\quad + \sin\left(\frac{\mu_{\lambda}+D_{\lambda}}{2}\tau\right)\sin\left(\frac{\mu_{\lambda}-D_{\lambda}-2\omega}{2}\tau\right) \\
&\quad + \sin\left(\frac{\mu_{\lambda}+D_{\lambda}}{2}\tau\right)\sin\left(\frac{\mu_{\lambda}-D_{\lambda}+2\omega}{2}\tau\right)\Bigg).
\end{aligned}$$

With

$$\int_{0}^{+\infty}\frac{d\tau}{\tau}\sin(x\tau)\sin(y\tau) = \frac{1}{2}\ln\left(\left|\frac{x+y}{x-y}\right|\right),$$

we finally end up with

$$\begin{aligned}
\lambda_{11}(\omega) = \lambda_{22}(\omega) &= \frac{i}{\pi}\sum_{\lambda}\Gamma_{\lambda}\Bigg(\frac{1}{2}\ln\left(\left|\frac{D_{\lambda}+\omega}{D_{\lambda}-\omega}\right|\right) \\
&\quad + \frac{1}{2}\ln\left(\left|\frac{\mu_{\lambda}+D_{\lambda}+\mu_{\lambda}-D_{\lambda}-2\omega}{\mu_{\lambda}+D_{\lambda}-\mu_{\lambda}+D_{\lambda}+2\omega}\right|\right) \\
&\quad + \frac{1}{2}\ln\left(\left|\frac{\mu_{\lambda}+D_{\lambda}+\mu_{\lambda}-D_{\lambda}+2\omega}{\mu_{\lambda}+D_{\lambda}-\mu_{\lambda}+D_{\lambda}-2\omega}\right|\right)\Bigg) \\
&= \frac{i}{2\pi}\sum_{\lambda}\Gamma_{\lambda}\left(\ln\left(\left|\frac{D_{\lambda}+\omega}{D_{\lambda}-\omega}\right|\right)+\ln\left(\left|\frac{\mu_{\lambda}-\omega}{D_{\lambda}+\omega}\right|\right)+\ln\left(\left|\frac{\mu_{\lambda}+\omega}{D_{\lambda}-\omega}\right|\right)\right) \\
&= \frac{i}{2\pi}\sum_{\lambda}\Gamma_{\lambda}\left(\ln\left(\left|\frac{D_{\lambda}+\omega}{D_{\lambda}-\omega}\right|\right)+\ln\left(\left|\frac{\mu_{\lambda}^2-\omega^2}{D_{\lambda}^2-\omega^2}\right|\right)\right) \\
&= \frac{i}{2\pi}\sum_{\lambda}\Gamma_{\lambda}\begin{cases}\ln\left(\left|\frac{\omega+D_{\lambda}+}{\omega-D_{\lambda}}\right|\right) & \text{for } \mu_{\lambda}\le -D_{\lambda} \\ \ln\left(\left|\frac{\omega+D_{\lambda}+}{\omega-D_{\lambda}}\right|\right)+\ln\left(\left|\frac{\omega^2-\mu_{\lambda}^2}{\omega^2-D_{\lambda}^2}\right|\right) & \text{for } -D_{\lambda}<\mu_{\lambda}<+D_{\lambda} \\ \ln\left(\left|\frac{\omega+D_{\lambda}+}{\omega-D_{\lambda}}\right|\right) & \text{for } \mu_{\lambda}\ge +D_{\lambda}\end{cases}.
\end{aligned}$$

For the off diagonal component we find

$$\begin{aligned}
\lambda_{12}(\omega) = -\lambda_{21}(\omega) &= \int_{-\infty}^{\infty}d\tau\,\mathrm{sign}(\tau)e^{+i\omega\tau}C_{12}(\tau) \\
&= \int_{-\infty}^{\infty}d\tau\,\mathrm{sign}(\tau)e^{+i\omega\tau}\frac{i}{2\pi\tau}\sum_{\lambda}\Gamma_{\lambda}\sin(X_{\lambda}\tau),
\end{aligned}$$

with $X_\lambda = -D_\lambda$ in region A, $X_\lambda = \mu_\lambda$ in region B and $X_\lambda = +D_\lambda$ in region C. We continue

$$\begin{aligned}
\lambda_{12}(\omega) = -\lambda_{21}(\omega) &= \frac{i}{2\pi}\sum_\lambda \Gamma_\lambda \left(\int_0^\infty - \int_{-\infty}^0 \right) \frac{d\tau}{\tau}\, e^{+i\omega\tau} \sin\left(X_\lambda \tau\right) \\
&= \frac{i}{2\pi}\sum_\lambda \Gamma_\lambda \left(\int_0^\infty \frac{d\tau}{\tau}\, e^{+i\omega\tau} \sin\left(X_\lambda \tau\right) - \int_\infty^0 \frac{-d\tau}{-\tau}\, e^{-i\omega\tau} \sin\left(-X_\lambda \tau\right) \right) \\
&= \frac{i}{2\pi}\sum_\lambda \Gamma_\lambda \left(\int_0^\infty \frac{d\tau}{\tau} \left(e^{+i\omega\tau} - e^{-i\omega\tau} \right) \sin\left(X_\lambda \tau\right) \right) \\
&= -\frac{1}{\pi}\sum_\lambda \Gamma_\lambda \int_0^\infty \frac{d\tau}{\tau} \sin\left(X_\lambda \tau\right) \sin\left(\omega\tau\right) \\
&= -\frac{1}{\pi}\sum_\lambda \Gamma_\lambda \frac{1}{2} \ln\left(\left| \frac{X_\lambda + \omega}{X_\lambda - \omega} \right| \right) \\
&= \frac{1}{2\pi}\sum_\lambda \Gamma_\lambda \ln\left(\left| \frac{\omega - X_\lambda}{\omega + X_\lambda} \right| \right) \\
&= \frac{1}{2\pi}\sum_\lambda \Gamma_\lambda \begin{cases} \ln\left(\left| \frac{\omega-(-D_\lambda)}{\omega+(-D_\lambda)} \right| \right) & \text{for } \mu_\lambda \le -D_\lambda \\ \ln\left(\left| \frac{\omega-\mu_\lambda}{\omega+\mu_\lambda} \right| \right) & \text{for } -D_\lambda < \mu_\lambda < +D_\lambda \\ \ln\left(\left| \frac{\omega-D_\lambda}{\omega+D_\lambda} \right| \right) & \text{for } \mu_\lambda \ge +D_\lambda \end{cases} .
\end{aligned}$$

E.8.5. Summary of the results

For flat bands at zero temperature, see Fig. E.1, Fig. E.2, Fig. E.3 and Fig. E.4, the time dependent correlation functions $C_{\alpha\beta}(\tau)$ are given by

$$C_{11}(\tau) = C_{22}(\tau) = \frac{1}{2\pi\tau}\sum_\lambda \Gamma_\lambda \left(\begin{cases} \sin\left(D_\lambda\tau\right) & \text{for } \mu_\lambda \le -D_\lambda \\ \sin\left(D_\lambda\tau\right) + i\left(\cos\left(D_\lambda\tau\right) - \cos\left(\mu_\lambda\tau\right)\right) & \text{for } -D_\lambda < \mu_\lambda < +D_\lambda \\ \sin\left(D_\lambda\tau\right) & \text{for } \mu_\lambda \ge +D_\lambda \end{cases} \right),$$

$$C_{12}(\tau) = -C_{21}(\tau) = \frac{i}{2\pi\tau}\sum_\lambda \Gamma_\lambda \left(\begin{cases} \sin\left(-D_\lambda\tau\right) & \text{for } \mu_\lambda \le -D_\lambda \\ \sin\left(\mu_\lambda\tau\right) & \text{for } -D_\lambda < \mu_\lambda < +D_\lambda \\ \sin\left(D_\lambda\tau\right) & \text{for } \mu_\lambda \ge +D_\lambda \end{cases} \right).$$

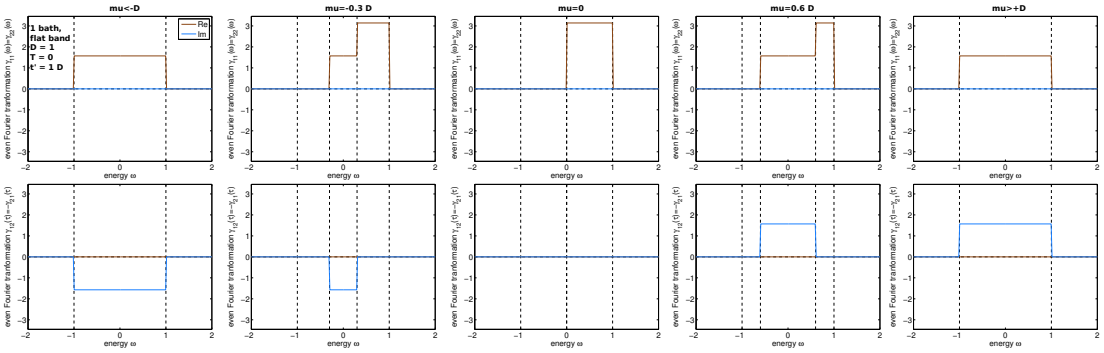

Figure E.1.: Coupling function $\Gamma(\omega)$ and distribution function $p_{\mathrm{FD}}(\omega)$ for one bath with constant density of states in the region $[-D, D]$ at zero temperature. The chemical potential is marked as a cyan vertical line.

The even Fourier transforms $\xi_{\alpha\beta}(\omega)$ read

$$\begin{aligned}
\xi_{11}(\omega) = \xi_{22}(\omega) &= \frac{1}{2}\sum_\lambda \Gamma_\lambda \left(\begin{cases} \theta(\omega + D_\lambda) - \theta(\omega - D_\lambda) & \text{for } \mu_\lambda \le -D_\lambda \\ -2\theta(\omega - D_\lambda) + \theta(\omega + \mu_\lambda) + \theta(\omega - \mu_\lambda) & \text{for } -D_\lambda < \mu_\lambda < +D_\lambda \\ \theta(\omega + D_\lambda) - \theta(\omega - D_\lambda) & \text{for } \mu_\lambda \ge +D_\lambda \end{cases} \right) \\
&= \frac{1}{2}\sum_\lambda \Gamma_\lambda \left[\theta(\omega + D_\lambda) - \theta(\omega - D_\lambda)\right]\left[\theta(\omega + \mu_\lambda) + \theta(\omega - \mu_\lambda)\right] , \\
\xi_{12}(\omega) = -\xi_{21}(\omega) &= \frac{i}{2}\sum_\lambda \Gamma_\lambda \left(\begin{cases} \theta(\omega + (-D_\lambda)) - \theta(\omega - (-D_\lambda)) & \text{for } \mu_\lambda \le -D_\lambda \\ \theta(\omega + \mu_\lambda) - \theta(\omega - \mu_\lambda) & \text{for } -D_\lambda < \mu_\lambda < +D_\lambda \\ \theta(\omega + D_\lambda)\theta(\omega - D_\lambda) & \text{for } \mu_\lambda \ge +D_\lambda \end{cases} \right) \\
&= \frac{i}{2}\sum_\lambda \Gamma_\lambda \left[\theta(\omega + D_\lambda) - \theta(\omega - D_\lambda)\right]\left[\theta(\omega + \mu_\lambda) - \theta(\omega - \mu_\lambda)\right] .
\end{aligned}$$

And for the odd Fourier transforms $\lambda_{\alpha\beta}(\omega)$ we find

$$\begin{aligned}
\lambda_{11}(\omega) = \lambda_{22}(\omega) &= \frac{i}{2\pi}\sum_\lambda \Gamma_\lambda \begin{cases} \ln\left(\left|\frac{\omega + D_\lambda}{\omega - D_\lambda}\right|\right) & \text{for } \mu_\lambda \le -D_\lambda \\ \ln\left(\left|\frac{\omega + D_\lambda}{\omega - D_\lambda}\right|\right) + \ln\left(\left|\frac{\omega^2 - \mu_\lambda^2}{\omega^2 - D_\lambda^2}\right|\right) & \text{for } -D_\lambda < \mu_\lambda < +D_\lambda \\ \ln\left(\left|\frac{\omega + D_\lambda}{\omega - D_\lambda}\right|\right) & \text{for } \mu_\lambda \ge +D_\lambda \end{cases} , \\
\lambda_{12}(\omega) = -\lambda_{21}(\omega) &= \frac{1}{2\pi}\sum_\lambda \Gamma_\lambda \begin{cases} \ln\left(\left|\frac{\omega - (-D_\lambda)}{\omega + (-D_\lambda)}\right|\right) & \text{for } \mu_\lambda \le -D_\lambda \\ \ln\left(\left|\frac{\omega - \mu_\lambda}{\omega + \mu_\lambda}\right|\right) & \text{for } -D_\lambda < \mu_\lambda < +D_\lambda \\ \ln\left(\left|\frac{\omega - D_\lambda}{\omega + D_\lambda}\right|\right) & \text{for } \mu_\lambda \ge +D_\lambda \end{cases} .
\end{aligned}$$

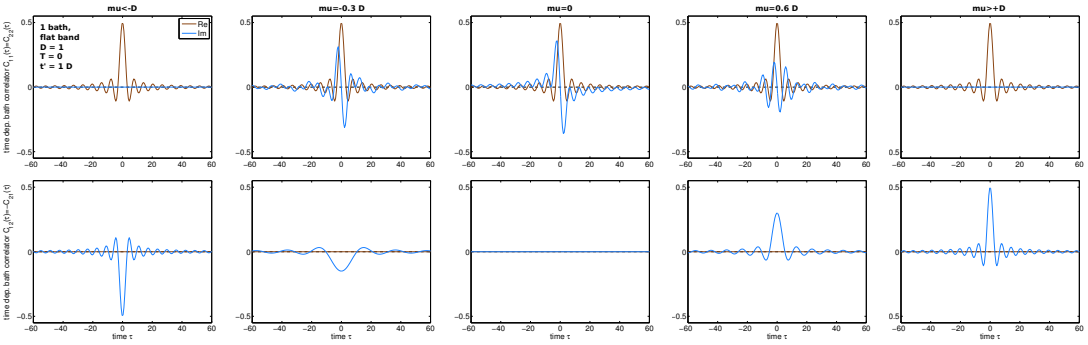

Figure E.2.: Time dependent bath correlation function $C_{\alpha\beta}(\tau)$ for one bath with constant density of states in the region $[-D, D]$ at zero temperature.

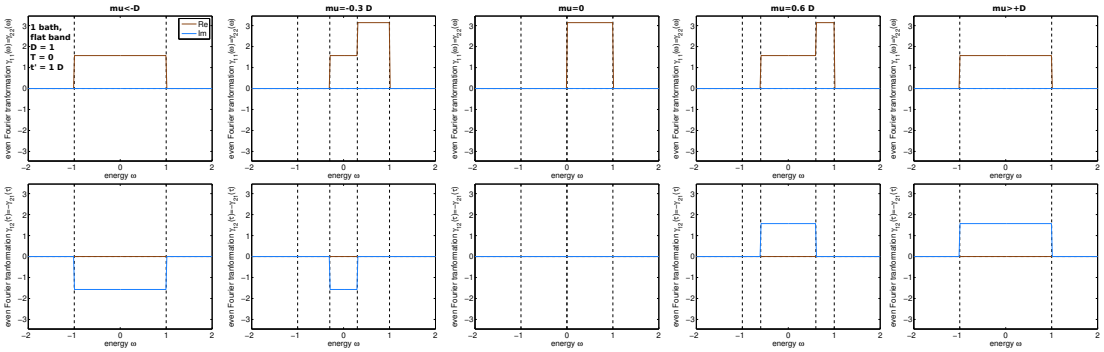

Figure E.3.: Even Fourier transform of the bath correlation function $\xi_{\alpha\beta}(\omega)$ for one bath with constant density of states in the region $[-D, D]$ at zero temperature.

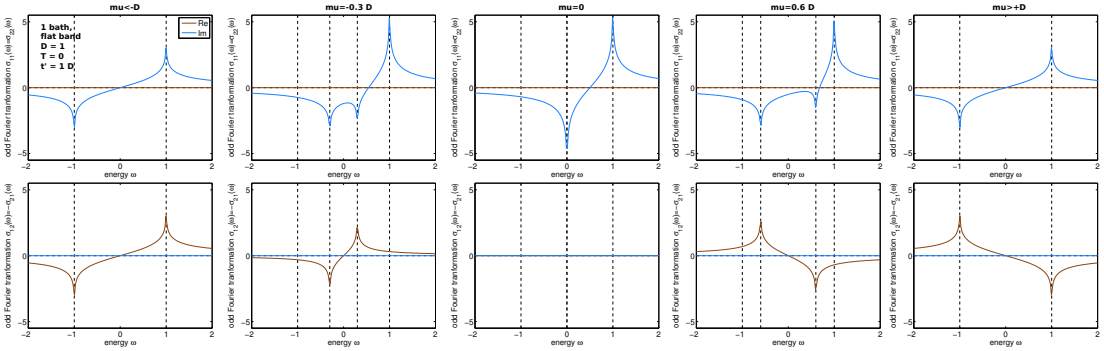

Figure E.4.: Odd Fourier transform of the bath correlation function $\lambda_{\alpha\beta}(\omega)$ for one bath with constant density of states in the region $[-D, D]$ at zero temperature.

F. Lindblad master equation for non-interacting fermions

In the following we consider fermions on a lattice described by a Hamiltonian

$$\hat{\mathcal{H}} = \hat{\mathcal{H}}_0 + \hat{\mathcal{H}}_I \,,$$

where the non-interacting part

$$\hat{\mathcal{H}}_0 = \hat{\mathcal{H}}_n + \hat{\mathcal{H}}_a = c_\mu^\dagger h_{\mu\nu} c_\nu + \left(c_\mu a_{\mu\nu} c_\nu + c_\mu^\dagger a_{\nu\mu}^* c_\nu^\dagger \right) ,$$

is quadratic in the fermion creation $c^\dagger$ and annihilation c operators, obeying the standard fermionic anti-commutation relations

$$\{c_\mu^\dagger, c_\nu^\dagger\} = \{c_\mu, c_\nu\} = 0, \{c_\mu^\dagger, c_\nu\} = \delta_{\mu\nu} \,, \tag{F.1}$$

where the anti-commutator is defined as $\{\hat{A}, \hat{B}\} = \{\hat{B}, \hat{A}\} = \hat{A}\hat{B} + \hat{B}\hat{A}$. Besides the normal part $\hat{\mathcal{H}}_n$ we explicitly take anomalous terms $\hat{\mathcal{H}}_a$ into account. Greek indices μ, ν quite generally denote compound indices of N fermionic quantum numbers where we have in mind for example a site i, orbital α and a spin σ index. Our notation relies on Einstein's summation convention where doubly occurring indices have to be summed over. The matrix representation of the normal part has to be hermitian

$$h_{\mu\nu} = h_{\nu\mu}^* \,,$$

and the anomalous part antisymmetric

$$a_{\mu\nu} = -a_{\nu\mu} \,.$$

Note that this implies zeros on the diagonal of $a_{\mu\nu}$. This leaves of course $\frac{(N+1)N}{2}$ independent parameters in $h_{\mu\nu}$ and $\frac{(N-1)N}{2}$ in $a_{\mu\nu}$, which are N^2 overall.

F.1. Open quantum systems and the Lindblad master equation

The Lindblad quantum master equation for the time evolution of the hermitian density operator $\hat{\rho}$ reads [454, 466, 456]

$$\dot{\hat{\rho}} = -i\hat{\hat{\mathcal{L}}}\hat{\rho} = -i\left([\hat{\mathcal{H}}, \hat{\rho}]_- + 2i \sum_{\mu\nu\alpha} \Gamma_{\mu\nu\alpha} \left(\hat{L}_{\mu\alpha} \hat{\rho} \hat{L}_{\nu\alpha}^\dagger - \frac{1}{2} \{ \hat{L}_{\nu\alpha}^\dagger \hat{L}_{\mu\alpha}, \hat{\rho} \} \right) \right) , \tag{F.2}$$

where $\hat{\hat{\mathcal{L}}}$ is the Lindbladian super-operator and $\hat{L}^{(\dagger)}_{\mu\alpha}$ are called dissipators with dissipation index α. The first term with the commutator $[\hat{A},\hat{B}]_- = -[\hat{B},\hat{A}]_- = \hat{A}\hat{B} - \hat{B}\hat{A}$ represents the unitary part of the time evolution, which is the only part present in closed systems. There arise two additional dissipative terms in open systems. The first one describes quantum jumps between the levels of the system, while the second term with the anti-commutator balances quantum fluctuations and quantum jumps and is needed for a trace preserving time evolution. In general there exist M^2-1 dissipators $\hat{L}^{(\dagger)}_{\mu\alpha}$ where M is the size of the Hilbert space. In the following we consider quadratic ones only i.e. the two normal options

$$\hat{L}_{\mu+} = c^\dagger_\mu, \hat{L}_{\mu-} = c_\mu \text{ with } \Gamma_{\mu\nu\alpha} = \Gamma_{\mu\nu+} \text{ and}$$
$$\hat{L}_{\mu+} = c_\mu, \hat{L}_{\mu-} = c^\dagger_\mu \text{ with } \Gamma_{\mu\nu\alpha} = \Gamma_{\mu\nu-},$$

as well as the two anomalous ones

$$\hat{L}_{\mu+} = c^\dagger_\mu, \hat{L}_{\mu-} = c^\dagger_\mu \text{ with } \Gamma_{\mu\nu\alpha} = \Upsilon_{\mu\nu+} \text{ and}$$
$$\hat{L}_{\mu+} = c_\mu, \hat{L}_{\mu-} = c_\mu \text{ with } \Gamma_{\mu\nu\alpha} = \Upsilon_{\mu\nu-}.$$

The dissipation matrices $\Gamma_{\mu\nu}$ are hermitian

$$\Gamma_{\mu\nu} = \Gamma^*_{\nu\mu},$$

due to the anti-commutation relation of the fermionic creation and annihilation operators and positive semidefinite in order to preserve the positivity of the density matrix during time evolution. The matrices $\Upsilon_{\mu\nu}$ fulfil

$$\Upsilon_{\mu\nu} = -\Upsilon_{\nu\mu}.$$

Time evolution with the Lindblad quantum master equation preserves the [61]

- trace of the density operator: $\mathrm{Tr}\,(\hat{\rho}(\tau)) = \mathrm{Tr}\,(\hat{\rho}(0))$,
- hermiticity of the density operator: $\hat{\rho}(\tau) = \hat{\rho}^\dagger(\tau)$ if $\hat{\rho}(0) = \hat{\rho}^\dagger(0)$,
- positivity of the density operator: $\langle\Psi|\hat{\rho}(\tau)|\Psi\rangle \geq 0 \;\forall\; \Psi$ if $\langle\Psi|\hat{\rho}(0)|\Psi\rangle \geq 0 \;\forall\; \Psi$.

It is helpful to split the Lindbladian into three parts

$$\hat{\hat{\mathcal{L}}} = \underbrace{\hat{\hat{\mathcal{L}}}_0 + \hat{\hat{\mathcal{L}}}_I}_{\text{unitary}} + \underbrace{\hat{\hat{\mathcal{L}}}_D}_{\text{dissipative}},$$

which are the unitary contributions of the non-interacting Hamiltonian $\hat{\mathcal{H}}_0$ and the interacting Hamiltonian $\hat{\mathcal{H}}_I$ as well as the non unitary dissipative terms.

Explicitly these terms read

$$\hat{\hat{\mathcal{L}}}_0\hat{\bullet} = [\hat{\mathcal{H}}_0, \hat{\bullet}]_- \tag{F.3a}$$
$$\hat{\hat{\mathcal{L}}}_I\hat{\bullet} = [\hat{\mathcal{H}}_I, \hat{\bullet}]_- \tag{F.3b}$$
$$\hat{\hat{\mathcal{L}}}_D\hat{\bullet} = 2i\sum_{\mu\nu\alpha}\Gamma_{\mu\nu\alpha}\left(\hat{L}_{\mu\alpha}\hat{\bullet}\hat{L}^\dagger_{\nu\alpha} - \frac{1}{2}\{\hat{L}^\dagger_{\nu\alpha}\hat{L}_{\mu\alpha}, \hat{\bullet}\}\right). \tag{F.3c}$$

In the following we will furthermore split $\hat{\hat{\mathcal{L}}}_0 = \hat{\hat{\mathcal{L}}}_n + \hat{\hat{\mathcal{L}}}_a$ where the normal component n includes the normal part of the non-interacting Hamiltonian $\hat{\mathcal{H}}_n$ and the anomalous component a holds the anomalous parts $\hat{\mathcal{H}}_a$. Likewise we decompose $\hat{\hat{\mathcal{L}}}_D = \hat{\hat{\mathcal{L}}}_{D_n} + \hat{\hat{\mathcal{L}}}_{D_a}$.

F.2. Lindbladian in super-fermion space

Here we consider the time evolution of the single-particle density matrix $\rho_{\mu\nu}$ as described by the Lindblad master equation Eq. (F.2). One elegant way of obtaining this, is by making use of the super-fermion formalism [467]. Introducing the left-vacuum $|I\rangle$ and the nonequilibrium wave function $|\rho(t)\rangle = \rho|I\rangle$ one can write the Lindblad master equation in a Schrödinger type formalism

$$\frac{d}{dt}|\rho(t)\rangle = -i\hat{\hat{\mathcal{L}}}\hat{\rho}|I\rangle\,.$$

F.2.1. Applying the super-operator

The problem is that $\hat{\rho}$ is trapped inside the super-operator. To shift it to the far right we use super-fermions $\tilde{c}_\mu/\tilde{c}_\mu^\dagger$ which commute with $\hat{\rho}$. To obtain super-fermions we have to shift all fermionic operators to the far right and apply them on $|I\rangle$ first. Note that the problem always occurs in the second part of the commutator while the first part is fine from the beginning.

We start out by considering the action of the non-interacting normal part $\hat{\hat{\mathcal{L}}}_n\hat{\rho}$ (Eq. (F.3a)).

$$\begin{aligned}
\hat{\mathcal{L}}_n|\rho(t)\rangle &= [\hat{\mathcal{H}}_n,\hat{\rho}]_-|I\rangle \\
&= \left(c_\mu^\dagger h_{\mu\nu}c_\nu\hat{\rho} - \hat{\rho}c_\mu^\dagger h_{\mu\nu}c_\nu\right)|I\rangle \\
&= \left(c_\mu^\dagger h_{\mu\nu}c_\nu\hat{\rho} - \hat{\rho}c_\mu^\dagger h_{\mu\nu}(-i\tilde{c}_\nu^\dagger)\right)|I\rangle \\
&= \left(c_\mu^\dagger h_{\mu\nu}c_\nu\hat{\rho} - \hat{\rho}h_{\mu\nu}(-i\tilde{c}_\nu^\dagger)(-c_\mu^\dagger)\right)|I\rangle \\
&= \left(c_\mu^\dagger h_{\mu\nu}c_\nu\hat{\rho} - \hat{\rho}h_{\mu\nu}(-i\tilde{c}_\nu^\dagger)(i\tilde{c}_\mu)\right)|I\rangle \\
&= \left(c_\mu^\dagger h_{\mu\nu}c_\nu - h_{\mu\nu}\tilde{c}_\nu^\dagger\tilde{c}_\mu\right)\hat{\rho}|I\rangle \\
&= \left(c_\mu^\dagger h_{\mu\nu}c_\nu - \tilde{c}_\mu^\dagger h_{\nu\mu}\tilde{c}_\nu\right)|\rho(t)\rangle \\
&= \left(c_\mu^\dagger h_{\mu\nu}c_\nu - \tilde{c}_\mu^\dagger h_{\mu\nu}^*\tilde{c}_\nu\right)|\rho(t)\rangle\,,
\end{aligned} \tag{F.4}$$

From line two to three we applied the fermion annihilation operator c_ν on the left vacuum, resulting in the creation of a super-fermion

$$\begin{aligned}
c_\mu|I\rangle &= -i\tilde{c}_\mu^\dagger|I\rangle \\
c_\mu^\dagger|I\rangle &= -i\tilde{c}_\mu|I\rangle\,.
\end{aligned} \tag{F.5}$$

Shifting $c_\mu^\dagger$ to the right and using the fermion - super-fermion anti-commutation relations

$$\{c_\mu,\tilde{c}_\nu\} = \{c_\mu^\dagger,\tilde{c}_\nu^\dagger\} = \{c_\mu,\tilde{c}_\nu^\dagger\} = 0\,. \tag{F.6}$$

Finally we used the fact that all super-fermions commute with the density operator $\hat{\rho}_{\mu\nu} = c_\mu^\dagger c_\nu$. This directly follows from Eq. (F.6).

The non-interacting anomalous part similarly yields

$$\hat{\mathcal{L}}_a|\rho(t)\rangle = [\hat{\mathcal{H}}_a, \hat{\rho}]_-|I\rangle = \left(c_\mu a_{\mu\nu} c_\nu - \tilde{c}_\mu a^*_{\mu\nu} \tilde{c}_\nu + c^\dagger_\mu a^*_{\nu\mu} c^\dagger_\nu - \tilde{c}^\dagger_\mu a_{\nu\mu} \tilde{c}^\dagger_\nu\right)|\rho(t)\rangle\,. \tag{F.7}$$

For the normal dissipative term we find

$$\begin{aligned}\hat{\mathcal{L}}_{Dn}|\rho(t)\rangle = 2i\Bigg(&\Gamma_{\mu\nu+}\left(c^\dagger_\mu \hat{\rho} c_\nu - \frac{1}{2} c_\nu c^\dagger_\mu \hat{\rho} - \frac{1}{2}\hat{\rho} c_\nu c^\dagger_\mu\right)\\ &+\Gamma_{\mu\nu-}\left(c_\mu \hat{\rho} c^\dagger_\nu - \frac{1}{2} c^\dagger_\nu c_\mu \hat{\rho} - \frac{1}{2}\hat{\rho} c^\dagger_\nu c_\mu\right)\Bigg)|\rho(t)\rangle\\ =\Bigg(&2\left(c^\dagger_\mu \Gamma_{\mu\nu+} \tilde{c}^\dagger_\nu + c_\nu \Gamma_{\nu\mu-} \tilde{c}_\mu\right)\\ &+ i\left(\Gamma_{\mu\nu+} - \Gamma_{\nu\mu-}\right)\left(c^\dagger_\mu c_\nu + \tilde{c}^\dagger_\nu \tilde{c}_\mu\right)\\ &- 2i\Gamma_{\mu\nu+}\delta_{\mu\nu}\Bigg)|\rho(t)\rangle\,.\end{aligned} \tag{F.8}$$

For the anomalous dissipative contribution we obtain

$$\begin{aligned}\hat{\mathcal{L}}_{Da}|\rho(t)\rangle = 2i\Bigg(&\Upsilon_{\mu\nu+}\left(c^\dagger_\mu \hat{\rho} c^\dagger_\nu - \frac{1}{2} c^\dagger_\nu c^\dagger_\mu \hat{\rho} - \frac{1}{2}\hat{\rho} c^\dagger_\mu c^\dagger_\nu\right)\\ &+\Upsilon_{\mu\nu-}\left(c_\mu \hat{\rho} c_\nu - \frac{1}{2} c_\nu c_\mu \hat{\rho} - \frac{1}{2}\hat{\rho} c_\nu c_\mu\right)\Bigg)|\rho(t)\rangle\\ =\Bigg(&c^\dagger_\mu 2\Upsilon_{\mu\nu+}\tilde{c}_\nu + c^\dagger_\mu i\Upsilon_{\mu\nu+} c^\dagger_\nu - \tilde{c}_\mu i\Upsilon_{\mu\nu+}\tilde{c}_\nu\\ &- \tilde{c}^\dagger_\mu 2\Upsilon^T_{\mu\nu-} c_\nu - c_\mu i\Upsilon^T_{\mu\nu-} c_\nu + \tilde{c}^\dagger_\mu i\Upsilon^T_{\mu\nu-}\tilde{c}^\dagger_\nu\Bigg)|\rho(t)\rangle\,.\end{aligned} \tag{F.9}$$

Note that in this chapter we discussed $\hat{\mathcal{L}}$ and not $-i\hat{\mathcal{L}}$.

F.2.2. Super-hole representation

We now change to a slightly more advantageous notation by introducing super-holes $\tilde{d}_\mu/\tilde{d}^\dagger_\mu$. This representation has the advantage that the system stays normal as long as the starting Hamiltonian is normal and only acquires anomalous terms if they are present from the beginning i.e. the super-space does not introduce anomalous contributions as in Eq. (F.8). The super-holes obey standard fermionic anti-commutation relations Eq. (F.1). In particular we apply a particle-hole transmutation to the super-fermion sector

$$\tilde{d}_\mu = \tilde{c}^\dagger_\mu \text{ and } \tilde{d}^\dagger_\mu = \tilde{c}_\mu\,.$$

The super-holes again anti-commute with the original fermions in the same fashion as the super-fermion Eq. (F.6).

From this we find for the normal part of the Lindbladian Eq. (F.4)

$$\hat{\mathcal{L}}_n|\rho(t)\rangle = \left(c^\dagger_\mu h_{\mu\nu} c_\nu + \tilde{d}^\dagger_\mu h_{\mu\nu}\tilde{d}_\nu - h_{\mu\nu}\delta_{\mu\nu}\right)|\rho(t)\rangle\,, \tag{F.10}$$

and for the anomalous part Eq. (F.7)

$$\hat{\mathcal{L}}_a|\rho(t)\rangle = \left(c_\mu a_{\mu\nu} c_\nu + \tilde{d}_\mu a_{\mu\nu} \tilde{d}_\nu + c_\mu^\dagger a_{\nu\mu}^* c_\nu^\dagger + \tilde{d}_\mu^\dagger a_{\nu\mu}^* \tilde{d}_\nu^\dagger\right)|\rho(t)\rangle \tag{F.11}$$

The dissipative part Eq. (F.8) becomes normal

$$\begin{aligned}\hat{\mathcal{L}}_{D_n}|\rho(t)\rangle = \Big(&2\left(c_\mu^\dagger \Gamma_{\mu\nu+} \tilde{d}_\nu - \tilde{d}_\mu^\dagger \Gamma_{\mu\nu-}^T c_\nu\right)\\ &+ i\left(\Gamma_{\mu\nu+} - \Gamma_{\mu\nu-}^T\right)\left(c_\mu^\dagger c_\nu - \tilde{d}_\mu^\dagger \tilde{d}_\nu\right)\\ &- i\left(\Gamma_{\mu\nu+} + \Gamma_{\mu\nu-}^T\right)\delta_{\mu\nu}\Big)|\rho(t)\rangle\,.\end{aligned} \tag{F.12}$$

For the anomalous dissipative contribution stays anomalous

$$\begin{aligned}\hat{\mathcal{L}}_{Da}|\rho(t)\rangle = \Big(&c_\mu^\dagger 2\Upsilon_{\mu\nu+} \tilde{d}_\nu^\dagger + c_\mu^\dagger i\Upsilon_{\mu\nu+} c_\nu^\dagger - \tilde{d}_\mu^\dagger i\Upsilon_{\mu\nu+} \tilde{d}_\nu^\dagger\\ &- \tilde{d}_\mu 2\Upsilon_{\mu\nu-}^T c_\nu - c_\mu i\Upsilon_{\mu\nu-}^T c_\nu + \tilde{d}_\mu i\Upsilon_{\mu\nu-}^T \tilde{d}_\nu\Big)|\rho(t)\rangle\,.\end{aligned} \tag{F.13}$$

The convenient end result for the non-interacting case is

$$\begin{aligned}\hat{\mathcal{L}}|\rho(t)\rangle = \Big(&c_\mu^\dagger\left(h_{\mu\nu} + i\Omega_{\mu\nu}\right)c_\nu + \tilde{d}_\mu^\dagger\left(h_{\mu\nu} - i\Omega_{\mu\nu}\right)\tilde{d}_\nu\\ &+ c_\mu^\dagger\left(2\Gamma_{\mu\nu+}\right)\tilde{d}_\nu - \tilde{d}_\mu^\dagger\left(2\Gamma_{\mu\nu-}^T\right)c_\nu + c_\mu^\dagger(2\Upsilon_{\mu\nu+})\tilde{d}_\nu^\dagger - \tilde{d}_\mu(2\Upsilon_{\mu\nu-}^T)c_\nu\\ &+ c_\mu(a_{\mu\nu} - i\Upsilon_{\mu\nu-}^T)c_\nu + \tilde{d}_\mu(a_{\mu\nu} + i\Upsilon_{\mu\nu-}^T)\tilde{d}_\nu + c_\mu^\dagger(a_{\nu\mu}^* + i\Upsilon_{\mu\nu+})c_\nu^\dagger + \tilde{d}_\mu^\dagger(a_{\nu\mu}^* - i\Upsilon_{\mu\nu+})\tilde{d}_\nu^\dagger\\ &- \left(h_{\mu\nu} + i\Lambda_{\mu\nu}\right)\delta_{\mu\nu}\Big)|\rho(t)\rangle\,.\end{aligned} \tag{F.14}$$

Where we introduced the following symbols:

$$\begin{aligned}\Lambda_{\mu\nu} &= \left(\Gamma_{\mu\nu+} + \Gamma_{\mu\nu-}^T\right), \Lambda = \mathrm{tr}\left(\Lambda_{\mu\nu}\right)\\ \Omega_{\mu\nu} &= \left(\Gamma_{\mu\nu+} - \Gamma_{\mu\nu-}^T\right), \Omega = \mathrm{tr}\left(\Omega_{\mu\nu}\right)\\ X_{\alpha\beta\pm} &= \left(\Upsilon_{\alpha\beta\pm} + \Upsilon_{\beta\alpha\pm}\right) = 0 \cdot \mathbb{1}_{\alpha\beta}\\ Y_{\alpha\beta\pm} &= \left(\Upsilon_{\alpha\beta\pm} - \Upsilon_{\beta\alpha\pm}\right)\\ A_{\mu\nu} &= \left(a_{\mu\nu} - a_{\nu\mu}\right) = -A_{\nu\mu} = 2a_{\mu\nu}\,.\end{aligned}$$

Note the order of indices in the last definition. Again note that this is $\hat{\mathcal{L}}$ and not $-i\hat{\mathcal{L}}$.

F.3. Time evolution of the single-particle density matrix

In the following we present two different, independent approaches to obtain the time evolution of the single-particle density matrix (equal time quadratic correlation function). They differ in computational complexity and stability. A third approach would be to do all calculations in the full Fock space, which results in an unfavourable scaling of the numeric algorithm.

F.3.1. Commutator approach

To actually evaluate the time evolution [467] of the density matrix $\langle\rho(t)\rangle = \langle I|\hat{\rho}|\rho(t)\rangle$, we make use of the fact that $\langle I|\hat{\mathcal{L}} = 0$

$$\dot{\rho}_{\alpha\beta} = \frac{d}{dt}\langle\rho(t)\rangle = -i\langle I|c_\alpha^\dagger c_\beta \hat{L}|\rho(t)\rangle = -i\langle I|\left[c_\alpha^\dagger c_\beta, \hat{L}\right]_-|\rho(t)\rangle\,.$$

Note that $c_\alpha^\dagger c_\beta \hat{L}$ would be a four-Fermi quantity, while the commutator is quadratic.

When dealing with anomalous systems we introduce the corresponding anomalous densities $\eta_{\alpha\beta}(t) = \langle I|c_\alpha c_\beta|\rho(t)\rangle$ and $\xi_{\alpha\beta}(t) = \langle I|c_\alpha^\dagger c_\beta^\dagger|\rho(t)\rangle$ in the same way as the normal density. Note that $\eta_{\alpha\beta} = -\eta_{\beta\alpha}$, $\xi_{\alpha\beta} = -\xi_{\beta\alpha}$ and $\rho_{\alpha\beta} = \rho^*_{\beta\alpha}$. In the general case we will acquire a coupled system of equations for $\rho_{\alpha\beta}, \eta_{\alpha\beta}$ and $\xi_{\alpha\beta}$.

Equations governing the time evolution

All that is left now is to evaluate the commutators $[c_\alpha^{(\dagger)} c_\beta^{(\dagger)}, \hat{L}]_-$ using Eq. (F.14). This is straight forwardly done by using the general properties of commutators

$$\begin{aligned}[\hat{A}, \hat{B}\hat{C}]_- &= [\hat{A}, \hat{B}]_-\hat{C} + \hat{B}[\hat{A}, \hat{C}]_- \\ &= \{\hat{A}, \hat{B}\}\hat{C} - \hat{B}\{\hat{A}, \hat{C}\}\,,\end{aligned}$$

as well as the elementary fermionic anti-commutation relations Eq. (F.1). Note that from now on the $-i$ of the time evolution is included in contrast to Eq. (F.14).

Introducing

$$\begin{aligned}K_{\alpha\beta} &:= (ih_{\alpha\beta} + \Lambda_{\alpha\beta}) \\ R_{\alpha\beta} &:= (ih_{\alpha\beta} - \Lambda_{\alpha\beta}) \\ F_{\alpha\beta} &:= (iA^*_{\alpha\beta} - X_{\alpha\beta+}) \\ G_{\alpha\beta} &:= (iA_{\alpha\beta} + X_{\alpha\beta-})\,,\end{aligned}$$

for the normal part $\rho_{\alpha\beta}$ we find

$$\dot{\rho}_{\alpha\beta} = \sum_\mu \left(R_{\mu\alpha}\rho_{\mu\beta} - K_{\beta\mu}\rho_{\alpha\mu} + G_{\alpha\mu}\eta_{\beta\mu} + F_{\beta\mu}\xi_{\alpha\mu} \right) + 2\Gamma_{\beta\alpha+}\,. \tag{F.15a}$$

The first anomalous component $\eta_{\alpha\beta}$ is given by

$$\dot{\eta}_{\alpha\beta} = \sum_\mu \left(K_{\beta\mu}\eta_{\mu\alpha} - K_{\alpha\mu}\eta_{\mu\beta} - F_{\beta\mu}\rho_{\mu\alpha} + F_{\alpha\mu}\rho_{\mu\beta} \right) - (iA^*_{\alpha\beta} + Y_{\alpha\beta+})\,. \tag{F.15b}$$

The second anomalous component $\xi_{\alpha\beta}$ is given by

$$\dot{\xi}_{\alpha\beta} = \sum_\mu \left(-R_{\mu\beta}\xi_{\mu\alpha} + R_{\mu\alpha}\xi_{\mu\beta} - G_{\beta\mu}\rho_{\alpha\mu} + G_{\alpha\mu}\rho_{\beta\mu} \right) + (-iA_{\alpha\beta} + Y^T_{\alpha\beta-})\,. \tag{F.15c}$$

It has been checked that Eq. (F.15c) is the hermitian conjugate of Eq. (F.15b) and vice versa, that Eq. (F.15a) is hermitian and that the fermionic relations $\dot{\eta}_{\alpha\beta} = -\dot{\eta}_{\beta\alpha}$ and $\dot{\xi}_{\alpha\beta} = -\dot{\xi}_{\beta\alpha}$ hold in Eq. (F.15).

The system above is for $3N^2$ variables and can be further reduced due to symmetry arguments: i) $\rho_{\alpha\beta} = \rho^*_{\beta\alpha}$, ii) $\xi_{\alpha\beta} = \eta^*_{\beta\alpha}$ and iii) $\eta_{\alpha\beta} = -\eta_{\beta\alpha}$. The fact that the diagonal anomalous densities vanish allows for reducing the dimension of the above system. Therefore we cast it into a form which describes the diagonal and upper triangle of ρ i.e. $\alpha \leq \beta$

$$\begin{aligned}
\dot{\rho}_{\alpha\beta} &= R_{\beta\alpha}\rho_{\beta\beta} - K_{\beta\alpha}\rho_{\alpha\alpha} \\
&+ \sum_{\mu<\beta} R_{\mu\alpha}\rho_{\mu\beta} - F_{\alpha\mu}\eta_{\mu\beta} + \sum_{\mu>\beta} R_{\mu\alpha}\rho^*_{\beta\mu} + F_{\alpha\mu}\eta_{\beta\mu} \\
&+ \sum_{\mu<\alpha} -K_{\beta\mu}\rho^*_{\mu\alpha} + G_{\beta\mu}\eta^*_{\mu\alpha} + \sum_{\mu>\alpha} -K_{\beta\mu}\rho_{\alpha\mu} - G_{\beta\mu}\eta^*_{\alpha\mu} \\
&+ 2\Gamma_{\beta\alpha+}\,,
\end{aligned}$$

as well as the upper triangle of η i.e. $\alpha < \beta$

$$\begin{aligned}
\dot{\eta}_{\alpha\beta} &= F_{\alpha\beta}\rho_{\beta\beta} - F_{\beta\alpha}\rho_{\alpha\alpha} \\
&+ \sum_{\mu<\beta} F_{\alpha\mu}\rho_{\mu\beta} - K_{\alpha\mu}\eta_{\mu\beta} + \sum_{\mu>\beta} F_{\alpha\mu}\rho^*_{\beta\mu} + K_{\alpha\mu}\eta_{\beta\mu} \\
&+ \sum_{\mu<\alpha} -F_{\beta\mu}\rho_{\mu\alpha} + K_{\beta\mu}\eta_{\mu\alpha} + \sum_{\mu>\alpha} -F_{\beta\mu}\rho^*_{\alpha\mu} - K_{\beta\mu}\eta_{\alpha\mu} \\
&- (iA^*_{\alpha\beta} + Y_{\alpha\beta+})\,.
\end{aligned}$$

The other components can be straightforwardly determined by the relations stated above.

Solution to the time dynamics and steady-state

The solution of Eq. (F.15) is straight forward and can for example be elegantly done in matrix notation. We reorder the matrices $\rho_{\alpha\beta}, \eta_{\alpha\beta}$ and $\xi_{\alpha\beta}$ in a suitable column vector form $\vec{\rho}, \vec{\eta}$ and $\vec{\xi}$ (for example column wise). We introduce a compound vector notation $\vec{\Xi} = (\vec{\rho}; \vec{\eta}; \vec{\xi})$. Performing the same reordering on the prefactors in Eq. (F.15) we call M the coefficients of $\vec{\Xi}$ and S the constant, inhomogeneous part. Then the time evolution takes the matrix form

$$\dot{\vec{\Xi}} = M\vec{\Xi} + \vec{S}\,,$$

which upon diagonalization of M

$$\begin{aligned}
\lambda &= U^{-1}MU \\
\vec{\zeta} &= U^{-1}\vec{\Xi}, \quad \vec{\Xi} = U\vec{\zeta} \\
\vec{\sigma} &= U^{-1}\vec{S}, \quad \vec{S} = U\vec{\sigma}\,,
\end{aligned}$$

where λ is diagonal and U the transformation which diagonalizes M, reads

$$\dot{\vec{\zeta}} = \lambda\vec{\zeta} + \vec{\sigma}\,.$$

The solution of this decoupled system of ordinary inhomogeneous differential equations, in the eigenmodes is

$$\vec{\zeta}_i(t) = \left(\zeta_i(0) + \frac{\sigma_i}{\lambda_{ii}}\right)e^{\lambda_{ii}t} - \frac{\sigma_i}{\lambda_{ii}}\,. \tag{F.16}$$

It can be shown that $\mathfrak{Re}(\lambda_i) < 0 \quad \forall \quad i$ so that the steady-state is given by

$$\vec{\zeta}_i(t \to \infty) = -\frac{\sigma_i}{\lambda_{ii}} \,. \tag{F.17}$$

Note that the numerical evaluation is extremely sensitive to values of σ which should be exactly zero but are very small but finite due to the transformation of s into the eigenbasis of L. Such errors get amplified beyond limits by dividing through small eigenvalues in Eq. (F.17).

Practical considerations

This time evolution of non-interacting open quantum systems scales like $\propto (N^2)^3 + N_t(N^2)^2$, where N is the number of distinct fermionic quantum numbers α (i.e. the system size times spin degeneracy), the squared comes essentially from the introduction of a super-space and is easily visible in the matrix reordering procedure in Sec. F.3.1 and the number of time slices of interest N_t. The complexity of the algorithm is essentially proportional to the full diagonalization of M which essentially scales with the third power plus corrections due to matrix vector multiplications which scale like the size squared albeit with a prefactor which is the number of time slices of interest. Note that for normal systems this scaling $\propto N^6$ makes accessing large system sizes even in the non-interacting system problematic. For full diagonalization ≈ 48 orbitals should be easily accessible on standard machines. The initial condition for time evolution is just given by $\rho_{\alpha\beta}(0), \eta_{\alpha\beta}(0)$ and $\xi_{\alpha\beta}(0)$ in concatenated reshaped form.

In short the evolution of the density matrix can be implemented by

- start with an initial density matrix $\Xi_{\alpha\beta}(0)$ and the dynamics M, S as described by the parameters of the Hamiltonian and the Lindbladian dissipators;
- reshape to matrix-vector form $\to \vec{\Xi}, M, \vec{S}$;
- solve the full eigenvalue problem for $M \to U, \lambda$;
- obtain $\vec{\sigma} = U^{-1}\vec{S}$;
- A) for time evolution:
  - obtain starting eigenmodes $\vec{\zeta}(0) = U^{-1}\vec{\Xi}(0)$;
  - loop desired times and evaluate $\vec{\zeta}(t)$ by Eq. (F.16);
  - transform back for all times $\vec{\Xi}(t) = U\vec{\zeta}(t)$;
- B) for the steady-state:
  - obtain steady-state eigenmodes $\vec{\zeta}(\infty)$ by Eq. (F.17);
  - transform back $\vec{\Xi}(\infty) = U\vec{\zeta}(\infty)$.

F.3.2. Nonequilibrium quasi-particles

After outlining the "commutator method" for obtaining the time evolution of the density matrix which could be obtained by solving an inhomogeneous system of differential equations by diagonalization we present an alternative "nonequilibrium quasi-particle" method. To start with we rewrite the Lindbladian in the super-hole picture Eq. (F.14) into a compact vector notation.

Defining

$$\vec{g} = \begin{pmatrix} \vec{c} \\ \vec{c}^\dagger \\ \vec{\bar{d}} \\ \vec{d}^\dagger \end{pmatrix}, \; \vec{g}^\dagger = \begin{pmatrix} \vec{c}^\dagger & \vec{c} & \vec{\bar{d}}^\dagger & \vec{\bar{d}} \end{pmatrix}, \; \vec{g}^\dagger \vec{g} = \begin{pmatrix} \vec{c}^\dagger \vec{c} & \vec{c}^\dagger \vec{c}^\dagger & \vec{c}^\dagger \vec{\bar{d}} & \vec{c}^\dagger \vec{\bar{d}}^\dagger \\ \vec{c}\vec{c} & \vec{c}\vec{c}^\dagger & \vec{c}\vec{\bar{d}} & \vec{c}\vec{\bar{d}}^\dagger \\ \vec{\bar{d}}^\dagger \vec{c} & \vec{\bar{d}}^\dagger \vec{c}^\dagger & \vec{\bar{d}}^\dagger \vec{\bar{d}} & \vec{\bar{d}}^\dagger \vec{\bar{d}}^\dagger \\ \vec{\bar{d}}\vec{c} & \vec{\bar{d}}\vec{c}^\dagger & \vec{\bar{d}}\vec{\bar{d}} & \vec{\bar{d}}\vec{\bar{d}}^\dagger \end{pmatrix},$$

so that

$$\mathcal{L} = \vec{g}^\dagger L \vec{g} + \vec{q}. \tag{F.18}$$

Bringing Eq. (F.14) by symmetrizing explicitly in the form above it becomes

$$\mathcal{L} = \vec{g}^\dagger \begin{pmatrix} \frac{1}{2}(h_{\mu\nu} + i\Omega_{\mu\nu}) & a^*_{\nu\mu} + i\Upsilon_{\mu\nu+} & \frac{1}{2}(2\Gamma_{\mu\nu+}) & \frac{1}{2}2\Upsilon_{\mu\nu+} \\ a_{\mu\nu} - i\Upsilon^T_{\mu\nu-} & \frac{1}{2}(-(h_{\nu\mu} + i\Omega_{\nu\mu})) & \frac{1}{2}2\Upsilon_{\mu\nu-} & \frac{1}{2}(2\Gamma^T_{\nu\mu-}) \\ \frac{1}{2}(-2\Gamma^T_{\mu\nu-}) & -\frac{1}{2}2\Upsilon_{\nu\mu+} & \frac{1}{2}(h_{\mu\nu} - i\Omega_{\mu\nu}) & a^*_{\nu\mu} - i\Upsilon_{\mu\nu+} \\ -\frac{1}{2}2\Upsilon^T_{\mu\nu-} & \frac{1}{2}(-2\Gamma_{\nu\mu+}) & a_{\mu\nu} + i\Upsilon^T_{\mu\nu-} & \frac{1}{2}(-(h_{\nu\mu} - i\Omega_{\nu\mu})) \end{pmatrix} \vec{g} - \mathrm{tr}\,(i\Lambda_{\mu\nu}), \tag{F.19}$$

where L and $\vec{q}$ can be conveniently read off. For normal systems ($a_{\mu\nu} \equiv \Upsilon_{\mu\nu\pm} \equiv 0$) the system above separates into two equivalent ones and one ends up in a reduced space

$$\mathcal{L} = \vec{g'}^\dagger \begin{pmatrix} h_{\mu\nu} + i\Omega_{\mu\nu} & 2\Gamma_{\mu\nu+} \\ -2\Gamma^T_{\mu\nu-} & h_{\mu\nu} - i\Omega_{\mu\nu} \end{pmatrix} \vec{g'} - \mathrm{tr}\,(h_{\mu\nu} + i\Lambda_{\mu\nu}) \;\text{ with } \vec{g'} = \begin{pmatrix} \vec{c} \\ \vec{\bar{d}} \end{pmatrix}.$$

Equations governing the time evolution

One diagonalizes L in Eq. (F.19)

$$\lambda = U^{-1} L U.$$

and obtains the nonequilibrium eigenmodes

$$\vec{\zeta} = U^{-1} \vec{g}$$
$$\vec{\bar{\zeta}} = \vec{g}^\dagger U.$$

Note that the fermionic commutation relations Eq. (F.1) hold for the nonequilibrium eigenoperators $\zeta/\bar{\zeta}$ but they are not hermitian conjugate. As a result we can write Eq. (F.18) in the ζ basis

$$\mathcal{L} = \vec{\bar{\zeta}} \lambda \vec{\zeta} + q. \tag{F.20}$$

The time evolution of an equal time quadratic expectation value $\langle\bar{\zeta}_\alpha\zeta_\beta\rangle = \langle I|\bar{\zeta}_\alpha\zeta_\beta|\rho(t)\rangle$ is given by

$$\begin{aligned}\frac{d\langle\bar{\zeta}_\alpha\zeta_\beta\rangle}{d\tau} &= -i\frac{d}{d\tau}\langle I|\bar{\zeta}_\alpha\zeta_\beta|\rho(t)\rangle \\ &= -i\langle I|\bar{\zeta}_\alpha\zeta_\beta\mathcal{L}|\rho(t)\rangle \\ &= -i\langle I|[\bar{\zeta}_\alpha\zeta_\beta,\mathcal{L}]_-|\rho(t)\rangle \\ &= -i\langle I|(\lambda_{\beta\beta}-\lambda_{\alpha\alpha})\bar{\zeta}_\alpha\zeta_\beta|\rho(t)\rangle \\ &= -i(\lambda_{\beta\beta}-\lambda_{\alpha\alpha})\langle\bar{\zeta}_\alpha\zeta_\beta\rangle\,,\end{aligned}$$

The solution of this decoupled system of differential equations is

$$\langle\bar{\zeta}_\alpha\zeta_\beta\rangle(\tau) = e^{-i(\lambda_{\beta\beta}-\lambda_{\alpha\alpha})\tau}\langle\bar{\zeta}_\alpha\zeta_\beta\rangle(0)\,.$$

A steady-state can only exist if $\mathfrak{Im}(\lambda_{\beta\beta}-\lambda_{\alpha\alpha}) \leq 0$, which is only guaranteed for $\lambda_{\gamma\gamma} - q$ but not for $\lambda_{\gamma\gamma}$ only. Next we transform to modes which fulfil this criterion

$$\begin{aligned}\varsigma_\gamma &= \begin{cases}\zeta_\gamma, & \text{if } \mathfrak{Im}(\lambda_{\gamma\gamma}) \leq 0 \\ \bar{\zeta}_\gamma, & \text{if } \mathfrak{Im}(\lambda_{\gamma\gamma}) > 0\end{cases} \\ \omega_\gamma &= -\lambda_{\gamma\gamma}\mathrm{sign}\left(\mathfrak{Im}(\lambda_{\gamma\gamma})\right)\,.\end{aligned}$$

Eq. (F.20) becomes in the ς basis

$$\begin{aligned}\mathcal{L} &= \sum_{\mathfrak{Im}(\lambda_{\gamma\gamma})\leq 0}\lambda_{\gamma\gamma}\bar{\zeta}_\gamma\zeta_\gamma + \sum_{\mathfrak{Im}(\lambda_{\gamma\gamma})>0}\lambda_{\gamma\gamma}\bar{\zeta}_\gamma\zeta_\gamma + q \\ &= \sum_{\mathfrak{Im}(\lambda_{\gamma\gamma})\leq 0}\omega_{\gamma\gamma}\bar{\varsigma}_\gamma\varsigma_\gamma - \sum_{\mathfrak{Im}(\lambda_{\gamma\gamma})>0}\omega_{\gamma\gamma}(1-\bar{\varsigma}_\gamma\varsigma_\gamma) + q \\ &= \sum_\gamma\omega_{\gamma\gamma}\bar{\varsigma}_\gamma\varsigma_\gamma + q + \sum_{\mathfrak{Im}(\lambda_{\gamma\gamma})>0}\lambda_{\gamma\gamma}\,,\end{aligned}$$

where the new constant is zero $v = q + \sum_{\mathfrak{Im}(\lambda_{\gamma\gamma})>0}\lambda_{\gamma\gamma}$ is zero. Note that in contrast to the commutator case, here $\mathcal{L}$ is really $\mathcal{L}$ and not $-i\mathcal{L}$.

Solution to the time dynamics and steady-state

Quadratic steady-state expectation values in the original $\vec{g}$ space are obtained from the modified nonequilibrium eigenmodes ς by

$$\langle g_\alpha^\dagger g_\beta\rangle(\infty) = \sum_{\mathfrak{Im}(\lambda_{\gamma\gamma})>0}((U^{-1})^T)_{\alpha\gamma}\lambda_{\gamma\gamma}(U^T)_{\gamma\beta}\,. \tag{F.21}$$

The time evolution is performed in the nonequilibrium eigenbasis ζ

$$\begin{aligned}\langle g_\alpha^\dagger g_\beta\rangle(\tau) &= ((U^{-1})^T)_{\alpha\gamma}\,e^{-i(\lambda_{\alpha\alpha}-\lambda_{\beta\beta})\tau}z(0)\,(U^T)_{\gamma\beta} \\ z(0) &= U^T\gamma(0)(U^{-1})^T\,,\end{aligned} \tag{F.22}$$

where $\gamma_{\alpha\beta}(0)$ is the initial density matrix in $\vec{g}$ space.

To transform any given $\rho_{\alpha\beta}$, $\eta_{\alpha\beta}$, $\xi_{\alpha\beta}$ into a form needed for propagation with Eq. (F.19)

we calculate the individual components of $\gamma_{\alpha\beta} = \langle g_\alpha^\dagger g_\beta \rangle = \langle I | \vec{g}^\dagger \vec{g} | \rho \rangle$ and re-express them in the quantities above by commuting and eliminating super-holes using relations Eq. (F.5)

$$\gamma_{\alpha\beta} = \langle g_\alpha^\dagger g_\beta \rangle = \begin{pmatrix} \rho_{\alpha\beta} & \xi_{\alpha\beta} & i(\mathbb{1} - \rho_{\alpha\beta}) & -i\xi_{\alpha\beta} \\ \eta_{\alpha\beta} & \mathbb{1} - \rho_{\alpha\beta}^T & -i\eta_{\alpha\beta} & i\rho_{\alpha\beta}^T \\ -i\rho_{\alpha\beta} & -i\xi_{\alpha\beta} & \mathbb{1} - \rho_{\alpha\beta} & -\xi_{\alpha\beta} \\ -i\eta_{\alpha\beta} & -i(\mathbb{1} - \rho_{\alpha\beta}^T) & -\eta_{\alpha\beta} & \rho_{\alpha\beta}^T \end{pmatrix}.$$

Again for normal systems this reduces to

$$\gamma'_{\alpha\beta} = \langle g_\alpha^{'\dagger} g_\beta^{'} \rangle = \begin{pmatrix} \rho_{\alpha\beta} & i(\mathbb{1} - \rho_{\alpha\beta}) \\ -i\rho_{\alpha\beta} & \mathbb{1} - \rho_{\alpha\beta} \end{pmatrix}.$$

Practical considerations

The algorithm is based on the diagonalization of the Lindbladian $\mathcal{L}$ in the original particle (c) and super-hole ($\tilde{d}$) space which we call ($\vec{g}$). The time evolution is done in the diagonalized non-hermitian quasi-particle space ζ. The space needed to directly extract the steady-state is the one where all positive imaginary parts of the eigenvalues in the ζ basis are particle hole transformed to the ς modes. Pure steady-state calculations scale like the solution of an eigenvalue problem and an inversion in $4N/2N$ dimensions in the anomalous/normal system which in leading order scales like $\propto 256/32N^3$. Time evolution calculations scale like the evaluation of an eigenvalue problem plus an inversion plus matrix multiplications in each time step in $4N/2N$ dimensions which amounts to $\propto (128/16 + 192/24N_\tau)N^3$

In short the evolution of the density matrix is easily implemented by

- start with an initial density matrix $\gamma_{\alpha\beta}(0)$ and the matrix L, q;
- solve the full eigenvalue problem for $L \to U, \lambda$;
- A) for time evolution:
  - obtain nonequilibrium eigenmodes ζ;
  - evaluate the time dependent density matrix by Eq. (F.22);
- B) for the steady-state:
  - obtain steady-state eigenmodes ς;
  - evaluate the steady-state density matrix by Eq. (F.21);

The procedure is numerically very sensitive. For a stable time evolution it is necessary to perform three numerical regularizations: i) Those exponents $(\lambda_{\alpha\alpha} - \lambda_{\beta\beta})$ which are supposed to be exactly zero due to round off errors and are not for numerical reasons should be set to zero manually. ii) Those exponents which couple to zero entries in the transformed density matrix $z_{\alpha\beta}$ should be set to zero. iii) The entries in the time dependent density matrix $\gamma_{\alpha\beta}$ which are not exactly zero due to round off errors arising from the transformation in the eigenbasis set to zero manually. For a stable evaluation of the steady-state also the resulting steady-state density matrix $\gamma_{\alpha\beta}(\infty)$ should be cleared from numerical noise arising from the transformation in the eigenbasis. Even more importantly when evaluating the constant contribution in the ς basis v and when choosing the states with $\mathfrak{Im}(\lambda_{\gamma\gamma}) > 0$ one has to try some cut-offs, maybe $> -|\epsilon|$ or so, otherwise one will end up in spurious steady-states. This point is numerically highly sensitive and it is best to check the steady-state calculation vs. the time evolution for large times and vs. the commutator method.

F.4. Single-particle Green's functions

We define the following single-particle Green's functions as a function of real time τ

$$
\begin{aligned}
G^{>}_{\alpha\beta}(\tau) &= -\imath\langle g_\alpha(\tau) g^\dagger_\beta\rangle \\
G^{<}_{\alpha\beta}(\tau) &= -\eta\imath\langle g^\dagger_\beta g_\alpha(\tau)\rangle \\
G^{K}_{\alpha\beta}(\tau) &= G^{>}_{\alpha\beta}(\tau) + G^{<}_{\alpha\beta}(\tau) \\
G^{R}_{\alpha\beta}(\tau) &= \Theta(\tau)\left(G^{>}_{\alpha\beta}(\tau) - G^{<}_{\alpha\beta}(\tau)\right) \\
G^{A}_{\alpha\beta}(\tau) &= -\Theta(-\tau)\left(G^{>}_{\alpha\beta}(\tau) - G^{<}_{\alpha\beta}(\tau)\right) ,
\end{aligned}
$$

where $\eta = -1$ for fermions, see Sec. 3.3.1.

The open quantum system described by the super-operator $\hat{\hat{\mathcal{L}}}$ (Eq. (3.43)) can be recast in an elegant way as a standard operator problem in a super fermion space with twice as many orbitals [467, 468, 469, 470]. The Fock space of the auxiliary problem formulated in $d\ /d^\dagger$: $\{|n\rangle\}$ with $\sum_n |n\rangle\langle n| = \hat{1\!\!1}, \langle n|m\rangle = \delta_{n,m}$ is augmented by a copy of super fermionic states $\tilde{d}\ /\tilde{d}^\dagger$: $\{|\tilde{n}\rangle\}$ with $\sum_{\tilde{n}} |\tilde{n}\rangle\langle\tilde{n}| = \hat{\hat{1\!\!1}}, \langle\tilde{n}|\tilde{m}\rangle = \delta_{\tilde{n},\tilde{m}}$. We rewrite the Lindblad master equation in the super Fock space spanned by $|n\rangle\otimes|\tilde{n}\rangle$. Introducing the left-vacuum $|I\rangle = \sum_{\{n\}} (-i)^{\Sigma n} |n\rangle\otimes|\tilde{n}\rangle$ and the nonequilibrium wave function $|\rho(t)\rangle = \hat{\rho}(t)|I\rangle$ one can write the Lindblad master equation in a Schrödinger type fashion [467] $\frac{d}{dt}|\rho(t)\rangle = \hat{\mathcal{L}}|\rho(t)\rangle$. Within a vector notation $\boldsymbol{g}^\dagger = \left(d^\dagger_0, \cdots, d^\dagger_{N_b}, \tilde{h}^\dagger_0, \cdots, \tilde{h}^\dagger_{N_b}\right)$, where the $\tilde{h}/\tilde{h}^\dagger$ operators are particle-hole transformed super-fermions $\tilde{d}^\dagger/\tilde{d}$, the non-interacting part of the Lindbladian becomes

$$
i\mathcal{L}_0 = \sum_\sigma \boldsymbol{g}^\dagger \begin{pmatrix} \boldsymbol{E} + i\boldsymbol{\Omega} & 2\boldsymbol{\Gamma}^{(2)} \\ -2\boldsymbol{\Gamma}^{(1)T} & \boldsymbol{E} - i\boldsymbol{\Omega} \end{pmatrix} \boldsymbol{g} - \mathrm{tr}\left(\boldsymbol{E} + i\boldsymbol{\Lambda}\right) , \tag{F.23}
$$

where $\boldsymbol{\Lambda} = \left(\boldsymbol{\Gamma}^{(2)} + \boldsymbol{\Gamma}^{(1)T}\right)$ and $\boldsymbol{\Omega} = \left(\boldsymbol{\Gamma}^{(2)} - \boldsymbol{\Gamma}^{(1)T}\right)$.

We start out by calculating the two time correlation function [456]

$$
\langle \hat{B}(t_2), \hat{A}(t_1)\rangle \equiv \mathrm{tr}_U\left(\hat{B}(t_2)\hat{A}(t_1)\hat{\rho}_U\right) = \mathrm{tr}\left(\hat{B}\hat{A}_{t_1}(t)\right)
$$

for $t = t_2 - t_1 > 0$, where $\hat{\rho}_U$ is the density operator of the universe, and $\mathrm{tr}_U = \mathrm{tr}\otimes\mathrm{tr}_E$ is the trace over the universe degrees of freedom, whereby tr is the one over the system, and tr_E the one over the environment. Here,

$$
A_{t_1}(t) = \mathrm{tr}_E\left(e^{-i\hat{\mathcal{H}}_U t}\hat{A}\hat{\rho}_U(t_1)e^{+i\hat{\mathcal{H}}_U t}\right)
$$

and $\hat{\mathcal{H}}_U$ is the total Hamiltonian of the universe.

By virtue of the Quantum regression theorem [456] which hold under the same assumptions for which Eq. (3.42) holds, one finds for $t > 0$

$$
\frac{d}{dt}\hat{A}_{t_1}(t) = \hat{\mathcal{L}}\hat{A}_{t_1}(t) ,
$$

which can be solved to yield

$$\langle \hat{B}(t_2), \hat{A}(t_1)\rangle = \mathrm{tr}\left(\hat{B}e^{\hat{\hat{\mathcal{L}}}t}(\hat{A}\hat{\rho}(t_1))\right).$$

Using this result we evaluate the greater Green's function for times $t > 0$ is defined as

$$\begin{aligned} G^{>,\infty}_{0,\mu\nu}(t) &:= -i\langle d_\mu(t) d^\dagger_\nu\rangle_\infty \\ &= -i\mathrm{tr}\left(d_\mu e^{\hat{\hat{\mathcal{L}}}t}\left(d^\dagger_\nu\hat{\rho}_\infty\right)\right) \\ &= -i\langle I| d_\mu e^{\hat{\mathcal{L}}t} d^\dagger_\nu|\rho_\infty\rangle. \end{aligned}$$

Diagonalizing the non-interacting non-hermitian Lindbladian Eq. (F.23) $\boldsymbol{\lambda} = \boldsymbol{U}^{-1}\boldsymbol{\mathcal{L}}\boldsymbol{U}$, we obtain nonequilibrium eigenmodes $\boldsymbol{\xi} = \boldsymbol{U}^{-1}\boldsymbol{g}$ / $\bar{\boldsymbol{\xi}} = \boldsymbol{g}^\dagger\boldsymbol{U}$, which are not hermitian conjugate but still fermionic commutation relations hold. As a result the non-interacting Lindbladian takes the form $\mathcal{L} = \bar{\boldsymbol{\xi}}\boldsymbol{\lambda}\boldsymbol{\xi} + \eta$. The expression for the greater Green's function can be readily evaluated in the nonequilibrium eigenmodes $\boldsymbol{\xi}$ of $\mathcal{L}$

$$\langle \xi_\alpha(t)\bar{\xi}_\beta\rangle_\infty := \langle I|\xi_\alpha e^{\hat{\mathcal{L}}t}\bar{\xi}_\beta|\rho_\infty\rangle = \langle I|e^{\hat{\mathcal{L}}t}e^{\lambda_{\alpha\alpha}t}\xi_\alpha\bar{\xi}_\beta|\rho_\infty\rangle = e^{\lambda_{\alpha\alpha}t}\langle I|\xi_\alpha\bar{\xi}_\beta|\rho_\infty\rangle,$$

since $\langle I|e^{\hat{\mathcal{L}}t} = \langle I|$. A steady-state can only exist if $\mathfrak{Re}(\lambda_{\gamma\gamma}) \le 0$, which is only guaranteed for $\lambda_{\gamma\gamma} - \eta$ but not for $\lambda_{\gamma\gamma}$. The left vacuum $\langle I|$ is the vacuum for the transformed modes

$$\begin{aligned} \varsigma_\gamma &= \begin{cases} \xi_\gamma, & \text{if } \mathfrak{Re}(\lambda_{\gamma\gamma}) \le 0 \\ \bar{\xi}_\gamma, & \text{if } \mathfrak{Re}(\lambda_{\gamma\gamma}) > 0 \end{cases} \\ \omega_\gamma &= -\lambda_{\gamma\gamma}\mathrm{sign}\left(\mathfrak{Re}(\lambda_{\gamma\gamma})\right). \end{aligned}$$

In this basis the Lindbladian becomes $\mathcal{L} = \sum_\gamma \omega_{\gamma\gamma}\bar{\varsigma}_\gamma\varsigma_\gamma + \upsilon$, where the new constant $\upsilon = \eta + \sum_{\mathfrak{Re}(\lambda_{\gamma\gamma})>0}\lambda_{\gamma\gamma}$ is zero. Transforming back to the orbital basis

$$\begin{aligned} \langle d_\alpha(t)d^\dagger_\beta\rangle_\infty &= \sum_{\gamma\epsilon} U_{\alpha\gamma}\langle\xi_\gamma(t)\bar{\xi}_\epsilon\rangle_\infty(U^{-1})_{\epsilon\beta} \\ &= \sum_{\gamma\epsilon} U_{\alpha\gamma}e^{\lambda_{\gamma\gamma}t}\langle I|\delta_{\gamma\epsilon} - \bar{\xi}_\epsilon\xi_\gamma|\rho_\infty\rangle(U^{-1})_{\epsilon\beta} \\ &= \sum_{\epsilon} U_{\alpha\gamma}e^{\lambda_{\gamma\gamma}t}\langle I|\sum_\gamma \delta_{\gamma\epsilon} - \Bigg(\sum_{\mathfrak{Re}(\lambda_{\gamma\gamma})\le 0}\bar{\varsigma}_\epsilon\varsigma_\gamma \\ &+ \sum_{\mathfrak{Re}(\lambda_{\gamma\gamma})>0}(\delta_{\gamma\epsilon} - \bar{\varsigma}_\epsilon\varsigma_\gamma)\Bigg)|\rho_\infty\rangle(U^{-1})_{\epsilon\beta} \\ &= \sum_{\epsilon} U_{\alpha\gamma}e^{\lambda_{\gamma\gamma}t}\langle I|\sum_\gamma \delta_{\gamma\epsilon} \\ &- \sum_{\mathfrak{Re}(\lambda_{\gamma\gamma})>0}\delta_{\gamma\epsilon}|\rho_\infty\rangle(U^{-1})_{\epsilon\beta} \\ &= \sum_\gamma U_{\alpha\gamma}e^{\lambda_{\gamma\gamma}t}D_{\gamma\gamma}(U^{-1})_{\gamma\beta}, \end{aligned}$$

since $|\rho_\infty\rangle$ is the vacuum of the ς modes. We introduced a matrix

$$D_{\gamma\gamma} = \begin{cases} 0 & \mathfrak{Re}(\lambda_{\gamma\gamma}) \le 0 \\ 1 & \mathfrak{Re}(\lambda_{\gamma\gamma}) > 0 \end{cases} ,$$

which selects exponentially growing eigenmodes and $\bar{D} = (\mathbb{1} - D)$ defines its complement. The component for $t < 0$ is obtained by taking the hermitian conjugate and exchanging t by $-t$ in the above expression. Then the greater Green's function is governed by contributions with $\mathfrak{Re}(\lambda_{\gamma\gamma}) \le 0$

$$G^{>,\infty}_{\mu\nu}(t) = \begin{cases} -i\left(\boldsymbol{U} e^{\boldsymbol{\lambda} t} \bar{\boldsymbol{D}} \boldsymbol{U}^{-1}\right)_{\mu\nu} & t \ge 0 \\ -i\left(\boldsymbol{U} e^{-\boldsymbol{\lambda} t} \bar{\boldsymbol{D}} \boldsymbol{U}^{-1}\right)^*_{\nu\mu} & t < 0 \end{cases} .$$

Its Fourier transform

$$G^{>,\infty}_{\mu\nu}(\omega) = \int_{-\infty}^{\infty} dt\, e^{i\omega t} G^{>,\infty}_{\mu\nu}(t) ,$$

yields

$$G^{>,\infty}_{\mu\nu}(\omega) = \left(\boldsymbol{U} \frac{1}{\mathbb{1} - i\boldsymbol{\lambda}\bar{\boldsymbol{D}}} \boldsymbol{U}^{-1}\right)_{\mu\nu} - \left(\boldsymbol{U} \frac{1}{\mathbb{1} - i\boldsymbol{\lambda}\bar{\boldsymbol{D}}} \boldsymbol{U}^{-1}\right)^*_{\nu\mu} ,$$

where $\mathbb{1}$ is the unit in the fermion+super-fermion space. Note that $G^{>,\infty}_{\mu\nu}(\omega) = G^{>,\infty *}_{\nu\mu}(\omega)$.

The lesser Green's function

$$G^{<,\infty}_{0,\mu\nu}(t) := i\langle d^\dagger_\nu(t) d_\mu\rangle_\infty ,$$

is evaluated in an analogous way and is governed by contributions with $\mathfrak{Re}(\lambda_{\gamma\gamma}) > 0$

$$G^{<,\infty}_{\mu\nu}(t) = \begin{cases} i\left(\boldsymbol{U} e^{-\boldsymbol{\lambda} t} \boldsymbol{D} \boldsymbol{U}^{-1}\right)^*_{\nu\mu} & t \ge 0 \\ i\left(\boldsymbol{U} e^{\boldsymbol{\lambda} t} \boldsymbol{D} \boldsymbol{U}^{-1}\right)_{\mu\nu} & t < 0 \end{cases} .$$

Its Fourier transform yields

$$G^{<,\infty}_{\mu\nu}(\omega) = \left(\boldsymbol{U} \frac{1}{\mathbb{1} - i\boldsymbol{\lambda}\boldsymbol{D}} \boldsymbol{U}^{-1}\right)_{\mu\nu} - \left(\boldsymbol{U} \frac{1}{\mathbb{1} - i\boldsymbol{\lambda}\boldsymbol{D}} \boldsymbol{U}^{-1}\right)^*_{\nu\mu} ,$$

which satisfies $G^{<,\infty}_{\mu\nu}(\omega) = G^{<,\infty *}_{\nu\mu}(\omega)$.

The Keldysh Green's function is given by contributions from all $\lambda_{\gamma\gamma}$: $G^{K,\infty}_{\mu\nu} = G^{>,\infty}_{\mu\nu} + G^{<,\infty}_{\mu\nu}$

$$G^{K,\infty}_{\mu\nu}(t) = \begin{cases} i\left(\boldsymbol{U} e^{-\boldsymbol{\lambda} t} \boldsymbol{D} \boldsymbol{U}^{-1}\right)^*_{\nu\mu} - i\left(\boldsymbol{U} e^{\boldsymbol{\lambda} t} \bar{\boldsymbol{D}} \boldsymbol{U}^{-1}\right)_{\mu\nu} & t \ge 0 \\ i\left(\boldsymbol{U} e^{\boldsymbol{\lambda} t} \boldsymbol{D} \boldsymbol{U}^{-1}\right)_{\mu\nu} - i\left(\boldsymbol{U} e^{-\boldsymbol{\lambda} t} \bar{\boldsymbol{D}} \boldsymbol{U}^{-1}\right)^*_{\nu\mu} & t < 0 \end{cases} .$$

Its Fourier transform yields

$$G^{K,\infty}_{\mu\nu}(\omega) = \left(\boldsymbol{U} \frac{1}{\mathbb{1} - i\boldsymbol{\lambda}} \boldsymbol{U}^{-1}\right)_{\mu\nu} - \left(\boldsymbol{U} \frac{1}{\mathbb{1} - i\boldsymbol{\lambda}} \boldsymbol{U}^{-1}\right)^*_{\nu\mu} , \tag{F.24}$$

for which $G^{K,\infty}_{\mu\nu}(\omega) = -G^{K,\infty}_{\nu\mu}(\omega)$ holds.

The retarded Green's function is given by $G^{R,\infty}_{\mu\nu}(t) = \theta(t)\left(G^{>,\infty}_{\mu\nu}(t) - G^{<,\infty}_{\mu\nu}(t)\right)$, where the step-function $\theta(t)$ selects times $t > 0$

$$G^{R,\infty}_{\mu\nu}(t) = \begin{cases} -i\left(\boldsymbol{U}e^{\boldsymbol{\lambda}t}\bar{\boldsymbol{D}}\boldsymbol{U}^{-1}\right)_{\mu\nu} - i\left(\boldsymbol{U}e^{-\boldsymbol{\lambda}t}\boldsymbol{D}\boldsymbol{U}^{-1}\right)^*_{\nu\mu} & t \geq 0 \\ 0 & t < 0 \end{cases}.$$

Its Fourier transform yields

$$G^{R,\infty}_{\mu\nu}(\omega) = \left(\boldsymbol{U}\frac{1}{\mathbb{1} - i\boldsymbol{\lambda}\bar{\boldsymbol{D}}}\boldsymbol{U}^{-1}\right)_{\mu\nu} - \left(\boldsymbol{U}\frac{1}{\mathbb{1} - i\boldsymbol{\lambda}\boldsymbol{D}}\boldsymbol{U}^{-1}\right)^*_{\nu\mu}. \tag{F.25}$$

The advanced Green's function is given by $G^{A,\infty}_{\mu\nu}(t) = \theta(-t)\left(G^{<,\infty}_{\mu\nu}(t) - G^{>,\infty}_{\mu\nu}(t)\right)$, where the step-function $\theta(-t)$ selects times $t < 0$

$$G^{A,\infty}_{\mu\nu}(t) = \begin{cases} 0 & t \geq 0 \\ i\left(\boldsymbol{U}e^{\boldsymbol{\lambda}t}\boldsymbol{D}\boldsymbol{U}^{-1}\right)_{\mu\nu} + i\left(\boldsymbol{U}e^{-\boldsymbol{\lambda}t}\bar{\boldsymbol{D}}\boldsymbol{U}^{-1}\right)^*_{\nu\mu} & t < 0 \end{cases}.$$

Its Fourier transform yields

$$G^{A,\infty}_{\mu\nu}(\omega) = \left(\boldsymbol{U}\frac{1}{\mathbb{1} - i\boldsymbol{\lambda}\boldsymbol{D}}\boldsymbol{U}^{-1}\right)_{\mu\nu} - \left(\boldsymbol{U}\frac{1}{\mathbb{1} - i\boldsymbol{\lambda}\bar{\boldsymbol{D}}}\boldsymbol{U}^{-1}\right)^*_{\nu\mu},$$

where $G^{R,\infty}_{\mu\nu} = -G^{A,\infty *}_{\nu\mu}$.

Next we show how to simplify the above expressions based on symmetries of the Lindbladian in the super-fermionic representation. We define matrices $\boldsymbol{V}$ which block diagonalize the non-interacting Lindbladian (Eq. (F.23)) $i\boldsymbol{\mathcal{L}}_0 = \boldsymbol{V}\boldsymbol{B}\boldsymbol{V}^{-1}$ with

$$\boldsymbol{B} = \sum_\sigma \begin{pmatrix} \boldsymbol{E} - i\boldsymbol{\Lambda} & \boldsymbol{0} \\ \boldsymbol{0} & \boldsymbol{E} + i\boldsymbol{\Lambda} \end{pmatrix},$$

where the two blocks are complex conjugate to each other and an Ansatz for $\boldsymbol{V}$

$$\boldsymbol{V} = \begin{pmatrix} \mathbb{1}_d & \boldsymbol{X} \\ -i\boldsymbol{X} & i(\mathbb{1}_d - \boldsymbol{X}) \end{pmatrix}, \boldsymbol{V}^{-1} = \begin{pmatrix} (\mathbb{1}_d - \boldsymbol{X}) & i\boldsymbol{X} \\ \mathbb{1}_d & -i\mathbb{1}_d \end{pmatrix},$$

where $\boldsymbol{X}$ is a hermitian matrix and $\mathbb{1}_d$ is the unit in either the fermion or the super-fermion space. The expression for the retarded Green's function Eq. (F.25) takes the form

$$\begin{aligned} \boldsymbol{G}^{R,\infty}_0(\omega) = \boldsymbol{V}\begin{pmatrix} (\omega\mathbb{1}_d - \boldsymbol{E} + i\boldsymbol{\Lambda})^{-1} & \boldsymbol{0} \\ \boldsymbol{0} & \boldsymbol{0} \end{pmatrix}\boldsymbol{V}^{-1} \\ + \left(\boldsymbol{V}\begin{pmatrix} \boldsymbol{0} & \boldsymbol{0} \\ \boldsymbol{0} & (\omega\mathbb{1}_d - \boldsymbol{E} - i\boldsymbol{\Lambda})^{-1} \end{pmatrix}\boldsymbol{V}^{-1}\right)^\dagger, \end{aligned}$$

which (for real ω) becomes independent of $\boldsymbol{X}$ and yields upon projection to the degrees of freedom of the fermions

$$\boldsymbol{G}^{R,\infty}_0(\omega) = (\omega\mathbb{1}_d - \boldsymbol{E} + i\boldsymbol{\Lambda})^{-1},$$

and

$$\boldsymbol{G}_0^{A,\infty}(\omega) = (\omega \mathbb{1}_d - \boldsymbol{E} - i\boldsymbol{\Lambda})^{-1}\,.$$

The Keldysh Green's function Eq. (F.24) takes the form

$$\begin{aligned}\boldsymbol{G}_0^{K,\infty}(\omega) = \boldsymbol{V}&\begin{pmatrix}(\omega \mathbb{1}_d - \boldsymbol{E} + i\boldsymbol{\Lambda})^{-1} & \boldsymbol{0}\\ \boldsymbol{0} & \omega \mathbb{1}_d - \boldsymbol{E} + i\boldsymbol{\Lambda})^{-1}\end{pmatrix}\boldsymbol{V}^{-1}\\ &+\left(\boldsymbol{V}\begin{pmatrix}(\omega \mathbb{1}_d - \boldsymbol{E} - i\boldsymbol{\Lambda})^{-1} & \boldsymbol{0}\\ \boldsymbol{0} & (\omega \mathbb{1}_d - \boldsymbol{E} + i\boldsymbol{\Lambda})^{-1}\end{pmatrix}\boldsymbol{V}^{-1}\right)^{\dagger},\end{aligned}$$

which yields upon projection to the degrees of freedom of the fermions

$$\begin{aligned}\boldsymbol{G}_0^{K,\infty}(\omega) &= (\omega \mathbb{1}_d - \boldsymbol{E} + i\boldsymbol{\Lambda})^{-1}(\mathbb{1}_d - 2\boldsymbol{X})\\ &\quad + (2\boldsymbol{X} - \mathbb{1}_d)(\omega \mathbb{1}_d - \boldsymbol{E} - i\boldsymbol{\Lambda})^{-1}\\ &= \boldsymbol{G}_0^{R,\infty}(\omega)(\mathbb{1}_d - 2\boldsymbol{X}) + (2\boldsymbol{X} - \mathbb{1}_d)\boldsymbol{G}_0^{A,\infty}(\omega)\,,\end{aligned}$$

which using $(\underline{\boldsymbol{G}}^{-1})^K = -(\underline{\boldsymbol{G}}^{-1})^R\boldsymbol{G}^K(\underline{\boldsymbol{G}}^{-1})^A$ yields

$$\begin{aligned}(\underline{\boldsymbol{G}}_0^{\infty -1})^K(\omega) &= (2\boldsymbol{X} - \mathbb{1}_d)(\omega \mathbb{1}_d - \boldsymbol{E} - i\boldsymbol{\Lambda})\\ &\quad + (\omega \mathbb{1}_d - \boldsymbol{E} + i\boldsymbol{\Lambda})(\mathbb{1}_d - 2\boldsymbol{X})\\ &= -2([\boldsymbol{X}, \boldsymbol{E}] + i\{\boldsymbol{X}, \boldsymbol{\Lambda}\}) + 2i\boldsymbol{\Lambda}\\ &= -2i\boldsymbol{\Omega}\,,\end{aligned}$$

since $[\boldsymbol{X}, \boldsymbol{E}] + i\{\boldsymbol{X}, \boldsymbol{\Lambda}\} = 2i\boldsymbol{\Gamma}^{(2)}$ which follows directly from the block elements of $i\boldsymbol{\mathcal{L}}_0 = \boldsymbol{V}\boldsymbol{B}\boldsymbol{V}^{-1}$. Altogether we find the convenient end result for the non-interacting Green's function of the fermionic orbitals

$$\underline{\boldsymbol{G}}_0^{\infty -1}(\omega) = \begin{pmatrix}\omega \mathbb{1}_d - \boldsymbol{E} + i\boldsymbol{\Lambda} & -2i\boldsymbol{\Omega}\\ \boldsymbol{0} & \omega \mathbb{1}_d - \boldsymbol{E} - i\boldsymbol{\Lambda}\end{pmatrix}.$$

G. Optimized representation of non-interacting electronic reservoirs

The ideas presented in this appendix have been discussed with Markus Aichhorn and Manuel Zingl who both fruitfully contributed to the developments. The study of the SIAM in [329] and the CPT based DMFT solver developed in [471] by Martin Nuss, Manuel Zingl and Markus Aichhorn as well as the distributed ED algorithm [472] and the efficient real frequency DMFT solver presented in [473] served as a seed for the need of an optimized bath in CPT. The scheme proposed here is useful for all CPT based methods in equilibrium or out-of-equilibrium when parts of the entire system are non-interacting. This is the case when studying the steady-state of small interacting devices contacted to infinite non-interacting leads under bias voltage as in the main part of this thesis. It is also useful when constructing finite size representations of hybridization functions as needed in the equilibrium DMFT problem, see also [474]. In a benchmark for a single correlated orbital we find that the optimization scheme is capable of reproducing even difficult observables, like the equilibrium Kondo temperature remarkably well, see also [357].

G.1. Reservoir representation

Within the steady-state quantum cluster methods stsCPT, stsVCA and meCPT, the electronic self-energy $\widetilde{\Sigma}_{\mathrm{sts}}(\omega)$ is approximated by the self-energy computed on a finite size reference system $\widetilde{\Sigma}_{\mathrm{rs}}(\omega)$. Consider a small interacting device $\hat{\mathcal{H}}^{\mathrm{S}}$ of size L_S, coupled by a single-particle hopping $\hat{\mathcal{H}}^{\mathrm{SE}}$ to non-interacting leads $\hat{\mathcal{H}}^{\mathrm{E}}$ of infinite size. A natural cluster decomposition for steady-state quantum cluster methods would be into $\hat{\mathcal{H}}^{\mathrm{S}}$ and $\hat{\mathcal{H}}^{\mathrm{E}}$ while treating the device-lead coupling $\hat{\mathcal{H}}^{\mathrm{SE}}$ within CPT perturbatively. Only the interacting subsystem $\hat{\mathcal{H}}^{\mathrm{S}}$ yields a contribution to the electronic self-energy $\widetilde{\Sigma}_{\mathrm{rs}}(\omega)$. That is the self-energy of an L_S site system is used. The non-interacting leads enter the calculation just via their local single-particle Green's function at the contact point $\widetilde{g}^{0\mathrm{E}}_{00}(\omega)$ which is typically available analytically [303].

However, electronic correlations inside the device can be treated more accurately when this perturbation lies further away from the interacting device i.e. when L_B orbitals of the non-interacting leads are incorporated in the central interacting cluster of size $L_C = L_S + L_B$. This implies that the electronic self-energy $\widetilde{\Sigma}_{\mathrm{rs}}(\omega)$ is now computed from an $L_C > L_S$ site interacting system, ultimately reaching its exact value at $L_C \to \infty$. In the following we shortly discuss the simplest way of incorporating a non-interacting reservoir partially into the interacting cluster: the chain representation. Leaving the non-interacting reservoir Green's function $\widetilde{g}^{0\mathrm{E}}_{00}(\omega)$ invariant, the non-interacting reservoir can always be transformed to a tridiagonal representation via unitary transformations. The reservoir on-site energies ϵ_i and nearest-neighbour-hopping t_i can be obtained using a Lanczos tridiagonalization procedure [329] yielding a chain representation of the reservoir. The on-site energies $\{\epsilon_1, \ldots, \epsilon_{L_B}\}$ and hopping $\{t_1, \ldots, t_{L_B-1}\}$ then enter the Hamiltonian of the interacting cluster. The complexity for solving this part grows exponentially with its size L_C. The new inter-cluster perturbation is the single-particle hopping t_{L_B}. The dynamics of the remainder of the non-interacting leads can still be solved exactly for example

via a continued fraction representation

$$g^{0\mathrm{E},R}(\omega) = \cfrac{1}{\omega^+ + \epsilon_{L_B+1} - \cfrac{t^2_{L_B+1}}{\omega^+ + \epsilon_{L_B+2} - \cfrac{t^2_{L_B+2}}{\omega^+ + \epsilon_{L_B+3} - \cfrac{t^2_{L_B+3}}{\omega^+ + \ldots}}}}.$$

This representation straight forwardly allows to successively incorporate parts of the reservoir into the interacting cluster. The situation is not so clear in other representations. Consider for example the case of a star geometry, where all reservoir orbitals couple once to the interacting device only. Then their on-site energies directly reflect their energetic location in the Green's function and the respective hopping their weight. Incorporating just any L_B of these star orbitals into the interacting cluster will lead to a poor self-energy due to the fragmentary contribution of the reservoir to the self-energy.

In general any unitary transformation on the non-interacting reservoir degrees of freedom leaves the physics of the interacting device invariant. It is however clear, that such a transformation will alter the electronic self-energy of the interacting cluster significantly due to the perturbative nature of CPT. However such transformations will also alter the off-diagonal perturbative blocks between the interacting cluster and the remaining reservoir, rendering the resulting perturbation in some cases larger than in other. There exist an infinite set of reservoirs of infinite size which all describe the non-interacting reservoir at the device exactly and which are related via unitary transformations. In the following we explore what characterizes good reservoirs in CPT and how to improve on the reservoir parametrization. We will present a way to efficiently construct reservoirs which are especially favourable for the CPT method. We conclude by presenting results for the physics of a single interacting orbital.

G.2. Optimized electronic reservoir

In the following, for illustration purposes, we restrict ourself to a single correlated orbital $L_S = 1$ coupled to one non-interacting reservoir of $L-1 \to \infty$ orbitals. We use a semicircular reservoir DOS, i.e. the local Green's function of a non-interacting semi-infinite tight binding chain. In general the non-interacting Green's function is specified by the non-interacting Hamiltonian H_0, that is a matrix in orbital space of size $L \times L$. Out of this space a cluster of size L_C is chosen such that it consists of the $L_S = 1$ device orbitals and the $L_C - L_S$ "first" reservoir orbitals (in any given order), this is the upper left $L_C \times L_C$ block in H_0 subsequently H_0^{cluster}. The remaining, lower $(L-L_C)\times(L-L_C)$ block describes the remainder of the reservoir, subsequently $H_0^{\mathrm{reservoir}}$. Note that explicitly $L_C - 1$ reservoir orbitals are also included in H_0^{cluster} and $H_0^{\mathrm{reservoir}}$ just describes the rest of the reservoir. In CPT both these Hamiltonians are solved exactly for their non-interacting single-particle Green's functions $\widetilde{g}^{0\mathrm{cluster}}(w)$ of size $L_C \times L_C$ and $\widetilde{g}^{0\mathrm{reservoir}}(w)$ of size $(L-L_C)\times(L-L_C)$. Subsequently they are joined to yield the $L \times L$ non-interacting single-particle Green's function of the full system $\widetilde{G}^{0-1}(w)$ by the CPT relation

$$\widetilde{G}^{0-1}(\omega) = \begin{pmatrix} \widetilde{g}^{0\mathrm{cluster}}(\omega) & 0 \\ 0 & \widetilde{g}^{0\mathrm{reservoir}}(\omega) \end{pmatrix}^{-1} - \widetilde{T},$$

which becomes exact as long as only non-interacting subsystems are considered. Here T is the inter-cluster perturbation which consists of the two off-diagonal blocks in H_0 connecting the interacting cluster and the remainder of the reservoir, i.e. $T = H_0(1:L_C, L_C+1:L) + H_0(L_C+1:L, 1:L_C)$. As soon as an interaction on the impurity is switched on, the non-interacting Green's

functions become replaced by their interacting equivalents. Then the CPT relation is no longer exact but a result of perturbation theory in T.

Therefore the CPT method itself suggests which reservoirs might be the best: Those which "minimize" the off diagonal perturbative elements $\|T\|$. Using unitary transformations just on the reservoir we can find those reservoirs with minimal $\|T\|$, which suggest the best system for the CPT perturbation theory and therefore the best self-energy, see Fig. G.1 (B).

The full non-interacting Hamiltonian reads for $L \to \infty$

$$H_0 = c_0^\dagger h_{00} c_0 + \sum_{i=1}^{L-1} c_i^\dagger h_{i0} c_0 + \sum_{i=1}^{L-1} c_0^\dagger h_{0i} c_i + \sum_{i,j=1}^{L-1} c_i^\dagger h_{ij} c_j \,,$$

where the impurity is denoted by 0 and all $L-1$ reservoir orbitals by i and j. We now perform a unitary transformation in the reservoir only, which leaves the impurity 0 invariant

$$\begin{aligned}
\underline{c}_\alpha &= \left(R^\dagger\right)_{i\alpha} c_i = R^*_{\alpha i} c_i \\
\underline{c}^\dagger_\alpha &= c_i^\dagger R_{i\alpha} \\
c_i &= R_{i\alpha} \underline{c}_\alpha \,, \\
c_i^\dagger &= \underline{c}^\dagger_\alpha \left(R^\dagger\right)_{i\alpha} = \underline{c}^\dagger_\alpha R^*_{\alpha i} \,,
\end{aligned}$$

with a unitary transformation $RR^\dagger = \mathbb{1}$. This leads to the reservoir-transformed Hamiltonian

$$\begin{aligned}
\underline{\mathrm{H}}_0 &= c_0^\dagger h_{00} c_0 + \sum_{i=1}^{L-1}\sum_{\alpha=1}^{L-1} \underline{c}^\dagger_\alpha R^*_{\alpha i} h_{i0} c_0 + \sum_{i=1}^{L-1}\sum_{\alpha=1}^{L-1} c_0^\dagger h_{0i} R_{i\alpha} \underline{c}_\alpha + \sum_{i,j=1}^{L-1}\sum_{\alpha,\beta=1}^{L-1} \underline{c}^\dagger_\alpha R^*_{\alpha i} h_{ij} R_{j\beta} \underline{c}_\beta \\
&= c_0^\dagger h_{00} c_0 + \sum_{\alpha=1}^{L-1} \underline{c}^\dagger_\alpha \underline{\mathrm{h}}_{\alpha 0} c_0 + \sum_{\alpha=1}^{L-1} c_0^\dagger \underline{\mathrm{h}}_{0\alpha} \underline{c}_\alpha + \sum_{\alpha,\beta=1}^{L-1} \underline{c}^\dagger_\alpha \underline{\mathrm{h}}_{\alpha\beta} \underline{c}_\beta \,,
\end{aligned}$$

with

$$\begin{aligned}
\underline{\mathrm{h}}_{\alpha 0} &= \sum_{i=1}^{L-1} R^*_{\alpha i} h_{i0} \\
\underline{\mathrm{h}}_{\alpha 0} &= \sum_{i=1}^{L-1} h_{0i} R_{i\alpha} \\
\underline{\mathrm{h}}_{\alpha\beta} &= \sum_{i,j=1}^{L-1} R^*_{\alpha i} h_{ij} R_{j\beta}.
\end{aligned}$$

The "energy" of a certain reservoir configuration H_0 is determined via the 2- norm of the off diagonal blocks T

$$E = \frac{1}{N_T} \sum_{ij} w_{ij} |T_{ij}|^2 \,, \tag{G.1}$$

where the number of elements in T is $N_T = L_C \cdot (L - L_C)$. Performing transformations on the reservoir degrees of freedom included in the interacting cluster does not influence the resulting self-energy in any way. The same is true for transformations on the reservoir orbitals in the remainder of the reservoir. This imposes a constraint on the energy: It has to be invariant with respect to such transformations, which is fulfilled by the two norm proposed above. In general one could think of a more complicated scheme including weighing factors w_{ij} which die off with

distance from the interacting device. We use $w_{ij} = 1$.

G.3. Optimization scheme

To find the minimum in energy Eq. (G.1) in the high dimensional space T_{ij}, we propose a simulated annealing strategy. We move through the space of possible H_0 by proposing random local updates R. In general any unitary updates $R = e^{iM}$, with $M = M^\dagger$ is allowed. Here we restrict ourselves to two-dimensional rotation matrices

$$R = \begin{pmatrix} 1 & 0 & \dots & 0 & 0 & \dots & 0 & \dots & 0 \\ 0 & 1 & \dots & 0 & 0 & \dots & 0 & \dots & 0 \\ \dots & \dots & \dots & \dots & \dots & \dots & \dots & \dots & 0 \\ 0 & 0 & \dots & \cos(\theta) & 0 & \dots & -\sin(\theta) & \dots & 0 \\ 0 & 0 & \dots & 0 & 1 & \dots & 0 & \dots & 0 \\ \dots & \dots & \dots & \dots & \dots & \dots & \dots & \dots & 0 \\ 0 & 0 & \dots & \sin(\theta) & 0 & \dots & \cos(\theta) & \dots & 0 \\ \dots & \dots & \dots & \dots & \dots & \dots & \dots & \dots & \dots \\ 0 & 0 & \dots & 0 & 0 & \dots & 0 & \dots & 1 \end{pmatrix},$$

An update $R(x, y, \phi)$ is drawn by choosing two random integers $x, y \in [1, L-1]$ representing the plane of rotation and one random double $\theta \in [0, 2\pi[$ representing the rotation angle.

Here we discuss a single interacting impurity in a particle-hole symmetric setting. Although reservoir rotations leave the particle-hole symmetry invariant on the L site H_0, they destroy it on the L_C site cluster in the interacting case. Therefore we split the reservoir space into an equal amount of positive and negative energy modes and one zero mode and perform updates simultaneously on the positive and negative modes which leaves the whole reservoir, the reservoir in the cluster as well as the remaining reservoir particle-hole invariant also in the interacting system.

To obtain a set of low energy, i.e. in the sense of CPT, reservoir configurations we propose a Monte Carlo update, see Fig. G.1 (A)

1. Given the non-interacting reservoir DOS, obtain H_0 in star form on $L-1$ reservoir orbitals by a Lanczos procedure.

2. Perform a global random update in all dimensions and therefore obtain a random starting representation of H_0.

3. From now on perform single random two dimensional rotation updates $R(x, y, \theta$ and accept them with probability

$$p = \min\left(1, e^{-\beta(E_{\text{trial}} - E)}\right).$$

   If rejected, stay with the old configuration. A suitable inverse temperature β has to be chosen according to the acceptance rate.

The resulting reservoir will

- minimize the perturbative matrix elements,
- leave the non-interacting Green's function invariant and
- fulfil particle-hole symmetry at the cluster level also for interacting systems.

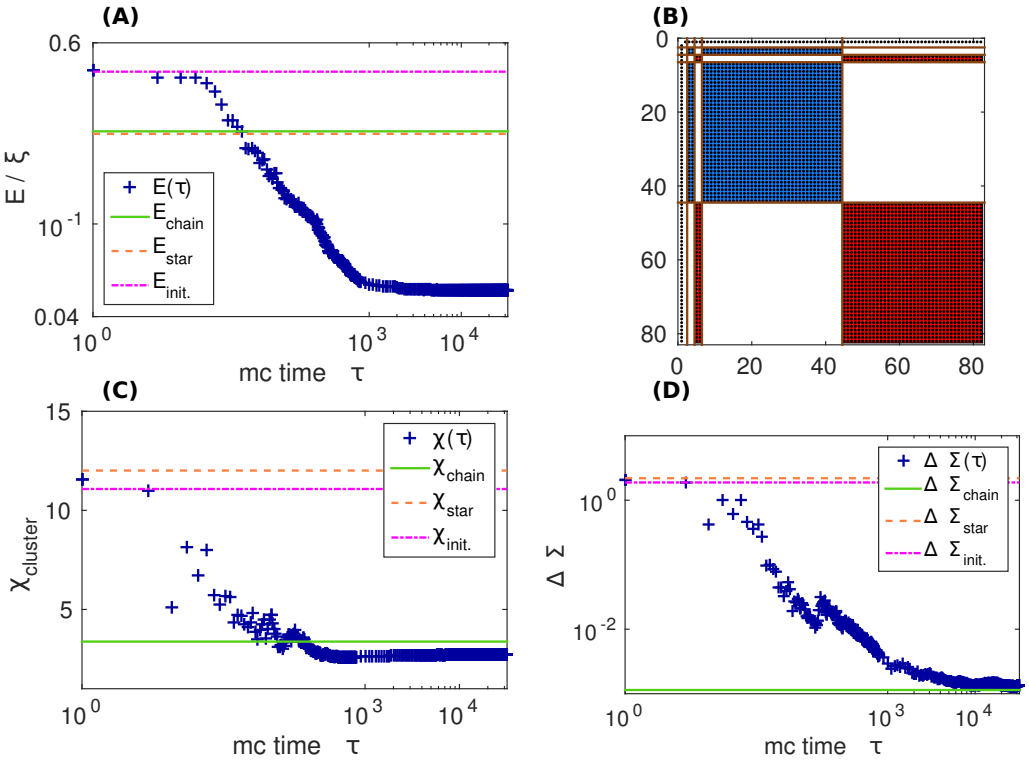

Figure G.1.: *Optimized representation of non-interacting reservoirs: optimization process.* **(A)** Minimization of the non-interacting reservoir representation. The Monte Carlo energy E is plotted vs. the Monte Carlo time τ in a doubly logarithmic fashion. In addition we show the initial energy (pink), the energy of an arbitrary star (orange) and the energy of a chain (green) representation. **(B)** Unitary updates are performed in the space of negative energies (blue) and the equivalent ones in the space of positive energies (red) to respect particle-hole symmetry. The diagonal blocks from top to bottom represent: 1) the impurity, 2) the zero mode inside the cluster, 3) two negative modes inside the cluster, 4) two positive modes inside the cluster, 5) the remaining negative modes in the reservoir and 6) the remaining positive modes in the reservoir. **(C)** Evolution of the hybridization function χ_{cluster}, generated by considering only the interacting cluster. **(D)** Evolution of the difference of the self-energy of the cluster to the self-energy of the full system $\Delta\Sigma$ as obtained by second order perturbation theory.

We gauge the quality of each reservoir representation by three indicators, see Fig. G.1 (C,D)

1. The energy E as defined in Eq. (G.1) which reflects the magnitude of the perturbation.

2. The influence of the CPT truncation can be judged on the non-interacting level. We compare the exact non-interacting DOS at the device $-\frac{1}{\pi}\mathfrak{Im}\left(g^{0R}_{00}(\omega)\right)$, that is the one yielded by the infinite reservoir to the one obtained by considering the orbitals in the interacting cluster only $-\frac{1}{\pi}\mathfrak{Im}\left(g^{0R}_{00,\mathrm{cluster}}(\omega)\right)$. The resulting quantity

$$\Delta\chi_{\mathrm{cluster}} = \int_{-\infty}^{\infty} d\omega \left|\mathfrak{Im}\left(g^{0R}_{00}(\omega)\right) - \mathfrak{Im}\left(g^{0R}_{00,\mathrm{cluster}}(\omega)\right)\right|^2 ,$$

   can readily be evaluated and reflects the ability of the interacting cluster to represent the reservoir degrees of freedom.

3. The influence of the CPT truncation should be judged on level of the self-energy. In analogy to $\Delta\chi_{\mathrm{cluster}}$ we define $\Delta\Sigma$ as the difference in cluster self-energy to the self-energy of the full infinite system

$$\Delta\Sigma = \int_{-\infty}^{\infty} d\omega \left|\Sigma_{00}(\omega) - \Sigma_{00,\mathrm{cluster}}(\omega)\right|^2 .$$

   Of course $\Sigma_{00}(\omega)$ can not be obtained exactly for interacting systems. This is why we propose a guess for this quantity for small U, based on second order perturbation theory. We evaluate both $\Sigma_{00,\mathrm{cluster}}(\omega)$ as well as $\Sigma_{00,\mathrm{cluster}}(\omega)$ using an integral over imaginary time τ [36, 42]

$$\Sigma^{(2)}_{00}(\omega_n) = U^2 \int_0^{\beta} d\tau (g^0_{00})^2(\tau) g^0_{00}(-\tau) e^{i\omega_n \tau} .$$

   Since we compute both $\Sigma_{00,\mathrm{cluster}}(\omega)$ and $\Sigma_{00,\mathrm{cluster}}(\omega)$ within this approximation and compare only quotients we can hope for a cancellation of perturbative errors.

A-priori a positive correlation of these three objects is not ensured but expected. In CPT one wants to use the best self-energy that is the minimum $\Delta\Sigma$, which however cannot be obtained exactly. A positive correlation of $\Delta\Sigma$ with $\Delta\chi_{\mathrm{cluster}}$ is for example assumed in ED based DMFT solvers. We will show below that both $\Delta\chi_{\mathrm{cluster}}$ and an approximate guess for $\Delta\Sigma$ correlate positively with E, validating the proposed scheme.

G.4. Optimization results

We start out by discussing the correlation of the three indicators $\Delta\chi_{\mathrm{cluster}}$, $\Delta\Sigma$ and E. In this section we use a particle-hole symmetric reservoir of 81 orbitals, a single interacting impurity and an interacting cluster of $L_C = 6$. That is the cluster hosts the impurity, one reservoir zero mode and two additional positive and negative reservoir modes each. In Fig. G.2 we plot the results of a typical annealing run (blue pluses). Fig. G.2 (A) shows that smaller perturbative elements E correlate positively with smaller $\Delta\chi_{\mathrm{cluster}}$, indicating a better representation of the non-interacting reservoir inside the interacting cluster. Fig. G.2 (B) shows the positive correlations of E with the guess for $\Delta\Sigma$. We compare the reservoir configurations to the random initial

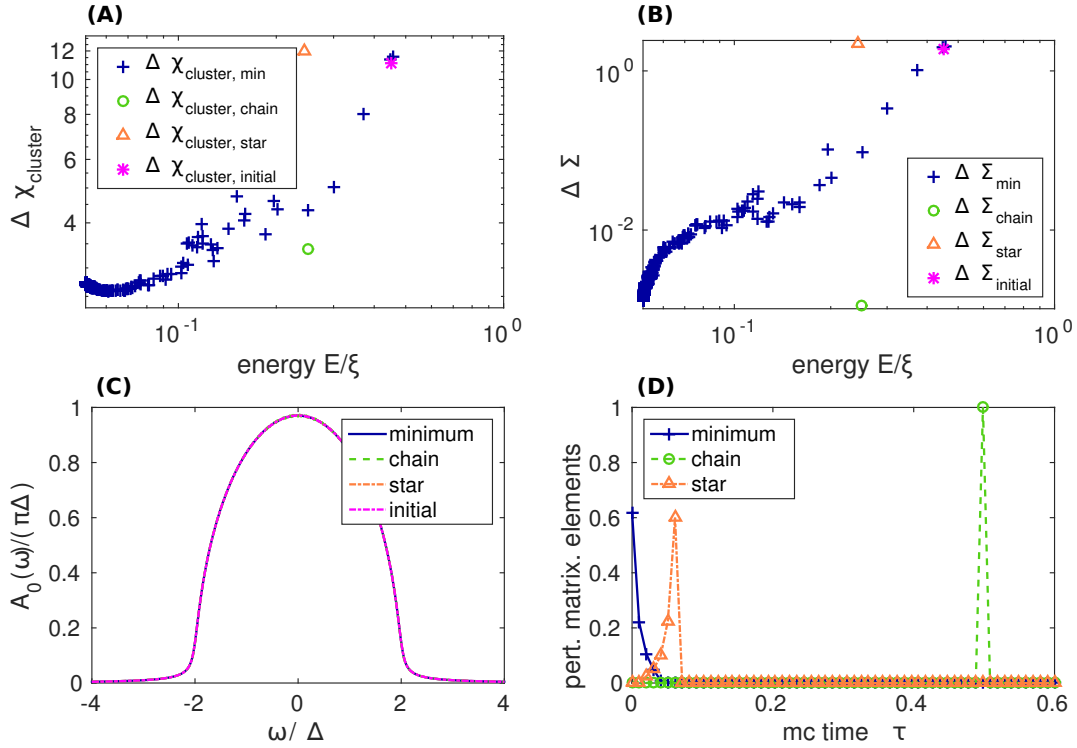

Figure G.2.: *Optimized representation of non-interacting reservoirs: optimized reservoir.* **(A)** Correlation of Monte Carlo energy E and the representation of the hybridization function by the interacting cluster only $\Delta\chi_{\text{cluster}}$. **(B)** Correlation of Monte Carlo energy E and the estimate for the error in the self-energy $\Delta\Sigma$, as obtained by second order perturbation theory. In both panel (A) and (B) we plot in addition the respective values for the chain (green), an arbitrary star (orange) and the initial (pink) representation. **(C)** The spectral function of the full system is invariant under change of basis. **(D)** Histogram of the perturbative matrix elements T_{ij} of the minimum energy (blue), the chain (green) and an arbitrary star (orange) representation.

configuration (pink star) which shows a much higher $\Delta\chi_{\text{cluster}}$ and a much higher $\Delta\Sigma$. When using a star representation of the reservoir and choosing five orbitals at random to enter the interacting cluster one again finds a much higher $\Delta\chi_{\text{cluster}}$ and a much higher $\Delta\Sigma$ with respect to the optimized results. The chain representation (green circles) hosts only one perturbative matrix element which is however large. The optimized representation can yield a better $\Delta\chi_{\text{cluster}}$, however the guess for $\Delta\Sigma$ of the chain seems to be as good as the one for the optimized result. The optimization procedure leaves the DOS of the non-interacting reservoir at the impurity invariant, see Fig. G.2 (C). Fig. G.2 (D) shows that as expected the number of perturbative matrix elements T_{ij} grows during the optimization but their magnitude becomes tiny as compared to the chain or the star.

In Fig. G.3 we present the resulting CPT spectral function $A(\omega)$ and self-energy $\Sigma(i\omega_n)$ for an interaction strength of $U = 2\,\Delta$. The arbitrary initial and star representations yield results far away from the chain and the optimized representation. Results obtained with the optimized

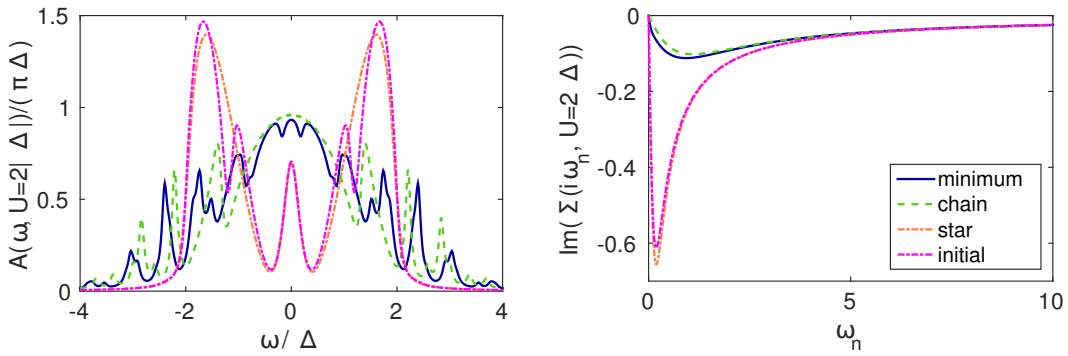

Figure G.3.: *Optimized representation of non-interacting reservoirs: Interacting spectral function and self-energy.* **(Left)** The CPT spectral function $A(\omega)$ at $U = 2\,\Delta$. **(Right)** The corresponding Matsubara self-energy $\Sigma(i\omega)$. The key is valid for both panels

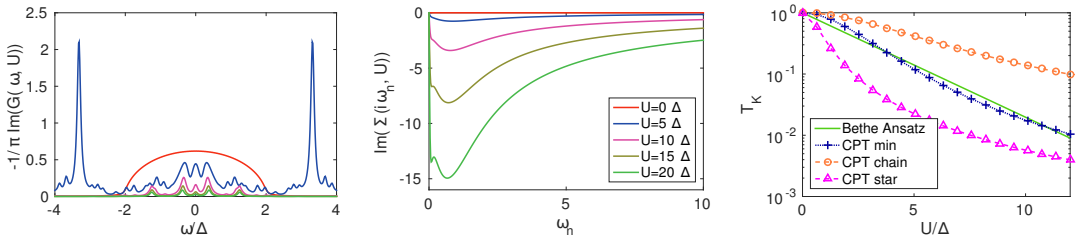

Figure G.4.: *Optimized representation of non-interacting reservoirs: Evolution with interaction strength.* **(Left)** Interacting spectral function as obtained by the optimized reservoir representation with CPT. **(Middle)** Matsubara self-energy as obtained by the optimized reservoir representation with CPT. The key is also valid for panel (A). **(Right)** CPT Kondo temperature as obtained by the optimized (blue), the chain (orange) and an arbitrary star (pink) representation.

reservoir are plotted in Fig. G.4 as a function of interaction strength U. Our results are based on $L_C = 6$ site clusters. Therefore dynamic quantities like the DOS show strong finite size effects. The quality of the approximation can however be judged by considering a static physical quantity like the Kondo temperature T_K [53]. Fig. G.4 shows that the optimized CPT representation yields results close to the Bethe Ansatz result [53] and outperforms CPT studies not using the optimization which also predict an exponential scaling of T_K, however with an underestimated exponential factor [357].

Bibliography

[1] M. Ferrero and O. Parcollet. *TRIQS: a Toolbox for Research in Interacting Quantum Systems.*

[2] R. Žitko. *"NRG Ljubljana" - open source numerical renormalization group code* (2013). V2.3.20.

[3] M. J. Frisch, G. W. Trucks, H. B. Schlegel, G. E. Scuseria, M. A. Robb, J. R. Cheeseman, G. Scalmani, V. Barone, B. Mennucci, G. A. Petersson, H. Nakatsuji, M. Caricato, X. Li, H. P. Hratchian, A. F. Izmaylov, J. Bloino, G. Zheng, J. L. Sonnenberg, M. Hada, M. Ehara, K. Toyota, R. Fukuda, J. Hasegawa, M. Ishida, T. Nakajima, Y. Honda, O. Kitao, H. Nakai, T. Vreven, J. A. Montgomery, Jr., J. E. Peralta, F. Ogliaro, M. Bearpark, J. J. Heyd, E. Brothers, K. N. Kudin, V. N. Staroverov, R. Kobayashi, J. Normand, K. Raghavachari, A. Rendell, J. C. Burant, S. S. Iyengar, J. Tomasi, M. Cossi, N. Rega, J. M. Millam, M. Klene, J. E. Knox, J. B. Cross, V. Bakken, C. Adamo, J. Jaramillo, R. Gomperts, R. E. Stratmann, O. Yazyev, A. J. Austin, R. Cammi, C. Pomelli, J. W. Ochterski, R. L. Martin, K. Morokuma, V. G. Zakrzewski, G. A. Voth, P. Salvador, J. J. Dannenberg, S. Dapprich, A. D. Daniels, Ã. Farkas, J. B. Foresman, J. V. Ortiz, J. Cioslowski, and D. J. Fox. *Gaussian09 Revision D.01.* Gaussian Inc. Wallingford CT 2009.

[4] P. Blaha, K. Schwarz, G. Madsen, D. Kvasnicka, and J. Luitz. *WIEN2K, An Augmented Plane Wave + Local Orbitals Program for Calculating Crystal Properties.* Karlheinz Schwarz, Techn. Universität Wien, Austria, Wien, Austria (2001).

[5] A. A. Mostofi, J. R. Yates, Y.-S. Lee, I. Souza, D. Vanderbilt, and N. Marzari. *wannier90: A tool for obtaining maximally-localised Wannier functions.* Computer Physics Communications **178** (9), 685 – 699 (2008).

[6] A. Kokalj. *Computer graphics and graphical user interfaces as tools in simulations of matter at the atomic scale.* Computational Materials Science **28** (2), 155 – 168 (2003).

[7] L. D. Landau. *The theory of a Fermi liquids.* J. Exptl. Theoret. Phys. **30**, 1058 (1956).

[8] L. D. Landau. *Oscillations of a Fermi liquid.* J. Exptl. Theoret. Phys. **32**, 59 (1957).

[9] L. D. Landau. *On the theory of the Fermi liquid,.* J. Exptl. Theoret. Phys. **35** (1958).

[10] G. Baym and C. Pethick. *Landau Fermi-Liquid Theory: Concepts and Applications.* John Wiley and Sons, 1 edition (1991). ISBN 0471824186.

[11] N. F. Mott. *The Basis of the Electron Theory of Metals, with Special Reference to the Transition Metals.* Proceedings of the Physical Society. Section A **62** (7), 416 (1949).

[12] J. Quintanilla and C. Hooley. *The strong-correlations puzzle.* Physics World **2**, 32–37 (2009).

[13] W. Kohn. *An essay on condensed matter physics in the twentieth century.* Rev. Mod. Phys. **71**, S59–S77 (1999).

[14] J. Bednorz and K. Müller. *Possible high T_c superconductivity in the Ba−La−Cu−O system.* Zeitschrift für Physik B Condensed Matter **64** (2), 189–193 (1986).

[15] N. F. Mott. *Metal-Insulator Transition.* Rev. Mod. Phys. **40**, 677–683 (1968).

[16] M. Imada, A. Fujimori, and Y. Tokura. *Metal-insulator transitions.* Rev. Mod. Phys. **70**, 1039–1263 (1998).

[17] S. Datta. *Quantum Transport: Atom to Transistor.* Cambridge University Press, 2nd edition edition (2005). ISBN 0521631459.

[18] D. K. Ferry, S. M. Goodnick, and J. Bird. *Transport in Nanostructures.* Cambridge University Press, 2nd edition edition (2009). ISBN 0521877482.

[19] Y. V. Nazarov and Y. M. Blanter. *Quantum Transport: Introduction to Nanoscience.* Cambridge University Press New York (2009). ISBN 0521832462.

[20] M. C. Rogge and R. J. Haug. *Noninvasive detection of molecular bonds in quantum dots.* Phys. Rev. B **78**, 153310 (2008).

[21] E. Assmann, P. Blaha, R. Laskowski, K. Held, S. Okamoto, and G. Sangiovanni. *Oxide Heterostructures for Efficient Solar Cells.* Phys. Rev. Lett. **110**, 078701 (2013).

[22] Z. Zhong, L. Si, Q. Zhang, W.-G. Yin, S. Yunoki, and K. Held. *Giant Switchable Rashba Effect in Oxide Heterostructures.* Advanced Materials Interfaces **2** (5) (2015).

[23] J. M. Luttinger. *An Exactly Soluble Model of a Many-Fermion System.* Journal of Mathematical Physics **4** (9), 1154–1162 (1963).

[24] C. A. M. dos Santos, M. S. da Luz, Y.-K. Yu, J. J. Neumeier, J. Moreno, and B. D. White. *Electrical transport in single-crystalline $Li_{0.9}Mo_6O_{17}$: A two-band Luttinger liquid exhibiting Bose metal behavior.* Phys. Rev. B **77**, 193106 (2008).

[25] J.-H. Chen, L. Li, W. G. Cullen, and E. D. W. M. S. Fuhrer. *Tunable Kondo effect in graphene with defects.* Nature Physics **7**, 535–538 (2011).

[26] W. Brenig and K. Schönhammer. *On the theory of chemisorption.* Zeitschrift für Physik **267**, 201–208 (1974).

[27] D. Vollhardt. *Normal ^{3}He: an almost localized Fermi liquid.* Rev. Mod. Phys. **56**, 99–120 (1984).

[28] G. Cuniberti, G. Fagas, and K. Richter. *Introducing Molecular Electronics.* Springer (2005). ISBN 3540279946.

[29] J. C. Cuevas and E. Scheer. *Molecular Electronics: An Introduction to Theory and Experiment.* World Scientific Publishing Company, 1 ed. edition (2010). ISBN 9814282588.

[30] I. Bloch, J. Dalibard, and W. Zwerger. *Many-body physics with ultracold gases.* Rev. Mod. Phys. **80**, 885–964 (2008).

[31] A. Nitzan and M. A. Ratner. *Electron Transport in Molecular Wire Junctions.* Science **300** (5624), 1384–1389 (2003).

[32] M. D. Ventra. *Electrical Transport in Nanoscale Systems.* Cambridge University Press, New York (2008). ISBN 0521896347.

[33] J. Park, A. N. Pasupathy, J. I. Goldsmith, C. Chang, Y. Yaish, J. R. Petta, M. Rinkoski, J. P. Sethna, H. D. Abruna, P. L. McEuen, and D. C. Ralph. *Coulomb blockade and the Kondo effect in single-atom transistors.* Nature **417** (6890), 722–725 (2002).

[34] R. H. M. Smit, Y. Noat, C. Untiedt, N. D. Lang, M. C. van Hemert, and J. M. van Ruitenbeek. *Measurement of the conductance of a hydrogen molecule.* Nature **419** (6910), 906–909 (2002).

[35] Xiao, Xu, and N. J. Tao. *Measurement of Single Molecule Conductance: Benzenedithiol and Benzenedimethanethiol.* Nano Letters **4** (2), 267–271 (2004).

[36] J. W. Negele and H. Orland. *Quantum Many-particle Systems.* Westview Press (1998). ISBN 0738200522.

[37] P. Delaney and J. C. Greer. *Correlated Electron Transport in Molecular Electronics.* Phys. Rev. Lett. **93**, 036805 (2004).

[38] M. Strange, I. S. Kristensen, K. S. Thygesen, and K. W. Jacobsen. *Benchmark density functional theory calculations for nanoscale conductance.* J. Chem. Phys. **128**, 114714 (2008).

[39] M. S. Green. *Markoff Random Processes and the Statistical Mechanics of Time Dependent Phenomena. II. Irreversible Processes in Fluids.* The Journal of Chemical Physics **22** (3), 398–413 (1954).

[40] R. Kubo. *Statistical-Mechanical Theory of Irreversible Processes. I. General Theory and Simple Applications to Magnetic and Conduction Problems.* Journal of the Physical Society of Japan **12** (6), 570–586 (1957).

[41] M. Nuss and M. Aichhorn. *Effective model for the electronic properties of quasi-one-dimensional purple bronze $Li_{0.9}Mo_6O_{17}$ based on ab initio calculations.* Phys. Rev. B **89**, 045125 (2014).

[42] A. Georges, G. Kotliar, W. Krauth, and M. J. Rozenberg. *Dynamical mean-field theory of strongly correlated fermion systems and the limit of infinite dimensions.* Rev. Mod. Phys. **68**, 13–125 (1996).

[43] C. Gros and R. Valenti. *Cluster expansion for the self-energy: A simple many-body method for interpreting the photoemission spectra of correlated Fermi systems.* Phys. Rev. B **48** (1), 418 (1993).

[44] Sénéchal, D. Perez, and M. Pioro-Ladriére. *Spectral Weight of the Hubbard Model through Cluster Perturbation Theory.* Phys. Rev. Lett. **84** (3), 522 (2000).

[45] M. Potthoff, M. Aichhorn, and C. Dahnken. *Variational Cluster Approach to Correlated Electron Systems in Low Dimensions.* Phys. Rev. Lett. **91** (20), 206402 (2003).

[46] M. Aichhorn, H. G. Evertz, W. von der Linden, and M. Potthoff. *Charge ordering in extended Hubbard models: Variational cluster approach.* Phys. Rev. B **70**, 235107 (2004).

[47] F. Wang, J. V. Alvarez, J. W. Allen, S.-K. Mo, J. He, R. Jin, D. Mandrus, and H. Hochst. *Quantum Critical Scaling in the Single-Particle Spectrum of a Novel Anisotropic Metal.* Phys. Rev. Lett. **103**, 136401 (2009).

[48] M. Greenblatt, W. McCarroll, R. Neifeld, M. Croft, and J. Waszczak. *Quasi two-dimensional electronic properties of the lithium molybdenum bronze, Li0.9Mo6O17.* Solid State Communications **51** (9), 671 – 674 (1984).

[49] U. Schollwöck. *The density-matrix renormalization group in the age of matrix product states.* Annals of Physics **326** (1), 96 – 192 (2011). January 2011 Special Issue.

[50] S. R. White. *Density-matrix algorithms for quantum renormalization groups.* Phys. Rev. B **48**, 10345–10356 (1993).

[51] G. Vidal. *Efficient Simulation of One-Dimensional Quantum Many-Body Systems.* Phys. Rev. Lett. **93**, 040502 (2004).

[52] M. Nuss, M. Ganahl, H. G. Evertz, E. Arrigoni, and W. von der Linden. *Steady-state and quench-dependent relaxation of a quantum dot coupled to one-dimensional leads.* Phys. Rev. B **88**, 045132 (2013).

[53] A. C. Hewson. *The Kondo Problem to Heavy Fermions.* Cambridge University Press (1997). ISBN 0521599474.

[54] M. Nuss, M. Ganahl, E. Arrigoni, W. von der Linden, and H. G. Evertz. *Nonequilibrium spatiotemporal formation of the Kondo screening cloud on a lattice.* Phys. Rev. B **91**, 085127 (2015).

[55] P. W. Anderson. *Localized Magnetic States in Metals.* Phys. Rev. **124**, 41–53 (1961).

[56] P. B. Wiegmann and A. M. Tsvelick. *Exact solution of the Anderson model: I.* Journal of Physics C: Solid State Physics **16** (12), 2281 (1983).

[57] A. M. Tsvelick and P. B. Wiegmann. *Exact solution of the Anderson model. II. Thermodynamic properties at finite temperatures.* Journal of Physics C: Solid State Physics **16** (12), 2321 (1983).

[58] K. G. Wilson. *The renormalization group: Critical phenomena and the Kondo problem.* Rev. Mod. Phys. **47** (4), 773–840 (1975).

[59] H. R. Krishna-murthy, J. W. Wilkins, and K. G. Wilson. *Renormalization-group approach to the Anderson model of dilute magnetic alloys. I. Static properties for the symmetric case.* Phys. Rev. B **21**, 1003–1043 (1980).

[60] E. H. Lieb and D. W. Robinson. *The finite group velocity of quantum spin systems.* Communications in Mathematical Physics **28**, 251–257 (1972).

[61] G. Schaller. *Non-Equilibrium Master Equations.* TU Berlin (2014).

[62] M. Nuss, C. Heil, M. Ganahl, M. Knap, H. G. Evertz, E. Arrigoni, and W. von der Linden. *Steady-state spectra, current, and stability diagram of a quantum dot: A nonequilibrium variational cluster approach.* Phys. Rev. B **86**, 245119 (2012).

[63] M. Nuss, E. Arrigoni, and W. von der Linden. *Non-linear transport through a strongly correlated quantum dot.* AIP Conference Proceedings **1485** (1), 302–306 (2012).

[64] A. V. Kretinin, H. Shtrikman, D. Goldhaber-Gordon, M. Hanl, A. Weichselbaum, J. von Delft, T. Costi, and D. Mahalu. *Spin-$\frac{1}{2}$ Kondo effect in an InAs nanowire quantum dot: Unitary limit, conductance scaling, and Zeeman splitting.* Phys. Rev. B **84**, 245316 (2011).

[65] M. Nuss, W. von der Linden, and E. Arrigoni. *Effects of electronic correlations and magnetic field on a molecular ring out of equilibrium.* Phys. Rev. B **89**, 155139 (2014).

[66] M. Nuss, G. Dorn, A. Dorda, W. von der Linden, and E. Arrigoni. *Master equation enhanced steady-state cluster perturbation theory: interaction induced quantum blocking* (2015). ArXiv:1505.01683.

[67] G. Begemann, D. Darau, A. Donarini, and M. Grifoni. *Symmetry fingerprints of a benzene single-electron transistor: Interplay between Coulomb interaction and orbital symmetry.* Phys. Rev. B **77**, 201406 (2008).

[68] E. Arrigoni, M. Knap, and W. von der Linden. *Nonequilibrium Dynamical Mean-Field Theory: An Auxiliary Quantum Master Equation Approach.* Phys. Rev. Lett. **110**, 086403 (2013).

[69] A. Dorda, M. Nuss, W. von der Linden, and E. Arrigoni. *Auxiliary master equation approach to nonequilibrium correlated impurities.* Phys. Rev. B **89**, 165105 (2014).

[70] M. Nuss, A. G. Dorda, M. Ganahl, H. G. Evertz, E. Arrigoni, and W. von der Linden. *Strong electronic correlations at high bias voltage and structured electronic leads* (2015). Unpublished.

[71] L. Mühlbacher, D. F. Urban, and A. Komnik. *Anderson impurity model in nonequilibrium: Analytical results versus quantum Monte Carlo data.* Phys. Rev. B **83**, 075107 (2011).

[72] M. Pletyukhov and H. Schoeller. *Nonequilibrium Kondo model: Crossover from weak to strong coupling.* Phys. Rev. Lett. **108**, 260601 (2012).

[73] A. V. Kretinin, H. Shtrikman, and D. Mahalu. *Universal line shape of the Kondo zero-bias anomaly in a quantum dot.* Phys. Rev. B **85**, 201301 (2012).

[74] C. L. Smallwood, C. Jozwiak, W. Zhang, and A. Lanzara. *An ultrafast angle-resolved photoemission apparatus for measuring complex materials.* Review of Scientific Instruments **83** (12), 123904 (2012).

[75] F. Schmitt, P. S. Kirchmann, U. Bovensiepen, R. G. Moore, L. Rettig, M. Krenz, J.-H. Chu, N. Ru, L. Perfetti, D. H. Lu, M. Wolf, I. R. Fisher, and Z.-X. Shen. *Transient Electronic Structure and Melting of a Charge Density Wave in TbTe3.* Science **321** (5896), 1649–1652 (2008).

[76] F. Schmitt, P. S. Kirchmann, U. Bovensiepen, R. G. Moore, J.-H. Chu, D. H. Lu, L. Rettig, M. Wolf, I. R. Fisher, and Z.-X. Shen. *Ultrafast electron dynamics in the charge density wave material TbTe 3.* New Journal of Physics **13** (6), 063022 (2011).

[77] M. Först, A. Frano, S. Kaiser, R. Mankowsky, C. R. Hunt, J. J. Turner, G. L. Dakovski, M. P. Minitti, J. Robinson, T. Loew, M. Le Tacon, B. Keimer, J. P. Hill, A. Cavalleri, and S. S. Dhesi. *Femtosecond x rays link melting of charge-density wave correlations and light-enhanced coherent transport in* $YBa_2Cu_3O_{6.6}$. Phys. Rev. B **90**, 184514 (2014).

[78] J. A. Sobota, S. Yang, J. G. Analytis, Y. L. Chen, I. R. Fisher, P. S. Kirchmann, and Z.-X. Shen. *Ultrafast Optical Excitation of a Persistent Surface-State Population in the Topological Insulator* Bi_2Se_3. Phys. Rev. Lett. **108**, 117403 (2012).

[79] J. A. Sobota, S.-L. Yang, A. F. Kemper, J. J. Lee, F. T. Schmitt, W. Li, R. G. Moore, J. G. Analytis, I. R. Fisher, P. S. Kirchmann, T. P. Devereaux, and Z.-X. Shen. *Direct Optical Coupling to an Unoccupied Dirac Surface State in the Topological Insulator* Bi_2Se_3. Phys. Rev. Lett. **111**, 136802 (2013).

[80] J. Graf, C. Jozwiak, C. L. Smallwood, H. Eisaki, R. A. Kaindl, D.-H. Lee, and A. Lanzara. *Nodal quasiparticle meltdown in ultrahigh-resolution pump-probe angle-resolved photoemission.* Nat Phys **7** (10), 805–809 (2011).

[81] C. L. Smallwood, J. P. Hinton, C. Jozwiak, W. Zhang, J. D. Koralek, H. Eisaki, D.-H. Lee, J. Orenstein, and A. Lanzara. *Tracking Cooper Pairs in a Cuprate Superconductor by Ultrafast Angle-Resolved Photoemission.* Science **336** (6085), 1137–1139 (2012).

[82] U. Bovensiepen and P. Kirchmann. *Elementary relaxation processes investigated by femtosecond photoelectron spectroscopy of two-dimensional materials.* Laser & Photonics Reviews **6** (5), 589–606 (2012).

[83] D. Fausti, R. I. Tobey, N. Dean, S. Kaiser, A. Dienst, M. C. Hoffmann, S. Pyon, T. Takayama, H. Takagi, and A. Cavalleri. *Light-Induced Superconductivity in a Stripe-Ordered Cuprate.* Science **331** (6014), 189–191 (2011).

[84] Z. Lenarčič and P. Prelovšek. *Ultrafast Charge Recombination in a Photoexcited Mott-Hubbard Insulator.* Phys. Rev. Lett. **111**, 016401 (2013).

[85] Z. Lenarčič and P. Prelovšek. *Charge recombination in undoped cuprates.* Phys. Rev. B **90**, 235136 (2014).

[86] H. Ehrke, R. I. Tobey, S. Wall, S. A. Cavill, M. Först, V. Khanna, T. Garl, N. Stojanovic, D. Prabhakaran, A. T. Boothroyd, M. Gensch, A. Mirone, P. Reutler, A. Revcolevschi, S. S. Dhesi, and A. Cavalleri. *Photoinduced Melting of Antiferromagnetic Order in* $La_{0.5}Sr_{1.5}MnO_4$ *Measured Using Ultrafast Resonant Soft X-Ray Diffraction.* Phys. Rev. Lett. **106**, 217401 (2011).

[87] E. J. Monkman, C. Adamo, J. A. Mundy, D. E. Shai, J. W. Harter, D. Shen, B. Burganov, D. A. Muller, D. G. Schlom, and K. M. Shen. *Quantum many-body interactions in digital oxide superlattices.* Nat Mater **11** (10), 855–859 (2012).

[88] M. Greiner, O. Mandel, T. Esslinger, T. W. Hänsch, and I. Bloch. *Quantum phase transition from a superfluid to a Mott insulator in a gas of ultracold atoms.* Nature **415** (6867), 39–44 (2002).

[89] R. Jordens, N. Strohmaier, K. Gunter, H. Moritz, and T. Esslinger. *A Mott insulator of fermionic atoms in an optical lattice.* Nature **455** (7210), 204–207 (2008).

[90] M. Cheneau, P. Barmettler, D. Poletti, M. Endres, P. Schausz, T. Fukuhara, C. Gross, I. Bloch, C. Kollath, and S. Kuhr. *Light-cone-like spreading of correlations in a quantum many-body system.* Nature **481** (7382), 484–487 (2012).

[91] K. E. Drexler. *Engines of Creation: The Coming Era of Nanotechnology.* Doubleday (1986). ISBN 0-385-19973-2.

[92] K. E. Drexler. *Nanosystems: Molecular Machinery, Manufacturing, and Computation.* New York: John Wiley and Sons (1992). ISBN 0-471-57547-X.

[93] R. P. Feynman. *Plenty of Room at the Bottom* (1959). Talk.

[94] H. W. Kroto, J. R. Heath, S. C. O'Brien, R. F. Curl, and R. E. Smalley. *C60: Buckminsterfullerene*. Nature **318** (6042), 162–163 (1985).

[95] S. L. di Vittorio, M. S. Dresselhaus, M. Endo, J.-P. Issi, and L. Piraux. *The Transport Properties of Activated Carbon Fibers*. Journal of Materials Research **6** (4) (1990).

[96] M. H. Grabert, Hermann amd Devoret. *Single Charge Tunneling: Coulomb Blockade Phenomena in Nanostructures*. Kluwer Academic/Plenum (1992). ISBN 0306442299.

[97] L. Kouwenhoven, C. Marcus, P. McEuen, S. Tarucha, R. Westervelt, and N. Wingreen. *Electron transport in quantum dots*. Kluwer Series, Proceedings of the NATO Advanced Study Institute on Mesoscopic Electron Transport **E345**, 105–214 (1997).

[98] M. Kastner. *The single electron transistor and artificial atoms*. Annalen der Physik **9** (11-12), 885–894 (2000).

[99] D. Kouwenhoven, L.P. amd Austing and S. Tarucha. *Few-electron Quantum Dots*. Reports on Progress in Physics **64** (6), 701–736 (2001).

[100] W. G. van der Wiel, S. De Franceschi, J. M. Elzerman, T. Fujisawa, S. Tarucha, and L. P. Kouwenhoven. *Electron transport through double quantum dots*. Rev. Mod. Phys. **75**, 1–22 (2002).

[101] L. Kouwenhoven and C. Marcus. *Quantum Dots*. Physics World **11** (6), 35–39 (1998).

[102] L. Gaudreau, A. Kam, G. Granger, S. A. Studenikin, P. Zawadzki, and A. S. Sachrajda. *A tunable few electron triple quantum dot*. Applied Physics Letters **95** (19), 193101 (2009).

[103] F. Molitor, S. Dröscher, J. Güttinger, A. Jacobsen, C. Stampfer, T. Ihn, and K. Ensslin. *Transport through graphene double dots*. Applied Physics Letters **94** (22), 222107 (2009).

[104] J. Eroms and D. Weiss. *Weak localization and transport gap in graphene antidot lattices*. New Journal of Physics **11** (9), 095021 (2009).

[105] J. R. Williams, A. J. Bestwick, P. Gallagher, S. S. Hong, Y. Cui, A. S. Bleich, J. G. Analytis, I. R. Fisher, and D. Goldhaber-Gordon. *Unconventional Josephson Effect in Hybrid Superconductor-Topological Insulator Devices*. Phys. Rev. Lett. **109**, 056803 (2012).

[106] H. Bruus and K. Flensberg. *Many-Body Quantum Theory in Condensed Matter Physics: An Introduction*. Oxford Univ Press (2004). ISBN 0198566336.

[107] W. Nolting. *Grundkurs Theoretische Physik 5/2: Quantenmechanik - Methoden und Anwendungen*. Springer Spektrum, 8. aufl. edition (2015). ISBN 3662442299.

[108] L. Gaudreau, S. A. Studenikin, A. S. Sachrajda, P. Zawadzki, A. Kam, J. Lapointe, M. Korkusinski, and P. Hawrylak. *Stability Diagram of a Few-Electron Triple Dot*. Phys. Rev. Lett. **97**, 036807 (2006).

[109] L. Gaudreau, A. S. Sachrajda, S. Studenikin, A. Kam, F. Delgado, Y. P. Shim, M. Korkusinski, and P. Hawrylak. *Coherent transport through a ring of three quantum dots*. Phys. Rev. B **80**, 075415 (2009).

[110] G. Austing, C. Payette, G. Yu, J. Gupta, G. Aers, S. Nair, S. Amaha, and S. Tarucha. *Slow and Fast Electron Channels in a Coherent Quantum Dot Mixer.* Japanese Journal of Applied Physics **49** (4S), 04DJ03 (2010).

[111] D. Goldhaber-Gordon, H. Shtrikman, D. Mahalu, D. Abusch-Magder, U. Meirav, and M. A. Kastner. *Kondo effect in a single-electron transistor.* Nature **391** (6663), 156–159 (1998).

[112] D. Goldhaber-Gordon, J. Göres, M. A. Kastner, H. Shtrikman, D. Mahalu, and U. Meirav. *From the Kondo Regime to the Mixed-Valence Regime in a Single-Electron Transistor.* Phys. Rev. Lett. **81**, 5225–5228 (1998).

[113] N. Agrait, A. L. Yeyati, and J. M. van Ruitenbeek. *Quantum properties of atomic-sized conductors.* Physics Reports **377** (2-3), 81 – 279 (2003).

[114] M. C. Petty. *Molecular Electronics: From Principles to Practice.* Wiley-Interscience; 1 edition (2008). ISBN 0470013087.

[115] A. Aviram and M. A. Ratner. *Molecular rectifiers.* Chemical Physics Letters **29** (2), 277 – 283 (1974).

[116] E. E. Polymeropoulos and J. Sagiv. *Electrical conduction through adsorbed monolayers.* The Journal of Chemical Physics **69** (5), 1836–1847 (1978).

[117] G. E. Moore. *Cramming more components onto integrated circuits.* Electronics **38** (8), 114–117 (1965).

[118] T. T. Heikkilan. *The Physics of Nanoelectronics: Transport and Fluctuation Phenomena at Low Temperatures.* Oxford Univ Press (2013). ISBN 0199592446.

[119] J. R. Heath. *Molecular Electronics.* Annual Review of Materials Research **39** (5624), 1–23 (2009).

[120] W. Liang, M. P. Shores, M. Bockrath, J. R. Long, and H. Park. *Kondo resonance in a single-molecule transistor.* Nature **417** (6890), 725–729 (2002).

[121] M. A. Reed, C. Zhou, C. J. Muller, T. P. Burgin, and J. M. Tour. *Conductance of a Molecular Junction.* Science **278** (5336), 252–254 (1997).

[122] E. Lörtscher, H. B. Weber, and H. Riel. *Statistical Approach to Investigating Transport through Single Molecules.* Phys. Rev. Lett. **98**, 176807 (2007).

[123] M. Kiguchi, O. Tal, S. Wohlthat, F. Pauly, M. Krieger, D. Djukic, J. C. Cuevas, and J. M. van Ruitenbeek. *Highly Conductive Molecular Junctions Based on Direct Binding of Benzene to Platinum Electrodes.* Phys. Rev. Lett. **101**, 046801 (2008).

[124] E. Lörtscher, H. B. Weber, and H. Riel. *Statistical Approach to Investigating Transport through Single Molecules.* Phys. Rev. Lett. **98**, 176807 (2007).

[125] L. Grill, M. Dyer, L. Lafferentz, M. Persson, M. V. Peters, and S. Hecht. *Nano-architectures by covalent assembly of molecular building blocks.* Nat Nano **2** (11), 687–691 (2007).

[126] W. Liang, M. P. Shores, M. Bockrath, J. R. Long, and H. Park. *Kondo resonance in a single-molecule transistor.* Nature **417** (6890), 725–729 (2002).

[127] S. Kubatkin, A. Danilov, M. Hjort, J. Cornil, J.-L. Bredas, N. Stuhr-Hansen, P. Hedegard, and T. Bjornholm. *Single-electron transistor of a single organic molecule with access to several redox states.* Nature **425** (6959), 698–701 (2003).

[128] L. H. Yu, Z. K. Keane, J. W. Ciszek, L. Cheng, J. M. Tour, T. Baruah, M. R. Pederson, and D. Natelson. *Kondo Resonances and Anomalous Gate Dependence in the Electrical Conductivity of Single-Molecule Transistors.* Phys. Rev. Lett. **95**, 256803 (2005).

[129] D.-H. Chae, J. F. Berry, S. Jung, F. A. Cotton, C. A. Murillo, and Z. Yao. *Vibrational Excitations in Single Trimetal-Molecule Transistors.* Nano Letters **6** (2), 165–168 (2006). PMID: 16464028.

[130] M. Poot, E. Osorio, K. O'Neill, J. M. Thijssen, D. Vanmaekelbergh, C. A. van Walree, L. W. Jenneskens, and H. S. J. van der Zant. *Temperature Dependence of Three-Terminal Molecular Junctions with Sulfur End-Functionalized Tercyclohexylidenes.* Nano Letters **6** (5), 1031–1035 (2006).

[131] H. B. Heersche, Z. de Groot, J. A. Folk, H. S. J. van der Zant, C. Romeike, M. R. Wegewijs, L. Zobbi, D. Barreca, E. Tondello, and A. Cornia. *Electron Transport through Single* Mn_{12} *Molecular Magnets.* Phys. Rev. Lett. **96**, 206801 (2006).

[132] E. A. Osorio, K. O'Neill, N. Stuhr-Hansen, O. F. Nielsen, T. Barnholm, and H. S. J. van der Zant. *Addition Energies and Vibrational Fine Structure Measured in Electromigrated Single-Molecule Junctions Based on an Oligophenylenevinylene Derivative.* Advanced Materials **19** (2), 281–285 (2007).

[133] A. Danilov, S. Kubatkin, S. Kafanov, P. HedegÃ¥rd, N. Stuhr-Hansen, K. Moth-Poulsen, and T. BjÃ¸rnholm. *Electronic Transport in Single Molecule Junctions: Control of the Molecule-Electrode Coupling through Intramolecular Tunneling Barriers.* Nano Letters **8** (1), 1–5 (2008). PMID: 18085806.

[134] L. Venkataraman, J. E. Klare, C. Nuckolls, M. S. Hybertsen, and M. L. Steigerwald. *Dependence of single-molecule junction conductance on molecular conformation.* Nature **442** (7105), 904–907 (2006).

[135] A. R. Champagne, A. N. Pasupathy, and D. C. Ralph. *Mechanically Adjustable and Electrically Gated Single-Molecule Transistors.* Nano Letters **5** (2), 305–308 (2005). PMID: 15794616.

[136] G. Binnig and H. Rohrer. *Scanning tunneling microscopy.* IBM Journal of Research and Development **30**, 4 (1986).

[137] N. Agra¨, J. G. Rodrigo, and S. Vieira. *Conductance steps and quantization in atomic-size contacts.* Phys. Rev. B **47**, 12345–12348 (1993).

[138] B. Xu and N. J. Tao. *Measurement of Single-Molecule Resistance by Repeated Formation of Molecular Junctions.* Science **301** (5637), 1221–1223 (2003).

[139] M. Koch, F. Ample, C. Joachim, and L. Grill. *Voltage-dependent conductance of a single graphene nanoribbon.* Nat Nano **7** (11), 713–717 (2012).

[140] S. Kawai, M. Koch, E. Gnecco, A. Sadeghi, R. Pawlak, T. Glatzel, J. Schwarz, S. Goedecker, S. Hecht, A. Baratoff, L. Grill, and E. Meyer. *Quantifying the atomic-level mechanics of single long physisorbed molecular chains.* Proceedings of the National Academy of Sciences **111** (11), 3968–3972 (2014).

[141] J. Repp, G. Meyer, S. M. Stojković, A. Gourdon, and C. Joachim. *Molecules on Insulating Films: Scanning-Tunneling Microscopy Imaging of Individual Molecular Orbitals.* Phys. Rev. Lett. **94**, 026803 (2005).

[142] B. J. van Wees, H. van Houten, C. W. J. Beenakker, J. G. Williamson, L. P. Kouwenhoven, D. van der Marel, and C. T. Foxon. *Quantized conductance of point contacts in a two-dimensional electron gas.* Phys. Rev. Lett. **60**, 848–850 (1988).

[143] D. A. Wharam, T. J. Thornton, R. Newbury, M. Pepper, H. Ahmed, J. E. F. Frost, D. G. Hasko, D. C. Peacock, D. A. Ritchie, and G. A. C. Jones. *One-dimensional transport and the quantisation of the ballistic resistance.* Journal of Physics C: Solid State Physics **21** (8), L209 (1988).

[144] N. D. Lang. *Resistance of atomic wires.* Phys. Rev. B **52**, 5335–5342 (1995).

[145] K. Hirose and M. Tsukada. *First-principles calculation of the electronic structure for a bielectrode junction system under strong field and current.* Phys. Rev. B **51**, 5278–5290 (1995).

[146] V. Mujica, A. E. Roitberg, and M. Ratner. *Molecular wire conductance: Electrostatic potential spatial profile.* The Journal of Chemical Physics **112** (15), 6834–6839 (2000).

[147] P. S. Damle, A. W. Ghosh, and S. Datta. *Unified description of molecular conduction: From molecules to metallic wires.* Phys. Rev. B **64**, 201403 (2001).

[148] M. Brandbyge, J.-L. Mozos, P. Ordejón, J. Taylor, and K. Stokbro. *Density-functional method for nonequilibrium electron transport.* Phys. Rev. B **65**, 165401 (2002).

[149] S.-H. Ke, H. U. Baranger, and W. Yang. *Electron transport through molecules: Self-consistent and non-self-consistent approaches.* Phys. Rev. B **70**, 085410 (2004).

[150] C. Zhang, X.-G. Zhang, P. S. Krstić, H.-p. Cheng, W. H. Butler, and J. M. MacLaren. *Electronic structure and spin-dependent tunneling conductance under a finite bias.* Phys. Rev. B **69**, 134406 (2004).

[151] J. Neaton, K. Khoo, C. Spataru, and S. G. Louie. *Electron transport and optical properties of carbon nanostructures from first principles.* Computer Physics Communications **169** (1â3), 1 – 8 (2005). Proceedings of the Europhysics Conference on Computational Physics 2004 {CCP} 2004 Europhysics Conference on Computational Physics 2004.

[152] A. R. Rocha, V. M. García-Suárez, S. Bailey, C. Lambert, J. Ferrer, and S. Sanvito. *Spin and molecular electronics in atomically generated orbital landscapes.* Phys. Rev. B **73**, 085414 (2006).

[153] K. Stokbro. *First-principles modeling of electron transport.* Journal of Physics: Condensed Matter **20** (6), 064216 (2008).

[154] T. Fließbach. *Statistische Physik: Lehrbuch zur Theoretischen Physik IV.* Spektrum Akademischer Verlag, 5 edition (2010). ISBN 3827425271.

[155] R. P. Feynman, R. B. Leighton, and M. Sands. *The Feynman Lectures on Physics including Feynman's Tips on Physics: The Definitive and Extended Edition.* Addison Wesley, 2 edition (2005). ISBN 0805390456.

[156] R. Shankar. *Principles of Quantum Mechanics.* Plenum Press, 2nd edition edition (2011). ISBN 0306447908.

[157] D. J. Griffiths. *Introduction to Quantum Mechanics.* Pearson Prentice Hall, 2nd edition edition (2004). ISBN 0131118927.

[158] W. Nolting. *Grundkurs Theoretische Physik 5/1: Quantenmechanik - Grundlagen.* Springer Spektrum, 8. aufl. edition (2013). ISBN 3642254020.

[159] E. Schrödinger. *An Undulatory Theory of the Mechanics of Atoms and Molecules.* Phys. Rev. **28**, 1049–1070 (1926).

[160] W. Heisenberg. *Über quantentheoretische Umdeutung kinematischer und mechanischer Beziehungen.* Zeitschrift für Physik **33** (1), 879–893 (1925).

[161] A. L. Fetter and J. D. Walecka. *Quantum Theory of Many-Particle Systems.* Dover Publications (2003). ISBN 0486428273.

[162] M. Born and R. Oppenheimer. *Zur Quantentheorie der Molekeln.* Annalen der Physik **389** (20), 457–484 (1927).

[163] P. Hohenberg and W. Kohn. *Inhomogeneous Electron Gas.* Phys. Rev. **136**, B864–B871 (1964).

[164] W. Kohn and L. J. Sham. *Self-Consistent Equations Including Exchange and Correlation Effects.* Phys. Rev. **140**, A1133–A1138 (1965).

[165] D. M. Ceperley and B. J. Alder. *Ground State of the Electron Gas by a Stochastic Method.* Phys. Rev. Lett. **45**, 566–569 (1980).

[166] J. Hubbard. *Electron Correlations in Narrow Energy Bands.* Proceedings of the Royal Society of London. Series A. **276** (1365), 238 –257 (1963).

[167] G. D. Mahan. *Many-Particle Physics.* Springer, 3 edition (2000). ISBN 0306463385.

[168] J. Friedel. *On some electrical and magnetic properties of metallic solid solutions.* Can. J. Phys. **34** (12A), 1190–1211 (1956).

[169] W. D. Haas and G. V. D. Berg. *The electrical resistance of gold and silver at low temperatures.* Physica **3** (6), 440 – 449 (1936).

[170] A. M. Clogston, B. T. Matthias, M. Peter, H. J. Williams, E. Corenzwit, and R. C. Sherwood. *Local Magnetic Moment Associated with an Iron Atom Dissolved in Various Transition Metal Alloys.* Phys. Rev. **125**, 541–552 (1962).

[171] J. Kondo. *Resistance Minimum in Dilute Magnetic Alloys.* Progress of Theoretical Physics **32** (1), 37–49 (1964).

[172] P. W. Anderson. *A poor man's derivation of scaling laws for the Kondo problem.* Journal of Physics C: Solid State Physics **3** (12), 2436 (1970).

[173] J. R. Schrieffer and P. A. Wolff. *Relation between the Anderson and Kondo Hamiltonians.* Phys. Rev. **149**, 491–492 (1966).

[174] S. Bravyi, D. P. DiVincenzo, and D. Loss. *Schrieffer-Wolff transformation for quantum many-body systems.* Annals of Physics **326** (10), 2793 – 2826 (2011).

[175] H. Bethe. *Zur Theorie der Metalle.* Zeitschrift für Physik **71** (3-4), 205–226 (1931).

[176] N. Andrei. *Diagonalization of the Kondo Hamiltonian.* Phys. Rev. Lett. **45**, 379–382 (1980).

[177] R. Bulla, T. A. Costi, and T. Pruschke. *Numerical renormalization group method for quantum impurity systems.* Rev. Mod. Phys. **80** (2), 395–450 (2008).

[178] K. Yosida and K. Yamada. *Perturbation Expansion for the Anderson Hamiltonian.* Progress of Theoretical Physics Supplement **46**, 244–255 (1970).

[179] K. Yamada. *Perturbation Expansion for the Anderson Hamiltonian. II.* Progress of Theoretical Physics **53** (4), 970–986 (1975).

[180] K. Yosida and K. Yamada. *Perturbation Expansion for the Anderson Hamiltonian. III.* Progress of Theoretical Physics **53** (5), 1286–1301 (1975).

[181] K. Yamada. *Perturbation Expansion for the Anderson Hamiltonian. IV.* Progress of Theoretical Physics **54** (2), 316–324 (1975).

[182] R. Hedden, V. Meden, T. Pruschke, and K. Schönhammer. *A functional renormalization group approach to zero-dimensional interacting systems.* Journal of Physics: Condensed Matter **16** (29), 5279 (2004).

[183] C. Karrasch, R. Hedden, R. Peters, T. Pruschke, K. Schönhammer, and V. Meden. *A finite-frequency functional renormalization group approach to the single impurity Anderson model.* Journal of Physics: Condensed Matter **20** (34), 345205 (2008).

[184] A. Isidori, D. Roosen, L. Bartosch, W. Hofstetter, and P. Kopietz. *Spectral function of the Anderson impurity model at finite temperatures.* Phys. Rev. B **81** (23), 235120 (2010).

[185] S. Nishimoto and E. Jeckelmann. *Density-matrix renormalization group approach to quantum impurity problems.* J. Phys.: Condens. Matter **16** (4), 613–625 (2004).

[186] S. Nishimoto, F. Gebhard, and E. Jeckelmann. *Dynamical mean-field theory calculation with the dynamical density-matrix renormalization group.* Physica B: Condensed Matter **378-380**, 283–285 (2006).

[187] R. Peters. *Spectral functions for single- and multi-Impurity models using DMRG.* Phys. Rev. B **84** (7), 075139 (2011).

[188] S. Florens and A. Georges. *Slave-rotor mean-field theories of strongly correlated systems and the Mott transitionin finite dimensions.* Phys. Rev. B **70** (3), 035114 (2004).

[189] P. Coleman. *New approach to the mixed-valence problem.* Phys. Rev. B **29** (6), 3035 (1984).

[190] T. Lobo, M. S. Figueira, and M. E. Foglio. *The atomic approach to the Anderson model for the finite U case: application to a quantum dot.* Nanotechnology **21** (27), 274007 (2010).

[191] R. Brako and D. M. Newns. *Slowly varying time-dependent local perturbations in metals: a new approach.* J. Phys. C **14** (21), 3065–3078 (1981).

[192] D. C. Langreth and P. Nordlander. *Derivation of a master equation for charge-transfer processes in atom-surface collisions.* Phys. Rev. B **43** (4), 2541 (1991).

[193] A. F. Otte, M. Ternes, K. von Bergmann, S. Loth, H. Brune, C. P. Lutz, C. F. Hirjibehedin, and A. J. Heinrich. *The role of magnetic anisotropy in the Kondo effect.* Nat Phys **4** (11), 847–850 (2008).

[194] I. Affleck. *Quantum Impurity Problems in Condensed Matter Physics* (2008). ArXiv:0809.3474.

[195] F. Steglich, J. Aarts, C. D. Bredl, W. Lieke, D. Meschede, W. Franz, and H. Schäfer. *Superconductivity in the Presence of Strong Pauli Paramagnetism: CeCu2Si2.* Phys. Rev. Lett. **43** (25), 1892 (1979).

[196] P. Coleman. *Heavy Fermions: electrons at the edge of magnetism.* arXiv:0612006 (2006).

[197] W. Metzner and D. Vollhardt. *Correlated Lattice Fermions in $d = \infty$ Dimensions.* Phys. Rev. Lett. **62**, 324–327 (1989).

[198] U. Brandt and C. Mielsch. *Thermodynamics and correlation functions of the Falicov-Kimball model in large dimensions.* Zeitschrift für Physik B Condensed Matter **75** (3), 365–370 (1989).

[199] E. Müller-Hartmann. *Correlated fermions on a lattice in high dimensions.* Zeitschrift für Physik B Condensed Matter **74** (4), 507–512 (1989).

[200] V. Janis. *A new construction of thermodynamic mean-field theories of itinerant fermions: application to the Falicov-Kimball model.* Zeitschrift für Physik B Condensed Matter **83** (2), 227–235 (1991).

[201] A. Georges and G. Kotliar. *Hubbard model in infinite dimensions.* Phys. Rev. B **45**, 6479–6483 (1992).

[202] M. Jarrell. *Hubbard model in infinite dimensions: A quantum Monte Carlo study.* Phys. Rev. Lett. **69**, 168–171 (1992).

[203] J. E. Hirsch and R. M. Fye. *Monte Carlo Method for Magnetic Impurities in Metals.* Phys. Rev. Lett. **56**, 2521–2524 (1986).

[204] J. E. Gubernatis, J. E. Hirsch, and D. J. Scalapino. *Spin and charge correlations around an Anderson magnetic impurity.* Phys. Rev. B **35**, 8478–8485 (1987).

[205] M. Feldbacher, K. Held, and F. F. Assaad. *Projective Quantum Monte Carlo Method for the Anderson Impurity Model and its Application to Dynamical Mean Field Theory.* Phys. Rev. Lett. **93**, 136405 (2004).

[206] E. Gull, A. J. Millis, A. I. Lichtenstein, A. N. Rubtsov, M. Troyer, and P. Werner. *Continuous – time Monte Carlo methods for quantum impurity models.* Rev. Mod. Phys. **83**, 349–404 (2011).

[207] S. Gull and G. Daniell. *Image reconstruction from incomplete and noisy data.* Nature **272** (5655), 686–690 (1978).

[208] J. Skilling. *Classic Maximum Entropy.* Kluwer Academic Publishers, Dordtrecht, 45–52 (1989).

[209] M. Caffarel and W. Krauth. *Exact diagonalization approach to correlated fermions in infinite dimensions: Mott transition and superconductivity.* Phys. Rev. Lett. **72** (10), 1545 (1994).

[210] R. Bulla, A. C. Hewson, and T. Pruschke. *Numerical renormalization group calculations for the self-energy of the impurity Anderson model.* Journal of Physics: Condensed Matter **10** (37), 8365 (1998).

[211] T. Pruschke, D. L. Cox, and M. Jarrell. *Transport Properties of the Infinite-Dimensional Hubbard Model.* EPL (Europhysics Letters) **21** (5), 593 (1993).

[212] T. Maier, M. Jarrell, T. Pruschke, and M. H. Hettler. *Quantum cluster theories.* Rev. Mod. Phys. **77**, 1027–1080 (2005).

[213] D. E. Logan and N. L. Dickens. *Magnetic properties of the Anderson model: A local moment approach.* EPL (Europhysics Letters) **54** (2), 227 (2001).

[214] N. Vidhyadhiraja and D. Logan. *Dynamics and scaling in the periodic Anderson model.* The European Physical Journal B - Condensed Matter and Complex Systems **39** (3), 313–334 (2004).

[215] D. J. García, K. Hallberg, and M. J. Rozenberg. *Dynamical Mean Field Theory with the Density Matrix Renormalization Group.* Phys. Rev. Lett. **93**, 246403 (2004).

[216] E. Jeckelmann. *Dynamical density-matrix renormalization-group method.* Phys. Rev. B **66**, 045114 (2002).

[217] S. Nishimoto, F. Gebhard, and E. Jeckelmann. *Dynamical density-matrix renormalization group for the Mott-Hubbard insulator in high dimensions.* Journal of Physics: Condensed Matter **16** (39), 7063 (2004).

[218] P. E. Dargel, A. Wöllert, A. Honecker, I. P. McCulloch, U. Schollwöck, and T. Pruschke. *Lanczos algorithm with matrix product states for dynamical correlation functions.* Phys. Rev. B **85**, 205119 (2012).

[219] M. Ganahl, P. Thunström, F. Verstraete, K. Held, and H. G. Evertz. *Chebyshev expansion for impurity models using matrix product states.* Phys. Rev. B **90**, 045144 (2014).

[220] M. Ganahl, M. Aichhorn, P. Thunström, K. Held, H. G. Evertz, and F. Verstraete. *Efficient DMFT impurity solver using real-time dynamics with Matrix Product States* (2014). ArXiv:1405.6728.

[221] W. G. v. d. Wiel, S. D. Franceschi, T. Fujisawa, J. M. Elzerman, S. Tarucha, and L. P. Kouwenhoven. *The Kondo Effect in the Unitary Limit.* Science **289** (5487), 2105–2108 (2000).

[222] S. Y. Müller, M. Pletyukhov, D. Schuricht, and S. Andergassen. *Magnetic field effects on the finite-frequency noise and ac conductance of a Kondo quantum dot out of equilibrium.* Phys. Rev. B **87**, 245115 (2013).

[223] D. Bohr and P. Schmitteckert. *The dark side of benzene: Interference vs. interaction.* Ann. Phys. **524**, 199204 (2012).

[224] J. Park, A. N. Pasupathy, J. I. Goldsmith, C. Chang, Y. Yaish, J. R. Petta, M. Rinkoski, J. P. Sethna, H. D. Abruna, P. L. McEuen, and D. C. Ralph. *Coulomb blockade and the Kondo effect in single-atom transistors.* Nature **417** (6890), 722–725 (2002).

[225] L. Tosi, P. Roura-Bas, and A. A. Aligia. *Non-equilibrium conductance through a benzene molecule in the Kondo regime.* Journal of Physics: Condensed Matter **24** (36), 365301 (2012).

[226] K. Richter. *Semiclassical Theory of Mesoscopic Quantum Systems.* Springer (1999). ISBN 3540665668.

[227] Y. Meir, N. S. Wingreen, and P. A. Lee. *Transport through a strongly interacting electron system: Theory of periodic conductance oscillations.* Phys. Rev. Lett. **66** (23), 3048–3051 (1991).

[228] Y. Meir and N. S. Wingreen. *Landauer formula for the current through an interacting electron region.* Phys. Rev. Lett. **68**, 2512–2515 (1992).

[229] Y. Meir, N. S. Wingreen, and P. A. Lee. *Low-temperature transport through a quantum dot: The Anderson model out of equilibrium.* Phys. Rev. Lett. **70** (17), 2601–2604 (1993).

[230] A.-P. Jauho, N. S. Wingreen, and Y. Meir. *Time-dependent transport in interacting and noninteracting resonant-tunneling systems.* Phys. Rev. B **50** (8), 5528–5544 (1994).

[231] P. Coleman, C. Hooley, and O. Parcollet. *Is the quantum dot at large bias a weak-coupling problem?* Phy. Rev. Lett. **86** (18), 4088–4091 (2001).

[232] F. Lesage and H. Saleur. *Boundary Interaction Changing Operators and Dynamical Correlations in Quantum Impurity Problems.* Phys. Rev. Lett. **80**, 4370–4373 (1998).

[233] A. Schiller and S. Hershfield. *Out-of-equilibrium Kondo effect: Response to pulsed fields.* Phys. Rev. B **62**, R16271–R16274 (2000).

[234] A. Komnik. *Transient dynamics of the nonequilibrium Majorana resonant level model.* Phys. Rev. B **79**, 245102 (2009).

[235] T. K. Ng and P. A. Lee. *On-Site Coulomb Repulsion and Resonant Tunneling.* Phys. Rev. **61** (15), 1768–1771 (1988).

[236] R. Aguado, G. Platero, C. Tejedor, and R. Lopez. *AC Kondo effect in quantum dots.* Physica B **258**, 256–259 (1998).

[237] A. Kaminski, Y. V. Nazarov, and L. I. Glazman. *Universality of the Kondo Effect in a Quantum Dot out of Equilibrium.* Phys. Rev. B **62** (12), 8154–8170 (2000).

[238] P. Mehta and N. Andrei. *Nonequilibrium Transport in Quantum Impurity Models: The Bethe Ansatz for Open Systems.* Phys. Rev. Lett. **96** (21), 216802 (2006).

[239] F. B. Anders. *Steady-State Currents through Nanodevices: A Scattering-States Numerical Renormalization-Group Approach to Open Quantum Systems.* Phys. Rev. Lett. **101** (6), 066804 (2008).

[240] F. B. Anders and S. Schmitt. *Quantum transport through a quantum dot: Combining the scattering-states numerical renormalization group with nonequilibrium Green functions.* Journal of Physics: Conference Series **220** (1), 012021 (2010).

[241] A. Rosch. *Wilson chains are not thermal reservoirs.* Eur. Phys. J. B **85**, 6 (2012).

[242] N. S. Wingreen and Y. Meir. *Anderson model out of equilibrium: Noncrossing-approximation approach to transport through a quantum dot.* Phys. Rev. B **49**, 11040–11052 (1994).

[243] T. Fujii and K. Ueda. *Perturbative approach to the nonequilibrium Kondo effect in a quantum dot.* Phys. Rev. B **68**, 155310 (2003).

[244] H. Schoeller and G. Schön. *Mesoscopic quantum transport: Resonant tunneling in the presence of a strong Coulomb interaction.* Phys. Rev. B **50** (24), 18436–18452 (1994).

[245] S. Hershfield, J. H. Davies, and J. W. Wilkins. *Probing the Kondo resonance by resonant tunneling through an Anderson impurity.* Phys. Rev. Lett. **67**, 3720–3723 (1991).

[246] H. Schoeller. *A perturbative nonequilibrium renormalization group method for dissipative quantum mechanics.* Eur. Phys. J. Special Topics **168**, 179–266 (2009).

[247] A. Rosch, J. Paaske, J. Kroha, and P. Wölfle. *The Kondo Effect in Non-Equilibrium Quantum Dots: Perturbative Renormalization Group.* J. Phys. Soc. Jpn. **74** (1), 118–126 (2005).

[248] F. B. Anders and A. Schiller. *Spin precession and real-time dynamics in the Kondo model:Time-dependent numerical renormalization-group study.* Phys. Rev. B **74** (24), 245113 (2006).

[249] D. Roosen, M. R. Wegewijs, and W. Hofstetter. *Nonequilibrium Dynamics of Anisotropic Large Spins in the Kondo Regime: Time-Dependent Numerical Renormalization Group Analysis.* Phys. Rev. Lett. **100**, 087201 (2008).

[250] B. Doyon and N. Andrei. *Universal aspects of nonequilibrium currents in a quantum dot.* Phys. Rev. B **73** (24), 245326 (2006).

[251] S. Weiss, J. Eckel, M. Thorwart, and R. Egger. *Iterative real-time path integral approach to nonequilibrium quantum transport.* Phys. Rev. B **77**, 195316 (2008).

[252] F. B. Anders and A. Schiller. *Real-Time Dynamics in Quantum-Impurity Systems: A Time-Dependent Numerical Renormalization-Group Approach.* Phys. Rev. Lett. **95**, 196801 (2005).

[253] M. Moeckel and S. Kehrein. *Interaction Quench in the Hubbard Model.* Phys. Rev. Lett. **100**, 175702 (2008).

[254] S. Kehrein. *Scaling and Decoherence in the Nonequilibrium Kondo Model.* Phys. Rev. Lett. **95** (5), 056602 (2005).

[255] A. J. Daley, C. Kollath, U. Schollwöck, and G. Vidal. *Time-dependent density-matrix renormalization-group using adaptive effective Hilbert spaces.* J. Stat. Mech. **2004** (04), P04005 (2004).

[256] S. R. White and A. E. Feiguin. *Real-Time Evolution Using the Density Matrix Renormalization Group.* Phys. Rev. Lett. **93** (7), 076401 (2004).

[257] P. Schmitteckert. *Nonequilibrium electron transport using the density matrix renormalization group method.* Phys. Rev. B **70**, 121302 (2004).

[258] F. Heidrich-Meisner, A. E. Feiguin, and E. Dagotto. *Real – time simulations of nonequilibrium transport in the single – impurity Anderson model.* Phys. Rev. B **79**, 235336 (2009).

[259] R. Gezzi, T. Pruschke, and V. Meden. *Functional renormalization group for nonequilibrium quantum many-body problems.* Phys. Rev. B **75**, 045324 (2007).

[260] S. G. Jakobs, V. Meden, and H. Schoeller. *Nonequilibrium Functional Renormalization Group for Interacting Quantum Systems.* Phys. Rev. Lett. **99** (15), 150603 (2007).

[261] P. Werner, T. Oka, M. Eckstein, and A. J. Millis. *Weak-coupling quantum Monte Carlo calculations on the Keldysh contour: Theory and application to the current-voltage characteristics of the Anderson model.* Phys. Rev. B **81** (3), 035108 (2010).

[262] G. Cohen, E. Gull, D. R. Reichman, and A. J. Millis. *Green's functions from real – time bold – line Monte Carlo: spectral properties of the nonequilibrium Anderson impurity model* (2013). ArXiv:1310.4151.

[263] J. E. Han. *Quantum simulation of many-body effects in steady-state nonequilibrium: Electron-phonon coupling in quantum dots.* Phys. Rev. B **73**, 125319 (2006).

[264] J. E. Han and R. J. Heary. *Imaginary-Time Formulation of Steady-State Nonequilibrium: Application to Strongly Correlated Transport.* Phys. Rev. Lett. **99**, 236808 (2007).

[265] A. Dirks, P. Werner, M. Jarrell, and T. Pruschke. *Continuous-time quantum Monte Carlo and maximum entropy approach to an imaginary-time formulation of strongly correlated steady-state transport.* Phys. Rev. E **82**, 026701 (2010).

[266] J. E. Han, A. Dirks, and T. Pruschke. *Imaginary-time quantum many-body theory out of equilibrium: Formal equivalence to Keldysh real-time theory and calculation of static properties.* Phys. Rev. B **86**, 155130 (2012).

[267] A. Dirks, J. E. Han, M. Jarrell, and T. Pruschke. *Imaginary-time quantum many-body theory out of equilibrium. II. Analytic continuation of dynamic observables and transport properties.* Phys. Rev. B **87**, 235140 (2013).

[268] M. Knap, W. von der Linden, and E. Arrigoni. *Nonequilibrium steady state for strongly correlated many-body systems: Variational cluster approach.* Phys. Rev. B **84**, 115145 (2011).

[269] F. Hofmann, M. Eckstein, E. Arrigoni, and M. Potthoff. *Nonequilibrium self-energy functional theory.* Phys. Rev. B **88**, 165124 (2013).

[270] P. Dutt, J. Koch, J. Han, and K. Le Hur. *Effective equilibrium theory of nonequilibrium quantum transport.* Annals of Physics **326** (12), 2963–2999 (2011).

[271] E. Muñoz, C. J. Bolech, and S. Kirchner. *Universal Out-of-Equilibrium Transport in Kondo-Correlated Quantum Dots: Renormalized Dual Fermions on the Keldysh Contour.* Phys. Rev. Lett. **110**, 016601 (2013).

[272] C. Jung, A. Lieder, S. Brener, H. Hafermann, B. Baxevanis, A. Chudnovskiy, A. Rubtsov, M. Katsnelson, and A. Lichtenstein. *Dual-fermion approach to non-equilibrium strongly correlated problems.* Ann. Phys. **524** (1), 49–61 (2012).

[273] A. M. Uimonen, E. Khosravi, A. Stan, G. Stefanucci, S. Kurth, R. van Leeuwen, and E. K. U. Gross. *Comparative study of many-body perturbation theory and time-dependent density functional theory in the out-of-equilibrium Anderson model.* Phys. Rev. B **84** (11), 115103 (2011).

[274] H. Schoeller and J. König. *Real-Time Renormalization Group and Charge Fluctuations in Quantum Dots.* Phys. Rev. Lett. **84**, 3686–3689 (2000).

[275] S. Smirnov and M. Grifoni. *Slave-boson Keldysh field theory for the Kondo effect in quantum dots.* Phys. Rev. B **84**, 125303 (2011).

[276] M. Schiro and M. Fabrizio. *Time-Dependent Mean Field Theory for Quench Dynamics in Correlated Electron Systems.* Phys. Rev. Lett. **105**, 076401 (2010).

[277] C. Timm. *Tunneling through molecules and quantum dots: Master-equation approaches.* Phys. Rev. B **77** (19), 195416 (2008).

[278] J. Eckel, F. Heidrich-Meisner, S. G. Jakobs, M. Thorwart, M. Pletyukhov, and R. Egger. *Comparative study of theoretical methods for nonequilibrium quantum transport.* New. J. Phys. **12**, 043042 (2010).

[279] S. Andergassen, V. Meden, H. Schoeller, J. Splettstoesser, and M. R. Wegewijs. *Charge transport through single molecules, quantum dots and quantum wires.* Nanotechnology **21** (27), 272001 (2010).

[280] L. D. Contreras-Pulido, J. Splettstoesser, M. Governale, J. König, and M. Büttiker. *Time scales in the dynamics of an interacting quantum dot.* Phys. Rev. B **85**, 075301 (2012).

[281] P. Schmidt and H. Monien. *Nonequilibrium dynamical mean-field theory of a strongly correlated system* (2002). ArXiv:cond-mat/0202046.

[282] J. K. Freericks, V. M. Turkowski, and V. Zlatić. *Nonequilibrium Dynamical Mean-Field Theory.* Phys. Rev. Lett. **97**, 266408 (2006).

[283] H. Aoki, N. Tsuji, M. Eckstein, M. Kollar, T. Oka, and P. Werner. *Nonequilibrium dynamical mean-field theory and its applications.* Rev. Mod. Phys. **86**, 779–837 (2014).

[284] C. Gramsch, K. Balzer, M. Eckstein, and M. Kollar. *Hamiltonian-based impurity solver for nonequilibrium dynamical mean-field theory.* Phys. Rev. B **88**, 235106 (2013).

[285] W. Nolting. *Grundkurs Theoretische Physik 7: Viel-Teilchen-Theorie.* Springer Spektrum, 8. aufl. edition (2015). ISBN 3642258077.

[286] V. S. Oudovenko, G. Pálsson, K. Haule, G. Kotliar, and S. Y. Savrasov. *Electronic structure calculations of strongly correlated electron systems by the dynamical mean-field method.* Phys. Rev. B **73**, 035120 (2006).

[287] J. M. Tomczak and S. Biermann. *Optical properties of correlated materials: Generalized Peierls approach and its application to VO_2.* Phys. Rev. B **80**, 085117 (2009).

[288] P. T. Jun and J. C. Light. *Emission characteristics of laser-driven dissipative coupled-cavity systems.* J. Chem. Phys. **85**, 5870 (1986).

[289] L. Vidmar, J. Bonča, M. Mierzejewski, P. Prelovšek, and S. A. Trugman. *Nonequilibrium dynamics of the Holstein polaron driven by an external electric field.* Phys. Rev. B **83**, 134301 (2011).

[290] M. Knap, E. Arrigoni, W. von der Linden, and J. H. Cole. *Emission characteristics of laser-driven dissipative coupled-cavity systems.* Phys. Rev. A **83**, 023821 (2011).

[291] A. Tomadin, S. Diehl, and P. Zoller. *Nonequilibrium phase diagram of a driven and dissipative many-body system.* Phys. Rev. A **83**, 013611 (2011).

[292] B. R. Mollow. *Power Spectrum of Light Scattered by Two-Level Systems.* Phys. Rev. **188**, 1969–1975 (1969).

[293] B. R. Mollow. *Pure-state analysis of resonant light scattering: Radiative damping, saturation, and multiphoton effects.* Phys. Rev. A **12**, 1919–1943 (1975).

[294] S. R. White. *Density matrix formulation for quantum renormalization groups.* Phys. Rev. Lett. **69**, 2863–2866 (1992).

[295] U. Schollwöck. *The density-matrix renormalization group.* Rev. Mod. Phys. **77**, 259–315 (2005).

[296] W. H. Press, S. A. Teukolsky, W. T. Vetterling, and B. P. Flannery. *Numerical Recipes 3rd Edition: The Art of Scientific Computing.* Cambridge University Press, 3 edition (2007). ISBN 0521880688.

[297] E. Rabel. *Diploma Thesis: Numerical Time Evolution of 1D Quantum Systems.* Graz University of Technology (2010).

[298] V. Zauner. *Diploma Thesis: Time Evolution of a Comoving Window: Simulation of Local Signals on Infnite One-Dimensional Spin Chains.* Graz University of Technology (2011).

[299] M. Ganahl. *Diploma Thesis: Simulation of Spin Transport in One Dimensional Quantum Heisenberg Spin 1/2 Systems in real time.* Graz University of Technology (2012).

[300] M. Ganahl. *Doctoral Thesis: Dynamics of Strongly Correlated One - Dimensional Quantum Systems using Matrix Product States.* Graz University of Technology (2012).

[301] G. W. Winkler. *Diploma Thesis: Interaction effects on quantum wires with strong spin-orbit coupling.* Graz University of Technology (2014).

[302] D. B. Steffelbauer. *Diploma Thesis: Andreev-Reflection in One-Dimensional Quantum Systems.* Graz University of Technology (2014).

[303] E. N. Economou. *Green's Functions in Quantum Physics.* Springer, 3rd ed. edition (2010). ISBN 3642066917.

[304] S. Sachdev. *Quantum Phase Transitions.* Cambridge University Press, 2 edition (2011). ISBN 0521514681.

[305] W. Brzezicki, J. Dziarmaga, and A. M. Oleś. *Exotic spin orders driven by orbital fluctuations in the Kugel-Khomskii model.* Phys. Rev. B **87**, 064407 (2013).

[306] M. H. Hettler, A. N. Tahvildar-Zadeh, M. Jarrell, T. Pruschke, and H. R. Krishnamurthy. *Nonlocal dynamical correlations of strongly interacting electron systems.* Phys. Rev. B **58**, R7475–R7479 (1998).

[307] M. H. Hettler, M. Mukherjee, M. Jarrell, and H. R. Krishnamurthy. *Dynamical cluster approximation: Nonlocal dynamics of correlated electron systems.* Phys. Rev. B **61**, 12739–12756 (2000).

[308] M. Jarrell, T. Maier, C. Huscroft, and S. Moukouri. *Quantum Monte Carlo algorithm for nonlocal corrections to the dynamical mean-field approximation.* Phys. Rev. B **64**, 195130 (2001).

[309] G. Kotliar, S. Y. Savrasov, G. Pálsson, and G. Biroli. *Cellular Dynamical Mean Field Approach to Strongly Correlated Systems.* Phys. Rev. Lett. **87**, 186401 (2001).

[310] A. N. Rubtsov, M. I. Katsnelson, and A. I. Lichtenstein. *Dual fermion approach to nonlocal correlations in the Hubbard model.* Phys. Rev. B **77**, 033101 (2008).

[311] A. Toschi, A. A. Katanin, and K. Held. *Dynamical vertex approximation: A step beyond dynamical mean-field theory.* Phys. Rev. B **75**, 045118 (2007).

[312] G. Rohringer, A. Toschi, H. Hafermann, K. Held, V. I. Anisimov, and A. A. Katanin. *One-particle irreducible functional approach: A route to diagrammatic extensions of the dynamical mean-field theory.* Phys. Rev. B **88**, 115112 (2013).

[313] C. Taranto, S. Andergassen, J. Bauer, K. Held, A. Katanin, W. Metzner, G. Rohringer, and A. Toschi. *From Infinite to Two Dimensions through the Functional Renormalization Group.* Phys. Rev. Lett. **112**, 196402 (2014).

[314] G. Knizia and G. K.-L. Chan. *Density Matrix Embedding: A Simple Alternative to Dynamical Mean-Field Theory.* Phys. Rev. Lett. **109**, 186404 (2012).

[315] G. Knizia and G. K.-L. Chan. *Density Matrix Embedding: A Strong-Coupling Quantum Embedding Theory.* Journal of Chemical Theory and Computation **9** (3), 1428–1432 (2013).

[316] I. W. Bulik, G. E. Scuseria, and J. Dukelsky. *Density matrix embedding from broken symmetry lattice mean fields.* Phys. Rev. B **89**, 035140 (2014).

[317] B.-X. Zheng and G. K.-L. Chan. *Ground-state phase diagram of the square lattice Hubbard model from density matrix embedding theory* (2015). ArXiv:1504.01784.

[318] B. G. H. and C. G. Kin-Lic. *Ground-state phase diagram of the square lattice Hubbard model from density matrix embedding theor* (2015). ArXiv:1309.2320.

[319] J. Hubbard. Proc. Roy. Soc. (London) A **281**, 401 (1964).

[320] D. Sénéchal, D. Perez, and D. Plouffe. *Cluster perturbation theory for Hubbard models.* Phys. Rev. B **66**, 075129 (2002).

[321] S. Pairault, D. Sénéchal, and A.-M. S. Tremblay. *Strong-Coupling Expansion for the Hubbard Model.* Phys. Rev. Lett. **80**, 5389–5392 (1998).

[322] D. Sénéchal. *An introduction to quantum cluster methods.* arXiv:0806.2690 (2009).

[323] D. Sénéchal. *Cluster Perturbation Theory.* In A. Avella and F. Mancini (eds.), *Strongly Correlated Systems: Theoretical Methods, Springer Series in Solid-State Sciences*, volume 171. Springer-Verlag Berlin Heidelberg, 1 edition (2012). ISBN 978-3-642-21831-6.

[324] W. Gasser, E. Heiner, and K. Elk. *Method Greenschen Funktionen in Der Festkörper Und Vielteilchenphysik.* Not Avail (2001). ISBN 3527402187.

[325] Z. Bai, J. Demmel, J. Dongarra, A. Ruhe, and H. van der Vorst. *Templates for the Solution of Algebraic Eigenvalue Problems: A Practical Guide (Software, Environments and Tools).* Society for Industrial and Applied Mathematics (1987). ISBN 0898714710.

[326] C. Lanczos. *An Iteration Method for the Solution of the Eigenvalue Problem of Linear Differential and Integral Operators.* Journal of research of the National Bureau of Standards **45**, 255–282 (1951).

[327] A. Weiße, G. Wellein, A. Alvermann, and H. Fehske. *The kernel polynomial method.* Rev. Mod. Phys. **78**, 275–306 (2006).

[328] F. Lin, E. Sorensen, C. Kallin, and A. Berlinsky. *Applications of Cluster Perturbation Theory Using Quantum Monte Carlo Data.* In *High-Performance Computing in an Advanced Collaborative Environment, 2006. HPCS 2006. 20th International Symposium on*, 27–27 (2006).

[329] M. Nuss. *Diploma Thesis: A cluster many-body approach to quantum impurity models.* Graz University of Technology (2011).

[330] M. Aichhorn. *Ordering Phenomena in Strongly-Correlated Systems: Cluster Perturbation Theory Approaches.* Ph.D. thesis, TU Graz (2004).

[331] M. Knap. *Masters thesis: Quantum many body properties of strongly correlated lattice bosons and polaritons* (2009). TU Graz.

[332] D. Sénéchal and A.-M. S. Tremblay. *Hot Spots and Pseudogaps for Hole- and Electron-Doped High-Temperature Superconductors.* Phys. Rev. Lett. **92**, 126401 (2004).

[333] F. Pollmann and G. Zwicknagl. *Spectral functions for strongly correlated* $5f$ *electrons.* Phys. Rev. B **73**, 035121 (2006).

[334] M. Kohno. *Mott Transition in the Two-Dimensional Hubbard Model.* Phys. Rev. Lett. **108**, 076401 (2012).

[335] M. Kohno. *Spectral properties near the Mott transition in the two-dimensional Hubbard model with next-nearest-neighbor hopping.* Phys. Rev. B **90**, 035111 (2014).

[336] M. Kohno. *Proceedings of the International Conference on Strongly Correlated Electron Systems: Relationship between Single-Particle Excitation and Spin Excitation at the Mott Transition.* JPS Conf. Proc. 3 **84**, 013020 (2014).

[337] M. Aichhorn and E. Arrigoni. *Weak phase separation and the pseudogap in the electron-doped cuprates.* EPL (Europhysics Letters) **72** (1), 117 (2005).

[338] C. Dahnken, M. Potthoff, E. Arrigoni, and W. Hanke. *Correlated band structure of electron-doped cuprate materials.* Low Temperature Physics **32** (4), 457–461 (2006).

[339] V. Hankevych, B. Kyung, A.-M. Dare, D. Senechal, and A.-M. Tremblay. *Strong- and weak-coupling mechanisms for pseudogap in electron-doped cuprates.* Journal of Physics and Chemistry of Solids **67** (1-3), 189 – 192 (2006). Spectroscopies in Novel Superconductors 2004.

[340] A.-M. S. Tremblay, B. Kyung, and D. Senechal. *Pseudogap and high-temperature superconductivity from weak to strong coupling. Towards a quantitative theory (Review Article).* Low Temperature Physics **32** (4), 424–451 (2006).

[341] M. G. Zacher, R. Eder, E. Arrigoni, and W. Hanke. *Stripes in Doped Antiferromagnets: Single-Particle Spectral Weight.* Phys. Rev. Lett. **85**, 2585–2588 (2000).

[342] W.-H. Leong, S.-L. Yu, T. Xiang, and J.-X. Li. *Localized in-gap state in a single-electron doped Mott insulator.* Phys. Rev. B **90**, 245102 (2014).

[343] M. Aichhorn, E. Y. Sherman, and H. G. Evertz. *Single-particle spectral function of quarter-filled ladder systems.* Phys. Rev. B **72**, 155110 (2005).

[344] M.C.Refolio and J. L. S. J. J. Verges. *The one-particle Green's function of one.dimensional insulating materials* (2004). ArXiv:cond-mat/0412565.

[345] W.-Q. Ning, H. Zhao, C.-Q. Wu, and H.-Q. Lin. *Phonon Effects on Spin-Charge Separation in One Dimension.* Phys. Rev. Lett. **96**, 156402 (2006).

[346] W. Z. Wang. *Model of a gate-controlled spin filter based on a polymer coupled to a quantum wire.* Phys. Rev. B **73**, 235325 (2006).

[347] W. H. C. Dahnken, E. Arrigoni. *Spectral Properties of High-Tc Cuprates via a Cluster-Perturbation Approach.* J. Low Temp. Phys. **126**, 949 (2002).

[348] M. Daghofer and A. Fischer. *Breaking of fourfold lattice symmetry in a model for pnictide superconductors.* Superconductor Science and Technology **25** (8), 084003 (2012).

[349] F. Manghi. *Multi-orbital cluster perturbation theory for transition metal oxides.* Journal of Physics: Condensed Matter **26** (1), 015602 (2014).

[350] F. Lin, E. S. Sørensen, C. Kallin, and A. J. Berlinsky. *Strong correlation effects in the fullerene C_{20} studied using a one-band Hubbard model.* Phys. Rev. B **76**, 033414 (2007).

[351] M. Daghofer, A. Nicholson, and A. Moreo. *Spectral density in a nematic state of iron pnictides.* Phys. Rev. B **85**, 184515 (2012).

[352] M. Hohenadler, M. Aichhorn, and W. von der Linden. *Spectral function of electron-phonon models by cluster perturbation theory.* Phys. Rev. B **68**, 184304 (2003).

[353] M. Hohenadler, M. Aichhorn, and W. von der Linden. *Single-particle spectral function of the Holstein-Hubbard bipolaron.* Phys. Rev. B **71**, 014302 (2005).

[354] J. Loos, M. Hohenadler, A. Alvermann, and H. Fehske. *Phonon spectral function of the Holstein polaron.* Journal of Physics: Condensed Matter **18** (31), 7299 (2006).

[355] M. Hohenadler, G. Wellein, A. Alvermann, and H. Fehske. *Many-polaron problem by cluster perturbation theory.* Physica B: Condensed Matter **378-380** (0), 64 – 65 (2006). Proceedings of the International Conference on Strongly Correlated Electron Systems {SCES} 2005 Proceedings of the International Conference on Strongly Correlated Electron Systems.

[356] H. Fehske and S. A. Trugman. *Polarons in Advanced Materials: Numerical solution of the Holstein polaron problem.* In A. S. Alexandrov (ed.), *Springer Series in Material Sciences*, volume 103, 393–461. Canopus/Springer Publishing, Bristol, Springer Verlag, Dordrecht (2006).

[357] M. Nuss, E. Arrigoni, M. Aichhorn, and W. von der Linden. *Variational cluster approach to the single-impurity Anderson model.* Phys. Rev. B **85**, 235107 (2012).

[358] C. Weber, A. Amaricci, M. Capone, and P. B. Littlewood. *Augmented hybrid exact-diagonalization solver for dynamical mean field theory.* Phys. Rev. B **86**, 115136 (2012).

[359] S. R. Hassan, S. Goyal, R. Shankar, and D. Sénéchal. *Quarter-filled Kitaev-Hubbard model: A quantum Hall state in an optical lattice.* Phys. Rev. B **88**, 045301 (2013).

[360] F. Grandi, F. Manghi, O. Corradini, C. M. Bertoni, and A. Bonini. *Topological invariants in interacting quantum spin Hall: a cluster perturbation theory approach.* New Journal of Physics **17** (2), 023004 (2015).

[361] M. G. Zacher, R. Eder, E. Arrigoni, and W. Hanke. *Stripes in doped antiferromagnets: bond-centered versus site-centered.* International Journal of Modern Physics B **14** (29n31), 3783–3790 (2000).

[362] A. Ovchinnikov, I. Bostrem, and V. Sinitsyn. *Cluster perturbation theory for spin Hamiltonians.* Theoretical and Mathematical Physics **162** (2), 179–187 (2010).

[363] T. Minh-Tien. *Quantum periodic cluster methods for strongly correlated electron systems* (2006). ArXiv:cond-mat/0602615.

[364] M. Potthoff. *Self-energy-functional approach to systems of correlated electrons.* Eur. Phys. J. B **32** (4), 429–436 (2003).

[365] M. Potthoff. *Self-energy-functional approach: Analytical results and the Mott-Hubbard transition.* Eur. Phys. J. B **36** (3), 335–348 (2003).

[366] M. Potthoff. *Self-energy-functional theory.* arXiv:1108.2183 (2011).

[367] M. Potthoff. *Self-Energy-Functional Theory.* In A. Avella and F. Mancini (eds.), *Strongly Correlated Systems: Theoretical Methods, Springer Series in Solid-State Science*, volume 171. Springer-Verlag Berlin Heidelberg, 1 edition (2012). ISBN 978-3-642-21831-6.

[368] E. Robert. *The Variational Cluster Approximation.* In E. Pavarini, E. Koch, and U. Schollwöck (eds.), *Emergent Phenomena in Correlated Matter Modeling and Simulation, Vol. 3.* Verlag des Forschungszentrum Jülich (2013). ISBN ISBN 978-3-89336-884-6.

[369] E. Robert. *Making Use of Self-Energy Functionals: The Variational Cluster Approximation.* In E. Pavarini, E. Koch, D. Vollhardt, and A. Lichtenstein (eds.), *DMFT at 25: Infinite Dimensions Modeling and Simulation, Vol. 4.* Verlag des Forschungszentrum Jülich (2014). ISBN ISBN 978-3-89336-953-9.

[370] J. M. Luttinger and J. C. Ward. *Ground-State Energy of a Many-Fermion System. II.* Phys. Rev. **118** (5), 1417 (1960).

[371] A. H. Nevidomskyy, D. Sénéchal, and A.-M. S. Tremblay. *Convexity of the self-energy functional in the variational cluster approximation.* Phys. Rev. B **77**, 075105 (2008).

[372] M. Aichhorn, E. Arrigoni, M. Potthoff, and W. Hanke. *Antiferromagnetic to superconducting phase transition in the hole- and electron-doped Hubbard model at zero temperature.* Phys. Rev. B **74** (2), 024508 (2006).

[373] D. Senechal, P.-L. Lavertu, M.-A. Marois, and A.-M. Tremblay. *Competition between Antiferromagnetism and Superconductivity in High-T c Cuprates.* Phys. Rev. Lett. **94**, 156404 (2005).

[374] M. Aichhorn, E. Arrigoni, M. Potthoff, and W. Hanke. *Phase separation and competition of superconductivity and magnetism in the two-dimensional Hubbard model: From strong to weak coupling.* Phys. Rev. B **76**, 224509 (2007).

[375] T. Yoshikawa and M. Ogata. *Role of frustration and dimensionality in the Hubbard model on the stacked square lattice: Variational cluster approach.* Phys. Rev. B **79** (144429), 1–7 (2009).

[376] H. Watanabe, T. Shirakawa, and S. Yunoki. *Microscopic Study of a Spin-Orbit-Induced Mott Insulator in Ir Oxides.* Phys. Rev. Lett. **105**, 216410 (2010).

[377] W. Koller and N. Dupuis. *Variational cluster perturbation theory for Bose Hubbard models.* J. Phys.: Condensed Matter **18** (41), 9525–9540 (2006).

[378] M. Balzer and M. Potthoff. *Variational cluster approach to ferromagnetism in infinite dimensions and in one-dimensional chains.* Phys. Rev. B **82**, 174441 (2010).

[379] W. Hanke, M. Aichhorn, E. Arrigoni, and M. Potthoff. *Correlated band structure and the ground-state phase diagram in high- cuprates.* Physica B: Condensed Matter **378-380** (0), 60 – 63 (2006). Proceedings of the International Conference on Strongly Correlated Electron Systems {SCES} 2005 Proceedings of the International Conference on Strongly Correlated Electron Systems.

[380] E. Arrigoni, M. Knap, and W. von der Linden. *Extended self-energy functional approach for strongly-correlated lattice bosons in the superfluid phase.* Phys. Rev. B **84** (1), 014535 (2011).

[381] M. Knap, E. Arrigoni, and W. von der Linden. *Variational cluster approach for strongly-correlated lattice bosons in the superfluid phase.* Phys. Rev. B **83** (13), 134507 (2011).

[382] M. Potthoff and M. Balzer. *Self-energy-functional theory for systems of interacting electrons with disorder.* Phys. Rev. B **75** (12), 125112 (2007).

[383] M. Knap, E. Arrigoni, and W. von der Linden. *Excitations in disordered bosonic optical lattices.* Phys. Rev. A **82** (5), 053628 (2010).

[384] M. Aichhorn, E. Arrigoni, M. Potthoff, and W. Hanke. *Variational cluster approach to the Hubbard model: Phase-separation tendency and finite-size effects.* Phys. Rev. B **74** (23), 235117 (2006).

[385] M. Balzer, B. Kyung, D. Senechal, A.-M. S. Tremblay, and M. Potthoff. *First-order Mott transition at zero temperature in two dimensions: Variational plaquette study.* EPL (Europhysics Letters) **85** (1), 17002 (2009).

[386] K. Fang, G. W. Fernando, and A. N. Kocharian. *Local electronic nematicity in the two-dimensional one-band Hubbard model.* Journal of Physics: Condensed Matter **25** (20), 205601 (2013).

[387] A. Yamada. *Magnetic phase diagram and Mott transition of the half-filled $\frac{1}{5}$-depleted Hubbard model with frustration.* Phys. Rev. B **90**, 245139 (2014).

[388] T. Schäfer, F. Geles, D. Rost, G. Rohringer, E. Arrigoni, K. Held, N. Blümer, M. Aichhorn, and A. Toschi. *Fate of the false Mott-Hubbard transition in two dimensions.* Phys. Rev. B **91**, 125109 (2015).

[389] S. Brehm, E. Arrigoni, M. Aichhorn, and W. Hanke. *Theory of two-particle excitations and the magnetic susceptibility in high-T c cuprate superconductors.* EPL (Europhysics Letters) **89** (2), 27005 (2010).

[390] E. Arrigoni, M. Aichhorn, M. Daghofer, and W. Hanke. *Phase diagram and single-particle spectrum of CuO 2 high- T c layers: variational cluster approach to the three-band Hubbard model.* New Journal of Physics **11** (5), 055066 (2009).

[391] T. Kaneko and Y. Ohta. *Excitonic phases in the two-orbital Hubbard model: Roles of Hund's rule coupling.* Journal of Physics: Conference Series **592** (1), 012096 (2015).

[392] P. Sahebsara and D. Sénéchal. *Antiferromagnetism and Superconductivity in Layered Organic Conductors: Variational Cluster Approach.* Phys. Rev. Lett. **97**, 257004 (2006).

[393] C.-C. Chen, M. van Veenendaal, T. P. Devereaux, and K. Wohlfeld. *Fractionalization, entanglement, and separation: Understanding the collective excitations in a spin-orbital chain.* Phys. Rev. B **91**, 165102 (2015).

[394] M. Knap, E. Arrigoni, and W. von der Linden. *Benchmarking the variational cluster approach by means of the one-dimensional Bose-Hubbard model.* Phys. Rev. B **81**, 235122 (2010).

[395] M. Knap, E. Arrigoni, and W. von der Linden. *Spectral properties of strongly correlated bosons in two-dimensional optical lattices.* Phys. Rev. B **81** (2), 024301 (2010).

[396] S. Ejima, H. Fehske, F. Gebhard, K. zu Münster, M. Knap, E. Arrigoni, and W. von der Linden. *Characterization of Mott-insulating and superfluid phases in the one-dimensional Bose-Hubbard model.* Phys. Rev. A **85**, 053644 (2012).

[397] K. Seki, R. Eder, and Y. Ohta. *BCS-BEC crossover in the extended Falicov-Kimball model: Variational cluster approach.* Phys. Rev. B **84**, 245106 (2011).

[398] S. Horiuchi, S. Kudo, T. Shirakawa, and Y. Ohta. *Antiferromagnetism versus Kondo screening in the two-dimensional periodic Anderson model at half filling: Variational cluster approach.* Phys. Rev. B **78**, 155128 (2008).

[399] S. Horiuchi, S. Kudo, T. Shirakawa, and Y. Ohta. *Antiferromagnetism and Kondo screening in the periodic anderson model: Variational cluster approach.* Journal of Physics: Conference Series **150** (4), 042060 (2009).

[400] M. Knap, E. Arrigoni, and W. V. D. Linden. *Spectral properties of coupled cavity arrays in one dimension.* Phys. Rev. B **81** (March), 1–16 (2010).

[401] M. Knap, E. Arrigoni, and W. von der Linden. *Quantum phase transition and excitations of the Tavis-Cummings lattice model.* Phys. Rev. B **82**, 045126 (2010).

[402] N. Ogawa, T. Kaneko, and Y. Ohta. *Dimensional crossover of the superfluid state in the attractive Hubbard model.* Journal of Physics: Conference Series **592** (1), 012103 (2015).

[403] K. Masuda and D. Yamamoto. *Variational cluster approach to s-wave pairing in heavy-fermion superconductors.* Phys. Rev. B **91**, 104508 (2015).

[404] X. Lu, L. Chioncel, and E. Arrigoni. *Time-reversal symmetry breaking phase in the Hubbard model: A variational cluster approach study.* Phys. Rev. B **85**, 125117 (2012).

[405] A. Yamada, K. Seki, R. Eder, and Y. Ohta. *Magnetic properties and Mott transition in the square-lattice Hubbard model with frustration.* Phys. Rev. B **88**, 075114 (2013).

[406] S. Goto, K. Masuda, and S. Kurihara. *Spontaneous loop-spin current with topological characters in the Hubbard model.* Phys. Rev. B **90**, 075102 (2014).

[407] M. Laubach, J. Reuther, R. Thomale, and S. Rachel. *Rashba spin-orbit coupling in the Kane-Mele-Hubbard model.* Phys. Rev. B **90**, 165136 (2014).

[408] S. Miyakoshi and Y. Ohta. *Coexistence of magnetic and topological phases in the asymmetric Kane-Mele-Hubbard model.* Journal of Physics: Conference Series **592** (1), 012129 (2015).

[409] A. Yamada. *Magnetic properties and Mott transition of the Hubbard model for weakly coupled chains on the anisotropic triangular lattice.* Phys. Rev. B **90**, 235138 (2014).

[410] A. Yamada. *Magnetic properties and Mott transition in the Hubbard model on the anisotropic triangular lattice.* Phys. Rev. B **89**, 195108 (2014).

[411] A. Yamada, K. Seki, R. Eder, and Y. Ohta. *Mott transition and ferrimagnetism in the Hubbard model on the anisotropic kagome lattice.* Phys. Rev. B **83**, 195127 (2011).

[412] S.-L. Yu and J.-X. Li. *Chiral superconducting phase and chiral spin-density-wave phase in a Hubbard model on the kagome lattice.* Phys. Rev. B **85**, 144402 (2012).

[413] S. Miyakoshi and Y. Ohta. *Antiferromagnetic topological insulator state in the correlated Bernevig-Hughes-Zhang model.* Phys. Rev. B **87**, 195133 (2013).

[414] X. Lu and E. Arrigoni. *Dispersive spectrum and orbital order of spinless p-band fermions in an optical lattice.* Phys. Rev. B **79**, 245109 (2009).

[415] M. Aichhorn, M. Hohenadler, C. Tahan, and P. B. Littlewood. *Quantum Fluctuations, Temperature, and Detuning Effects in Solid-Light Systems.* Phys. Rev. Lett. **100**, 216401 (2008).

[416] S.-L. Yu, X. C. Xie, and J.-X. Li. *Mott Physics and Topological Phase Transition in Correlated Dirac Fermions.* Phys. Rev. Lett. **107**, 010401 (2011).

[417] M. Hohenadler, M. Aichhorn, L. Pollet, and S. Schmidt. *Polariton Mott insulator with trapped ions or circuit QED.* Phys. Rev. A **85**, 013810 (2012).

[418] W. Brzezicki, M. Daghofer, and A. M. Oleś. *Mechanism of hole propagation in the orbital compass models.* Phys. Rev. B **89**, 024417 (2014).

[419] R. Eder, A. Dorneich, and H. Winter. *Single-particle spectra of charge-transfer insulators by cluster perturbation theory: The correlated band structure of NiO.* Phys. Rev. B **71**, 045105 (2005).

[420] R. Eder. *From cluster to solid: Variational cluster approximation applied to* NiO. Phys. Rev. B **76**, 241103 (2007).

[421] R. Eder. *Spin-state transition in $LaCoO_3$ by variational cluster approximation.* Phys. Rev. B **81**, 035101 (2010).

[422] L. Chioncel, H. Allmaier, E. Arrigoni, A. Yamasaki, M. Daghofer, M. I. Katsnelson, and A. I. Lichtenstein. *Half-metallic ferromagnetism and spin polarization in* CrO_2. Phys. Rev. B **75**, 140406 (2007).

[423] R. Eder. *Correlated band structure of NiO, CoO, and MnO by variational cluster approximation.* Phys. Rev. B **78**, 115111 (2008).

[424] H. Allmaier, L. Chioncel, and E. Arrigoni. *Titanium nitride: A correlated metal at the threshold of a Mott transition.* Phys. Rev. B **79**, 235126 (2009).

[425] H. Allmaier, L. Chioncel, E. Arrigoni, M. I. Katsnelson, and A. I. Lichtenstein. *Half-metallicity in NiMnSb: A variational cluster approach with ab initio parameters.* Phys. Rev. B **81**, 054422 (2010).

[426] L. Chioncel, I. Leonov, H. Allmaier, F. Beiuşeanu, E. Arrigoni, T. Jurcuţ, and W. Pötz. *Electronic correlations in short-period $(CrAs)_n/(GaAs)_n$ ferromagnetic heterostructures.* Phys. Rev. B **83**, 035307 (2011).

[427] C. Morari, H. Allmaier, F. Beiuşeanu, T. Jurcuţ, and L. Chioncel. *Electronic structure and magnetic properties of metallocene multiple-decker sandwich nanowires.* Phys. Rev. B **85**, 085413 (2012).

[428] N.-H. Tong. *Extended variational cluster approximation for correlated systems.* Phys. Rev. B **72** (11), 115104 (2005).

[429] S. Filor and T. Pruschke. *Variational cluster approximation to the thermodynamics of quantum spin systems.* New Journal of Physics **16** (6), 063059 (2014).

[430] M. Z. Asadzadeh, E. Arrigoni, and F. Michele. *Quench dyanamics in the transverse field Ising model: non-equilibirum cluster perturbation theory approach* (2015). To be published.

[431] M. Balzer and M. Potthoff. *Nonequilibrium cluster perturbation theory.* Phys. Rev. B **83**, 195132 (2011).

[432] M. Knap, E. Arrigoni, and W. von der Linden. *Vibration-mediated correlation effects in the transport properties of a benzene molecule.* Phys. Rev. B **88**, 054301 (2013).

[433] M. Sorantin. *Diploma Thesis: Theoretical investigations of vibronic effects on the steady state current through a molecular ring structure.* Graz University of Technology (2015).

[434] L. Keldysh. *Diagram technique for nonequilibirum processes.* Zh. Eksp. Teor. Fiz. **47**, 1515 (1965).

[435] J. Schwinger. *Brownian Motion of a Quantum Oscillator.* J.Math. Phys. **2**, 407 (1961).

[436] R. Feynman and F. V. Jr. *The theory of a general quantum system interacting with a linear dissipative system.* Ann. Phys. **24** (0), 118 – 173 (1963).

[437] H. Haug and A. Jauho. *Quantum Kinetics in Transport and Optics of Semiconductors.* Springer-Verlag GmbH, 2., corr. printing edition (1996). ISBN 3540616020.

[438] J. Rammer and H. Smith. *Quantum field-theoretical methods in transport theory of metals.* Rev. Mod. Phys. **58** (2), 323 (1986).

[439] L. P. Kadanoff and G. Baym. *Quantum Statistical Mechanics: Green's Function Methods in Equilibrium and Nonequilibrium Problems.* W.A. Benjamin, 1 edition (1962). ISBN B0007DKBI6.

[440] R. Kubo, T. Morikazu, and N. Hashitsume. *Statistical Physics II: Nonequilibrium Statistical Mechanics.* Springer, 2 edition (2003). ISBN 354053833X.

[441] A. Altland and B. D. Simons. *Condensed Matter Field Theory.* Cambridge University Press, 2 edition (2010). ISBN 0521769752X.

[442] J. Rammer. *Quantum Field Theory of Non-equilibrium States.* Cambridge University Press, reissue edition (2011). ISBN 0521188008.

[443] A. Kamenev. *Non-Equilibrium Systems.* Camebridge University Press (2013). ISBN 9780521760829.

[444] J. Viljas. *On the calculation of Green' s functions in nonequilibrium Fermi systems* (2008). Http://ltl.tkk.fi/ jviljas/.

[445] D. Ryndyk, R. Gutierrez, B. Song, and G. Cuniberti. *Green Function Techniques in the Treatment of Quantum Transport at the Molecular Scale.* In I. Burghardt, V. May, D. A. Micha, and E. R. Bittner (eds.), *Energy Transfer Dynamics in Biomaterial Systems*, volume 93 of *Springer Series in Chemical Physics*, 213–335. Springer Berlin Heidelberg (2009). ISBN 978-3-642-02305-7.

[446] T. Kita. *Introduction to Nonequilibrium Statistical Mechanics with Quantum Field Theory.* Progress of Theoretical Physics **123** (4), 581–658 (2010).

[447] A. Jauho. *Introduction to the Keldysh Nonequilibrium Green Function Technique* (2006). Http://nanohub.org/resources/1877.

[448] A. Kamenev. *Many-body theory of non-equilibrium systems* (2004). Cond-mat/0412296.

[449] R. van Leeuwen, N. E. Dahlen, G. Stefanucci, C.-O. Almbladh, and U. von Barth. *Introduction to the Keldysh Formalism.* In *Lect. Notes Physics 706.* Springer-Verlag Berlin Heidelberg (2006). Lecture notes.

[450] J. Keller and M. Jarrell. *The Non-Equilibrium Green Function Method* (2011). Lecture Notes.

[451] J. Jaklič and P. Prelovšek. *Lanczos method for the calculation of finite-temperature quantities in correlated systems.* Phys. Rev. B **49**, 5065–5068 (1994).

[452] M. Aichhorn, M. Daghofer, H. G. Evertz, and W. von der Linden. *Low-temperature Lanczos method for strongly correlated systems.* Phys. Rev. B **67**, 161103 (2003).

[453] P. Prelovsek and J. Bonca. *Ground State and Finite Temperature Lanczos Methods.* In A. Avella and F. Mancini (eds.), *Strongly Correlated Systems: Numerical Methods.* Springer Berlin Heidelberg (2013).

[454] H.-P. Breuer and F. Petruccione. *The Theory of Open Quantum Systems.* Oxford University Press (2002). ISBN 0198520638.

[455] C. Cohen-Tannoudji, J. Dupont-Roc, and G. Grynberg. *http://www.amazon.com/Atom-Photon-Interactions-Basic-Processes-Applications/dp/0471293369.* Wiley-VCH (1998). ISBN 0471293369.

[456] H. J. Carmichael. *Statistical Methods in Quantum Optics 1: Master Equations and Fokker-Planck Equations.* Springer (2010). ISBN 3642081339.

[457] G. Schaller. *Open Quantum Systems Far from Equilibrium.* Springer, Cham ; New York, auflage: 2014 edition (2014). ISBN 9783319038766.

[458] M. G. Zacher, R. Eder, E. Arrigoni, and W. Hanke. *Evolution of the stripe phase as a function of doping from a theoretical analysis of angle-resolved photoemission data.* Phys. Rev. B **65**, 045109 (2002).

[459] M. Jurow, A. E. Schuckman, J. D. Batteas, and C. M. Drain. *Porphyrins as molecular electronic components of functional devices.* Coordination Chemistry Reviews **254** (19-20), 2297 – 2310 (2010). Supramolecular approaches to nano and molecular electronics.

[460] A. Yella, H.-W. Lee, H. N. Tsao, C. Yi, A. K. Chandiran, M. Nazeeruddin, E. W.-G. Diau, C.-Y. Yeh, S. M. Zakeeruddin, and M. Grätzel. *Porphyrin-Sensitized Solar Cells with Cobalt (II/III)-Based Redox Electrolyte Exceed 12 Percent Efficiency.* Science **334** (6056), 629–634 (2011).

[461] R. Pariser and R. Parr. *A Semi-Empirical Theory of the Electronic Spectra and Electronic Structure of Complex Unsaturated Molecules. I.* Journal of Chemical Physics **21** (466), 767 (1953).

[462] J. A. Pople. *Electron interaction in unsaturated hydrocarbons.* Transactions of the Faraday Society **49**, 1375 (1953).

[463] D. A. Ryndyk, A. Donarini, M. Grifoni, and K. Richter. *Many-body localized molecular orbital approach to molecular transport.* Phys. Rev. B **88**, 085404 (2013).

[464] J. Merino and R. H. McKenzie. *Effective Hamiltonian for the electronic properties of the quasi-one-dimensional material* $Li_{0.9}Mo_6O_{17}$. Phys. Rev. B **85**, 235128 (2012).

[465] P. Jordan and E. Wigner. *Über das Paulische Äquivalenzverbot.* Zeitschrift für Physik **47** (9-10), 631–651 (1928).

[466] H. J. Carmichael. *An Open Systems Approach to Quantum Optics: Lectures Presented at the Universite Libre De Bruxelles October 28 to November 4, 1991 (Lecture Notes in Physics New Series M).* Springer-Verlag (1993). ISBN 0387566341.

[467] A. A. Dzhioev and D. S. Kosov. *Super-fermion representation of quantum kinetic equations for the electron transport problem.* J. Chem. Phys. **134**, 044121 (2011).

[468] M. Schmutz. *Real-time green's functions in many body problems.* Zeitschrift für Physik B Condensed Matter **30** (1), 97–106 (1978).

[469] U. Harbola and S. Mukamel. *Superoperator nonequilibrium Green's function theory of many-body systems; applications to charge transfer and transport in open junctions.* Physics Reports **465** (5), 191 – 222 (2008).

[470] T. Prosen. *Third quantization: a general method to solve master equations for quadratic open Fermi systems.* New Journal of Physics **10** (4), 043026 (2008).

[471] M. J. Zingl. *Diploma Thesis: Real-frequency impuritys sovler for dynamical mean-field theory based on cluster perturbation theory.* Graz University of Technology (2014).

[472] M. Granath and H. U. R. Strand. *Distributional exact diagonalization formalism for quantum impurity models.* Phys. Rev. B **86**, 115111 (2012).

[473] Y. Lu, M. Höppner, O. Gunnarsson, and M. W. Haverkort. *Efficient real-frequency solver for dynamical mean-field theory.* Phys. Rev. B **90**, 085102 (2014).

[474] D. Sénéchal. *Bath optimization in the cellular dynamical mean-field theory.* Phys. Rev. B **81**, 235125 (2010).